

**MISSISSIPPI
ACADEMY OF SCIENCES**



Supplemental Issue

30th Annual Southern Biomedical Engineering Conference

Digest of Papers

April 11-12, 2014

Beachfront Marriott,

Gulfport, MS

Major Sponsor

Mississippi Academy of Science

Journal of the Mississippi Academy of Sciences

Volume 59

April 2014

Supplemental Issue 1



Editor

Michelle Tucci
University of Mississippi Medical Center

Associate Editors

Hamed Benghuzzi
University of Mississippi Medical Center

Kenneth Butler
University of Mississippi Medical Center

Editorial Board

Gregorio Begonia
Jackson State University

Maria Begonia
Jackson State University

Ibrahim O. Farah
Jackson State University

Robin Rockhold
University of Mississippi Medical Center

Program Editors

Michelle Tucci
University of Mississippi Medical Center

Kenneth Butler
University of Mississippi Medical Center

The Journal of the Mississippi Academy of Sciences (ISSN 0076-9436) is published in January (annual meeting abstracts), April, July, and October, by the Mississippi Academy of Sciences. Members of the Academy receive the journal as part of their regular (nonstudent) membership. Inquiries regarding subscriptions, availability of back issues, and address changes should be addressed to The Mississippi Academy of Sciences, Post Office Box 55709, Jackson, MS 39296-5709, telephone 601-977-0627, or email msacademyofscience@comcast.net.

Contents

143 SOUTHERN BIOMEDICAL ENGINEERING CONFERENCE

147 KEYNOTE SPEAKER

148 OVERVIEW OF ANNUAL MEETING

PAPERS

158 Session I
170 Session II
196 Session III
217 Poster Session
306 Session IV
327 Session V
351 Session VI
371 Session VII
394 AUTHOR INDEX



30th Annual SOUTHERN BIOMEDICAL ENGINEERING CONFERENCE

April 11-12, 2014

.....
Program Co-Chairs

Hamed A. Benghuzzi, Ph.D.
Department of Health Sciences
University of Mississippi Medical Center
Jackson, MS 39216

Michelle A. Tucci, Ph.D.
Department of Orthopedics
University of Mississippi Medical Center
Jackson, MS 39216

Program Committee

Amol Janorkar, Ph.D.	Aaron Puckett, Ph.D.	Adel Mohamed, M.D.	Gerri Wilson, PhD,
Ibrahim Farah, Ph.D.	Ken Butler, Ph.D.	Jafar Vossoughi, Ph.D.	Mary Green
Joseph A. Cameron, Ph.D.	Lynne Jones, Ph.D.	Elgenaid Hamadain, Ph.D	Lisa McCammon

SBEC HISTORY

The Southern Biomedical Engineering Conference (SBEC) series was conceived by bioengineering professionals from academia and industry located primarily in the South of the United States in 1982. The first Southern Biomedical Engineering Conference was held at the LSU Medical Center, Shreveport, Louisiana, in 1982. Since then it has been held annually in different cities, mostly in the southern United States, and has grown to become a global event that regularly attracts attendees from all over the world. Submitted Papers are peer-reviewed, and those papers accepted for presentation and publication appear in the yearly issue of SBEC proceedings.

The SBEC serves a special purpose by emphasizing participation from young professionals and advanced students. Since established investigators present papers in the same sessions with the students, it encourages a high level of professionalism as a standard for young investigators and students. Submission of papers from individuals from around the world is encouraged. However, if their papers are accepted, an author or co-author must attend the conference to present their work and to interact with other attendees. In keeping with the emphasis on student participation, the SBEC presents best paper and presentation awards to undergraduate, graduate, and professional students.

Conference Information

The format of the conference is to have a single session, with each presentation limited to 15 minutes (12-minute presentation and three minute discussions). Room assignments for each session will be posted at the conference.

The Conference will be held at the **Courtyard by Marriott Gulfport Beachfront** which is located approximately 75 miles east of New Orleans, LA on interstate 10, and 65 miles from Mobile International Airport. SBEC participants can make reservations by calling the hotel directly at 1-228-864-4310. Please indicate that you are attending the SBEC to receive the discounted rate. The hotel is easily accessible from I-10 East and West, Exit at Gulfport Interstate 49 South toward interstate 90. Take a left on interstate 90 and it is approximately 0.5 miles on the left hand side.

Registration and Fees

Initial on-site registration will be held from 5:00 –8:00 p.m., Thursday, April 10, 2014.

Participants may register anytime afterwards. Participants are encouraged to preregister by returning the registration post-marked by March 30, 2014 to take advantage of the reduced registration rates.

Fees before April 4, 2014

Students: \$175
Faculty/Staff: \$250

Fees after April 4, 2014

Students: \$200
Faculty/Staff: \$325

Session Chairs

Session I (Neuroengineering)

Session Chair: Ramesh Patel Co-Chair: Ibrahim Farah

Session II (Tissue Engineering)

Session Chair: LaShan Simpson Co-Chair: Stacy Vance

Session III (Drug Delivery)

Session Chair: Ken Butler Co-Chair: Felix Adah

Poster Session

**Session Co-Chairs: Ham Benghuzzi, Michelle Tucci, Joseph A. Cameron, Mary Green,
Zelma Cason and Ken Heard**

Session IV (Imaging/Data Management)

Session Chair: Tom Rich Co-Chair: Felicia Tardy

Session V (CVD/Health Care)

Session Chair: Subrata Suha Co-Chair: Jafar Vossoughi

Session VI (Trauma Bone and Cartilage)

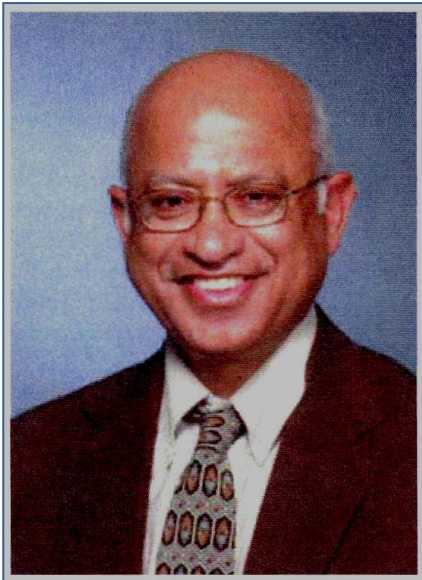
Session Chair: Amol Janorkar Co-Chair: Renee Wilkins

Session VII (Modeling)

Session Chair: Elgenaid Hamadain Co-Chair: Aaron Puckett

Session VIII (Cancer)

Session Chair: Pradip Biswas Co-Chair: LaToya Moore



2014 Keynote Speaker

March 12, 2014

Ethical Challenges in Biomedical Research

Given by

Subrata Saha, Ph.D.

Editor-in-Chief, Journal of Long Term Effects of Medical Implants; Ethics in Biology; Engineering & Medicine
Director, Biomedical Engineering Program, School of Graduate Studies
Research Professor and Director of Musculoskeletal Research. Department of Orthopaedic Surgery and Rehabilitation Medicine.
Professor, Dept. Physiology & Pharmacology
SUNY Downstate Medical Center

Dr. Subrata Saha is the Director of Musculoskeletal Research and Research Professor in the Department of Orthopaedic Surgery & Rehabilitation Medicine at SUNY Downstate Medical Center in Brooklyn, New York. Dr. Saha received a BS in Civil Engineering from Calcutta University in 1963, an MS in Engineering Mechanics from Tennessee Technological University in 1969, and Engineering and PhD degrees in Applied Mechanics from Stanford University in 1972 and 1974, respectively. He has been a faculty member at Yale University, Louisiana State University Medical Center, Loma Linda University, Clemson University, and Alfred University. Dr. Saha has received many awards from professional societies, including Orthopedic Implant Award, Dr. C. P. Sharma Award, Researcher of the Year Award, C. William Hall Research Award in Biomedical Engineering, Award for Faculty Excellence, Research Career Development Award from NIH, and Engineering Achievement Award. He is a Fellow of the Biomedical Engineering Society (BMES), The American Society of Mechanical Engineers (ASME), and the American Institute for Medical and Biological Engineering (AIMBE). He currently chairs the Bioethics Committee of the International Federation of Medical and Biological Engineering (IFMBE) and the Development Committee of Sigma Xi, and is Co-Chair of the International Committee of AIMBE. He is the immediate past chair of the Ethics Committee of the American Association of Dental Research (AADR).

He has received numerous research grants from federal agencies (NIH and NSF), foundations, and industry. Dr. Saha is the founder of the Southern Biomedical Engineering Conference Series, and he also started the International Conference on Ethical Issues in Biomedical Engineering. Dr. Saha has published over 118 papers in journals, 45 book chapters and edited volumes, 382 papers in conference proceedings, and 151 abstracts. His research interests are bone mechanics, biomaterials, orthopedic and dental implants, drug delivery systems, rehabilitation engineering, and bioethics.

Abstract:

During the last fifty years, the field of biomedical engineering has been largely responsible for the dramatic advances in modern medicine. These include advanced therapeutic and diagnostic techniques (e.g., total joint replacements, heart-lung machines, artificial heart, computed tomography and magnetic resonance imaging) and that in turn has significantly improved the life span and quality of life of our patients. However, biomedical technology has also contributed to new ethical dilemmas and has challenged some of our moral values. Some of the areas that have shown immense promise but also raised public concern are Nanobiotechnology, stem cell research, cloning, genetic engineering and synthetic biology. Other topics that also often face ethical scrutiny are animal research, clinical trials and conflicts-of-interest. A discussion of ethical issues associated with these topics will be presented.



OVERVIEW OF PROGRAM

Thursday April 10, 2014

5:00-8:00 Registration and Reception

Hotel Lobby

Friday April 11, 2014

8:00 AM-4:00 PM Registration

8:30-8:35 AM Opening of the Meeting
Dr. Ham Benghuzzi, Program Chair

April 11, 2014 Scientific Sessions

Friday Morning	Talk #	Conference Room
Time		Session I: Neuroengineering Session Chair: Ramesh Patel Co-Chair: Ibrahim Farah
8:35	1	Resetting of the Epileptic Brain by Seizures Dr. Leonidas Iasemidis, Louisiana Tech
9:00	2	WEARABLE EEG SYSTEM FOR DROWSINESS DETECTION Jenny Wang, Janet Spoonamore, Cliff Wang NC School of Science and Math, 1219 Broad St, Durham, NC 27705 NC State University, Raleigh, NC 27695
9:15	3	THE ROLE OF THE HYOID apparatuses OF WOODPECKERS FOR ENERGY dissipation Nayeon Lee ^{a,c} , R. Prabhu ^{a,c} , Lakiesha N. Williams ^{a,c} , M.F. Horstemeyer ^{b,c} a Department of Agricultural and Biological Engineering, Mississippi State University, Mississippi State, MS 39762-9632, USA b Department of Mechanical Engineering, Mississippi State University, Mississippi State, MS 39762-9552, USA c Center for Advanced Vehicular Systems, Mississippi State University, Mississippi State, MS 39762-5405, USA
9:30	4	Tracking of hMSCs Preconditioned with 0.5% O ₂ in Association with Stroke Utilizing 1H and ²³ Na MRI at 21.1 T Jens T. Rosenberg ^{1,2} , Avigdor Leftin ³ , Fabian Calixto Bejarano ¹ , Michael M. Davidson ^{1,4} , Michelle Baird ¹ , Lucio Frydman ^{1,3} , Teng Ma ² And Samuel C. Grant ^{1,2} ¹ The National High Magnetic Field Laboratory, ² Chemical And Biomedical Engineering, Famu-Fsu College Of Engineering, And ³ Department Of Biological Science, The Florida State University, ⁴ Department Of Chemical Physics, Weizmann Institute Of Science
9:45	5	PLATELET-RICH PLASMA EFFECTS ON DEGENERATIVE DISC DISEASE: ANALYSIS OF HISTOLOGY AND IMAGING IN AN ANIMAL MODEL. Tucci, MA ¹ , Gullung, GB ¹ , Woodall, JW ¹ , James, JR ² , Black DA ¹ , McGuire, RA ¹ ¹ Orthopedic Surgery and Rehab and ² Department of Radiology, University of Mississippi Medical Center, Jackson, MS
10:00		BREAK

Friday Morning	Talk #	Conference Room
Time		Session II (Tissue Engineering) Session Chair: LaShan Simpson Co-Chair: Stacy Vance
10:15	6	TREATMENT OF VASCULAR CALCIFICATION BY ELASTIN-TARGETED NANOPARTICLES Kevin A. Bennett, C. LaShan Simpson. Mississippi State, MS 39762
10:30	7	ENDOTHELIALIZED IN VITRO TUBULAR SILICONE SCAFFOLDS Marzieh K Atigh ¹ , Kristen Smith ² , Saami K. Yazdani ³ ¹ Department of Mechanical Engineering, University of South Alabama, Mobile, Alabama. ² Spanish Fort High School, Spanish Fort, Alabama ³ Department of Mechanical Engineering, University of South Alabama, Mobile, Alabama
10:45	8	SYNTHESIS AND CHARACTERIZATION OF AN ELASTIN-LIKE-POLYPEPTIDE-POLYARGININE CONJUGATE FOR THREE-DIMENSIONAL CELL CULTURE C. Andrew Weeks and Amol V. Janorkar* Department of Biomedical Materials Science, School of Dentistry, University of Mississippi Medical Center, Jackson, MS 39216
11:00	9	THE CORRELATION BETWEEN NEOVASCULARIZATION AND MACROPHAGE POPULATIONS UNDER THE INFLUENCE OF ANDROGENS Kenneth R. Butler, PhD, Hamed A. Benghuzzi, PhD, Michelle Tucci, PhD, Aaron D. Puckett, PhD University of Mississippi Medical Center, Jackson, Mississippi—USA
11:15	10	INTERCELLULAR SIGNALING BY CYCLIC AMP-CONTAINING MICROPARTICLES. Scruggs AK ¹ , Sayner SL ² , Bauer N ¹ , and Rich TC ¹ . ¹ Departments of Pharmacology, ² Cell Biology and Neuroscience, and the ^{1,2} Center for Lung Biology, Colleges of Medicine and Engineering, University of South Alabama, Mobile AL 36688.
11:30	11	QUANTITATIVE EVALUATION OF FRET-BASED cAMP MEASUREMENTS Kristal J. Webb ¹ , Silas J. Leavesley ^{2,3} , Thomas C. Rich ^{1,3} ¹ Center for Lung Biology and Departments of ² Chemical Engineering and ³ Pharmacology Colleges of Medicine and Engineering, University of South Alabama, Mobile, Alabama, 36688

12:00- 1:00 Visit the Poster Area

Friday Afternoon	Talk #	Conference Room
Time		Session III (Drug Delivery) Session Chair: Ken Butler Co-Chair: Felix Adah
1:00	12	ANDROGEN ADMINISTRATION AND FIBROBLAST BEHAVIOR IN THE TISSUE-IMPLANT RESPONSE Kenneth R. Butler, PhD, Hamed A. Benghuzzi, PhD, Michelle Tucci, PhD, Aaron D. Puckett, PhD University of Mississippi Medical Center Jackson, Mississippi—USA
1:15	13	ELASTIN LIKE POLYPEPTIDE-COLLAGEN COMPOSITE HYDROGELS FOR DRUG DELIVERY APPLICATIONS Shruti S. Amruthwar and Amol V. Janorkar* Department of Biomedical Materials Science, School of Dentistry, University of Mississippi Medical Center, 2500 N. State Street, Jackson, MS 39216
1:30	14	KERATIN AS A NOVEL DRUG CARRIER FOR DRUG COATED BALLOONS Emily Turner ¹ , Seth Tomblyn ² , Luke Burnett ² , Saami K. Yazdani ¹ ¹ Mechanical Engineering, University of South Alabama

		² KeraNetics, Winston-Salem, NC 27101
1:45	15	SUSTAINED DELIVERY OF MANNOSE 6 PHOSPHATE FOR TENDON HEALING Michelle Tucci, David Black, Gerri Wilson, and Ham Benghuzzi, University of Mississippi Medical Center, Jackson, MS 39216
2:00	16	THE USE OF ANTIOXIDANT LOADED TCP DEVICES TO SUPPRESS THE METABOLIC ACTIVITY OF SK-OV-3 OVARIAN CANCER LIKE CELLS Jennifer L. Harpole, PhD, Michelle Tucci, PhD, Hamed Benghuzzi, PhD University of Mississippi Medical Center, Jackson, MS 39216
2:15	17	MARKOV CHAIN BASED PREDICTIVE (BCI) SPELLER Jenny Wang, Janet Spoonamore, Cliff Wang NC School of Science and Math, 1219 Broad St, Durham, NC 27705 NC State University, Raleigh, NC 27695
2:30		break

April 11, 2014
3:00-5:00 PM Poster Session

Scientific Sessions-Poster Session

Presenter and Title	P#
Session Co-Chairs: Ham Benghuzzi, Michelle Tucci, Joseph A. Cameron, Mary Green, Zelma Cason and Ken Heard THE EFFECTS OF THYMOQUINONE AND GREEN TEA EXTRACT ON LDL MODIFICATION IN HUMAN AORTIC ENDOTHELIAL CELLS Felicia M. Tardy ¹ , Hamed Benghuzzi ¹ , and Michelle Tucci ² ¹ School of Health Related Professions and ² Department of Orthopedic Surgery University of Mississippi Medical Center, Jackson, MS 39216	1
IDENTIFICATION OF EPILEPTIC BRAIN STATES ON THE BASIS OF MATCHING PURSUIT DECOMPOSITION OF EEG Rui Liu ¹ , Ioannis Vlachos ¹ , Joshua Adkinson ¹ , Leonidas Iasemidis ^{1,2} ¹ Louisiana Tech University, Biomedical Engineering, Ruston, LA ² Louisiana State University Medical School, Shreveport, LA	2
MORPHOLOGICAL EVALUATION OF KIDNEY CELLS FOLLOWING CYCLORSPORINE ADMINISTRATION Stacy Hull Vance, Michelle Tucci and Hamed Benghuzzi Clinical Health Sciences Graduate Program, School of Health Related Professions, University of Mississippi Medical Center, Jackson, Mississippi, USA	3
EPILEPTIC FOCUS CONNECTIVITY PATTERNS DURING SEIZURES IN TEMPORAL LOBE EPILEPSY Joshua Adkinson, Rui Liu, Ioannis Vlachos, Leonidas Iasemidis Louisiana Tech University Biomedical Engineering, Ruston, LA	4
STUDY OF EPILEPTIC SEIZURE SUSCEPTIBILITY BY SPECTRAL ANALYSIS OF THE EEG Ankit, Yiannis, Iasemidis, Rui Lui, Joshua Adkinson ¹ Louisiana Tech University, Biomedical Engineering, Ruston, LA ² Louisiana State University Medical School, Shreveport, LA	5
QUANTITATIVE EEG ANALYSIS FOR DIFFERENTIATION OF SLEEP DISORDERS Sai Mohan Rudarshetty, Ashmit Pyakurel, Rui Lui, Bharath Red Karamuri, Leon D Iasemidis, Ioannis Vlachos ¹ Louisiana Tech University, Biomedical Engineering, Ruston, LA ² Louisiana State University Medical School, Shreveport, LA	6
INFLAMMATORY RESPONSE TO TRAUMA: A PROSPECTIVE CLINICAL STUDY Arun Aneja M.D., Ph.D., Edward Yang B.S., Lusha Xiang M.D., Boshen Liu B.S., Peter Mittwede B.S., Clark Walker M.D., Robert Hester Ph.D., George Russell M.D. University of Mississippi Medical Center , Jackson, MS	7
MORPHOLOGICAL EFFECTS OF GENISTEIN, THYMOQUINONE, 5-FU, AND LASER THERAPY ON LARYNGEAL CARCINOMA CELLS Osasu Adah, Gerri Wilson, Felix Adah, Michelle Tucci, and Hamed Benghuzzi Departments of Orthopaedic Surgery and Rehabilitation and Clinical Health Sciences University of Mississippi Medical Center, Jackson, Mississippi	8
MORPHOLOGICAL EVALUATION OF A549 CELLS FOLLOWING THE EXPOSURE TO OMEGA FATTY ACIDS IN CULTURE Jana Bagwell, Michelle Tucci, Ham Benghuzzi University of Mississippi Medical Center, Jackson, MS 39216	9

IMPACT OF HEARING AID USE IN INDIVIDUALS WITH UNILATERAL SENSORY HEARING IMPAIRMENTS Charles E. Bishop, Au.D. and Elgenaid Hamadain, Ph.D. University of Mississippi Medical Center ,Jackson, MS 39216	10
PREDICTING OVERALL SURVIVAL IN PATIENTS WITH METASTATIC MELANOMA ON ANTI-ANGIOGENIC THERAPY AND RECIST STABLE DISEASE ON INITIAL POST-THERAPY IMAGES USING CT TEXTURE ANALYSIS - A SECONDARY ANALYSIS OF A PHASE II PROSPECTIVE CLINICAL TRIAL Mark Gray, Andrew Smith, Xu Zhang, Haowei Zhang, Sara Martin del Campo, Elgenaid Hamadain, William Carson University of Mississippi Medical Center	11
DIFFERENTIAL BIOTHERAPEUTIC ADVANTAGES OF HONEY IN TARGETING THE WARBURG EFFECT AND SURVIVAL OF MRC-5 AND A549 CELL LINES Ibrahim O. Farah Department of Biology, Jackson State University, Jackson, MS 39217, USA	12
NOVEL APPLICATION FOR MONITORING COMPLIANCE WITH HAND HYGIENE AND ISOLATION ATTIRE AT A UNIVERSITY HOSPITAL Elham Ghonim, and Hamed Benghuzzi University of Mississippi Medical Center, Jackson, MS 39216	13
THE EFFECT OF TRANSCUTANEOUS ELECTRICAL NERVE STIMULATION AT ACUPUNCTURE POINTS ON SPINAL MOTOR NEURON EXCITABILITY IN PEOPLE WITHOUT KNOWN NEUROMUSCULAR DISEASES Min Huang ¹ , Howe Liu ¹ , Jian-Wei Gu ² , Ham Benghuzzi ¹ , Xuexiang Wang ² , Antonio V Hayes ³ , Rebecca H. Pearson ¹ , Felix Adah ¹ , and Dobrivoje S Stokic ² . ³ Neurophysiological Research Laboratories, The Methodist Rehabilitation Center, Jackson; ² Department of Physiology, and ¹ Department of Physical Therapy, University of Mississippi Medical Center, Jackson, MS	14
THE EFFECT OF MANNOSE 6 PHOSPHATE IN REDUCING TRANSFORMING GROWTH FACTOR PROLIFERATION OF MCCOY FIBROBLAST CELLS Gerri Wilson, David Black, Michelle Tucci, and Hamed Benghuzzi University of Mississippi Medical Center, Jackson, MS 39216	15
MORPHOLOGICAL CHANGES TO LNCAP CELLS SUBJECTED TO TREATMENT WITH EPIGALLOCATECHIN-3-GALLATE, THYMOQUINONE, AND TANNIC ACID La'Toya Richards Moore*, PhD MLS (ASCP) ^{CM} , Hamed Benghuzzi, PhD Michelle Tucci, PhD, Elgenaid Hamadain, PhD University of Mississippi Medical Center, Jackson, MS 39216	16
PLATELET-RICH PLASMA EFFECTS ON HEALING TISSUE INTERFACES: HISTOLOGICAL ANALYSIS IN A SPINAL DECOMPRESSION MODEL James Woodall MD, PhD; Michelle Tucci PhD; Robert McGuire MD University of Mississippi Medical Center, Jackson, MS 39216	17
USE OF TCPL CERAMIC IMPLANTS TO DELIVER ESTROGEN IN OSTEOPOROTIC FEMALE RATS Jill White, Gerri Wilson, Zelma Cason, Hamed Benghuzzi, and Michelle Tucci University of Mississippi Medical Center, Jackson, MS 39216	18
SPHEROID ORGANIZATION AND ADIPOGENESIS ON COPOLYMERS OF ELASTIN-LIKE POLYPEPTIDES Paul A. Turner and Amol V. Janorkar* Department of Biomedical Materials Science, School of Dentistry, University of Mississippi Medical Center, , Jackson, MS 39216	19
THE EFFECTS OF SUSTAINED DELIVERY OF ANTIOXIDANTS ON LPS STIMULATED RAW 264.7 MACROPHAGES Renee Wilkins, Michelle Tucci, Ham Benghuzzi University of Mississippi Medical Center, Jackson, MS 39216	20
THE USE OF ANTIOXIDANT TO SUPPRESS THE METABOLIC ACTIVITY OF SK-OV-3 OVARIAN CANCER LIKE CELLS Jennifer L. Harpole, PhD, Michelle Tucci, PhD, Hamed Benghuzzi, PhD University of Mississippi Medical Center, Jackson, MS 39216	21
EVALUATING EFFECTIVENESS OF LABORATORY TRAINING OF CYTOTECHNOLOGY STUDENTS USING TURNINGPOINT, A PRODUCT OFFERING OF TURNING TECHNOLOGIES, INC. Ken Heard, Zelma Cason, Ron Landreth, Hamed Benghuzzi University of Mississippi Medical Center, Jackson, MS 39216	22
THE EFFECTS OF SUSTAINED DELIVERY OF ESTROGEN ON THE GLOMERULI PATHOLOGY Zelma Cason, Michelle Tucci, Hamed Benghuzzi University of Mississippi Medical Center, Jackson, MS 39216	23



MORPHOLOGICAL CHANGES TO LNCAP CELLS SUBJECTED TO TREATMENT WITH EPIGALLOCATECHIN-3-GALLATE, THYMOQUINONE, AND TANNIC ACID La'Toya Richards Moore*, PhD; MLS (ASCP) ^{CM} , Hamed Benghuzzi, PhD; FBSE; FAIMBE, Michelle Tucci, PhD, Elgenaid Hamadain, PhD University of Mississippi Medical Center Jackson, MS 39216	24
FROM EMERGENCY DEPARTMENT TO PRIMARY CARE: CONTINUITY OF CARE Linda M. Watkins MSN, RN, FNP-C and Elgenaid Hamadain, PhD University of Mississippi Medical Center Jackson, MS 39216	25
STATISTICAL DECISION MAKING ON HOW TO SELECT THE BEST STATISTICAL TECHNIQUE Elgenaid Hamadain, Ph.D. Department of Diagnostics and Clinical Health Sciences University of Mississippi Medical Center, Jackson, MS 39216	26
INDUCTION OF INTERLEUKIN-6 UPON THE SUSTAINED DELIVERY OF DANAZOL USING ADULT RATS AS A MODEL Hamed Benghuzzi*, Michelle Tucci, Adel Mohamed, and Joseph A. Cameron** University of Mississippi Medical Center, Jackson, MS 39216, and ** Jackson State University, Jackson, MS 39216	27
ASSESSING THE MORPHOLOGY OF HUMAN GINGIVAL FIBROBLASTS UPON EXPOSURE TO DENTAL ADHESIVES IN THE PRESENCE OF <i>PORPHYROMONAS GINGIVALIS</i> LIPOPOLYSACCHARIDE Angelia D. Garner, Michelle A. Tucci, Hamed A. Benghuzzi University of Mississippi Medical Center, Jackson, MS 39216, and ** Jackson State University, Jackson, MS 39216	28
DESIGN AND OPTIMIZATION OF A HIGH POWERED HYPERSPECTRAL ILLUMINATION SOURCE FOR PRE-CLINICAL AND CLINICAL IMAGING Arslan Arshad ¹ , Thomas Rich ^{2,3} , and Silas Leavesley ^{1,3} ¹ Chemical and Biomolecular Engineering, University of South Alabama, ² Center for Lung Biology, University of South Alabama, ³ Pharmacology, University of South Alabama	29

End of Friday's Sessions

April 12, 2014
Scientific Sessions

Saturday Morning	Talk #	Conference Room
Time		Session IV (Imaging/Data Management) Session Chair: Tom Rich Co-Chair: Felicia Tardy
8:30	18	AN EXCITATION-SCANNING HYPERSPECTRAL MICROSCOPE FOR BIOMEDICAL IMAGING OF GFP IN HIGHLY AUTOFLUORESCENT LUNG TISSUE Peter Favreau ^{1,2} , Thomas Rich ^{2,3} , Ashley Stringfellow ² , Diego Alvarez ^{2,4} , Prashant Prabhat ⁵ , Silas Leavesley ^{1,3} ¹ Chemical and Biomolecular Engineering, University of South Alabama, ² Center for Lung Biology, University of South Alabama, ³ Pharmacology, University of South Alabama, ⁴ Internal Medicine, University of South Alabama, ⁵ Semrock, Inc., A Unit of IDEX Corp.
8:45	19	HYPERSPECTRAL FRET IMAGING AND ANALYSIS APPROACHES TO DETERMINE cAMP COMPARTMENTALIZATION IN PMVECs Naga S. Annamdevula ¹ , Andrea Britain ² , Thomas C. Rich ^{2,3} , Silas J. Leavesley ^{1,2} ¹ Department of Chemical and Biomolecular Engineering, ² Department of Pharmacology, ³ Center for Lung Biology, University of South Alabama, Mobile, AL, 36688
9:00	20	Transverse Relaxations of Selectively Excited Metabolites in Stroke at 21.1 T Jens T Rosenberg ^{1,3} , Noam Shemesh ² , Jean-Nicolas Dumez ² , Lucio Frydman ^{1,2} and Samuel C. Grant ^{1,3} ¹ National High Magnetic Field Laboratory, The Florida State University, ² Chemical Physics, Weizmann Institute of Science, ³ Chemical & Biomedical Engineering, FAMU-FSU College of Engineering, The Florida State University

3:00	38	DEVELOPMENT OF A THREE-DIMENSIONAL DIGITAL IMAGE CORRELATION FOR DISPLACEMENT AND STRAIN MEASUREMENT OF SEEDED ENDOTHELIAL CELLS Emily Gould, Nicholas Carroll, Dr. Gail D. Jefferson, and Dr. Saami K. Yazdani Department of Mechanical Engineering, 150 Jaguar Drive, Shelby Hall, Mobile, AL 36688
3:15	39	DEVELOPMENT OF SILICONE CORONARY BIFURCATION MODELS FOR <i>IN VITRO</i> FLOW EVALUATION Alex Parks, Saami K. Yazdani Department Of Mechanical Engineering University Of South Alabama
3:30	40	HIGHLY SENSITIVE CONTINUOUS FLOW MICROFLUIDIC CHIP SENSOR WITH INTEGRATED BI/SB THERMOPILE FOR BIOCHEMICAL APPLICATIONS Varun Kopparthy ^{1,2} , Joshna Nimmala ^{1,2} , Eric. J. Guilbeau ^{1,2} ¹ Center for Biomedical Engineering and Rehabilitation Science, ² Institute for Micromanufacturing, Louisiana Tech University, Ruston, LA, 71272
4:00		BREAK

Saturday Afternoon	Talk #	Conference Room
Time		Session VIII (Cancer) Session Chair: Pradip Biswas Co-Chair: LaToya Moore
4:15	41	MULTIFUNCTIONAL NANOPLATFORMS FOR TARGETED MDRB AND CANCER THERANOSTIC APPLICATIONS Paresh Chandra Ray Department of Chemistry, Jackson State University, Jackson, MS, USA
4:30	42	PROBING G-PROTEIN COUPLED RECEPTOR CONFORMATIONAL DYNAMICS USING HUMAN COMPUTER INTERFACES Dr. Rajendram Rajnarayanan University of Buffalo
4:45	43	THE ROLE OF RESVERATROL IN PREVENTION AND THERAPY OF HORMONE-DEPENDENT CANCERS: IN SILICO STUDIES Chakraborty S ¹ , Zhang L ² , Lin SY ² , Rimando AM ³ , Biswas PK ¹ and Levenson AS ^{2*} ¹ Laboratory of Computational Biophysics & Bioengineering, Depart of Physics, Tougaloo College, Tougaloo, MS ² Cancer Institute and Department of Pathology, University of Mississippi Medical Center, Jackson, MS ³ United States Department of Agriculture, Agricultural Research Service, Natural Products Utilization Research Unit, University, MS
5:00	44	INHIBITION OF CYTOMEGALOVIRUS INFECTION AND PHOTOTHERMAL LYSIS OF INFECTED CELLS USING BIOCONJUGATED GOLD NANOPARTICLES Bernadette M. DeRussy ¹ , Madeline A. Aylward ¹ , Zhen Fan ² , Paresh C. Ray ² and Ritesh Tandon ^{1*} ¹ Department of Microbiology, University of Mississippi Medical Center, 2500 North State Street, Jackson, MS 39216, USA. ² Department of Chemistry and Biochemistry, Jackson State University, 1400 J.R Lynch Street, Jackson, MS 39217, USA.
5:15	45	HORMONE-INDEPENDENT DRUG DESIGNING FOR BREAST CANCERS TARGETING RECEPTOR DIMERIZATION INTERFACE Pradip K Biswas ¹ , Rajendram Rajnarayanan ² , Sandipan Chakraborty ¹ , and Nicholas Rader ¹ ¹ Laboratory of Computational Biophysics & Bioengineering Department of Physics, Tougaloo College, Tougaloo MS 39174 ² Department of Pharmacology and Toxicology, University of Buffalo, Buffalo, NY 14260



5:30- 6:30 PM FREE TIME

6:30-8:30 PM Banquet and Key Note Speaker and Student Awards

NOTE PAGE

NOTE PAGE

WEARABLE EEG SYSTEM FOR DROWSINESS DETECTION

Jenny Wang, Janet Spoonamore, Cliff Wang

NC School of Science and Math, 1219 Broad St, Durham, NC 27705

NC State University, Raleigh, NC 27695

ABSTRACT

Each year a high percentage of accidents are caused by drowsy drivers. We propose using Electroencephalography (EEG) signal to detect driver fatigue and alert drivers of potential drowsiness. EEG data sets of both alert and drowsy state were captured. The raw EEG data was transformed to frequency domain and band filtered into eight distinct frequency bands, from Delta to high Gamma band. Nonlinear Energy Operator was used to identify power spikes in each band. We studied and compared the spectrum power patterns of each band, between alert and drowsy state. Experiment results have shown that certain EEG band spectrum power spikes are reliable bio-indicators for detecting common fatigue phenomena, such as eye blinking, eye closing, and yawning. Based on this observation, we developed the fatigue detection algorithm and a corresponding Smartphone App for drowsy detection.

Keywords: EEG Signal processing, Drowsy Detection, Power Spike Detection

INTRODUCTION

Every year, a high percentage of traffic accidents are caused by drowsy drivers. The National Highway Traffic Safety Administration estimates that 100,000 police-reported crashes are the direct result of driver fatigue each year, resulting in an estimated 1,550 deaths, 71,000 injuries, and \$12.5 billion in monetary losses [1]. Previous efforts include lane deviation measurements or eye tracking, but these approaches can be highly subjective [2]. This project studies the measurable differences in EEG power output between the alert and drowsy states and identifies EEG power signatures for drowsiness detection.

METHODS

A. EEG Data Collections

A low cost single channel dry EEG system, a headset with a sensor band on the forehead and a clip on the ear lobe, was used to capture EEG signal under non-clinical settings [3, 4]. The EEG headset was linked to a PC via Bluetooth to record the EEG data. EEG data was recorded for 90 to 120 seconds in 4 scenarios: (1) a concentrated fully alert state; (2) blinking in drowsy state; (3) eye closing in drowsy state; and (4) yawning in drowsy state. The alert state data was captured when the subjects were solving a math problem. This data set is the baseline for the study. The drowsy state data was recorded late at night when the subjects showed visible signs of drowsiness.

B. EEG Signal Processing and Analysis

Due to the complexity of raw EEG signals, it is difficult to analyze and compare sets of raw EEG signals directly [5]. This study focuses on the frequency domain analysis of EEG signals and examines EEG spectrum power changes in response to the onset of fatigue indicators. EEG data in this study was digitized at a sampling rate of 512Hz, converted to frequency domain via FFT and split into eight frequency bands (Delta, Theta, low Alpha, high Alpha, low Beta, high Beta, low Gamma, and high Gamma). The power output in each band, which corresponds to different neurological activities [6], was calculated every second and analyzed to identify a correlation between spectrum power changes and the onset of fatigue events such as eye closing.

C. Power Spike Analysis

To uniquely identify the onset of drowsy indicators, two approaches were adopted to identify EEG signal power spikes.

- 1) Absolute Value Threshold: a threshold value of 3x the mean baseline power is applied to the EEG power data to identify peaks.
- 2) Nonlinear Energy Operator (NEO): NEO was derived from the idea of tracking the energy of a linear oscillator with both kinetic and potential energy, and was used to detect spikes in captured EEG signals in the time domain [7-9]. We use NEO method to detect peaks in EEG signal power level.

For a discrete signal $x(n)$, such that $n \in 0,1,2 \dots N$, the NEO operator is defined as:

$$\psi[x(n)] = x^2(n) - x(n+1)x(n-1) \quad . \quad (\text{eq.1})$$

And the threshold used in the NEO method is defined as:

$$Tr = c \frac{1}{N} \sum_{n=1}^N \psi_s[x(n)] \quad (\text{eq.2})$$

Where N is the number of samples and c is a scaling factor.

The two metrics were used to quantify the strength of EEG signal response:

1) Response Strength:

The ratio between the mean peak power and mean alert state power (the baseline) is calculated. This ratio provides a quantitative measure of the relative strength of a drowsiness EEG power spike.

2) Participation:

The number of identified peaks represents the participation rate of the response. A strong participation shows that the specific frequency band is more reliable and more responsive to the presence of drowsiness bio-indicator.

RESULTS

A. EEG Response to Eye Blinking

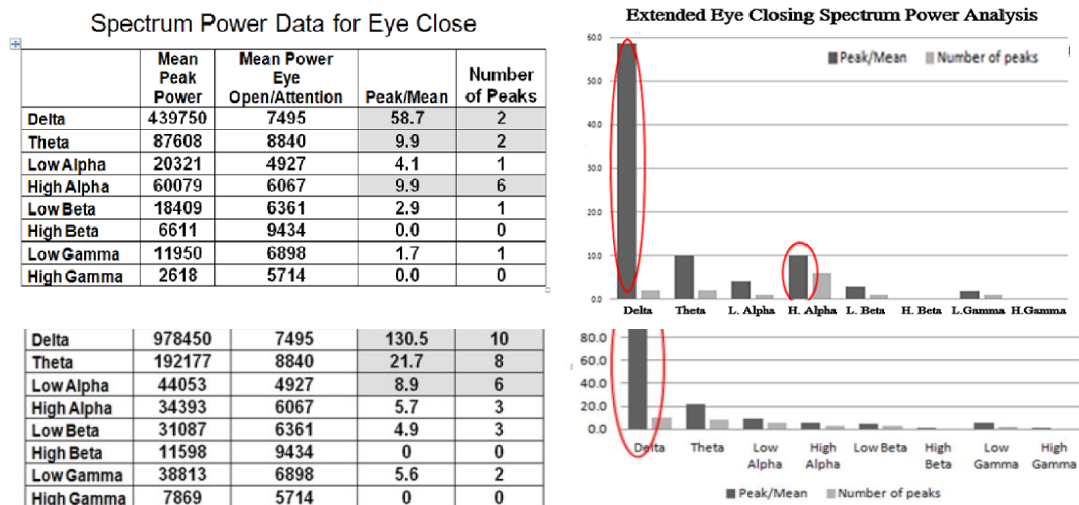
EEG power spikes in response to each eye blink were identified. The Response Strength and the Participation of each band were calculated and listed in Figure 1. These results indicate that 1) the Delta frequency band responded strongly to the eye blinking bio-indicator, with the peak to mean ratio over 100; 2) the Theta and low Alpha band responses were less powerful, with lower participation rates. The other 5 bands produced no reliable responses; thus, they are not suitable for blink detection.

Figure 1 Spectrum power analysis for eye blinking, from Delta to High Gamma band.

B. EEG Response to Eye Closing

Figure 2 contains the EEG response to eye closing, showing that only the lowest four frequency bands, Delta to high Alpha responded to eye closing. Delta power spiked when the eye closed and reopened. In between the closing/reopening action, the high Alpha power was elevated. The combination of Delta spikes and elevated high Alpha power represents a reliable detection pattern for this extended eye closing bio-indicator.

Figure 2 Spectrum power analysis for extended eye closing, from Delta to High Gamma band.



C. EEG Response to Eye Closing

Figure 3 shows each band's power in response to yawns. The key observations are 1) all eight bands participated with peak to mean ratios of at least 5; and 2) the response is very strong in each band. For example, the Delta band peak to mean ratio is 163, stronger than the corresponding ratios from both eye blinking (130) and extended eye closing (58.7).

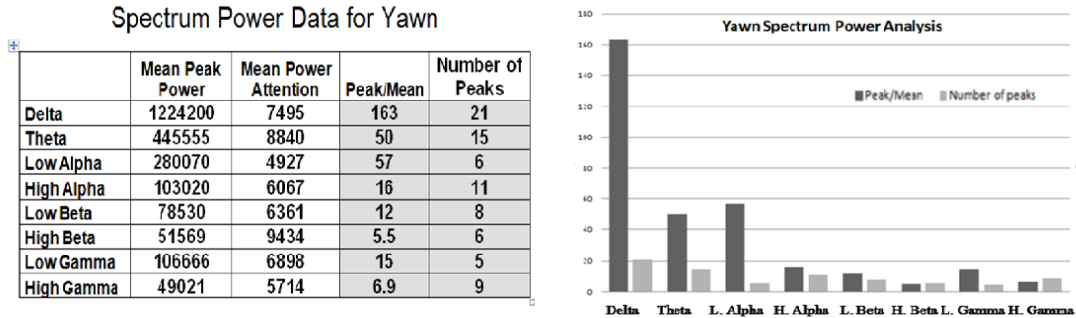


Figure 3 Spectrum power analysis for yawning, from Delta to High Gamma band.

DISCUSSION

Experiment results confirmed that the 3 bio-indicators of drowsiness produced uniquely identifiable EEG patterns in the form of power spikes in certain frequency band. To demonstrate the viability of this new idea for potential commercialization, a Smartphone App was developed on a java Android mobile development platform using Eclipse. The wearable low cost EEG headset is paired with a Smartphone via Bluetooth. EEG data is captured real time through the headset and streamed to the Smartphone. The per-band power level of the captured EEG signal is calculated every second. Using the peak detection algorithm developed in this study, the Smartphone App continuously monitors the per-second EEG power measurement to identify the potential onset of drowsiness indicators. When the EEG signal power spikes up due to the presence of sleepy indicators, the Smartphone will emit a visual and audio alert, consisting of screen flashes and loud beeps to alert the driver.

Using EEG to track Drowsiness

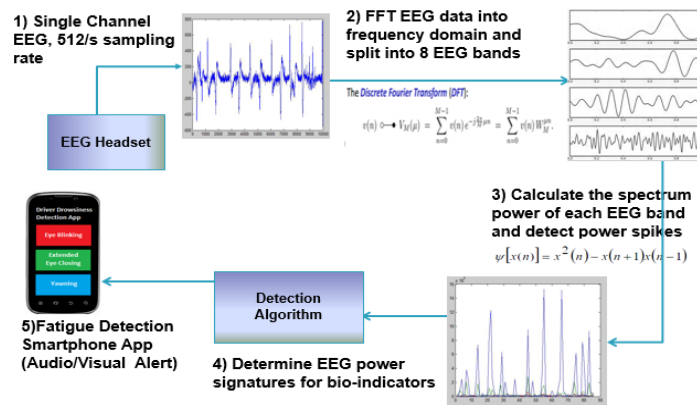


Figure 4 A portable drowsiness detection system linking EEG headset to a Smartphone

CONCLUSIONS

Using EEG power patterns to detect drowsiness is a new concept that has not been done before. In this study, we carried out frequency domain EEG signal analysis and determined that EEG spectrum power change is a good indicator for detecting fatigue/sleepiness. Experimental data from human subjects confirmed that EEG power patterns can reliably detect the presence of drowsiness indicators. Furthermore, detection algorithms based on EEG frequency band response were created.

A prototype that demonstrated the commercialization potential of this new technique was created. This initial system has been tested successfully on drowsy subjects. A widespread adoption of this technology will no doubt make our roads safer, and save lives.

REFERENCES

- [1] National Sleep Foundation <http://drowsydriving.org/about/facts-and-stats/> & <http://www.sleepfoundation.org/article/sleep-topics/drowsy-driving>
- [2] Q. Wang, J. Yang, M. Ren, “Driver Fatigue Detection: A Survey”, *WCICA 2006*. The Sixth World Congress on Intelligent Control and Automation, Pages: 8587 – 8591
- [3] NeuroSky’s eSense™ Meters and Detection of Mental State, September 2009, web site: <http://www.neurosky.com/AcademicPapers.aspx>
- [4] G. Rebolledo-mendez , I. Dunwell , E. A. Martínez-mirón , D. Vargas-cerdán , S. Freitas, F. Liarokapis , A. R. García-gaona, “Assessing NeuroSky's usability to detect attention levels in an assessment exercise”, in *Human-Computer Interaction. New Trends Lecture Notes in Computer Science*, Vol. 5610, pp 149-158 , 2009
- [5] Y. Yosui, “A Brainwave Signal Measurement and Data Processing Technique for Daily Life Applications”, in *J Physiol Anthropol*, vol. 28(3):145-50, 2009;
- [6] A. Juozapavičiūsa, G. Bacevičiūsa, D. Bugelskisa, R. Samaitien, “EEG analysis – automatic spike detection”, in *Nonlinear Analysis: Modeling and Control*, Vol. 16, No. 4, 375–386, 2011
- [7] S. Mukhopadhyay, G. C. Ray, “A New Interpretation of Nonlinear Energy Operator and Its Efficacy in Spike Detection”, in *IEEE Trans. On Biomed. Eng.*, vol.45, no.2, pp.180-187, Feb. 1998.
- [8] M. Malarvili, H. Hassanpour, M. Mesbah, B. Boashash, “A histogram-based electroencephalogram spike detection”, in *Proc of the Eighth International Symposium on Signal Processing and Its Applications*, 2005.
- [9] P. Maragos, J. Kaiser, and T. Quatieri, “On amplitude and frequency demodulation using energy operators”, in *IEEE Trans. Signal Processing*, vol. 41, pp. 1532-1550, Apr. 1993.

THE ROLE OF THE HYOID APPARATUSES OF WOODPECKERS FOR ENERGY DISSIPATION

Nayeon Lee^{a,c} (nayeon@cavs.msstate.edu), R. Prabhu^{a,c} (rprabhu@abe.msstate.edu), Lakiesha N. Williams^{a,c} (lwilliams@abe.msstate.edu), M.F. Horstemeyer^{b,c} (mfhorst@cavs.msstate.edu)

a Department of Agricultural and Biological Engineering, Mississippi State University, Mississippi State, MS 39762-9632, USA

b Department of Mechanical Engineering, Mississippi State University, Mississippi State, MS 39762-9552, USA

c Center for Advanced Vehicular Systems, Mississippi State University, Mississippi State, MS 39762-5405, USA

ABSTRACT

In order to examine the role of the hyoid apparatuses of woodpeckers with respect to energy mitigation, we investigated its unique geometry using FEA (finite element analysis). It is believed that the hyoid apparatus' role is to aid in protecting the woodpecker's brain from damage by dissipating stress waves due to impact while pecking. The woodpecker's hyoid apparatus has a unique structure compared to other birds' hyoid apparatus as it starts at the tip of the beak, which is the tongue, surrounds the woodpeckers' skull, and ends at the root of the upper beak. The hyoid apparatus has cartilage at its core, and the cartilage is surrounded by muscle. In this study, we constructed the model of the hyoid apparatus using ABAQUS-explicit FEA software, applied a blast pressure, and measured the change in pressures along various locations on the apparatus. The results showed that the impending longitudinal stress wave was decreased by 97.5% at the free end of the forked geometry, while the shear stress increased 74.7% at the same free end. We believe that this is due to the spiral geometry of the hyoid apparatus. The analysis of the woodpecker's hyoid apparatus provides additional insight into energy dissipation from the perspective of novel biological structural materials. Our focus is to develop protective gear for soldiers and athletes based on such designs in nature.

Keywords: Woodpecker; Hyoid; Energy dissipation; Finite element analysis

INTRODUCTION



Figure 1. X-ray CT of the hyoid apparatus in a golden-fronted woodpecker, *Melanerpes aurifrons*, (highlighted in red) surrounds the skull of woodpecker. (Photo courtesy of Digital Morphology, 2004)

A woodpecker has a unique structure of a hyoid apparatus compared to the hyoid apparatus of other birds'. The hyoid apparatus starts at the beak tip, surrounds the skull, and ends at the upper beak/front head intersection as shown in Fig. 1, while other birds' hyoid apparatus starts at the beak tip and ends at the neck. The tip of the hyoid apparatus is a tongue having with several barbs to facilitate grabbing insects [1, 2]. According to Zhou et al. [3], the hyoid apparatus of woodpeckers have a high strength and elasticity, and the reported elastic modulus of the hyoid cartilage is about 1.72 - 3.70 GPa.

Several researchers have studied the relationship between geometry and wave propagation of various materials. Johnson et al. [4] reported that the spiral geometry dissipate energy better than that of a cylinder geometry, and the tapered geometry mitigates energy better compared to a straight geometry. The waves of helical waveguides were studied by Treysede et al. [5, 6]. In this study, we investigated the role of the hyoid apparatus for dissipating energy with regard to its geometry.

METHODS

We studied the hyoid apparatus on the adult Red-Bellied Woodpecker, *Melanerpes carolinus*, which is a medium sized bird living in southern United States. The Red-Bellied Woodpecker pecks trees to make a nest or seek insects. Non-living woodpeckers were obtained from the collections of the Department of Wildlife, Fisheries and Aquaculture at Mississippi State University. Hyoid apparatuses were separated from the body of woodpecker. The structure of the woodpecker hyoid apparatus was characterized by using ZEISS Axiovert 200 optical microscope.

Finite element analysis of the hyoid apparatus was performed using the commercial code, ABAQUS-Explicit. The generated model consists of two material parts which are bone/cartilage and muscle. The properties used for the simulation is organized in Table 1. The blast impact was 0.44 MPa with duration of 3.8e-5 seconds.

Table 1. Material properties used for the simulation.

Material properties		Values
Skeleton [3, 7]	Young's modulus	3.72 GPa
	Poisson ratio	0.3
	Density	1850 kg/m ³
Muscle [8]	Elastic modulus	0.5 GPa
	Poisson ratio	0.4
	Density	1000 kg/m ³

RESULTS

1. Microstructure and Model Development of the Hyoid Apparatus

The microstructure of the hyoid apparatus is shown in Fig. 2. It is comprised of core cartilage/bone and muscle encasing the hyoid cartilage fully, and the cartilage part changes gradually from being thick (3 mm diameter) and rigid at the beak tip to being thin (1 mm diameter) and flexible at the end [9]. The model of the hyoid apparatus was built based on the observed microstructure.

2. Energy Mitigation

To examine the role of the hyoid apparatus on dissipating shock energy, the model was subjected to a stress wave impact. As shown in Fig. 3, the blast impact was loaded at the tip, and the impulse was analyzed at 4 regions: the tip, the bone split region, the back, and the free end. In Fig. 3, the deformation of the model was exaggerated by 10 times to show the deformation clearly. Most of the deformation was occurred at the free end in the lateral direction. Fig. 4 illustrates the amount of the longitudinal impulse and transverse impulse at the 4 regions. Impulse is defined as the following:

$$J = \int_{t_1}^{t_2} \nabla p \, dt \quad (\text{eq.1})$$

where J is impulse, t is time, and p is pressure. As the pressure wave traveled from the tip to the free end, the longitudinal impulse decreased about 97.5 % while the transverse impulse increased about 74.7 %.

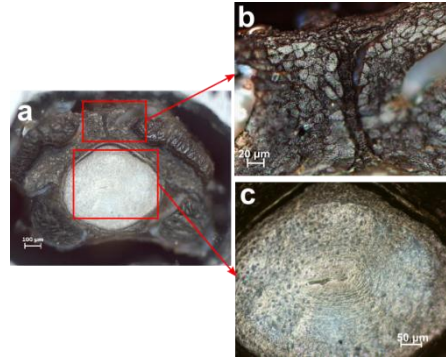


Figure 2. Optical microscopy of the microstructure of the hyoid apparatus of the woodpecker; (a) cross-sectional view of the entire hyoid apparatus, (b) the muscle part, and (c) the cartilage part.

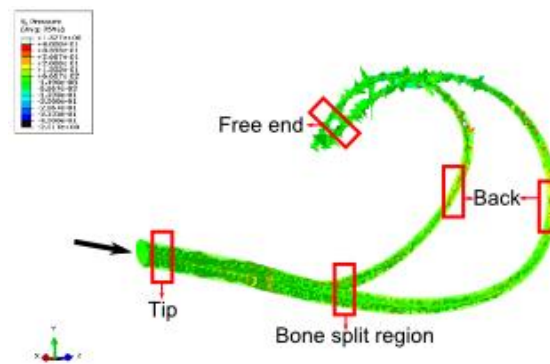


Figure 3. The pressure contour with exaggerated deformation of the hyoid apparatus showing most of the lateral deformation occurring at the free end. The black arrow indicates the impact load. The impulse was analyzed at the 4 region: tip, bone split region, back, and free end.

DISCUSSION

Two factors resulted in a remarkable decrease impulse while the stress wave traveled along the hyoid apparatus. One factor is the thinning structure, and another factor is curvature of the hyoid apparatus. The introduction of shear stresses at the bone split region, back, and free end due to curvature caused conversion of the stress wave from the longitudinal to the transverse wave. The longitudinal and shear bulk velocities are defined as:

$$c_l = \sqrt{\frac{E(1-\nu)}{\rho(1+\nu)(1-2\nu)}}, \quad c_s = \sqrt{\frac{E}{2\rho(1+\nu)}} \quad (\text{eq.2})$$

The benefit of the conversion of the stress wave from the longitudinal to the shear wave decreases the wave speed. The decreased wave speed is less harmful. Also, these shear stresses introduce lateral deformation. The tapered structure augments lateral deformation, which aids in dissipating energy and results in reducing the final impulse. The energy dissipating mechanism that the woodpecker's hyoid apparatus uses can be applied to man-made gear for soldiers and athletes.

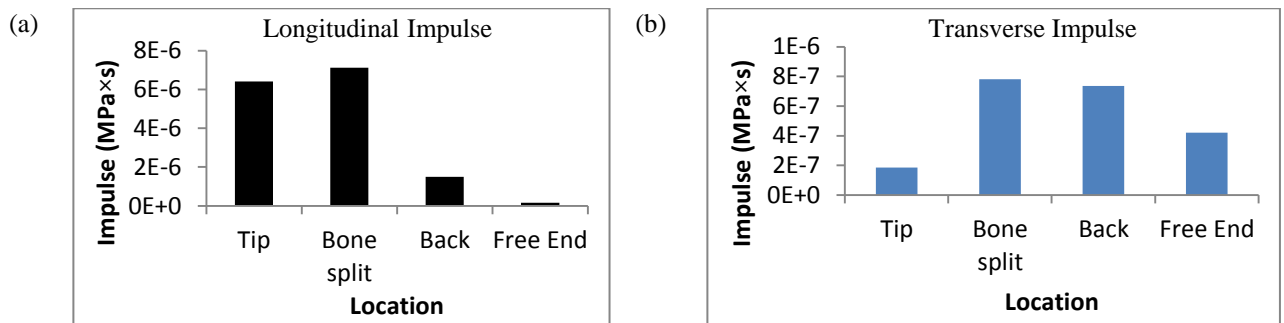


Figure 4. (a) The longitudinal impulse and (b) the transverse impulse of the hyoid apparatus.

CONCLUSIONS

The unique structure of the hyoid apparatus allows the woodpecker to catch insects from holes of trees. In this study, we also showed that the hyoid apparatus functions to dissipate energy. The tapered structure and curvature of the hyoid apparatus introduce shear stresses and lateral deformation by converting longitudinal stresses to transverse stresses, which help to protect the woodpeckers' head from experiencing abnormally high stresses while pecking.

ACKNOWLEDGMENTS

The authors would like to thank The Department of Agricultural and Biological Engineering for financial support of this study, The Department of Mechanical Engineering and The Center of Advanced Vehicular Systems (CAVS) at Mississippi State University. Also, the authors gratefully acknowledge Dassault Systems Simulia Corporation for the use of Abaqus software.

REFERENCES

- [1] P. Villard, J. Cuisin, and W. Karasov, "How do woodpeckers extract grubs with their tongues? A study of the guadeloupe woodpecker (*melanerpes herminieri*) in the french west indies," *The Auk*, vol. 121, pp. 509-514, 2004.
- [2] S. Emura, T. Okumura, and H. Chen, "Scanning electron microscopic study of the tongue in the Japanese pygmy woodpecker (*Dendrocopos kizuki*)," *Okajimas folia anatomica Japonica*, vol. 86, pp. 31-35, 2009.
- [3] P. Zhou, X. Kong, C. Wu, and Z. Chen, "The Novel Mechanical Property of Tongue of a Woodpecker," *Journal of Bionic Engineering*, vol. 6, pp. 214-218, 2009.
- [4] K. Johnson, Horstemeyer, M.F., Williams, L., Liao, J., Lee, N. , "Geometric effects on stress wave propagation," *Journal of Biomechanical Engineering*, 2014.
- [5] F. Treyssède and L. Laguerre, "Investigation of elastic modes propagating in multi-wire helical waveguides," *Journal of Sound and Vibration*, vol. 329, pp. 1702-1716, 2010.
- [6] F. Treyssède, "Elastic waves in helical waveguides," *Wave motion*, vol. 45, pp. 457-470, 2008.
- [7] O. Riekkinen, M. Hakulinen, M. Lammi, J. Jurvelin, A. Kallioniemi, and J. Töyräs, "Acoustic properties of trabecular bone—relationships to tissue composition," *Ultrasound in medicine & biology*, vol. 33, pp. 1438-1444, 2007.
- [8] M. G. Urbanek, E. B. Picken, L. K. Kalliainen, and W. M. Kuzon, "Specific force deficit in skeletal muscles of old rats is partially explained by the existence of denervated muscle fibers," *The Journals of Gerontology Series A: Biological Sciences and Medical Sciences*, vol. 56, pp. B191-B197, 2001.
- [9] W. J. Bock, "Functional and evolutionary morphology of woodpeckers," *Ostrich: Journal of African Ornithology*, vol. 70, pp. 23-31, 1999.

TRACKING OF HMSCS PRECONDITIONED WITH 0.5% O₂ IN ASSOCIATION WITH STROKE UTILIZING ¹H AND ²³Na MRI AT 21.1 T

Jens T. Rosenberg^{1,2}, Avigdor Leftin³, Fabian Calixto Bejarano¹, Michael M. Davidson^{1,4}, Michelle Baird¹, Lucio Frydman^{1,3}, Teng Ma² and Samuel C. Grant^{1,2}

¹The National High Magnetic Field Laboratory, ²Chemical and Biomedical Engineering, FAMU-FSU College of Engineering, and ³Department of Biological Science, The Florida State University, ⁴Department of Chemical Physics, Weizmann Institute of Science

ABSTRACT

As evaluated by ultra-high field ¹H and ²³Na MRI, human mesenchymal stem cells (hMSCs) exposed to 2% O₂ (hypoxia) have shown enhanced therapeutic effects once transplanted into an ischemic brain. In this study, we further investigate hypoxic preconditioning by using a sublethal exposure, 0.5% O₂, prior to intra-arterial injection of cells in to a stroked rat brain. Preconditioned hMSCs were transfected with an iron based contrast agent (SPIOs) for cell tracking. Serial MRI at 21.1 T was performed to acquire ¹H and ²³Na images of lesion progression and cell migration. Images of the ischemic stroke [1] lesion show increased signal as evidenced by the influx of extracellular water. Increases in tissue sodium concentration are seen by ²³Na MRI, and the SPIO labeled cells are visualized as signal voids. Histological tissue sections show the localization of the iron-labeled hMSCs in brain tissue. With Na MRI, the sublethal pretreatment showed a trend towards increased stroke recovery compared to normoxic and control; however, statistical significance was not reached. In fact, the 2% hypoxic pre-treatment is the only test group showing a significant difference as evaluated with Na MRI. With the respect to the permanence of the hMSCs, the average decrease is lower for the sublethal cells compared to both the 2% hypoxic pretreatment and to normoxic cells, but again statistical significance was not achieved. In conclusion, this study shows limited benefits for the sublethal pretreatment compared to previous hypoxic protocols.

Keywords: Stroke, hSMCs, cell therapy, sublethal exposure, hypoxia, iron oxide, MRI, celltracking

INTRODUCTION

Introduction: Mesenchymal stem cells (MSCs) have gained increased interest in the field of tissue regeneration because of their availability, ease of expansion and multipotency [1-3]. MSCs are known to secrete factors for regulating inflammatory processes as well as neuronal growth factors [4] in association with neural damage. Human MSCs (hMSCs) exposed to low oxygen tension (hypoxia), which is a native physiological condition, may enhance therapeutic effects. Prior studies in our lab [5] have shown that hypoxic culture can enhance stroke recovery as evaluated by ultra-high field ¹H and ²³Na MRI. In this *in vivo* study, transient hypoxic preconditioning is evaluated by using a sub-lethal 0.5% O₂ exposure just prior to injecting the cells systemically in a stroked rat model. The sub-lethal O₂ pretreatment of the hMSCs have shown to increase the expression of trophic factors, down-regulate inflammatory genes, and increase cell viability under ischemic stress [6]. hMSCs also were transfected with superparamagnetic iron oxide (SPIO) nanoparticles prior to being injected intra-arterially to treat ischemic stroke resulting from a middle cerebral artery occlusion (MCAO). Serial MRI at 21.1 T was performed to acquire ¹H and ²³Na images of lesion progression and cell migration.

METHODS

HMSCs were cultured following Grayson *et al* [7] and incubated continuously under either 20% O₂ (Normoxic) or 2% O₂ (hypoxic 2%) [5] or pre-conditioned in 0.5% O₂ (hypoxic 0.5%) for 24 hours just prior to injection. For tracking, cells were transfected with 0.86- μ m fluorescent iron oxides (Bangs Laboratory) for 12 hours. Immediately following a 1-h transient MCAO [8], 1×10^6 cells suspended in sterile PBS were injected through the exposed common carotid artery (CCA) of Sprague-Dawley rats [9]. For control, five animals were injected with saline instead of cells. *In vivo* MRI was performed 24 hours, 72 hours and 7 days after surgery utilizing high resolution, T₂-weighted (T2W) spin echo, gradient recalled echo (GRE), 3D ²³Na GRE at 21.1 T for increased sensitivity. *Ex vivo* imaging was performed at 11.75 T using a 100- μ m 3D GRE sequence. Correlative histology was done on 20- μ m brain sections treated with Hoechst nuclear stain and human antibody (Spring BioScience). Stroke lesions were determined based on volumetric changes on ¹H and ²³Na images using AMIRA (FEI Visualization Science Group, Burlington MA). Pixels were defined as being part of a MPIO labeled cell if any of its signal were less than the average signal of a ROI on the contralateral side minus three times its standard deviations. All work has been conducted in accordance with FSU Animal Care and User committee.

RESULTS

In vivo images of the ischemic stroke lesion (red circles in Figure 1) show increased signal as evidence of the influx of extracellular water. Increases in tissue sodium concentration (TSC) are seen with ²³Na MRI. On 2D GRE images, labeled cells are visualized as signal voids. Also in Fig. 1, a tissue section taken from an animal 24-hour post stroke and injection with hypoxic 0.5% O₂ pretreated cells is displayed. The tissue is stained with human anti-mitochondria antibody (green), red is from the fluorescent Bangs particles and blue is Hoescht nuclear stain. Immunohistochemistry shows the localization of labeled cells within brain tissue. In Figure 2, there is no significant difference for the sub-lethal pretreated hMSCs with respect to T₂ lesion volume compared to other culture conditions. With ²³Na MRI, the sub-lethal pretreatment shows a slight increase in stroke recovery compared to normoxic and control (saline) specimen but no statistical significance is evident. In fact, the hypoxic 2% culture is the only condition showing significantly difference as evaluated with ²³Na MRI. In Figure 3, the average percent decrease in signal voids (indicative of cell engraftment) is lower for the sub-lethal cells compared to both the hypoxic 2% and normoxic conditions, but no statistical significance is achieved.

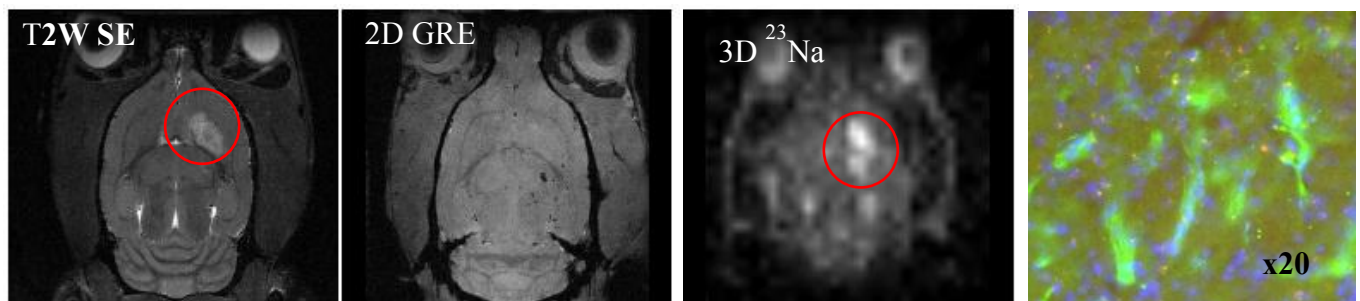


Figure 1: Images of a representative animal at 24 hours post-surgery showing the stroke (a) iron labeled cells (b) and stroke with sodium MRI (c) and histology (d) showing the iron labeled cells in the stroked tissue confirming the contrast seen with MRI. In (d) the green fluorescent is the hSMCs labeled with a human mitochondria antibody, red are the bangs particles and blue is Hoescht nuclear stain.

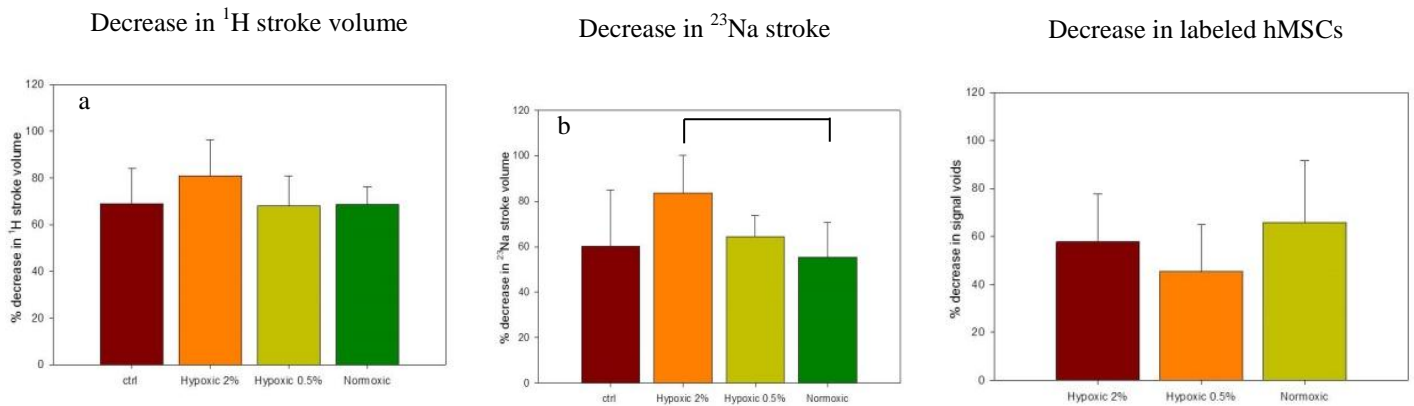


Figure 2: Graphs of percent decrease in stroke lesion volume as measured with ¹H (a), ²³Na (b) MRI and decrease in hMSCs as determined by the signal voids generated from the iron oxides inside the cells. Significance determined with ANOVA and LSD post hoc test ($p < 0.05$)

DISCUSSION

This study investigated the presumed increased therapeutic properties of pretreated hMSCs under a sub-lethal, 0.5% O₂ exposure prior to transplanting them into a stroked brain. The study shows that these cells are delivered to the brain with the intra-arterial injection as seen on the 2D GRE image and tissue section stained for anti-human mitochondria. However, no significant increase in therapeutic properties evident with the sub-lethal, 0.5% O₂ pretreatment as measured by volumetric changes of the stroke region, beyond the possibility of an initially higher engraftment and permanence of cells compared to other conditions. A long-term hypoxic culture at 2% O₂ provides significant recovery as seen with ²³Na MRI [5].

CONCLUSIONS

Despite the promising *in vitro* results with hSMCs cultured under sub-lethal conditions in regards to increased properties associated with stroke lesion recovery (expression of trophic factors, down-regulate inflammatory genes, and increase cell viability), this treatment does not appear increase the cells therapeutic properties in association with an ischemic stroke.

ACKNOWLEDGMENTS

Funding provided by the NSF and National High Magnetic Field Laboratory (DMR-0654118), the American Heart Association Grant-in-Aid (10GRNT3860040), ERC Advanced Grant (246754), a Helen Kimmel Award for Innovative Investigation, Kamin-Yeda Grant Israel (711237), DIP Grant Germany (710907), and NSF IRFP and Fulbright (AL).

REFERENCES

- [1] M. E. Bernardo, N. Zaffaroni, F. Novara, A. M. Cometa, M. A. Avanzini, A. Moretta, D. Montagna, R. Maccario, R. Villa, M. G. Daidone, O. Zuffardi and F. Locatelli, "Human bone marrow derived mesenchymal stem cells do not undergo transformation after long-term in vitro culture and do not exhibit telomere maintenance mechanisms," *Cancer Res.*, vol. 67, pp. 9142-9149, Oct 1, 2007.
- [2] M. F. Pittenger, A. M. Mackay, S. C. Beck, R. K. Jaiswal, R. Douglas, J. D. Mosca, M. A. Moorman, D. W. Simonetti, S. Craig and D. R. Marshak, "Multilineage potential of adult human mesenchymal stem cells," *Science*, vol. 284, pp. 143-147, Apr 2, 1999.

- [3] A. J. Friedenstein, R. K. Chailakhjan and K. S. Lalykina, "The development of fibroblast colonies in monolayer cultures of guinea-pig bone marrow and spleen cells," *Cell Tissue Kinet.*, vol. 3, pp. 393-403, Oct, 1970.
- [4] N. Pavlichenko, I. Sokolova, S. Vijde, E. Shvedova, G. Alexandrov, P. Krouglyakov, O. Fedotova, E. G. Gilerovich, D. G. Polyntsev and V. A. Otellin, "Mesenchymal stem cells transplantation could be beneficial for treatment of experimental ischemic stroke in rats," *Brain Res.*, vol. 1233, pp. 203-213, Oct 3, 2008.
- [5] J. T. Rosenberg, K. Sellgren, M. A. Davidson, T. Ma and S. C. Grant, "*MR contrast and biological impacts of intracellular superparamagnetic iron oxides on human mesenchymal stem cells with long-term culture and hypoxic exposure*," in Melbourne, Australia, 2012, .
- [6] L. Wei, J. L. Fraser, Z. Y. Lu, X. Y. Hu and S. P. Yu, "Transplantation of hypoxia preconditioned bone marrow mesenchymal stem cells enhances angiogenesis and neurogenesis after cerebral ischemia in rats," *Neurobiol Dis*, vol. 46, pp. 635-645, Jun, 2012.
- [7] W. L. Grayson, T. Ma and B. Bunnell, "Human mesenchymal stem cells tissue development in 3D PET matrices," *Biotechnol. Prog.*, vol. 20, pp. 905-912, May-Jun, 2004.
- [8] E. Z. Longa, P. R. Weinstein, S. Carlson and R. Cummins, "Reversible middle cerebral artery occlusion without craniectomy in rats," *Stroke*, vol. 20, pp. 84-91, Jan, 1989.
- [9] K. Uluc, A. Miranpuri, G. C. Kujoth, E. Akture and M. K. Baskaya, "Focal cerebral ischemia model by endovascular suture occlusion of the middle cerebral artery in the rat," *J. Vis. Exp.*, vol. (48). pii: 1978. doi, pp. 10.3791/1978, Feb 5, 2011.

TREATMENT OF VASCULAR CALCIFICATION BY ELASTIN-TARGETED NANOPARTICLES**Kevin A. Bennett, C. LaShan Simpson**

Box 9632

130 Creelman St.

Mississippi State, MS 39762

ABSTRACT

Vascular calcification is the deposition of calcium mineral in blood vessels and can cause increased vascular stiffness, resulting in an increased risk for cardiovascular complications. It has recently been determined that calcification resembles the active process of bone formation, with smooth muscle cells being able to differentiate into bone-forming osteoblast-like cells. Another key characteristic of vascular calcification is the breakdown of elastin, the protein responsible for providing blood vessels their elasticity. It is believed that degraded elastin could provide sites for the initiation of vascular calcification. A recent study has shown that bone-absorbing cells, osteoclasts, can demineralize calcified elastin. To improve upon this study, degraded elastin-targeted nanoparticles will be used to target sites of calcification and cause resident macrophages, inflammatory cells believed to be involved in vascular calcification, to differentiate into osteoclasts. Iron oxide nanoparticles, which have already been used in the imaging of macrophage-rich areas in arteries with magnetic resonance imaging (MRI), will be modified with anti-tropoelastin antibodies. Once injected, the nanoparticles will target sites of calcification, acting as a contrast agent for MRI and delivering 1,25 dihydroxyvitamin D₃ and macrophage colony-stimulating factor to the nearby macrophages and circulating monocytes to induce osteoclastic differentiation and facilitate demineralization of the calcified arteries. With an estimated 18 million people dying from cardiovascular diseases world wide, research in this field is essential, and this proposed research could be pivotal in the understanding, treatment, and diagnosis of vascular calcification.

Keywords: vascular calcification, degraded elastin, iron oxide nanoparticles, osteoclast demineralization

INTRODUCTION

Arterial calcification is the calcification of blood vessels, which occur in both the inner (intimal) and middle (medial) layers, and is associated with atherosclerosis, diabetes, and chronic kidney disease [1]. The mineral deposits cause increased vascular stiffness, possibly leading to hypertension, left ventricular hypertrophy, myocardial infarction, and heart failure [2,3]. Recently, research has shown that the process of vascular calcification resembles the process of bone formation, involving bone forming cells, osteoblasts, and bone absorbing cells, osteoclasts. It has been determined that the vascular smooth muscles cells (VSMCs), pericytes, and myocytes found in blood vessels are capable of differentiating into osteoblast-like cells that deposit the hydroxyapatite minerals [4]. This process is mediated through various signaling molecules that are typically present in bone. Potential treatments for vascular calcification have been tested, such as bisphosphonates, statins, and other drugs, and while they have shown varying degrees of success, most of these therapies are preventative and work to prevent the onset and progression [1]. While surgical procedures, such as stents, balloon angioplasty, and bypass surgery, can be used to treat calcification associated atherosclerosis, these treatments often have complications and high rates of restenosis. No treatments that reverse the mineralization currently exist.

In addition to high phosphate and calcium levels, the disruption and degradation of elastin has been implicated in the onset and progression of vascular calcification [3,4]. Elastin is an extracellular matrix protein that provides blood vessels, among other organs, their elasticity. Tropoelastin, the soluble precursor of elastin, consists of both hydrophobic and hydrophilic domains. Elastin is formed by the crosslinking of these hydrophilic domains, resulting in a very stable protein that is typically not broken down [5]. The breakdown of elastin is typically associated with protease activity, such as matrix metalloproteinase (MMP), and has been observed in almost all types of vascular calcification. It was then determined that elastin peptides released from elastin breakdown caused an increase in osteogenic response in smooth muscle cells [4,6]. Recently, it was also shown that elastin degradation preceded vascular calcification in a Uremic mouse model of Chronic Kidney Disease. They suggested that elastin degradation, while not able to solely cause calcification, provides sites for calcification to occur [3].

In 2007, a novel study was conducted by Simpson et al, in which they used mature osteoclasts to demineralize calcified elastin *in vitro* and *in vivo* [2]. To improve upon this work, the differentiation of resident cells into osteoclasts will be induced through the delivery of proteins. Macrophages, inflammatory cells that have been shown to be involved in arterial calcification [7], differentiate from the same lineage as osteoclasts. However, there is also evidence to suggest that mature macrophages can transdifferentiate into osteoclasts as well through the exposure of certain proteins, such as 1,25 dihydroxyvitamin D₃ and macrophage colony-stimulating factor (M-CSF) [8]. Because of the similarities of bone formation and vascular calcification, targeted delivery to the sites of vascular calcification is imperative and will be achieved through the use of nanoparticles (NPs). NPs are nano-sized engineered particles that have received considerable attention for use in drug delivery due to several key advantages: small size to avoid clearance from immune system, ability for site-specific delivery, and controllable release rate [9]. NPs have been used for the treatment and diagnosis of various diseases. In particular, iron oxide NPs coated in a polymer, dextran, have been FDA approved for their use in magnetic resonance imaging (MRI) and have been used to image macrophage-rich areas in the vasculature. To improve upon this targeting mechanism and to ensure delivery to sites of arterial calcification, additional targeting of degraded elastin will be developed.

Overall, the goal of this research will be to develop NPs that target sites of vascular calcification through degraded elastin. In addition, the proteins needed for the differentiation of the macrophages into osteoclasts will be incorporated in these NPs. Once injected, they should target sites of vascular calcification in blood vessels, releasing the proteins and inducing osteoclastic differentiation of the resident macrophages. These osteoclasts will then demineralize the calcified vessels.

METHODS

In Vitro Model of Calcification

An *in vitro* calcification model will be established. Human VSMCs, all between passage 2 and passage 6, will be seeded on purified elastin in standard six wells plates. The elastin will be obtained from porcine aortas and purified as previously described [2,6]. The cells will be cultured with standard growth media, changing it every 2-3 days, until the cells have become confluent. Then, half of the wells on each plate will serve as a control group and continue to be cultured in standard growth media. The other three wells will be cultured in a media containing 10 mM β-glycerophosphate and 100 nM Dexamethasone to promote calcification. The media will be changed every 2-3 days for 3 weeks. Calcium and phosphorus levels will be analyzed using atomic absorption spectrophotometer and molybdate complexation assay, respectively, as previously described [6]. Calcification will be visually observed using alizarin staining. Elastin degradation will be verified through quantification of soluble elastin peptides using a competitive enzyme-linked immunosorbent assay (ELISA), as previously described [2]. Briefly, rabbit anti-elastin antibody will be used as the primary antibody and detection will be completed using goat anti-rabbit IgG-peroxidase conjugate and H₂O₂/ortho-phenylene diamine hydrochloride. It will also be visual observed by staining the elastin using Verhoeff-van Gieson's stain. All assays will be done in triplicate.

Specificity of Anti-tropoelastin Antibody

To test the affinity and specificity of rabbit anti-tropoelastin antibody for the degraded elastin, ELISA testing will be done. The anti-tropoelastin antibody targets a hydrophilic domain involved in crosslinking and not found in stable elastin. Two antigens will be used, purified elastin that will be obtained as described in the calcification model and the degraded elastin obtained from the calcification model at multiple concentrations. The detection will be completed using goat anti-rabbit IgG-peroxidase conjugate and H₂O₂/ortho-phenylene diamine hydrochloride.

Differentiation of RAW 264.7 Macrophage Cells

To test the ability for the macrophages to differentiate, RAW 264.7 cells, a murine macrophage cell line, will be cultured in various concentrations of 1,25 dihydroxyvitamin D₃, and M-CSF *in vitro*. Validation of the osteoclast phenotype will be confirmed through staining for multiple nuclei using hematoxylin and eosin (H&E) staining and the activity of tartrate-resistant acid phosphatase (TRAP). In addition, the cells will be cultured on Hydroxyapatite-coated quartz discs to test their demineralization ability. Demineralization will be observed using von Kossa staining. Using the data, the minimum concentration of proteins needed to induce the differentiation can be determined.

Antibody Conjugated Nanoparticles

Vitamin D₃ and M-CSF will be encapsulated in polymer coated iron oxide NPs using various encapsulation methods. The drug loading and release rate will be tested by using high performance liquid chromatography (HPLC), and the size of the nanoparticles can be determined with transmission electron microscopy and dynamic light scattering. It has been determined that the ideal size for NPs to avoid clearance from the body is between 10-100 nm [9]. The bioactivity of the released proteins will be tested on cell cultures of the RAW 264.7 cells with media containing the protein loaded NPs. The ability of the cells to differentiate into osteoclasts will be verified using the same techniques as described during the bulk addition of proteins.

Calcification Analysis

RAW 264.7 cells will be cultured on calcified elastin obtained from the calcification model in a six well plate using standard growth media, replacing every 2-3 days, until reaching confluency. Then, half the wells will continue to receive the standard growth media, while the other half will receive growth media with the protein loaded NPs. Time points will be taken at 7, 14, and 21 days. The degree of reduction in calcification will be quantified by measuring the calcium and phosphate levels and observed visually using the method described in the original calcification model.

RESULTS

Although this research has not currently yielded results, it is expected that the anti-tropoelastin conjugated NPs will be able to bind specifically to sites of degraded elastin. It is also expected that the RAW 264.7 cells will be able to transdifferentiate into osteoclasts.

DISCUSSION

The aim of this research is to develop a potential treatment for vascular calcification by using elastin-targeted nanoparticles to induce the differentiation of resident macrophages into osteoclasts. Current treatments only prevent the onset or progression of the calcification and must be given to at-risk patients before calcification occurs [1]. Thus, the development of a treatment that can reverse mineralization is becoming essential. In the United States alone, approximately 715 thousand people experience heart attacks, 67 million people (1 in 3) suffer from hypertension, and one in nine deaths are contributed to heart failure [10]. Therefore, a treatment for calcification could have far reaching impact on society. Also, this research will provide additional insight on certain aspects of vascular calcification, such as macrophages' ability to transdifferentiate into osteoclasts and the structure of degraded elastin. In addition, the nanoparticles targeted to degraded elastin can provide another method of delivery for other vascular calcification treatments and could be a pivotal step in the creation of a new treatment.

CONCLUSIONS

With strong evidence to suggest that degraded elastin is associated with vascular calcification, NPs targeted to degraded elastin represent a novel way to delivery drugs and proteins to sites of vascular calcification. Using these NPs to differentiation of resident macrophages into osteoclasts, a treatment for calcification can be developed. This treatment is unique in that it uses the body's own cells to differentiate into bone absorbing cells to reverse the process and does not need to be administered before the calcification is noticed. With an estimated 18 million people dying from cardiovascular diseases worldwide each year [9], research in this field is becoming increasingly important.

ACKNOWLEDGMENTS

The authors acknowledge the department of Agricultural and Biological Engineering at Mississippi State University

REFERENCES

- [1] M. Wu, C. Rementer, and C.M. Giachelli. "Vascular Calcification: An Update on Mechanisms and Challenges in Treatment." *Calcif Tissue Int*, vol. 93, pp. 365-73, Mar. 2013.
- [2] C.L. Simpson et al. "Toward cell therapy for vascular calcification: osteoclast-mediated demineralization of calcified elastin." *Cardiovasc Pathol*, vol. 16, pp. 29-37, Jan. – Feb. 2007.

- [3] A. Pai, E.M. Leaf, M. El-Abbadi, and C.M. Giachelli. "Elastin Degradation and Vascular Smooth Muscle Cell Phenotype Change Precede Cell Loss and Arterial Medial Calcification in a Uremic Mouse Model of Chronic Kidney Disease." *The Am J Pathol*, vol. 178, pp. 764-73, Feb. 2011.
- [4] A. Simionescu, K. Philips, and N. Vyavahare. "Elastin-derived peptides and TGF- β 1 induce osteogenic responses in smooth muscle cells." *Biochem Biophys Res Commun*, vol. 334, pp. 524-32, Aug. 2005.
- [5] W.F. Daamen, J.H. Veerkamp, J.C.M van Hest, and T.H. van Kuppevelt. "Elastin as a biomaterial for tissue engineering." *Biomaterials*, vol. 28, pp. 4378-98, Oct. 2007.
- [6] J.S. Lee et al. "Elastin Calcification in the Rat Subdermal Model is Accompanied by Up-Regulation of Degradative and Osteogenic Cellular Response." *Am J Pathol*, vol. 168, pp. 490-98, Feb. 2006.
- [7] K. Ikeda et al. "Macrophages play a unique role in the plaque calcification by enhancing the osteogenic signals exerted by vascular smooth muscle cells." *Biochem Biophys Res Commun*, vol. 425, pp. 39-44, Aug. 2012.
- [8] T.T Yang, A. Sabokbar, C.L.M.H Gibbons, and A. Athanasou. "Human mesenchymal tumour-associated macrophages differentiate into osteoclastic bone-resorbing cells." *J Bone Joint Surg Br*, vol. 84, pp. 452-6, Apr. 2002.
- [9] C. Psarros, R. Lee, M. Margiaritis, and C. Antoniadis. "Nanomedicine for the prevention, treatment and imaging of atherosclerosis." *Maturitas*, vol. 73, pp. 52-60, Sep. 2012.
- [10] Center for Disease Control and Prevention. "Fact Sheets" Internet: http://www.cdc.gov/dhdspl/data_statistics/fact_sheets, [January 31, 2014]

ENDOTHELIALIZED IN VITRO TUBULAR SILICONE SCAFFOLDS

Marzieh K Atigh¹, Kristen Smith², Saami K. Yazdani³

¹ Department of Mechanical Engineering, University of South Alabama, Mobile, Alabama.

² Spanish Fort High School, Spanish Fort, Alabama

³ Department of Mechanical Engineering, University of South Alabama, Mobile, Alabama.

ABSTRACT

More than 81 million Americans suffer from some form of cardiovascular disease, making it the leading cause of death in the country. Atherosclerosis, the major cause of cardiovascular disease, is a condition in which an artery wall thickens and narrows as a result of the accumulation of fatty materials. Clinical studies has shown that plaque growth occur in specific regions of the artery, correlating with areas of flow disturbances. Endothelial cells align the inner surface of the blood vessel, and are susceptible to adverse changes in these flow-disturbed regions. It is hypothesized that these flow disturbances reduce the endothelial cells ability to function optimally, eventually leading to disease initiation such as lesion development and eventually to clinical complications. Therefore, the purpose of this project was to make an *in vitro* endothelial cell culture system, which mimics the geometry and hemodynamic conditions of an artery. A bioreactor system was developed to seed endothelial cells on the inner surface of silicone tubes. Briefly, silicone tubes with arterial geometry and similar mechanical compliance were created using Sylgard 184 elastomeric kit. The tubes were then sterilized with 70% sulfuric acid and coated with fibronectin. The inner surface of the tubes was then seeded with rat aortic endothelial cells. The bioreactor was then placed inside an incubator for a period of 48 hours. The result demonstrated endothelial cells successfully attached to the inner surface of the sylgard tube. This system can be used to examine endothelial cell responses to flow and flow gradients under defined and controllable conditions and potentially to assess cell behavior to varying therapeutic treatments.

Keywords: Atherosclerosis, Endothelial Cells, *in vitro*, Hemodynamics, Cell Culture.

INTRODUCTION

Heart disease is one of the most important and common causes of death and disability in the United States and throughout the world [1]. Cardiovascular disease, also known as heart and vessel disease consist of numerous problems, many of which lead to a process called artherosclerosis [3]. Atherosclerosis is a condition in which an artery wall thickens and then narrows as a result of accumulation of fatty materials in the luminal region.

Endothelial cells align the lumen or inner surface of the blood vessel, and are susceptible to adverse changes due to local changes in the mechanical environment [4]. Plaque growth has shown to occur in specific regions of the artery, correlating with areas of flow disturbances [1]. It is hypothesized that these flow disturbances reduce the endothelial cells ability to function optimally, eventually leading to disease initiation such as lesion development and eventually to clinical complications. Complex hemodynamic forces resulting in low wall shear stress values stimulate dysfunction of endothelial cell [5]. Due to the difficulty of studying ECs *in vivo*, an *in vitro* endothelial cell culture system was created, which mimics the geometry and hemodynamic conditions of an artery *in vivo* [2]. The goal of our study was to therefore create a model of an endothelialized artery to study the impact of hemodynamics on cell behavior. This system has the potential to examine endothelial cell response to varying flow conditions mimicking a wide range of arterial hemodynamics.

MATERIALS AND METHODS

Cell culture

Rat endothelial cells (P.2), were provided from Department of Biomedical Sciences at University of South Alabama. ECs were first grown on 100cm dishes under controlled condition.

The media contained a mixture of 50% DMEM high glucose (Hyclone, Thermo Scientific, Utah), 50% DMEM low glucose (Hyclone, Thermo Scientific, Utah), and supplemented with 10% Bovine Growth Calf Serum (Hyclone, Thermo Scientific, Utah) and 1% Antibiotic/Antimycotic solution (Hyclone, Thermo Scientific, Utah).

Silicon tubular model

Sylgard 184 Silicone Elastomer Kit (Dow Corning, Michigan) was used to create tubular model, which mimics the elastic modulus of soft tissue. The Sylgard tubular models had an approximately 5 mm diameter, which match the average diameter of the inlet region of the anatomical model.

The tubular models were first incubated in 70% sulfuric acid for 20 minutes, followed by sterilization, and then coated with fibronectin (Millipore, California) for 24 hours. The cell suspension (2.4×10^5 cells/mL) was pipetted into each model (Fig. 1). Then the models were placed in the incubator and rotated every 15 minutes for one hour until all sides were seeded.

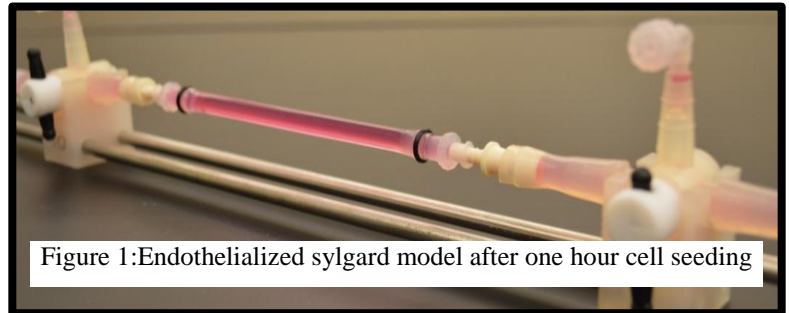


Figure 1: Endothelialized sylgard model after one hour cell seeding

Bioreactor system and the experiment

A bioreactor system was designed to provide an environment suited for EC growths, which mimicked physiologic flow and pressure conditions. The bioreactor consisted of a perfusion flow loop system composed of fresh cell culture media, a gear pump connected to a PC to control the flow waveform and flow rate within our endothelialized tubular models.

The entire apparatus was maintained inside an incubator for a period of 48 hours and exposed to steady (first 24 hours) and pulsatile flow. At the end of each experiment, the EC seeded on the tubular model were fixed by using 10% Formalin (SF 98-4, Fisher Scientific, New Jersey) and visualized under a light microscope (Micromaster, Fisher Scientific, New Jersey). High-resolution images were captured with microscope camera at two different magnifications, 40x and 60x.

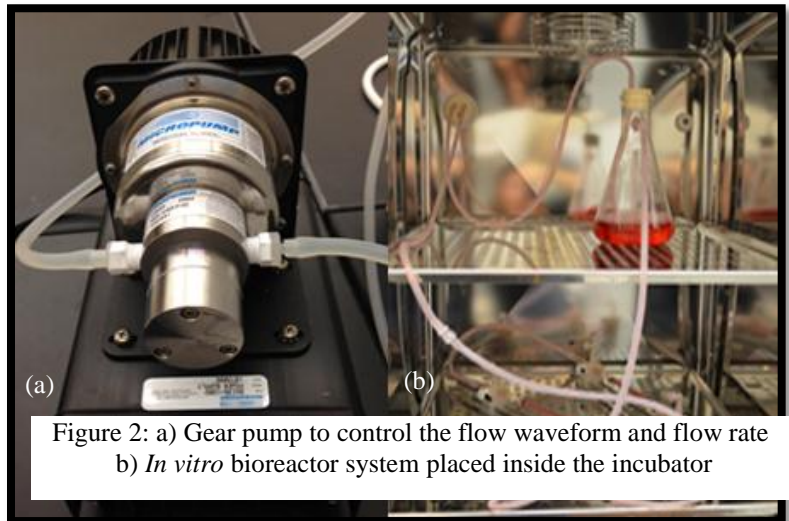


Figure 2: a) Gear pump to control the flow waveform and flow rate
b) *In vitro* bioreactor system placed inside the incubator

RESULTS

Endothelial cells were successfully grown to in culture (Fig. 3a). Sylgard tubular models with a uniform wall thickness of 0.65mm and inner diameter of 6.75mm were developed and prepared for EC seeding. All bioreactor runs were successful for the 48 hour flow conditioning period. As shown in figure 3a ECs successfully attached to the inner surface of the sylgard tube and after 48 hours, remained adhered and showed complete confluency.

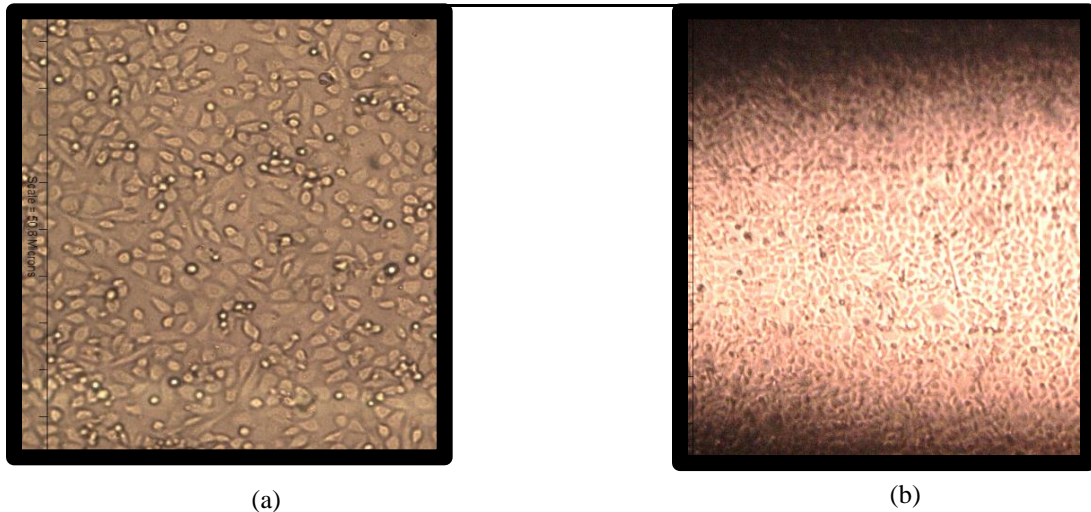


Fig. 3: Cultured Endothelial Cell. (a) Phase-contrast image of cultured Endothelial Cell (60X). (b) High power (40X) phase-contrast image of endothelial Cell seeded on sylgard tube following 48 hour of seeding.

DISCUSSION

In this study, we developed an *in vitro* endothelial cell culture system, which mimics the geometry and hemodynamic conditions of an artery. Rat endothelial cell were grown, pipetted, and cultured into sylgard tube. Using a bioreactor system, ECs remained adherent following 48 hours of steady flow conditions. This system has the potential to examine endothelial cell response to varying flow conditions mimicking arterial hemodynamics.

The importance of such a system is emphasized by the need for understanding ECs behavior and their interaction to blood flow for clinical use such vascular stents [6]. This non-obstructive optical method of observing EC can pave the way to study the interaction of endothelial cells and stents with varying parameters, including different coating and drug release profile. By understanding the EC response to these factors, potentially, this *in vitro* model can be used to optimize design parameters.

Thus far, we have shown that cells remain attached following 48 hour steady state flow conditions. Both the waveform (from steady to pulsatile) and shear values will be increased to produce better EC alignment to flow. Furthermore, we plan to change the mechanical properties (stiffness) of the sylgard model to better understand the relationship of endothelial cells and elastic modulus. Indeed the ECs has been playing a significant role in developing complications like atherosclerosis due to hemodynamic forces at flow disturbed regions such as bifurcations. Future studies will investigate these phenomena by developing such a system consisting of bifurcation models under physiological conditions.

Nevertheless, the highlight of this study is the use of hemodynamics environment to study the behavior of ECs in order to provide better therapeutic treatments.

CONCLUSIONS

The *in vitro* cell culture model system has been presented to simulate the geometry of an artery *in vivo*, and to study ECs behavior to flow gradients. This model successfully shows cultured ECs remained adherent to steady flow conditions and developed into a confluent layer of endothelium. Our project will contribute to a better understanding of ECs behavior to their mechanical environment and to serve as a platform to test future arterial treatment strategies.

ACKNOWLEDGMENTS

We would like to thank Dr. Diego Alvarez of the Department of Pharmacology at University of South Alabama Collage of Medicine for providing endothelial cells and guidance and Mr. John Lyons and Mr. Terry Pritchett for technical support.

REFERENCES

- [1] J. Becherman, "Atherosclerosis and Coronary Artery Disease", Heart Disease Health Center, [Online]. Available: <http://www.webmd.com/heart-disease/atherosclerosis-and-coronary-artery-disease>. February, 2012. [2]
- [2] M. A. Punched, E. D. O'Cearbhail, J. N. Mackle, "Evaluation of Human Endothelial Cells Post Stent Deployment in a Cardiovascular Simulator *In Vitro*," Annual of Biomedical Engineering, Vol. 37, No.7, pp. 1322-1330, July, 2009.
- [3] S. Joshi. M. Girgus. "Atherosclerosis", American Heart association, [Online]. Available: http://www.heart.org/HEARTORG/Conditions/CholesterolWhyCholesterolMatters/AtherosclerosisUCM_305564_Article.jsp. 18. December, 2013.
- [4] M. A. Farcas, L. Rouleau, R.L. Leask, "The development of 3-D, *in vitro*, endothelial culture models for the study of coronary artery disease," Biomedical Engineering Online, October, 2009.
- [5] J. A. Lamack, H. A. Himburg, X. Li, M. H. Friedman, "Interaction of Wall Shear Stress Magnitude and Gradient in the Prediction of Arterial Macromolecular Permeability," Annual of Biomedical Engineering, Vol. 33, No.4, pp. 457-464, April, 2005.
- [6] S. K. Yazdani, J. L. Berry, "*In vitro* stent induced SMC proliferation," Department of Biomedical Engineering, Wake Forest University.

SYNTHESIS AND CHARACTERIZATION OF AN ELASTIN- LIKE-POLYPEPTIDE- POLYARGININE CONJUGATE FOR THREE-DIMENSIONAL CELL CULTURE

C. Andrew Weeks and Amol V. Janorkar*

Department of Biomedical Materials Science, School of Dentistry, University of Mississippi Medical Center,
2500 N. State St., Jackson, MS 39216

* Corresponding author (Email: ajanorkar@umc.edu; Phone: 1-601-984-6170; Fax: 1-601-984-6087)

ABSTRACT

We have synthesized an elastin-like-polypeptide-polyarginine (ELP-PA) conjugate to be used as coating material for cell culture. Following synthesis and isolation of ELP-PA, the material was chemically characterized by sodium dodecyl sulfate polyacrylamide gel electrophoresis (SDS-PAGE) and o- Pthalaldehyde (OPA) primary amine assay. We then created two coating materials by diluting the ELP- PA product with neat ELP to render a “low charge” ELP/ELP-PA blend and a “high charge” ELP/ELP- PA blend. The resulting materials were deposited as thin films atop tissue culture polystyrene (TCPS) surfaces. The hydrophobicities of these surfaces were measured using water contact angle goniometry. Surface topography of dry coatings was explored using atomic force microscopy (AFM). Surface texture under culture conditions was assessed by optical microscopy. Our data indicates that higher amine content lowers water contact angle and significantly affects surface topography of the resultant coating.

Key Words: Elastin-like polypeptide, chemical conjugation, surface characterization

INTRODUCTION

An improved *in vitro* hepatic cellular model is needed to study and treat liver diseases [1]. Elastin-like polypeptides (ELPs) are a class of genetically modified, *E.Coli*-generated polypeptides that have demonstrated promise as cell culture substrates [2-5]. Furthermore, a culture surface of hydrophobic ELP molecules conjugated with a polyelectrolyte (polyethyleneimine, PEI) has been shown to induce primary rat hepatocytes to self-arrange into 3D spheroidal aggregates [6]. Cells of these spheroids demonstrate increased production and cell function more closely aligned to that of *in vivo* hepatocytes compared to cells comprising a traditional monolayer morphology [6]. However, PEI is highly cytotoxic. Arginine-based polycations have been shown to have orders of magnitude higher general biocompatibility than PEI [7]. The objective of this research was to prepare and thoroughly characterize two charged ELP/ELP-PA blend coating materials that may be used for future cell culture studies. Our future studies will aim to elicit superior hepatocyte response using an ELP-PA conjugate coating surface.

MATERIALS AND METHODS

Chemical conjugation of ELP to PA: Expression and purification of ELP with a primary sequence of [VPGVG]₄₀, where G = glycine, P = proline, and V = valine, and a molecular weight of 17,00 Da has been described elsewhere [8]. ELP was conjugated to PA (molecular weight = 10,000 Da) by first dissolving ELP in 0.1 M MES buffer solution to create a 5 mg/mL solution. 10x molar excess (with respect to ELP) PA was then added. 10x molar excess 1-ethyl-3-[3-dimethylaminopropyl] carbodiimide hydrochloride (EDC) and N-Hydroxysuccinimide (NHS) were added to activate the carboxyl group of ELP to facilitate the formation of a peptide bond between ELP and PA (Figure 1). The mixture was titrated to a pH of 6.5 and left to react overnight under gentle rotation at 4 C. NaCl was then added to make a 5 M NaCl solution. This was heated to 40 C (above ELP's inverse transition temperature), causing ELP and ELP-PA to precipitate from solution. Precipitated ELP and ELP-PA was removed via centrifugation, resuspended in DI water, and dialyzed against DI.

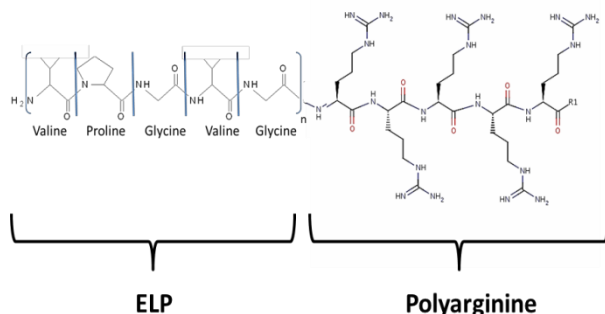


Figure 1. Representation of ELP-PA conjugate Overnight.

SDS-PAGE: Aqueous solutions of ELP and ELP/ELP-PA blend were mixed with SDS detergent, heated to 95 °C for 5 minutes, and placed at the top of equivalent separate lanes of a 20% polyacrylamide gel (Lonza). Gels were subjected to a -150 V electric potential for 75 minutes and stained with a copper stain solution.

OPA assay: When o-Phthalaldehyde (OPA) bonds to primary amine groups within an aqueous solution it gains the ability to fluoresce. We placed 20 μL of a 5 mg/mL solution of reaction product (ELP-PA and unreacted ELP) and neat ELP within separate wells of a 96 well plate and added 200 μL of OPA solution. By comparing the intensity of amine-bound OPA in ELP/ELP-PA solutions with that of neat ELP at excitation/emission of 360/460, we qualitatively assessed the amine:mass ratio of our ELP-PA product. This fluorescence intensity guided the dilution of the ELP-PA with neat ELP to create both a low charge ELP/ELP-PA blend and a high charge ELP/ELP-PA blend.

Coating: Coating materials were applied to 100 mm tissue culture polystyrene (TCPS) dish surfaces. 30 L of 5 mg/mL aqueous solutions of each material was carefully placed onto a section of TCPS surface. This solution was allowed dry overnight under ambient conditions, rendering a 0.5 mg/cm² circular film having a 6 mm diameter.

Goniometry: Using a pipette mounted on a support apparatus (to provide experimental consistency), we placed a 5 L drop of 5 M NaCl aqueous solution on the coating surface. The contact angle was recorded 10 seconds after placing the drop by a ramé-hart 100 contact angle goniometer.

AFM: Atomic force microscopy was performed with a Bioscope Catalyst AFM in ScanAssyst mode at a rate of 0.5 Hz and resolution of 512 samples per line. The topography of a 100 m x 100 m section of each coating was mapped in dry air with a silicon nitride cantilever tip.

Optical microscopy: Surface topography under culture conditions was assessed by taking images of coating films at 400x with an optical microscope 1 hour after addition of Dulbecco's modified Eagle's medium (DMEM) supplemented with 10% fetal bovine serum (FBS) and antibiotics.

Statistical analysis: All experiments were performed in triplicate and reported as mean \pm 95% confidence intervals. Statistical evaluation was performed with ANOVA and Games Howell post hoc analysis procedure for unequal variances. Values with $p \leq 0.05$ were deemed significantly different.

RESULTS

SDS-PAGE (Figure 2) revealed the molecular weights of the ELP-PA reaction products. Comparing the reaction product in the third lane with the protein ladder in the first lane and neat ELP in the second lane, unreacted ELP at 17,000 Da and the ELP-PA conjugate at 27,000 Da were noted. Fluorescence intensities of the two ELP/ELP-PA blends are shown in Figure 3. The fluorescence intensity of the high charge blend is over 3 times that of the low charge blend due to additional OPA binding with amines of PA. AFM surface analysis revealed intricate patterns formed by the charged material during solvent evaporation and coating deposition. Linear and circular depression patterns observed in the surfaces

were believed to develop as ELP and ELP-PA molecules likely phase segregated during the drying process (Figure 4). We surmise that the conjugated (hydrophilic) ELP-PA precipitated later from solution compared to the hydrophobic ELP molecules and could be disproportionately present near the walls of the pictured surface pits. Optical microscopy of the coatings in culture conditions showed that surface morphology changed significantly over the course of an hour and appeared to be dependent on ELP-PA content. In the future, we will investigate if and how such changes in surface morphology affect cell movement throughout cell culture. Goniometry measurements showed a statistically significant difference in water contact angle between the two ELP/ELP-PA blends (Figure 6). The high charged blend has a much lower water contact angle compared to that of the low charge material.

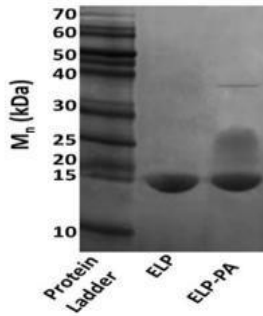


Figure 2. SDS-PAGE gel of ELP-PA

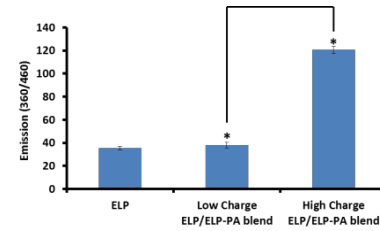


Figure 3. OPA fluorescence of ELP and ELP/ELP-PA blends indicating primary amine content. * denotes statistically distinct ($p < 0.05$) results.

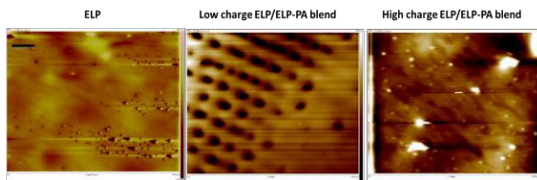


Figure 4. 100 μm x 100 μm AFM height images of coating surfaces. Scale bar: 10 μm .

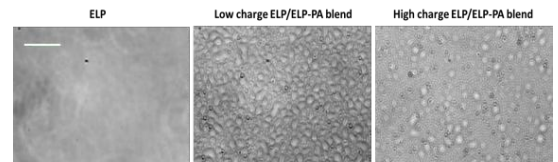


Figure 5. 400x micrographs of culture surfaces one hour after addition of culture

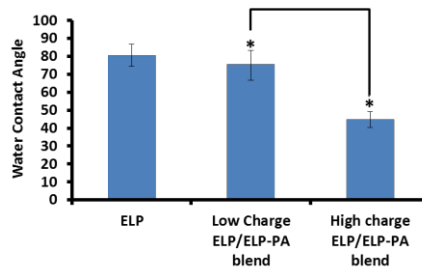


Figure 6. Water contact angle of ELP/ELP-PA films. * denotes statistically distinct ($p < 0.05$) results.

We successfully created an ELP-PA conjugate for future use as a more biocompatible hepatocyte culture surface than ELP-polyethyleneimine. SDS-PAGE analysis showed a light but clearly present conjugated product and no unreacted polyarginine. AFM and optical microscopy suggest significant topological and material distribution

differences between the three coatings, and we hypothesize that these differences will significantly affect cell movement and performance. The high charge ELP/ELP-PA blend surface had a statistically significant lower water contact angle than the low charge ELP/ELP-PA blend surface. This suggests that amine groups from the PA are more prevalent at the surface of high charge ELP/ELP- PA blend, protonating the surface and increasing its hydrophilicity overall.

CONCLUSIONS

Two ELP/ELP-PA blends were synthesized. The higher amine content of the high charge ELP/ELP-PA surface made a more hydrophilic and resulted in a lower water contact angle than that of the low charge ELP/ELP-PA blend. Surface topography given by AFM suggests separation of charged and uncharged portions of the materials during coating deposition. We hope to ultimately correlate coating properties with performance of hepatocytes spheroidal aggregates grown atop the ELP-PA surfaces.

ACKNOWLEDGEMENTS

Financial support from the National Science Foundation (NSF Award No. 1033525) is gratefully acknowledged. This work made use of instruments in the Department of Biomedical Materials Science User Facility.

REFERENCES

- [1] Xia L, Sakban RB, Qu Y, Hong X, Zhang W, Nugraha B, et al. Tethered spheroids as an *in vitro* hepatocyte model for drug safety screening. *Biomaterials* 2012;33:2165-76.
- [2] Shang Y, Yan Y, Hou X. Stimuli responsive elastin-like polypeptides and applications in medicine and biotechnology. *Journal of Biomaterials Science, Polymer Edition* 2014;25:101-20.
- [3] Turner PA, Harris LM, Purser CA, Baker RC, Janorkar AV. A surface-tethered spheroid model for functional evaluation of 3T3-L1 adipocytes. *Biotechnology and bioengineering* 2014;111:174-83.
- [4] Turner PA, Weeks CA, McMurphy AJ, Janorkar AV. Spheroid organization kinetics of H35 rat hepatoma model cell system on elastin-like polypeptide-polyethyleneimine copolymer substrates. *Journal of Biomedical Materials Research - Part A* 2014;102:852-61.
- [5] Wheeler TS, Sbravati ND, Janorkar AV. Mechanical & cell culture properties of elastin-like polypeptide, collagen, bioglass, and carbon nanosphere composites. *Annals of biomedical engineering* 2013;41:2042-55.
- [6] Janorkar AV, Rajagopalan P, Yarmush ML, Megeed Z. The use of elastin-like polypeptide- polyelectrolyte complexes to control hepatocyte morphology and function *in vitro*. *Biomaterials* 2008;29:625-32.
- [7] Zern BJ, Chu H, Osunkoya AO, Gao J, Wang Y. A biocompatible arginine-based polycation. *Advanced Functional Materials* 2011;21:434-40.
- [8] Wu Y, Mackay JA, McDaniel JR, Chilkoti A, Clark RL. Fabrication of elastin-like polypeptide nanoparticles for drug delivery by electrospraying. *Biomacromolecules* 2009;10:19-24.

THE CORRELATION BETWEEN NEOVASCULARIZATION AND MACROPHAGE POPULATIONS UNDER THE INFLUENCE OF ANDROGENS

Kenneth R. Butler, PhD, Hamed A. Benghuzzi, PhD, Michelle Tucci, PhD, Aaron D. Puckett, PhD
University of Mississippi Medical Center
Jackson, Mississippi—USA

ABSTRACT

Macrophages and blood vessels are critical components in the biocompatibility and functionality of implantable ceramic materials used in drug delivery applications. As part of the chronic inflammatory response, macrophages surround the implant, establishing the tissue-implant interface and produce cytokines critical for recruitment of other complementary cells involved in the response. Neovascularity also occurs and allows more direct access of cells and support in the tissue-implant response. The purpose of this study was to examine the correlation of macrophage and neovascularization by further defining their presence and relationship in the fibrous tissue capsule of calcium phosphate (TCP) ceramic drug delivery systems. Sixteen animals in four experimental groups were implanted with one TCP bioceramic each. Group I animals were implanted with a sham TCP ceramic not containing a steroid hormone (control group). Group II animals received the testosterone loaded TCP ceramic. Group III animals were implanted with the dihydrotestosterone loaded ceramic. Group IV animals received the androstenedione ceramic. At 90 days post-implantation, the implants and fibrous tissue capsules were extracted. Determination of macrophage populations and neovascularity was conducted microscopically following H&E staining and aided by ImagePro digital analysis software. Overall, macrophage counts were highly and significantly correlated with vascularity ($p < 0.05$). In individual group analysis, macrophages and vascularity in Groups II, III, and IV were highly correlated, while correlations for Group I was not statistically significant. These findings suggest that presence of macrophages is be directly related to neovascularity.

Keywords: androgens, angiogenesis, neovascularity, macrophage, tissue-implant response, intraperitoneal, correlation

INTRODUCTION

Previous studies in our laboratory have quantified the tissue implant response surrounding tricalcium phosphate (TCP) bioceramic implants and have demonstrated how this response may be modified in the presence of androgens [1-3]. Subsequent studies revealed the extent to which androgens modify the tissue-implant response with respect to the presence of macrophages and neovascularization [4, 5]. To date, there is little data elucidating the relationship between vascularity and macrophages in the fibrous tissue capsule surrounding TCP bioceramic implants. The purpose of this study was to examine the relationship between macrophages and neovascularization in the fibrous tissue capsule surrounding TCP implants loaded with three androgenic hormones. We hypothesized that low levels of neovascularization would be reflected in low macrophage counts.

METHODS

Sixteen Sprague-Dawley male albino rats weighing 280-300g were obtained (Holtz Company, Madison, WI), acclimatized in the animal care facility for two weeks prior to surgery, and randomly divided into three experimental groups ($n=4$ /group) and 1 control group ($n=4$). The tricalcium-phosphate bioceramic implants were prepared according to standard laboratory protocol [1, 3-5]. Surgery on all animals was performed according to a standard laboratory protocol reviewed and approved by the University of Mississippi Medical Center Animal Care and Use Committee and has been described previously [1, 3-5]. Animals in Group I were designated for the implantation of the sham TCP ceramics (control), animals in Group II were designated for T-TCP (testosterone) implantation, animals in Group III were selected for the implantation of the D-TCP (dihydrotestosterone) ceramic devices, and animals designated in Group IV were implanted with the A-TCP (androstenedione) ceramic. All animals in this investigation were kept on a 12-hour day/night cycle and were fed Purina Rodent Chow 5001 (Ralston Purina, St. Louis, MO) and water *ad libitum*.

The TCP ceramic implants and their fibrous capsules were collected, observed grossly, photographed, and fixed in 10% neutral buffered formalin at 90 days post-implantation. Processing of these tissues included infiltration with paraffin and routine histologic processing.

Three inch glass microscope slides were coated with chrome-alum adhesive to aid in the tissue attachment to the glass slide [3]. Three to five sections were cut at 5 μm and mounted onto glass slides every 25 μm throughout the entire depth of the fibrous tissue mounted in the paraffin blocks.

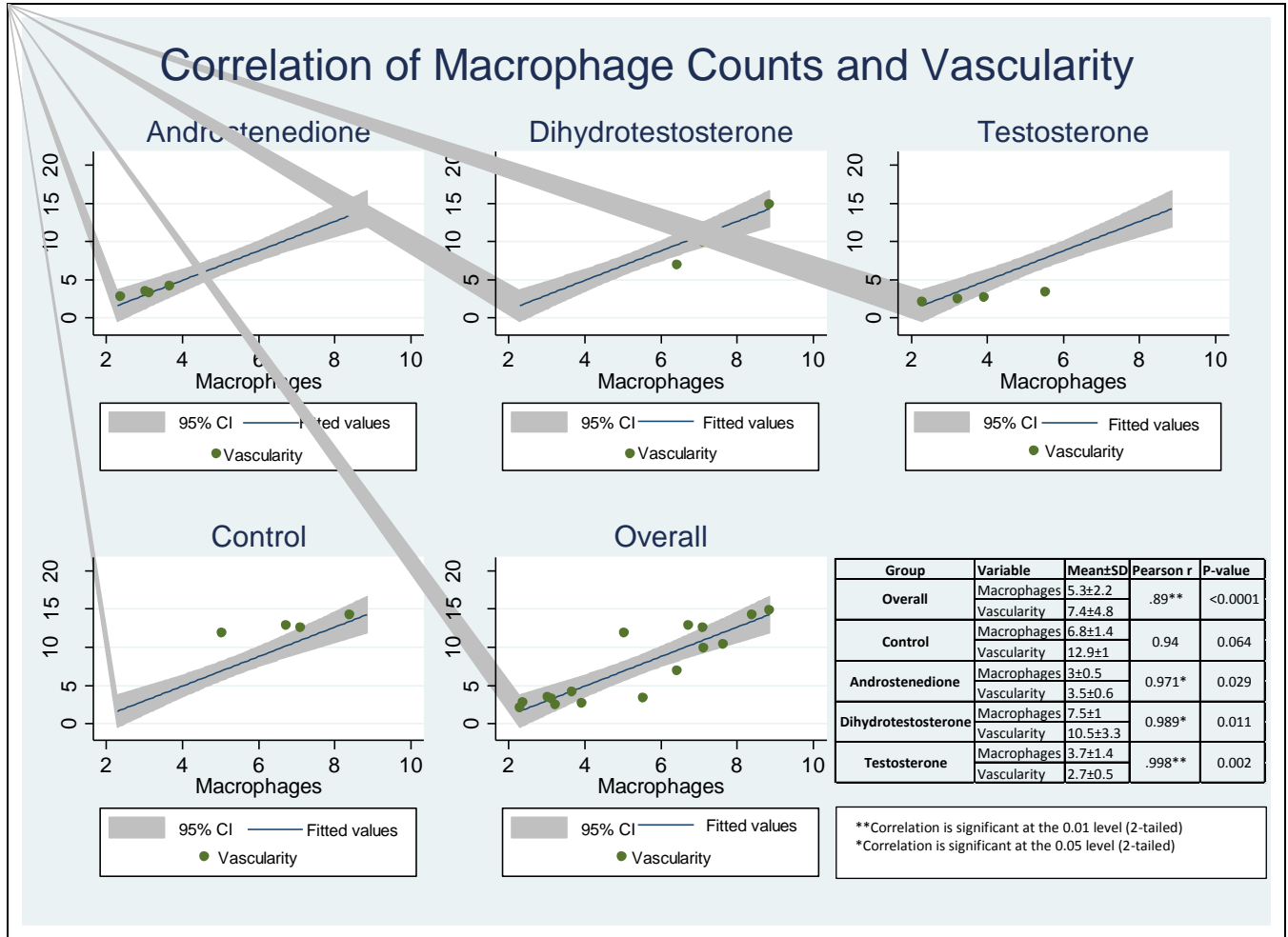
Tissues were stained with hematoxylin and eosin (H&E), Masson's trichrome, and Papanicolaou stains. Histologic sections prepared from the tissue directly surrounding the implants were evaluated using the light microscope and Image Pro Plus digital analysis software (Media Cybernetics, Silver Spring, MD) on captured images [3]. Blood vessels in the fibrous tissue capsule were quantified by counting numbers of vessels per high power field (HPF) with the assistance of the digital analysis software using a semi-automated method [3, 5]. Macrophages were identified based on cellular morphology and imaging characteristics and reported as the number of cells/HPF [4]. To minimize bias and variability, a minimum of 10 fields per slide were randomly examined throughout the depth of the tissue capsule on 125 randomly selected slides per animal to thoroughly examine the depth of the tissue.

Statistical analysis was conducted using Stata version 12 statistical software (StataCorp, College Station, TX). Quantification of neovascularity and macrophage counts throughout the different layers of fibrous tissue were expressed as mean \pm sd. The number of blood vessels and macrophages in each group were compared using Pearson's correlation coefficient (Pearson r , $\alpha=0.05$).

RESULTS

Upon extraction of the implants from the peritoneal cavity, multiple stains revealed fibrous tissue of varying degrees of thickness for all four groups. Morphometric analysis revealed both macrophages and vascularity were highly variable among the four groups (Figure). The control group had the highest number of blood vessels/HPF, while Group III had the highest number of macrophages. The statistical analysis revealed macrophages and vascularity were highly and significantly correlated in each of the three experimental groups. The most interesting finding was the correlation of macrophages and vascularity in the control group. Analysis revealed these counts were highly correlated, but this group failed to demonstrate statistical significance ($r=0.94$, $p=0.064$). The number of blood vessels/HPF was two times higher compared to the number of macrophages/HPF. In the experimental groups, the number of macrophages/HPF more closely mirrored the number of blood vessels/HPF. To better demonstrate the positive linear relationship, the number of macrophages/HPF was plotted against the number of blood vessels/HPD for each of the four groups and a composite where data were combined. Overall, macrophages and vascularity were highly correlated when tested together as a composite ($r=0.89$, $p<0.0001$). The data suggest that although androgenic hormones tend to suppress vascularity, vascularity was highly correlated to macrophage counts in all treatment groups. Correlation in the control group was not statistically significant, providing evidence that androgenic hormones may strongly influence neovascularization.

Figure 1 shows the correlation of macrophage counts and vascularity (y-axis) in fibrous tissue surrounding TCP ceramic implants loaded with testosterone, dihydrotestosterone, androstenedione, and control. Overall, macrophages and vascularity were highly correlated when tested together as a composite. Though androgenic hormones tend to suppress vascularity, vascularity was highly correlated to macrophage counts in all treatment groups. Correlation in the control group was not statistically significant.



DISCUSSION

In this investigation, we demonstrated macrophage counts and vascularity to be highly and significantly correlated in all three experimental groups treated with androgenic hormones. In the control group, though highly correlated, statistical significance was not obtained. This was a surprising finding indicating certain androgens, particularly testosterone and androstenedione, appear to have more of an effect on blood vessel development compared to dihydrotestosterone. Previous investigations support these findings [3-5].

Dihydrotestosterone and androstenedione appeared to inhibit macrophage migration and attraction to the implant compared to testosterone and control. This could be advantageous in extending the life of the implant. Fewer macrophages at the tissue implant interface could reduce the amount of degradative enzymes and other reactive oxygen intermediates as they act to dissolve the implant [4]. Likewise, the reduced vascularity observed in the testosterone treated group was unexpected. Previous reports indicated the testosterone treated groups demonstrated fewer blood vessels/HPF, but the blood vessels present had greater diameter compared to control helping to sustain macrophage counts [5].

The strengths of this study include the use of digital analysis software to aid in data collection, the care taken to treat all animals in exactly the same manner, and the use of genetically related animals to minimize variation. This study is not without limitations. Previous experiments have demonstrated as few as three animals per group were adequate to determine significant differences among groups [2, 6-8]. While the number of animals per group was low, the number of observations per slide per animal was high to further minimize variability. Another limitation concerns the use of morphometry to identify the number macrophages and blood vessels/HPF. In

doing so, without immunohistochemical staining, we may underestimate the number of proliferating or budding vessels or macrophages [9]. However, this is not a major concern since the histomorphometric evaluation occurred 90-days post-implantation allowing the tissue-implant response to fully stabilize.

CONCLUSIONS

The findings from this study demonstrate that macrophage populations and vascularity are highly correlated. The number of macrophages present in the tissue-implant response appears to be directly proportional to the number of blood vessels per high power field. These findings suggest macrophages participating in the tissue implant response are dependent on the vascularity of the fibrous tissue capsule surrounding the implants. This information could be advantageous as sustained release technologies are further enhanced for potential use in humans.

ACKNOWLEDGMENTS

The authors thank Ms. Gerri Wilson and Ms. Lisa McCammon, from the Department of Orthopedic Surgery and Rehabilitation for their technical and administrative support.

REFERENCES

- [1] K. Butler, H. Benghuzzi, P. Bajpai, A. Puckett, M. Tucci, Z. Cason, and B. England, "One year histopathological evaluation of fibrous tissue surrounding TCPL implants using adult rats as a model," *Biomed Sci Instrum*, vol. 33, pp. 233-9, 1997.
- [2] K. Butler, A. Puckett, and H. Benghuzzi, "Quantitative analysis of the cellular components of the fibrous tissue matrix surrounding ALCAP, HA, and TCP bioceramics using adult male rats as a model," *Biomed Sci Instrum*, vol. 35, pp. 267-72, 1999.
- [3] K. R. Butler, Jr. and H. A. Benghuzzi, "Morphometric analysis of the hormonal effect on tissue-implant response associated with TCP bioceramic implants," *Biomed Sci Instrum*, vol. 39, pp. 535-40, 2003.
- [4] K. R. Butler, Jr., H. Benghuzzi, M. Tucci, and A. Puckett, "Androgen administration and macrophage behavior in the tissue-implant response - biomed 2011," *Biomed Sci Instrum*, vol. 47, pp. 228-33, 2011.
- [5] K. R. Butler, H. Benghuzzi, M. Tucci, and A. Puckett, "Neovascularization is influenced by androgenic hormones in the tissue implant response," *Biomed Sci Instrum*, vol. 48, pp. 49-56, 2012.
- [6] K. Butler, H. Benghuzzi, and A. Puckett, "Cytological evaluation of the tissue-implant reaction associated with S/C and I/P implantation of ALCAP and HA bioceramics in vivo," *Pathol Res Pract*, vol. 197, pp. 29-39, 2001.
- [7] K. Butler, H. Benghuzzi, M. Tucci, and Z. Cason, "A comparison of fibrous tissue formation surrounding intraperitoneal and subcutaneous implantation of ALCAP, HA, and TCP ceramic devices," *Biomed Sci Instrum*, vol. 34, pp. 18-23, 1997.
- [8] K. R. Butler, H. A. Benghuzzi, and A. Puckett, "Morphometric evaluation of tissue-implant reaction associated with ALCAP and TCP bioceramics in vivo," *J Invest Surg*, vol. 14, pp. 139-52, May-Jun 2001.
- [9] S. Henno, J. C. Lambotte, D. Glez, M. Guigand, G. Lancien, and G. Cathelineau, "Characterisation and quantification of angiogenesis in beta-tricalcium phosphate implants by immunohistochemistry and transmission electron microscopy," *Biomaterials*, vol. 24, pp. 3173-81, Aug 2003.

INTERCELLULAR SIGNALING BY CYCLIC AMP-CONTAINING MICROPARTICLES.

Scruggs AK¹, Sayner SL², Bauer N¹, and Rich TC¹.

¹Departments of Pharmacology, ² Cell Biology and Neuroscience, and the ^{1,2} Center for Lung Biology, Colleges of Medicine and Engineering, University of South Alabama, Mobile AL 36688.

ABSTRACT

Microparticles (MPs) are extracellular vesicles 0.1 to 1 μm in diameter that are released from many cell types under physiological and pathophysiological conditions. Endothelial-derived MPs are found circulating in blood and communicate with downstream target cells in a paracrine fashion. MPs contain a variety of functional protein and RNA that are likely to contribute to the information content delivered to target cells by MPs. The Bauer and Sayner laboratories recently determined that cyclic adenosine monophosphate (cAMP), a ubiquitous second messenger, is found in MPs from pulmonary microvascular endothelial cells (PMVECs); ongoing studies suggest that MPs isolated from PMVECs treated with β adrenergic agonists have increased cAMP levels. We developed mathematical models of MP-target cell interactions in order to better understand how cAMP and enzymes in the cAMP signaling pathway delivered by MPs may alter target cell signaling. Simulations indicate that if cAMP contained in one MP were released into a near-membrane compartment of a target cell, cAMP levels within that compartment would be sufficient to activate protein kinase A for several minutes. However, if cAMP were released into the larger volume of the bulk cytoplasm it would have little or no effect on target cell function. These data indicate that a single MP may deliver cAMP payloads sufficient to trigger sustained responses in a target cell and may contribute to MP-mediated signaling events.

Keywords: microparticles, cAMP, PKA, pulmonary microvascular endothelial cells

INTRODUCTION

Microparticles (MPs) are submicron vesicles released into the extracellular environment. Endothelial-derived MPs circulate in the bloodstream and their number increases in pathological states involving vascular injury or inflammation. MPs contain proteins, microRNA, and mRNA, and are a novel form of intercellular communication [1]. MPs alter target cell function, for example, MPs isolated from diabetic patients have pro-thrombotic effects on target cells [2]. Recent studies demonstrated that MPs from pulmonary microvascular cells (PMVECs) contain cAMP, a ubiquitous second messenger that regulates a wide variety of cell functions [3]. This observation suggests that MPs initiate signaling events via the cAMP signaling pathway. To test the plausibility of this hypothesis we developed simple mathematical models describing the kinetics and subcellular distribution of cAMP signals. cAMP was either assumed to be released and rapidly distributed throughout the cytosol, or cAMP was assumed to be released into a near-membrane compartment in which it rapidly equilibrated and subsequent flux into the cytosol was slow. Models simulated effects of MP-mediated cAMP release into target cells and assessed the ability of this exogenous cAMP signal to trigger cellular responses.

METHODS

Cell Culture. Rat PMVECs were provided by the cell culture core of the Center for Lung Biology, University of South Alabama. Cells were grown to confluence on 150mm culture dishes and maintained in DMEM supplemented with 10% FBS, 100 $\mu\text{g}/\text{ml}$ streptomycin, and 100 U/ml penicillin, pH 7.4, at 37°C, in a humidified atmosphere of 95% air and 5% CO₂, as described previously [4].

Microparticle Collection. PMVECs were treated with 10 μM rolipram and 1 μM isoproterenol or vehicle control prior to isolation of MPs. Media from three confluent 150mm culture dishes was combined and subjected to serial centrifugation (1000 x g for 10 min and 100,000 x g for 45 min) to isolate MPs. MPs were resuspended in 0.5 mL of lysis buffer. cAMP was measured with radioimmunoassays [4]. cAMP levels were normalized to total protein levels.

Model Description. We developed models that describe the time course of MP-induced cAMP signals in PMVECs. These models included basal cAMP production, cAMP hydrolysis, and the two compartment model included a simplified description of the spatial spread of cAMP signals. The two models considered were a model in which the cAMP levels rapidly equilibrate within PMVECs (Fig. 1A); and a model in which cAMP levels near the plasma membrane readily equilibrate, but the flux between the near-membrane compartment (C1) and the bulk cytosol (C2) is markedly hindered (Fig. 1B). Realistic rates of cAMP turnover and diffusion between compartments were

estimated from previous studies [5, 6]. Mathematical descriptions of MP-target cell interactions were coded in the MATLAB programming environment using the Runge Kutta solver. Equations are described below.

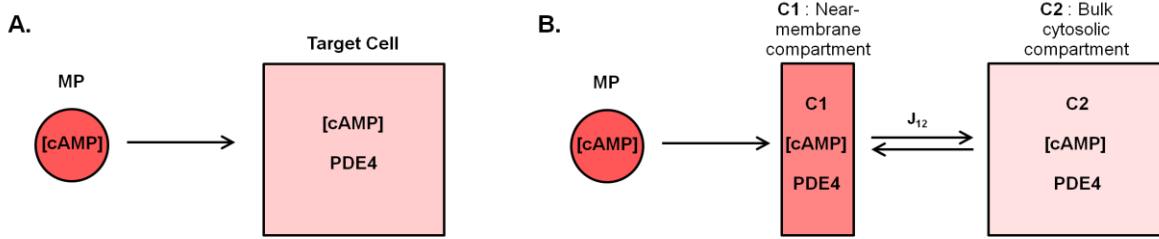


Figure 1. Compartmentalized cell model used to evaluate the potential of cAMP contained within a MP to trigger responses in target cells. (A) One compartment model: MP-mediated delivery of cAMP to the bulk cytosol of the target cell. (B) Two compartment model: MP-mediated delivery of cAMP to near-membrane compartment within the target cell. C1, near-membrane microdomain within the target cell; C2, bulk cytosol of the target cell; MP, microparticle; PDE4, type 4 phosphodiesterase; J_{12} , cAMP diffusion flux between compartments C1 and C2.

One Compartment Model:

$$\frac{d[\text{cAMP}]}{dt} = \frac{AC_{\text{basal}} - E_{\text{PDE}}}{V} \quad (1)$$

$$E = \frac{V_{\text{max}} * [\text{cAMP}]}{[\text{cAMP}] + K_m * \left(1 + \frac{[I]}{K_I}\right)} \quad (2)$$

Two Compartment Model:

$$\frac{d[\text{cAMP}]_{\text{C1}}}{dt} = \frac{AC_{\text{basal}} - E_{\text{PDE-C1}} - k_1 * [\text{cAMP}]_{\text{C1}} + k_2 * [\text{cAMP}]_{\text{C2}}}{V_1} \quad (3)$$

$$\frac{d[\text{cAMP}]_{\text{C2}}}{dt} = \frac{-E_{\text{PDE-C2}} + k_1 * [\text{cAMP}]_{\text{C1}} - k_2 * [\text{cAMP}]_{\text{C2}}}{V_2} \quad (4)$$

$$E_{\text{PDE-C1}} = \frac{V_{\text{max1}} * [\text{cAMP}]_{\text{C1}}}{[\text{cAMP}]_{\text{C1}} + K_{m1} * \left(1 + \frac{[I]}{K_I}\right)} \quad (5)$$

$$E_{\text{PDE-C2}} = \frac{V_{\text{max2}} * [\text{cAMP}]_{\text{C2}}}{[\text{cAMP}]_{\text{C2}} + K_{m2} * \left(1 + \frac{[I]}{K_I}\right)} \quad (6)$$

where, $[\text{cAMP}]_{\text{C1}}$ and $[\text{cAMP}]_{\text{C2}}$ are the cAMP concentrations in compartments 1 and 2, AC_{basal} is basal adenylyl cyclase activity (cAMP synthesis), V_{max} is the maximal rate of cAMP hydrolysis by PDE, K_{m1} is the Michaelis constant for PDE activity, $[I]$ is the concentration of PDE inhibitor, K_I is the inhibitor dissociation constant, k_1 and k_2 are the cAMP flux coefficients between C1 and C2, and V_1 and V_2 are the volumes of C1 and C2. Parameters used in the one and two compartment models were adapted from [5, 6] and references therein. Parameters for the two compartment model: $V = 4$ pL, $V_{\text{max}} = 0.415$ $\mu\text{M/s}$, $K_m = 2$ μM , and $AC_{\text{basal}} = 1.25 * 10^{-2}$ $\mu\text{M/s}$. Parameters for the one compartment model: $V_1 = 0.04$ pL, $V_2 = 4$ pL, $k_1 = 1.4 * 10^{-16}$ L/s, $k_2 = 1.4 * 10^{-16}$ L/s, $V_{\text{max1}} = 0.415$ $\mu\text{M/s}$, $V_{\text{max2}} = 0.415$ $\mu\text{M/s}$, $K_{m1} = 2$ μM , $K_{m2} = 2$ μM , $K_I = 0.1$ μM , and $AC_{\text{basal}} = 1.25 * 10^{-2}$ $\mu\text{M/s}$. Inhibitor concentration was either 0 or 3 μM , as indicated. Release of cAMP from MPs into target cells was assumed to occur instantaneously.

RESULTS

We first evaluated the cAMP content of MPs released from PMVECs. We observed that MPs released from PMVECs did contain cAMP, similar to previous reports [3]. We next observed that MPs released from PMVECs pretreated with 10 μM isoproterenol (a β -adrenergic agonist) and 10 μM rolipram (a PDE4 inhibitor) had markedly elevated cAMP levels (Bauer and Sayner, data not shown). We first sought to assess the ability of MP-mediated increases in cytosolic cAMP levels to activate downstream cAMP effectors using a one compartment model.

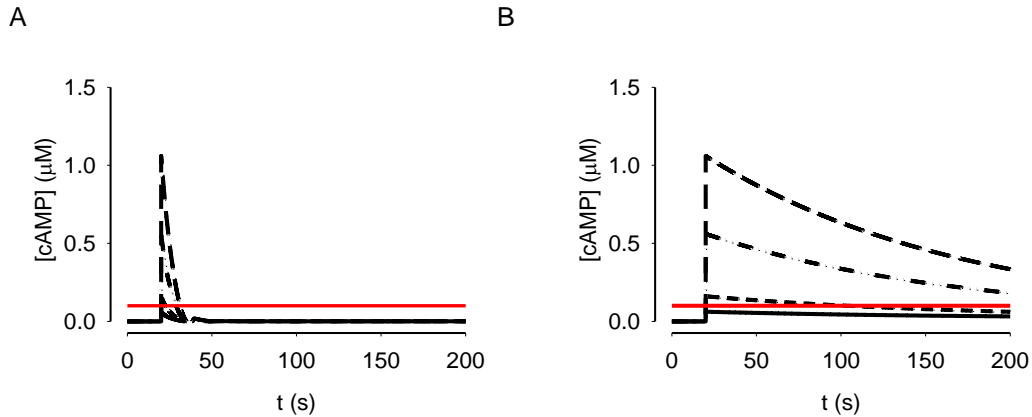


Figure 2. Simulated cellular cAMP levels after delivery of the contents of a single MP (at 20 s) to a target cell. cAMP concentrations contained within MPs: solid line, 1 μM ; dotted line, 10 μM ; short dash 100 μM ; dash-dot-dash, 500 μM , and long dash, 1,000 μM . The cAMP concentration that elicits half maximal activation of high affinity effectors ($EC_{50} = 0.1 \mu\text{M}$) are indicated by red lines. (A) MPs cause transient increases in cAMP concentration that are sufficient to activate high affinity cAMP effectors. (B) MPs trigger sustained increases in cAMP levels in the presence of PDE inhibitors.

The release of cAMP from a single MP-mediated transient increases cAMP levels in the cytosol of target cells (Fig. 2A). Transient cAMP responses elicited by MPs containing cAMP levels $\geq 100 \mu\text{M}$ was sufficient to briefly activate the primary cAMP effectors, PKA type 1 ($EC_{50} \sim 100 \text{ nM}$, red line) and PKA type 2 ($EC_{50} \sim 200 \text{ nM}$), but would have little or no effect on lower affinity effectors including CNG channels and EPAC ($EC_{50} \geq 1 \mu\text{M}$). Simulations in which PDE activity (cAMP hydrolysis) was inhibited, a typical experimental protocol, revealed a sustained increase in cAMP levels that would be sufficient to activate PKA (Fig. 2B).

We next simulated the ability of MP-mediated cAMP signals to elicit responses in the subplasmalemmal region of PMVECs using a two compartment model. Simulations indicated that a single MP with as little as 10 μM cAMP was sufficient to transiently activate PKA (Fig. 3A, red line). MPs containing higher cAMP concentrations were sufficient to activate lower affinity cAMP effectors (green line). Simulations indicated that under these conditions little or no activation of cytosolic effectors would occur (Fig 3B). Inhibition of PDE activity contributed to more sustained cAMP responses in both subcellular compartments (Fig. 3C, D).

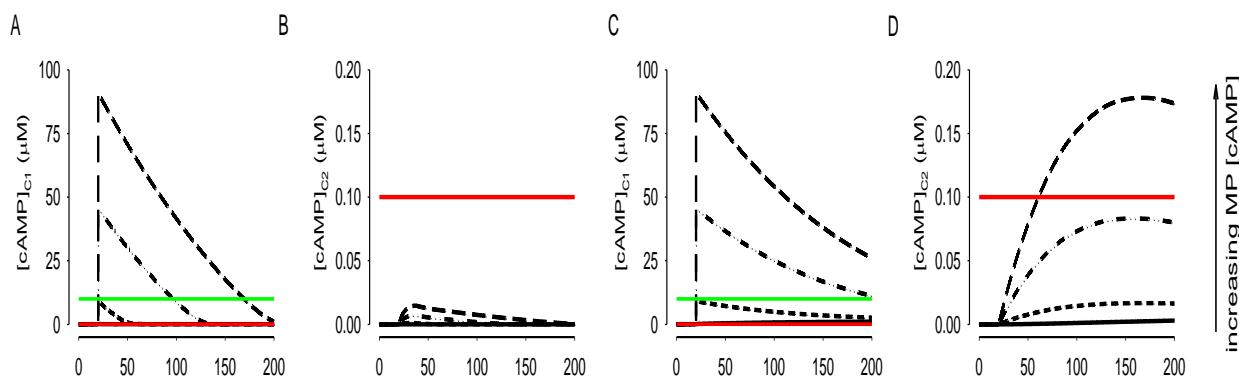


Figure 3. Simulated cAMP levels after delivery of the contents from a single MP (20 s) to a target endothelial cell. cAMP concentrations in MPs are as follows: solid line, 1 μM ; dotted line, 10 μM ; short dash 100 μM ; dash-dot-dash, 500 μM ; and long dash, 1 mM. cAMP concentrations that elicit half maximal activation of high affinity effectors ($EC_{50} = 0.1 \mu\text{M}$) are indicated by red lines, and concentrations that elicit half maximal activation of low affinity effectors ($EC_{50} = 10 \mu\text{M}$) are indicated by green lines. (A) MPs containing $\geq 500 \mu\text{M}$ cAMP caused sustained cAMP levels in C1 sufficient to activate known effectors. (B) MPs trigger small increases in cAMP levels in C2 that were not sufficient to activate effectors. (C, D) Simulations indicate that the rate of decay of cAMP signals in C1 (C) and C2 (D) are reduced by PDE inhibitors.

DISCUSSION

The simulations presented here indicate that MP-mediated increases in cAMP are insufficient to substantially activate downstream effectors within the cytosol of PMVECs. MP-mediated increases in cAMP levels in the near-membrane compartment of target cells is sufficient to activate known cAMP effectors. Inhibition of PDE activity slowed the decay in cAMP signals but had little effect on peak cAMP levels. MPs that contained $\geq 500 \mu\text{M}$ cAMP caused increases in cAMP levels sufficient to activate high and low affinity effectors in the near-membrane compartment of target cells. High cAMP concentrations may occur in MPs that contain adenylyl cyclase. In the future it will be interesting to examine potential roles of MP-mediated transfer of other proteins in the cAMP signaling pathway.

CONCLUSIONS

The simulations presented here indicate that MP-mediated increases in target cell cAMP levels are sufficient to activate downstream effectors in localized compartments of target cells.

ACKNOWLEDGMENTS

This work was supported by NIH awards P01H066299, R03H110828 and AHA awards 11GRNT7430039, 11SDG7390037.

REFERENCES

- [1] L. A. Hargett and N. N. Bauer, "On the origin of microparticles: From "platelet dust" to mediators of intercellular communication," *Pulm. Circ.*, vol. 3, pp. 329-340, 2013.
- [2] A. D. Terrisse, N. Puech, S. Allart, P. Gourdy, J. M. Xuereb, B. Payrastre, and P. Sié, "Internalization of microparticles by endothelial cells promotes platelet/endothelial cell interaction under flow," *J. Thromb. Haemost.*, vol. 8, pp. 2810-2819, 2010.
- [3] L. A. Hargett, L. Brown, S. Sayner, and N. Bauer, "Microparticles from pulmonary microvascular endothelial cells contain cyclic adenosine monophosphate," *Am. J. Respir. Crit. Care Med.*, vol. 185, pp. A4819, 2012.

- [4] S. L. Sayner, M. Alexeyev, C. W. Dessauer, and T. Stevens, "Soluble adenylyl cyclase reveals the significance of cAMP compartmentation on pulmonary microvascular endothelial cell barrier," *Circ. Res.*, vol. 98, pp. 675- 681, 2006.
- [5] T. C. Rich, K. A. Fagan, T. E. Tse, J. Schaack, D. M. F. Cooper, and J. W. Karpen, "A uniform extracellular stimulus triggers distinct cAMP signals in different compartments of a simple cell," *Proc. Natl. Acad. Sci. USA*, vol. 98, pp. 13049-13054, 2001.
- [6] W. P. Feinstein, B. Zhu, S. J. Leavesley, S. L. Sayner, and T. C. Rich, "Assessment of cellular mechanisms contributing to cAMP compartmentalization in pulmonary microvascular endothelial cells," *Am. J. Physiol. Cell Physiol.*, vol. 302, pp. C839-C852, 2012.

A QUANTITATIVE EVALUATION OF FRET-BASED cAMP MEASUREMENTS

Kristal J. Webb¹, Silas J. Leavesley^{2,3}, Thomas C. Rich^{1,3}

¹Center for Lung Biology and Departments of ²Chemical Engineering and ³Pharmacology
Colleges of Medicine and Engineering, University of South Alabama, Mobile, Alabama, 36688

ABSTRACT

In the last decade, several probes for measuring cyclic nucleotide signals in single cells have been developed. However, few studies have attempted to evaluate the ability of these probes to discern mechanisms of signaling specificity. Thus, we developed mathematical descriptions of cyclic nucleotide–probe interactions to assess the strengths and weaknesses of these probes for measurement of cyclic nucleotide signals. Our simulations indicate that care must be taken when interpreting data obtained using these probes. The most commonly used cyclic nucleotide probes are FRET–based. Current FRET probes have a low signal-to-noise ratio, are susceptible to environmental changes (e.g., pH), and are subject to photobleaching. Our models describe the kinetic properties of FRET–based probes used to measure cAMP signals. Simulations indicate that these probes are adequate to detect slow cAMP oscillations. Unfortunately, concentrations of fluorescent probes cannot be estimated in single cells. Thus, we cannot predict the magnitude of cyclic nucleotide buffering by heterologously–expressed probes. Model simulations suggest that buffering may dramatically alter the kinetics of free cAMP signals. Finally, the ability of these probes to discriminate between cAMP levels in intact cells has not been adequately assessed. We are currently using both spectrofluorometric and imaging measurements to estimate the dynamic range of these probes. These studies will facilitate the quantitative use of FRET probes for the measurement of intracellular processes in living cells.

Keywords: Förster resonance energy transfer, live cell imaging, quantitative image analysis, cAMP, cGMP, PKA, Epac

INTRODUCTION

Over the last decade a variety of fluorescence- and Förster resonance energy transfer (FRET)-based sensors for intracellular signals have been developed. The sensors are typically described as high resolution, real-time sensors for use in single cells. We have previously used both experimental measurements and mathematical models to assess the utility of these sensors for detecting intracellular signals [1-3]. This approach has been particularly useful in assessing the effects of kinetics of the sensors and changes in environmental factors such as pH on the interpretation of apparent FRET signals. FRET-based sensors typically have low signal-to-noise ratios due to their relatively weak signals. Although FRET-based sensors have been used in a wide variety of studies, the sensitivity and dynamic range of these sensors has not been adequately assessed. To address this limitation we estimated the ability of a FRET-based cyclic AMP (cAMP) sensor to detect changes in cAMP. This sensor is a chimera in which a cyclic nucleotide-binding domain (Epac) is sandwiched between cyan fluorescent protein (CFP, the FRET donor) and yellow fluorescent protein (YFP, the FRET acceptor) [4]. We assessed the sensitivity of this probe by measuring the response of the probe to increasing cAMP concentrations using a lysed cell preparation. The lysed cell preparation allowed exposure of the FRETbased sensor to known cAMP concentrations and measurement of FRET signals using a spectrofluorimeter. We also assessed FRET responses in live cells using a Nikon A1R spectral confocal microscope system.

METHODS

Cell Culture and Protein Expression. HEK-293 cells were maintained and FRET-based cAMP probes were transfected as described previously [2]. In brief, cells were grown to confluence on 100 mm culture dishes and maintained in MEM supplemented with 10% FBS, 100 µg/ml streptomycin, and 100 U/ml penicillin, pH 7.4, at 37°C, in a humidified atmosphere of 95% air and 5% CO₂. Approximately 96 hours prior to experiments cells were plated on 100 mm dishes (spectrofluorimeter) or 35 mm cover slips (microscopy). Approximately 48 hours prior to experiments cells were transfected with cDNA encoding the FRET-based probes using the Fugene 6 reagent.

Spectrofluorimetry. Spectrofluorimetric experiments were performed as previously described [2, 5]. Cells were harvested, resuspended in standard extracellular buffer (~10⁶ cells/mL), lysed with 20 strokes of a dounce, and placed into a stirred cuvette. 10 µM rolipram was added to inhibit PDE activity. cAMP concentration-response was measured by adding known concentrations of cAMP to the cuvette (as indicated). FRET responses were measured

using excitation wavelengths of 415 or 505 nm and an emission range from 450 to 650 nm or 520 to 650 nm, in 1 nm increments, respectively.

Confocal Microscopy. Spectral microscopy experiments were conducted on a Nikon AIR confocal microscope as described previously [2]. Coverslips were placed in an experimental chamber in 2 mL of extracellular buffer. Spectral image stacks were acquired every 10 s, using 405 nm excitation and 432 to 606 nm emission, in 6 nm increments. 30 s after initiation of image acquisition, cAMP accumulation was triggered by addition of 10 μ M rolipram and 10 μ M forskolin (an adenylyl cyclase activator).

Data Analysis. Image and data analysis were performed as previously described [2, 5]. Briefly, custom scripts were written in MATLAB (MathWorks) for processing fluorescence emission spectra. Five FRET analysis techniques for spectrofluorometric data were utilized: two fluorescence filter sets, three fluorescence filter sets, three fluorescence filter sets corrected for donor concentration, acceptor–donor peak intensity ratio, and linear unmixing. Image data were analyzed using linear unmixing.

Statistical Analysis. Results are expressed as mean \pm SD. One-way ANOVA and Tukey’s HSD tests were used to determine significant differences between cAMP levels or time. Analyses were carried out using Prism (v5.01; GraphPad Software, Inc.). Differences were considered significant if $P < 0.01$.

RESULTS

We evaluated the effects of cAMP concentration on FRET levels in lysed cells (Fig. 1). We evaluated both traditional two filter set and three filter set techniques, and a three filter set with correction for donor concentration to assess FRET levels. In addition, we used two spectral approaches that have higher signal-to-noise ratios than standard FRET measurements, acceptor–donor peak intensity ratio and linear unmixing [2]. As expected, FRET levels decreased with increasing cAMP concentration. We utilized statistical analysis to determine the sensitivity of this FRET-based cAMP probe, as described in the Methods. The results indicate that 5- to 10-fold increases in cAMP levels were required for statistically significant changes in FRET levels. This suggests that under nearly ideal conditions – precisely controlled cAMP levels in a heavily buffered, lysed cell preparation, measured with a spectrofluorimeter – only 4 statistically significant FRET levels could be determined.

We next evaluated the number of statistically significant steps that can be determined from typical, live cell FRET measurements. We used both rolipram and forskolin to inhibit cAMP hydrolysis and trigger increased cAMP synthesis, and thus to induce large increases in cAMP levels within the cell. We observed that following treatment with both rolipram and forskolin, FRET levels decreased indicating an increase in intracellular cAMP. The unfiltered FRET response has a relatively high standard deviation (Fig. 2A). As anticipated, filtering the data at 0.025 Hz reduced the standard deviation of the FRET signal (Fig. 2B). (It is important to note that FRET data are not typically filtered.) We were able to differentiate three distinct levels in the filtered FRET response. Finally, we evaluated the ability to distinguish relative rather than absolute FRET levels by normalizing FRET responses (F) to basal FRET levels (F₀) (Fig. 2C). Again, only three distinct FRET levels were observed.

The three distinct FRET levels that were observed allow us to estimate the overall change in rolipram/forskolin-induced cAMP levels. Basal free cAMP levels are thought to be between 50-100 nM [6]. 5- to 10-fold increases in cAMP are required for statistically significant changes in FRET. Thus, the rolipram/forskolin-induced FRET response likely represents an increase in cAMP from basal levels to a plateau of 1.25 to 10 μ M cAMP.

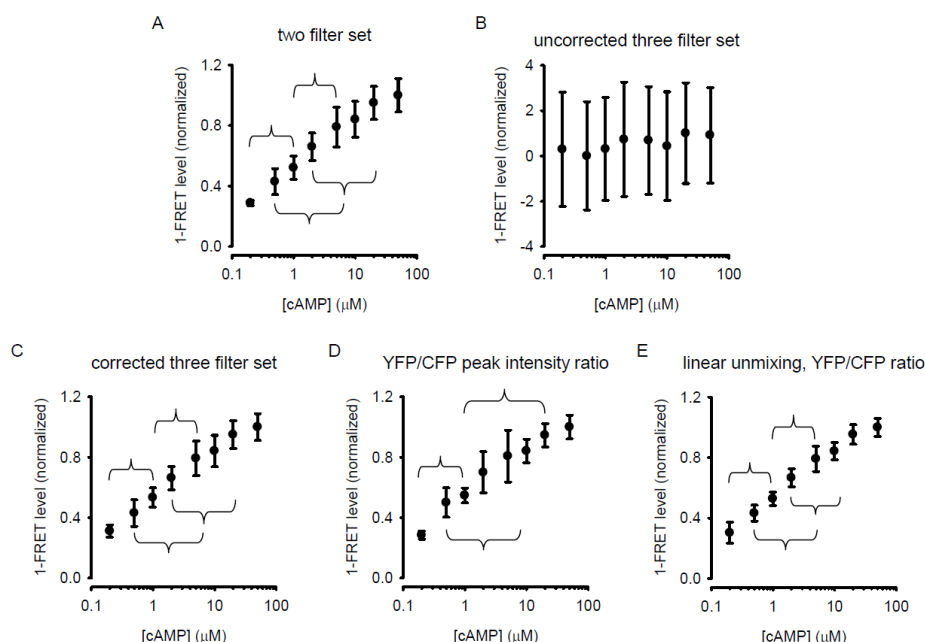


Figure 1. Sensitivity of FRET-based cAMP measurements. cAMP concentration response of FRET-based probes analyzed with typical two and three filter set approaches as well as spectral approaches as indicated. Data were obtained from lysed cell preparations as described in the Methods. Brackets indicate significant changes in FRET measurements ($P < 0.01$). Data represent mean \pm SD of 3 experiments.

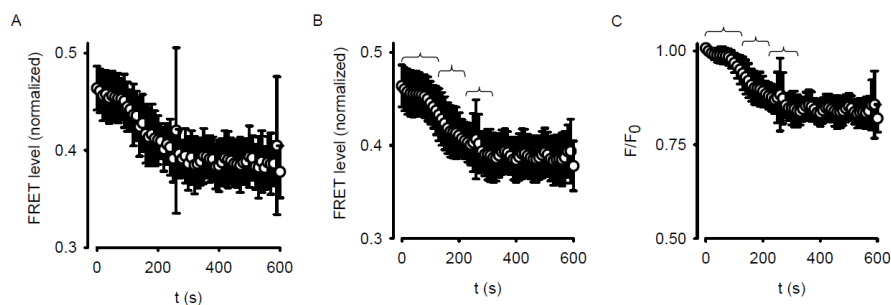


Figure 2. FRET-based measurement of cAMP levels in living cells. Images were acquired using a Nikon A1R spectral confocal microscope as described in Methods. cAMP accumulation was triggered by addition of 10 μ M rolipram and 10 μ M forskolin. Brackets indicate a significant change in the FRET signal ($P < 0.01$). (A) Unfiltered time course of rolipram/forskolin- induced FRET signal. Typically FRET measurements are not appropriately filtered. (B) FRET signal filtered with a Butterworth filter at 0.025 Hz. (C) FRET data normalized to baseline FRET measurements (initial 30 s). Data are the mean \pm SD of 15 cells from 3 coverslips.

DISCUSSION

We have assessed the ability of a FRET-based cAMP probe to detect changes in cAMP levels. Our results suggest that this probe can detect 5- to 10-fold changes in cAMP. This result implies that great care must be taken in interpreting results from this and other FRET probes. For example, only three distinct FRET levels can be assessed from the FRET signal depicted in Fig. 2B,C. In the future it will be important to assess the ability of other FRET probes to detect changes in cAMP levels, particularly probes that have been reported to have a high signal range [7].

CONCLUSIONS

Data presented here suggest that the FRET-based cAMP probe and acquisition techniques used in this study are only able to detect 5- to 10-fold changes in cAMP concentrations. This conclusion is problematic given that the spectral acquisition and linear unmixing approaches used here are among the fluorescence imaging approaches with highest signal-to-noise ratio. Taken together, these results indicate that better microscopy approaches or fluorescent probes with higher signal-to-noise ratio need to be developed to quantitatively assess the dynamics of intracellular signaling.

ACKNOWLEDGMENTS

We would like to thank V. O. Nikolaev for providing cDNA encoding the FRET-based sensor. This work was supported by NIH awards P01HL066299, R01HL094455, T32HL076125, and S10RR027535.

REFERENCES

- [1] T. C. Rich and J. W. Karpen, "Cyclic AMP sensors in living cells: what signals can they actually measure?" *Ann. Biomed. Eng.*, vol. 30, pp. 1088-1099, 2002.
- [2] S. J. Leavesley, A. L. Britain, L. K. Cichon, V. Nikolaev, and T. C. Rich, "Assessing FRET using spectral techniques," *Cytometry A*, vol. 83, pp. 898-912, 2013.
- [3] T. C. Rich, K. J. Webb, and S. J. Leavesley, "Perspectives on: Cyclic nucleotide microdomains and signaling specificity: Can we decipher the information content contained within cyclic nucleotide signals?" *J. Gen. Physiol.*, vol. 143, pp. 17-27, 2014.
- [4] V. O. Nikolaev, M. Bünemann, L. Hein, A. Hannawacker, and M. J. Lohse, "Novel single chain cAMP sensors for receptor-induced signal propagation," *J. Biol. Chem.*, vol. 279, pp. 37215-37218, 2004.
- [5] T. C. Rich, A. L. Britain, T. Stedman, and S. J. Leavesley, "Hyperspectral Imaging of FRET-based cGMP probes," *Meth. Mol. Biol.*, pp. 73-88, 2013.
- [6] W. P. Feinstein, B. Zhu, S. J. Leavesley, S. L. Sayner, and T. C. Rich, "Assessment of cellular mechanisms contributing to cAMP compartmentalization in pulmonary microvascular endothelial cells," *Am. J. Physiol. Cell Physiol.*, vol. 302, pp. C839-C852, 2012.
- [7] J. B. Klarenbeek, J. Goedhart, M. A. Hink, T. W. Gadella, and K. Jalink, "A mTurquoise-based cAMP sensor for both FLIM and ratiometric read-out has improved dynamic range," *PLoS One*, vol. 6, pp. e19170, 2011.

ANDROGEN ADMINISTRATION AND FIBROBLAST BEHAVIOR IN THE TISSUE-IMPLANT RESPONSE

Kenneth R. Butler, PhD, Hamed A. Benghuzzi, PhD, Michelle Tucci, PhD, Aaron D. Puckett, PhD

University of Mississippi Medical Center
Jackson, Mississippi—USA

ABSTRACT

The purpose of this study was to further evaluate the presence of fibroblasts in the fibrous tissue capsules surrounding tricalcium phosphate (TCP) bioceramics loaded with androstenedione, dihydrotestosterone, and testosterone to that of a control to further explore the mechanisms involved in the tissue-implant response. The effect of steroid hormones on the chronic inflammatory response has been widely reported in the scientific literature. Sixteen animals in four experimental groups were implanted with one TCP bioceramic each. Group I animals were implanted with a sham TCP ceramic not containing a steroid hormone (control group). Group II animals received the testosterone loaded TCP ceramic. Group III animals were implanted with the dihydrotestosterone loaded ceramic. Group IV animals received the androstenedione ceramic. At 90 days post-implantation, the animals were euthanized. The implants and fibrous tissue capsules surrounding them were extracted and evaluated microscopically following routine H&E staining aided by ImagePro digital analysis software. Both Groups II and III demonstrated higher fibroblast counts per high power field compared to Groups I (control) and IV (androstenedione). Testosterone and dihydrotestosterone significantly intensified fibroblast migration into the fibrous tissue capsule surrounding the implants. The results of this study indicate that these hormones can significantly influence fibroblast behavior in the tissue-implant response.

Keywords: androgen, testosterone, fibroblast, tissue-implant response, migration, intraperitoneal, tricalcium phosphate, bioceramic

INTRODUCTION

Fibroblast migration is an important phenomenon associated with the tissue-implant reaction surrounding implanted devices. As part of the chronic inflammatory reaction working through complex cytokine signaling interactions, activated fibroblasts exit near-by vascularity, migrate to the area surrounding the implant, and work closely with macrophages in an effort to seal the implanted material away from the body within a layer of fibrous tissue. Fibroblasts secrete a collagenous extracellular matrix providing support to the developing tissue. For the purposes of sustained drug delivery, this fibrous tissue formation provides support and stability to the implant and is complete with a rich vascular network that develops as the tissue-implant reaction evolves.

Previous studies in our laboratory have attempted to quantify the fibrous tissue components associated with the tissue-implant response used in drug delivery applications. Initial studies, using manual techniques, revealed differences in fibrous tissue component based on type of material as well as the biologicals that were being delivered [1-7]. Often, large standard deviations were observed when multiple observers were involved in the data collection. As subsequent studies evolved and these morphometric methods were improved with digital quantitation technologies, variability was decreased significantly [4, 8-11]. The goal of this investigation was to further quantify and elucidate the role of fibroblasts in the fibrous tissue surrounding tricalcium phosphate (TCP) bioceramic implants in context of recent work on macrophage populations and neovascularity. This study contributes quantitative data regarding the effects of exogenous male hormones have on the presence of fibroblasts at 90 days post implantation using semi-automated digital morphometric techniques.

METHODS

Sixteen Sprague-Dawley male albino rats weighing 280-300g were obtained (Holtz Company, Madison, WI), acclimatized in the animal care facility for two weeks prior to surgery, and randomly divided into three experimental groups (n=4/group) and 1 control group (n=4). The tricalcium-phosphate bioceramic implants were prepared according to standard laboratory protocol [1, 9-11]. Surgery on all animals was performed according to a standard laboratory protocol reviewed and approved by the University of Mississippi Medical Center Animal Care and Use Committee and has been described previously [1, 9-11]. Animals in Group I were designated for the implantation of the sham TCP ceramics (control), animals in Group II were designated for T-TCP (testosterone)

implantation, animals in Group III were selected for the implantation of the D-TCP (dihydrotestosterone) ceramic devices, and animals designated in Group IV were implanted with the A-TCP (androstenedione) ceramic. All animals in this investigation were kept on a 12-hour day/night cycle and were fed Purina Rodent Chow 5001 (Ralston Purina, St. Louis, MO) and water *ad libitum*.

The TCP ceramic implants and their fibrous capsules were collected, observed grossly, photographed, and fixed in 10% neutral buffered formalin at 90 days post-implantation. Processing of these tissues included infiltration with paraffin and routine histologic processing.

Three inch glass microscope slides were coated with chrome-alum adhesive to aid in the tissue attachment to the glass slide [11]. Three to five sections were cut at 5 μm and mounted onto glass slides every 25 μm throughout the entire depth of the fibrous tissue mounted in the paraffin blocks.

Tissues were stained with hematoxylin and eosin (H&E), Masson's trichrome, and Papanicolaou stains. Histologic sections prepared from the tissue directly surrounding the implants were evaluated using the light microscope and Image Pro Plus digital analysis software (Media Cybernetics, Silver Spring, MD) on captured images [11, 12]. Fibroblasts were quantified by counting numbers of cells per high power field (HPF) with the assistance of the digital analysis software using a semi-automated manual tag method [10, 11]. Fibroblasts were identified based on cellular morphology and imaging characteristics and reported as the number of cells/HPF [9]. To minimize bias and variability, a minimum of 10 fields per slide were randomly examined throughout the depth of the tissue capsule on 125 randomly selected slides per animal to thoroughly examine the depth of the tissue.

Statistical analysis was conducted using Stata version 12 statistical software (StataCorp, College Station, TX). Quantification fibroblast counts throughout the different layers of fibrous tissue were expressed as mean \pm sd for each group. The number of fibroblasts in each group were compared using analysis of variance (ANOVA, $\alpha=0.05$) and Dunnett's t for post-hoc analysis ($\alpha=0.05$).

RESULTS

Fibroblasts found in the fibrous tissue capsules surrounding the implants were highly variable among the four groups as presented in the Figure. Dihydrotestosterone treatment demonstrated the most fibroblasts in the fibrous tissue capsule/HPF (65 ± 3), with testosterone treatment demonstrating 37 ± 2 fibroblasts/HPF, androstenedione yielded 31 ± 3 fibroblasts/HPF, compared to control with 30 ± 3 fibroblasts/HPF. ANOVA demonstrated statistically significant differences in mean numbers of fibroblasts between groups ($F=81.63$, $p<0.001$). Post-hoc analysis using the Dunnett's t ($\alpha = 0.05$), revealed the difference in the mean number of fibroblasts observed in the fibrous tissue capsules extracted from the control group was significantly different that the means observed in testosterone and dihydrotestosterone treated groups. The mean difference between the control and androstenedione treated group was not statistically different.

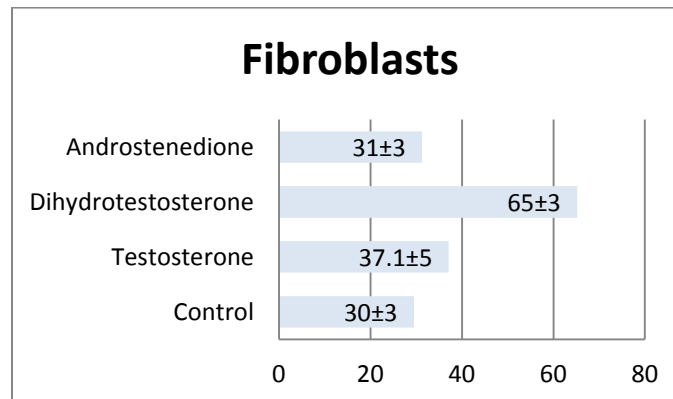


Figure. In this analysis, fibroblasts within the fibrous tissue capsules of three experimental groups were compared to control. Fibroblast counts in the androstenedione treated group were similar to control. Counts in the dihydrotestosterone and testosterone treated groups were significantly higher compared to control.

Table. Multiple comparisons: Dunnett t (2 sided)^a comparing the mean number of fibroblasts/HPF to control group. The number of fibroblasts in the testosterone and dihydrotestosterone treated groups demonstrated significant differences compared to control.

Experimental Groups	Control	Mean Difference (Groups-Control)	Std. Error	p-value	95% CI
Testosterone	Control	7.53*	2.60	0.03*	0.56-14.49
Dihydrotestosterone		35.66*	2.60	<0.001*	28.69-42.63
Androstenedione		1.79	2.60	0.83	-5.18-8.76

*The mean difference is significant at the 0.05 level. ^aDunnett's t-tests treat one group as a control, and compare all other groups against it.

DISCUSSION

Marked variation can be appreciated in the architectural patterns of the tissue extracted from the four groups. In previous studies, fibrous tissue reactions in soft tissue revealed that different types of ceramic materials without drugs or biologicals elicit a markedly different fibrous tissue response based on the composition of the fibrous tissue capsule [1-3, 5]. Subsequent studies revealed the sustained release of biological hormones demonstrated significant differences in fibroblast populations [11]. In this study, significant differences were found in fibroblast distribution on digital analysis with small standard deviations. Dihydrotestosterone treated animals demonstrated a much higher fibroblast distribution in the fibrous capsule than the other three groups. In this and previous studies, fibroblast production has corresponded well with increased collagen production [11]. The presence of fibroblasts, in the testosterone treated group was similar to dihydrotestosterone. It appears that steroid hormones effect fibroblast distribution by different mechanisms. This is also apparent in the androstenedione treated group which demonstrated similar fibroblast counts as the control. Androstenedione is a precursor to testosterone, while dihydrotestosterone is a downstream metabolite of testosterone.

From the data obtained in this study, it appears that the physiochemical effects of testosterone and dihydrotestosterone play a major role in fibroblast migration and possibly collagen production in these groups. Testosterone does appear to exhibit anabolic effects with large numbers of fibroblasts being present in tissue surrounding the implants. However, there did appear to be degenerated zones between the functional capsule and the indistinct interface of this group. The similarities in larger fibroblast counts of these two groups could be explained by the possibility of active conversion of testosterone to dihydrotestosterone. The control and androstenedione treated groups demonstrated similar fibroblast counts. In a previous study, the fibrous tissue from the androstenedione treated group consisted primarily of adipose tissue and little other cellular constituents [11]. Conversely, the fibrous tissue extracted from the testosterone and dihydrotestosterone treated groups consisted heavily of collagen and little adipose tissue [11].

CONCLUSIONS

Two of the experimental groups receiving steroid hormones demonstrated different fibroblast population counts when compared to the control group. Their distribution within the fibrous tissue capsule is highly dependent on the physiochemical characteristics of the hormone being delivered. While these hormones are from the same family, our findings suggest that any change in compound will significantly change the fibroblastic composition of the tissue capsule surrounding the implant.

The quantitation procedures used for this application have been adapted from Image Pro digital analysis software and can provide researchers methods that can be more easily reproduced. The data that was produced from the image analysis ensured little variability from animal to animal within groups. It will continue to be part of the evaluation process associated with the tissue-implant reaction to sustained release drug delivery systems.

ACKNOWLEDGMENTS

The authors thank Ms. Gerri Wilson and Ms. Lisa McCammon, from the Department of Orthopedic Surgery and Rehabilitation for their technical and administrative support.

REFERENCES

- [1] K. Butler, H. Benghuzzi, P. Bajpai, A. Puckett, M. Tucci, Z. Cason, and B. England, "One year histopathological evaluation of fibrous tissue surrounding TCPL implants using adult rats as a model," *Biomed Sci Instrum*, vol. 33, pp. 233-9, 1997.
- [2] K. Butler, H. Benghuzzi, and A. Puckett, "Cytological evaluation of the tissue-implant reaction associated with S/C and I/P implantation of ALCAP and HA bioceramics in vivo," *Pathol Res Pract*, vol. 197, pp. 29-39, 2001.
- [3] K. Butler, H. Benghuzzi, M. Tucci, and Z. Cason, "A comparison of fibrous tissue formation surrounding intraperitoneal and subcutaneous implantation of ALCAP, HA, and TCP ceramic devices," *Biomed Sci Instrum*, vol. 34, pp. 18-23, 1997.
- [4] K. Butler, H. Benghuzzi, and S. Tucci, "Tissue-implant response following soft tissue implantation of poly-L-lysine coated UHMW-polyethylene into adult male rats," *Biomed Sci Instrum*, vol. 37, pp. 19-24, 2001.
- [5] K. Butler, A. Puckett, and H. Benghuzzi, "Quantitative analysis of the cellular components of the fibrous tissue matrix surrounding ALCAP, HA, and TCP bioceramics using adult male rats as a model," *Biomed Sci Instrum*, vol. 35, pp. 267-72, 1999.
- [6] K. R. Butler, H. A. Benghuzzi, and A. Puckett, "Morphometric evaluation of tissue-implant reaction associated with ALCAP and TCP bioceramics in vivo," *J Invest Surg*, vol. 14, pp. 139-52, May-Jun 2001.
- [7] M. Callender, H. Benghuzzi, M. Tucci, A. Mohamed, Z. Cason, L. Lemos, and A. Tsao, "Immunochemical and histopathological evaluation associated with sustained delivery of 5-alpha androstane-3-one using adult rats as a model," *Biomed Sci Instrum*, vol. 32, pp. 55-62, 1996.
- [8] K. R. Butler, Jr., H. Benghuzzi, M. Tucci, and A. Puckett, "Amino Acid coated uhmw-pe implants modify macrophage migration in the tissue-implant response - biomed 2011," *Biomed Sci Instrum*, vol. 47, pp. 240-5, 2011.
- [9] K. R. Butler, Jr., H. Benghuzzi, M. Tucci, and A. Puckett, "Androgen administration and macrophage behavior in the tissue-implant response - biomed 2011," *Biomed Sci Instrum*, vol. 47, pp. 228-33, 2011.
- [10] K. R. Butler, H. Benghuzzi, M. Tucci, and A. Puckett, "Neovascularization is influenced by androgenic hormones in the tissue implant response," *Biomed Sci Instrum*, vol. 48, pp. 49-56, 2012.
- [11] K. R. Butler, Jr. and H. A. Benghuzzi, "Morphometric analysis of the hormonal effect on tissue-implant response associated with TCP bioceramic implants," *Biomed Sci Instrum*, vol. 39, pp. 535-40, 2003.
- [12] H. Benghuzzi, "Histomorphometric analysis: comparative study of manual and digital image analysis using reproductive organ as a model," *Biomed Sci Instrum*, vol. 38, pp. 29-34, 2002.

ELASTIN LIKE POLYPEPTIDE-COLLAGEN COMPOSITE HYDROGELS FOR DRUG DELIVERY

APPLICATIONS

Shruti S. Amruthwar and Amol V. Janorkar*

Department of Biomedical Materials Science, School of Dentistry, University of Mississippi Medical Center,
2500 N. State Street, Jackson, MS 39216

* Corresponding author (Email: ajanorkar@umc.edu; Phone: 1-601-984-6170; Fax: 1-601-984-6087)

ABSTRACT

We compared the release characteristics of the collagen and elastin-like polypeptide (ELP)-collagen composite hydrogels loaded with a model protein (bovine serum albumin, BSA) and a commonly used antibiotic (doxycycline). Both BSA and doxycycline showed a gradual time dependent release and the release kinetics followed the power law model demonstrating that the release from the collagen and ELP-collagen hydrogels was predominantly through Fickian diffusion. The ELP-collagen hydrogels, in general, showed a slower release of the bioactive agents compared to the collagen hydrogels. These results suggested that drug molecular weight, target loading, and inter-chain interactions between collagen, ELP, and the bioactive agents were significant factors that affected the release kinetics.

Key Words: Elastin-like polypeptide, collagen, hydrogel, drug delivery

INTRODUCTION

Special attention has been given to collagen-based hydrogels for drug delivery applications [1-5], but they suffer many drawbacks such as rapid degradation, poor mechanical properties, and possible antigenicity [5]. Cross-linking of collagen or blending with other polymers minimizes these drawbacks [5]. Such modifications may also modulate drug release behavior and obtain a sustained drug release profile that is essential to assure total eradication of pathogenic bacteria from the wound area and assure good healing [6]. Here, we report the drug release behavior of collagen-based composite hydrogels prepared by incorporating a recombinant form of elastin called ELP. ELPs have been used for tissue engineering and drug delivery [7]. Previous studies included chemically cross-linked ELP microparticles and films, respectively, for delivery of model drug molecules (BSA and prednisone acetate) and antibiotics (vancomycin and cefazolin) [8,9], and ELP nanoparticles prepared by electrospraying for delivery of chemotherapeutics [10].

Recently, we prepared non-crosslinked ELP-collagen composite hydrogels by utilizing the gelation behavior of collagen at 37°C [11] and demonstrated that the ELP-collagen hydrogels displayed equivalent biocompatibility compared to the neat collagen hydrogels and allowed MC3T3-E1 pre-osteoblast cell attachment, differentiation, and subsequent mineralization over a 3-week culture period [12]. In this paper, we report on their drug release characteristics. Specifically, the collagen and ELP-collagen (3:1 weight ratio of ELP:collagen) hydrogels were prepared and loaded with two different amounts (1.5 and 3.0% w/w) of a model protein (BSA) and a commonly used antibiotic in periodontal therapy (doxycycline hyclate) and the release was followed. The drug release data was then fit to the power law model and relevant model parameters were calculated. The hydrogels were also characterized for their *in vitro* antimicrobial activity.

MATERIAL AND METHODS

Preparation of collagen and ELP-collagen hydrogels: Expression and purification of ELP with a primary sequence of [VPGVG]₁₂₀, where G = glycine, P = proline, and V = valine, and a molecular weight of 51,000 Da has been described elsewhere [11]. To prepare ELP-collagen hydrogels, 25 mg ELP, DI water (160 L), 10 X PBS (200 L), 1 N NaOH (40 L), and type I collagen (rat tail, 1.6 mL) were gently mixed and incubated at 37°C in a humidified environment for 24 h.

Bioactive agent release: BSA or doxycycline (1.5 or 3.0% w/w) was added to above solution and the gelation procedure was followed. Hydrogels were washed with 1 mL PBS, incubated in 1 mL of PBS at 37°C in a humidifier, and the supernatants were analyzed by an NDS 1000 spectrophotometer. The amount of BSA

or doxycycline released was determined by measuring the absorbance at specific wavelength (280 and 345 nm, respectively) and comparing to pre-prepared calibration curves. The percent release was the ratio of the measured amount to the initial loading multiplied by 100.

Determination of power law parameters for bioactive agent release: We evaluated the bioactive agent release profiles using the power law model: $(M_t/M_0) = k t^n$, where M_t = amount of drug released in time t , M_0 = initial drug loading, t = time, k = release rate constant which primarily depends on the geometry of the hydrogel, and n = power law exponent indicative of release mechanism [13].

Determination of bioactivity of the released doxycycline: Bioassays were performed using the disk diffusion method [14]. *E. coli* bacteria (BLR-DE3) were multiplied in a Luria Bertani nutrient broth in suspension culture at 275 rpm for 8 h at 37°C and swabbed onto petri dishes containing Luria Bertani agar. The collagen and ELP-collagen hydrogels with or without doxycycline were placed on the surface of the agar plates and incubated at 37°C for 18 h. The inhibition of bacterial growth was observed by comparing the zones of inhibition created around the hydrogels.

Statistical analysis: All experiments were performed in triplicate and reported as mean \pm 95% confidence intervals. Statistical evaluation was done using ANOVA with Bonferroni and Games-Howell post hoc tests for equal and unequal variances. Values with $p \leq 0.05$ were deemed significantly different.

RESULTS

First, we verified the structural integrity of our hydrogels. The UV-Vis spectra of the supernatants collected at the various time points from neat collagen and ELP-collagen hydrogels did not show the characteristic absorbance at 280 nm and thus, confirmed that a significant amount of collagen or ELP was not released into the supernatant due to matrix degradation (data not shown). The collagen hydrogels loaded with 1.5% w/w BSA (Fig. 1a red diamonds) and 3.0% w/w BSA (Fig. 1b red diamonds) showed a gradual time-dependent release to reach 18.1 ± 2.5 and $17.7 \pm 2.1\%$ over the 168-h period, respectively. On the other hand, ELP-collagen hydrogels containing 1.5% w/w BSA (Fig. 1a purple triangles) and 3.0% w/w BSA (Fig. 1b purple triangles) showed a gradual time-dependent release behavior to reach 12.5 ± 1.7 and $17.1 \pm 2.9\%$, respectively. Comparison of the release profiles for collagen hydrogels against ELP-collagen hydrogels loaded with 1.5% w/w BSA (Fig. 1a) revealed that a lower amount of BSA was released from the ELP-collagen hydrogels ($p < 0.05$). However, for 3.0% w/w BSA loaded hydrogels (Fig. 1b) no statistical difference was observed after the initial 6 h.

Next, we studied the release of doxycycline from collagen and ELP-collagen hydrogels. As shown in Figs. 2a and 2b (red diamonds), the collagen gels loaded with 1.5 and 3.0% w/w doxycycline showed the majority of release (20.6 ± 2.8 and $19.1 \pm 3.4\%$, respectively; $p > 0.05$) occurring in the initial 9 h. On the other hand, ELP-collagen hydrogels containing 1.5 and 3.0% w/w doxycycline (purple diamonds in Figs. 2a and 2b) showed a more gradual release (6.6 ± 1.6 and $11.1 \pm 0.5\%$, respectively; $p < 0.05$) occurring in the initial 9 h. Comparison among the release profiles revealed that a significantly lower amount of doxycycline was released from the ELP-collagen hydrogels at all time points ($p < 0.05$).

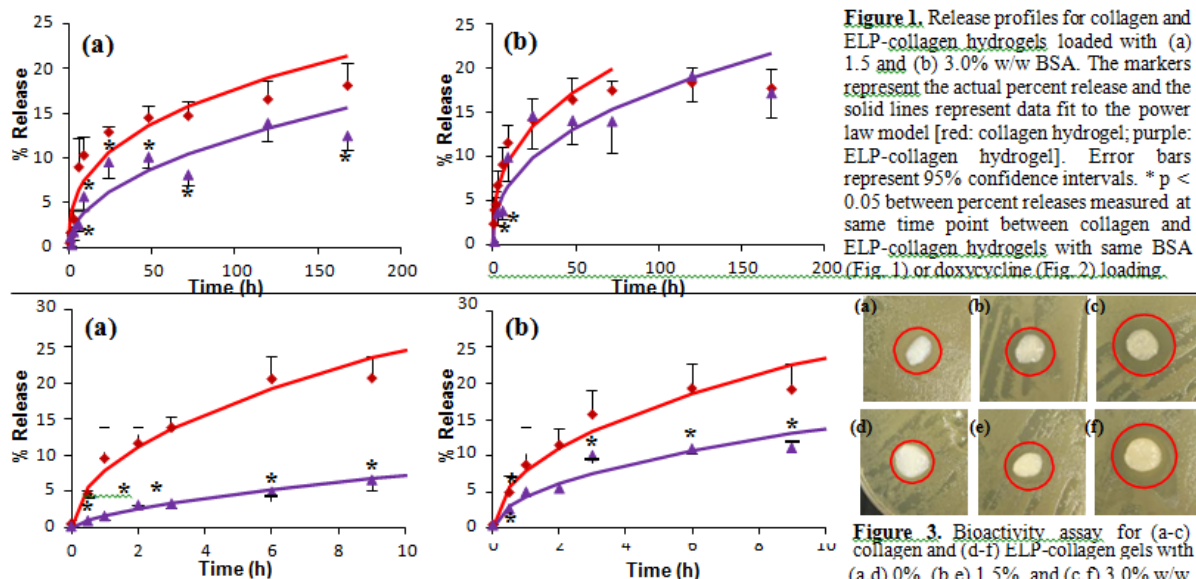


Figure 2. Release profiles for collagen and ELP-collagen hydrogels loaded with (a) 1.5 and (b) 3.0% w/w doxycycline [red: collagen hydrogel; purple: ELP-collagen hydrogel].

Figure 1. Release profiles for collagen and ELP-collagen hydrogels loaded with (a) 1.5 and (b) 3.0% w/w BSA. The markers represent the actual percent release and the solid lines represent data fit to the power law model [red: collagen hydrogel; purple: ELP-collagen hydrogel]. Error bars represent 95% confidence intervals. * $p < 0.05$ between percent releases measured at same time point between collagen and ELP-collagen hydrogels with same BSA (Fig. 1) or doxycycline (Fig. 2) loading.

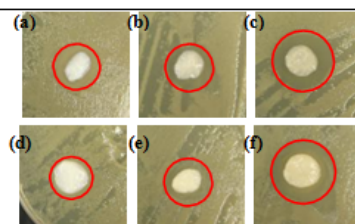


Figure 3. Bioactivity assay for (a-c) collagen and (d-f) ELP-collagen gels with (a, d) 0%, (b, e) 1.5%, and (c, f) 3.0% w/w doxycycline. The red circles indicate the zones of inhibition.

The disk diffusion assay confirmed the bioactivity of the released antibiotic (Fig. 3). Comparison of the zones of inhibition created by doxycycline released from the collagen (Figs. 3b and 3c) and ELP-collagen hydrogels (Figs. 3e and 3f) were equivalent. The negative controls, which were the collagen and ELP-collagen hydrogels without doxycycline showed minimal zones of inhibition (Figs. 3a and 3d).

Table 1. Power law model parameters for the various collagen and ELP-collagen hydrogels loaded with BSA and doxycycline.

Target loading (%w/w)	n	k	$t_{0.5}$ (days)
BSA Release from Collagen Hydrogels			
1.5	$0.36 \pm 0.02_{\#}$	$3.40 \pm 0.25_{\#}$	$80.9 \pm 16.1^*$
3.0	$0.36 \pm 0.03_{\#}$	$4.29 \pm 0.41_{\#}$	$43.0 \pm 14.3^*$
BSA Release from ELP-Collagen Hydrogels			
1.5	$0.47 \pm 0.02_{\#}$	$1.38 \pm 0.10_{\#}$	$84.2 \pm 11.9^*$
3.0	$0.41 \pm 0.02_{\#}$	$2.70 \pm 0.20_{\#}$	$56.6 \pm 9.0^*$
Doxycycline Release from Collagen Hydrogels			
1.5	$0.49 \pm 0.04_{\#}$	$7.98 \pm 0.59_{\#}$	$1.8 \pm 0.2_{\#}$
3.0	0.47 ± 0.03	$7.96 \pm 0.51_{\#}$	$2.1 \pm 0.3_{\#}$
Doxycycline Release from ELP-Collagen Hydrogels			
1.5	$0.63 \pm 0.06_{\#}$	$1.71 \pm 0.19_{\#}$	$9.7 \pm 3.0_{\#}$
3.0	$0.50 \pm 0.03^*$	$4.38 \pm 0.30_{\#}$	$5.7 \pm 1.1_{\#}$

* $p < 0.05$ between same hydrogels (collagen or ELP-collagen) with different loading of the same bioactive agent (BSA or doxycycline)
 $\# p < 0.05$ between different hydrogels (collagen and ELP-collagen) with the same loading of the same bioactive agent (BSA or doxycycline)

DISCUSSION

We analyzed the release behavior using the power law model of drug release. The model parameters (n and k) were obtained by plotting the $\log(\% \text{ drug release})$ versus $\log(\text{time})$. The slope of the best-fit line gave the power law exponent (n) and the y- intercept gave the $\log(k)$. These are summarized in Table 1. Our hydrogels were of cylindrical geometry, for which according to Siepmann and Peppas, $n = 0.45$ indicated diffusion-controlled

Fickian release and $n = 0.89$ indicated swelling- controlled Case-II release [13]. It is clear from Table 1 that the n values for all of our hydrogels were close to 0.45, indicating that the release was dominated by the diffusion-controlled Fickian mechanism. Using n and k values, we then calculated the time required to release 50% of the bioactive agent ($t_{0.5}$). These values (Table 1) indicate following: (1) Doxycycline release from the collagen hydrogels was significantly faster than that from the ELP-collagen hydrogels. (2) BSA release from the collagen hydrogel was marginally faster than that from the ELP-collagen hydrogel. (3) Release was faster for the higher (3.0% w/w) than the lower (1.5% w/w) target loading. This was expected and true for both collagen and ELP-collagen hydrogels. (4) Release was faster for doxycycline compared to BSA. Again, this was expected, true for both collagen and ELP-collagen hydrogels, and can be related to the molecular weights of BSA and doxycycline.

The release behavior of the high molecular weight BSA from our hydrogels agrees well with that reported by Bergeron et al. where collagen hydrogel showed gradual release of bone morphogenetic protein-9 that followed the power law model [3]. Another study reported that collagen hydrogels released up to 50% of the initially loaded human serum albumin over a 72-h period and followed the power law model [4]. On the other hand, as observed in case of our ELP-collagen hydrogels, composites of collagen with other polymers have been shown to modulate this release behavior. For example, composite hydrogels of collagen and BSA-loaded alginate microparticles showed a sustained release of up to 50% of initially loaded BSA over an 11-day period [1] and hyaluronic acid-collagen composite hydrogels released up to 50% of initially loaded DNA over a 1-week period [2]. When drugs are incorporated in a polymer matrix, the polymer may interact with the drugs and reduce their bioactivity by changing the molecular configuration [10]. Therefore, it was important to investigate the bioactivity of the released doxycycline. Our doxycycline-loaded collagen and ELP-collagen hydrogels showed considerable level of bioactivity in the disk diffusion tests (Fig. 5) and demonstrated that collagen and ELP did not interfere with the bioactivity of doxycycline.

CONCLUSIONS

BSA and doxycycline release from our hydrogels followed the power law model of drug release and revealed that the addition of ELP resulted in a composite hydrogel with a more gradual bioactive agent release. These results suggest a potential advantage during *in vivo* applications with a faster release of the antibiotic preventing post-operative infections and a slower, sustained release of the high molecular weight growth factors (similar to BSA) allowing sufficient time for tissue healing and regeneration.

ACKNOWLEDGEMENTS

Financial support by the School of Dentistry through the intramural research support program is gratefully acknowledged. This work made use of instruments in the Department of Biomedical Materials Science User Facility.

REFERENCES

1. Liu W, Griffith M and Li F 2008 *J. Mater. Sci. Mater. Med.* **19** 3365-71
2. Segura T, Chung P H and Shea L D 2005 *Biomaterials.* **26** 1575-84
3. Bergeron E, Leblanc E, Drevelle O, Giguère R, Beauvais S, Grenier G and Fauchoux N 2012 *Tissue. Eng.* **18A** 342-52
4. Maeda M, Tani S, Sano A and Fujioka K 1999 *J. Control.*

- Rel.* **62** 313-24
5. Friess W 1998 *Eur. J. Pharma. Biopharma.* **45** 113-36
 6. Huang L, Nagapudi K, Apkarian R P and Chaikof E L 2001 *J. Biomat. Sci. Polym. Ed.* **12** 979-93
 7. Turner P A, Joshi G V, Weeks C A, Williamson R S, Puckett A D, and Janorkar A V 2013 *NanoLIFE.* **3** 134300201-26
 8. Na K, Jung J, Lee J and Hyun J 2010 *Langmuir.* **26** 11165-9
 9. Adams S B, Shamji M F, Nettles D L, Hwang P and Setton L A 2009 *J. Biomed. Mater. Res.* **90B** 67-74
 10. Wu Y, MacKay J A, McDaniel J R, Chilkoti A and Clark R L 2009 *Biomacromolecules.* **10** 19-24
 11. Amruthwar S S, Puckett A D and Janorkar A V 2013 *J. Biomed. Mater. Res. Part A.* **101A** 2383-91
 12. Amruthwar S S and Janorkar A V 2013 *Dent. Mater.* **29**, 211-20
 13. Siepmann J and Peppas N A 2001 *Adv. Drug. Del. Rev.* **48** 139-57
 14. Barry A L, Coyle M B, Thornsberry C, Gerlach E H and Hawkinson R W 1979 *J. Clinical. Microbiol.* **10** 885-9

KERATIN AS A NOVEL DRUG CARRIER FOR DRUG COATED BALLOONS**Emily Turner¹, Seth Tomblyn², Luke Burnett², Saami K. Yazdani¹**¹Mechanical Engineering, University of South Alabama²KeraNetics, Winston-Salem, NC 27101**ABSTRACT**

Drug coated balloons (DCB) represent a novel approach to develop a superior intervention for the treatment of peripheral artery disease (PAD). Currently, DCB are coated with anti-proliferative drugs which combat neointimal hyperplasia reducing the occurrence of restenosis. The common anti-proliferative drug used in DCB is paclitaxel, which when coated alone shows very poor retention rates due to its diffusion from the treated artery following deployment. Multiple excipients have marginally improved the retention of paclitaxel in the arterial wall such as urea, iopromide, polysorbate and sorbitol carriers, however retention rates are still less than 10% following a 24-hour period. Keratin, a protein derived from human hair, is a potential option for an excipient due to its intrinsic scaffolding characteristics and biocompatibility. The goal of this project was to evaluate the possibility of keratin as an excipient for paclitaxel and its efficacy in the inhibition of neointimal hyperplasia. Additionally, nonionic contrast medium, iohexol, was used as an additional excipient based on its previous success as a carrier for paclitaxel. Briefly, a cell proliferation assay was performed *in vitro* in which various combinations of keratin, paclitaxel, and iohexol were coated on the bottom of 6-well plates to form a hydrogel on which cells were seeded and proliferation was determined microscopically. Finally, a 4% solution of Keratose- α , a form of keratin, was dissolved in 1x PBS and an angioplasty balloon was coated using a dipping technique. To evaluate the coating thickness, the Keratose- α coated balloon was embedded in OCT, sectioned and stained by Hematoxylin, and evaluated by light microscopy. The results demonstrated inhibited cell proliferation in the cell proliferation assay. The coating on the balloon demonstrated uniform coating circumferentially with coating thicknesses ranging from 5 to 20 microns. These studies highlight the potential of a new biomaterial that can provide a safe and controllable drug release profile for treatment of PAD.

Keywords: Peripheral artery disease, Drug-coated balloon, Paclitaxel, Keratin

INTRODUCTION

Stents have become the hallmark treatment of coronary artery disease (CAD), but are unable to translate to peripheral artery disease (PAD) treatment due to their susceptibility to biomechanical stress and possibility of strut fracture [1]. Furthermore, small diameter peripheral vessels, often occluded in diabetic patients, are not conducive to stent intervention leaving percutaneous transluminal angioplasty (PTA) as the primary treatment for PAD [2]. Success of arterial disease intervention is limited to the restenosis of the artery following treatment. Factors involved in restenosis include early vascular recoil, negative vascular remodeling, and neointimal hyperplasia [3, 4, 5, 6]. Neointimal hyperplasia, or the thickening of the arterial wall, can be combated through the use of antiproliferative drugs such as paclitaxel and has become the primary drug coating in the development of drug-coated balloons (DCB) [7]. A widely used chemotherapeutic, paclitaxel, acts to inhibit cell proliferation by stabilizing and preventing depolymerization of microtubules thereby reducing the severity of neointimal hyperplasia and restenosis [7, 8, 9]. However, paclitaxel delivery alone shows little efficacy in arteries since the drug simply diffuses away following deployment [11]. Delivery to the arteries was improved when paclitaxel was combined with hydrophilic contrast medium, iopromide, suggesting that a drug carrier is needed to increase drug retention within the artery [12]. Various other excipients have marginally improved the retention of paclitaxel in the arterial wall such as urea, polysorbate and sorbitol, and shellac acid carriers [13, 14, 15]. There exists still a need for a more durable, longer-lasting drug carrier to elongate arterial drug delivery and further inhibit neointimal hyperplasia and restenosis. Keratin shows unique promise in this application due to its stability, scaffolding capabilities, and biocompatibility [16, 17, 18]. An endogenous structural protein, keratin, has shown good compatibility in cell culture studies and has been demonstrated as a carrier for Cipro® antibiotic by KeraNetics LLC (Winston-Salem, NC) [16]. KeraNetics also demonstrated that by altering the keratin concentration within a keratin hydrogel, the release kinetics could be altered. De Guzman, et al. showed that keratose hydrogel capsule implanted in mouse subcutaneous layer shows a degradation of 92% at 8-weeks following implantation and that resorbed material was replaced with endogenous collagen [17]. By optimizing the make-up of a keratin-paclitaxel (specifically keratose) coating therein lies the ability to control the concentration and dissociation of paclitaxel within the affected artery allowing long- or short-

term delivery of the drug, increasing overall retention and providing a controllable drug (paclitaxel) release profile to fully combat neointimal hyperplasia.

METHODS

Cell seeding and proliferation

Pig endothelial cells were cultured in DMEM/50% High Glucose with 10% calf serum and 1% penicillin/streptomycin. Keratin hydrogels were prepared by reconstituting lyophilized keratose- α (KOS- α) with deionized water at a 4% weight to volume ratio and incubated overnight at 37°C. Following incubation, the KOS- α solution was coated onto the bottom of 6-well plates following combinations described in Table 1. KOS- α , paclitaxel, and iohexol concentrations were determined based on previous methods in the literature and carried out as duplicates [18, 19]. Iohexol was used in place of iopromide. It exhibits comparable characteristics to the more commonly used iopromide [20]. The plate coatings were left to dry for four days at room temperature receiving 48 hours of UV sterilization. 7.0×10^4 endothelial cells were seeded onto each well and confluence was evaluated microscopically 3 and 48 hours following seeding.

Table 1. Plate coating combinations.

Well	KOS- α	Paclitaxel (6 mg/mL)	Iohexol (300 mg/mL)
1	-	-	-
2	-	3 μ g/mm ²	0.197 M
3	4%	-	-
4	4%	-	0.197 M
5	4%	3 μ g/mm ²	-
6	4%	3 μ g/mm ²	0.197 M

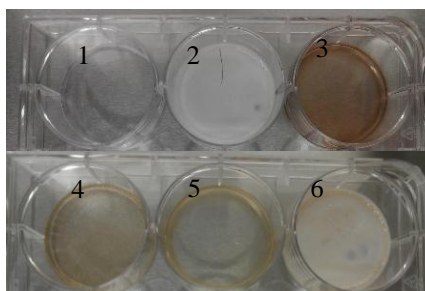
Balloon coating Lyophilized KOS- α was combined with 1x phosphate buffered saline (PBS) to form a 4% weight to volume mixture. Commercially available balloon catheters were procured and coated with the 4% KOS- α solution using a dipping method. The balloon was coated with a second layer following a drying time of 20 minutes. To evaluate the coating thickness, the KOS- α coated balloon was embedded in OCT, sectioned at 15 microns, and stained by Hematoxylin. Thickness of KOS- α coating was evaluated with Micromaster light microscope (Thermo Fisher Scientific, Rockford, IL) and Micron imaging software (Westover Scientific, Mill Creek, WA).

RESULTS

Cell proliferation assay

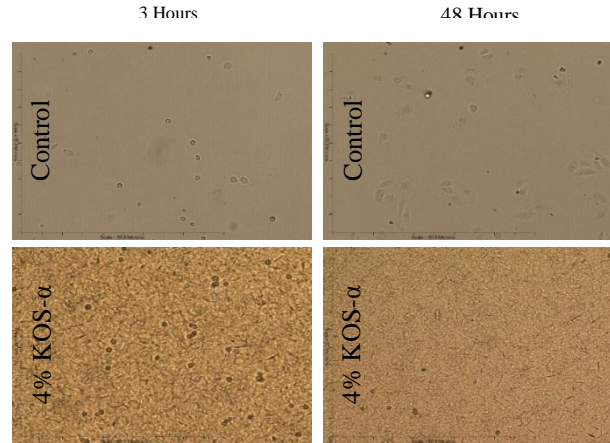
The plate coatings formed a uniform hydrogel layer with the KOS- α and iohexol coating on well four forming a semi-crystalline layer (Fig. 1).

Figure 1. Plate coatings corresponding to Table 1. 4% KOS- α and iohexol coating (4) form semi-crystalline layer.



The KOS- α (3), KOS- α and iohexol (4), and KOS- α and paclitaxel (5) coatings all appeared to mix throughout the media upon cell seeding and precipitate back to the bottom 3 hours following. The KOS- α and iohexol (4), KOS- α and paclitaxel (5), and KOS- α , paclitaxel, and iohexol (6) coatings microscopically showed a precipitate on the well bottom with a crystalline layer on top which the endothelial cells settled. The control (1) showed cell adhesion and proliferation. Cell proliferation seemed to be stunted in KOS- α , paclitaxel, and iohexol (6) with similar cell numbers between 3 and 48 hours following cell seeding (Fig. 2). Coating combinations of paclitaxel and iohexol (2), KOS- α (3), KOS- α and iohexol (4), and KOS- α and paclitaxel (5) showed a decrease in cell numbers between 3 and 48 hours (Fig. 2).

Figure 2. Cell proliferation assay of pig endothelial cells of control and 4% KOS- α hydrogel coating at 3 and 48 hours following seeding.



Balloon coating

The balloon was coated using the dipping technique and crystallization of 4% KOS- α was observed (Fig. 3). Sectioning of the balloon demonstrated uniform coating circumferentially with the coating thicknesses ranging from 4 to 7 microns.

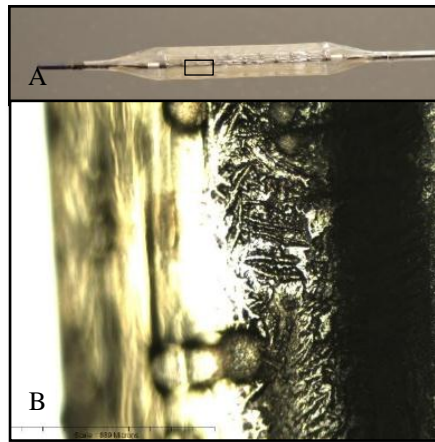


Figure 3. 4% KOS- α balloon coating. A) Balloon following coating, B) Crystallization observed at 10x magnification

DISCUSSION

The mixing and re-precipitation of coating and cell media were shown in the KOS- α (3), KOS- α and iohexol (4), and KOS- α and paclitaxel (5) wells suggests that the integrity of the hydrogel was compromised following cell seeding. Although paclitaxel and iohexol (2), KOS- α (3), KOS- α and iohexol (4) and KOS- α and paclitaxel (5) showed a decrease in cell proliferation, control (1), and KOS- α , paclitaxel, and iohexol (6) showed an increase. The next steps in establishing the effect of the coating combinations on cell proliferation should include a revised method for viewing total number of cells within and determine optimal combinations to decrease cell proliferation and effectively neointimal hyperplasia once correlated *in vivo*.

The results from the balloon coating demonstrates the KOS- α thickness can be achieved on the angioplasty balloon allowing calculated delivery of distinct doses of paclitaxel. Next steps directed toward the balloon coating involve a bench top flow model in which the DCB can be delivered to the porcine native porcine artery to determine the lifetime of the coating exposed to pulsatile flow and pharmacokinetic analyses determining dosage delivery and retention to the artery.

CONCLUSIONS

This project further tests the biocompatibility of keratin and shows its ability to be used as a coating in DCBs. By combining keratin, keratose specifically, and contrast medium, iohexol, there exists potential to develop the next generation coating for DCB. Optimizing the make-up of the coating, leads to the ability to control the concentration and dissociation of paclitaxel within the affected artery allowing long- or short-term delivery of the drug. Such an ability will provide a means for repeated drug delivery and in the future, could be coupled with various other drugs for direct delivery into the arteries.

ACKNOWLEDGMENTS

The authors would like to thank KeraNetics, LLC for providing the lyophilized keratin and Robert Barrington and Diego Alvarez of the University of South Alabama School Of Medicine for their help in balloon sectioning and staining.

REFERENCES

- [1] Scheinert D, Scheinert S, Sax J, Piorkowski C, Braunlick S, Ulrich M, Biamino G, Schmidt A. *Prevalence and clinical impact of stent fractures after femoropopliteal stenting*. Journal of the American College of Cardiology, 2005; 45:312-315.
- [2] Arom KV, Jotisakulratana V, Pitiguagool V, Banyatpiyaphod S, Asawapiyanond S, Pamornsing P, Suwannakijboriharn C, Ruengsakulrach P. *Can Surgeons Do Complete Revascularization in Diabetic Patients Using the Off-Pump Technique?* Innovations, 2007; 2:1-6.
- [3] Lincoff AM, Popma JJ, Ellic SG, Hacker JA, Topol EJ. *Abrupt vessel closure complicating coronary angioplasty: clinical, angiographic and therapeutic profile*. Journal of the American College of Cardiology, 1992; 19:926-935.
- [4] Post MJ, Borst C, Kuntz RE. *The relative importance of arterial remodeling compared with intimal hyperplasia in lumen renarrowing after balloon angioplasty. A study in the normal rabbit and the hypercholesterolemic Yucatan micropig*. Circulation, 1994; 89:2816-2821.
- [5] Strauss BH, Chisholm RJ, Keeley FW, Gotlieb AI, Logan RA, Armstrong PW. *Extracellular matrix remodeling after balloon angioplasty injury in a rabbit model of restenosis*. Circulation, 1994; 75:650-658.
- [6] Gertz SD, Gimple LW, Banai S, Ragosta M, Powers ER, Roberts WC, Perez LS, Sarembock IJ. *Geometric remodeling is not the principal pathogenetic process in restenosis after balloon angioplasty. Evidence from correlative angiographic-histomorphometric studies of atherosclerosis arteries in rabbits*. Circulation, 1994; 90:3001-3008.
- [7] Heldman AW, Cheng L, Jenkins GM, Heller PF, Kim D, Ware M, Nater C, Hruban RH, Rezai B, Abella BS, Bunge KE, Kinsella JL, Sollott SJ, Lakatta EG, Brinker JA, Hunter WL, Froehlich JP. *Paclitaxel stent coating inhibits neointimal hyperplasia at 4 weeks in a porcine model of coronary restenosis*. Circulation, 2001; 103:2289-2295.
- [8] Schiff PB, Fant J, Horwitz SB. *Promotion of microtubule assembly in vitro by taxol*. Nature, 1979; 277:665-667.
- [9] Jordan MA, Toso RF, Thrower D, Wilson L. *Mechanism of mitotic block and inhibition of cell proliferation by taxol at low concentrations*. Proc Natl Acad Sci USA, 1993; 90:9552-9556.
- [10] Levin AD, Vukmirovic N, Hwang CW, Edelman ER. *Specific binding to intracellular proteins determines arterial transport properties for rapamycin and paclitaxel*. Proc Natl Acad Sci USA, 2004; 101:9463-9467.
- [11] Cortese B, Micheli A, Picchi A, Coppolaro A, Bandinelli L, Severi S, Limbruno U. *Paclitaxel-coated balloon versus drug-eluting stent during PCI of small coronary vessels, a prospective randomized clinical trial*. Heart, 2010; 96:1291-1296.

- [12] Scheller B, Speck U, Schmitt A, Bohm M, Nickenig G. *Addition of paclitaxel to contrast media prevents restenosis after coronary stent implantation*. Journal of the American College of Cardiology, 2003; 42:1450-1420.
- [13] Kelsch B, Scheller B, Biedermann M, Clever YP, Schaffner S, Mahnkopf D, Speck U, Cremers B. *Dose response to Paclitaxel-coated balloon catheters in the porcine coronary overstretch and stent implantation model*. Investigative Radiology, 2011; 46:255-263.
- [14] Scheinert D, Duda S, Zeller T, Krankenberg H, Ricke J, Bosiers M, Tepe G, Naisbitt S, Rosenfield K. *The LEVANT I trial for femoropopliteal revascularization*. JACC: Cardiovascular Interventions, 2014; 7:10-19.
- [15] Posa A, Nyolczas N, Hemetsberger R, Pavo N, Petnehazy O, Petrasi Z, Sangiorgi G, Gyongyosi M. *Optimization of drug-elution balloon use for safety and efficacy: Evaluation of the 2nd generation paclitaxel-elution DIOR-balloon in porcine coronary arteries*. Catheterization and Cardiovascular Interventions, 2010; 76:395-403.
- [16] Hill P, Brantley H, Van Dyke M. *Some properties of keratin biomaterials: Kerateines*. Biomaterials, 2010; 31:585-593.
- [17] De Guzman RC, Merrill MR, Richter JR, Hamzi RI, Greengauz-Roberts OK, Van Dyke ME. *Mechanical and biological properties of keratose biomaterials*. Biomaterials, 2011; 32:8205-8217.
- [18] Burnett LR, Rahmany MB, Richter JR, Aboushwareb TA, Eberli D, Ward CL, Orlando G, Hantgan RR, Van Dyke ME. *Hemostratic properties and the role of cell receptor recognition in human hair keratin protein hydrogels*. Biomaterials, 2013; 34:2632-2640.
- [19] Clever YP, Cremer B, Kraub B, Bohm M, Speck U, Laufs U, Scheller B. *Paclitaxel and sirolimus differentially affect growth and motility of endothelial progenitor cells and coronary artery smooth muscle cells*. EuroInt, 2011; 7:K32-K42.
- [20] Goldberg SN, Abrahams J, Drayer BP, Golding S, Bernardino M, Brunetti J. *A comparison of iopromide with iopamidol and iohexol for contrast-enhanced computed tomography*. Investigational Radiology, 1994; 29:S76-S83,S93.

THE USE OF ANTIOXIDANT LOADED TCP DEVICES TO SUPPRESS THE METABOLIC ACTIVITY OF SK-OV-3 OVARIAN CANCER LIKE CELLS

Jennifer L. Harpole, MS, Michelle Tucci, PhD
Hamed Benghuzzi, PhD

Clinical Health Sciences, University of Mississippi Medical Center, Jackson, MS 39216

ABSTRACT

Ovarian cancer is the leading cause of mortality among gynecologic cancers. Recent studies have indicated that antioxidant exposure may slow the progression in major neoplastic diseases. The objective of this study was to investigate the synergistic effect of antioxidants Thymoquinone (TQ) and Epigallocatechin-3-gallate (EGCG) using SK-OV-3 cell line as a model. A total of 144 wells were plated with 10^5 SK-OV-3 ovarian cancer cells. The wells were divided into 4 groups of 72 wells for conventional and sustained delivery, respectively. Each group was subdivided into 4 groups of 6 wells. Group 1 served as control and groups 2, 3, and 4 were treated with TQ (16 μ M), EGCG (3 μ g/ml), and TQ + EGCG, respectively. Biomarker evaluations were performed following standard lab techniques. The results of the study revealed: (1) there were no differences in cellular protein concentrations between TQ, EGCG, and control in conventional and sustained delivery for 24 and 48 phases; conversely at 72 hours, protein concentration of TQ was significantly increased in conventional and unchanged in sustained delivery ($p < 0.05$) and (2) an increase in nitric oxide following administration of EGCG and combination therapy at 24 and 72 hours regardless of route of administration. Overall conclusion: the results of this study provided the literature with more insights regarding manipulation of ovarian cancer behavior through potent antioxidants such as TQ and EGCG. The results also indicated the use of sustained delivery of TQ + EGCG inhibited the metabolic activities of SK-OV-3 ovarian cancer cell line in culture.

Keywords: SK-OV-3 ovarian cancer cells, Thymoquinone, EGCG, Sustained Drug Delivery, Conventional Drug Delivery

INTRODUCTION

Ovarian cancer is the leading cause of mortality among the gynecologic cancers. The cause of ovarian cancer is unknown. Ovarian cancer is a very devastating disease and is rarely diagnosed in its early stages. There is very little research on the use of TQ and EGCG on the cell line SK-OV-3 of ovarian cancer. TQ has antioxidant effects and has been shown to protect against heart, liver and kidney damage in animal studies, as well as having possible anti-cancer effects. Other results indicate that TQ inhibits tumor angiogenesis and tumor growth and could be used as a potential drug candidate for cancer therapy. There is increasing evidence to show that EGCG – along with other flavanoids – can be beneficial in treating brain, prostate, cervical and bladder cancers. The results of this study will provide the literature with more insight about the mode of action of antioxidants in the progression of ovarian cancer. The cell line SK-OV-3 is an ovarian adenocarcinoma and was obtained from ATCC. It is derived from the ascites of the metastatic site. It is epithelial-like and was isolated in 1973. SK-OV-3 is a hypodiploid human cell line. SK-OV-3 cells are resistant to tumor necrosis factor and to several cytotoxic drugs including diphtheria toxin, cis-platinum, and adriamycin [1].

METHODS

To find these desired results, there will be 4 groups. Group 1 served as control and groups 2, 3, and 4 were treated with TQ (16 μ M), EGCG (3 μ g/ml), and TQ + EGCG, respectively. Each group will be terminated at 24, 48, and 72 hours. A total of 144 wells were plated with 10^5 SK-OV-3 ovarian cancer cells, respectively. The wells were divided into groups of 72 wells. Each group was subdivided into 4 groups of 6 wells. The antioxidants will be administered through the ceramic drug delivery system. A capsule will be placed in the petri dish with the cells and the antioxidants will diffuse into and surrounding the cells to elicit the appropriate reaction. The BCA assay is a biochemical assay for determining the total concentration of protein in a solution and measures the metabolic activity of the cells. The malinodialdehyde determination assay (MDA) levels were used to determine the membrane and cellular damage of each cell group. The MDA levels were determined using the known standard laboratory procedure [2]. Nitrogen dioxide can be assayed spectrophotometrically by measuring the accumulation of its stable degradation products, nitrate and nitrite. The nitric oxide assay measures cell viability. The glutathione

assay measures the glutathione peroxidase that is used to evaluate cell injury. It is one of the key enzymes in the cellular defense against oxidative stress and the hepatocyte growth factor receptor.

RESULTS

Conventional Delivery

No differences were seen in cellular protein concentrations between control, TQ, and EGCG for the duration of the study. The data shows that treatment with TQ and EGCG alone caused a significant increase in cellular protein concentration at 72 hours following treatment compared to control and combination of TQ and EGCG. Combination treatment at 24 and 48 hours had protein concentrations similar to control, TQ, and EGCG-treated cells.

The results show an increase in nitric oxide following the administration of EGCG alone and in combination with TQ compared with TQ alone or untreated control cells. The difference was approximately three-fold higher for EGCG alone at 24 and 48 hours and two-fold higher at 72 hours. The difference was approximately three-fold higher for the combination of TQ and EGCG at 24 and 72 hours and two-fold higher at 48 hours. This difference was statistically different ($p < 0.05$).

Conventional delivery of TQ, EGCG, and combination of TQ and EGCG did not cause changes in intracellular GSH concentration for 24 or 48 hours. By 72 hours, there was a significant three-fold decrease in intracellular GSH concentration in cells treated with combination of TQ and EGCG when compared to the control. Cells treated with TQ and EGCG alone were similar to the control.

Sustained Delivery

Cellular protein concentrations for the treated groups were not statistically different ($p < 0.05$) for the duration of the study. Protein concentration ranged between 100 to 170 μg in all treatment groups after 24 hours, 120 to 190 μg 48 hours following treatment, and 210 to 310 μg 72 hours following treatment. The treated groups were not statistically different ($p < 0.05$) for the duration of the study.

Nitric oxide concentration ranged between 20 to 80 μM in all treatment groups after 24 hours, 30 to 90 μM 48 hours following treatment, and 10 to 70 μM 72 hours following treatment.

Sustained delivery of TQ, EGCG, and combination of TQ and EGCG did not cause changes in intracellular GSH concentration for 24 or 48 hours. By 72 hours, there was a significant two-fold decrease in intracellular GSH concentration in cells treated with EGCG when compared to the control. There was a significant three-fold decrease in intracellular GSH concentration in cells treated with TQ and the combination of TQ and EGCG when compared to the control.

The MDA levels evaluate for membrane and cellular damage of the groups. After analysis, there was no damage to the SK-OV-3 ovarian cancer cells for the conventional method or sustained drug delivery.

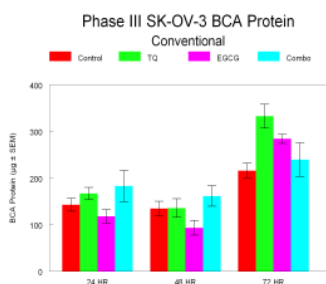


Figure 1: The effects of conventional delivery of TQ, EGCG, and the combination of TQ and EGCG on SK-OV-3 ovarian cancer cells at 24, 48, and 72 hours.

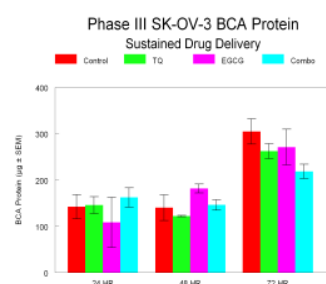


Figure 2: The effects of sustained drug delivery of TQ, EGCG, and the combination of TQ and EGCG on SK-OV-3 ovarian cancer cells at 24, 48, and 72 hours.

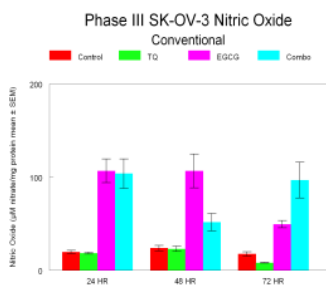


Figure 3: Nitric Oxide evaluation following conventional delivery of TQ, EGCG, and the combination of TQ and EGCG on SK-OV-3 ovarian cancer cells at 24, 48, and 72 hours.

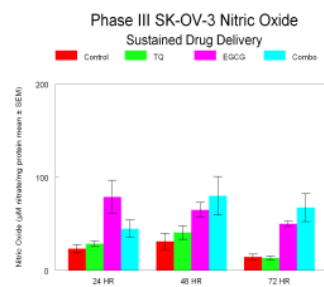


Figure 4: Nitric Oxide evaluation following sustained delivery of TQ, EGCG, and the combination of TQ and EGCG on SK-OV-3 ovarian cancer cells at 24, 48, and 72 hours.

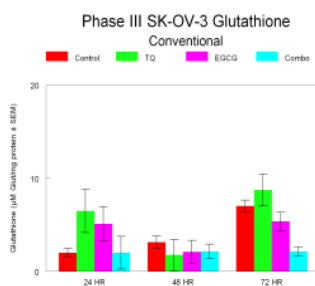


Figure 5: GSH evaluation following conventional delivery of TQ, EGCG, and the combination of TQ and EGCG on SK-OV-3 ovarian cancer cells at 24, 48, and 72 hours.

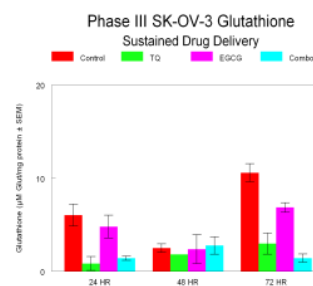


Figure 6: GSH evaluation following sustained delivery of TQ, EGCG, and the combination of TQ and EGCG on SK-OV-3 ovarian cancer cells at 24, 48, and 72 hours.

DISCUSSION

Ceramic drug delivery devices (CDDD) are particularly promising as delivery systems because they are capable of the storage and release of hydrophilic and hydrophobic compounds, and low and high molecular weight molecules over extended intervals. Also, these delivery systems which are capable of delivering a wide variety of chemicals and biologicals can be used in other applications including veterinary medicine, pisciculture, and agriculture [3]. This study was utilized to determine if there were any effects on the cells after treatment of two different delivery methods: conventional delivery (CD) and sustained delivery (SD) of natural potential chemotherapeutic agents.

The results on antioxidants in colon cancer cells and ovarian cancer cells when compared show that the antioxidants affected them differently. In conventional delivery, the administration of TQ to the SK-OV-3 cells was increased at 72 hours just as the colon cancer cells were increased. In sustained delivery, there were no differences when the antioxidants were administered to the ovarian cancer cells, but there was a decrease in the protein levels in the colon cancer cells [4].

When compared to our study, the dose was 50µM which is a high dose. The ovarian cancer cell line had an increase in nitric oxide levels when exposed to EGCG at all phases through conventional delivery. Through sustained delivery, the nitric oxide levels of the ovarian cell when treated with TQ and EGCG were the same as the control levels in all phases. This demonstrates that the antioxidants were more effective on the colon cancer cells than the ovarian cancer cells [4].

According to Martin *et al.* (2006), the result of the conventional delivery of TQ was that there was a slight increase in glutathione at 48 hours. The result of sustained delivery is that there was an initial increase at 24 hours after TQ

was added. At 48 hours, there was a time dependent increase in the TQ group. This shows that TQ affects the glutathione differently in neuroblastoma cells and ovarian cancer cells. TQ caused increase in neuroblastoma cells; whereas, it caused the ovarian cells to decrease or remain unchanged in both conventional and sustained delivery [5].

The MDA levels in the PANC-1 cells showed a statistically significant increase with the treatment of 25 μ M TQ+EGCG in comparison to the control groups at all phases using sustained delivery. At 24 hours of sustained delivery, the MDA levels were most markedly increased when TQ and TQ+EGCG were administered. However, all MDA levels showed cellular damage at all phases. This study had results that were the opposite of our study because we had no cellular injury to either of the ovarian cancer cell lines by the conventional or sustained delivery method [6].

CONCLUSIONS

Antioxidants may be used as an alternative method of treatment and offer patients and their families' options in managing their disease. The use of antioxidants has proven to offer promising effects as chemopreventive agents of ovarian cancer. The data of this study suggest that combination therapy with antioxidants is an effective means of generating physiological responses, such as cell suppression, decrease in protein levels, and cell cycle disruption. Future studies are needed to further investigate the possibilities of antioxidant treatment and prevention of ovarian cancer.

REFERENCES

- [1] "SK-OV-3." ATCC, 1973.
<http://www.atcc.org/ATCCAdvancedCatalogSearch/ProductDetails/tabid/452/Default.aspx?ATCCNum=HTB-77&Template=cellBiology>
- [2] Hansen, JT, H Benghuzzi, M Tucci, and Z Cason. "The role of black seed in the proliferation and biochemical marker levels of Hep-2 cells." *Biomedical Science Instrumentation*. 39:371-6 (2003): Print.
- [3] Benghuzzi, H. A., B. G. England, and P. K. Bajpai. "Characterization of Ceramic Drug Delivery Devices: The Effect of Various Temperatures of Incubation on the Delivery of Biologicals." *Biomedical Sciences Instrumentation*. (1992): Print.
- [4] Norwood, Anne A., Michelle Tucci, and Hamed Benghuzzi. "A Comparison of 5-Fluorouracil and Natural Chemotherapeutic Agents, EGCG and Thymoquinone, Delivered by Sustained Drug Delivery on Colon Cancer Cells." *Biomedical Sciences Instrumentation*. (2007): Print.
- [5] Martin, Tina Mitchell, Hamed Benghuzzi, and Michelle Tucci. "The effect of conventional and sustained delivery of thymoquinone and levodopa on SH-SY5Y human neuroblastoma cells." *Biomedical Sciences Instrumentation*. 42: 332-337 (2006): Print.
- [6] Tan, Mary, Anne Norwood, Merilyn May, Michelle Tucci, and Hamed Benghuzzi. "Effects of (-)epigallocatechin gallate and Thymoquinone on Proliferation of a PANC-1 Cell Line in Culture." *Biomedical Sciences Instrumentation*. 42: 363-369 (2006): Print.

MARKOV CHAIN BASED PREDICTIVE (BCI) SPELLER

Jenny Wang, and Janet Spoonamore,
NC School of Science and Math, 1219 Broad St, Durham, NC 27705
NC State University, Raleigh, NC 27695

ABSTRACT

Brain-Computer Interfaces (BCI) allow for hands free communication by correlating visual stimulation with surface electroencephalograph (EEG) signal responses. To overcome inefficiency in the current BCI speller, we created a Markov-chain based predictive method to help enhance letter selection. Based on the observation that the 100 most commonly used English words make up about half of all written material and the 300 most commonly used words make up about 65% of all written material, we analyzed the 100 and 300 most commonly used words and calculated the first order Markov Transition probability of next alphabetic character given the current letter. Based on the Markov transition probability, we created three optimized visual stimulation patterns for text input: 1) ordered row and column flashing of next possible letters in decreasing probability; 2) ordered row and column flashing of next possible letters after re-arranging the list to top left corner diagonally; 3) ordered single character flashing of next possible letters in decreasing probability. Our simulation results showed a significant speed up in text entry over current methods.

Keywords: Brain-Computer Interfaces, Markov Analysis, Predictive text input, Visual Speller

INTRODUCTION

Brain-Computer Interfaces (BCI) [1], which is based on the correlation of P300 evoked reaction potentials (ERPs) with visual stimuli, has enabled severely disabled people to interact with computers. The visual stimulus comes from a 6 by 6 display of 26 letters, digits and other commands. A single or a group of letters flashes based on a predetermined order. When users concentrate on the letter they want to select, a P300 response is evoked when the letter of choice is flashing. The FD-Speller (Farwell and Donchin) was first proposed in [2] by flashing rows and columns of letters in random order. Users selected a letter by evoking a P300 signal when both the row and column containing that letter were flashed. Another scheme, called the SD-Speller, was proposed in order to elicit a more reliable P300 signal [3]. Instead of flashing rows and columns, SD-Speller highlights each letter individually. Other efforts include a revised 7 x12 display layout with different flash patterns [4].

A common weakness of these spellers is that they assume equal probability of appearance for each letter, while in reality letters do appear at different frequencies. Randomized flashing schemes led to inefficiency. This project focuses on improving current BCI speller by using the 1st order Markov transition probability of the most commonly used words to re-arrange letter flashing pattern and to re-order the flashing sequence.

METHODS

A. Analysis of Commonly Used Words

The most commonly used first 25 words make up about one-third of all printed material in English, while the first 100 words and 300 words make up about one-half and sixty-five percent of all written material [5]. We analyzed the frequencies of letters appearing in the first 100 and 300 word sets. Based on the frequency of appearance, we calculated the transition probability $P(X_{i+1}=x_{i+1}|X_i=x_i)$ from the current letter X_i where $x_i \in \{a, b, \dots, x, y, z\}$ to next letter X_{i+1} where $x_{i+1} \in \{a, b, \dots, x, y, z\}$ at each letter position (from the 1st letter position to the 9th letter position, since these most frequently used words have fewer than 10 letters). Based on the 26 by 26 Markov transition probability matrix for each letter at its current location, we can create a list of the possible next letters.

B. New Predictive Speller

Using the Markov transition probability, three new visual speller schemes were created:

New FD1: Given the current letter and its transition probability to the next letter, a list of possible next letters can be obtained. Instead of flashing rows and columns randomly, only the rows and columns that contain the possible next letter will be flashed in the order of descending probability.

New FD2: To make the above scheme more efficient, the list of possible next letters will be rearranged starting from the top left corner diagonally. Thus, the letter in the top left corner can be selected in two flashes, while the adjacent two letters can be selected in three flashes, etc. This re-arrangement to the top left corner of the 6 by 6 paradigm further minimizes the total number of flashes.

New SD1: The original SD scheme flashes letters in random order. To improve efficiency, our SD1 method flashes only the most likely next letters in the order of descending probability.

RESULTS

We analyzed both the 100 and 300 most frequently used words, and calculated the transition probability at each letter location. Figure 1 (Left) shows the list of possible next letters in descending probability given the first letter of a word in our 100 and 300 word set. For example, if *t* is the first letter, there are four possible second letters in the 100 word set and eight possible next letters in the 300 word set. Figure 1 (Right) shows the letter transition probabilities from first letter *t* to the possible second letter.

	a	b	c	d	e	f
First 100 Words	nbrlst	euy	ao	oai	a	lor
First 300 Words	nbrsdfgimtw	eoaiuy	aohilu	oia	anvxy	oair
	g	h	i	j	k	l
First 100 Words	eo	aeio	ntfs			oi
First 300 Words	orie	eaio	ntdfms	u	ein	ieao
	m	n	o	p	q	r
First 100 Words	aoy	ou	nfirtu	ae		
First 300 Words	aoeliuy	eoaiu	nfulprtvw	aleiou		eiu
	s	t	u	v	w	x
First 100 Words	oah	hiow	ps		haeior	
First 300 Words	oetahcimpu	hoareiuw	nsp	e	haeoir	
	y	z				
First 100 Words	o					
First 300 Words	oe					

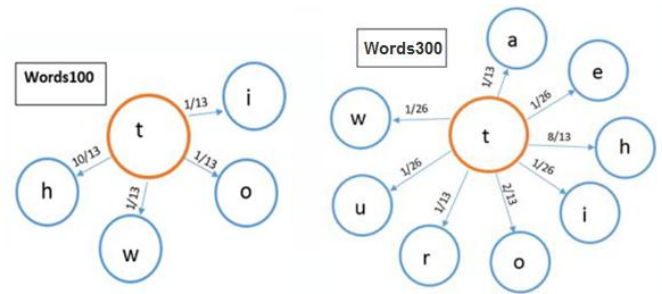


Figure 1 (Left) shows the lists of possible second letter in descending probability; (Right) A Markov transition probability diagram for both the 100 word and 300 word sets given the first letter as “*t*”.

Figure 2 shows the transition probability from the 1st letter to 2nd letter. It can be seen that the 100 word and 300 word vocabulary sets have different transition probabilities. The 300 word transition matrix has more non-zero entries due to the increase of word in the set. In both charts, the transition probability from *t* to *h* is the highest.

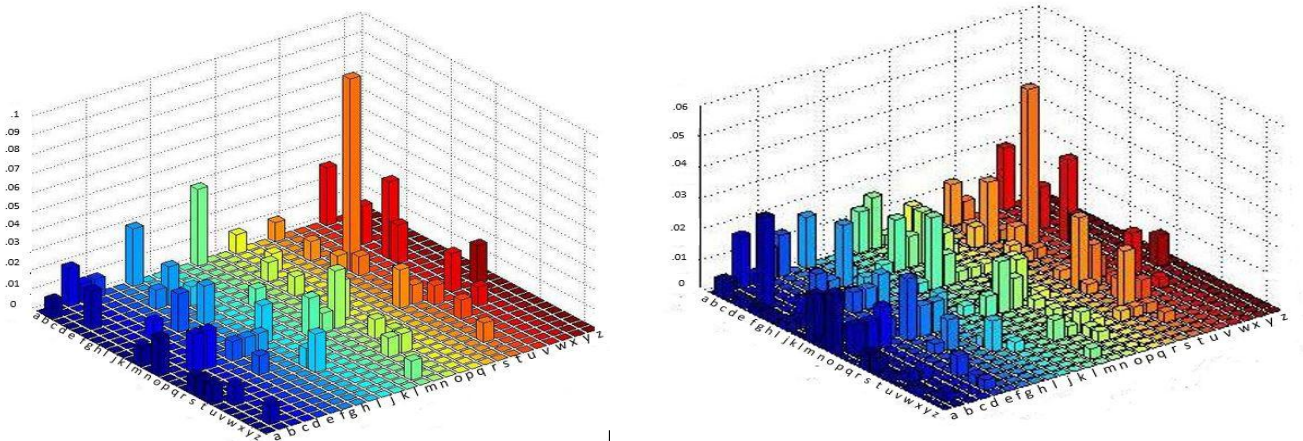


Figure 2 (Left) The 26x26 transition probability from the 1st letter to the 2nd letter of the 100 most commonly used words; (Right) The 26x26 transition probability from the 1st letter to the 2nd letter of the 300 most commonly used words.

We compared the performance of our new schemes with the existing FD and SD scheme via simulation. Test paragraphs were created using the 100 and 300 most commonly used word sets, and spelled by each of the mechanisms. Assuming flashing periods of 100ms followed by 100ms rest periods, we ran the simulation for a total of 1000 times and obtained the average time required to input one word under error free, 10% error and 30% error conditions. Figure 3 shows the performance comparison among the five schemes. The 10% error and 30% error cases cover the scenario that a user missed the correct selection and has to go through the selection sequence again.

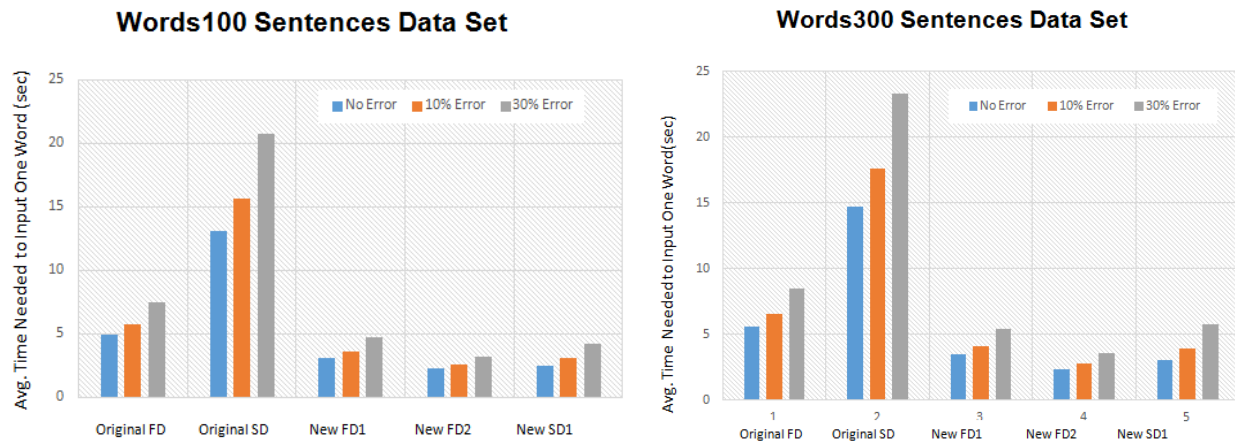


Figure 3 (Left) Average time needed to spell a word in a test paragraph formed from the 100 most frequently used words.

(Simulation based on 100ms flash time followed by 100ms delay interval); (Right) Average time to spell a word in a test paragraph formed from the 300 most frequently used words.

DISCUSSION

The transition probability matrix represents the statistical property of a selected vocabulary set. The first order Markov Chain transition matrix provides a good way to predict the next letter, once the current letter has been selected. The second order Markov Chain transition matrix may offer more accurate word predictions, but was not used due to its size ($26 \times 26 \times 26$), and the limited usefulness (can only start predicting at the 3rd letter). Using the probability learned from the vocabulary set, our new schemes only flash the possible next letters (in decreasing probability from most likely to least). In our new FD2 scheme, rearranging the most likely letters to the top left corner further improved the FD performance. The original SD scheme was not efficient since it may have to flash through the whole alphabet one letter a time in a randomized order. Our revised SD scheme is much more efficient since it goes through the possible letters based on the order of decreasing probability, and as a result drastically cuts input time.

As with any predictive algorithm, the performance of our system relies on how closely the test data (input text) resembles the training data (the vocabulary set). In reality, the two sets will never be exactly the same. For example, in calculating transition matrix, we assumed that each word in the 100 or 300 word set was used the same number of times, while in real life (modeled by our test paragraphs) these words appear in varying frequencies. An additional challenge is to deal with words outside the training vocabulary set. The predictive method may not be effective in such cases. But as long as the majority of the input text is using words from the training set, our predicative methods provide a significant speed-up over current randomized schemes.

CONCLUSIONS

Using the statistical properties of the underlying vocabulary set to predict next letter, we created three new visual speller schemes that offer prioritized flashing of most likely letters. For input text that resembles the training vocabulary, our methods can achieve a significant increase in entry speed and provides an enhanced user experience. We plan to carry out future work to verify the effectiveness of our new visual speller schemes on human subjects under a clinical setting.

REFERENCES

- [1] J. Wolpaw, N. Birbaumer, D. MacFarland, G. Pfurtscheller and T. Vaughan, 'Brain-computer interface for communication and control', in *Clin. Neurophysiol.*, 113:767-791, 2002.
- [2] L. Farwell, E. Donchin "Talking off the top of your head: toward a mental prosthesis utilizing event related brain potentials", in *Electroencephalogr Clin Neurophysiol* 70(6):510-523
- [3] C Guan, M. Thulasidas, J. Wu, "High performance P300 speller for brain-computer interface", IEEE International Workshop on Biomedical Circuits and Systems, 2004
- [4] J. Jin, Eric W. Sellers, X. Wang, "Targeting an efficient target-to-target interval for P300 speller brain-computer interfaces", in *Medical & Biological Engineering & Computing*, Vol. 50 No. 3
- [5] E. Fry, J. Kress, D. Fountoukidis, "*The Reading Teachers Book of Lists*", Jossey-Bass; 5th edition (April 14, 2006)

THE EFFECTS OF THYMOQUINONE AND GREEN TEA EXTRACT ON LDL MODIFICATION IN HUMAN AORTIC ENDOTHELIAL CELLS

Felicia M. Tardy¹, Hamed Benghuzzi¹, and Michelle Tucci²

¹School of Health Related Professions and ²Department of Orthopedic Surgery
University of Mississippi Medical Center, Jackson, MS 39216

ABSTRACT

Oxidatively modified low-density lipoprotein (LDL) has been implicated in the development of cardiovascular disease, the leading cause of morbidity and mortality worldwide. While the exact mechanism by which oxidized LDL contributes to CVD has not been fully elucidated, it is believed that inhibiting LDL oxidation may provide protection against CVD. Previous studies have indicated that antioxidants such as green tea (GT) and thymoquinone (TQ) may reduce the damage caused by oxidized LDL. Therefore, the specific aim of this study is to determine the effects of GT and TQ on the modification of LDL using endothelial cells as a model. Male and female human aortic endothelial cells (HAEC) were challenged with LDL, alone or in combination, with TQ and GT, and the functional capacity of the cells was evaluated. Results of the study suggest that TQ and GT may be effective in preventing the damage caused by LDL oxidation.

Keywords: cardiovascular disease, green tea, thymoquinone, endothelial cells, LDL, antioxidants

INTRODUCTION

A report by the American Heart Association estimates that approximately 83.6 million American adults have one or more types of CVD [1]. Although mortality rates from CVD have declined nearly 30% in the past few years, it still remains the leading cause of death for both males and females in the US [2]. With CVD being the leading global cause of disease burden, and healthcare costs continuing to soar, researchers are seeking for alternative therapies to treat CVD.

The fact that researchers have considered CVD an inflammatory process has received much attention in the last few decades. Atherosclerosis is believed to result from injury to the vascular endothelium by lipids, primarily LDL. Once LDL attaches to the endothelium, it soon becomes oxidized by surrounding cells, initiating an inflammatory response that ultimately leads to the formation of atherosclerotic plaque [3].

Numerous studies have investigated the effects of green tea consumption on CVD risk. Nagao and colleagues looked into the relationship of ingesting green tea high in catechins and body fat. They concluded that consumption of green tea high in catechins may promote weight loss and reduce CVD risk [4]. Sung et al. evaluated the effect of green tea consumption on atherosclerotic markers in men. Their study suggests that green tea has an *in vivo* antioxidant effect and may influence markers for atherosclerosis [5].

Several previous studies in our lab suggest that treating cells with TQ may reduce the effects of damage caused by oxidation. Vance et al. treated Rhesus monkey kidney epithelial cells (RMKEC) with various doses of TQ and observed them for signs of cellular damage. Increased concentrations of TQ raised glutathione levels without causing cellular damage, suggesting that TQ may protect RMKEC from oxidative damage [6].

Because GT has been shown to be effective at reducing CVD risk, and TQ has demonstrated protective effects against oxidative damage, these two antioxidants were selected for the current investigation.

METHODS

Cell Cultures: Human aortic endothelial cells (HAEC) of male and female origin were obtained from Invitrogen, in Frederick, MD. The cells were grown in Medium 200 supplemented with Low Serum Growth Supplement (Invitrogen). The cells were grown in tissue culture flasks in a humidified incubator at 37°C with 5% CO₂. The cells were propagated and grown to confluency, and then they were subcultured into 24-well plates. Next, cells were challenged with one of the following: control, LDL (408 mg/dL), LDL+TQ (5 μM), LDL+GT (10 μM), and LDL+TQGT. After incubating for 24, 48, or 72 hours, the supernatant was removed and biochemical analyses were performed.

Cell Viability and Proliferation: The MTT assay was used to determine cell viability and proliferation and can

detect the presence of 200 to 50,000 cells. To perform the assay, Medium 200 (100 μ L) was added directly to each of the wells in the cell culture plate. Next, 10 μ L of MTT/phosphate buffer solution was added to the wells. The cell culture plate was incubated at 37° for 4 hours to allow MTT cleavage to occur. Color development solution (10 μ L), isopropanol with 0.04 N HCl, was added to the samples. The medium in sample wells was read on an ELISA plate reader at 630 nm. The absorbance measured was directly proportional to the number of cells present (Chemicon® International).

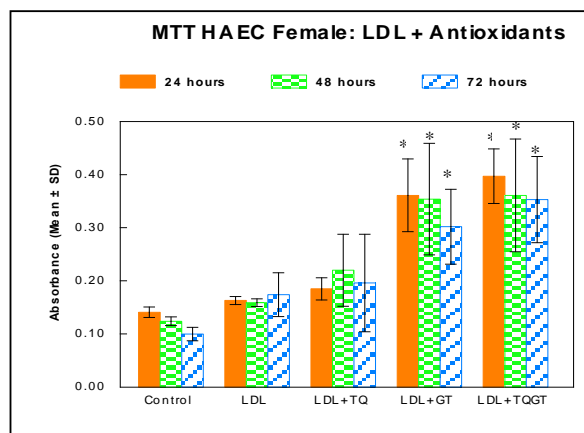
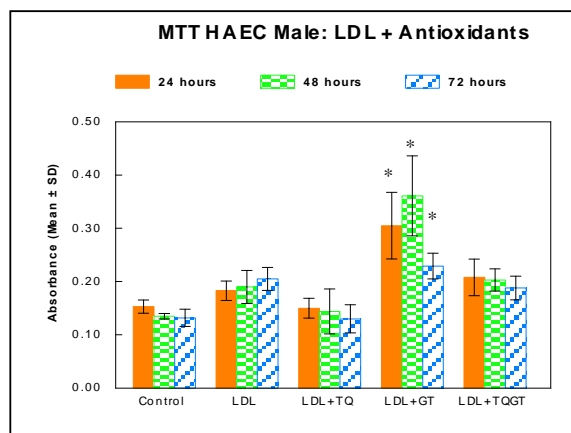
Lactate Dehydrogenase: Lactate dehydrogenase (LD) activity was measured using a quantitative kinetic assay. To perform this assay, 1.0 mL of reagent containing 7.5 mM NAD, 55 mM L-lactate, and buffer pH 8.95, was added to tubes and prewarmed in a heat block at 37° for 5 minutes. Next, 50 μ L of sample (supernatant) was added to the warmed reagent, mixed, and heated for 30 seconds. An initial reading (A_1) was taken on the spectrophotometer at 340 nm, and the sample was returned to the heat block for one minute. A second absorbance reading (A_2) was recorded next. The difference in the two absorbance readings ($A_2 - A_1$) was multiplied by a factor of 3376. Results were expressed in U/L.

Statistical Analysis: Statistical analysis was performed using Jandel Computer Statistical Analysis Software (Sigma STAT). Differences among the control and experimental groups were detected using one-way analysis of variance (ANOVA), while Tukey's test was used to make pairwise comparisons. The results were expressed as the mean \pm standard deviation (SD).

RESULTS

Observations of the study indicate that male HAEC challenged with LDL, alone or in combination with antioxidants, resulted in differences in cell proliferation. This excludes the group that was given LDL+TQ, which had cell numbers nearly identical to the control for all durations. Proliferation in groups challenged with LDL alone steadily increased throughout the experimental phases. The most dramatic changes in proliferation were seen in the LDL+GT group. Statistically significant ($p < 0.05$) increases were observed throughout the extent of the incubation periods. Proliferation was also enhanced in cells treated with LDL+TQGT. In this group, MTT levels were increased throughout the experimental phases compared to the controls. These differences were not statistically significant (Figure 1).

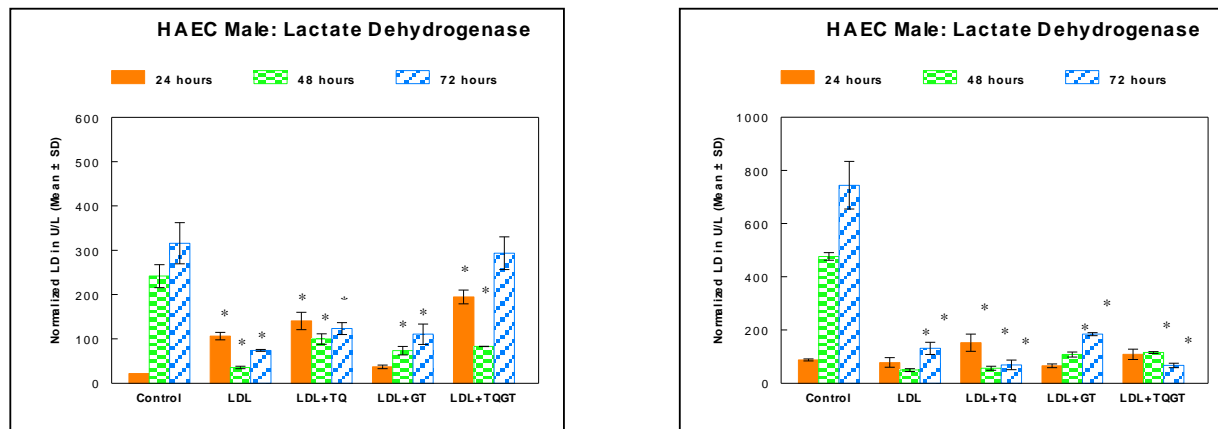
Female endothelial cells challenged with LDL or LDL+TQ had elevated MTT levels at all incubation periods when compared to the control; however, the slight increases were not statistically significant. Similar to male HAEC, LDL+GT also positively affected proliferation for the extent of the experiment. In contrast, the group receiving LDL+TQGT displayed the greatest cell numbers in female HAEC. Increases in MTT levels for cells treated with LDL+GT and LDL+TQGT were both statistically significant ($p < 0.05$) (Figure 2).



Figures 1 and 2. MTT (proliferation) levels of LDL-challenged HAEC male and HAEC female exposed to TQ and GT, alone or in combination, at 24, 48, and 72 hours incubation. The control was the non-treated group. Values are expressed as the mean \pm SD. (* $p < 0.05$)

Significant differences were noted for lactate dehydrogenase activity among male HAEC groups treated with LDL and antioxidants, alone or in combination. At 24 hours, groups treated with LDL, LDL+TQ, and

LDL+TQGT were all significantly higher than control ($p < 0.05$). A reversal of this trend was seen at 48 hours. In this duration, all experimental groups were significantly lower than control. A combination of LDL+TQGT amounted to a small reduction in lactate dehydrogenase activity, but this reduction was insignificant (Figure 3).



Figures 3 and 4. Normalized lactate dehydrogenase levels of LDL-challenged HAEC male and HAEC female exposed to TQ and GT, alone or in combination, at 24, 48, and 72 hours incubation. The control was the non-treated group. Values are expressed as the mean \pm SD. (* $p < 0.05$)

Normalized lactate dehydrogenase results for HAEC female treated with antioxidants also resulted in significant differences. LDL+TQ treated cells did increase substantially from the control. The difference was statistically significant ($p < 0.05$). When compared to male HAEC, female HAEC displayed a similar trend in lactate dehydrogenase activity at 48 hours and 72 hours. Groups treated with LDL alone, LDL+TQ, LDL+GT, and LDL+TQGT were all significantly lower than controls ($p < 0.05$) at these durations (Figure 4).

DISCUSSION AND CONCLUSION

In male endothelial cells treated with LDL, proliferation rates increased throughout the duration of the experiment, when compared to control. Similarly, increases were seen in lactate dehydrogenase levels early in the experiment. At 48 hours, however, lactate dehydrogenase levels were significantly lower than the control. The addition of antioxidants to HAEC male challenged with LDL caused the cells to behave in a normal fashion, with the exception of GT, which induced proliferation. Assessment of morphological features indicated that LDL alone or in combination with antioxidants caused changes in cellular appearance.

Female endothelial cells increased in proliferation when challenged with LDL. The addition of antioxidants with LDL enhanced proliferation, with significantly higher cell numbers in groups treated with LDL+GT and LDL+TQGT. While proliferation rates in HAEC female increased, the opposite was seen in lactate dehydrogenase levels. LDL alone or in combination with antioxidants caused significantly lower levels at 48 and 72 hours. Morphological evaluation showed that LDL challenge resulted in alterations in cellular appearance. The addition of antioxidants in the presence of LDL did not prevent changes in morphology.

While antioxidants appeared to reduce the effects of LDL damage in male endothelial cells, the same effect was not observed in female endothelial cells. Overall, results of this study suggest that TQ and EGCG may be effective treatments for CVD; however, further studies are needed.

ACKNOWLEDGEMENT

This project was supported by the University of Mississippi Medical Center, School of Health Related Professions Development Fund, Jackson, MS.

REFERENCES

- [1] A.S. Go *et al.*, “Heart disease and stroke statistics—2013 update: a report from the American Heart Association,” *Circulation*, vol. 127, pp. e6-e245, Dec. 2012.
- [2] D. Lloyd-Jones *et al.*, “Heart disease and stroke statistics—2010 update. A report from the American Heart Association,” *Circulation*, vol.121, e1-e170, 2010.
- [3] S. Fox, *Human Physiology*, 11th ed., New York: McGraw-Hill, 2009.
- [4] T. Nagao *et al.*, “A green tea extract high in catechins reduces body fat and cardiovascular risks in humans,” *Obesity*, vol. 15, pp. 1473-1483, 2007.
- [5] H. Sung, *et al.*,”The effects of green tea ingestion over four weeks on atherosclerotic markers,” *Annals of Clinical Biochemistry*, vol. 42, pt. 4, pp. 292-297, 2005.
- [6] S. Vance *et al.*,”Thymoquinone supplementation and its effect on kidney tubule epithelial cells *in vitro*,” *Biomedical Sciences Instrumentation*, vol. 44, pp. 477-482, Apr. 2008.

IDENTIFICATION OF EPILEPTIC BRAIN STATES ON THE BASIS OF MATCHING PURSUIT DECOMPOSITION OF EEG

Rui Liu¹, Ioannis Vlachos¹, Joshua Adkinson¹, Leonidas Iasemidis^{1,2}

¹Louisiana Tech University, Biomedical Engineering, Ruston, LA

²Louisiana State University Medical School, Shreveport, LA

ABSTRACT

The epileptic brain typically transits into seizures (ictal states) with preceding (preictal) and following (postictal) states, while it behaves “normally” between seizures (interictal states). We set to automatically identify these brain states from the electroencephalogram (EEG). The ability to differentiate between epileptic brain states can find many valuable applications in the management of epilepsy. A time-frequency analysis via multivariate matching pursuit (MMP), which efficiently decomposes a multichannel signal into basic waveforms (e.g., Gabor functions), was performed peri-ictally and interictally to long-term intracranial multi-channel EEG recordings from 4 patients with intractable epilepsy. Novel features capturing EEG’s complexity, frequency content and energy were estimated from the resulted data. We used these features together with their time lags in a 4-class support vector machine (SVM) classification scheme per patient and tested it under a leave-one-out cross-validation (LOOCV) strategy. Synthetic Minority Oversampling Technique (SMOTE) was also used to treat the highly imbalanced datasets due to considerably longer span of the interictal state compared to the span of the other states. Our analytical scheme achieved high sensitivity in detecting each state in all 4 patients (e.g., 83%, 95%, 100% and 100% for the preictal state per patient respectively). These results suggest potential employment of the devised scheme to a wide range of applications, from seizure prediction and in-time intervention to abolish an upcoming seizure, to accurate and objective monitoring of seizure susceptibility over time, to fast and robust detection of different epileptic brain states hidden in days-long inpatient EEG recordings.

Keywords: Multivariate Matching Pursuit, EEG, Brain States, Seizures, Epilepsy

INTRODUCTION

Epilepsy is characterized by recurrent seizures and is among the most common disorders of the nervous system, second only to stroke and Alzheimer disease, and affects 1% to 2% of the world’s population. Due to the unpredictable occurrence of epileptic seizures, patients with epilepsy are at higher risk of injury in their daily life. Seizures occur when a large group of neurons suddenly begins to discharge in a highly organized rhythmic pattern. Iasemidis and colleagues [1] have postulated in the past that seizures result from nonlinear chaotic mechanisms. A characteristic of chaotic systems is that they can demonstrate intermittent state transitions into and out of more ordered states. In this point of view, brain resetting, in which dynamics of cortical areas that converged during the preictal and ictal state diverge in the postictal state, may be captured by nonlinear signal analysis and help with understanding of the mechanisms of ictogenesis. By using measures of time-frequency analysis of multivariate EEG and subsequent SVM classification, we seek to identify the distinct states of the brain on its route into and out of seizures.

The organization of this paper is as follows. The measures employed in the time-frequency analysis of multivariate EEG patterns and the methodology on identification of each brain dynamic state are described in the Methods section. In the Results section, the EEG data and the results of a patient-specific state classification approach are presented. Discussion of the obtained results follows.

METHODS AND MATERIALS

The state identification algorithm consisted of a feature extraction and a classification scheme applied to each EEG segment. Long-term intracranial, 28-channel EEG recordings from 4 patients diagnosed with temporal lobe epilepsy were analyzed. The clinical reports specified a total of 44 seizures in this dataset. We assumed 2 minute periods before seizure onsets as preictal states, the seizures themselves as ictal states and 2 minute periods after seizure ends as postictal states. To reduce possible influence of seizure-related activity on interictal states, interictal states were assumed to be at least one hour before preictal states and one hour after postictal states. In continuous EEG recordings, interictal state is always much longer than the other 3 states and dominates the recordings. Using

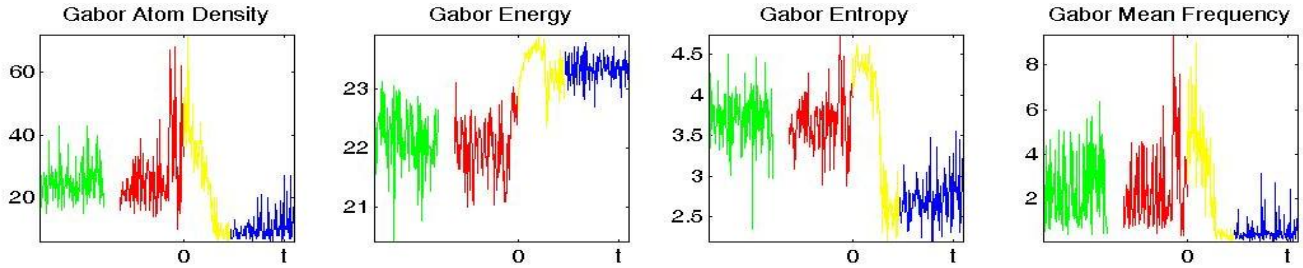


Fig. 1. Values of the four features extracted from MMP interictally and around a seizure. Features presented in green color stand for interictal state; red, yellow and blue correspond to preictal, ictal and postictal states respectively.

the whole interictal periods in our analysis was computationally cumbersome so, in order to include as many different patterns as possible, interictal segments were selected randomly from each patient's interictal periods (accounting to approximately 2 hours of data), while successive non-overlapping EEG data segments in preictal, ictal and postictal states were considered for analysis.

A. Feature Extraction

Multivariate Matching Pursuit [2] (MMP) is an adaptive approximation to a multichannel signal. MMP decomposes the signal into basic waveforms (e.g. Gabor functions) that are automatically selected from a redundant functions dictionary. Gabor functions are mainly sinusoids modulated by Gaussian envelopes:

$$g_{\gamma}(t) = \frac{\sqrt[4]{2}}{\sqrt{s}} e^{-\pi((t-u)/s)^2} e^{i\xi} \quad (\text{eq.1})$$

Four features capturing EEG's complexity with respect to its frequency content and energy were estimated from the MMP decomposition, namely: Gabor atom density (GAD) [3], Gabor energy (GE), Gabor entropy (GEntropy) and Gabor mean frequency (GMF). The estimation was performed on multichannel EEG segments of 1 second duration. The selected features estimate the complexity of EEG signals as follows: GAD is the number of Gabor functions (atoms); GE is the signal energy estimated from the decomposition; GEntropy is the energy-based entropy estimated similarly to wavelet entropy [4] and GMF is the average value of the extracted Gabor atoms frequencies.

B. Classifier

Four-feature sets corresponding to the four epileptic brain states were analyzed by means of support vector machine (SVM) classification [5,6]. In order to also incorporate the short-term dynamics of those features, nine time lags (1 sec each) of them were used as additional features. This made the time span of each feature vector equal to 10 seconds. To compensate for the highly imbalanced length of datasets in interictal versus peri-ictal periods, Synthetic Minority Over-sampling Technique (SMOTE) [7] was used with artificial data being added during the training phase.

Training and testing of peri-ictal data. For peri-ictal data, a leave-one-out (seizure) cross-validation (LOOCV) approach was used, where the SVM was trained on peri-ictal data from all seizures except one seizure and the whole interictal data of the same patient. Then testing was performed on the peri-ictal data from the excluded seizure. The process was repeated on the peri-ictal data from all seizures in the same patient and classification results for each segment of peri-ictal data were obtained.

Training and testing of interictal data. The previous procedure is not applicable to interictal data, so we opted for a 10-fold cross-validation scheme. The SVM was trained on data from all peri-ictal data segments and 90% of the interictal data per patient, while the remaining 10% of interictal data was reserved for testing. This process was repeated 10 times, each time for a different 10% of interictal data, thus classification results for all interictal data were obtained.

C. Post-processing classification of peri-ictal states

Finally, a majority voting strategy was implemented on the previously obtained classification results. For example, if the majority of 1sec segments in a 2min peri-ictal epoch were classified by the algorithm as preictal, the whole 2min epoch is characterized as preictal. This strategy considerably improved our classification results at the expense of time resolution (classification of 1sec segments versus post-processing classification of 2min epochs).

RESULTS

Fig. 1 shows an example of the 4 different features extracted from MMP decomposition per brain state. In Table I we present the SVM-classification results from testing of the algorithm for peri-ictal states of one seizure (seizure 4) that was left out from training in Patient 3. For this seizure, the vast majority of the data was classified correctly. From this table, sensitivity for each of the three states (pre-ictal, ictal, post-ictal) was estimated as 95%, 88.24% and 95.83%, with corresponding specificities 95.82%, 100% and 97.91% respectively. Fig. 2 shows the classification percentage of 1sec segments in the three peri-ictal states across all 9 seizures and interictal states for Patient #3. In this patient, at least 85% of the data segments from each state were classified correctly. Classification results from all 4 patients are presented in Table II and evaluated by means of sensitivity. The left side of the table (columns 3-6) is based on classification from SVM of 1sec individual EEG segments while the right side (columns 7-9) on 2min EEG epochs comprised of consecutive 1sec EEG segments.

Table I. Confusion Table for the three (true) peri-ictal states of seizure 4 (Patient 3)

Classified State \ True State	interictal	preictal	ictal	postictal	Total number of segments
Preictal	2	114	0	4	120
ictal	3	10	105	1	119
postictal	5	0	0	115	120

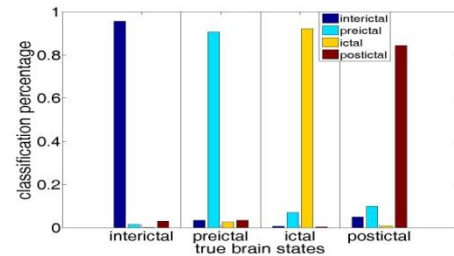


Fig. 2. Classification results from 1sec EEG segments across all seizures and interictal data (Patient 3)

Table II. Classification results for sensitivity of interictal and peri-ictal states per patient

Patient	#seizures	From 1-sec EEG segment				From 2-min EEG epochs		
		interictal	preictal	ictal	postictal	Preictal	ictal	postictal
#1	6	99.14%	61.11%	84.64%	78.75%	83.33%	83.33%	83.33%
#2	23	86.62%	77.64%	90.86%	88.91%	95.65%	100%	100%
#3	9	95.56%	89.91%	92.12%	83.61%	100%	88.89%	88.89%
#4	6	87.16%	80.97%	81.91%	80.42%	100%	100%	100%

DISCUSSION

Even though for interictal data across all patients we were able to achieve consistently high sensitivity (>85%) using 1sec segment classification without post-processing (see Table II, column 3), the results for peri-ictal states were mixed with considerable misclassifications for some patients/states, indicating the need for a post-processing scheme like majority voting. This scheme (Table II, columns 7-9) correctly classified the peri-ictal states of all seizures, except one out of the six seizures of patient #1, one preictal state of patient #2, and one ictal and one postictal state of patient #3.

CONCLUSIONS

Four novel features (Gabor atom density, Gabor energy, Gabor entropy, Gabor mean frequency) were used to analyze and characterize the epileptic brain's states. The above features, when used under an SVM classification setup combined with time lags and adjusting for special data conditions (minority class revision, cross-validation schemes, post processing), performed remarkably well for the task of epileptic brain states identification. This brain state identification algorithm could in the future be improved and adapted for monitoring seizure susceptibility over time and seizure prediction.

REFERENCES

- [1] L. D. Iasemidis, D. Shiau, J. C. Sackellares, P. M. Pardalos, and A. Prasad, "Dynamical resetting of the human brain at epileptic seizures: application of nonlinear dynamics and global optimization techniques," *IEEE Transactions on Biomedical Engineering*, vol. 51, pp. 493-504, 2004.
- [2] C. Sieluzycski, R. Konig, A. Matysiak, R. Kus, D. Ircha, and P. J. Durka, "Single-trial evoked brain responses modeled by multivariate matching pursuit," *IEEE Transactions on Biomedical Engineering*, vol. 56, pp. 74-82, 2009.
- [3] C. C. Jouny, P. J. Franaszczuk, and G. K. Bergey, "Characterization of epileptic seizure dynamics using Gabor atom density," *Clinical Neurophysiology*, vol. 114, pp. 426-437, 2003.
- [4] O. A. Rosso, S. Blanco, J. Yordanova, V. Kolev, A. Figliola, M. Schurmann, and E. Basar, "Wavelet entropy: a new tool for analysis of short duration brain electrical signals," *Journal of Neuroscience Methods*, vol. 105, pp. 65-75, 2001.
- [5] J. Han, M. Kamber, and J. Pei, *Data Mining: Concepts and Techniques*, 3rd ed., Morgan Kaufmann, 2011.
- [6] C. Chang and C. Lin, "LIBSVM: a library for support vector machines," *ACM Transactions on Intelligent Systems and Technology*, vol. 2, no. 3, pp. 27:1-27, 2011.
- [7] N. V. Chawla, K. W. Bowyer, L. O. Hall, and W. P. Kegelmeyer, "SMOTE: synthetic minority oversampling technique," *Journal of Artificial Intelligence Research*, vol. 16, pp. 321-357, 2002.

MORPHOLOGICAL EVALUATION OF KIDNEY FOLLOWING CYCLOSPORINE ADMINISTRATION

Stacy Hull Vance, Michelle Tucci and Hamed Benghuzzi

University of Mississippi Medical Center, Jackson, Mississippi, USA

ABSTRACT

Cyclosporine (CsA) is extracted from *Tolypocladium inflatum* Gams, which is metabolized through the superfamily of hepatic isoenzymes P-450. CsA has a mean life of 6.4-8.7 h, although this varies among different individuals. Ninety percent of the drug is withdrawn through biliary excretion and only 6% appears unchanged in the urine. The exact mechanism of action of CsA is unknown; however, CsA has the ability to act on the immune system by blocking the biosynthesis of some lymphokines produced by T lymphocytes and interleukine-2 synthesis at the transcriptional level. It has been suggested that CsA acts by interacting with cytoplasmic membrane and activates the intracellular calcium pathway, or binds to cytoplasmic proteins (Parra, 2003). At toxic levels, CsA also has the ability to cause renal damage and histological changes that can affect the function of a transplanted kidney (Kahn, 1989, Wang, 1994, Bagnis, 1996, Hansen, 1996). **Hypothesis:** A: Cyclosporine is a potent immunosuppressive agents that act on many cells of the body, including epithelial cells and may cause a decrease in the cell proliferation and increase markers for cell damage. **Specific Aim :** To evaluate kidney epithelial cells after exposure to various doses (low, medium, and high) of CsA and to measure changes in cellular proliferation, morphology and function with time. **Results:** The results from our study indicates that the administration of CsA will result in cellular destruction and dysfunction. **Conclusion:** The findings from our study indicate that the overall the administration of cyclosporine resulted in changes as early as 24 hours in comparison to the control. By 72 hours the group treated with cyclosporine displaced devastating morphological changes, which can ultimately result in kidney dysfunction in comparison to the control.

Keywords: RHKEC, Rhesus Monkey, Kidney cells, Cell Line, Epithelial Cells,

INTRODUCTION

Cyclosporine (CsA) is extracted from *Tolypocladium inflatum* Gams, which is metabolized through the superfamily of hepatic isoenzymes P-450. CsA has a mean life of 6.4-8.7 h, although this varies among different individuals. Ninety percent of the drug is withdrawn through biliary excretion and only 6% appears unchanged in the urine. The exact mechanism of action of CsA is unknown; however, CsA has the ability to act on the immune system by blocking the biosynthesis of some lymphokines produced by T lymphocytes and interleukine-2 synthesis at the transcriptional level. It has been suggested that CsA acts by interacting with cytoplasmic membrane and activates the intracellular calcium pathway, or binds to cytoplasmic proteins (Parra, 2003). At toxic levels, CsA also has the ability to cause renal damage and histological changes that can affect the function of a transplanted kidney (Kahn, 1989, Wang, 1994, Bagnis, 1996, Hansen, 1996). Some of the typical signs of CsA usage include reduced glomerular filtration and changes in intrarenal hemodynamic function, which can start to occur after one week of usage (Tegzess, 1988, Kahan, 1989). Endothelial dysfunction and hypertension are common complications of calcineurin inhibitors, such a cyclosporine and Tacrolimus. Calcineurin inhibitors exert its effects on vasomotor tone. Oxidative stress induced by superoxide has been implicated as a cause of hypertension. NADPH oxidase is the main source of superoxide production in phagocytic and vascular cells. The p22^{phox} subunit is involved in NADPH oxidase activation. Kidney and heart transplant patients that are treated with cyclosporine have been shown to have an increase in reactive oxygen species production, upregulation of the nitric oxide synthase gene expression, and nitrite/nitrate levels. Using p22^{phox} as a marker of oxidative stress, there was not a significant difference between the group treated with cyclosporine or tacrolimus when compared to normotensive healthy controls (Calo, 2002).

In the early stages of CsA administration kidney damage can occur, which causes alterations in intrarenal hemodynamics related to afferent arteriolar vasoconstriction, causing a decrease in glomerular filtration rate, renal plasma flow, loss of proximal tubular cells brush border, proximal tubule dilatation, swelling, necrosis, and infiltration of white blood cells in the kidney cortex. Renal tubular toxicity induced by CsA can be acute with the appearance of oligoanuria, presence of atrophic tubules, and edema. In addition, CsA can induce a subacute

syndrome with giant mitochondria, isometric vacuolization, and microcalcifications in proximal tubules. CsA causes an imbalance of the cellular oxidative status because of increased formation of free radicals, which can be attributed to degradation of membrane phospholipids. In *in vitro* studies, CsA has induced lipid peroxidation in rat kidney and liver microsomes. *In vivo* studies have demonstrated that lipid peroxidation induced by CsA was dose-dependent and paralleled the renal function, measured as decreased glomerular filtration rate, and renal blood flow, and increase renal vascular resistance. In the rat glomeruli treated with CsA, showed a dose dependent increase in enzyme activity.

Hypothesis A: Cyclosporine is a potent immunosuppressive agents that act on many cells of the body, including epithelial cells and may cause a decrease in the cell proliferation and increase markers for cell damage.

Specific Aim : To evaluate kidney epithelial cells after exposure to various doses (low, medium, and high) of CsA and to measure changes in cellular proliferation, morphology and function with time.

Rationale: Renal damage caused by therapeutic treatment with CsA has been previously documented; however, the exact mechanism by which this drug causes nephrotoxicity has yet to be clarified. TGF- β induces the synthesis of numerous extra cellular matrix (ECM) proteins such as fibronectin and collagen; decreases matrix degradation by down regulating proteases inhibitors; enhances the expression of integrins on the cell surface; facilitates deposition of matrix; and is a major regulator in the healing process (Border, 1990). Previous findings in our laboratory showed increasing doses of Cort to RMKC caused a decrease in cell number and an increase in cellular damage (Vance, 2003).

MATERIALS AND METHODS

The RMKEC cell line was obtained from the American Type Culture Collection (ATCC) and grown in 24 well plates on coverslips. Each group was treated with CsA 10 μ g/ml, 25 μ g/ml, or 50 μ g/ml of cyclosporine respectively. After treatment and incubation, the supernatant were removed from the wells and the coverslips were mounted on a glass slide. The slides were stained with H&E stain and digitized using Image Pro.

RESULTS

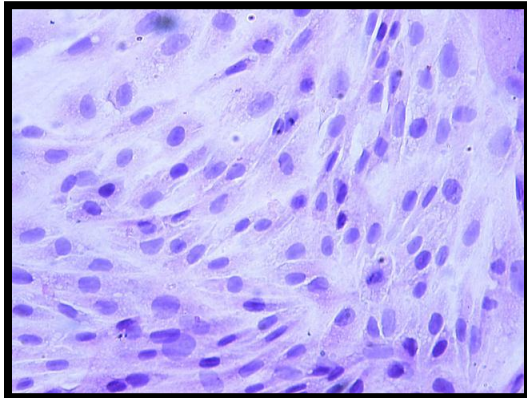


Figure 6: Morphology (H & E) of RMKEC cells exposed to conventional delivery of low, medium, and high doses of Cyclosporine. The control group (all images shown above) was the non-treated group at 24 hours. Cells were digitized using Image Pro Plus Software at 40X.

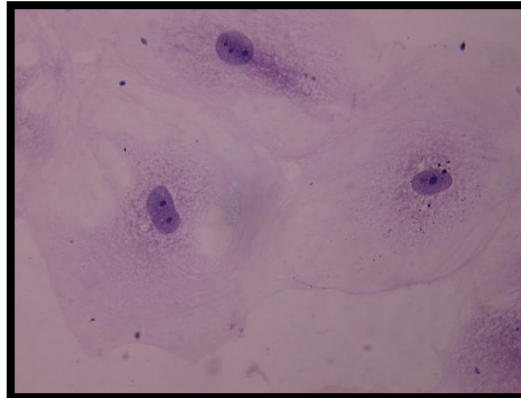


Figure 7: Morphology (H & E) of RMKEC cells exposed to conventional delivery of low dose of Cyclosporine 10 at 24 hours (all images shown above) Cells were digitized using Image Pro Plus Software at 40X.

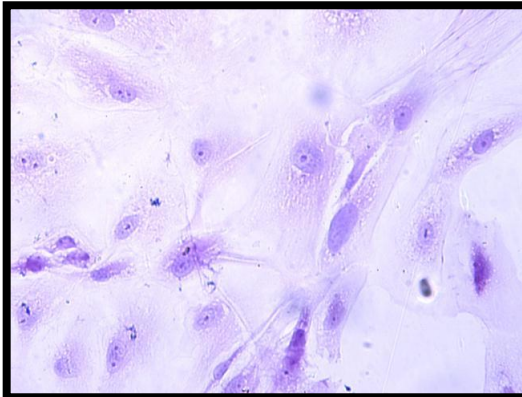
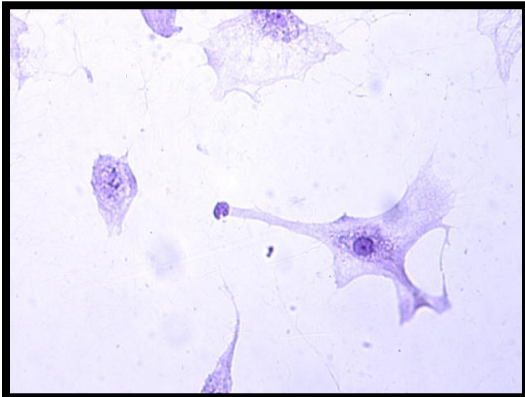


Figure 8: Morphology (H & E) of RMKEC cells exposed to conventional delivery of medium dose of Cyclosporine 25 at 24 hours (all images shown above). Cells were digitized using Image Pro Plus Software at 40X.

Figure 9: Morphology (H & E) of RMKEC cells exposed to conventional delivery of high dose of Cyclosporine 50 at 24 hours (all images shown above). Cells were digitized using Image Pro Plus Software at 40X.

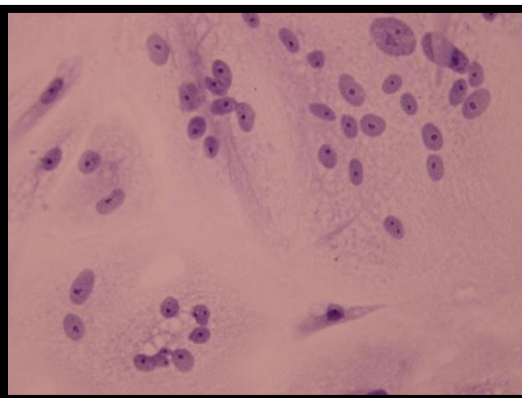
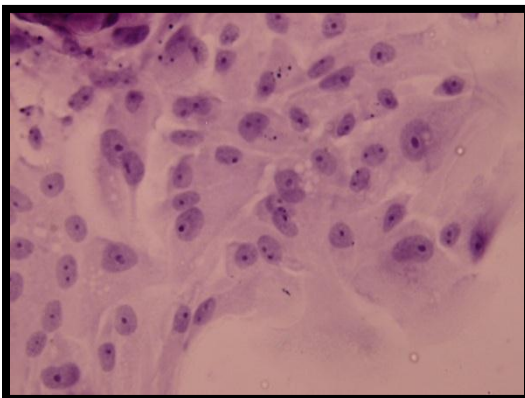


Figure 10: Morphology (H & E) of RMKEC cells exposed to conventional delivery of low, medium, and high doses of Cyclosporine. The control group (all images shown above) was the non-treated group at 48 hours. Cells were digitized using Image Pro Plus Software at 40X.

Figure 11: Morphology (H & E) of RMKEC cells exposed to conventional delivery of low dose of Cyclosporine 10 at 48 hours (all images shown above). Cells were digitized using Image Pro Plus Software at 40X.

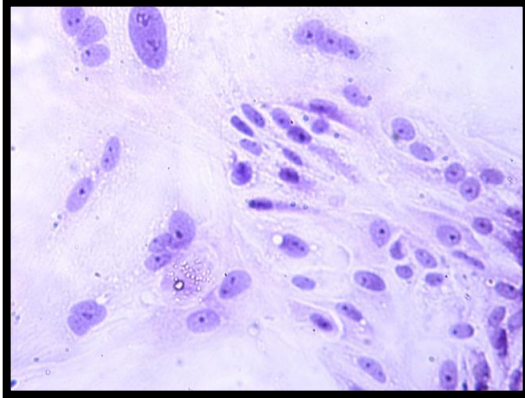
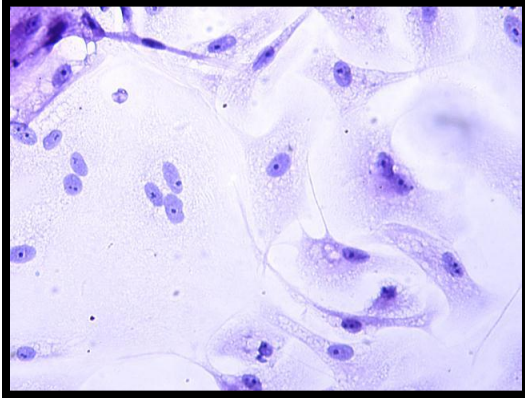


Figure 12: Morphology (H & E) of RMKEC cells exposed to conventional delivery of medium dose of Cyclosporine 25 at 48 hours (all images shown above). Cells were digitized using Image Pro Plus Software at 40X.

Figure 13: Morphology (H & E) of RMKEC cells exposed to conventional delivery of high dose of Cyclosporine 50 at 48 hours (all images shown above). Cells were digitized using Image Pro Plus Software at 40X.

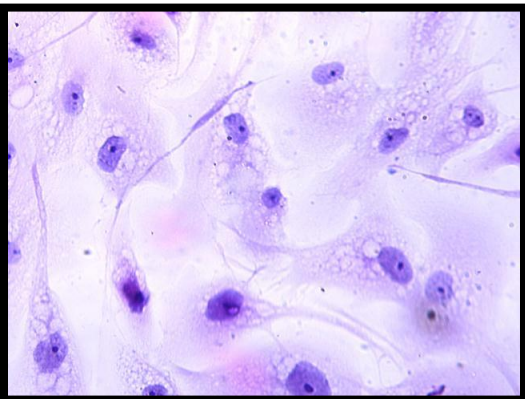
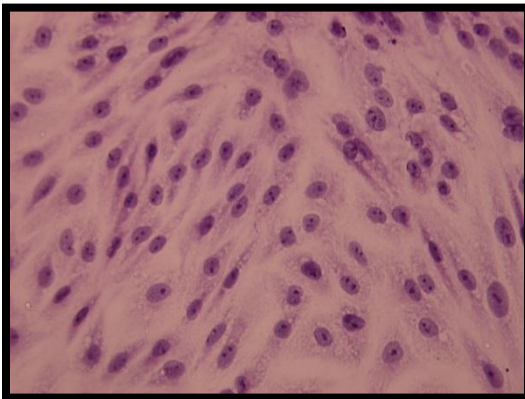


Figure 14: Morphology (H & E) of RMKEC cells exposed to conventional delivery of low, medium, and high doses of Cyclosporine. The control group (all images shown above) was the non-treated group at 72 hours. Cells were digitized using Image Pro Plus Software at 40X.

Figure 15: Morphology (H & E) of RMKEC cells exposed to conventional delivery of low dose of Cyclosporine 10 at 72 hours (all images shown above). Cells were digitized using Image Pro Plus Software at 40X.

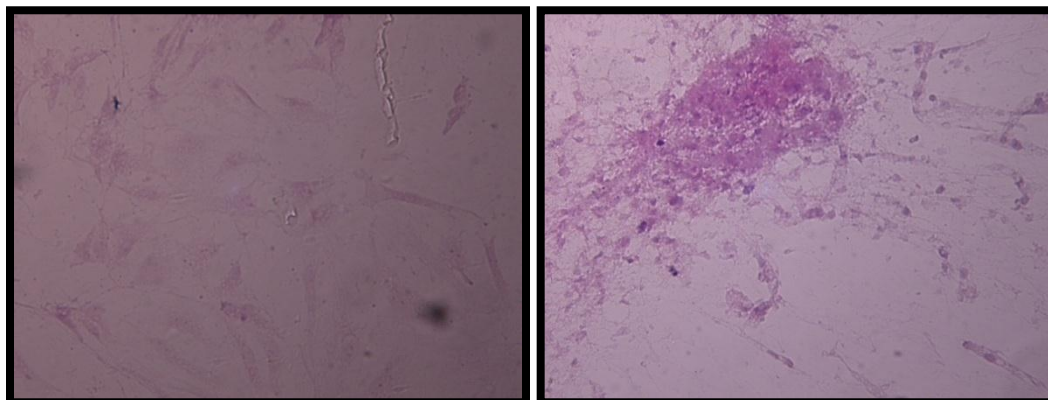


Figure 16: Morphology (H & E) of RMKEC cells exposed to conventional delivery of medium dose of Cyclosporine 25 at 72 hours (all images shown above). Cells were digitized using Image Pro Plus Software at 40X.

Figure 17: Morphology (H & E) of RMKEC cells exposed to conventional delivery of High dose of Cyclosporine 50 at 72 hours (all images shown above). Cells were digitized using Image Pro Plus Software at 40X.

DISCUSSION

Cyclosporine (CsA) is one of the most widely used drugs in organ transplantation. CsA administration following transplantation is associated with 1-year graft survival rates of approximately 90% (Harihran et al., 2000), but the major drawback is associated with renal vasoconstriction (English et al., 1987). Long term CsA use has been linked to structural changes in the kidney which leads to an irreversible decline in kidney function. Long term use is associated with interstitial fibrosis and tubular atrophy. The mechanism or events leading to CsA nephrotoxicity is currently unknown. Several studies suggest that CsA mode of action through an induction of apoptosis (Jennings 2007,). Baker et al., (2007) examined CsA on the viability of cultured proximal tubular epithelial cells by measuring cell death by apoptosis or necrosis. Their findings showed CsA at concentrations of $< 10 \mu\text{g/mL}$ did not result in increased apoptotic behavior. Furthermore when CsA given at concentrations $> 10\mu\text{g/mL}$ the results showed increased cell death. Jennings et al., (2007) also demonstrated that CsA can induce senescence in renal tubular epithelial cells. They showed CsA induced H_2O_2 production, which ultimately caused cell cycle arrest in the G0/G1 phase.

CONCLUSION

Irreversible cell damage can occur by electrophilic radicals that can react with oxygen giving rise to reactive oxygen species. ROS that have the ability to react with intracellular molecules, unsaturated fatty acids, and transmembrane proteins with oxidizable amino acids. The cellular changes that occurred resulted in alterations of ionic gradients, disruption of several membrane functions, and induced free radical production. Patients treated with CsA have a lower prevalence of bacterial and fungal infections, but a higher incidence rate of viral infections and pneumocystis carinii pneumonia. Renal dysfunction is the main complication associated with CsA treatment, which results in 30% of patients having moderate to severe kidney damage. The findings from our study indicate that the overall administration of cyclosporine resulted in changes as early as 24 hours in comparison to the control. By 72 hours the group treated with cyclosporine displaced devastating morphological changes, which can ultimately result in kidney dysfunction in comparison to the control.

REFERENCES

- Calo, L., Davis, P., Giacon, B., Pagnin, E., Sartori, M., Riegler, P., et al., (2002). Oxidative stress in kidney transplant patients with calcineurin inhibitor-induced hypertension: Effect of ramipril. *J Cardiovasc Pharmacol*, 40(4), 625-631.
- Hansen JM, Olsen NV, Leyssac PP.(1996) Renal effects of amino acids and dopamine in renal transplant recipients treated with or without cyclosporin A. *Clin Sci (Lond)*. Oct;91(4):489-96.
- Hariharan S, Johnson CP, Bresnahan BA, Taranto SE, McIntosh MJ, Stablein D. (2000) Improved graft survival after renal transplantation in the United States, 1988 to 1996. *N Engl J Med*. Mar 2;342(9):605-12.
- Jennings P, Koppelstaetter C, Aydin S, Abberger T, Wolf AM, Mayer G, Pfaller W. (2007) Cyclosporine A induces senescence in renal tubular epithelial cells. *Am J Physiol Renal Physiol*. Sep;293(3):F831-8. Epub Jun 27.
- Kahn D, Mazzaferro V, Cervio G, Venkataramanan R, Makowka L, Van Thiel DH, Starzl TE. (1989) Transplant Proc. Correlation between dose and level of cyclosporine after orthotopic liver transplantation. *Feb;21(1 Pt 2):2240-1*
- Parra, C., Conejo, G., Carballo, A., & De Arriba, G. (2003). Antioxidant nutrients protect against cyclosporine a nephrotoxicity. *Toxicology*, 15(189(1-2)), 99-111.
- Tegzess AM, Doorenbos BM, Minderhoud JM, Donker AJ. (1988) Prospective serial renal function studies in patients with nonrenal disease treated with cyclosporine A. *Transplant Proc*. Jun;20(3 Suppl 3):530-3.
- Wang C, Salahudeen AK. (1994) Cyclosporine nephrotoxicity: attenuation by an antioxidant-inhibitor of lipid peroxidation in vitro and in vivo. *Transplantation*. Oct 27;58(8):940-6.

EPILEPTIC FOCUS CONNECTIVITY PATTERNS DURING SEIZURES IN TEMPORAL LOBE EPILEPSY

Joshua Adkinson, Rui Liu, Ioannis Vlachos, Leonidas Iasemidis

Louisiana Tech University
Biomedical Engineering, Ruston, LA

ABSTRACT

About 1% of the global population is afflicted with epilepsy and, of all adult epilepsy patients, 60% have focal epilepsy. It has been observed that, during the course of secondarily generalized focal seizures, epileptic activity propagates from focal to other brain sites. This could reflect changes in connectivity mappings. Computer assisted analysis of recorded electrographic activity of the brain (EEG) can allow the characterization and quantification and of brain connectivity patterns during seizures. We developed a method that uses the measure of Generalized Partial Directed Coherence (GPDC) to estimate the effective connections between brain sites, and by the use of surrogate data analysis determines the statistically significant ones. Assuming that the brain functions as a network of directionally interconnected nodes, we then use these derived connections to estimate the inward and outward density of connections for each node over time during seizures. The method was applied to EEG recordings of seizures from three patients with focal temporal lobe epilepsy. In 16 of 19 recorded clinical seizures across these patients, at the start of seizures, a relatively consistent and distinct increase of density of inward connections at focal brain sites was observed, accompanied by an increase of density of outward connections at non-focal brain sites. For some seizures and patients reversal of this pattern was observed as seizures were progressing. Subclinical seizures did not exhibit such a consistent or distinct pattern of connectivity. These findings shed further light on the underlying mechanisms governing seizure spatiotemporal dynamics and could be useful in the elucidation of seizure generation, accurate focus localization and seizure control.

Keywords: Network Connectivity, GPDC, Graph Theory, Epilepsy, Seizure Dynamics

INTRODUCTION

Epilepsy is one of the most common neurological disorders afflicting approximately 1% of the global population [1]. The disorder is characterized by intermittent abnormal events (seizures) which, if not controlled, can have adverse effects on a patient's physical, emotional, and social well-being. Seizures result from a sudden onset of synchronous firing of neurons in the brain. This activity can be recorded from electrodes placed on the surface of the head (scalp EEG) or inside the brain (intracranial EEG). Of all patients with epilepsy, approximately 60% experience focal (partial) epilepsy [2]. Focal epilepsy is characterized by seizures emanating from a pathological region (focus) and usually propagating through its connections to other (non-pathological) brain sites. It has been shown in the past that changes occur in the functional connections of the epileptic focal region during a seizure [3-5].

Graph theory is a field of mathematics that studies the pairwise relationship between multiple components of a structure. A graph is made of nodes (structural components) and edges. The edges of a graph may represent any quantifiable relationship between two nodes in the structure. The power of graph theory lies in the ability to apply abstract concepts developed under a purely theoretical framework to any field of study where a given structure can be expressed as a graph. This mathematical approach has been applied to brain network connectivity to better understand the structural and functional/effective relationship of regions of the brain [6], and has been shown to be an effective method for quantifying the relationship between brain sites during epileptic seizures [3]. In the presented work, we employ the novel measure of generalized partial directed coherence (GPDC) [7] and simple graph theoretical measures to study the interactions of the epileptogenic focus during seizure.

METHODS

The initial step in our method was the estimation of the directed coupling between EEG signals from different brain sites by GPDC. Let $\mathbf{X}(t) = (X_1(t), \dots, X_n(t))'$ be an n -dimensional time series vector representing

the recorded EEG signals at n brain sites, with each vector component $X_i(t)$ denoting the signal recorded at the i^{th} recording site. A vector autoregressive model VAR(p) of order p for \mathbf{X} is constructed as:

$$\mathbf{X}(t) = \sum_{\tau=1}^p \boldsymbol{\gamma}(\tau) \mathbf{X}(t - \tau) + \boldsymbol{\epsilon}(t)$$

where $\boldsymbol{\gamma}(\tau)$ are the $n \times n$ coefficient matrices of the model and the residuals $\boldsymbol{\epsilon}(t)$ follow a multivariate Gaussian white noise process. GPDC measures the direct effect of process j to i at frequency f as:

$$GPDC_{j \rightarrow i}(f) = \frac{|B_{ij}(f)|/\sigma_{ii}}{\sqrt{\sum_{k=1}^n |B_{kj}(f)|^2 / \sigma_{kk}^2}}$$

where σ_{ii} are obtained from the covariance matrix $\mathbf{S} = [\sigma_{ij}]_{i,j=1,\dots,n}$ of the noise process $\boldsymbol{\epsilon}(t)$, $B_{ij}(f)$ is the $(i, j)^{th}$ element of the matrix $\mathbf{B}(f) = \mathbf{I} - \sum_{\tau=1}^p \boldsymbol{\gamma}(\tau) e^{-i2\pi f \tau}$ and \mathbf{I} is the $n \times n$ identity matrix.

The GPDC values were estimated over the frequency range 0.1-50 Hz in non-overlapping 3sec duration EEG segments that span each seizure. The average $GPDC_{j \rightarrow i}$ value over this frequency band was used as the index of directional connectivity from electrode/region j to i .

The next step was to evaluate the statistical significance of the identified directional connections. This was assessed through improved amplitude-adjusted Fourier transformed (IAAFT) surrogate analysis [8] at the 95% significance level. After determination of the significant connections, the adjacency matrix \mathbf{A} was created with elements $a_{i,j}$ taking value 1 when there is a significant connection from electrode i to j and 0 if not. The matrix \mathbf{A} captures the directional connections the network in the brain may have with a resolution of 3 seconds.

The last step was to define indices of connectivity per brain site as the total number of connections arriving to a node (in-degree) and the total number of connections originating from a node (out-degree). This concept is illustrated in Figure 1. The left panel (Fig. 1A) shows the adjacency matrix of the graph that is depicted in the right panel (Fig. 1B) along with the in-degrees and out-degrees for each node. The above process was repeated for non-overlapping consecutive 3sec EEG segments over each entire seizure epoch to capture the connectivity patterns in the brain during seizures.

RESULTS

The analyzed data were intracranial EEG (iEEG) recordings from three patients diagnosed with focal epilepsy and included 9, 5 and 5 clinical seizures respectively. The iEEG data were recorded with 28 implantable electrodes: two strips of 4 electrodes each in the left (LOF) and right (ROF) orbito-frontal areas, two strips of 4 electrodes each in the left (LST) and right (RST) sub-temporal areas, and two depth electrodes of 6-contacts each in the left (LTD) and right (RTD) hippocampi.

The in-degree and out-degree values for each node were estimated per 3sec EEG segments during each seizure. Figure 2 shows the in-degree and out-degree connectivity values over time for all recording channels of one representative seizure epoch from each of the three patients.

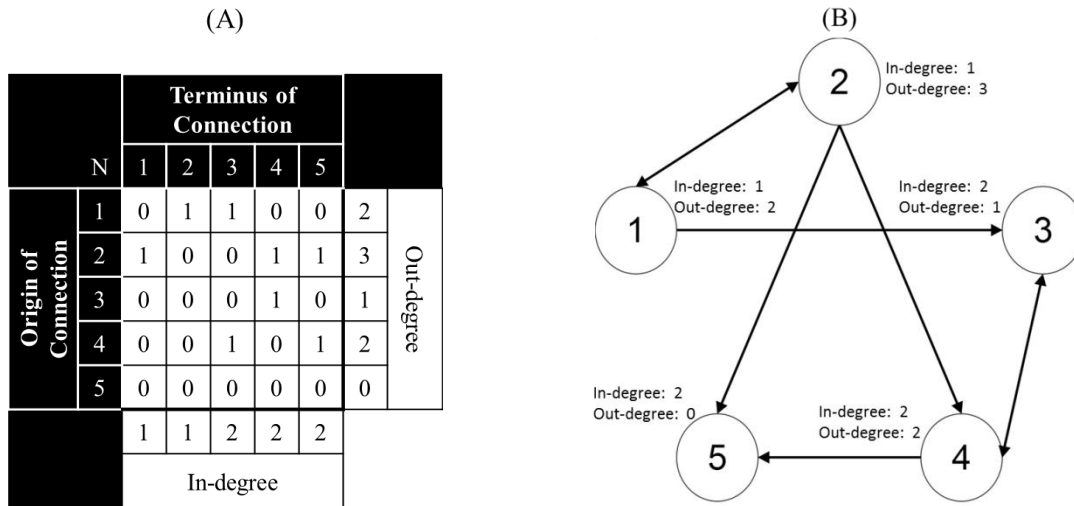


Figure 3. An adjacency matrix and its resulting graph. In (A), a value of 1 represents a connection between two nodes and a value of 0 represents no connection. Since the edges between nodes have directionality (see arrows on the edges of (B)), the adjacency matrix is not symmetric. The in-degree and out-degree of a node are determined by taking the sum of the columns and rows of the adjacency matrix, respectively.

In 7 out of 9 clinical seizures recorded from Patient 1, at the beginning of the seizures (0-30sec), there was a comparatively higher number of incoming and a lower number of outgoing connections at the epileptogenic focus than the other brain sites (Fig. 2A). Patient 2 showed the same pattern of connectivity at the focus at the beginning of 4 out of 5 recorded complex partial seizures (Fig. 2B). In Patient 3, all 5 of his complex partial seizures exhibited the same connectivity pattern for the incoming and outgoing interactions of the focus at the beginning of his seizures. Patients 1 and 2 showed a reversal in their connectivity patterns at the epileptogenic focus as seizures progressed, meaning that there was a decrease in the number of inward connections and an increase in the number of outward connections by seizure's end. For Patients 1 and 2, this reversal occurred approximately midway through the ictal (seizure) period (see Fig. 2A and 2B). No such reversal was observed in Patient 3. In subclinical seizures from all patients, no such significant or consistent patterns were observed.

CONCLUSIONS

In this work, the generalized partial directed coherence (GPDC) measure of directed connectivity between brain regions was used in conjunction with statistically significant in-degree and out-degree measures of graph connectivity to quantify the connectivity over time of the epileptogenic focus during seizures. All three epileptic patients we studied exhibited focal seizures and, at the onset of 16 of the total of 19 clinical seizures that were recorded, a higher number of incoming connections to the epileptogenic focal region and a simultaneous reduction in the number of outgoing connections from that region was observed. These results suggest that: a) the changing behavior of the focus during seizures may be explained via its connectivity patterns with other brain sites, b) directional effective connectivity patterns, in particular high in-degree and low out-degree connectivity of the focus, may be used to localize the focus from EEG epochs close to seizure onsets, c) based on the observed reversal of connectivity patterns of the focus after seizure onset in the majority of seizures, seizures may indeed serve as resetting mechanisms of the epileptogenic focus network [9]. Investigations into the specificity of these findings to ictal versus interictal periods are currently under way.

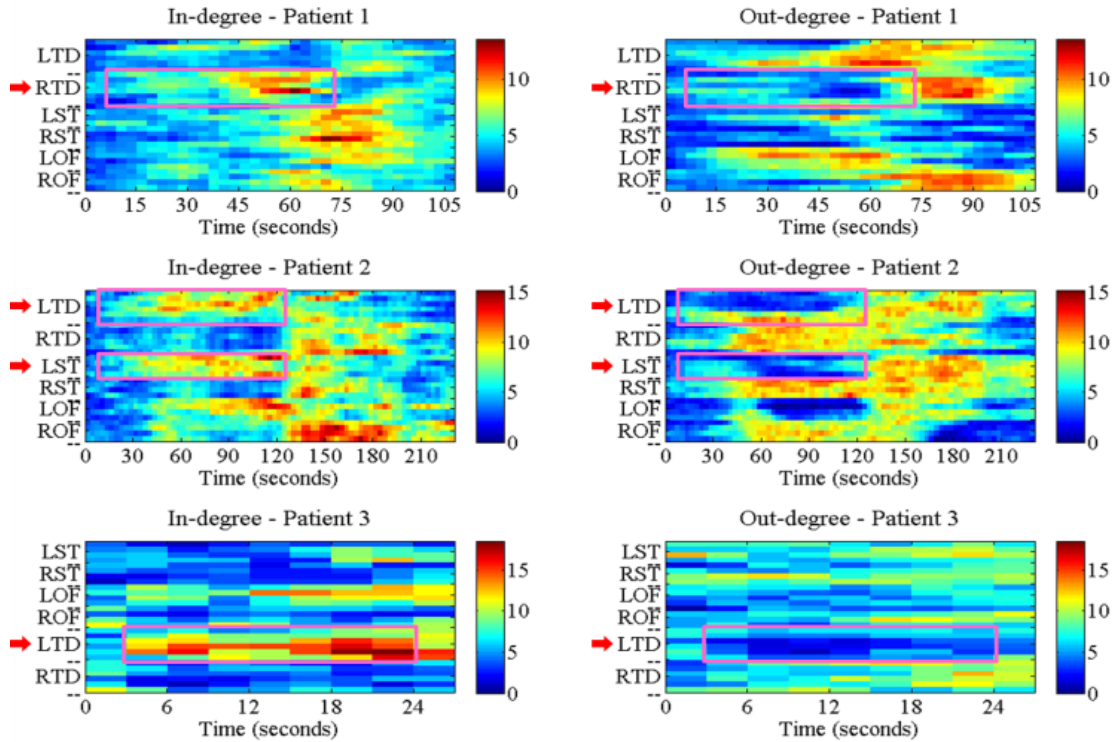


Figure 4. In-degree and out-degree values during seizure, per site, for each of the 3 patients. The ictal period begins at 0 seconds, and the color scheme represents the number of connections either from a given electrode or to a given electrode. Blue color represents smaller number of connections while red represents higher number. The red arrow to the left of each plot points to the physician assessed focal region. The pink outlines show where an increase in the in-degree and decrease in the out-degree of the epileptic focus is observed.

REFERENCES

- [1] A. K. Ngugi, C. Bottomley, I. Kleinschmidt, J. W. Sander and C. R. Newton, "Estimation of the burden of active and life-time epilepsy: a meta-analytic approach," *Epilepsia*, vol. 51, no. 5, pp. 883–90, May 2010.
- [2] W. A. Hauser, J. F. Annegers and W. A. Rocca, "Descriptive Epidemiology of Epilepsy: Contributions of Population-Based Studies From Rochester, Minnesota," *Mayo Clinic Proc.*, vol. 71, no. 6, pp. 576-586, Jun. 1996.
- [3] G. Varotto, L. Tassi, S. Franceschetti, R. Spreafico and F. Panzica, "Epileptogenic networks of type II focal cortical dysplasia: a stereo-EEG study," *Neuroimage*, vol. 61, no. 3, pp. 591–598, Jul. 2012.
- [4] F. Bartolomei, F. Wendling, J. Régis, M. Gavaret, M. Guye and P. Chauvel, "Pre-ictal synchronicity in limbic networks of mesial temporal lobe epilepsy," *Epilepsy Research*, vol. 61, no. 1–3, pp. 89-104, Sept. 2004.
- [5] Z. Haneef, A. Lenartowicz, H. J. Yeh, H. S. Levin, J. Engel and J. M. Stern, "Functional connectivity of hippocampal networks in temporal lobe epilepsy," *Epilepsia*, pp. 137–145, Dec. 2013.
- [6] M. Rubinov and O. Sporns, "Complex network measures of brain connectivity: uses and interpretations," *Neuroimage*, vol. 52, no. 3, pp. 1059–1069, Sep. 2010.
- [7] L. A. Baccala, K. Sameshima and D. Y. Takahashi, "Generalized Partial Directed Coherence," *Proc. of the 2007 15th Intl. Conf. on Digital Signal Processing*, pp.163-166, Jul. 2007.
- [8] T. Schreiber and A. Schmitz, "Improved surrogate data for nonlinearity tests," *Phys. Rev. Lett.*, vol. 635, p. 4, Sep. 1996.
- [9] L.D. Iasemidis, "Seizure Prediction and its Applications", *Neurosurg. Clin. N. Am.*, vol. 22, pp. 489-506, 2011.

INFLAMMATORY RESPONSE TO TRAUMA: A PROSPECTIVE CLINICAL STUDY**Arun Aneja M.D., Ph.D., Edward Yang B.S., Lusha Xiang M.D., Boshen Liu B.S., Peter Mittweide B.S., Clark Walker M.D., Robert Hester Ph.D., George Russell M.D.**University of Mississippi Medical Center
Department of Orthopedics
2500 North State St, Jackson MS 39211**ABSTRACT**

Traumatic injury is often accompanied with hemorrhagic shock, hemodynamic instability, exaggerated inflammatory response and multiple organ failure. Inflammatory mediators and cytokines are known to increase vascular filtration, and cause tissue edema during the inflammatory response that leads to increased morbidity and mortality. We hypothesize that patients with major orthopedic trauma demonstrate an elevated inflammatory response that is even more so exaggerated in the obese trauma patient. Sixty five adult trauma patients admitted to a Level I trauma service were enrolled. Approximately half of the participants were obese. Race, age, gender, BMI, New Injury Severity Score (NISS), and severity of head and/or extremity injury of the patients were recorded. Blood samples were collected 24 hours after admission. Each blood sample was analyzed for inflammatory and stress hormone components. Obese patients had longer length of hospital stay, higher plasma glucose levels, and BUN levels. The obese trauma patient also displayed an altered immune response with elevated inflammatory cytokine (IL-8), but lower anti-inflammatory cytokine IL-10 levels. These markers did correlate with longer hospital length of stay indicating that obese trauma patients have an exaggerated and altered inflammatory response. The results provided from this study will help us in elucidating future studies directed at treatment against the exaggerated inflammatory response in hopes of decreasing morbidity and mortality associated with trauma.

Keywords: inflammation, cytokines, IL-6, IL-8, IL-10, obesity, trauma, glucose, lactate, creatinine

INTRODUCTION

Trauma is the leading cause of mortality in patients under the age of 50. It is associated with an inflammatory response with hormonal, immunologic and metabolic mediators [1,2]. Traumatic injury has been shown to increase serum levels of inflammatory cytokines, free fatty acids, and triglycerides [1-4]. Markedly elevated cytokines and inflammatory markers, in turn, are correlated with the development of posttraumatic complications such as multi organ dysfunction syndrome (MODS), acute respiratory distress syndrome (ARDS), and systemic inflammatory response syndrome (SIRS) [2-6]. These markers are thought to hold the key to identifying patients at risk for development of posttraumatic complications. Among those markers include: C-reactive protein (CRP), tumor necrosis factor- α (TNF- α), IL-1, IL-6, IL-8, and IL-10 [2-4].

Obesity is associated with a systemic state of low grade inflammation characterized by endothelial cell dysfunction, oxidative stress, and activation of circulating immune cells [7,8]. Adipocytes produce and release various cytokines (IL-1, TNF- α , CRP, adiponectin, etc.) that mediate the inflammatory response accompanying obesity [7]. Clinical studies report that obese patients (BMI \geq 30) have a significantly higher propensity for post injury complications such as system organ failure, ARDS, myocardial infarction, and renal failure [9]. Obesity has also been associated with prolonged mechanical ventilation and longer Intensive Care Unit (ICU) and hospital stays in polytrauma patients [9]. Individuals with a BMI \geq 35 are thought to be at highest risk with a 2.8 times greater likelihood to die after being injured than lean patients (BMI \leq 25) with similar injury severity scores (ISS) [10].

Though many theories have been postulated to explain the disparity in outcome between these two patient groups, we believe that obese patients have an exaggerated cytokine response to trauma which may predispose them to a higher rate of posttraumatic complications. This assumption has been tested and proven in our animal studies and warrants clinical studies [11,12].

METHODS

This study was a prospective cross-sectional study of male and female trauma patients between the ages of 18 and 70 years admitted to a Level I trauma center with multisystem injuries. The study was approved by the

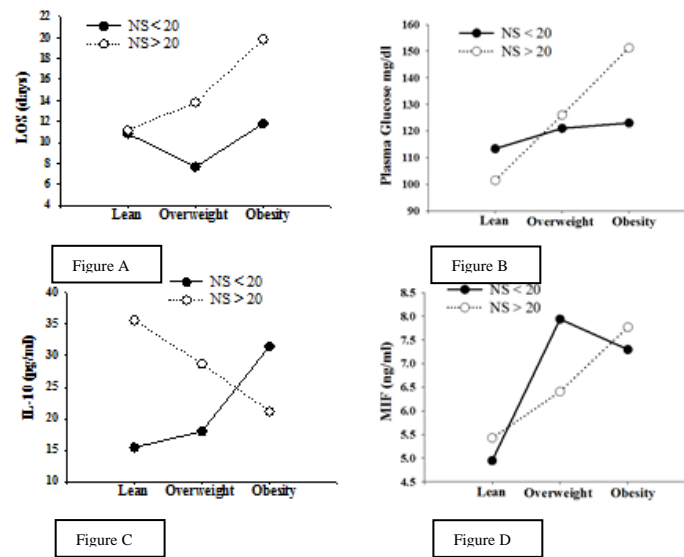
institutional review board, and written or verbal informed consent was obtained from patient or immediate family member before enrollment. Patients were excluded from the study if the medical record contained a diagnosis of acquired immunodeficiency syndrome (AIDS), chronic use of steroids, renal or hepatic failure, or lung disease (chronic obstructive pulmonary disease, emphysema, tuberculosis, or asthma). Between July 1st 2012, and June 30th 2013, we approached patients who met the above-mentioned inclusion criteria when research personnel were available until we had achieved the desired number of participants (n = 60). A total of 65 patients were enrolled. The patients were divided into three groups according to BMI: normal weight (BMI < 25 kg/m²), overweight (BMI ≥25 kg/m² and BMI < 30 kg/m²), and obese (BMI ≥30 kg/m²). Twenty mL of blood was collected on each patient within 24 hours of arrival (Day 1 blood sample). Trauma patients were also divided into new injury severity score (NISS) less than 20, and NISS > 20 to stratify the severity of injury as mild or severe. The NISS score has been shown to be a better predictor of extended hospitalization, post injury death, and multiple organ failure in trauma outcome research [13].

The blood samples of 49 patients were processed and plasma was extracted. The serum concentrations of IL-6, IL-8, IL-10, and macrophage migration inhibitory factor (MIF) were determined in the Physiology Laboratory at a Biomedical Science Building in a Level I academic medical center. Quantitative sandwich enzyme immunoassay kits (ELISA) from R&D Systems (Minneapolis, MN 55413) were used by following the manufacturer's instructions. The assays had 100% reactivity with all of the measured cytokines.

The primary outcome was the relationship between BMI and acute inflammatory response (within 24 hours) measured by secretion of cytokines. Blood markers of interest included MIF, IL-6, IL-8, and IL-10. Anthropometrical measures, including age, sex, height, body weight, and BMI, were collected upon admission from the hospital computer charts and via the university trauma registry. Day 1 glucose and blood urea nitrogen (BUN) levels were also obtained from the computer chart records. Patient demographics were summarized by means and SDs for continuous variables and frequencies and percentages for categorical or discrete variables. Cytokine levels were summarized by means and SDs. Twenty four hour cytokine levels were compared using the Wilcoxon signed-rank test. The strength of the association between BMI and early and late cytokine levels was assessed using the Spearman's rank correlation coefficient. All statistical analyses were performed using SAS1 Version 9.1.3 (SAS Institute, Inc, Cary, NC, USA). We considered p values of less than 0.05 significant.

RESULTS

Of the 65 patients enrolled in the study, 49 had their blood analyzed. Of those 49 patients, 10 were female and 39 were male. Twenty three patients were Caucasian, 25 were African American and 1 was Native American. Fourteen patients had normal BMI, 9 patients were overweight, and 26 patients were obese. The NISS ranged from 4 to 39 with the mean at 17.3. Obese patients with severe trauma had a longer length of hospital stay (20.2 ± 9.70 days) that was significantly greater ($p=0.035$) than lean patient with severe trauma (10.2 ± 5.78 days) and significantly greater ($p=0.003$) than obese patients with mild trauma (8.83 ± 6.97 days). This is shown as Figure A. As shown in Figure B obese patients with severe trauma had higher glucose levels (149.8 ± 52.9 mg/dl) than lean patients with severe trauma (102.8 ± 7.90 mg/dl) though this was not significantly greater ($p=0.054$). As shown in Figure C, obese patients with severe trauma had lower levels of IL-10 (26.9 ± 19.5 pg/ml) than lean patients with severe trauma (31.8 ± 22.3 pg/ml), though this was not significantly different ($p=0.067$). As shown in Figure D obese patients with severe trauma had higher MIF levels (6.62 ± 4.98 ng/ml) than lean patients with severe trauma (6.23 ± 5.15 ng/ml), though this was again not significantly different ($p=0.885$). There were no significant differences in IL-6 among the various groups, however, lean patient with severe trauma had higher IL-8 levels (55.0 ± 23.5 pg/ml) that was significantly greater ($p=0.003$) than lean patients with mild trauma (16.4 ± 8.63 pg/ml). Obese patients with severe trauma had higher BUN levels (15.5 ± 7.13 mg/dl) that was significantly greater ($p=0.041$) than lean patients with severe trauma (8.16 ± 3.66 mg/dl).



DISCUSSION

Obese patients with severe trauma present acutely with higher glucose levels, higher BUN levels and display a different inflammatory response than lean patients with severe trauma resulting in longer hospital length of stay. Pape et al showed IL-6 to be a reliable index of the magnitude of systemic inflammation, while Giannoudis et al reported that elevated levels of IL-10 correlated with the development of sepsis [5,6]. Another clinical study found the ratio of IL-6 to IL-10 to better correlate with injury severity after major trauma, recommending that it be used to predict degree of injury following trauma [14]. CRP is thought to predict postoperative organ failure with an accuracy of 70% while IL-1, TNF- α , and lactate have good correlation with initial degree of hemorrhage and non-survival after ARDS and MODS [15,16]. MIF is thought to be responsible for early polymorphonuclear cell activation and respiratory burst in severe trauma patients and correlates with higher morbidity [17]. Although there is much controversy about which marker is the most reliable predictor of outcome following trauma, there is overwhelming consensus that use of such biochemical markers to identify “at risk” trauma patients may facilitate clinical decision making and treatment.

It has been shown that obese human patients (BMI ≥ 30) have more than double the incidence of perioperative complications after operative treatment of pelvic ring injuries than non-obese patients (BMI < 30) [18]. The complication profile was even higher in another study evaluating complications of acetabular fracture surgery in morbidly obese patients (BMI ≥ 40) [19]. The morbidly obese group had a significant increase in estimated blood loss, operative time, and length of hospital stay compared to non-morbidly obese group (BMI < 40) [19]. Obesity recently has been shown to be associated with a pro-inflammatory state after total hip arthroplasty (THA) with increased cytokine levels and poor outcomes [20]. Only a few reports have suggested that IL-6 levels are exaggerated in severely obese patients after surgery [20,21]. Winfield et al actually stated that obese patients sustaining severe injury had a depressed early cytokine response compared to patients with normal BMI conferring the obese patient increased susceptibility to nosocomial infection and late multi organ failure [22]. Nonetheless, all these various studies demonstrated that the obese trauma patient has an altered inflammatory response that is different from the lean trauma patient with increased morbidity and mortality.

The limitations of this study include a very small sample size that is likely underpowered, though the objective was to perform a pilot study. Another limitation is the fact that we only looked at the inflammatory response 24 hours after injury. Our future studies will examine the inflammatory response at multiple later time intervals. Some patients may have received surgery immediately upon arrival elevating biomarker data, but as long as patients in each BMI category were equally likely to receive surgery, uniformity was obtained.

Elucidating the physiologic response of obese patients to trauma may lead to more effective treatment modalities and algorithms to improve the outcome for both lean and obese patient populations.

Developing the optimal pharmacotherapy regiment for the inflammatory syndromes associated with trauma depends on a detailed understanding of the patho-physiology of the inflammatory cascade coupled with discovery based basic and clinical science research. We believe that the inflammatory response to trauma results in morbidity in both lean and obese groups, however, it appears to be more so exaggerated and better characterized in the obese.

CONCLUSIONS

Obese patients with severe trauma present with higher glucose levels, higher BUN levels and display a different inflammatory response than lean patients with severe trauma that leads to increased morbidity with longer hospital length of stay.

ACKNOWLEDGMENTS

Funding for this study was received from the Mid America Orthopedic Association Resident Grant

REFERENCES

1. Choban PS, Weireter LJ, Maynes C: Obesity and increased mortality in blunt trauma. *J Trauma* 1991;31:1253-1257.
2. Roberts CS, Pape HC, Jones AL, et al: Damage Control Orthopedics: Evolving concepts in the treatment of patients who have sustained orthopaedic trauma. *AAOS Inst Cour Lec* 2005;54:447-469.
3. Hilebrand F, Giannoudis PV, Krettek C, Pape HC: Damage control: extremities. *Injury, Int. J. Care Injured* 2004;35:678-679.
4. Frink M, Heieh YC, Hsieh CH, Pape HC, Choudhry MA, Schwacha MG, Chaudry IH: Keratinocyte-Derived chemokine plays a critical role in the induction of systemic inflammation and tissue damage after trauma-hemorrhage. *Shock* 2007;28: 201-07.
5. Pape HC, Schmidt RE, Rice J, et al: Biochemical changes after trauma and skeletal surgery of the lower extremity: Quantification of the operative burden. *Crit Care Med* 2000;28:3341-3448.
6. Giannoudis PV, Smith RM, Perry SL, Windsor AJ, Dickinson RA, Bellamy MC: Immediate IL-10 expression following major orthopedic trauma: Relationship to anti-inflammatory response and subsequent development of sepsis. *Intensive Care Med* 2000;26:1076-1081.
7. Singer G, Granger ND: Inflammatory responses underlying the microvascular dysfunction associated with obesity and insulin resistance. *Microcirculation* 2007;14:375-387.
8. Xiang L, Naik J, Hester RL. Exercise-induced increase in skeletal muscle vasodilatory responses in obese Zucker rats. *Am J Physiol Regul Integr Comp Physiol.* 2005; 288(4):R987-91.
9. Brown CV, Neville AL, Rhee P, Salim A, Velmahos GC, et al: The impact of obesity on the outcomes of 1,153 critically injured blunt trauma patients. *J Trauma* 2005;59:1048-1051.
10. Byrnes MC, McDaniel MD, Moore MB, Helmer SD, Smith SR: The effect of obesity on outcomes among injured patients. *J Trauma* 2005;58:232-237.
11. Xiang L, Hester RL, Fuller WL, Sebai ME, Mittwede PN, Jones EK, Aneja A, Russell GV: Orthopedic Trauma-Induced Pulmonary Injury in the Obese Zucker Rat. *Microcirculation* 2010;17(8):650-659.
12. Xiang L, Lu S, Fuller WL, Aneja A, Russell GV, Jones LB, Hester R: Impaired blood pressure recovery to hemorrhage in obese Zucker rats with orthopedic trauma. *Am J Physiol Heart Circ Physiol* 2011;302(1):340-348.
13. Balogh ZJ, Varga E, Tomka J, Suveges G, Toth L, Simonka JA: The new injury severity score is a better predictor of extended hospitalization and intensive care unit admission than the injury severity score in patients with multiple orthopaedic injuries. *J Orthop Trauma* 2003;17(7):508-512.
14. Taniguchi T, Koido Y, Aiboshi J, Yamashita T, Suzuki S, Kurokawa A: The ratio of interleukin 6 to interleukin 10 correlates with severity in patients with chest and abdominal trauma. *Am J Emerg Med* 1999;17:548-551.
15. Waydhas C, Nast-Kolb D, Trupka A, et al: Posttraumatic inflammatory response, secondary operations, and late multiple organ failure. *J Trauma* 1996;40:624-631.
16. Roumen RM, Redl H, Schlag G, Zilow G, Sandtner W, Koller W, et al. Inflammatory mediators in relation to the development of multiple organ failure in patients after severe blunt trauma. *Crit Care Med* 1995;23:474-80.

17. Shih HC, Huang MS, Lee CH: Polymorphonuclear cell priming associated with NF-kB activation in patients with severe injury is partially dependent on macrophage migration inhibitory factor. *J Am Coll Surg* 2010;6;791-797.
18. Russell GV, Qin Z, Dews RC: Body Mass Index: The Role it plays in the complications of operatively treated pelvic fractures. *2007 AAOS Annual Meeting*, Paper No. 359.
19. Russell GV, Dews RC, Graves M, Porter S, Qin Z: *Morbid Obesity*: Is operative treatment of displaced acetabular fractures worth the risk? *2006 OTA Annual Meeting*, Paper No. 41.
20. Motaghedi R, Babe JJ, Memtsoudis SG, Kim DH, Beathe JC, Paroli L et al. Association of obesity with inflammation and pain after total hip arthroplasty. *Clin Orthop Relat Res* 2013 Oct 5. [Epub ahead of print]
21. Gletsu N, Lin E, Zhu JL, Khaitan L, Ramshaw BJ, Farmer PK, Ziegler TR, Papanicolaou DA, Smith CD. Increased plasma interleukin 6 concentrations and exaggerated adipose tissue interleukin 6 content in severely obese patients after operative trauma. *Surgery* 2006;140:50-57.
22. Winfield RD, Delano MJ, Cuenca AG, Cendan JC, Lottenberg L, Efron PA, et al. Obese patients show a depressed cytokine profile following severe blunt injury. *Shock* 2012;37(3):253-6.

MORPHOLOGICAL EFFECTS OF GENISTEIN, THYMOQUINONE, 5-FU, AND LASER THERAPY ON LARYNGEAL CARCINOMA CELLS

Osasu Adah, Gerri Wilson, Felix Adah, Michelle Tucci, and Hamed Benghuzzi
Departments of Orthopaedic Surgery and Rehabilitation and Clinical Health Sciences
University of Mississippi Medical Center, Jackson, Mississippi

Abstract

Low level laser therapy (LLLT) may enhance or decrease cell proliferation, but more on the stimulation side of cellular activities. The precise biochemical mechanisms underlying the therapeutic effects of LLLT are not yet well-established. From observation, it appears that LLLT has a wide range of effects at the molecular, cellular, and tissue levels. In addition, its specific modes of action may vary among different applications. Within the cell, there is strong evidence to suggest that LLLT acts on the mitochondria to increase adenosine triphosphate (ATP) production, modulate reactive oxygen species (ROS), and induce transcription factors. LLLT has shown promise for down regulating inflammation by reducing the presence of reactive oxygen species (ROS). In normal cells, high levels of ROS are damaging to the cells and the cells have the ability to squelch the production of ROS enzymatically. Cancer cells exhibit elevated levels of ROS due to their accelerated metabolism needed to maintain proliferation. The goals of this experiment were (1) to determine the effects of LLLT for a period of 30 minutes on laryngeal cancer cell survival; and (2) to determine the effects of natural chemotherapeutic agents or a known conventional chemotherapeutic agent, 5-FU, along with exposure to LLLT on cancer cell growth. Cells were treated with laser, Thymoquinone (TQ), Genistein (G), 5FU, or laser in the presence of TQ, G, or 5-FU for 30 minutes followed by incubation for a period of 24 hours. The cells were harvested and cellular protein, intracellular glutathione, and morphology were evaluated. The results show a decrease in cell numbers following treatment with TQ and 5 FU for 24, 48, and 72 hours, while genistein treatment showed changes in cell number after 72 hours. Interestingly, the cells in the presence of Laser were reduced within 24 hours, and treatments with Laser + 5-FU, Laser + G, and Laser + TQ were significantly reduced further than when given the compound alone. The results show that laser and chemotherapeutic interventions may be synergistic and beneficial treatment for laryngeal cancer. These findings are important since laryngeal cancer is difficult to resect, and laser therapy could be guided into the area to reduce the tumor size or used following resection.

Keywords

Carcinoma, Laryngeal, Laser, Cell Proliferation, Genisten, Thymoquinone, 5-Fu, Growth.

INTRODUCTION

Nasopharyngeal carcinoma (NPC), which is a type of head and neck cancer, is the most common type of squamous cell carcinoma, and it is the second most common head and neck cancer. According to the National Institute of Cancer, in 2013 there were an estimated 12,260 new cases and 3,630 deaths. The location of the tumor makes it hard to detect due to its anatomic proximity to critical structures and infamous choice for distant metastases. Subsequent rates of local and distant metastases are high. The non-specific nature of nasal and aural symptoms also increases the likelihood to misdiagnose and leads NPC to often be diagnosed at advanced stages. Various modalities are used in the treatment of the cancer including 5-Fluorouracil (5-FU) [4] but not without some side effects. There is no accepted and efficacious regimen for the treatment of NPC. The use of natural compounds that stop cancer in G1 phase of the cell cycle may provide an alternative to 5-FU drug regime. The literature is replete with reports documenting the effect of low level laser therapy (LLLT) on cellular modulation (increase or decrease cell proliferation) [5,6,7, 8, and 9]. *Kreisler et al.* [7] reported the use of LLLT of 809 nm at energy level of 1.96 – 7.84 J/cm² increased the proliferation activity of human laryngeal carcinoma cell *in vitro*. Other studies by the same authors [5, 6] showed increased cell proliferation of periodontal ligament cells and human gingival fibroblast cells cultured respectively. A study by *Werneck et al.* [10] reported that two LLLT units (685 nm and 830 nm) tested separately significantly increase H. Ep2 (laryngeal carcinoma cells) when treated with 4J/cm². Investigational studies have been conducted utilizing laser (LLLT) as a means to alter cellular proliferation thus decreasing the number of cancer cells within the body [□3]. The problem with most cancer management is the side effects the therapeutic intervention may elicit. Chemotherapy side effects are well known including weakness, anemia, and in

some cases infertility, limb deformity and development of other malignancies [14]. On the other hand, LLLT have limited systemic effects and may be implicated in toxic reduction in the body [15, 16].

Recently, laser treatment had been tried on tumor of the bone. *Renno et al.* [13] investigated the effects of LLLT of different wavelengths (670 nm, 780 nm and 830 nm) on osteoblast and osteosarcoma (cancerous) cells. The researchers reported that 830 nm laser increased osteoblast proliferation significantly and reduced osteosarcoma cells significantly, but the 670 nm and 780 nm lasers both increased osteoblast and osteosarcoma proliferation. The LLLT of 830 nm wavelengths induced osteoblast (good bone cells) at energy level of 10 J/cm² and did not increase osteosarcoma (cancerous) bone cells unlike the other lasers in the study. The energy delivered by the three different lasers is 0.5, 1, 5, and 10 J/cm² levels. Also, Renno and co-researchers reported an increase in Alkaline phosphatase (ALP) activity in the osteoblast line using the 830 nm laser irradiation at 10 J/cm² whereas there was no increase in ALP activity in the osteosarcoma line other lasers used in the study. The 830 nm laser used in the study that did not lead to the cancer proliferating is used being used in this study. This contrasting action of LLLT may be based on the parameters and the energy impacted to the tissues. Various types of cells respond differently to laser irradiation, depending on irradiation parameters [8].

Due to the insignificant improvement of the survival rate of those affected by NPC and that the tumors are almost impossible to resect, there is a critical need for more efficient biotherapy to treat such cancer. The LLLT may become a viable alternative modality for the treatment of NPC in view of the fact the energy level can be modulated on the right wavelength. The use of laser therapy may also be able to reach the tumor by fibro optics and in conjunction with chemotherapeutic agents may provide a better prognosis for patients with NPC. In the literature, studies that tested dual effects of LLLT and any other anti cancer agents such as 5-FU, Genistein (G), and Thymoquinone (T) are limited. Therefore, the goals of this study were (1) to determine the effects of LLLT for a period of 30 minutes on laryngeal cancer cell survival; and (2) to determine the effects of natural chemotherapeutic agents or a known conventional chemotherapeutic agent, 5-FU, along with exposure to LLLT on cancer cell growth. We hypothesized that low level light laser treatment alone and in combination with genistein or 5-FU is capable of reducing tumor load of an NPC cell line.

MATERIALS AND METHODS

Treatment of Cells: Cells were treated with TQ, Genistein or 5-fluorouracil in a 24 well plate and all were incubated for 24, 48, and 72 hour intervals. Cells were treated alone with 10 joules of laser therapy or were treated 30 minutes with chemotherapeutic agents prior to laser therapy

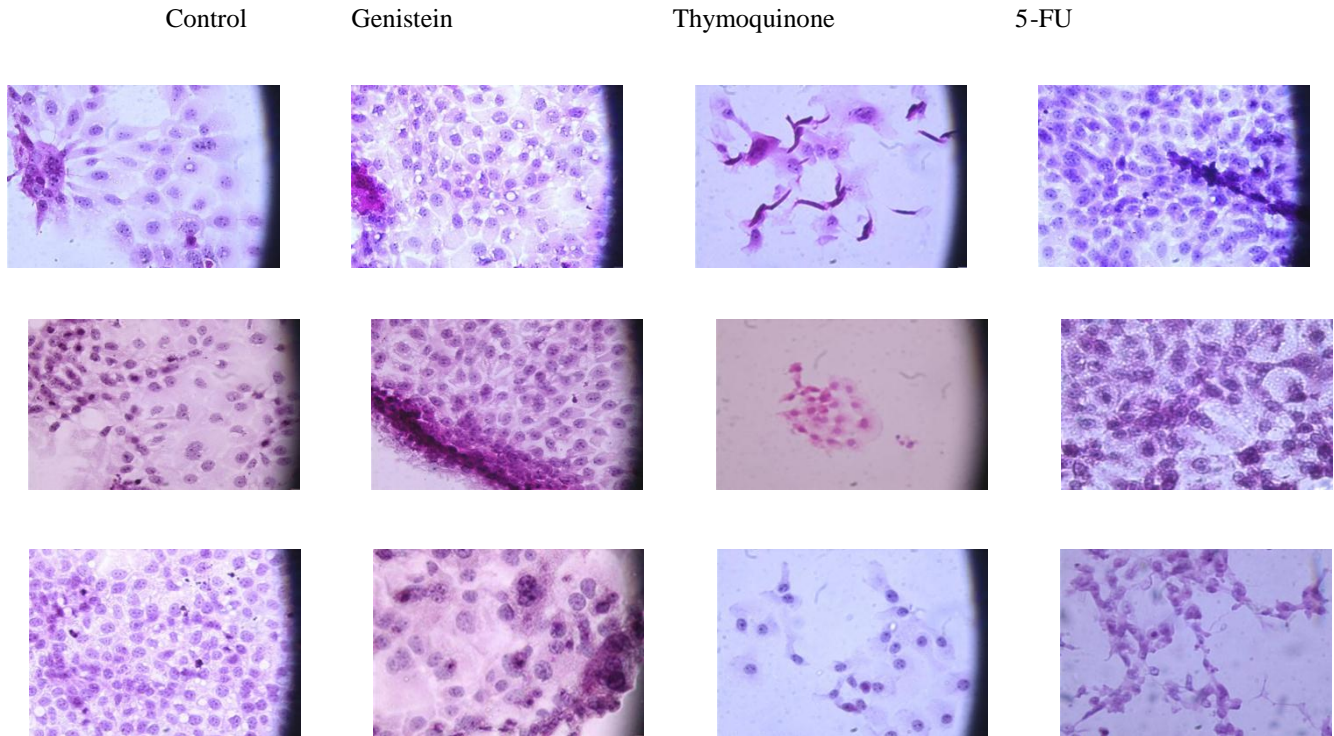
Cell Collection: After incubation, the supernatant was collected and frozen. All cells except the last row were scraped from the wells and collected for protein assay.

Protein Assay: The Initial step in the protein assay process involved making the standard solution. Standard was then added to columns 1 and 2 on the cell plate followed by 25 μ L of cells into the remaining wells. The working reagent was determined by multiplying the number of wells with standards and cells by 0.2mL, which is equal to the total WR. The equation $1/50=x/\text{total amount of WR}$ gave the amount of reagent B when solved for X. By subtracting the amount of reagent B from the total WR, the amount of reagent A was calculated. There was an incubation for 30 minutes at 37^o C, covered. After incubation, plate was read using Magellan software.

Morphology: The cells were grown on sterile, circular coverslips and analyzed morphologically by staining the coverslips using the H&E method. Cells were evaluated under light microscopy and digitized.

RESULTS AND DISCUSSION

Our results show changes in cellular morphology within 24-48 hours following treatment with TQ and 5-FU (Figures 1a-c). Cells treated with 5-FU had more prominent nucleolus loss of nuclear detail as early as 24 hours following treatment. Cells treated with genistein appeared further differentiated than control cells. TQ treated cells after 24 hours showed loss of adhesiveness and an adaptive response to treatment. By 72 hours cells treated with TQ showed presence of mitotic figures. At 72 hours the 5-FU treated cells were anucleated with vacuolization of the cytoplasm. Cells treated with genistein show modest effects after 72 hours of treatment.



Figures 1: Top, middle and bottom rows with H&E of FaDu cells after respective treatments for 24, 48, and 72 hours, respectively (40x magnification).

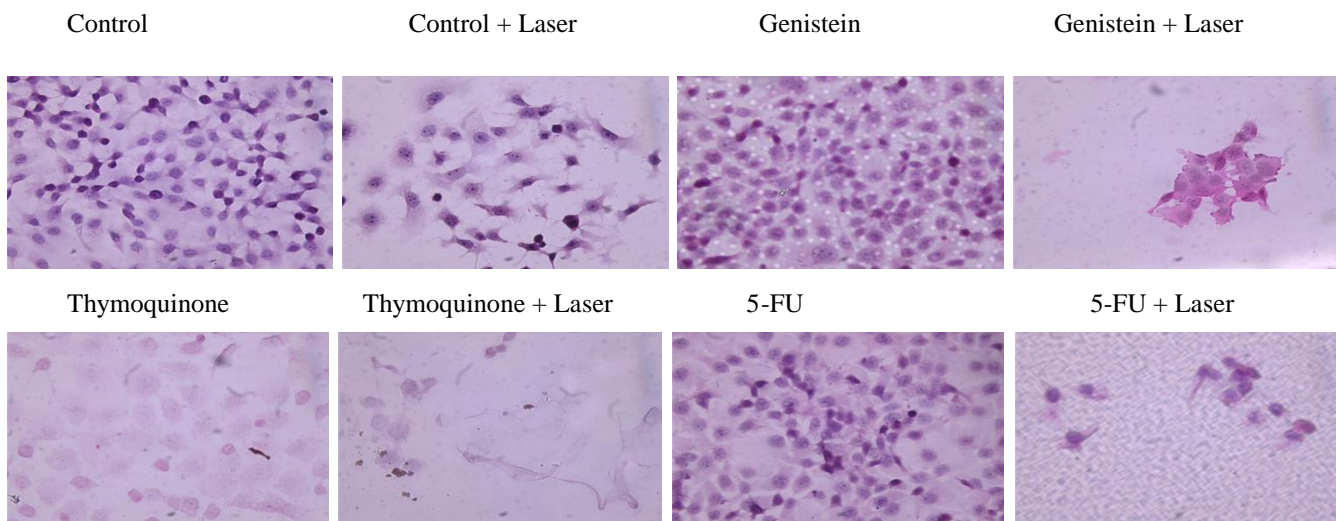


Figure2: H&E of FaDu cells after respective treatments for 24 hours (40x magnification).

Low level light laser treatment reduced cell number within 24 hours following a single dose treatment. Combining the chemotherapeutic drugs with the laser therapy had even a greater (Figures 2). The changes in morphology are consistent with the changes in cellular protein (Figure 3). The variety of chemotherapeutic drugs stops cells in several phases of the cell cycle. The cell cycle is divided into four parts normally: G1, S, G2, and M.

Each chemotherapeutic drug is cell cycle specific. The literature suggests that cancer cells treated with known chemotherapeutic agent 5-FU stops division of cell in the S phase of the cell cycle [2]. Limited and conflicting information exists regarding natural agents, genistein and TQ; however, both have been shown to stop cells in the G0-G1 phase of the cell cycle and induce apoptosis [3]. Low level light therapy or cold laser has shown controversy in the literature when it comes to treating cancer. Studies by *Kreisler et al.* [5, 6, and 7] produced cell proliferation including on human laryngeal carcinoma *in vitro* at energy level of 1.96 – 7.84 J/cm² after using a LLLT of 809 nm wavelength which is contrary to the result of the study. *Pinheiro et al.* [9] reported that LLLT with 635 nm wavelength did not significantly stimulate H. Ep2 cells, whereas, the LLT with a wavelength of 670 nm wavelength significantly stimulate H. Ep2 compared to the control with energy of irradiation being 0.04 – 0.48J/cm². Other researchers [10] who used LLLT with wavelengths of 685 nm and 830 nm respectively significantly increased the proliferation of H.Ep2 which is contrary the results of this study. On the other hand the cell apoptosis seen in the laser group is similar to the results of *Renno et al.* [13] that reported increase in normal osteoblast and reduction in osteosarcoma cells after treating with LLLT with 830 nm wavelengths and total energy impact of 10 J/cm². In our present study we impacted a total energy into each well using LLLT of 830 nm wavelength. The conflicting results one may observe in the literature may be due to time of exposure, treatment and wavelength or parameters used [10, 8]. Our results clearly demonstrate a reduction in tumor cells following treatment with TQ and 5-FU alone and when combined with laser therapy there appears to be a synergistic effect. Genistein at the dose chosen shows more of an effect after 72 hours, but when combined with laser treatment there was even a more significant reduction at 24 hours than laser alone.

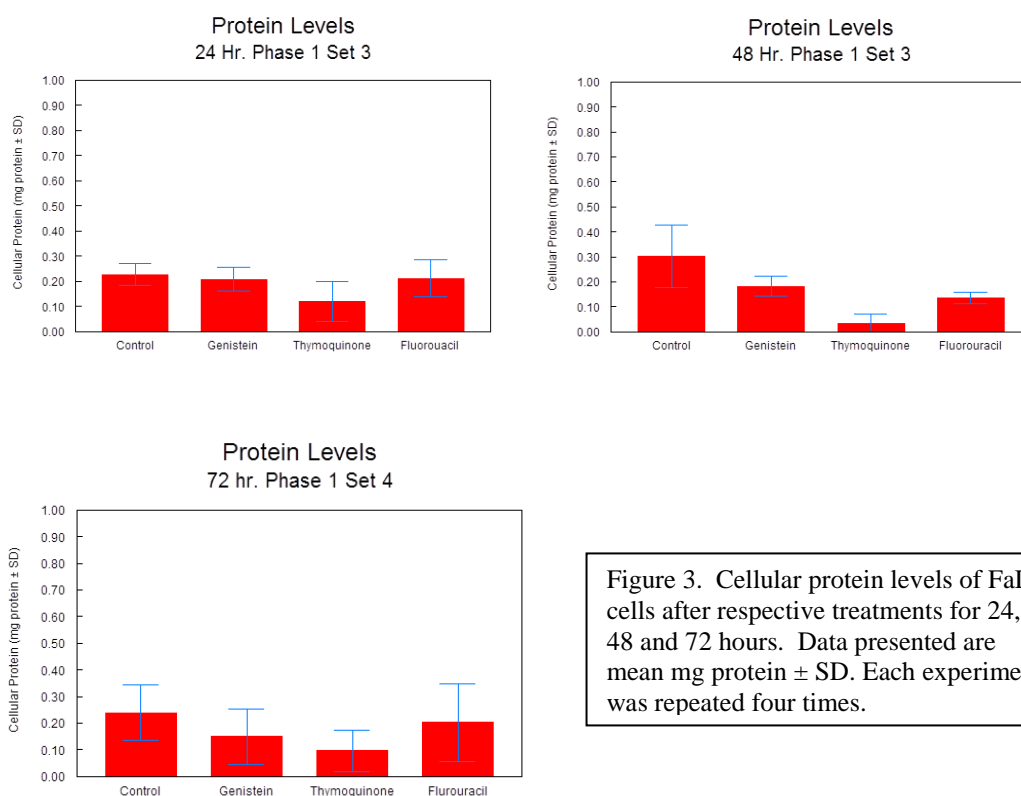


Figure 3. Cellular protein levels of FaDu cells after respective treatments for 24, 48 and 72 hours. Data presented are mean mg protein ± SD. Each experiment was repeated four times.

CONCLUSION

Overall, laser therapy in this particular cell line appears to reduce the tumor cell load within 24 hours of treatment. TQ also significantly affects the number of cells in a similar fashion as a known chemotherapeutic agent, 5-FU. Genistein's effects occur over time and may actually stimulate cell proliferation in the initial phases. The

combination of laser with the chemotherapeutic agent may alter the cells permeability and offer a greater response than when cells are treated with either laser or drug alone. More work is needed to determine the exact mechanism of cold laser cell reduction to determine the right parameters for cancer treatment efficacy

ACKNOWLEDGEMENT

This work was supported by the Mississippi INBRE, funded by an Institutional Development Award (IDeA) from the National Institute of General Medical Sciences of the National Institutes of Health under grant number P20GM103476.

REFERENCES

- [1]. Edwards JP, Zhang X, Frauwirth KA, Mosser DM. Biochemical and functional characterization of three activated macrophage populations. *J Leukoc Biol* 2006;80:1298–1307. [PubMed: 16905575].
- [2]. Wilkes GM, Burke, MB (2008). *Oncology Nursing Drug Handbook 2009*; 0763765856; Jones & Bartlett Publishers
- [3]. Tan M, Norwood A, May M, Tucci M, Benghuzzi H. Effects of (-)epigallocatechin gallate and thymoquinone on proliferation of a PANC-1 cell line in culture. *Biomed Sci Instrum.* 2006;42:363-71.
- [4]. Furusaka T, Matsuda A, Tanaka A, Matsuda H, Ikeda. Superselective intra-arterial chemoradiation therapy for functional laryngeal preservation in advanced squamous cell carcinoma of the glottic larynx. *MActa Otolaryngol.* 2013 Jun;133(6):633-40.
- [5]. Kreisler M, Christoffers AB, Willershausen B, d'Hoedt B. Effect of low-level GaAlAs laser irradiation on the proliferation rate of human periodontal ligament fibroblasts: an in vitro study. *J Clin Periodontol.* 2003 Apr;30(4):353-8.
- [6]. Kreisler M, Christoffers AB, Willershausen B, d'Hoedt B. Low level 809-nm diode laser-induced in vitro stimulation of the proliferation of human gingival fibroblasts. *Lasers Surg Med.* 2002;30(5):365-9
- [7]. Kreisler M, Christoffers AB, Willershausen B, d'Hoedt B. Low-level 809 nm GaAlAs laser irradiation increases the proliferation rate of human laryngeal carcinoma cells in vitro. *Lasers Med Sci.* 2003;18(2):100-3.
- [8]. Peplow PV, Chung TY, Baxter GD. Laser photobiomodulation of proliferation of cells in culture: a review of human and animal studies. *Photomed Laser Surg.* 2010 Aug;28 Suppl 1:S3- 40.
- [9]. Pinheiro AL, do Nasclento SC, de Vieira AL, Rolim AB, da Silva PS, Brugnera A Jr. Does LLLT stimulate laryngeal carcinoma cells? An in vitro study. *Braz Dent J.* 2002;13(2):109-12.
- [10]. Werneck CE¹, Pinheiro AL, Pacheco MT, Soares CP, de Castro JL. Laser light is capable of inducing proliferation of carcinoma cells in culture: a spectroscopic in vitro study. *Photomed Laser Surg.* 2005 Jun;23(3):300-3.
- [11]. Ju YH, Allred KF, Allred CD, Helferich WG. Genistein stimulates growth of human breast cancer cells in a novel, postmenopausal animal model, with low plasma estradiol concentrations. *Carcinogenesis.* 2006 Jun;27(6):1292-9.
- [12]. Allred CD, Allred KF, Ju YH, Virant SM, Helferich WG. Soy diets containing varying amounts of genistein stimulate growth of estrogen-dependent (MCF-7) tumors in a dose-dependent manner. *Cancer Res.* 2001 Jul 1;61(13):5045-50
- [13]. Renno, AC, McDonnell, PA, Parizotto, NA and Laakso, EL. The effects of laser irradiation on osteoblast and osteosarcoma cell proliferation and differentiation in vitro. *Photomed Laser Surg.* 2007;25(4):275-280.
- [14]. Jully B, and Rajkumar, T. Potential molecular targets for Ewing's sarcoma therapy. *Indian J Med Paeditr Oncol.* 2012; 33(4):195-202.
- [15]. Rhee, CK, He, JY, Ahn, JC, Chung, PS and Suh, MW. Effect of low-level laser therapy on cochlear hair cell recovery after gentamicin-induced ototoxicity. *Lasers Med Ssc.* 2012; 27(5):987-992.
- [16]. Achilla, JR, Moreira, MS, Miyagi, SP, Bombana, AC, Gutknecht, N, and Marques, MM. Single session of Nd:YAG laser intracanal irradiation neutralizes endotoxin in dental root dentin. *J Biomed Opt.* 2012;17(11):18002

MORPHOLOGICAL EVALUATION OF ADENOCARCINOMA HUMAN ALVEOLAR BASAL EPITHELIAL LIKE CELL LINE UPON THE EXPOSURE TO OMEGA FATTY ACIDS ON IN CULTURE

Jana Bagwell, Michelle Tucci, and Ham Benghuzzi

University of Mississippi Medical Center
Jackson, MS

ABSTRACT

The A549 cell line in which is derived from adenocarcinoma human alveolar basal epithelial cells has been used as a model for cancer research. This cell line has shown good suitability as a model for respiratory studies due to presence of type II alveolar functionality. Additionally, this cell type secretes surfactant that contains phospholipids in which plays a major role in reducing alveolar surface tension. The objective of this study was to evaluate the morphological features of the A549 cells upon the exposure to low and high doses of omega fatty acids. Sterile aseptic techniques were followed throughout the experimentations by following standard lab protocols. Morphological evaluation was conducted by using two different standard staining protocols namely: hematoxylin & eosin (H-E) stain was used (to evaluate general qualitative assessment of cell characteristics); and the alcian blue stain (to identify mucin production and assess the ability of the cells to produce phospholipid surfactant). A549 cells were treated with a low and high concentration of flaxseed oil, providing omega 3-6-9 fatty acids and allowed to incubate for 24, 48 and 72 hours. The results of this study revealed: (i) at the end 24 hours of incubation, the cells showed slight indication of growth qualitatively compared to the control group; (ii) at the end 48 and 72 hours of incubation, an increase in growth was observed with islands of confluent cells forming when compared to the control group; (iii) maintenance of cell functionality was observed by evidence of alcian blue mucopolysaccharide staining in and around the peripheral of the cell; (iv) no visible signs of debris or cytotoxicity were noted at both low and high doses and at all three incubation intervals. The results of this pilot study suggest that the exposure of omega fatty acids to A549 cells can provide an adequate matrix for defining and identifying the components of an asthma inflammatory condition. Further investigations are highly recommended to assess the quantitative measurements of cell viability, integrity and actual cell count as well as functional capacity.

Keywords: A549 cell line, omega fatty acids, mucopolysaccharide, surfactant, hematoxylin and eosin, alcian blue

INTRODUCTION

Omega-3 fatty acid in dietary oils, such as flaxseed or fish oil, is described as an anti-inflammatory agent that reduces inflammation throughout the body. Omega-3 is part of a larger group of fatty acids consisting of both monounsaturated and polyunsaturated fatty acids containing two or more double bonds. Mammals do not have the desaturase enzymes required to synthesize omega-3 (α -linolenic acid or ALA) and omega-6 (linoleic acid or LA), thus they are termed essential fatty acids and must be supplied by the human daily diet.[1] Omega-9 fatty acid, termed oleic and stearic acids, is produced by the body naturally, therefore it is labeled nonessential. The importance of omega-3 in the process of inflammation was first observed in a late 1970's study of the dietary intake of omega-3 in a population of Greenland compared to individuals in Denmark. The subjects in Greenland, who had a much larger intake of dietary omega-3, had lower incidence of autoimmune and inflammatory disorders, such as psoriasis, asthma and type-1 diabetes.[2] Most of these diseases are characterized by inappropriate activation of T cells, ultimately resulting in destruction of host tissues. [3].

The anti-inflammatory process of omega fatty acid starts with the competition between the omega-3 and omega-6 fatty acids in prostaglandin formation. Eicosapentaenoic acid (EPA), an omega-3 fatty acid, competes with arachidonic acid (AA), an omega-6 fatty acid that converts from LA, for prostaglandin and leukotriene synthesis at the cyclooxygenase and lipoxygenase level. [3] When the human diet consist of high EPA, as well as, docosahexaenoic acid (DEA), both omega-3 fatty acids, there is a decrease in pro-inflammatory eicosanoids, prostaglandin E2 and leukotriene B4. These substances, which are derived from the AA and have been associated with inflammatory processes.[4]

In addition, the proper ratio of omega-6 to omega-3 has been shown in many studies to be very important in the inflammatory process. It has been well documented that the intake of omega-6 is too high in the modern Western diet. The ratio for omega-6:omega-3 should be 4:1 or lower for optimum benefits, but is close to 20:1 to

25:1 in current Western diets.[1] A 2006 study by Oddy, et al, studied the association between the ratio of omega-6 to omega-3 fatty acids and risk for current asthma in children. They found a statistically significant difference in a diet with increased omega-3 and reduced omega-6 acids to protect children against symptoms of asthma.[5]

Omega fatty acid supplements have become readily available to consumers. The current ratio of many commercially sold over-the-counter omega 3-6-9 blends is often 4:1:1, with omega-3 being four times that of omega-6 and omega-9.

This study utilizes the A549 cell line which was first developed in 1972 by D.J. Giard, et al, through the removal and culturing of cancerous lung tissue in the explanted tumor of a 58 year old Caucasian male. These cells have been derived from a single parent cell.[6] When examined by electron microscopy, the cells contain multilamellar cytoplasmic inclusion bodies typical of those found in type II alveolar epithelial cells of the lung. At early and late passage levels, Leiber et al. report that these cells suggest a pattern of phospholipid synthesis that is expected to be responsible for pulmonary surfactant synthesis.[7]

METHODS

R-mix shell vials (containing both human lung carcinoma [A549] and mink lung [Mv1Lu] cells) were obtained from Quidel, Diagnostic Hybrids Inc. (Athens, Ohio) and grown in RPMI 1640 media and supplemented with 10% newborn calf serum and 1% antibiotic/antimycotic solution (10,000 I.U./mL penicillin, 10,000 µg/mL streptomycin and 25µg/mL amphotericin B) in a humidified atmosphere of 5% carbon dioxide at 37°C.

After the transport media was removed from the vials, the RPMI and treatment was simultaneously added. Treatment of cells with omega fatty acid mixture was accomplished by adding NatureMade® Flaxseed oil suspension containing a ratio of 4.5:1:1 omega 3:6:9 ratio [one softgel contained alpha linolenic acid (omega-3) 500 mg; linoleic acid (omega-6) 110 mg, and oleic acid (omega-9) 120 mg]. At incubation intervals of 24, 48 and 72 hours, all experimental groups were stained with hematoxylin and eosin stain (H-E) and alcian blue stain.

Morphological evaluation was performed using the H-E staining procedure according to standard laboratory procedure. Hematoxylin will stain basophilic structures such as nuclei, chromatin, and ribosomes a deep purple or blue. Eosin is an acidic stain that stains acidophilic structures red, such as the cell membrane. Structure and integrity of the cells were reviewed by the same individual in order to maintain consistency of subjective values. Assessments were recorded for all slides. Criteria for morphological evaluation include size and shape of cell, appearance of nucleus and cytoplasm, assessment of nuclear/cytoplasm ratio and observation of cytotoxic effects.

Alcian blue stains acid mucosubstances and acetic mucins.[8] Because type II alveolar cells secrete surfactant, the majority of which is dipalmitoylphosphatidylcholine, the alcian blue dye will give a blue color to mucopolysaccharides present in or on the cells. This stain was used to qualitatively assess the functionality of the cell after treatment was added. Standard laboratory staining procedures were used for the alcian blue staining.

The study was divided into 3 groups for which each staining method was applied: (1) untreated control cells, (2) low concentration omega fatty acid treatment (5 µL), (3) high level concentration omega fatty acid treatment (15 µL). Each 5 µL dose provided the following amounts of each omega acid: 2.50 mg (omega-3), 0.55 mg (omega-6), and 0.60 mg (omega-9). Each group had 15 shell vials per group, and each set was assessed at time intervals of 24, 48, and 72 hours of incubation in sets of 5; N=45 for H-E evaluation, N=45 for alcian blue evaluation.

RESULTS

Observations of morphology utilized the H-E stained cells using light microscopy on 40x objective magnification and Image Pro Digital Analysis to document analyses. All groups, from untreated control cells to low and high dose of treatment were observed with prominent well-defined, round to oval nuclei with evenly dispersed chromatin. Most cells had intact nuclear membranes without vacuolization. Occasional mitotic figures were observed. The nucleoli were clearly visible and most cells contained one or two nucleoli, with occasional multiple nucleoli.

The cytoplasm was free from debris and with no disruption to the cellular membrane. No bizarre shapes or fragmented cells were noted. The predominant cytoplasm to nucleus ratio observed was 2:1. Occasional cytoplasmic vacuoles were present, but no overall evidence of cytotoxicity was evident in the cytoplasm.

At the 24 hour interval, the A549 cells showed no signs of stress and compared quite adequately to the non-treated cells. The qualitative observation of growth appeared to be equal between the control cells and both treatments at the 24 hour time interval. However, at the 48 hour interval, the cells began to show larger growth in culture in both the low and high dose groups when compared to the control group. At the 72 hour interval, the

observation was not only of continued viability, but rapid growth consisting of islands of confluent cells developing in low and high dose cell groups. Both of these treatment groups exhibited packed cells uniformly-shaped and merging together, see Figure 1-3.

The Alcian blue stains were also viewed with light microscopy on 40x objective magnification. As previously stated, the alcian blue stains mucopolysaccharides in and around the perimeter of the cell with a light blue color. The cells continued to produce phospholipid substances throughout all incubation periods and with all groups of concentration, see Figure 4.

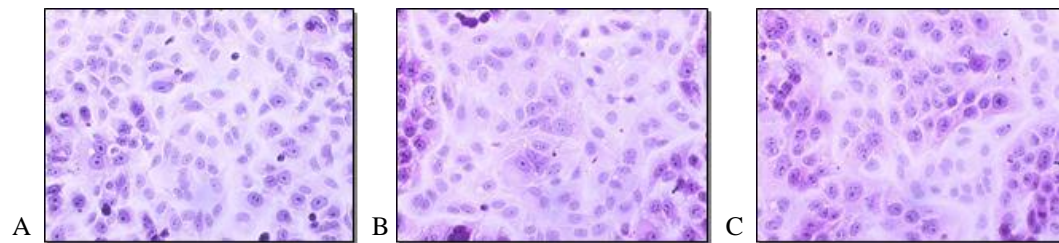


Figure 1a-c: H-E stained A549 cells with no treatment (control) at 24 hours (a), 48 hours (b), and 72 hours (c).

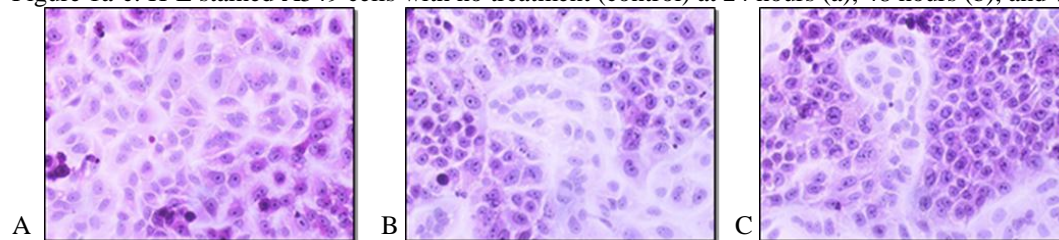


Figure 2a-c: H-E stained A549 cells with low conc. omega fatty acids; 24 hours (a), 48 hours (b), and 72 hours (c).

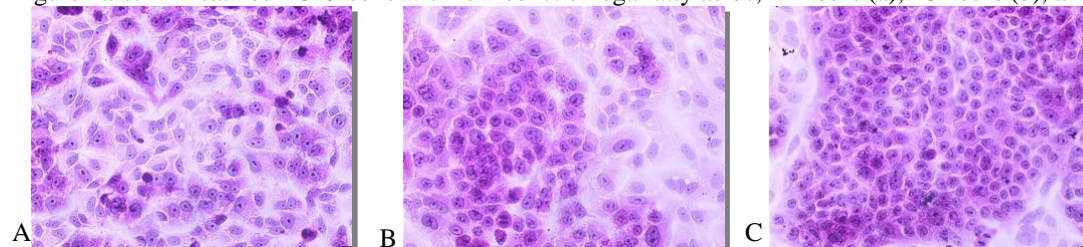


Figure 3a-c: H-E stained A549 cells with high conc. omega fatty acids; 24 hours (a), 48 hours (b), and 72 hours (c).

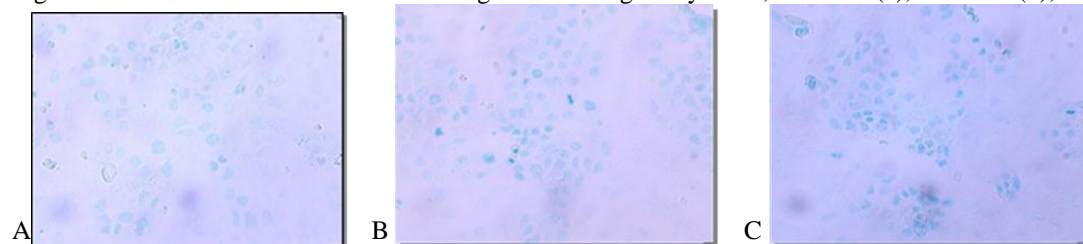


Figure 4a-c: alcian blue stained A549 cells no treatment control 72hours (a), low conc. 72 hours (b), and high conc. 72 hours (c).

DISCUSSION

This study gives good indication that omega fatty acid treatment at the concentrations set forth in this pilot study will not induce cytotoxicity to A549 cell line. The cells readily adapted to their environment and had abundance of growth. The alcian blue staining of each group provided evidence that the A549 cell as a type II alveolar cell did not lose the functionality to produce phospholipid surfactant in this study group.

CONCLUSIONS

This pilot study gives good support to the thought that the A549 cell line is a useful model for epithelial airway studies. Furthermore, it will be an adequate matrix for defining and identifying the components of an asthma inflammatory condition. This study was for morphological and qualitative assessment only. More evidence, such as quantitative measurement of cell viability, integrity and actual cell count, is necessary to support definitive conclusions.

REFERENCES

- [1] Harris, R.E., *Inflammation in the pathogenesis of chronic diseases : the COX-2 controversy*. Subcellular biochemistry. 2007, New York: Springer. xiii, 323 p.
- [2] Kromann, N. and A. Green, *Epidemiological studies in the Upernavik district, Greenland. Incidence of some chronic diseases 1950-1974*. Acta Med Scand, 1980. **208**(5): p. 401-6.
- [3] Simopoulos, A.P., *Omega-3 fatty acids in inflammation and autoimmune diseases*. J Am Coll Nutr, 2002. **21**(6): p. 495-505.
- [4] Wall, R., et al., *Fatty acids from fish: the anti-inflammatory potential of long-chain omega-3 fatty acids*. Nutr Rev, 2010. **68**(5): p. 280-9.
- [5] Oddy, W.H., et al., *Ratio of omega-6 to omega-3 fatty acids and childhood asthma*. J Asthma, 2004. **41**(3): p. 319-26.
- [6] Giard, D.J., et al., *In vitro cultivation of human tumors: establishment of cell lines derived from a series of solid tumors*. J Natl Cancer Inst, 1973. **51**(5): p. 1417-23.
- [7] Lieber, M., et al., *A continuous tumor-cell line from a human lung carcinoma with properties of type II alveolar epithelial cells*. Int J Cancer, 1976. **17**(1): p. 62-70.
- [8] Klatt, E.C. *Alcian Blue Surgical Pathology - Histology Staining Manual*. 2014 [cited 2014 February 1]; Available from: <http://library.med.utah.edu/WebPath/HISTHTML/MANUALS/ALCIAN.PDF>.

IMPACT OF HEARING AID USE IN INDIVIDUALS WITH UNILATERAL SENSORY HEARING IMPAIRMENTS

Charles E. Bishop, Au.D. and Elgenaid Hamadain, Ph.D.

School of Health Related Professions
University of Mississippi Medical Center
2500 North State St.
Jackson, MS 39216

ABSTRACT

Unilateral sensory hearing loss poses particular hearing difficulty for individuals in the way of reduced localization of sound and understanding speech in the presence of background noise. At present it is not clear in the published literature whether conventional hearing aids help individuals with this kind of impairment. To assess this we evaluated the speech perception in noise and hearing handicap outcome of 22 individuals dispensed a hearing aid for a three month field trial. Our results were found to be consistent with distinct improvements in speech perception in noise, as measured by the Quick speech in noise test (QuickSIN), presented at 0 and 45 degrees azimuth, with speech and noise spatially separated in sound field, with and without a hearing aid. Also, we noted reduced self-perceived hearing handicap in these individuals, as measured by the abbreviated profile of hearing aid benefit (APHAB) questionnaire.

Keywords: Unilateral hearing loss, asymmetrical hearing loss, hearing aid outcome, APHAB, QuickSIN

INTRODUCTION

Individuals with at least moderate, unilateral, sensory hearing impairment have distinct hearing problems related especially to the localization of sound and understanding speech in noise. Etiologies that result in such impairments include noise trauma, Meniere's disease, and sudden idiopathic hearing loss. A common clinical finding associated with unilateral impairments is impaired supra-threshold word recognition. Conventional wisdom is that unilateral hearing loss with impaired word recognition negates good outcome with use of amplification on the impaired side. The central hypothesis of our study is that a multi-channel, digital hearing aid, dispensed in such a way that maximizes speech intelligibility index (SII) after three months of use, can provide subjective benefit as well as improved speech intelligibility in noise, in our study participants.

METHODS

We evaluated performance on an objective measure of speech perception in noise (QuickSIN) and a on a subjective, self-report, hearing handicap questionnaire (APHAB) of a group of 22 individuals with unilateral, moderate to severe, sensory hearing impairment. The APHAB was administered before the participants were dispensed a hearing aid ("unaided" condition), and performed again after at least three months of hearing aid use ("aided" condition). This questionnaire was administered by interview and the participants answered questions for the aided condition while viewing their previous responses for the unaided condition. Questionnaire data were compared to published norms. The procedure for administering the QuickSIN involved stimulus and noise presentations in sound field at 0 degree and 45 degree azimuths, with speech and noise spatially separated. This was performed also in the unaided and aided conditions. Additionally, the direction of speech and competing noise signals were alternated, such that data regarding performance on this measure could be assessed with speech directed toward and away from the better ear.

RESULTS

Female (n/%)	12.0, 54.5
Age (median, range)	62.5, 66.0
	*50yr-60yr (n/%) 9.0, 40.9
	61yr-70yr (n/%) 8.0, 36.4
	71yr-80yr (n/%) 5.0, 22.7
Better Ear PTA4 (mean, SE)	20.8, 2.4
Better Ear WRS % (mean, SE)	96.2, 1.1
Worse Ear PTA4 (mean, SE)	65.7, 2.2
Worse Ear WRS % (mean, SE)	37.5, 4.2
Etiology of Hearing Loss (n/ %)	--
	Sudden/Idiopathic 19.0, 86.3
	Slowly Progressive 2.0, 9.1
	Meniere's 1.0, 4.5
Worse Ear-UnAided SII (mean, SE)	4.3, 1.8
Worse Ear-Aided SII (mean, SE)	39.4, 1.8
Outcome After Study (n, %)	--
	Continued Use (purchase or other) 12.0, 54.5
	Discontinued Use 10.0, 45.5

Table 1: Participant characteristics. *Included in this group is one individual with outlying age (14 yrs). "PTA4" is the average of the air-conducted, pure tone, audiometric frequencies that correlate with speech understanding (average of 500, 1000, 2000, and 4000 Hz). "WRS" denotes the word recognition score, which is the percentage of mono-syllabic words understood at comfortably loud presentation levels. "SII" is the speech intelligibility index.

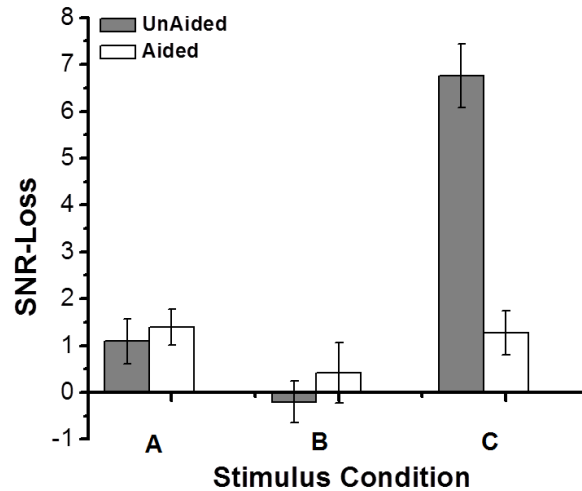


Figure 1: QuickSIN results in sound field for three conditions: A=speech and noise presented together at 0 degrees, B=speech presented 45 degrees toward better ear and noise presented 45 degrees toward worse ear, and C=speech presented 45 degrees toward worse ear and noise presented 45 degrees toward better ear. Difference between "unaided" and "aided" results for condition C were statistically significant ($p < 0.05$).

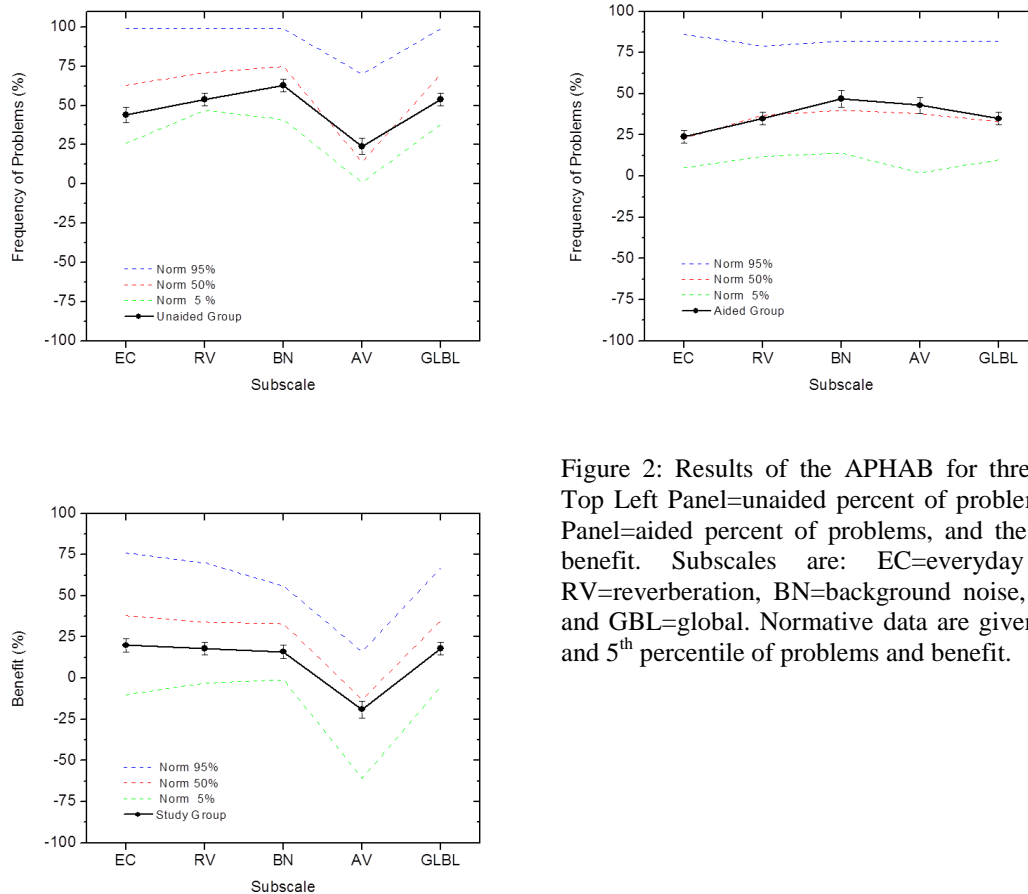


Figure 2: Results of the APHAB for three conditions: The Top Left Panel=unaided percent of problems, the Top Right Panel=aided percent of problems, and the Left Panel=aided benefit. Subscales are: EC=everyday communication, RV=reverberation, BN=background noise, AV=aversiveness and GBL=global. Normative data are given for the 95th, 50th and 5th percentile of problems and benefit.

DISCUSSION/CONCLUSIONS

Our data show that hearing aid use by the participants in our study provided measurable improvements on the QuickSIN for the condition where speech is directed toward the worse ear and noise is directed toward the better ear. Though the hearing aid did not provide enhancement in the other conditions (such as when speech is directed toward the better ear and noise is directed toward the worse ear), it was neither a detriment. These findings were supported by the APHAB questionnaire, wherein participants reported overall improved function in most listening conditions, such as in noise and reverberant conditions. We feel that these results support the notion that a hearing aid used by individuals with moderate or worse "aidable" sensory hearing loss in one ear is a viable approach that should be considered when counseling patients.

ACKNOWLEDGMENTS

All hearing aids used in this study were generously donated by Starkey Hearing Technologies.

DIFFERENTIAL BIOTHERAPEUTIC ADVANTAGES OF HONEY IN TARGETING THE WARBURG EFFECT AND SURVIVAL OF MRC-5 AND A549 CELL LINES

Ibrahim O. Farah

Department of Biology, Jackson State University, Jackson, MS 39217, USA

ABSTRACT

Lung cancer is one of the most prevalent and deadly cancers in United States. Experimental evidence support that cancer cells do exhibit higher glycolytic rates than normal cells (Warburg effect). To exploit this unique cancer-dependent ATP generation phenomenon, we hypothesize that exposure of cancer cells to organic inhibitors of glycolysis would negatively impact their survival and alter their growth and viability resulting from the vast decrease in their essential glycolytic ATP production; no negative consequences will be seen on normal lung cells. The human lung fibroblast cell line MRC-5 and the human alveolar epithelial cell line A549 were used as models for normal lung and lung cancer in vitro in this study. Using standard methods, both cell lines were maintained and exposed to honey reagent at concentration levels ranging from 31.3-2,000 $\mu\text{g/ml}$ in 96 well plates in quadruplets and experiments repeated at least three times using MTT, and cell counting (T4 Cellometer) assays as well as phase-contrast photo-imaging. Our results indicate that exposure of both cell lines to this natural organic nutraceutical resulted in concentration dependent cell destruction/cell survival depending on the cell line exposed. Honey showed statistically significant ($p < 0.05$) differential negative effects on the A549 line in comparison to its unexposed control as well as to its effects on the MRC-5 cell line. Results show a promising role of honey as a metabolite of interest for selective management of cancerous cells.

Keywords: Warburg effect, glycolysis inhibition, lung cancer, natural organics, T4 cellometer, bioenergetics, biotherapeutics

INTRODUCTION

Cancerous cells exhibit higher glycolytic rates than normal cells (the Warburg effect). This has been generally attributed to injury to mitochondrial respiration [1, 2, 3 and 4] that results in a compensatory increase in glycolytic ATP production. Mitochondrial respiration can be negatively affected by mutations within the mitochondrial DNA (mtDNA). Mutations within the mtDNA have been found in various malignancies including breast, prostate, and pancreatic cancers [5, 6, 7, and 8].

In attempting to exploit this unique cancer-dependent ATP generation phenomenon, we propose that exposure of cancerous cells to organic inhibitors of glycolysis would lead to cell utilization of these inhibitors by cancerous cells to satisfy their energy supply needs. Their high demand for glucose and their dependence on cellular glycolytic machinery can differentially lead to blockage of glucose metabolism and the consequent demise of cancerous cells through the inhibition of their sole energy generating mechanisms [9, 10, 11 and 12].

We therefore hypothesized that normal cells will have the ability to escape demise from the organic inhibitors' effects while cancerous cells will be killed off at lower concentrations that can be benign or actually do not influence normal cellular glucose metabolism. This means that delivery of organic inhibitors at the optimized dose can be a means of selectively causing the demise of cancerous cells while leaving normal cells intact [13, 14].

Based on this hypothesis, we studied the viability patterns of two possible differential energy-inhibiting metabolites for cancerous versus normal lung cells. The objective of this research was to assess the differential role of a natural organic product; honey, in being utilized as possible energetic inhibitors cancerous lung cells.

METHODS

Reagents: F-12K, Dulbecco's Modified Eagle's (DMEM) culture media, Phosphate- buffered saline (PBS), Trypsin EDTA, Fetal bovine serum (FBS), Penicillin-Streptomycin, A549 human lung cancer cell

line, and MRC-5 human normal lung cells line were each purchased from American Type Culture Collection (ATCC) located in Manassas, VA, USA. Honey was from a commercially marketed grade A pure source.

Cell Culture: A549, human lung cancer cell line was cultured in F-12k media. The F-12k medium was a mixture of 85% F-12K media, 10% FBS, and 5% penicillin. The cell culture was started with a mixture of 4ml of the F-12K media and 1 ml of A-549 cells in a 5ml flask (Corning Company). MRC-5, a normal human lung cell line was cultured in DMEM media composed of a mixture of 85% DMEM media, 10% FBS, and 5% penicillin. The cells were maintained at 37°C and 5% CO₂ in a humidified incubator. Once each cell line became confluent cells were trypsinized (Trypsin EDTA) and counted by the use of a hemocytometer. From the cell count appropriate dilution were made for specific plating necessary to deliver constant number of cells for exposure studies ($C_1V_1=C_2V_2$). **MTT assay:** The purpose of the MTT assay was to measure cellular metabolic viability (reduction of tetrazolium by the mitochondria). The yellow tetrazolium MTT (3-(4, 5-dimethylthiazolyl-2)-2, 5-diphenyltetrazolium bromide) is reduced by metabolically active cells to generate the reduced agent. The purple formazan that results within the cell was solubilized in DMSO and measured by spectrophotometric methods (Thermo Scientific, Multiskan Ascent from Waltham, MA, USA). After incubation for 72 hours in the 96 wells plate, the cells were examined by using a phase-contrast microscope for cell morphology and growth/damage parameters. This was followed by the MTT assay. Briefly, the chemical mixture was removed from the 96 well plates and 10 µL of MTT reagent were added to each well. The 96 well plates were incubated at 37°C and 5% CO₂ for 2 to 4 hours until the purple precipitate was visible. Hundred (100) µl of detergent reagent (DMSO) were added to each of the 96 well plate and set for 10 minutes before proceeding to the next step where the 96 well plates were positioned into the spectrophotometer and the absorbance was recorded at 570 nm. Several concentrations of honey in DMSO were evaluated ranging from 0 (control) to 2000 µg/ml. Tests were done in quadruplets and experiments were repeated three times (12 data points per concentration). **The T4 Cell Analyzer:** Cell Analysis by High Content Cell Analyzer (HCCA); Nexcelom, Bioscience in Lawrence, MA, USA: Once cell growth became maximal at confluence, cells were exposed to each organic chemical mixture at 2,000 µg/mL concentration for 48 hours in an incubator at 37°C and 5% CO₂. After 48 hours incubation period, cells were trypsinized, centrifuged, and resuspended in fresh media of 2 mL volumes for counting. Lastly, 20µl of the cell-containing media and 20 µL of trypan blue were mixed and injected into a slide and read by the high content cell analyzer, which will automatically calculate the % of viable cells in 1 ml of sample. Chemically exposed cells were compared to control cells in at least duplicate samples/chemical exposure for and in-between cell lines. **Statistical Analysis:** The viability parameters of both the A549 and MRC-5 were determined by using the ANOVA and Student's T-test (at the level of <0.05 for statistical significance), for treated A549 compared to MRC-5 cell line and their respective controls. Data was also normalized through the use of percentages and tested for statistical significance based on comparisons of differences in the computed means, standard deviations/errors, and p-values.

RESULTS

This study investigated the in-vitro responses of the A549 and MRC-5 cell lines upon their exposure to honey. Results of the MTT assay are presented in Fig 1A and 1B and Tables 1 and 2. As can be seen, honey boosted the metabolic activity of MRC-5 while differentially declining the metabolic activity of the A549 cell line (Fig 1A and 1B). Cell display Figures IIA and IIB show the phase-contrast photo-display for the effects of honey on the A549 cell line comparing control to exposed cells. As can be seen, the exposed cell morphology and confluency are different; cells are smaller and their numbers are lower compared to the control cell display. The results of the T4 cell analysis showed statistically significant differences ($p<0.05$) between the MRC-5 and the A549 cell lines. Viability of the MRC-5 was

at 100% for both control and treated cells. In contrast, the viability of the A549 showed 100% versus 72.55 % for the control and treated cell respectively. When both treated cell lines were compared for true viability, there was highly statistically significant difference between the two confirming the findings with the MTT assay as to the differential response of these cell lines to honey (Table 3).

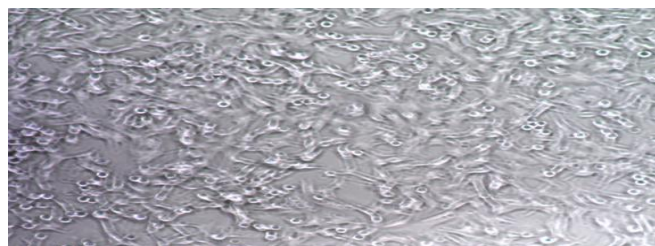
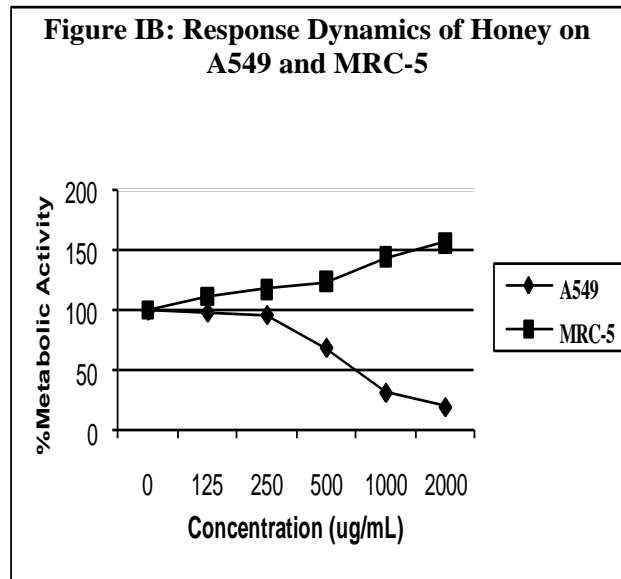
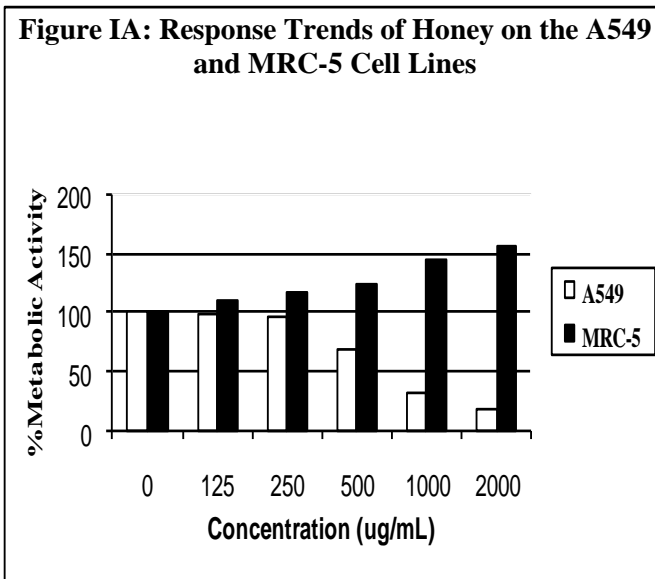


Figure IIA: A549 Control (Honey; 0 $\mu\text{g/ml}$) cell



Figure IIB: Honey (2,000 $\mu\text{g/ml}$) on A549 cell

Table 1: ANOVA Mean Comparisons, Statistical Significance, and P-values for A549 cell line using MTT assay data for 2,000 $\mu\text{g/ml}$ of Honey at 48 hrs. of incubation

Chemical	Mean of Control	Mean of Test Chemical	P- Value	Level of Statistical Significance
Honey	0.87 ± 0.07	0.17 ± 0.03	0.001*	Highly Statistically Significant metabolic injury

Table 2: ANOVA Mean Comparisons, Statistical Significance, and -values for MRC-5 and A549 cell lines using the MTT normalized data.

Chemical	Mean of A549	Mean of MRC5	P- Value	Level of Statistically Significance
Honey	76.84±8.76	152.08±23.19	0.002	Highly Statistically Significant metabolic boost to MRC-5 and injury to A549.

Table 3: T4 Cellometer per cent (%) Data** and T-test Statistical Analysis of Exposure of A549 to Honey

Chemical	Control A549	Treated A549	P-Value	Control MRC-5	Treated MRC-5	P-Value	Treated A549	Treated MRC-5	P-Value
Honey	100%	72.55%	0.018*	100%	99.95%	0.500	72.55%	99.95%	0.005*

DISCUSSION

Lung cancer is one of the most prevalent and deadly cancers in the United States. This study evaluated the metabolic as well as actual viability of the A549 and MRC-5 cell lines upon exposure to honey aiming at inhibiting glycolysis in cancer cells. Glycolysis was closely examined in light of research by others that have proven that cancer cells exhibit a higher glycolytic rate than normal cells [1, 2, 3, 4 and 5]. This major influx of glycolysis is caused by deregulated metabolism within the cell with special reference to impaired mitochondria as a hallmark of the cancer phenotype. The root of the deregulated metabolism could in general stem from damage and impairment of genetic stability, as well as the presence of hypoxic environments (6, 7, and 8]. Deregulated metabolism results in uncontrollable cell proliferations that lead to the development of the cancer phenotype. During this endeavor, A549 and MRC-5 cell lines were exposed to honey for three different time periods (24, 48, and 72 h), and assessed for the impairment of metabolic viability by the MTT assay, and the High Content Cell Analyzer (HCCA; T4) for cell death was used to assess the true survival of the A549 and MRC-5 cell lines upon their exposure to honey [12, 13 and 14-19].

As can be seen from the results in Figures 1A and 1B of the MTT assay, honey declined the metabolic viability of the A549 cell line, which was significantly instigated at 500ug/mL. In contrast to its negative effects on the A549 cell line, honey contributed significantly to the metabolic boost of the MRC-5 cell line. The metabolic viability of the MRC-5 increased steady and differentially from 125µg/mL to 2000µg/mL and exceeded the metabolic viability level of their control. For statistical analysis as based on Table 1, ANOVA analysis showed that the p-value for the A549 cell line exposed to honey as compared to its control was 0.001 which is extremely statistically significant towards the metabolic cell injury to the A549 cell line. In Figure IA, the A549 cell line control had substantial cell viability and maintained its normal morphological structure, however, when exposed to the highest concentrations of honey, the metabolic viability declined along with its normal morphological structure as shown in figure IB.

In Table 2, the ANOVA analysis also determined that the p-value for the comparison of A549 and MRC-5 cell lines exposed to honey was highly statistically significant with a p-value of 0.002 (A549 metabolic injury vs. MRC-5 metabolic boost), and in Table 3, the HCCA; T4 analysis, determined that the level of difference for the A549 cell line compared to its control was statistically significant at a p-value of 0.018, however, the MRC-5 cell line compared to its control provided a level of difference that

was not significant at a p-value of 0.500 showing no cellular death to support the previous finding with the MTT testing. The cell analyzer also provided a comparison of the MRC-5 and A549 cell line which exhibited a level of difference that was highly statistically significant with a p-value of 0.005 in support of the previous differential findings with the MTT assay (actual death of the A549 vs. no death to the MRC-5 cell line). The assessments used during this research proved that honey is an effective anti-proliferative agent in lung cancer which was in agreement with earlier findings by others that showed that honey is an effective anti-proliferation agent in the treatment of colon cancer [20, 21, 22, and 23].

CONCLUSIONS

It is concluded that treatment with 62.6-2,000 µg/ml of honey produced moderate inhibitory effects and proved to be a differential killing agent to the lung cancer cell line (A549). In contrast, honey served as an activator of metabolism in the normal lung fibroblast cell line (MRC-5), where honey provided healthy metabolic outcomes. Additionally, Honey did also show a differential effect and caused more damage to the A549 cancer cell line when compared to the MRC-5 cell line using the T4 cell counting techniques (actual cell death). The major findings from this study is that there is great potential for using natural organics in the differential destruction of lung cancer as based on the survival responses of the A549 and MRC-5 cell lines to honey. Further studies are warranted to establish the ideal conditions for selective killing of other cancer cell lines in terms of organic concentrations, incubation time, and combination synergy of the effective products.

ACKNOWLEDGMENTS

This research is supported by NIH/NCRR RCMI grant # G12007581.

REFERENCES

1. Warburg, Otto. (1956). "On the Origin of Cancer Cells." *Science*. <http://www.sciencemag.org>, 2007.
2. H. Bucay "The biological significance of cancer: Mitochondria as a cause of cancer and the inhibition of glycolysis with citrate as a cancer treatment *Medical Hypotheses*, Volume 69, Issue 4, Pages 826-828A, 1989.
3. R. Buc, S. Demaugre, M. Moncion and N. Leroux "Metabolic consequences of pyruvate kinase inhibition by oxalate in intact hepatocytes". *Biochemie*. 63(7): 595-602, 1981.
4. Lung Cancer Facts. National Lung Cancer Partnership. 2009.
5. Carew, Jennifer and pen Huang "Mitochondrial defects in cancer." *Molecular Cancer*. Vol. 1:9, 2002.
6. National Cancer Institute "Understanding Cancer Series: Cancer" 2006
7. M. Reimann "Normal Growth and Cancer. Philadelphia and Montreal: Lippincott Company". p.295, 1963.
8. "Safety (MSDS) data for ascorbic acid". Oxford University.10-09, 2005.
9. T. St. John "With Every Breath: A Lung Cancer Guidebook." www.lungcancerguidebook.org, 2003.
10. Woodard, Gladys "The effect of 2-Deoxy-D-glucose on glycolysis and respiration on tumor and normal tissues". *Biochemical Research Foundation*. Vol.14:599-605, 1954.
11. Xu, Rui-hua, Helene Pelicano, Yan Zhou, Jennifer S. Carew, Li Feng, Kapil N. Bhalla, Micheal J. Keating, and Peng Huane "Inhibition of Glycolysis in Cancer Cells: A Novel Strategy to Overcome Drug Resistance Associated with Mitochondrial Respiratory Defect and Hypoxia." *Cancer Research*. Vol.65: 613-615, 2005.
12. . J.B. Jacobs "Characteristics of a human diploid cell designated MRC-5." *Nature*. 168-170, 1970.
13. S.A. Ahmed, R.M. Gogal, and J.E. Walsh "A new rapid and simple non-radioactive assay to monitor and determine the proliferation of lymphocytes: an alternative to [3H] thymidine incorporation assay." *J Immunol. Methods*. Vol.170 (2): 211-24, 1994.
14. M. Nociari, A. Shalev, P. Benias , and C. Russo "A novel one-step, highly sensitive fluorometric assay to evaluate cell-mediated cytotoxicity." *J Immunol Methods*. Vol.78, 221-27, 1998.

15. L.A. Knowles, B.S. Raval, H.W. Harris, and R.M. Ratcliffe "Effect of ascorbate on the activity of hypoxia-inducible factor in the cancer cells." *Cancer Research United Kingdom Oncology Laboratory*. Vol. 63(8): 17648, 2003.
16. H. Liu, S. Niramol, P. Waldemar and T. J. Lampidis "Hypoxia increases tumor cell sensitivity to glycolytic inhibitors: a strategy for solid tumor therapy (Model C). *Biochemical Pharmacology*, Volume 64, Issue 12. Pages 1745-1751, 2002.
17. D.R. Lide "Handbook of Data on Organic Compounds, 3rd ed; CRC Press: Boca Raton, FL. p.4386, 1994.
18. H. Liu, N. Savaraj, W. Priebe W, and T.J. Lampidis "Hypoxia increases tumor cell sensitivity to glycolytic inhibitors: a strategy for solid tumor therapy (Model C)." *Biochem. Pharmacol.* 64(12): 1745-51, 2002.
19. Roudier, Bachelet, and Perrin "Pyruvate reduces DNA damage during hypoxia and after reoxygenation in hepatocellular carcinoma cells." Vol. 274 Issue 19 pp. 5188-98, 2007.
20. J. Murray "The Hive: The Story of the Honeybee. London, Great Britain." 2006.
21. National Honey Board "Carbohydrate and sweetness of Honey." [http:// www.honey.com/ downloads/carb.pdf](http://www.honey.com/downloads/carb.pdf). 2008.
22. M. Samitra, C. Gayuthm, and K. Sugna "Influence of Honey on Energy Metabolism during Wound Healing in Rats." University of Kentucky. Vol.1:6. 2009.
23. L.N. Sandier "Honey Bee Nutrition and Supplemental feeding." Beekeeping in United States. 2007.

NOVEL APPLICATION FOR MONITORING COMPLIANCE WITH HAND HYGIENE AND ISOLATION ATTIRE AT A UNIVERSITY HOSPITAL

Elham Ghonim, and Hamed Benghuzzi
University of Mississippi Medical Center
Jackson, MS 39110

ABSTRACT

Issue: Strict adherence to good techniques in hand hygiene (HH) and isolation precautions (IP) can prevent at least a third of infections acquired as a result of hospitalization. Compliance with these practices remains poor in many hospitals. Monitoring employees for compliance with these practices is costly, labor intensive, and may result in confrontation between observers and health care workers (HCWs). To facilitate observation for compliance and circumvent said problems we created a novel desktop and handheld computer application. Observed episodes of non-compliance generated instant email notifications to offenders with escalating penalties for repeated offenses. .

Project: Pilot project began on Sept 1, 2012, in four inpatient hospital wards. Monitoring in all wards began January 1, 2013 (25 inpatient units within 4 hospitals). A minimum of 80 observations per month were required for each unit. Data was collected by volunteer nurses, medical students, and unit secretaries. Data included: Name of observer and the person observed, date, time, unit, occupation, HH indication, the method used to perform HH, type of IP, and compliance with the required isolation attire. The application was linked to the human resources database and allowed the display of images of observed care providers, ending problems with mis-attribution.

Results: From January- December 2013, a total of 22,338 HH observations were collected from the four wards; 15,446 nurses, compliance 99%, and 2585 physicians, compliance 96%. Over three thousand HCWs were monitored for compliance with isolation attire; 2416 nurses, compliance 98%, and 334 physicians, compliance 99%. Rates of infections were monitored prior to and after the application, as a secondary outcome, where the decline was detected in the number of hospital acquired central line associated blood stream infection.

Keywords: Hand hygiene, isolation precautions, uScrub, handheld device, infection prevention program

INTRODUCTION

Hand Hygiene (HH) is the simplest, cheapest, and most important modality to prevent the spread of nosocomial pathogens in healthcare facilities. Compliance with HH remains poor in many institutions (R. Douglas Scott 2009, Perencevich et al., 2007). Reasons for poor compliance include lack of perception that HH is beneficial, understaffing, lack of time, lack of access to sinks and HH supplies among others (Pessoa-Silva, et al., 2005, Dubbert, et al., 1990). Strategies to improve compliance include providing education, performance feedback, and education on the association between reduced infection rate and performing HH (Dubbert, et al., 1990, White CM, et al., 2011, Lam BCC, et al., 2004, Mathur P 2011, Pittet D. et al., 2000, Sayed et al., 2011). Placing patients colonized or infected with multi-drug resistance organisms (MDROs) in isolation can reduce the spread of infections in hospitalized neonates, pediatric, and adult patients (Morioka. I, et al., 2013, Matsushima A, et al., 2011, Song X, et al., 2010, Lecornet E, et al., 2007, Bosnak, et al., 2007). Monitoring for compliance with HH and isolation precautions (IP) is an essential function of a hospital infection prevention program. At our institution monitoring for compliance with HH and use of appropriate isolation attire was performed by the infection preventionists (IPs) during their daily work rounds. Such efforts yielded an unacceptably low a number of observations on a limited number of work shifts. In addition, attempts at correction of non-compliant employees led to frequent confrontations. Other efforts, including patient and family surveys and monitoring for amounts of HH products (liquid soap, alcohol-based hand cleaners) used on patient care units did not yield information useful to target improvement efforts. The overall compliance with HH and IP was perceived as no better than 50%. In order to raise numbers of observations and increase compliance with HH and IP the division of information system (DIS) developed a comprehensive facility-wide program that utilized volunteer observers who monitored HH and IP using a single application. Furthermore, escalating series of consequences for healthcare workers (HCWs) chronically non-compliant with HH and IP were approved by hospital administration. The program yielded dramatic improvements in quality of care as indicated by reducing the number of central line associated blood stream infections (CLABSIs).

METHODS

This study was undertaken as a quality improvement plan. As such, it received a waiver of formal review by the institutional review board at the University of Mississippi Medical Center. The implementation of the program started on January 1st, 2011.

Our facility is a 722 bed tertiary referral medical-surgical hospital that serves as the major teaching affiliate of the University of Mississippi School of Medicine. The hospital serves as the only level one trauma center in the state of Mississippi. All medical and surgical sub-specialties are represented. In the year of the described intervention 2013 the hospital experienced 29,536 inpatient admissions and 110,645 unique outpatient visits.

Protocol and Data Collection: Prior to the intervention monitoring compliance with HH was performed using the iScrub® application (January 2011 through December 2012) developed by the University of Iowa Computational Epidemiology Research Group for use on the Apple iPhone® or iTouch® device (Hlady, et al., 2012). This application was attractive since it was available free of charge, requires minimal training, contains mechanisms to minimize data entry error, and decreases the amount of time required to process and feedback results” as compared to traditional methods using pen and paper. Details of this intervention are described in a previous paper (Ghonim et al., 2013).

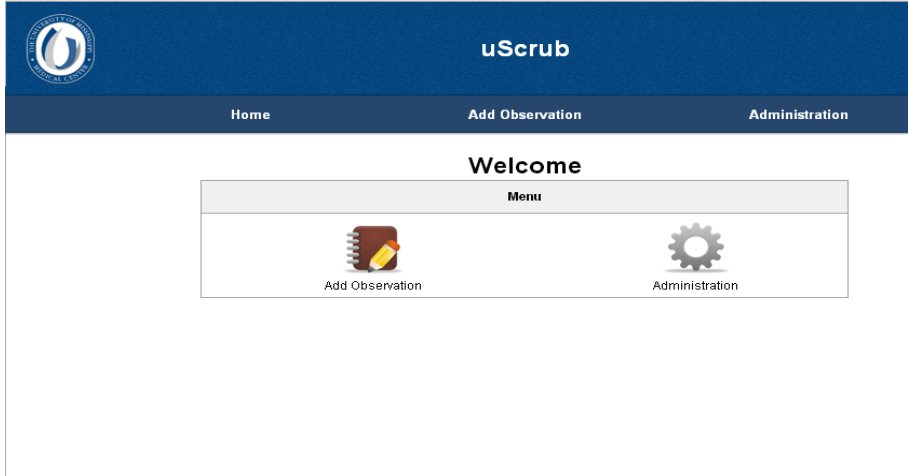
Several shortcomings were associated with the iScrub® system. First, there was the expense incurred to purchase over fifty iTouch devices. Also devices or their chargers were frequently lost or misplaced, leading to absent HH observations on some patient care units. iScrub® collected data were sent via WiFi to the Infection Prevention Department email box and then downloaded to an electronic database, SharePoint®, where it was available on the hospital intranet system for review by stakeholders in near real time. Due to weak WiFi signals in some location within the facility, multiple observations were lost, with no alert to the observers. Additionally; iScrub® allowed us to collect data regarding HH but was less robust in collecting data on compliance with isolation guidelines. Lastly, we had problems with attribution. In an institution such as ours, with over 13,000 employees and students, duplication of names was common and led to complaints of mis-attribution of those identified as non-compliant.

To address these issues we developed the “u Scrub” application with the help of the Division of Information System. Since desktop computers are abundant on all patient care units we developed a program that could be loaded on any computer in our facility. This circumvented the need to purchase handheld devices and eliminated the problem with their loss or lack of electrical charge. The application records the number of observations sent and an alert that the observation was sent to the shared website for analysis. We included expanded fields, from those available in iScrub® to collect a more detailed description of job categories, plus additional information regarding compliance with isolation attire. We also added an interface with a centralized personnel database. When a provider’s name is entered in the program pictures of all healthcare providers with the same name appear in a window. This ended issues with mis-attribution. In September 2012 we piloted the program in all four patient care units in our 82 bed adult intensive care hospital. In January 2013 uScrub was implemented in all patient care units.

January 2013 – December 2013 center wide monitoring of HH and IP, in 25 inpatient units within 4 separate hospital wards: Adult Critical Care Hospital, Women and Infants Hospital, Children’s Hospital, and Adult Medical/Surgical Hospital were performed using the uScrub. By consensus from administration in the effort to ensure a culture of compliance with HH, we adopted an escalating set of penalties for those repeatedly non-compliant (Ghonim E, et al., 2013). On August 2013, the quality board approved same consequences for not complying with IP.

HCWs were required to wash their hands prior to entering and upon leaving patient rooms. Wash in/Wash out was our HH indication during the intervention. Data was collected 24 hours/ day, seven days/week at the unit level by over one hundred anonymous nursing volunteers, medical students, and unit secretaries. Data included: Name of observer and observe, date, time, unit, occupation, HH indication, the method used to perform HH, type of isolation precaution, and required isolation attire (figure 1).

Figure 1: uScrub Screen Shots for Monitoring for Compliance with Hand Hygiene and Isolation Attire
 A; Choose add observation



B; Choose Job category



C; Type observe name



D; Choose a location



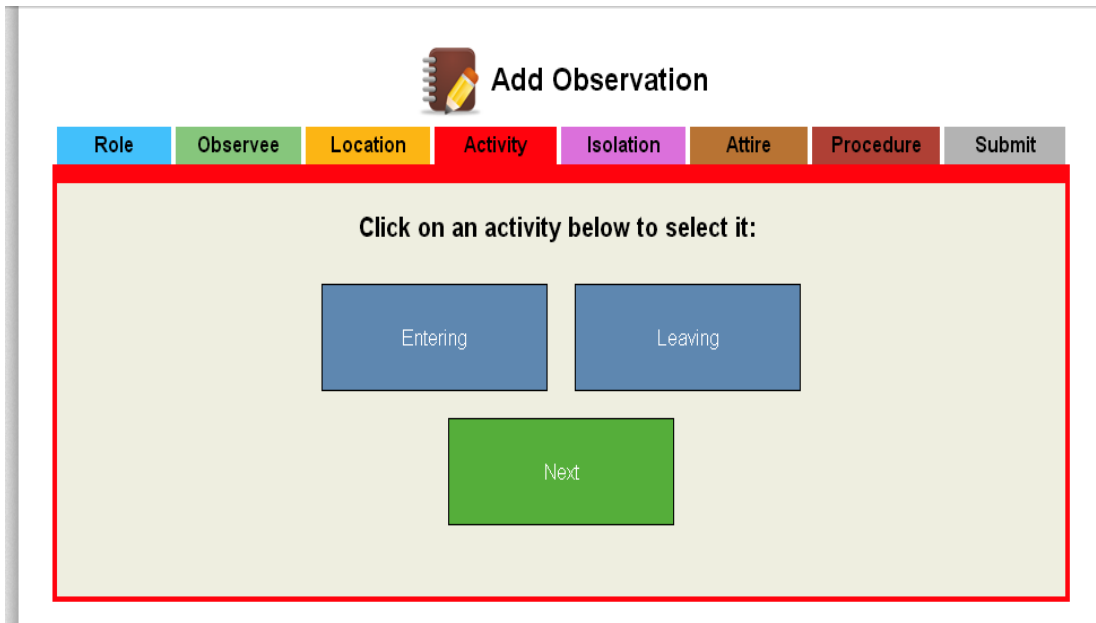
Add Observation

Role Observee **Location** Activity Isolation Attire Procedure Submit

Click on a location below to select it:

Adult Tower - 2 North

E; Choose hand hygiene indication



Add Observation

Role Observee Location **Activity** Isolation Attire Procedure Submit

Click on an activity below to select it:

Entering Leaving

Next

F; Choose Type of isolation or NA if isolation is not required

Add Observation

Role | Observee | Location | **Activity** | **Isolation** | Attire | Procedure | Submit

Click below to choose an isolation:

Contact | Droplet | Airborne

Contact and Airborne | Contact and Droplet

Contact, Droplet and Airborne | N/A

Next

G; Choose required isolation attire

Add Observation

Role | Observee | Location | Activity | Isolation | **Attire** | Procedure | Submit

Click below to choose attire:

Gloves | Gown | N95 Mask | Surgical Mask

Gloves and Gown | Gloves, Gown, and Surgical Mask | Gloves, Gown, and N95 Mask

N/A

Next

H; Submit Observation

Add Observation

Role | Observee | Location | Activity | Isolation | Attire | Procedure | **Submit**

Enter any notes below (optional):

The page at <https://apps.umc.edu> says:
Thanks for your submission.

Submit

RESULTS

During January – December 2013, 26,764 HH observations were collected from four hospital wards compared to 24,977 and 26,657 observations during 2012 and 2011 calendar year respectively. Our program led to a continuous increase in compliance rates among physicians and sustained high rate among nurses (Table 1). Total HH Observations among nurses were 16,517, with 100% average compliance rate, and 3,055 observations among physicians with a compliance rate of 97%. Highest compliance was observed from the Children’s Hospital (table 2). Noncompliance occurred at a similar frequency both before and after patient contact. Alcohol hand rub has been the most frequently used methods to perform HH. Noncompliance occurrences at BMTU were not observed among physicians or nurses.

Table1: Comparison of hand hygiene vital data analysis during 2013, 2012, and 2011 calendar year.

Calendar Year	Total # of Observations	Total % Compliance	% MD Compliance	% RN Compliance
2011	26657	95%	88%	98%
2012	24977	98%	95%	99%
2013	26764	98%	96%	99%

Table 2: uScrub® hand hygiene vital data analysis – 2013 Calendar Year

Location	Total Observations	RN	MD	RN compliance	MD Compliance
Adult	9626	6232	817	100%	97%
Batson	4754	2615	298	100%	100%
Wiser	5433	3532	909	100%	99%
Critical Care	6951	4138	1031	99%	92%
Total	26,764	16517	3055	100%	97%

Prior to the uScrub application no data was stated for compliance with IP among staff. After the execution of the program, over four thousand HCWs were monitored for compliance with IP, 2,898 nurses with a compliance average of 98% and 404 physicians with a compliance average of 95%. Adult Hospital had the highest rate of compliance with IP, where the critical Care Hospital had the lowest rate of compliance (Table 3).

Table 3: uScrub Isolation Attire vital Data Analysis- 2013 Calendar Year

Location	Total Observations	Total %	RN	MD	RN compliance	MD Compliance
Adult	1248	99%	870	80	99%	94%
Batson	1483	98%	1018	82	97%	99%
Wiser	113	98%	77	21	99%	98%
Critical Care	1330	96%	933	221	97%	88%
Total	4,174	98%	2,898	404	98%	95%

To strengthen the culture of compliance with HH and IP, monthly surveillance for central line associated blood stream infections (CLABSIs) was performed. Retrospective surveillance during the iScrub period (2011 and 2012 calendar years) and the year during the intervention (2013) were performed by the infection prevention department. Data was represented as the number of infections per 1000 central line days. All four hospital wards participated in the monthly surveillance. Standardized infection ratio (SIR), and P value was calculated by the National Healthcare Network (NHSN) (table 4). Largest significant reduction was observed from locations with the sickest patient population and largest central line utilization ratio such as the Critical Care Hospital (Table 5), and the Neonatal Intensive Care Unit (Table 6).

Table 4: Central Line Associated Blood Stream Infection (CLABSIs) Center Wide Vital Data Analysis

Calendar Year	CLABSI Infection Count	CLABSI Number Expected	Central Line Days	SIR	SIR_pval	CLABSI Rate /1000 Line Days
2011	64	90	39225	0.713	0.0026	1.6
2012	102	104	45547	0.979	0.4416	2.2
2013	69	114	52315	0.604	0.00	1.3

Table 5: Central Line Associated Blood Stream Infection (CLABSIs) at the Critical Care Hospital

Calendar Year	CLABSI Infection Count	CLABSI Number Expected	Central Line Days	SIR	SIR_pval	CLABSI Rate/1000 Line Days
2011	28	32	12270	0.9	0.3	2.3
2012	30	32	12252	0.9	0.4	2.4
2013	16	35	13097	0.5	0.0	1.2

Table 6: Central Line Associated Blood Stream Infection (CLABSIs) at the Neonatal Intensive Care Unit

Calendar Year	CLABSI Infection Count	CLABSI Number Expected	Central Line Days	SIR	SIR_pval	CLABSI Rate/1000 Line Days
2011	13	12.186	4884	1.067	0.4453	2.7
2012	17	17.865	7034	0.952	0.4814	2.4
2013	13	19.428	7500	0.669	0.0833	1.7

DISCUSSION

Traditional methods for monitoring HH and IP include HCWs self-reporting; which proved to have poor validity in several studies. Measuring the consumption of HH products over identified time, does not indicate which job category is in compliance/ noncompliance with HH or the indication of hand hygiene. WHO identifies direct observation to be the gold standard for monitoring HH; however, it is labor intensive and carries the possibility that staff members might change their behavior when they realize that they are being monitored for compliance (Haas J.P. and Larson E.L., 2007).

Electronic monitoring has been introduced and used by multiple institutions; these systems provide continuous monitoring for HH. The benefits of such product include continuous monitoring of HH compliance and utilization of less manpower by hospital administration; disadvantage is that it is expensive to install (Swoboda, et al., 2004, Venkatesh, et al., 2008, Boyce, et al., 2008, Shaud, et al., 2010; Edmond, et al., 2010, Haas and Larson, 2007).

Monitoring compliance with IP is done by direct observations in most health care facilities and outpatient clinics. In our institution, direct observation in collecting HH and IP utilizing IPs had multiple disadvantages which include but not limited to; not being able to monitor most of the health care workers who come in contact with the patient, collection of a small number of observations, possible confrontations between IPs and staff, in addition, no observations were collected in wards where patient service is provided behind closed doors. These disadvantages did not help in creating a culture of compliance with HH and IP, providing an accurate feedback to staff and stakeholders, or gain the administration support needed for the success of the program. The use of electronic monitoring was a financial burden for an academic teaching facility that contains 25 inpatient units and 722 beds. iScrub® was an affordable methodology that we utilized for two calendar years utilizing nursing volunteers (Ghonim et al., 2013). However, multiple disadvantages were associated with the use of the iScrub®.

Establishment of the “uScrub” has multiple advantages most remarkable were: sustaining a high number of HH observations, sustaining an increase in compliance with HH, obtaining data for compliance with IP among HCWs. Adding, easy utilization of the application and spread of its use among all staff without the need to purchase or charge hand held devices. The General impact of the success of the program was measured by the achievement of a significant reduction in the infection rate and the number of CLABSI. Furthermore, the uScrub application aided in maintaining a continuous increase in compliance of HH and IP center wide without adding a financial burden to our budget.

Limitations

In this study HH and IP observations were collected mostly by using nursing staff, which might create a bias in collecting observations of physicians versus nursing staff observations. This led us to creation another intervention using the uScrub utilizing physicians and administration Champions.

REFERENCES

- Douglas Scott II., Kilgore, Meredith L. PhD; Ghosh, Kathakali MS; Beavers, C Martin BS; Wong Daisy Y. PhD; Hymel, Patrick A. Jr MD; Brossette, Stephen E. MD, PhD. The direct medical costs of healthcare-associated infections in U.S. hospitals and the benefits of prevention 2008; 6:101-104.
- Perencevich EN, Stone PW, Wright SB et al. Raising standards while watching the bottom line: making a business case for infection control. *Infect Control Hosp Epidemiol.* 2007; 28:1121-33.
- Pessoa-Silva CL, Posfay-Barbe K, Pfister R, Touveneau S, Perneger TV, Pittet D. “Attitudes and perceptions toward HH among healthcare workers caring for critically ill neonates” *Infection control and hospital epidemiology* 2005; 26:305-11.
- Dubbert, P. M., Dolce, J., Richter, W., Miller, M., & Chapman, S. W. Increasing ICU staff handwashing: effects of education and group feedback. *Infect Control Hosp Epidemiol* 1990; 11: 191-193.
- White MC, Statile AM, Conway PH, Schoettker PJ, Solan LG, Vidwan N, Warrick SD, Yau C, and Connelly BL. Utilizing improvement science methods to improve physician compliance with proper HH. *Official journal of the American academy of pediatrics* 2012;129:1042-50.
- Lam B, Lee J, and Y.L.Lau. HH Practices in a Neonatal Intensive Care Unit: A multimodal Intervention and Impact on Nosocomial Infection. *Pediatrics* 2004;10: 114-e565.
- Mathur P. HH: back to the basics of infection control. Department of Laboratory Medicine, Jai Prakash Narain Apex Trauma Centre, All India Institute of Medical Sciences, New Delhi, India Year : 2011;134: 611-620.
- Pittet D, Hugonnet S, Harbarth S, Mourouga P, Sauvan V, Touveneau S, Pernger T, and Members of the infection Control programme. Effectiveness of a hospital-wide programme to improve Compliance with HH. *The lancet* 2000; 356:1307-12.
- Syed ZB, Waleed MH, Abdulkareem B, Wail HA, Talal K, Mohammad IF. Hand Hygiene compliance rate among healthcare professional. *Saudi MD J* 2011; Vol. 32(5): 515-519.
- I. Morioka, M. Yahata, A. Shibata, A. Miwa, T. Yokota, T. Jikimoto, M. Nakamura, J. J. Lee, H. Yoshida, H. Yamada, S. Arakawa, K.Iijima: Impact of pre-emptive contact precautions for outborn neonates on the

- incidence of healthcare-associated methicillin-resistant *Staphylococcus aureus* transmission in a Japanese Neonatal intensive care unit. *Journal of Hospital Infection* 2013; 84: 66-70.
- Matsushima A, Tasaki O, Tomono K, et al. Pre-emptive contact precautions of intubated patients reduced healthcare-associated methicillin-resistant *Staphylococcus aureus* transmission and infection in an intensive care unit. *J Hosp Infect* 2011;79:97-101.
- Song X, Cheung S, Klontz K, Short B, Campos J, Singh N. A stepwise approach to control an outbreak and ongoing transmission of methicillin-resistant *Staphylococcus aureus* in a neonatal intensive care unit. *AM J Infect Control* 2010;38:607-611
- Lecornet E, Robert J, Jacqueminet S. Preemptive isolation to prevent methicillin-resistant *Staphylococcus aureus* cross transmission in diabetic foot. *Diabetes Care* 2007;30:2341-2342.
- Bosnak V.K, Mustafa Namiduru, Ilkay Karaoglan, and Ayse Ozlem Mete. Evaluation of compliance in control and prevention study of Vancomycin resistant *Enterococcus* outbreak. *The scientific World Journal* 2013;10:1155-1162.
- Hlady CS., Curtis D.E., Fries J, Yang M, Segre A.M., Polgreen P.M.. 21st Annual Scientific Meeting Of the Society for Healthcare Epidemiology of America: A Pilot Intervention with Feedback from a Companion Website 2011
- Ghonim E, Nolan R, Benghuzzi H, Increasing Hand Hygiene Compliance by Use of a Novel Hand Held Device at a University Hospital. *Biomed Sci Instrum.* 2013 Apr 5; 49:32-39. PMID: 23686178
- Haas JP, Larson EL. Measurement of Compliance with HH. *J Hosp Infect* 2007;66:6-14
- Swoboda SM, Earsing K, Strauss K, Lane S, Lipsett PA. Electronic monitoring and voice prompts improve HH and decrease nosocomial infections in an intermediate care unit. *Crit Care Med* 2004;32:358-63
- Venkatesh AK, Lankford MG, Rooney DM, Blachford T, Watts CM, Noskin GA: use of electronic alerts to enhance HH compliance and decrease transmission of vancomycin-resistant enterococcus in a hematology unit. *Am J Infect Control* 2008;36: 199-205
- Boyce JM. HH compliance monitoring: current perspectives from the USA. *Journal of hospital infection* 2008; 70: 2-7.
- Sahud AG, Bhanot N, Radhakrishnan A, Bajwa R, Manyam H, Post JC: An electronic. Hand hygiene surveillance device: a pilot study exploring surrogate markers for HH compliance *Infect Control Hosp Epidemiol* 2010; 31:634-9.
- Edmond MB, Goodell A, Zuelzer W, Sanogo K, Elam K, Bearman G: Successful use of alcohol sensor technology to monitor and report HH compliance. *J Hosp Infect* 2010; 76:364-5.

THE EFFECT OF TRANSCUTANEOUS ELECTRICAL NERVE STIMULATION AT ACUPUNCTURE POINTS ON SPINAL MOTOR NEURON EXCITABILITY IN PEOPLE WITHOUT KNOWN NEUROMUSCULAR DISEASES.

Min Huang¹, Howe Liu¹, Jian-Wei Gu², Ham Benghuzzi¹, Xuexiang Wang², Antonio V Hayes³, Rebecca H. Pearson¹, Felix Adah¹, and Dobrivoje S Stokic³. ³Neurophysiological Research Laboratories, The Methodist Rehabilitation Center, Jackson; ²Department of Physiology, and ¹Department of Physical Therapy, University of Mississippi Medical Center, Jackson, MS

ABSTRACT

Background and Purpose: Any changes in the Hoffmann reflex (H-reflex) reflect the changes in spinal motor neuron excitability. The purpose of this study was to determine whether transcutaneous electrical nerve stimulation (TENS), applied over the acupuncture points, would alter the soleus muscle's H-reflex. **Subjects:** Forty-five volunteers without known neuromuscular diseases (mean years of age=25, SD=7.3, range=21-47) were studied. **Methods:** Subjects were randomly divided into three groups: control (C), TENS stimulation at sensory threshold (ST) and 1.5 times sensory threshold (1.5 ST), and TENS was administered for 15 minutes. Stimulation intensity varied according to group assignment. H-reflexes were recorded before and at 0, 5 and 10 minutes after TENS. **Results:** H-reflex amplitudes significantly increased following TENS at both the ST and 1.5 ST in 10 minutes, whereas H-reflex amplitudes did not change in 0 and 5 minutes following TENS at both the ST and 1.5 ST. **Conclusion:** Both of the low and high-intensity TENS at the acupuncture points increase H-reflex amplitudes in subjects without known neuromuscular diseases. **Clinical Relevance:** This study suggests that TENS at the acupuncture points may facilitate the recovery of patient with diagnosis of stroke

Keywords: Acupuncture, TENS stimulation, Hoffmann reflex, Neuromuscular Diseases

INTRODUCTION

Patients with upper motor neuron syndrome (eg, a lesion of the central nervous system stroke, spinal cord lesion) often display spasticity [1-7], a complex motor disorder characterized by a velocity-dependent increase in muscle resistance to passive stretch with exaggerated tendon jerks, caused by hyperexcitability of the stretch reflex [8]. Commonly associated symptoms include impaired movement, painful muscle spasms, stiffness and disturbed sleep. Severe or long-standing spasticity may lead to contractures and joint ankylosis, which can severely restrict the patient's care and rehabilitation [9]. Therefore, an effective treatment is important to increase the motor function, facilitate self-care and decrease painful, harmful effects of spastic contractions. Therapeutic treatments, including pharmacological agents and physical therapy, have been used to ameliorate spasticity. However, pharmacologic reduction of spasticity is often associated with severe side effects including sedation, generalized muscle weakness, and hepatotoxicity [10]. Therefore, physical therapy is getting more and more attention in the management of spasticity.

The Hoffmann (H) reflex is widely acknowledged as an indirect indicator of spinal motor neuron excitability. It is well documented that any changes in H-reflex amplitude, latency and recovery time reflect the changes in spinal motor neuron excitability [8,11,12]. Acupuncture is considered an effective therapeutic modality for a wide range of diseases and conditions in Eastern cultures. Western interest in acupuncture is generally related to the treatment of pain [13-15]. In addition to its use in pain management, the scope of research using this modality has broadened considerably to many other medical problems including cardiovascular related medical problems [16], HIV [17], central nervous system ischemia [18] and stroke [19]. Several studies [11,12] have found that the use of acupuncture can alter the sensitivity of spinal motor neuron excitability as evidenced by the changes in H-reflex. Yu and associates [11] have shown that acupuncture at the points of Yang Ling Chuan, Hsuan Chung, Kun Lun, Feng Shih and Cheng Shan can prolong the H-reflex recovery time following the double-stimulation of popliteal tibial nerve in stroke patients with the paralysis of the lower limb. Our previous results demonstrated that low intensity TENS increases H-reflex amplitudes in subjects without known neuromuscular diseases while high intensity TENS had little influence on H-reflex amplitudes [8]. A recent study from Ge *et al.* shows that TENS at intramuscular trigger points increases H-reflex [29]. A study from Chang *et al.* shows that TENS with surface electrodes on Hegu

acupoint increases the amplitude of the H-reflex [12]. However, the changes in H-reflex in soleus in response to the acupoint stimulation on Hegu (in the hand) could be different from the H-reflex response following the acupoint stimulation in the leg. The effect of TENS, administered via non-invasive surface electrodes to acupoints in the leg, on H-reflex of the soleus muscle has not been previously studied. Therefore, the main purpose of the present study is to determine the effect of TENS, administered to acupuncture points, on spinal motor neuron excitability, as reflected by the H-reflex of the soleus muscle, in volunteers having no known neuromuscular diseases. Despite numerous studies, demonstrating that TENS can alter the H-reflex response, considerable controversy exists regarding the effect of stimulus intensity on the H-reflex. Some authors [20,21] reported that that hypertonicity and tonus decreases when TENS was below sensory threshold (ST). Other authors [22-24] have suggested that the stimulation should be above ST and just below motor threshold (MT). Stimulus intensity also varies in people with no known muscular diseases. Our previous results [8], along with the study from Delwaide and associates [25], have shown that mild stimulus increases the amplitude of H-reflex of the soleus muscle whereas a strong stimulus caused no changes or a brief decrease in the H-reflex. However, other authors [26] have observed that a mild stimulus caused a decrease in the soleus muscle's H-reflex. In the present study we focused on the potential differential effects that stimulus intensity at the acupuncture points might have on this reflex. Our hypothesis is that TENS at the acupuncture points will influence the H-reflex in healthy subjects and that this influence will vary in magnitude depending on the stimulus intensity.

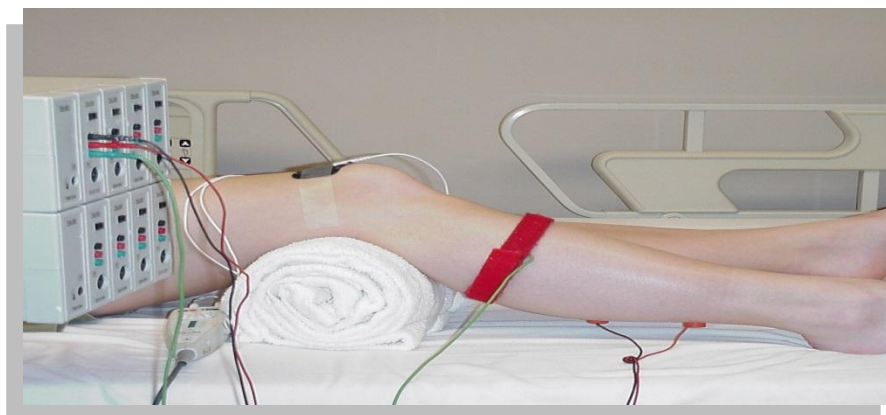
METHODS

Subjects: This study was conducted on 45 (26 males, 19 females) volunteer subjects, with no known neuromuscular disease, with an age range from 21 to 47 years old. Subjects were informed of the nature of the experiment, benefits and risks involved in participation, and all signed **an informed consent document**. **Subjects were randomly divided into 3 groups determined by TENS stimulus intensity as follows: control (C), sensory threshold (ST), and 1.5 ST. The demographics of our study are illustrated in the table below:**

Groups	Males	Females	Total #	Mean Age
Control	11	5	16	24.43
ST	8	7	15	25.33
ST 1.5	7	7	14	25.21
Totals	26	19	45	24.98

Set-up

Subject positioning: Each subject rested supine on a bed. Towel rolls were placed under the right knee and ankle, so that the heel would be off the surface of the bed and so that reflex movements of the ankle were unrestricted.



H-reflex protocol. H-reflex recording performed by an experienced EMG technologist, using a commercially available electrodiagnostic apparatus (Viking IV-D). First, an H-reflex recruitment curve recorded to determine the current necessary to produce a maximal H-reflex and a maximal M-wave (short-latency orthodromic motor response). The current were subsequently adjusted to elicit reproducible H-reflexes that measured between 20% and 40% of the maximum M-wave, a size known to be sensitive to both excitatory and inhibitory influences [27]. Following this procedure, 10 H-reflexes recorded in complete relaxation before and 3 times after TENS. An H-reflex evoked every 10 seconds using a 1-millisecond stimulus duration.

TENS stimulation apparatus: Transcutaneous electrical nerve stimulation administered with a Grass S-88 stimulator [Grass instruments, Division of Astro-Med Inc, 600 E Greenwich Ave, West Warwick, RI 02893] through 4 carbon-rubber surface electrodes [4.3 cm long × 3.7 cm wide or 1.25 inches in diameter) at the acupuncture points. The stimulus delivered as 3-second trains, with a 2-second intertrain (off) period. Each train consisted of 100-microsecond square waves occurring at 20 Hz [total of 60 pulses). These stimulus parameters were similar to those used to reduce spasticity, hyperreflexia, and clonus [1,2,4,8,22,28] using these stimulus settings, each subject tested to determine the sensory or 1.5 times ST at the following four acupuncture points of Yang Ling Chuan, Kun Lun, Feng Shih and Cheng Shan as previously described [11]. The TENS administered either at ST or at 1.5 times ST (1.5ST), depending on a group assignment.

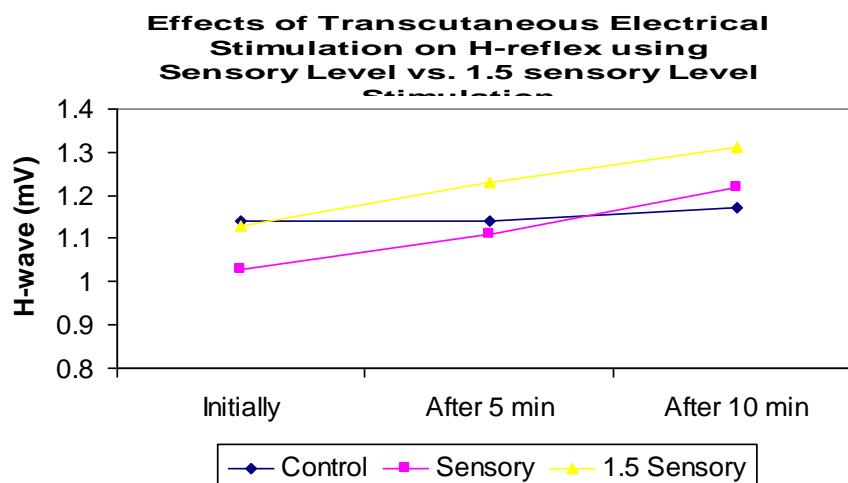
Experimental protocol: Subjects were randomly assigned to one of three groups (control, ST stimulation and 1.5 ST stimulation groups) in which electrical stimulation administered for 15 minutes. The subjects in the control group had the electrode placement as the two experimental groups, but did not receive electrical stimulation. The subjects in the ST stimulation group received electrical stimulation at the acupuncture points with stimulation intensity at the level of ST. The subjects in the 1.5 ST group received electrical stimulation at the acupuncture points with stimulation intensity at the level of 1.5 ST. Immediately before the period of electrical stimulation, 10 consecutive H-reflexes elicited, and their amplitudes averaged to yield the baseline value. Following the period of stimulation, 3 sets of 10 H-reflexes each obtained starting (1) at the end of stimulation, (2) five minutes following the end of stimulation, and (3) ten minutes following the end of stimulation.

Data Analysis: Repeated ANOVA test were used to compare the statistical significance between the groups and the differences before and after electrical stimulation. Data were expressed as means ± SE.

RESULTS

There was a significant increase ($P < 0.05$) in H-reflex response following transcutaneous electrical stimulation at sensory threshold and 1.5 sensory threshold levels at acupuncture sites.

There was more of an increase in H-reflex response following stimulation at 1.5 sensory threshold levels.



DISCUSSION

We have investigated the effect of TENS with ST and 1.5 ST at acupuncture points on the lower limb on H-reflex. In our study, the results supported the hypothesis that stimulus intensity would play an important role in determining the extent to which TENS influenced the H-reflexes. In subjects with no known neuromuscular diseases, we found that low-intensity TENS at acupuncture points increased H-reflex amplitudes; high-intensity stimulation at acupuncture points caused significant higher increase in amplitude of H-reflex.

These results tend to be in partly agreement with the research findings from Delwaide and associates [25] in which they found that mild stimulation (2-3 times ST) of the sural nerve caused a brief increase of the soleus muscle's H-reflex, whereas a strong (painful) stimulus caused a brief decrease of the soleus H-reflex. The observations of Delwaide and associates [25] correlate well with our findings that TENS delivered at ST resulted in an increase in the soleus muscle's H-reflex, whereas TENS delivered at 1.5 ST caused an higher increase in amplitude of H-reflex.

The fact that our results only partly support the findings of Delwaide and associates [25] may be attributed, in part, to the fact that we used different intensity. Delwaide and associates [25] used painful stimulus as higher stimulation intensity as compared to 1.5 ST as high stimulation intensity used in the present study. At 1.5 ST, subjects felt strong, but not painful. Therefore, our data seem to indicate that TENS utilizing a strong stimulus, but not painful, significantly increased the amplitude of H-reflex.

The present study results also confirmed our previous findings [8] at which low intensity TENS increased amplitude of H-reflex, but high intensity TENS did not alter the amplitude of H-reflex. The possible explanation for the difference between the present study and our previous study is the difference in stimulation sites. The present study used acupuncture points as compared to non-acupuncture points used in our previous study. Acupuncture points may be more sensitive than non-acupuncture sites. Further research required to confirm our hypothesis.

In summary, the present study results indicate that both of the low and high intensity TENS at acupuncture points increase H-reflex amplitudes in subjects without known neuromuscular disease.

CONCLUSION AND CLINICAL IMPLICATIONS

This study shows that TENS at acupuncture points results in an increase in H-reflex response. As patients diagnosed with stroke [cerebral vascular accident] often present with flaccidity and decreased H-reflex response, TENS at acupuncture points could potentially be used clinically to increase H-reflex response and ultimately decrease flaccidity.

REFERENCES

1. Alfieri V. Electrical treatment of spasticity: reflex tonic activity in hemiplegic patients and selected specific electrostimulation. *Scand J Rehabil Med.* 1982;14:177-182.
2. Franek A, Turczynski B, Opara J. Treatment of spinal spasticity by electrical stimulation. *J Biomed Eng.* 1988;10:266-270.
3. Robinson CJ, Kett NA, Bolam JM. Spasticity in spinal cord injured patients, 1: short-term effects of surface electrical stimulation. *Arch Phys Med Rehabil.* 1988;69:598-604.
4. Seib TP, Price R, Reyes MR, Lehmann JF. The quantitative measurement of spasticity: effect of cutaneous electrical stimulation. *Arch Phys Med Rehabil.* 1994;75:746-750.
5. Goulet C, Arsenault AB, Bourbonnais D, et al. Effects of transcutaneous electrical nerve stimulation on H-reflex and spinal spasticity. *Scand J Rehabil Med.* 1996;28:169-176.
6. Hummelsheim H, Maier-Loth ML, Eickhof C. The functional value of electrical muscle stimulation for the rehabilitation of the hand in stroke patients. *Scand J Rehabil Med.* 1997;29:3-10.
7. Schindler-Ivens S, Shields RK. Low frequency depression of H-reflexes in humans with acute and chronic spinal-cord injury. *Exp Brain Res* 2000; 133:233-241.
8. Hardy SGP, Spalding TB, Liu H, Nick TG, Pearson RH, Hayes AV, Stokic DS. The effect of transcutaneous electrical stimulation on spinal motor neuron excitability in people without known neuromuscular diseases: the roles of stimulus intensity and location. *Phys Ther.* 2002; 82:354-363.
9. Anonymous. The management of spasticity. *Drug & Therapeutics Bulletin* 2000; 38:44-46.
10. Ciccone CD. *Pharmacology in Rehabilitation.* 3rd edition, F. A. Davis, Philadelphia, 2002; pp 167-182.
11. Yu YH, Wang HC, Wang ZJ. The effect of acupuncture on spinal motor neuron excitability in stroke

- patients. *Chin. Med J* 1995; 56:258-263.
12. Chang QY, Lin JG, Hsieh CL. Effect of manual acupuncture and transcutaneous electrical nerve stimulation on the H-reflex. *Acupuncture & Electro-Therapeutics Res. InT. J* 2001; 26: 239-251.
 13. Wang X. Electroimpulse acupuncture treatment of 110 cases of abdominal pain as a sequela of abdominal surgery. *J. Tradit. Chin. Med.* 1988; 8:269-270.
 14. Christensen PA, Noreng M, Andersen PE, Nielsen JW. Electroacupuncture and postoperative pain. *Br. J. Anaesth* 1989; 62:258-262.
 15. Filshie, J. and White, A. *Medical Acupuncture: A Western Scientific Approach*, Churchill Livingstone, Philadelphia, 1998.
 16. Chiu Yj, Chi A, Reid IA. Cardiovascular and endocrine effects of acupuncture in hypertensive patients. *Clinical & Experimental Hypertension* 1997; 19(7): 1047-63.
 17. Galantino MLA, Eke-okoro ST, Findley TW, Condoluci D. Use of noninvasive electroacupuncture for the treatment of HIV-related peripheral neuropathy: a pilot study. *Journal of Alternative and Complementary Medicine* 1999; 5(2):135-142.
 18. Ying SX, Cheng JS. Neuoprotective effects of electro-acupuncture in a gerbil model of transient cerebral ischemia and reperfusion. *Chinese Journal of Neuroscience* 1994; 1(1): 33-36.
 19. Chen A. Effective acupuncture therapy for stroke and cerebrovascular diseases. Part I. *Am J Acupunct* 1993; 21:105-122.
 20. Dimitrijevic MM. Mesh-glove, 1: a method for whole-hand electrical stimulation in upper motor neuron dysfunction. *Scand J Rehabil Med.* 1994;26:183-186.
 21. Dimitrijevic MM, Soroker N. Mesh-glove, 2: modulation of residual upper limb motor control
 22. Dewald JP, Given JD, Rymer WZ. Long-lasting reductions of spasticity induced by skin electrical stimulation. *IEEE Trans Rehabil Eng.* 1996;4:231-242.
 23. Carmick J. Managing equinus in children with cerebral palsy: electrical stimulation to strengthen the triceps surae muscle. *Dev Med Child Neurol.* 1995;37:965-975.
 24. Carmick J. Use of neuromuscular electrical nerve stimulation and a dorsal wrist splint to improve the hand function of a child with spastic hemiparesis. *Phys Ther.* 1997;77:661-671.
 25. Delwaide PJ, Crenna P, Fleron MH. Cutaneous nerve stimulation and motoneuron excitability, I: soleus and tibialis anterior excitability after ipsilateral and contralateral sural nerve stimulation. *J Neurol Neurosurg Psychiatry.* 1981;44:699-707.
 26. Goulet CG, Arsenault AB, Bourbonnais D, Levin MF. Effects of transcutaneous electrical nerve stimulation on the H-reflex of muscles of different fibre type composition. *Electromyogr Clin Neurophysiol.* 1997;37:335-342.
 27. Crone C, Hultborn H, Mazieres L, et al. Sensitivity of monosynaptic test reflexes to facilitation and inhibition as a function of the test reflex size: a study in man and the cat. *Exp Brain Res.* 1990;81:35-45.
 28. King TI 2nd. The effect of neuromuscular electrical stimulation in reducing tone. *Am J Occup Ther.* 1996;50:62-64.
 29. Ge HY, Serrao M, Andersen OK, Graven-Nielsen T, Arendt-Nielsen L. Increased H-reflex response induced by intramuscular electrical stimulation of latent myofascial trigger points. *Acupunct Med.* 2009; 27(4): 150-4.

THE EFFECT OF MANNOSE-6-PHOSPHATE IN REDUCING TRANSFORMING GROWTH FACTOR PROLIFERATION OF MCCOY FIBROBLAST CELLS

Gerri A. Wilson, David A. Black, Michelle A. Tucci, and Ham A. Benghuzzi
University of Mississippi Medical Center, Jackson, MS 39216

ABSTRACT

Surgically repaired tendons are plagued by complications related to the healing response. Adhesion formation between the tendon and its sheath or surrounding tissues inhibits free gliding and results in a loss of excursion. The random orientation of collagen deposition at the site of repair creates a focal area of weakness, thereby rendering the tendon prone to rupture at this point. Even the strongest, most technically precise repair can be negated by excessive scar tissue. No widely accepted therapy currently exists to promote healing and prevent fibrosis in surgically repaired tendons. Transforming growth factor beta (TGF- β) is considered the active factor during healing that leads to scar formation. It does so by binding with a mannose-6-phosphate/IGF-II receptor on the Golgi apparatus, which changes the extracellular matrix and ultimately leads to fibrosis. Therefore, inhibiting TGF- β may be one method to reduce scar formation. The goal of this study was to determine the effects of mannose-6-phosphate (M6P) in inhibiting transforming growth factor β 1 (TGF- β 1) proliferation of fibroblast cells. McCoy fibroblasts were treated with low, medium, and high concentrations of mannose-6-phosphate for periods of 24, 48, and 72 hours, and with low, medium, and high concentrations of TGF- β 1 for periods of 24, 48, and 72 hours. Cell proliferation, damage, and morphology were evaluated at each time point. The results show that low dose TGF- β 1 treatment resulted in significant increases in cell number with distinct cytological changes within 48 hours of treatment. Mannose-6-phosphate reduced cell number within the first 48 hours and appeared to be dose dependent. A competitive assay was then developed using low concentration TGF- β 1 and medium concentration M6P at 48 hours to determine if M6P could interfere with TGF- β 1-induced fibroblast cell growth. Cell proliferation, damage, and morphology were evaluated. The results show that M6P is capable of reducing TGF- β 1-induced fibroblast proliferation, and it is suggested that this effect is through competitive inhibition of the M6P/IGF-II receptor of fibroblasts.

Keywords: mannose-6-phosphate, transforming growth factor- β , fibrosis

INTRODUCTION

Tendon healing is plagued by the complications of rupture and adhesion formation. Both of these tend to occur early in healing and are due to improper regulation of collagen formation. Flexor tendon repairs are plagued by the formation of peripheral adhesions that limit motion. An important aspect of tendon healing is the timing and degree of collagen expression during the repair process. Connective tissue growth factor (CTGF) is a member of a family of regulatory proteins, which along with transforming growth factor beta (TGF- β), plays a central role in Type I collagen and extracellular matrix (ECM) production [1]. Over-expression of CTGF has been noted in multiple fibrotic tissues [2-5]. Increased expression of CTGF is enhanced by placing tissues under hypoxic conditions [6]. CTGF has been shown to up-regulate TGF- β , which is the major player in fibrosis through induction of ECM fabrication, and is additionally recognized to play an important role in continued signaling for CTGF [7]. This cooperative role of TGF- β and CTGF in fibrotic pathways presents a viable target for therapy in tissue fibrosis.

Our lab has shown that fructose-1,6-bisphosphate (FBP) is an intermediate in glycolysis which, if provided to cells, could allow them to bypass two ATP-requiring steps for energy production. Huang and colleagues have previously shown that treatment of cells placed under hypoxic conditions with FBP decreases production of CTGF to near control conditions [8]. Mannose-6-phosphate (M6P), a natural sugar, is known to isomerize to fructose-6-phosphate (F6P), an intermediate of glycolysis in the step prior to FBP. Therefore, one might hypothesize that treatment with M6P may decrease production of CTGF by decreasing the need for substrate-level phosphorylation, which would be vital in hypoxic conditions. Alternatively, latent TGF- β is activated through its binding with the M6P/IGF-II receptor [9]. M6P has been shown to interact with the M6P/IGF-II receptor on fibroblasts. Therefore, competitive inhibition of the activation of TGF- β through treatment with M6P is considered another method by which M6P may inhibit fibrosis. It is thought that M6P may have more potential for reducing fibrosis than FBP because its mechanism of action is not dependent upon a hypoxic environment.

Since M6P acts at the same receptor as TGF- β 1 on fibroblasts, it is possible that treatment with M6P may inhibit fibrosis. Our goal was to determine if M6P could prevent or reduce TGF- β 1-induced fibroblast proliferation. This study is clinically important since no current adjunct therapy is available to prevent scar formation.

METHODS

Cell Culture: McCoy [McCoyB] (ATCC[®] CRL-1696[™]) fibroblasts were obtained from American Type Culture Collection (ATCC, Rockville, MD) and supplemented with Dulbecco's Modified Eagle's Medium (DMEM) + 5% fetal bovine serum + 1% antibiotic/antimycotic solution in T-75 culture flasks where they were grown to confluence under normoxic conditions at 37°C.

Cell Culture for M6P Concentration Studies: Once confluent, the cells were plated on 24-well plates where row A served as a control, row B served as 0.005 μ M (Low) M6P (Sigma-Aldrich) treatment, row C served as 0.05 μ M (Medium) M6P treatment, and row D served as 0.5 μ M (High) M6P treatment. Columns 5 and 6 of each plate contained coverslips for staining.

Cell Culture for TGF- β 1 Concentration Studies: Once confluent, the cells were plated on 24-well plates where row A served as a control, row B served as 200 ng (Low) TGF- β 1 (Sigma-Aldrich) treatment, row C served as 1,000 ng (Medium) TGF- β 1 treatment, and row D served as 2,000 ng (High) TGF- β 1 treatment. Columns 5 and 6 of each plate contained coverslips for staining.

Cell Culture for Competitive Study: Once confluent, the cells were plated on 24-well plates where row A served as a control, row B served as 0.05 μ M (Medium) M6P (Sigma-Aldrich) treatment, row C served as 200 ng (Low) TGF- β 1 (Sigma-Aldrich) treatment, and row D served as the M6P/TGF- β 1 combination treatment. Columns 5 and 6 of each plate contained coverslips for staining.

Cell Count: At the end of each 24, 48, and 72 hour incubation period, cell counts were performed using standard hemacytometer techniques. Briefly, an aliquot of the cell suspension was diluted in a 1:1 volume of trypan blue prior to adding 10 μ l of cell/dye mixture to each chamber of the hemacytometer. The average number of cells per square was multiplied by the dilution factor prior to multiplying it by 10,000 to determine the average number of cells per milliliter.

Glutathione (GSH) Assay: Oxidative damage to the cells was assessed by utilizing an enzyme assay to determine glutathione peroxidase levels and subsequently estimate glutathione levels. Decreases in cellular glutathione concentrations correlate directly with cellular viability. Briefly, 0.05 mL of standard and samples were placed in corresponding wells of a 96-well plate. Then, 0.1 mL of reaction mixture consisting of 5 mL DNTB, 5 mL NADPH, 5.75 mL buffer solution, and 0.01 mL GSH reductase was added to each well. The plate was placed in a microtiter plate reader and the absorbances were measured at a wavelength of 405 nm with a repeat reading after 30 minutes of incubation at 37°C. The concentrations of glutathione in the samples were determined based upon the linear equation of the line for the standard curve; the resultant concentrations were normalized to their respective cell count and reported as nM/10,000 cells.

Malondialdehyde (MDA) Assay: Cellular membrane damage was assessed by analyzing the levels of malondialdehyde bis diethyl acetal levels in the supernatant. This was accomplished by measuring thiobarbituric acid reactive substance (TBARS). Briefly, a standard curve using 1,1,3,3-tetraethoxypropane was prepared, and 0.1 mL of supernatant from the samples were added to respectively labeled 5 mL glass test tubes. Then, 0.5 mL of trichloroacetic acid (20% w/v) was added to all tubes and allowed to stand for 1 minute before adding 0.5 mL of thiobarbituric acid (0.67% in 0.2M NaOH). All tubes were then incubated in a 100°C shaking water bath for 45 minutes. They were then allowed to cool for 5 minutes prior to being centrifuged at 2500 rpm for 10 minutes. An aliquot of 0.1 mL was withdrawn from each standard and sample and placed in corresponding wells of a 96-well microtiter plate. The absorbances were then measured at a wavelength of 562 nm using a microtiter plate reader. The concentrations of MDA in the samples were determined based upon the linear equation of the line for the standard curve; the resultant concentrations were normalized to their respective cell count and reported as nM/10,000 cells.

Morphological Evaluation: The standard hematoxylin and eosin (H&E) procedure was used to demonstrate cellular morphology on the coverslips from columns 5 and 6. The coverslips were mounted on glass slides following the H&E staining procedure and subsequently were evaluated for general features (e.g., arrangement of cells), cytoplasmic features (e.g., size, shape, staining reaction), and nuclear features (e.g., size, shape, nucleoli). The slides were then digitized using Image-Pro Plus (Media Cybernetics, Inc.; Rockville, MD).

Statistics: Data analysis was performed using PASW Statistics (SPSS, Chicago) Version 18.0. Descriptive statistics generated included mean (\bar{y}) and standard error of the mean (SEM), represented in the form $\bar{y} \pm \text{SEM}$. One-way ANOVA was performed for each experiment to determine any differences in response based on treatment. Multiple comparison procedures were done using Tukey's method when warranted by significant ANOVA results. All graphs were created using SlideWrite Plus (Advanced Graphics Software, Inc.; Encinitas, CA).

RESULTS

Cell Counts for M6P Study: Fibroblast cells treated with low (0.005 μM) and medium (0.05 μM) concentrations of M6P after 24 hours showed a trend toward increases in cell number. Treatment with high dose (0.5 μM) M6P produced cell numbers that were more similar to control (Figure 1). ANOVA showed that none of the treatment groups represented a significant difference in cell count from control. After 48 and 72 hours of culturing the cells with M6P, cell numbers were suppressed when compared with control untreated cells. Low dose treatment at 48 and 72 hours produced a significantly lower cell count than control.

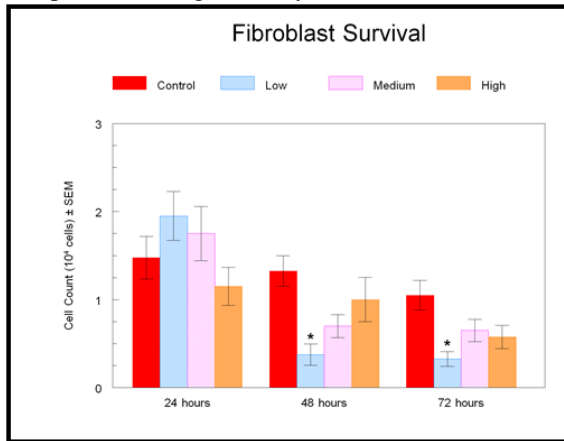


Figure 1. Cell count representing mitotic activity of McCoy fibroblasts supplemented with media alone (Control), media plus 0.005 μM M6P, media plus 0.05 μM M6P, or media plus 0.5 μM M6P at 24, 48, and 72 hours. Data is presented as mean cell count $\times 10^4$ cells \pm SEM. * $p < 0.05$ versus control

Cell Counts TGF- β 1 Study: After 24 hours, cells in the untreated control group showed significantly greater mitotic activity than cells in the medium (1200 ng/mL) and high (2000 ng/mL) groups. Mitotic activity for cells treated with low dose TGF- β 1 (200 ng/mL) was not significantly different from Control. At 48 hours, low dose treatment showed significantly greater mitotic activity than all other groups. By 72 hours, no significant differences were seen among the groups (Figure 2).

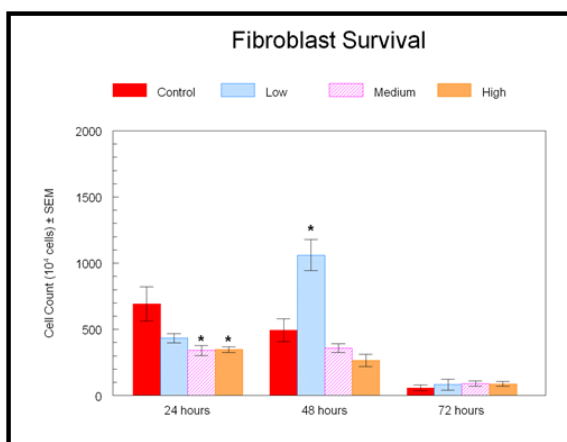


Figure 2. Cell count representing mitotic activity of McCoy fibroblasts supplemented with media alone (Control), media plus 200 ng TGF- β 1, media plus 1000 ng TGF- β 1, or media plus 2000 ng TGF- β 1 at 24, 48, and 72 hours. Data is presented as mean cell count $\times 10^4$ cells \pm SEM. * $p < 0.05$ versus control

Choice of Doses and Time Point for Competitive Study: Since the 0.05 μ M dose of M6P was the lowest dose that did not show evidence of significantly decreasing mitotic activity or increasing cellular damage and the 200 ng dose of TGF- β 1, at 48 hours, showed the most significant increase in mitotic activity over Control, these doses and the 48 hour time point were chosen for the competitive study.

Cell Count for Competitive Study: The cell count for the group treated with TGF- β 1 alone revealed significantly greater mitotic activity than that of the control cells whereas the mitotic activity of the groups treated with M6P alone and with both TGF- β 1 and M6P were not significantly different from the untreated control group (Figure 3).

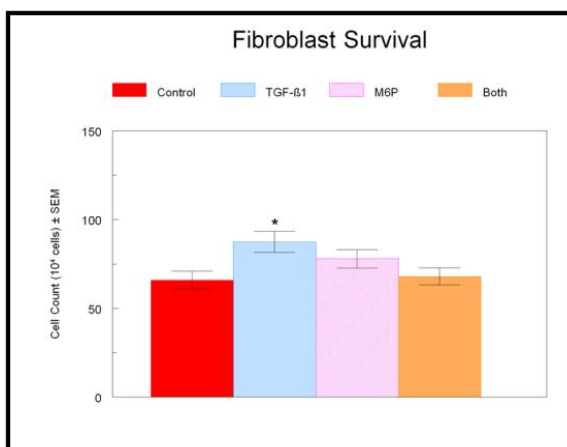


Figure 3. Cell count representing mitotic activity of McCoy fibroblasts supplemented with media alone (Control), media plus 200 ng TGF- β 1, media plus 0.05 μ M M6P, or media plus 200 ng TGF- β 1 and 0.05 μ M M6P (Both) at 48 hours. Data is presented as mean cell count $\times 10^4$ cells \pm SEM. * $p < 0.05$ versus control

GSH: The GSH assay revealed no significant difference between any of the three treatment groups and Control group (Figure 4).

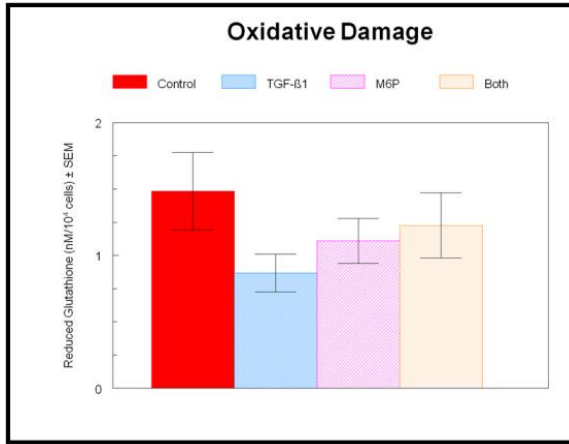


Figure 4. GSH assay showing oxidative damage seen in McCoy fibroblasts supplemented with media alone (Control), media plus 200 ng TGF-β1, media plus 0.05 μM M6P, or media plus 200 ng TGF-β1 and 0.05 μM M6P (Both). Data is presented as reduced glutathione (nM/10⁴ cells) ± SEM. * p<0.05 versus control

MDA: The MDA assay showed that all three treatment groups had significantly lower cell membrane damage than the Control group (Figure 5).

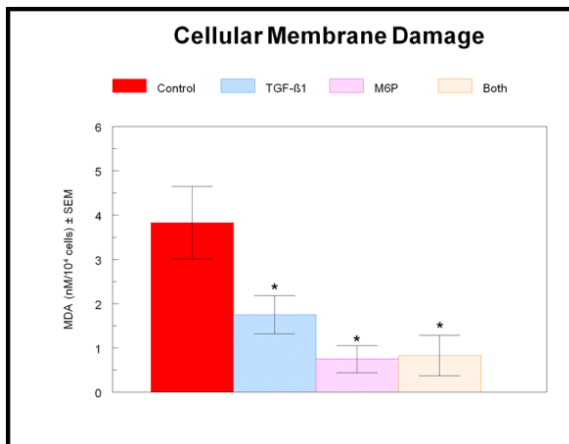


Figure 5. MDA assay showing cellular membrane damage seen in McCoy fibroblasts supplemented with media alone (Control), media plus 200 ng TGF-β1, media plus 0.05 μM M6P, or media plus 200 ng TGF-β1 and 0.05 μM M6P (Both). Data is presented as MDA (nM/10⁴ cells) ± SEM. * p<0.05 versus control

Morphological Evaluation: Cells were evaluated 48 hours after treatment and were compared to the untreated control cells. Observations are reported in Table 1 and can be seen in Figure 6.

Table 1. Cellular Morphology at 48 Hours

	Control	M6P	TGF-β1	Both
48 Hours	<p><u>General:</u> numerous singles and few loosely cohesive aggregates.</p> <p><u>Cytoplasmic:</u> few small, round; numerous spindle-shaped with few extensions; few with hydropic swelling having multiple extensions; scant with well-defined borders.</p> <p><u>Nuclear:</u> basophilic; hyperchromatic; multiple micronucleoli.</p>	<p><u>General:</u> similar to Control.</p> <p><u>Cytoplasmic:</u> similar to Control except exhibited increased number of spindle-shaped having multiple extensions and more with hydropic swelling.</p> <p><u>Nuclear:</u> similar to Control.</p>	<p><u>General:</u> similar to Control except numerous tightly cohesive aggregates.</p> <p><u>Cytoplasmic:</u> similar to Control except many with round and irregular shapes and more extensions.</p> <p><u>Nuclear:</u> similar to Control.</p>	<p><u>General:</u> similar to Control.</p> <p><u>Cytoplasmic:</u> similar to Control.</p> <p><u>Nuclear:</u> similar to Control.</p>

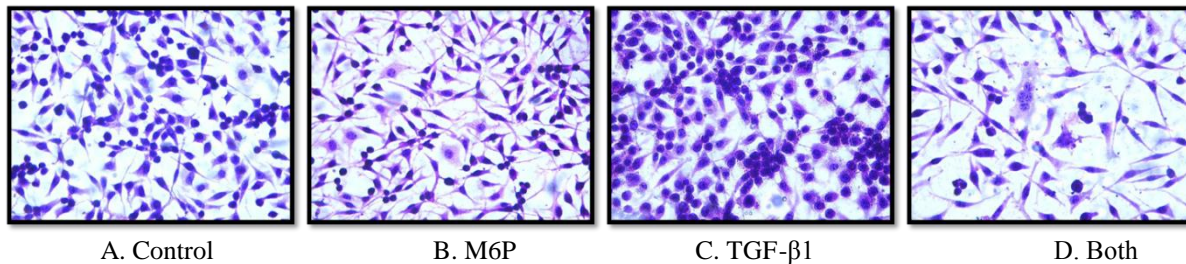


Figure 6A-D. Representative photomicrographs of H&E stained McCoy fibroblasts 48 hours after no treatment (A), treatment with 0.05 μM M6P (B), treatment with 200 ng TGF- β 1 (C), or treatment with 200 ng TGF- β 1 and 0.05 μM M6P (D). 400x

DISCUSSION

After an injury, the already tenuous blood supply of tendons is interrupted, creating a focal area of ischemia. Under such conditions, fibroblasts in the tendon have been shown to up-regulate the production of scar collagen. The collagen produced in such settings is not arranged in the typical parallel bundles seen in strong, healthy tendons. Instead, it forms a disorganized mesh that adheres to surrounding tissues, inhibiting the free gliding of the tendon. At the site of the scar, the tendon is never as strong as its pre-injury state because the fibers are not all aligned with the axis of force through the tendon. The overriding biological derangement responsible for this fibrotic response is hypoxia that precludes aerobic metabolism. In a hypoxic environment, hypoxia-inducible factor-1 α (HIF-1 α) production is up-regulated in fibroblasts, inducing the cells to produce CTGF and TGF- β . These two molecules interact with receptors on the fibroblasts to up-regulate the production of collagen. With this information in mind it is reasonable to examine HIF-1 α , CTGF, and TGF- β as potential targets for inhibition of fibrosis.

Fibroblasts throughout the body have a receptor known as the M6P/IGF-II receptor, so named for two of its common ligands. An important additional ligand active at the M6P/IGF-II receptor is TGF- β . TGF- β interaction with the M6P/IGF-II receptor causes up-regulation of CTGF production by fibroblasts, resulting in increased production of collagen by the fibroblasts. Since both TGF- β 1 and M6P bind reversibly at the M6P/IGF-II receptor, M6P may competitively inhibit the binding of TGF- β 1. This would effectively inhibit the up-regulation of CTGF and collagen production by the fibroblasts.

Previous studies in our lab have shown that F6P but not M6P under hypoxic conditions is capable of decreasing HIF-1 α and CTGF, suggesting M6P has a mechanism of action unrelated to isomerization to F6P. Studies in our lab on tendon healing have shown that M6P is capable of reducing scar tissue. This investigation has helped to provide the mechanism of action for M6P. In the experiments examining the effect of M6P on fibroblasts and its interaction with TGF- β 1, three things were determined: 1) M6P was not harmful to fibroblasts at either the medium or high doses of the concentrations tested; 2) TGF- β 1 significantly increased the mitotic activity of fibroblasts at the lowest of the concentrations tested; 3) the medium concentration of M6P was able to inhibit the action of the low dose of TGF- β 1 on fibroblast mitotic activity.

CONCLUSIONS

Overall, our results show that M6P is capable of reducing TGF- β 1-induced fibroblast proliferation and suggest that this is accomplished through competitive inhibition of the M6P/IGF-II receptor of fibroblasts.

ACKNOWLEDGMENTS

The authors would like to acknowledge the support from the Department of Diagnostic and Clinical Health Sciences and the Department of Orthopedic Surgery and Rehabilitation at the University of Mississippi Medical Center.

REFERENCES

- [1] T. Quan, Y. Shao, T. He, J. J. Voorhees, and G. J. Fisher, "Reduced expression of connective tissue growth factor (CTGF/CCN2) mediates collagen loss in chronologically aged human skin," *J Invest Dermatol*, vol. 130, pp. 415-24, Feb 2010.
- [2] X. M. Chen, W. Qi, and C. A. Pollock, "CTGF and chronic kidney fibrosis," *Front Biosci (Schol Ed)*, vol. 1, pp. 132-41, 2009.
- [3] A. Dessein, C. Chevillard, V. Arnaud, X. Hou, A. A. Hamdoun, H. Dessein, *et al.*, "Variants of CTGF are associated with hepatic fibrosis in Chinese, Sudanese, and Brazilians infected with schistosomes," *J Exp Med*, vol. 206, pp. 2321-8, Oct 26 2009.
- [4] Y. Matsui and J. Sadoshima, "Rapid upregulation of CTGF in cardiac myocytes by hypertrophic stimuli: implication for cardiac fibrosis and hypertrophy," *J Mol Cell Cardiol*, vol. 37, pp. 477-81, Aug 2004.
- [5] C. Clavel, V. Barragan-Montero, X. Garric, J. P. Moles, and J. L. Montero, "Synthesis and biological activity of M6-P and M6-P analogs on fibroblast and keratinocyte proliferation," *Farmaco*, vol. 60, pp. 721-5, Sep 2005.
- [6] D. F. Higgins, M. P. Biju, Y. Akai, A. Wutz, R. S. Johnson, and V. H. Haase, "Hypoxic induction of Ctgf is directly mediated by Hif-1," *Am J Physiol Renal Physiol*, vol. 287, pp. F1223-32, Dec 2004.
- [7] S. Sonnylal, X. Shi-Wen, P. Leoni, K. Naff, C. S. Van Pelt, H. Nakamura, *et al.*, "Selective expression of connective tissue growth factor in fibroblasts in vivo promotes systemic tissue fibrosis," *Arthritis Rheum*, vol. 62, pp. 1523-32, May 2010.
- [8] D. Haung, A. Adah, R. Richardson, C. Pierce, A. Whittington, and T. Taylor, "Defining the role of hif-1 ? And ctgf in fibrosis - biomed 2009," *Biomed Sci Instrum*, vol. 45, pp. 340-5, 2009.
- [9] A. Ghahary, E. E. Tredget, L. Mi, and L. Yang, "Cellular response to latent TGF-beta1 is facilitated by insulin-like growth factor-II/mannose-6-phosphate receptors on MS-9 cells," *Exp Cell Res*, vol. 251, pp. 111-20, Aug 25 1999.

MORPHOLOGICAL CHANGES TO LNCaP CELLS SUBJECTED TO TREATMENT WITH EPIGALLOCATECHIN-3-GALLATE, THYMOQUINONE, AND TANNIC ACID

La'Toya Richards Moore*, PhD; MLS (ASCP)^{CM}, Hamed Benghuzzi, PhD;FBSE;FAIMBE, Michelle Tucci, PhD, Elgenaid Hamadain, PhD

Medical Laboratory Science Department, University of Mississippi Medical Center, Jackson, MS 39216

ABSTRACT

Research studies on nutritional supplements and cancer risk has demonstrated that antioxidants and their derivatives play a major role in combating prostate cancer and reducing the risk of prostate cancer in men. It has been suggested that ample amounts of antioxidants, such as vitamin E, selenium, and their constituents may be effective in decreasing both the risk and incidence of prostate cancer. Epidemiological studies have evaluated these agents in certain populations and in specific prostate cell lines to compare the risk reduction as well as the magnitude of risk reduction [1,2]. The aim of this study was to use the human LNCaP prostate cancer cell line to analyze the morphological effects of conventional treatment with low and high doses of epigallocatechin-3-gallate (EGCG), thymoquinone (TQ), and tannic acid (TA) at 24, 48, and 72 hours. After 48 and 72 hours of incubation, the groups treated with the lower doses of EGCG, TQ, and TA revealed hyperchromatic, irregular, and fewer cells. Upon treatment with higher doses of EGCG and TQ, cells were also irregular and fewer in number after 48 and 72 hours of incubation. Overall findings of this study showed suppressed cell growth and cell number after conventional treatment with EGCG, TQ, and TA. This suppression may be due to disruptions in several cell-cycle checkpoints and the role of antioxidants along with their chemopreventive properties. Further research is needed in this era to assist with remedies for prostate cancer prevention.

Keywords: antioxidants, prostate cancer, epigallocatechin-3-gallate, thymoquinone, tannic acid, LNCaP, treatment

INTRODUCTION

In males, prostate cancer is a major public health issue and the leading cause of cancer-related deaths [3,4]. Over ten years ago, there were nearly 200,000 new cases of prostate cancer predicted [4]. The clinical lifetime prostate cancer risk is around 10% for men in the U.S. and usually 3% of these males die from the condition.

Antioxidants are substances responsible for protecting cells from free radical damage, implicated in the development of certain cancers. Examples of antioxidants include substances such as lycopene, beta-carotene, vitamins A, E, C, and other substances. Agents like vitamin E, lycopene, and selenium have been reported to prevent prostate cancer development [5]. The biochemical nature of these agents suggests that they act primarily through antioxidant-related pathways. However, the manner of this biological activity has not been thoroughly investigated.

Research has also suggested that antioxidants like vitamin E may fight prostate cancer. A study on nutritional supplements and cancer risk evaluated the result of seven randomized clinical trials. Cohort and case-control studies demonstrated the protective effects of vitamin E against prostate cancer. Overall, there was limited evidence regarding the protective effects of nutrients from supplements against several cancers [6].

MATERIALS AND METHODS

Table I below represents the behavior and response of LNCaP cells to treatment with various doses of the antioxidants epigallocatechin-3-gallate (EGCG), thymoquinone (TQ), and tannic (TA) at 24, 48, and 72 hours of incubation according to the experimental design.

TABLE 1. Experimental Design

	GROUP	EGCG	TQ	TA	N	Duration
1	Control	—	—	—	24	24,48,72
2	EGCG LD	10 µg/ml	—	—	24	24,48,72

3	EGCG HD	100 µg/ml	—	—	24	24,48,72
4	TQ LD	—	10 µg/ml	—	24	24,48,72
5	TQ HD	—	100 µg/ml	—	24	24,48,72
6	TA LD	—	—	10 µg/ml	24	24,48,72
7	TA HD	—	—	100 µg/ml	24	24,48,72

Cell Line and Culture: The LNCaP cell line, purchased from the American Type Culture (ATCC, Rockville, MD), was utilized in this study. These cells were slow-growers and tended to grow in clusters. After subculture, the cells were allowed to incubate undisturbed for the first 48 hours. Cells were then allowed to incubate and reattach. Finally, old medium was removed and replaced with fresh medium.

Cell Count: Upon treatment of the cells with the various doses of the antioxidants, incubation occurred for 24, 48, and 72 hours. Supernatant was removed and cells were placed in media after being scraped from the tubal walls. A hemacytometer was utilized to count the cells following standard laboratory procedure.

Morphological Evaluation: A certain number of microtiter plate wells were used for morphological evaluation. Cells were plated, cover slipped, and washed after the desired incubation periods. To stain the slides, Hematoxylin and Eosin staining procedures were utilized. After staining, slides were mounted and cover slips were applied. To evaluate the cell morphology, a standard light microscope was used. The morphological evaluation criteria were as follows:

TABLE 2. Morphological Evaluation Criteria

GROUPS	CELL SIZE	SHAPE	NUCLEUS	NUCLEUS SIZE	CYTOPLASM	STAIN
Control	Small	Round	Hyperchromasia	Prominent	Well-defined	Coarse
EGCG LD; EGC G HD	Medium	Oblong	Hypochromasia	Single	Clusters	Pink
TQ LD; TQ HD	Large	Irregular		Multiple	Irregular	Vacuoles
TA LD; TA HD		Oval				

Statistical Analysis: One Way Analysis of Variance was performed to determine if there was a significant difference (at the 5% level of significance) among different experimental groups using the Jandel Computer Statistical Analysis Software (Sigma Stat). For mean separation, Student Newman Keules was utilized.

RESULTS

Cell Count Results: Following 24 hours of incubation, the TQHD showed the greatest decrease in cell count in comparison to the control. The next groups which showed the greatest decrease in cell count were the TAHD, TALD, and EGCGHD groups. The EGCGLD group demonstrated a slight decrease in cell count in comparison to the control. After 48 hours of incubation, the TAHD group showed the greatest decrease in cell count followed by the TALD and TQHD groups. Finally, after 72 hours of incubation, both the TAHD and TQHD groups maintained decreased cell counts followed by the TALD group. Again, the EGCGHD group was the next group to show a

decreased cell count followed by the slight decrease in the EGCGLD group.

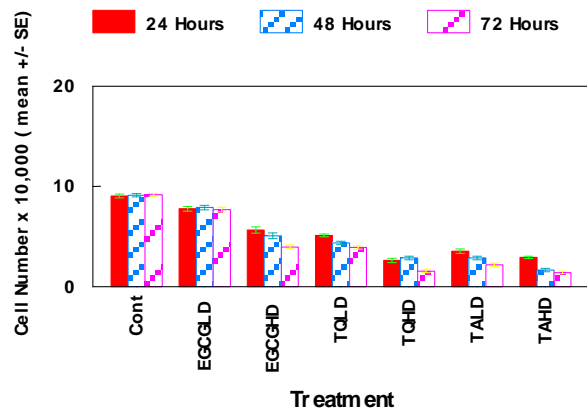
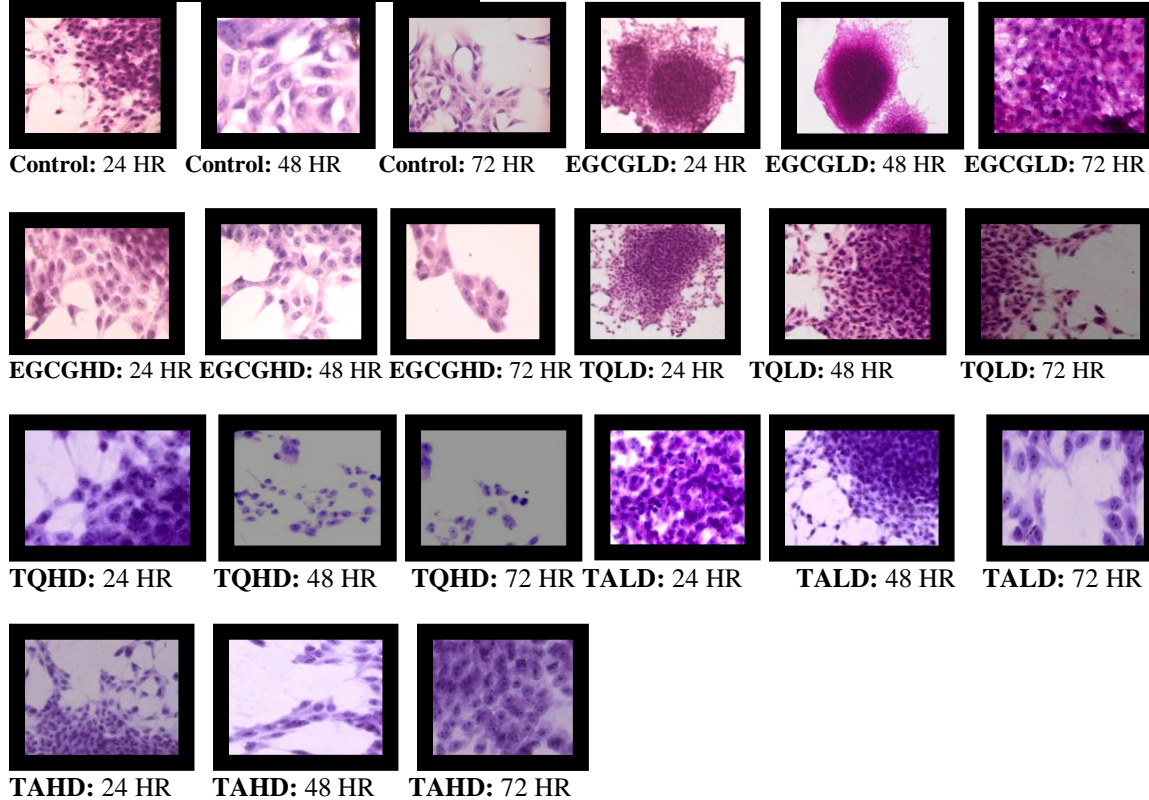


Figure 1: The effect of various doses of conventional delivered EGCG (low dose 10 $\mu\text{g/ml}$, high dose 100 $\mu\text{g/ml}$), TQ (low dose 10 $\mu\text{g/ml}$, high dose 100 $\mu\text{g/ml}$), and TA (low dose 10 $\mu\text{g/ml}$, high dose 100 $\mu\text{g/ml}$, on the proliferation rate of LNCaP cells at 24, 48, and 72 hours. Data presented is expressed as means \pm SEM. Data revealed significant differences in treatment groups at 24, 48, and 72 hours when compared to the control ($p < 0.05$).

Morphology Figures (40X Magnification)



Morphology Results: Following 24 hours of incubation, the control group showed medium sized healthy cells which were round in appearance. The nucleus was prominent and the membranes were well-defined. The

background was clear and there was no evidence of structural damage. After 48 hours of incubation, the control group cells were still healthy and round in appearance. The cells remained healthy, medium-shaped, with a well-defined nucleus after 72 hours of incubation. Cells treated with low doses of EGCG appeared medium and round with a hyperchromatic nucleus after 24 hours of incubation. Cells portrayed the same characteristics with an irregular cytoplasm after 48 hours of incubation. Following 72 hours of incubation, the cytoplasm was irregularly spindle-shaped and cells were medium and round. Cells treated with high doses of EGCG revealed medium, round cells with a hyperchromatic nucleus and apparent nucleoli. Characteristics remained the same after 48 hours of incubation. Cells remained hyperchromatic with an irregular cytoplasm after 72 hours. Cells treated with low doses of TQ appeared clustered, round, and irregular after 24 hours of incubation. After 48 and 72 hours of incubation, cells portrayed similar characteristics with a hyperchromatic nucleus. Cells treated with high doses of TQ were round, irregular, and fewer in number in comparison to the control. After 48 hours, cells were round and scattered with an irregular cytoplasm. Vacuolization and swelling was evident. After 24 hours of incubation, cells treated with low doses of TA were medium and round with a prominent and hyperchromatic nucleus. After 48 and 72 hours of incubation, cells were decreased and they remained round with an irregular cytoplasm. Following 24 hours of incubation, cells treated with high doses of TA were medium and round with a well-defined nucleus and apparent nucleoli. Cells became more scattered after 48 hours and remained round with apparent nucleoli after 72 hours.

DISCUSSION

In this study, we used lipid soluble antioxidants such as thymoquinone, epigallocatechin-3-gallate, and tannic acid as experimental agents for the conventional treatment to observe morphological changes in the LNCaP cell line. Results of our study revealed that both cell growth and mitotic ability of the cells were suppressed following treatment with conventional doses of EGCG, TQ, and TA. All treatment groups showed a dose-dependent trend, with the exception of the TA groups. However, the most potent group was the high dose TQ group, in comparison to all other groups. Although all treatment groups resulted in cell growth suppression, conventional treatment with TQ may mean that the containment of cells is a possibility for a number of years. Salim and researchers yielded support to this hypothesis by demonstrating that treatment with TQ inhibited carcinogenesis by suppressing cell proliferation in the colonic mucosa. This study also demonstrated that there was evidence of cell disruption as well as cellular events with treatment from high doses of TQ.

CONCLUSIONS

Data of this study demonstrated that antioxidants such as thymoquinone, epigallocatechin-3-gallate, and tannic acid may yield promising effects for targeting prostate cancer treatment. Not only are the treatments effective, but they are also safer and inexpensive. The data of this study suggested that conventional treatment with the various antioxidants resulted in an overall suppression of cell growth and mitotic ability. Overall conclusions of this study showed that antioxidant treatment played a major role in morphological changes in the LNCaP cell line. Additional studies are needed to dissect the modes of behavior and mechanisms involved to offer safer and effective remedies for prostate cancer.

ACKNOWLEDGMENTS

We would like to acknowledge the Medical Laboratory Science Department, the School of Health Related Professions, and the Department of Orthopedics at the University of Mississippi Medical Center for their valuable support during this research process. In addition, we offer a great deal of thanks to the Southern Biomedical Engineering Conference and the Sponsors.

REFERENCES

- [1] Ni, J., Yeh, S., Pang, S. (2007) Differential retention of α -vitamin E is correlated with its transporter gene expression and growth inhibition efficacy in prostate cancer cells. *The Prostate* 67:463-417.
- [2] Morrissey, C., Vessella, R. (2007) The role of tumor microenvironment in prostate cancer bone metastasis. *Journal of Clinical Biochemistry* 101: 873-886.
- [3] [Greenlee RT](#), [Hill-Harmon MB](#), [Murray T](#), [Thun M](#). (2001) *Cancer Statistics*. [CA Cancer J Clin](#).1:15-36.
- [4] American Cancer Society. (2002) *Cancer Facts and Figures*. Atlanta, Ga.
- [5] Gronberg H. (2003) Prostate cancer epidemiology. *Lancet*. 361: 859-864.
- [6] Patterson,R.E., White, E., Kristal, A.R., Neuhausser, M.L., and Potter, J. D. (1997) Vitamin supplements and cancer risk: the epidemiologic evidence. *Cancer Causes and Control* 8: 786-802.

SPHEROID ORGANIZATION AND ADIPOGENESIS ON COPOLYMERS OF ELASTIN-LIKE POLYPEPTIDES

Paul A. Turner and Amol V. Janorkar*

Department of Biomedical Materials Science, School of Dentistry, University of Mississippi Medical Center, 2500
N. State Street, Jackson, MS 39216

* Corresponding author (Email: ajanorkar@umc.edu; Phone: 1-601-984-6170; Fax: 1-601-984-6087)

ABSTRACT

In this paper, we have demonstrated spheroid formation and differentiation of primary human adipose-derived stem cells (hASCs) with respect to spheroid dimensions and functional markers (protein and triglyceride accumulation, Oil red-O staining, CD36 expression). We propose spheroid culture techniques to be especially beneficial to adipogenesis by promoting cell-cell interactions and downregulating mitosis by minimizing surface interaction. Our spheroid culture also provides the unique benefit of maintained surface anchorage while allowing uninhibited cell expansion during lipogenesis.

Key Words: Elastin-like polypeptide, human, adipocyte, spheroid

INTRODUCTION

Our work has shown that the culture surfaces made using positively charged elastin-like polypeptide-polyethyleneimine (ELP-PEI) conjugates induced H35 rat hepatoma [1] as well as Swiss 3T3-L1 mouse fibroblast (CL-173) [2] spheroid formation. We believe that the multicellular interaction and growth arrest of preadipocytes and the adipose-derived stem cells will promote differentiation, thereby enhancing the expression of adipose-specific functionality. Following our previous studies using model cell lines [1,2], we sought to prove the feasibility of using our *in vitro* model to evaluate human adipocyte response to similar microenvironments. While murine cells are popular subjects for tissue engineering feasibility studies, the use of primary human adipose tissue will be ideal for establishing clinical relevance of our *in vitro* model. The large volume of discarded adipose and clinical connections allow us the opportunity to study the impact of spheroid culturing techniques on hASC viability, differentiation, and overall functionality. Human preadipocytes were cultured using similar methods pioneered with H35 and 3T3-L1 model cells, though using maintenance media optimized for human-derived cells [3-5]. Our experiments utilized normally discarded breast or abdominal whole adipose tissue provided during elective procedures from patients and in accordance with the University of Mississippi Medical Center Institutional Review Board (IRB) protocol. Donated adipose tissue was dissected and digested to harvest hASCs for subsequent culturing using techniques demonstrated by Flynn [6], adopted from methods developed by Hauner, Skurk, and Wabitsch [7]. However, differentiation was induced via hormone cocktail based on IBMX and dexamethasone [8, 9] to maintain consistency with our previous outcomes obtained from mouse 3T3-L1 cells [2].

MATERIALS AND METHODS

hASC Cell Culture: Whole breast adipose tissue was collected and maintained in sterile Na⁺/Ca⁺⁺ free PBS, arriving in the lab immediately after extraction. In a sterile environment, the tissue was placed in a tissue culture dish, minced into small (~1 mm³) sections, and washed with PBS to help remove blood, oil, serum, other vascular components, and lymph vessels. The tissue fragments were then digested in 20 mg/mL BSA for 20 minutes at 37°C in a shaker bath. The tissue was then filtered through sterile layered cotton mesh to remove undigested fragments. Cell media (DMEM, 10% FBS, pen/strep) was then added to the filtrate and the cells allowed to gravity separate. The supernatant was aspirated to remove mature adipocytes and the remaining filtrate centrifuged at 1200 g for 5 minutes. The cell pellet was suspended in preadipocyte media (DMEM + 10% calf serum) at room temperature. The remaining cells were pelleted again, resuspended in whole media, and filtered through a 60- μ m mesh nylon net. The remaining hASCs were cultured on TCPS dishes in 50:50 DMEM:Ham's F12 + 10% calf serum at 37°C and 5% CO₂, with regular media changes every 2-3 days. Cells were used for experiment prior to their 6th passage. hASC differentiation was carried out for 72 hours in media containing 50:50 DMEM:Ham's F12 media supplemented with 1 μ M dexamethasone, 0.5 mM IBMX, 0.1 U/mL insulin, 1 μ M indomethacin, and 100 units/mL penicillin - 100 μ g/mL streptomycin.

Induction of Adiposity: Maintenance medium was prepared by supplementing 50/50 DMEM/F-12 with 2% albumin, 0.2 U/mL insulin, and 100 units/mL penicillin - 100 μ g/mL streptomycin.

Optical Microscopy Cells were observed using an Olympus IX-81 microscope (Olympus, Center Valley, PA) equipped with an environmental chamber (LiveCell, Pathology Devices, Westminster, MD), which maintained normal culture conditions (37°C temperature, 70% relative humidity, and 5% CO₂). Slidebook software (Intelligent Imaging, Denver, CO) was used for image analysis. Spheroid dimensions were tracked by time-lapse imaging and measured with ImageJ digital analysis software.

Biochemical Characterization of Cell Lysate: hASC spheroids were removed after 5 and 10 days of maturation by aspiration and collected in filter columns (Millipore). hASCs in monolayer were collected by trypsinization. All aliquots were centrifuged for 2 min at 1000 rpm, resuspended in PBS, and lysed using a Branson Digital Sonifier 450 (Danbury, CT). Following chromatic assays were measured on an absorbance plate reader (Biotek ELx800, Winooski, VT) with a 540 nm filter.

Total Protein Assay: A chromatic BCA total protein assay kit was purchased from Thermo Fisher Scientific (Rockford, IL) and performed on cell lysates in accordance with the manufacturers' suggested protocols. Cell protein concentration was quantified by comparison against standard curves constructed from serially-diluted albumin stocks. Assays were performed in triplicate for each sample taken from three experimental wells, yielding nine total measurements per condition. Total protein data was subsequently used to normalize individual markers collected with the other assays.

Triglyceride Assay: Intracellular triglyceride accumulation and free glycerol were measured using a Serum Triglyceride Determination Kit (Sigma Aldrich). Measurements were quantified by comparison with a glycerol standard solution (Sigma Aldrich).

CD36 ELISA Assay: An ELISA assay specific to mouse CD36 fatty acid transport protein was purchased from Abcam (Cambridge, MA) and performed in accordance with manufacturer's protocols. Assays were performed in triplicate for each culture condition, one sample per experimental well, yielding a total of three measurements per condition. Though manufacturer's specifications state that the kit's antibodies were specifically tested for mouse CD36, we detected sufficient cross-reactivity to obtain qualitative data for the human cells.

Statistical Analysis: All experiments were performed in triplicate and reported as mean \pm 95% confidence intervals. Statistical evaluation was done using ANOVA with Bonferroni and Games-Howell post hoc tests for equal and unequal variances. Values with $p \leq 0.05$ were deemed significantly different.

RESULTS

Measurements taken from hASC micrographs (Figure 1) tracked spheroid organization and growth throughout differentiation and maturation. Prior to differentiation, hASC spheroids achieved an average diameter of only ~25 μ m, though spheroid size gradually increased to ~45 μ m by day 10 during maturation. Variation in spheroid diameters also increased with longer culture times.

After differentiation and 8 days of maturation, 2-D hASCs qualitatively assessed with Oil Red-O staining (Figure 2, left) showed small amounts of lipid accumulation in most (multilocular) cells. Alizarin Red staining was also performed on 2-D hASCs (Figure 2, right) to determine the potential for osteogenic differentiation. These cultures showed few positive alizarin-red stained cells. These results confirmed that the hASCs were preferentially differentiated along the adipocytic lineage.

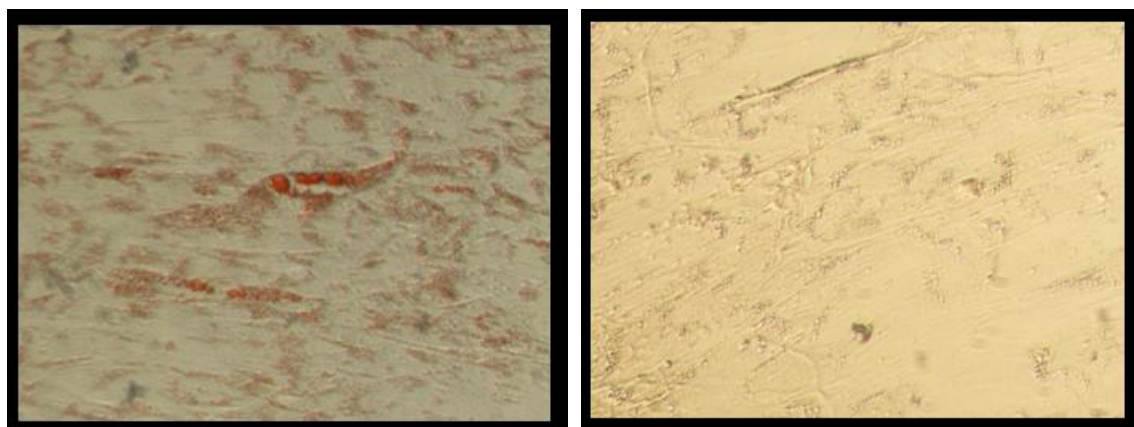
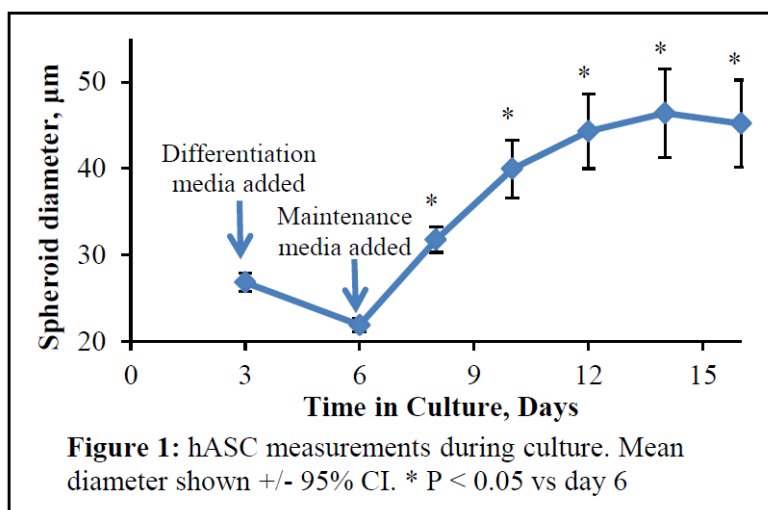
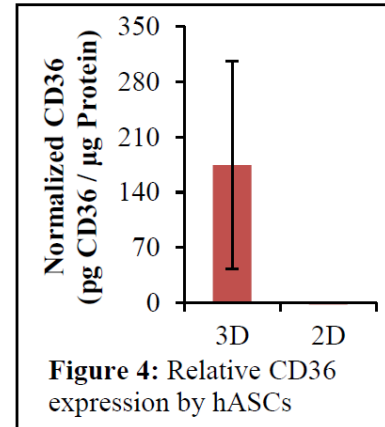
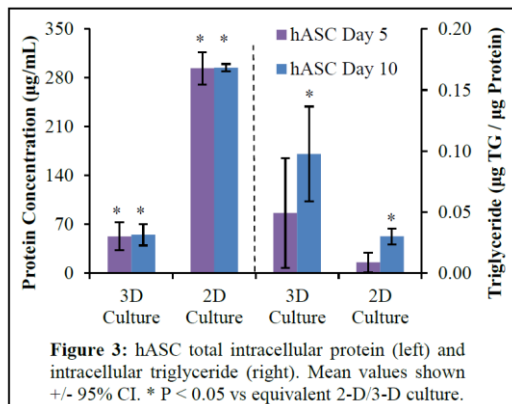


Figure 2: Histological staining of maturing hASCs after 8 days in maintenance media. Oil Red-O (left) and Alizarin Red (right).

Total intracellular protein measured in hASC samples collected after 5 and 10 days of maturation (Figure 3) showed almost a 6 fold increase protein content in 2-D cultures compared to 3-D spheroids. Protein content was indistinguishable between the two time points for both cultures, indicating a steady state culture condition had been achieved. Analysis of intracellular triglyceride accumulation in hASCs (Figure 3) was slightly increased in 3-D spheroid cultures compared to equivalent 2-D monolayer cultures. The triglyceride accumulation also increased between samples analyzed on days 5 and 10 in both culture conditions.



Relative CD36 expression in 3-D and 2-D cultures was measured with an ELISA assay specific to extracellular CD36 proteins (Figure 4). Though the signal from 2-D cultures was negligible, 3-D cultures showed a substantial expression of the fatty acid transporter.

DISCUSSION

The overall differentiation and maturation process in hASCs compared well with our previous studies analyzing 3T3-L1 adipocytes on the same surface. Similar to 3T3-L1 preadipocytes, undifferentiated hASC showed spheroid formation achieving an aggregate size of 25 µm. As previously observed in 3T3-L1 cultures [2], treatment with differentiation hormones prompted increased cell aggregation resulting in a maximum average sustained spheroid diameter of 45 µm. However, the aggregates observed in hASC cultures were much smaller than similarly differentiated 3T3-L1 cells, whose spheroids achieved dimensions of up to 120 µm. In both studies, increased spheroid sizes correlated with increased intracellular triglyceride. Histological staining attested to the functional competency of the differentiated cells, Oil Red-O showing multiple small lipid droplets in most cells, while low alizarin red staining indicating insignificant osteogenesis. However, the differentiation potential of the hASCs appeared lower than that of the 3T3-L1 cells, which showed a much higher degree of Oil Red-O staining after a shorter culture period [2]. CD36 (FAT) has previously been found in both 3T3-L1 mouse [10, 11] and human adipocytes [10], associated with both long-chain fatty acid transport [11] and advanced glycation end products [10]. Thus, CD36, an important marker for physiological homeostasis and differentiated function, was also found to be upregulated by cells in our spheroid model.

CONCLUSIONS

hASCs were found to exhibit functional markers characteristic of adipogenesis including triglyceride accumulation and CD36 expression in correlation with spheroid formation and growth. These outcomes suggest that our spheroid model is a more physiologically-relevant representation of adipogenesis and deserves further investigation and optimization.

ACKNOWLEDGEMENTS

Financial support by the Intramural Research Support Programs from the School of Dentistry and the University of Mississippi Medical Center is gratefully acknowledged. This study was approved by the UMMC Institutional Review Board (Approval # 2012-0004). This work made use of instruments in the Department of Biomedical Materials Science User Facility.

REFERENCES

1. Turner, P.A., et al., *J Biomed Mater Res A*, 2014. **102**(3): p. 852-61.
2. Turner, P.A., et al., *Biotechnol Bioeng*, 2014. **111**(1): p. 174-83.
3. Bunnell, B.A., et al., *Methods*, 2008. **45**(2): p. 115-20.
4. O'Connor, K., et al., *Biotechnology Letters*, 2003. **25**(23): p. 1967-1972.
5. Vallée, M., et al., *Pathologie Biologie*, 2009. **57**(4): p. 309-317.
6. Flynn, L., et al., *Woodhouse, J Biomed Mater Res A*, 2006. **79**(2): p. 359-69.
7. Hauner, H.S., et al., *Cultures of Human Adipose Precursor Cells. From: Methods in Molecular Biology, in Adipose Tissue Protocols*, G. Ailhaud, Editor. 2001, Humana Press, Inc: Totawa, NJ. p. 239-247.
8. Higuchi, M., et al., *Stem Cells Dev*, 2013. **22**(6): p. 878-88.
9. Mbalaviele, G., et al., *J Biol Chem*, 2000. **275**(19): p. 14388-93.
10. Kuniyasu, A., et al., *FEBS Lett*, 2003. **537**(1-3): p. 85-90.
11. Pohl, J., et al., *Mol Biol Cell*, 2005. **16**(1): p. 24-31.

THE EFFECTS OF SUSTAINED DELIVERY OF ANTIOXIDANTS ON LPS STIMULATED RAW 264.7 MACROPHAGES

Renee Wilkins, Michelle Tucci, Ham Benghuzzi

University of Mississippi Medical Center
Jackson, MS 39216

ABSTRACT

The use of sustained drug delivery has been implicated as a means of improving the effectiveness of epigallocatechin-3-gallate (EGCG) and thymoquinone (TQ). Both of these antioxidants are dose dependent in their actions; therefore, finding the most effective dose may offer a better understanding of the mechanisms of each of these antioxidants actions. Further, finding the most effective dose and utilizing it in a sustained method could offer an even better scenario. The goal of this study was to determine the effects of sustained delivery of EGCG and/or TQ on macrophages challenged with lipopolysaccharide (LPS). Tricalcium phosphate (TCP) capsules were loaded with EGCG (10 μ M) and/or TQ (10 μ M) and placed in wells containing macrophages challenged with LPS (0.01 μ g/mL) for 72, 96 and 120 hours. Cellular viability was assessed by cell number and cellular morphology. Cellular glutathione levels, malondialdehyde and nitric oxide levels determined cellular function. Inflammatory markers were quantitated by the use of multiplex ELISA technology. Nitric oxide levels remained elevated in all treatment groups, with the highest observed in the EGCG treatment group. Prolonged delivery of LPS on EGCG and TQ treated cells had various effects on the secretion of activated cytokines, including TNF- α , IL-1 α , and IL-6, as well as the anti-inflammatory, IL-10. This study suggests that sustained delivery of EGCG and/or TQ may not be able to efficiently reduce the effects of prolonged LPS stimulation.

Keywords: antioxidants, epigallocatechin-3-gallate, lipopolysaccharide, macrophages, thymoquinone, inflammation, drug delivery

INTRODUCTION

It is widely known that prolonged inflammation can lead to tissue damage as a result of increased production of reactive oxygen species, and ultimately, oxidative stress. Antioxidants are compounds that have been shown to protect the body from the harmful effects of oxidative stress as a result of the inflammatory process [1]. The goal of this study was to investigate the effects of sustained delivery of the antioxidants EGCG and TQ as anti-inflammatory agents in a model of inflammation. TQ, a lipophilic antioxidant, has been shown to be anti-inflammatory, anti-neoplastic and anti-microbial [2, 3, 4]. Water soluble EGCG has also been shown to have similar properties [5, 6]. Sustained delivery using ceramics is a promising area because of the ability to control features such as porosity and hardness. These characteristics allow for a wide variety of substances such as antioxidants to be incorporated into the device. Both EGCG and TQ are dose dependent in their actions and utilizing the most effective dose in a sustained method could provide valuable knowledge in the prevention and treatment of inflammation [7, 8]. To investigate the effects of sustained delivery of EGCG and TQ, we hypothesized that antioxidants alone and in combination would restore inflammatory markers in macrophages receiving prolonged stimulation with LPS. Although extensive studies have used EGCG and TQ in a drug delivery system (DDS), few have used them in macrophages in a model of inflammation.

METHODS

Cell Culture: The RAW 264.7 macrophages were obtained from American Type Culture Collection (Rockville, MD). RAW macrophages were cultured and plated in 24-well tissue culture plates (Corning, Costar-24) at a density of 1.0×10^6 cells/well in 1.0 mL of Roswell Park Memorial Institute (RPMI) 1640 medium with 20% fetal calf serum and 1% antibiotics. After overnight incubation, cells in each well were rinsed with fresh RPMI medium and treated with antioxidants [EGCG (10 μ M); TQ (10 μ M)] and LPS.

Cell Viability: At the end of each phase, cells were dislodged from the bottom of the culture well and resuspended in phosphate buffered saline (PBS). The cells were centrifuged and the pellet was washed with PBS and

centrifuged. The resultant cell pellet was resuspended in 300 μ L of PBS and 20 μ L was removed for hemacytometer counts.

H&E Staining: Cells were grown in 24 well plates on cover slips for morphological evaluations. Cells were fixed in 200 μ L of 95% ethanol, followed by rehydration in a series of 70% and 50% ethanol. The cover slips were rinsed in water then stained with hematoxylin and washed with water, 50% ethanol and 95% ethanol. The cells on the cover slips were stained with eosin before washing with a series of ethanol concentrations. The cover slips were removed from the wells with and dipped in xylene. The coverslips were mounted cell side up on clear glass slides and covered with clear coverslips (22x22mm).

Glutathione (GSH): GSH concentration was determined by the use of the glutathione recycling assay [9]. This method is based on the reduction of 5,5-dithiobis (2-nitrobenzoic acid; DNTB) to 2-nitro-5-thiobenzoic acid (a yellow colored product) by glutathione and the recycling of glutathione disulfide to glutathione by glutathione reductase. Absorbance was read (492 nm) initially and then again after a 30 minute incubation using a microtiter plate reader. The GSH results were compared to a standard curve for final analysis.

Malondialdehyde (MDA): MDA is used for the determination of cellular membrane damage. Supernatants were combined with 20% trichloroacetic acid and allowed to precipitate for two minutes before adding 0.67% thiobarbituric acid in 2.0M NaOH. The samples were vortexed and heated to 100°C for 40 minutes and centrifuged at 1500 rpms for 10 minutes. The absorbance of the supernatants after centrifugation were read at 532 nm and compared to a standard curve.

Nitric Oxide (NO): Standard laboratory procedure was utilized to determine the amount of NO in the RAW 264.7 cells. One hundred μ L of supernatant were incubated with 14 mU of nitrate reductase with 40 μ M Nicotinamide Adenosine Dinucleotide Phosphate (NADPH) and 20nM Tris buffer (ph 7.6) for 5 minutes. Water was added and equal amounts of Greiss reagent well complete the reaction. The sample was incubated for approximately 30 minutes and then read at 492 nM. Nitrate was quantified by a reference to a standard curve generated by dissolving 1-50,000nM of sodium nitrate (NaNO₂) in the assay medium.

Multiplex ELISA: A 16-plex mouse cytokine screening kit (Quansys Biosciences) was used to determine cytokine levels in the supernatants. This ELISA-based test uses 16 distinct capture antibodies absorbed to each well of a 96-well plate. After running the assay, the chemiluminescent light emitted from each well of the plate was captured on a BioRad ChemiDoc XRS imaging system. The image was then auto-processed using Quansys Q-View™ Software and concentrations for each analyte were output for the sample.

Ceramic Fabrication: The method for preparing the microcrystals of tri-calcium phosphate (TCP) was developed by Benghuzzi and Bajpai [10]. After preparation of the TCP, the capsules were fabricated by weighing 1g of TCP, 0.02 g of Vancomycin, and 0.01 g of lysine (used as a binder). The calcined material was pressed using a 2/32-die set at a compression load of 5000 lbs. UV light was used for sterilization during the time the capsules were loaded with antioxidants.

Statistics: The data collected from the experiments was statistically analyzed using Jandel Computer Statistical Software (SigmaSTAT). Differences among the experimental and control groups were determined by statistical analysis and ANOVA were used to compare groups. Means plus or minus the standard error of the mean (SEM) was used to express the data. The Tukey's post hoc testing was used for multiple comparisons of the means. Finally, all graphs were assembled using Slide Write Computer Software. Significance (P-value) was set at $p < 0.05$.

RESULTS

Cell Counts: At 72 hours, only the group treated with EGCG (plus LPS) was significantly lower ($p < 0.05$) than the control and sham groups. Cells treated with TQ and the combination of EGCG and TQ (plus LPS) were significantly decreased ($p < 0.05$) from the control and sham groups at 96 hours. By 120 hours, all treatment groups were close to the control and sham values and no significant differences were observed.

Normalized Glutathione: After daily administration of 0.01 μ g/mL of LPS, all groups were significantly higher ($p < 0.05$) than control and sham groups at 72 hours. Only the TQ treated group and the EGCG plus TQ treated group were significantly higher than the controls at 96 hours. By 120 hours, EGCG groups and the combination group showed a significant increase in GSH levels.

Normalized MDA: At 72 hours, only the cells treated with EGCG were significantly higher ($p < 0.05$) than the untreated control and sham groups. Only the groups treated with TQ were significantly higher ($p < 0.05$) than the controls at 96 hours, although all groups appeared to have more membrane damage than the controls. Less cellular

membrane damage was observed at 120 hours in all treatment groups in comparison to the control and sham groups, although only the EGCG and combination groups were significantly lower ($p < 0.05$).

Normalized Nitric Oxide: All treatment groups had significantly elevated levels of NO at 72 and 96 hours. At 120 hours, the EGCG groups and the combination groups were significantly higher than the control and sham groups, but the TQ treated groups returned to a level close to the control value. Interestingly, the highest increase in NO occurred in the EGCG treated groups and the lowest levels of NO occurred in the TQ treated groups.

Multiplex ELISA:

IL-1 β : Control and sham groups remained similar throughout the duration of the phase (Figure 1A). The LPS control had higher concentrations of IL-1 β compared to the control groups, but the treatment groups showed even higher levels at 72 and 96 hours. By 120 hours, IL-1 β remained increased in the LPS control, but the treatment groups had returned to concentrations at or below control values.

IL-6: Figure 1B shows that IL-6 levels were the most elevated in the LPS control during 72, 96 and 120 hour intervals. Control and sham groups were similar to each other for all durations and remained much lower than the LPS controls. Groups treated with antioxidants were decreased from the LPS control groups during 72, 96 and 120 hours. Although the treatment groups were higher than control values during the 72 and 96 hour period, concentrations did decrease to at or below control levels by 120 hours.

IL-10: Control and sham groups were similar during each duration of testing. LPS controls had the highest concentrations of IL-10 compared to all groups (Figure 1C). At 72 and 96 hours, groups treated with antioxidants were decreased from the LPS control; and by 120 hours, concentrations had decreased to levels at or below control values.

TNF- α : Figure 1D shows concentrations for the cytokine TNF- α . Control and sham concentrations were similar and were at levels almost undetectable. The LPS control groups were slightly higher than the control and sham groups. At 72 hours, all groups treated with antioxidants were slightly higher than the LPS control, but were drastically increased at 96 hours. By 120 hours, only the groups treated with EGCG (plus LPS) and the combination of EGCG and TQ (plus LPS) remained elevated.

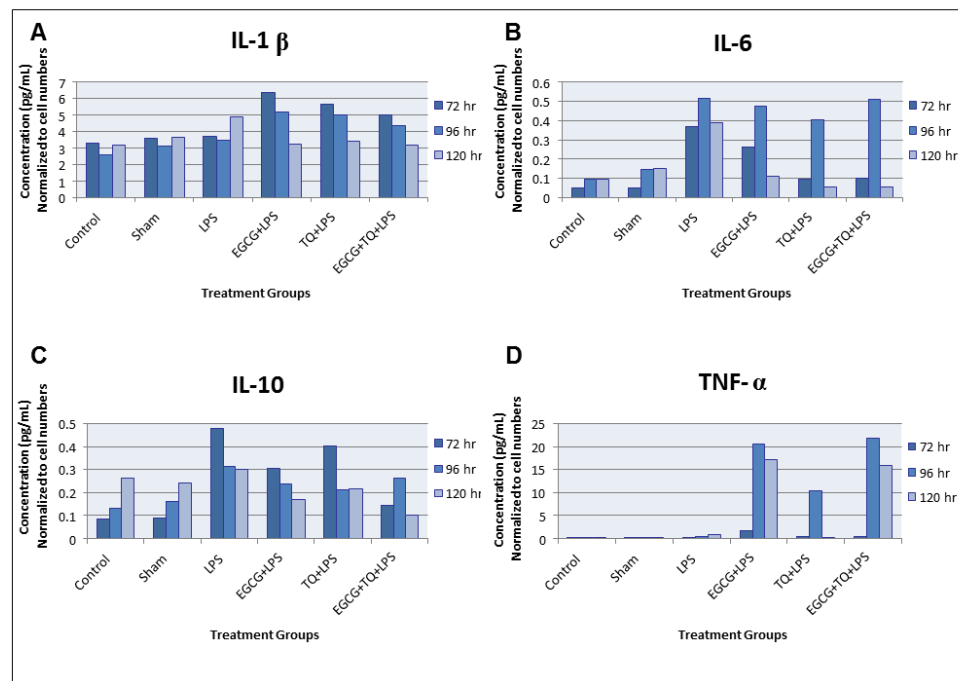


Figure 1: Multiplex ELISA results from the supernatants of RAW 264.7 macrophages after daily administration of LPS and sustained delivery with EGCG and/or TQ. The figures are represented as follows: A, IL-1 β ; B, IL-6; C, IL-10; and D, TNF- α . Results are normalized to mean cell numbers and displayed in pg/mL.

DISCUSSION

This study is the first to use drug delivery using antioxidants on RAW 264.7 macrophages. Therefore, there are no studies available investigating the effects of sustained delivery of EGCG and TQ on cytokine levels of RAW 264.7 macrophages. In our study, prolonged delivery of LPS on EGCG and TQ treated cells had different effects on the secretion of activated cytokines, including proinflammatory TNF- α , interleukin IL-1 $\alpha\beta$, and IL-6, as well as the anti-inflammatory, IL-10.

LPS is known to induce the expression of IL-1 β in macrophages. During inflammation, the increases in the release of IL-1 β lead to cell or tissue damage [11]. Therefore, decrease in the release of IL-1 β from macrophages may slow down the inflammatory responses to LPS stimulation. Our study showed that IL-1 β remained slightly higher than the control levels from 72 to 120 hours indicating that IL-1 β suppression was not altered by treatment with EGCG and/or TQ.

Our study showed during prolonged incubation with LPS, IL-10 levels were elevated. This is an important observation since it has been documented that LPS can induce IL-10 in macrophages [12]. Although IL-10 levels in the treatment groups were not higher than the LPS control, they remained elevated in comparison to the controls. Since IL-10 is known to downregulate proinflammatory cytokines, induction of IL-10 could reduce the LPS induced response [13]. In this study, it appeared that IL-10 may have had an impact on IL-6 levels, since IL-6 was decreased from the LPS values.

After prolonged incubation with LPS, there was actually an increase in TNF- α in the treatment groups (96 & 120 h), which conflicted with other studies. In the literature, TNF- α has been shown to be reduced in the presence of antioxidants [14, 15]. On the other hand, there was a study conducted where EGCG at a concentration of 10 μ M markedly increased TNF- α in RAW 264.7 macrophages [16]. The author attributed these differences to possibly the biochemical nature of the antioxidants and/or the cell types used. Although TQ was also elevated, the increase occurred only during one time period and could be the result of factors previously mentioned.

CONCLUSIONS

Previous studies in our lab have indicated that EGCG and TQ possess anti-inflammatory properties that may be useful as therapeutic agents to combat inflammation. Each of these antioxidants has been shown to have anti-cancer properties via separate mechanisms, but may have a similar target in models of inflammation. Both EGCG and TQ act as pro-oxidants toward cancerous cells and individually can be strong inhibitors of angiogenesis or mitosis. Excessive concentrations of EGCG and TQ or the type of cell line used may play a role in the chemoprotective properties of each of these phytochemicals, but lower non-toxic concentrations may contribute to the reduction of inflammation.

This study also suggests that sustained delivery of EGCG and/or TQ may not be able to efficiently reduce the effects of prolonged LPS stimulation. The continuous stimulation of LPS may be too overwhelming for the macrophages thus inhibiting the benefits of antioxidant therapy. Further investigations need to be conducted to understand the mechanisms of these observations.

REFERENCES

- [1] S. R. Maxwell, "Prospects for the use of antioxidant therapies," *Drugs*, 49(3), 345-61, 1995.
- [2] M. A. El-Gazzar, R. El Mezayen, J. C. Marechi, M. R. Nicolls, A. Canastar, and S. C. Dreskin, "Thymoquinone attenuates proinflammatory responses in lipopolysaccharide-activated mast cells by modulating NF-kappaB nuclear transactivation," *Biochimica et Biophysica Acta*, 1770(4), 556-64, 2007.
- [3] M. Roepke, A. Diestel, K. Bajbouj, d. Walluscheck, P. Schonfeld, A. Roessner, et al, "Lack of p53 augments thymoquinone-induced apoptosis and caspase activation in human osteosarcoma cells," *Cancer Biology & Therapy*, 6(2), 160-9, 2007.
- [4] A. Osterburg, J. Gardner, S. H. Hyon, A. Neely, and B. Babcock, "Highly antibiotic-resistant *Acinetobacter aumannii* clinical isolates are killed by the green tea polyphenol (-)-epigallocatechin-3-gallate (EGCG)," *Clinical Microbiology and Infection*, 15(4), 341-6, 2009.
- [5] G. Peng, D. A. Dixon, S. J. Muga, T. J. Smith, and M. J. Wargovich, "Green tea polyphenols (-)-epigallocatechin-3-gallate inhibits cyclooxygenase-2 expression in colon carcinogenesis," *Molecular Carcinogenesis*, 45(5), 309-19, 2006.

- [6] H. S. Youn, J. Y. Lee, S. I. Saitoh, K. Miyake, K. W. Kang, Y. J. Choi, et al, "Suppression of MyD88-TRIF-dependent signaling pathways of Toll-like receptor by (-)-epigallocatechin-3-gallate, a polyphenol component of green tea," *Biochemical Pharmacology*, 72(7), 850-9, 2006.
- [7] S. Crouvezier, B. Powell, D. Keir, and P. Yaqoob, "The effects of phenolic components of tea on the production of pro- and anti-inflammatory cytokines by human leukocytes in vitro," *Cytokine*, 13(5), 2880-6, 2001.
- [8] H. S. El-Abhar, D. M. Abdallah, and S. Saleh, "Gastroprotective activity of Nigella sativa oil and its constituent, thymoquinone, against gastric mucosal injury induced by ischaemia/reperfusion in rats," *Journal of Ethnopharmacology*, 84(2-3), 251-8, 2003).
- [9] M. A. Baker, G. J. Cerniglia, A. Zaman, "Microtiter plate assay for the measurement of glutathione and glutathione disulfide in large numbers of biological samples," *Analytical Biochemistry*, vol. 190, pp. 360-65, 1990.
- [10] H. A. Benghuzzi and P. K. Bajpai, "Effects of delivering different amounts of DHT by ceramic implants on reproductive system of male rats," *Biomedical Sciences Instrumentation*, 25, 179-189, 1989.
- [11] M. A. West, S. C. Seatter, J. Bellingham, and L. Clair, "Mechanisms of reprogrammed macrophage endotoxin signal transduction after lipopolysaccharide pretreatment," *Surgery*, 118(2), 220-8, 1995.
- [12] C. Wu, T. Chen, T. Chen, W. Ho, W. Chiu, and R. Chen, "Nitric oxide modulates pro- and anti-inflammatory cytokines in lipopolysaccharide-activated macrophages," *The Journal of TRAUMA Injury, Infection and Critical Care*, 55(3), 540-45, 2003.
- [13] R. de waal Malefyt, J. Abrams, B. Bennett, C. Figdor, and J. E. de Vries, "Interleukin 10 (IL-10) inhibits cytokine synthesis by human monocytes: an autoregulatory role of IL-10 produced by monocytes," *The Journal of Experimental Medicine*, 174(5), 1209-20, 1991.
- [14] A. El-Mahmoudy, Y. Shimizu, T. Shiina, H. Matsuyama, H. Nikami, and T. Takewaki, "Macrophage-derived cytokine and nitric oxide profiles in type I and type II diabetes mellitus: effect of thymoquinone," *Acta Diabetologica*, 42(1), 23-30, 2005.
- [15] F. Yang, W. J. de Villiers, C. J. McClain, and G. W. Varilek, "Green tea polyphenols blood endotoxin-induced tumor necrosis factor-production and lethality in a murine model," *Journal of Nutrition*, 128(12), 2334-40, 1998.
- [16] A. Murakami, D. Takahashi, K. Hagihara, K. Koshimizu, and H. Ohigashi, "Combinatorial effects of nonsteroidal anti-inflammatory drugs and food constituents on production of prostaglandin E₂ and tumor necrosis factor- α in RAW264.7 murine macrophages," *Bioscience, Biotechnology and Biochemistry*, 102, 47-90, 2003.

THE USE OF ANTIOXIDANTS TO SUPPRESS THE SK-OV-3 CELL LINE IN OVARIAN CANCER

Jennifer L. Harpole, MS, Michelle Tucci, PhD

Hamed Benghuzzi, PhD

Clinical Health Sciences, University of Mississippi Medical Center, Jackson, MS 39216

ABSTRACT

Ovarian cancer is the leading cause of mortality among the gynecologic cancers and is the 5th most common cancer among women. Recent studies have indicated that antioxidant exposure may slow the progression in major neoplastic diseases. The objective of this study was to investigate the pathophysiological effects of Thymoquinone (TQ) and Epigallocatechin-3-gallate (EGCG) using the SK-OV-3 cell line as a model. A total of 72 wells were plated with (10^5) SK-OV-3 ovarian cancer cells according to standard lab protocols. Each group was subdivided into 4 groups of 6 wells each. Group 1 served as control and groups 2, 3, and 4 were treated with TQ (16 μ M), EGCG (3 μ g/ml), and TQ + EGCG, respectively. Biomarker and morphological evaluations were performed following standard lab techniques. The results of the study revealed: (1) an increase in cellular protein concentration of the combination at 24 and 48 hours phases ($p < 0.05$); (2) an increase in nitric oxide following administration of EGCG and the combination at 24 and 48 hours; conversely at 72 hours, there was no significant difference between all agents ($p < 0.05$); (3) TQ and EGCG were shown to induce intracellular oxidative stress (glutathione levels) at the end of 72 hour phase; (4) there were no membrane or cellular damage to the cells at all phases. The results of this study provided the literature with more insights regarding manipulation of ovarian cancer behavior through potent antioxidants such as TQ and EGCG in culture.

Keywords: Ovarian Cancer, Thymoquinone, EGCG, SK-OV-3 ovarian cancer cells

INTRODUCTION

Ovarian cancer is the leading cause of mortality among the gynecologic cancers. Ovarian cancer is the fifth most common cancer among women, and it causes more deaths than any other type of female reproductive cancer. The cause of ovarian cancer is unknown. The cell line SK-OV-3 is an ovarian adenocarcinoma and was obtained from ATCC. It is derived from the ascites of the metastatic site. It is epithelial-like and was isolated in 1973. Another name for SK-OV-3 is HTB-77. SK-OV-3 is a hypodiploid human cell line. SK-OV-3 cells are resistant to tumor necrosis factor and to several cytotoxic drugs including diphtheria toxin, cis-platinum, and adriamycin [1].

Among many natural compounds, TQ and EGCG exhibit a high probability for chemoprevention. EGCG has synergistic properties with other natural compounds [2]. EGCG and green tea extracts have been shown to have a wide range of target organs which is a property that standard cancer drugs do not possess [3]. TQ and EGCG exhibits its chemopreventative actions by multiple pathways which results in the outcomes of apoptosis, cell cycle arrest, growth inhibition, antiangiogenesis, and inhibition of metastasis [2]. Past and current research of antioxidants continues to provide hopeful findings concerning the success of deterring certain disease processes such as cancers [4]. Antioxidants have been shown to play an important role in protecting cells from free radical damage, which is implicated in cancer development [5]. The goal is to show that with the correct therapy combination the progression of ovarian cancer can be slowed so the disease process can be stopped.

METHODS

To find these desired results, there will be 4 groups. Group 1 served as control and groups 2, 3, and 4 were treated with TQ (16 μ M), EGCG (3 μ g/ml), and TQ + EGCG, respectively. Each group will be terminated at 24, 48, and 72 hours. A total of 144 wells were plated with 10^5 SK-OV-3 ovarian cancer cells. The wells were divided into groups of 72 wells. Each group was subdivided into 4 groups of 6 wells. The BCA assay is a biochemical assay for determining the total concentration of protein in a solution. The total protein level should measure the metabolic activity of the cells. The malindialdehyde determination assay (MDA) levels were used to determine the membrane and cellular damage of each cell group. The MDA levels were determined using the known standard laboratory procedure as exhibited by [6]. Nitrogen dioxide can be assayed spectrophotometrically by measuring the accumulation of its stable degradation products, nitrate and nitrite. The nitric oxide assay measures cell viability. The glutathione assay measures the glutathione peroxidase that is used to evaluate cell injury. It is one of the key

enzymes in the cellular defense against oxidative stress and the hepatocyte growth factor receptor. A morphological evaluation will be performed using a standard light microscope. Morphological evaluation was done using Hematoxylin and Eosin (H & E) staining procedure according to our laboratory protocol. This technique was performed to assess the structure and integrity of the cells in a representative well sample. Criteria for morphological evaluation will include cell size, shape, and appearance of nucleus, nucleus size, cytoplasm, and nucleolus.

RESULTS

In the BCA assay, no differences were seen in cellular protein concentrations between control, TQ, and EGCG for the duration of the study. The data shows combination treatment caused a significant increase in cellular protein concentration at 24 and 48 hours following treatment compared to control and treatment with TQ and EGCG alone. Combination treatment at 72 hours had protein concentrations similar to control, TQ, and EGCG-treated cells. The results of the nitric oxide assay show an increase in nitric oxide following the administration of EGCG alone and in combination with TQ compared with TQ alone or untreated control cells. The difference was approximately three-fold higher and this difference was statistically different ($p < 0.05$). By 48 hours, the nitric oxide levels were still elevated in EGCG and combination groups but the levels were not statistically different ($p < 0.05$) from control or TQ treatment alone. By 72 hours, there were no differences in nitric oxide levels between the groups. According to the glutathione assay, a single dose of TQ, EGCG, and combination of TQ and EGCG did not cause changes in intracellular GS concentration for 24 or 48 hours. By 72 hours, there was a significant two-fold increase in intracellular GSH concentration in cells treated with TQ and three-fold increase in GSH concentration in cells treated with EGCG. The combination treatment was similar to control values. After MDA analysis, there was no damage to the SK-OV-3 ovarian cancer cells. The morphological evaluation of SK-OV-3 ovarian cancer cells when the cells were treated with TQ shows a medium-sized cell that is oval-shaped with a single nucleus. At 24 hours, the chromatin was coarse and the cells were arranged in a sheet-like fashion. There was occasional vacuolization with a background containing debris. At 48 and 72 hours, the chromatin was hyper chromatic and the cells were arranged in clusters. The cells had occasional vacuolization with a background containing debris. When the SK-OV-3 cells are treated with EGCG at 24 hours, the cells were large, spindle-shaped and had multiple nuclei. The nuclei were oval and had hyper chromatic chromatin. The cells were arranged in clusters having severe vacuolization and a debris-filled background. At 48 hours, the cells were small, spindle-shaped and arranged in clusters. The cells have a single, oval nucleus that is hyper chromatic. There is severe vacuolization and debris in the background. At 72 hours, the cells were round, small and arranged in a single-like fashion. The nucleus is oval, singular and has hyper chromatic chromatin. It has occasional vacuolization and debris in the background. When the SK-OV-3 cells are treated with TQ+EGCG at 24 hours, the cells were medium, spindle-shaped and had a single nucleus. The nucleus was oval and had coarse chromatin. The cells were arranged as singles having occasional vacuolization and a clear background. At 48 hours, the cells were small, spindle-shaped and arranged singly. The cells have a single, oval nucleus that has coarse chromatic. There is severe vacuolization and a clear background. At 72 hours, the cells were round, small and arranged in a single-like fashion. The nucleus is oval, singular and has hyper chromatic chromatin. It has occasional vacuolization and a clear background.

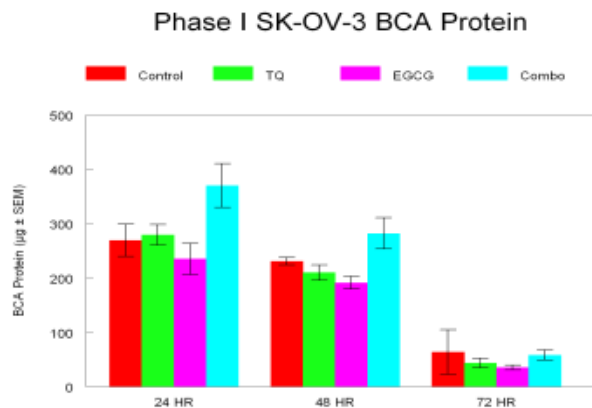


Figure 1: The effects of conventional delivery of TQ, EGCG and the combination of TQ and EGCG on SK-OV-3 ovarian cancer cells at 24, 48, and 72 hours.

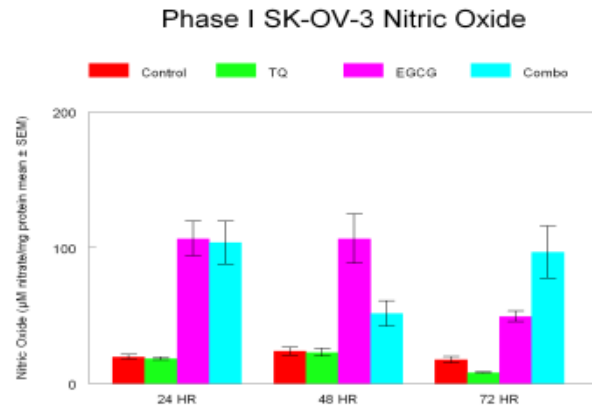


Figure 2: The effects of conventional delivery of TQ, EGCG and the combination of TQ and EGCG on SK-OV-3 ovarian cancer cells at 24, 48, and 72 hours.

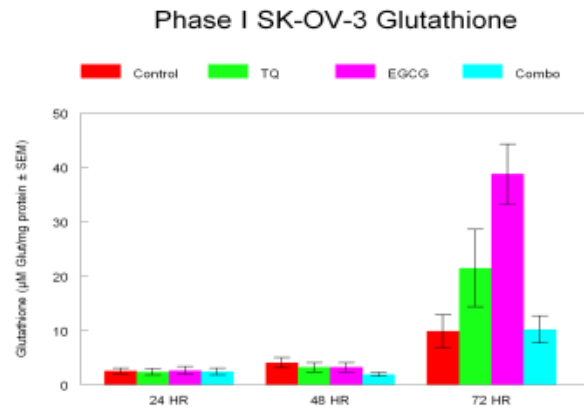
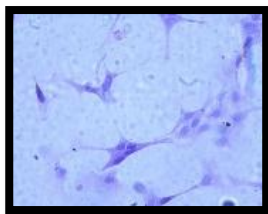


Figure 3: The effects of conventional delivery of TQ, EGCG, and the combination of TQ and EGCG on SK-OV-3 ovarian cancer cells at 24, 48, and 72 hours.

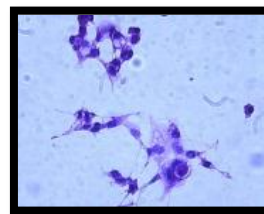
24 Hours



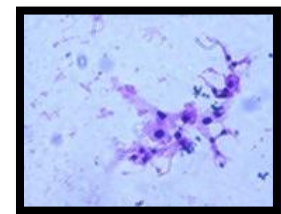
Control



TQ

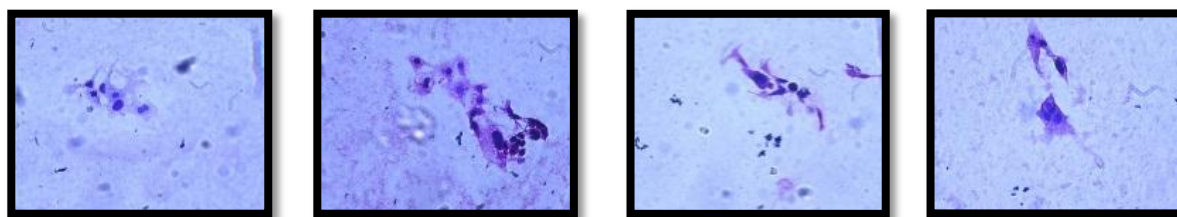


EGCG



TQ and EGCG

48 Hours



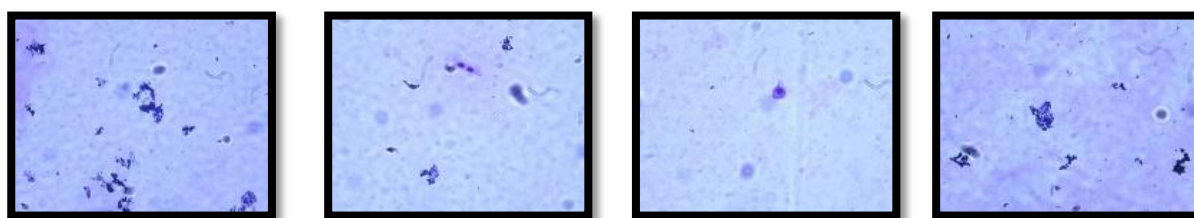
Control

TQ

EGCG

TQ and EGCG

72 Hours



Control

TQ

EGCG

TQ and EGCG

DISCUSSION

Antioxidants work to prevent or delay the development of cancer by inhibiting oxidative radical damage or by increasing the cellular glutathione detoxifying systems within the cells. A review of the literature suggests that antioxidants have the ability to increase apoptosis in cancer cells by holding cells within the cell cycle and increasing the activity of various caspases and p53. Other investigators suggest that increasing concentrations of antioxidants may also reduce radical formation no longer acting as a cell protectant but insulting the cellular membrane and causing cytolysis. Work on numerous cell lines in our labs have shown positive outcomes in regards to using TQ and EGCG alone and in combination to impair cell proliferation and induce cytolysis. The investigation and findings on SK-OV-3 ovarian cancer cells are interesting because this cell line is thought to be resistant to other chemotherapeutic drugs. In reviewing the literature, there is a difference in the susceptibility of ES-2 and SK-OV-3 cells to TQ and EGCG. In fact, Stellar *et al.* (1995) found ES-2 ovarian cells were inhibin A resistant while SK-OV-3 cells were not [7]. A study by Chan *et al.* (1997) shows that peritoneal cells were inhibited by EGCG which was caused by the excessive oxidative damage to the cells therefore enhancing apoptosis. In our study, 50 μM EGCG caused the ovarian cancer cells to secrete nitric oxide which may enhance vasodilation leading to increased blood flow to the tissue or it may increase nitric oxide radicals that ultimately increase apoptosis [8]. According to Tan *et al.* (2006) TQ suppressed the growth of PANC-1 cell line. The high dose of 50 $\mu\text{g}/\text{dL}$ TQ which is 3.0 μM significantly decreased cell proliferation at all phases with an increase in glutathione content. However, this study used a much lower dose of TQ than was used in our study. These results with such different dosages could be used to justify more studies with ovarian cancer cells using a much lower dosage [9]. Richards *et al.* (2006) study is different from our study because the concentrations are different than our concentration of 50 μM and the levels of MDA are decreased when compared to the control; whereas, in our study, the MDA levels are neither increased nor decreased when compared to the control [5].

CONCLUSIONS

The use of antioxidants has proven to offer promising effects as chemopreventive agents of ovarian cancer. Antioxidants may be used as an alternative method of treatment and offer patients and their families' options in managing their disease. The data of this study suggest that combination therapy with antioxidants is an effective

means of generating physiological responses, such as cell suppression, decrease in protein levels, and cell cycle disruption. Future studies are needed to further investigate the possibilities of antioxidant treatment and prevention of ovarian cancer.

REFERENCES

- [1] "SK-OV-3." ATCC, 1973.
<http://www.atcc.org/ATCCAdvancedCatalogSearch/ProductDetails/tabid/452/Default.aspx?ATCCNum=HTB-77&Template=cellBiology>
- [2] Kim, Myung Jin, Hyung Kim, Jin Chung, Tae Sung Jeong, and Hae Ryoung Park. "(-)-Epigallocatechin-3-Gallate (EGCG) Increases the Viability of Serum-Starved A549 Cells Through Its Effect on Akt." *The American Journal of Chinese Medicine*. 37:4 723-734 (2009): Print.
- [3] White, Patricia Oyetakin, Heather Tribout, and Elma Baron. "Protective Mechanisms of Green Tea Polyphenols in Skin." *Oxidative Medicine and Cellular Longevity*. (2012): Print.
- [4] Norwood, Anne A., Michelle Tucci, and Hamed Benghuzzi. "A Comparison of 5-Fluorouracil and Natural Chemotherapeutic Agents, EGCG and Thymoquinone, Delivered by Sustained Drug Delivery on Colon Cancer Cells." *Biomedical Sciences Instrumentation*. (2007): Print.
- [5] Richards, La'Toya Ross, Pamala Jones, James Hughes, Hamed Beghuzzi, and Michelle Tucci. "LNCaP Cells Exposed to Ceramic Drug Delivery Treatment with Epigallocatechin-3-Gallate, Thymoquinone, and Tannic Acid." *Biomedical Sciences Instrumentation*. (2007): Print.
- [6] Hansen, JT, H Benghuzzi, M Tucci, and Z Cason. "The role of black seed in the proliferation and biochemical marker levels of Hep-2 cells." *Biomedical Science Instrumentation*. 39:371-6 (2003): Print.
- [7] Steller, Michael D. Tanya J. Shaw, and Barbara C. Vanderhyden. "Inhibin Resistance is Associated with Aggressive Tumorigenicity of Ovarian Cancer Cells." *Molecular Cancer Research*. 3: 50-61 (2005): Print.
- [8] Chan, MM, D Fong, CT Ho, and HI Huang. "Inhibition of inducible nitric oxide synthase gene expression and enzyme activity by epigallocatechin gallate, a natural product from green tea." *Biochemical Pharmacology*. 12: 1281-6 (1997): Print.
- [9] Tan, Mary, Anne Norwood, Merilyn May, Michelle Tucci, and Hamed Benghuzzi. "Effects of (-)epigallocatechin gallate and Thymoquinone on Proliferation of a PANC-1 Cell Line in Culture." *Biomedical Sciences Instrumentation*. 42: 363-369 (2006): Print.

INDUCTION OF INTERLEUKIN-6 UPON THE SUSTAINED DELIVERY OF DANAZOL USING ADULT RATS AS A MODEL

Hamed Benghuzzi*, Michelle Tucci, Adel Mohamed, and Joseph A. Cameron**

University of Mississippi Medical Center, Jackson, MS 39216, and ** Jackson State University, Jackson, MS 39216

ABSTRACT

The specific objective of this study was to evaluate the physiological responses associated with sustained delivery of Danazol (D) through hydroxyapatite phosphate lysine (HAL) devices in a rat model. A total of twenty four rats were distributed randomly into three equal groups. Rats in group II were implanted (S/C) with empty HAL devices and served as sham controls. Group III rats were implanted with 1.61 (5ng/ml) g/cm³ devices containing 80 mg D each. Group I animals served as unimplanted controls. Upon sacrifice (6 weeks), the vital and reproductive organs were collected, fixed, embedded, and sectioned (H&E) by using standard lab protocols. Blood samples (500 ul) were collected three times per week and processed for biochemical analysis. Data obtained from this study revealed that HAL devices were capable of releasing D at sustained levels for 6 weeks. The release profiles ranged between 5 to 9 ng/ml serum. Biochemical analysis of the serum revealed that there is remarkable reduction in LH, FSH, and IL-1 (52%). In contrast, the level of IL-6 increased (58%) in experimental animals compared to the sham operated animals. Histopathological evaluation showed an increase the wet weights of ventral prostate as well as an atrophied testicular tissues upon the exposure to D compared to control animals. There were no significant changes observed in vital organ tissues (spleen, kidneys, adrenals and heart). In addition, physiological levels of D could cause severe prostatic hypertrophy and regression to spermatogenesis after 6 weeks in rats.

KEYWORDS

Danazol, Drug Delivery Systems, Androgens, Bioceramics, Cytokines, Reproductive Organs, Prostate

INTRODUCTION

Several studies have documented that there are several factors implicated in local gonadal control [1-9]. These local factors include regulatory hormone such as corticotropin releasing hormone and somatostatin, as well as several growth factors and cytokines [4-6]. The growth factors and cytokines are of particular interest because they are involved in all aspects of the fluid homodynamic. The elevation of these factors were attributed to the changes in various cellular growth, altered gene expression, and often changes in phenotype [4-6]. This study explored the changes of both local and systemic control factors associated with continuous delivery of D by HAL delivery devices.

Danazol is a derivative of the synthetic androgen ethisterone also known as 17-alpha-ethinyl testosterone. It was approved by the FDA as the drug of choice to treat endometriosis. Even though D was documented to be effective to treat endometriosis, its use was limited by its aggressive behavior and masculinizing side-effects. Previous studies in our laboratory have shown that sustained delivery of D can induce azoospermia in adult rats. Danazol has been also used for other indications, namely in the management of menorrhagia, fibrocystic breast disease, immune thrombocytopenic purpura, breast pain (mastodynia) and hereditary angioedema. The effect of D on the status of inflammatory mediators such as Interleukin-6 (IL-6) and Interleukin-1 has not been investigated. IL-6 is an known to be an essential immune protein in the hematopoietins family with many previous names, including interferon- β 2 (IFN- β 2), B-cell stimulatory factor-2 (BSF-2), hepatocyte stimulating factor (HSF), cytotoxic T-cell differentiation factor (CDF), and hybridoma/plasmacytoma growth factor (HPGF/HGF), but given its final distinction as IL-6 in the late 1988. It is a monomer of 184 amino acids produced by T-cells, macrophages, and endothelial cells found on a single gene located at 7p21. IL-6 is released in response to infection, burns, trauma, and neoplasia, and its functions range from key roles in acute-phase protein induction to B- and T- cell growth and differentiation. As mediator to the inflammatory cascade, IL-6 is released in response to IL-1 and TNF-b. The IL-6 receptor is found on many cell surfaces, including resting normal T-cells, activated normal B-cells, myeloid cell lines, hepatoma cell lines, myeloma cell lines, and on Epstein-Barr virus (EBV) modified B-cells, in which it promotes proliferation.

MATERIAL AND METHODS

Fabrication of HAL:

The microcrystals of HAL were prepared by following standard laboratory procedure in which explained elsewhere unless otherwise indicated [7]. The synthesized material was calcined at 1200°C for one hour. The calcined HAL was then placed on an automatic Tyler sieve stack (75, 60, 45, <38 μm) to obtain particles 1-38 μm . The calcined material was sintered at 1350°C for 24 hours. The sintered HAL powder, were combined with D, then were cold pressed into cylindrical form (final density of $1.61 \pm 0.03 \text{ gm/cm}^3$ and surface area of $3.33 \pm 0.21 \text{ cm}^2$) using a 3/8" die set at a compression load of 5000 Kg.[7-9]

Animals:

A total of 24 Sprague Dawley rats weighing 280-320 gm were divided randomly into three groups of 8 rats each. Group II animals were implanted with empty HAL capsules and served as sham implanted group. Group III animals were implanted with D filled HAL capsules (80 mg D). All rats were acclimatized one week prior to surgery. During the entire duration of this study, the rats were kept on a 12-h day/night cycle, and were fed Purina Rodent Chow, and water ad libitum.

Ceramic Implantation:

Rats were anesthetized with zylazin and ketamins according to institutional approved protocol, and their hind-limbs shaved and scrubbed with providone iodine. The sterilized ceramics were inserted under the skin using standard aseptic techniques. After implantation, the site was sealed with wound clips, and the animals were injected with 0.1 ml of 200,000 units of Penicillin G. At the end of the experiment (6 weeks) testes, epididymis, seminal vesicles, ventral prostate, spleen, adrenals, kidneys, lungs, and hearts were removed and weighted on an analytical balance. The data collected were analyzed by analysis of variance at $p > 0.05$.

Collection of Blood:

A total of 1 ml of blood was collected (three times per week) by nicking the tip of the tail and gently massaging the tail until the appropriate amount was collected. The blood was allowed to clot for 30 min. at room temperature, then the samples were reamed to pull the clot away from the side of the tubes. The tubes were then centrifuged at 2,500 rpm for 15 min. The serum was collected and stored in 0.1 ml aliquots at -20°C

Analysis of IL-1 β and IL-6 by sandwich enzyme linked immunoabsorbent assay (ELISA):

Aliquots of 100 μl from collected serum samples or standard proteins of IL-1 β were added in triplicate to the wells of a microtiter plates containing either anti-IL-1 β or IL-6, and allowed to incubate at 4°C overnight for maximum binding. The plates were washed several times with 200 μl of PBS containing 0.5% tween, then 100 μl of either anti IL-1 β conjugated to peroxidase or IL-6 conjugated with peroxidase were added for 2 hours at room temperature on a shaking platform oscillating at 150 rpm. At the end of the incubation period the plates were washed 5 times with 200 μl of PBS containing 0.5% tween and then developed for peroxidase with 50 μl of phenylaminodiamine in citric acid buffer (pH 5.0). After 20 minutes the reaction was stopped with the addition of 50 μl 2N H₂SO₄ and the product was measured at 409 nm. The standard curve was generated using the absorbances versus known concentrations of IL-1 β or IL-6. Concentration of cytokine in tissue was then calculated. In order to standardize the assay the values were divided by the serum protein concentration.

Protein Assay:

A standard bicinchoinic acid (BCA) assay for the protein determination was used following standard laboratory procedure as described by Pierce (Pierce Laboratory, Rockford, IL). Briefly, a standard curve is generated using 2mg/ml, 1mg/ml, 0.5mg/ml, 0.25mg/ml, 0.125mg/ml and 0 mg/ml of bovine serum albumin (BSA) in phosphate buffer. Ten microliter aliquots of the standard solutions or unknown samples were added to the wells of a microtiter plate in triplicate. A reaction mixture consisting of BCA and copper sulfate in a ratio of 50:1 was prepared. Two hundred microliters of the reaction mixture were placed in each well containing standard or unknown sample. The microtiter plates were then incubated at 37°C for 30 min. until sufficient color developed.

At the end of the incubation period the microtiter plate was read at 562 nm using a Bio Rad plate reader. A standard curve was generated from absorbances versus concentration of BSA. Unknown protein was determined using the linear equation for the best fit line.

RESULTS AND DISCUSSIONS

The body weights of all animals are reported in Table 1. The rats implanted with the D filled devices had slightly increased body weight at the end of the experiment. This increase in body weight is possibly due to the anabolic effects of the D. Since D is an anabolic steroid of abuse, and D is known to have receptors on other organs besides the male sex organs such as the heart and the liver, all organs were collected at the 6 week phase. The results showed that there were no changes in the weights of the liver, spleen, heart, lung, kidney and adrenal glands (Table 2). However, when the seminal vesicles, prostate, epididymis, and testis were analyzed, the results revealed that there were gross and anatomical differences in these tissues (Table 3). The data demonstrated that the weights of seminal vesicles and ventral prostate increased significantly by 6 weeks in the D treated group, and the epididymis and testis decreased significantly for the D implanted group in comparison with sham treated group (Table 3). Morphological evaluations of cross sections of prostatic tissues showed cuboidal hyperplastic activities in conjunction with hypertrophy. Other investigators have shown that in men with prostate hypertrophy was associated with a marked increase in androgen content [10,11]. This was attributed to synthesis of messenger RNA that codes for the proteins necessary for cell growth and function. [11-16]. Histological evaluation of the testis showed that the rats treated with D were azoospermic and compared to control and sham groups. It is well documented that normal functioning of the testis relies mainly on the action of follicle stimulating hormone (FSH) on the Sertoli cells and lutenizing hormone (LH) on the Leydig cells which subsequently acts on the seminiferous tubules to maintain testis function. The current postulation states that most of the endocrine regulation of spermatogenesis is manifested through the locally produced hormones on the Sertoli cells [18]. Data collected from this study indicated that there was a slight decrease in both LH and FSH levels in D treated animals compared to sham and control animals. It appears likely that local cell-cell communication and production of glycoproteins secreted by the Sertoli cells *in vivo* have direct regulatory roles in germinal cell development and in other biological processes related to reproduction [19]. Pollanen *et al* demonstrated that the cytokine IL-1 may have an effect on reproductive tissues and suggested that cytokines could be one of the major spermatogonial growth factors [20]. Circulating levels of cytokines in the serum were analyzed and are reported in Table 4. The analysis revealed that D treated animals had a 52% decrease in IL-1 activity, and a 58% increase in IL-6 activity. The decrease in circulating IL-1 activity may be a direct effect of the increased level observed in IL-6. The interleukins which were originally thought to mediate communication uniquely between cells of the immune system, have subsequently been found to exert effects on many cells outside the immune system, and to regulate the production of each type of growth factor. IL-6 has been shown to be a potent inhibitor of circulating IL-1 [20-21]. Decreased levels of IL-1 noticed in this study would partially account for the azoospermic condition of the D treated rats [20].

Table 1
Body weights of rats at the end of the 2,4, and 6 week duration. Weights are expressed as means in grams ± SD.

Groups	0 Week	2 Week	4 Week	6 Week
Sham	276 ±9	286 ±10	311 ±12	341 ±11
Control	269 ±16	291 ±9	321 ±20	339 ±20
D Treated	273 ±11	321 ±20	359 ±18	421 ±10

Table 2
Organ Weights for Sham and D implanted rats at the end of 6 weeks. All measurements are presented as means in grams \pm SD.

Group	Heart	Spleen	Kidney	Adrenal
Sham	1.62 \pm 0.16	0.91 \pm 0.12	1.85 \pm 0.20	0.50 \pm 0.02
Control	1.61 \pm 0.22	0.88 \pm 0.09	1.73 \pm 0.28	0.48 \pm 0.09
D	1.77 \pm 0.16	0.92 \pm 0.27	1.93 \pm 0.26	0.53 \pm 0.07

Table 3
Accessory Sex Organ Weights for Sham and D implanted rats at T (6 weeks). All measurements are tabulated as means in grams \pm SD.

Groups	Seminal Vesicle	Prostate	Epididymis	Testes
Sham	0.81 \pm 0.21	0.72 \pm 0.16	0.42 \pm 0.06	3.21 \pm 0.39
Control	0.99 \pm 0.10	0.81 \pm 0.20	0.39 \pm 0.05	3.41 \pm 0.28
D	1.40 \pm 0.2*	1.60 \pm 0.25*	0.19 \pm 0.02*	1.20 \pm 0.19*

Table 4
Cytokine IL-1 (pg/mg protein) levels obtained from serum samples obtained from sham and experimental animals.

Groups	0 Time	2 Week	4 Week	6 Week
Sham	71 \pm 7	72 \pm 5	73 \pm 10	77 \pm 12
Control	70 \pm 16	69 \pm 10	75 \pm 13	75 \pm 14
D Treated	39 \pm 10	33 \pm 7	30 \pm 8	31 \pm 7

Table 5
IL-6 (pg/mg protein) levels obtained from serum samples obtained from sham and experimental animals.

Groups	0 Time	2 Week	4 Week	6 Week
Sham	21 \pm 2	22 \pm 4	25 \pm 8	28 \pm 6
Control	24 \pm 5	28 \pm 9	27 \pm 4	27 \pm 6
D Treated	44 \pm 8	46 \pm 4	54 \pm 11	57 \pm 8

Table 5
Concentration of Serum Proteins in the plasma of samples obtained from sham operated and DHT-TCPL implanted adult rats (means \pm SD).

Groups	0 Week	2 Week	4 Week	6 Week
Sham	65 \pm 5	70 \pm 3	71 \pm 7	70 \pm 9
Control	66 \pm 7	68 \pm 8	76 \pm 10	72 \pm 3
D Treated	74 \pm 9	75 \pm 14	78 \pm 12	72 \pm 13

CONCLUSIONS

This experiment demonstrates that HAL capsules are capable of delivering D in a sustained manner for 6 weeks. The results also reveal that D delivered at a sustained manner resulted in systemic modifications. In addition, sustained delivery of D stimulated the IL-6 secretion and inhibited IL-1 levels in adult rats.

ACKNOWLEDGMENTS

The authors wish to express their gratefulness to the School of Health Related Professions and Department of orthopedic surgery at the University of Mississippi Medical Center.

REFERENCES

1. Benghuzzi H, Cason Z, Tucci M, Cameron JA, Mohamed A. (2011). *Biomed Sci Instrum*;47:189-94. PMID:21525619 [PubMed]
2. Benghuzzi Ham, Michelle Tucci. (2008); Vol 44, 94-99.
3. Benghuzzi H, Powell P, Tucci M, Cameron J. (2009) *Biomed Sci Instrum*;45:413-8. PMID: 19369798 [PubMed]
4. Bruchovsky N and Wilson JD (1968). *J Biol Chem* 243:2012
5. Bruchovsky N and Wilson JD (1968). *J Biol Chem* 243:5953
6. Catt KJ, Harwood RN, Clayton RN, Davies TF, Chan V, Katikineni M, Nozu and Dufau ML (1980). *Rec Prog Horm Res* 36:357:557-622.
4. Benahmed M, Sordoillet C, Chauvin MA, and Morera AM (1990) In: *Gonadotropin Releasing hormone and Gonadal Peptides*, Edited by Franchimont P, Elsevier Amsterdam.
5. Bellve AR and Zheng W (1989). *J Reprod Fert* 85:771-793.
6. Risberdger GP and de Krestser DM (1989) In: *The testis*, edited by Burger H and de Kretser DM, Raven Press, New York pp 255-268.
7. Benghuzzi, H.A., B.G. England, P.K. Bajpai and B.F. Giffin, *Journal of Clinical Materials* (CMU-9201). In Press.
8. Benghuzzi, H.A., B.G. England, R.M. Possley and P.K. Bajpai. *Proceedings of the 11th Southern Biomedical Engineering Conference*. Oct. 2-4, 1992. Memphis, TN. John Ray (Editor), pp. 28-29, 1992.
9. Benghuzzi, H.A., B.G. England, and P.K. Bajpai. *Biomedical Sciences Instrumentation (ISA, Paper #92-0131)*. Vol. 28. pp. 129-134, 1992.
10. Sitter DK and Wilson JD (1980). *J Clin Invest* 49:1737
11. Wilson JD (1980). *Am J Med* 68:745
12. Coffey DS (1986). In: *Campbell's Urology*, Vol 1 5th edition, edited by Walsh PC, Gittes RF, Perlmutter AD, and Stamey TA. WB Saunders, Philadelphia pg 233.
13. Wilson JD and Gloyna RE (1970). *Recent Prog Horm Res* 26:309-311.
14. Walsh PC (1975). *Urol Clin N Am* 2:125-130.
15. Coffey DS, Isaacs JT (1981). *Urology* 17:17-20.
16. Trachtenberg J, Bujnovszky P and Walsh PC (1989). *J Clin Endocrin Metab* 54:17.
17. Athony CT, Kovacs WJ and Skinner MK (1989). *Endocrinology* 125:2628-2630.
18. Fritz I (1978). In: *Biochemical Actions of Hormones Vol 5*. edited by G Litwack. Academic Press, New York, pp 249-278.
19. Griswald MD, Morales C and Slyvester SR. (1989): *Oxford Rev Reprod Biol* 10:124-161.
20. Pollanen P, Soder O and Parvinen M (1989): *Reprod Fert. Develo* 1:85-87.
21. Mizel SM, Dayer JM, Krane SM, and Mergenhagen SE (1981). *Proc Natl Acad Sci USA* 78:2874.

ASSESSING THE MORPHOLOGY OF HUMAN GINGIVAL FIBROBLASTS UPON EXPOSURE TO DENTAL ADHESIVES IN THE PRESENCE OF *PORPHYROMONAS GINGIVALIS* LIPOPOLYSACCHARIDE

Angelia D. Garner, Michelle A. Tucci, Hamed A. Benghuzzi
(ADG/HAB): Clinical Health Sciences Graduate Program,
University of Mississippi Medical Center, Jackson, MS 39216
(MAT): Department of Orthopedic Surgery,
University of Mississippi Medical Center, Jackson, MS 39216

ABSTRACT

This study aims to assess the morphology of human gingival fibroblasts upon exposure to dental adhesives in the presence of *Porphyromonas gingivalis* lipopolysaccharide (*LPS-PG*). Dental caries is not the only common disease of the oral cavity; periodontal disease has significant prevalence in the adult population. The fibroblasts were exposed to 0.1g of dental adhesives (PMMA, OptiBond®, and Prime & Bond®) in combination with *Porphyromonas gingivalis* lipopolysaccharide (2 µL) at phases of 24, 48, and 72 hours. At 48 hours, the cells exposed to the Prime & Bond® adhesive combined with *LPS-PG* (25.954±4.153 IU/mg Protein) demonstrated statistically significant increase (P=0.003) in LDH activity in the media compared to the control (7.014±1.395 IU/mg Protein). No significant differences in intracellular levels were detected at 24, 48, or 72 hours. Morphological evaluation at all phases demonstrated that the exposure of the cells to the three dental adhesives in combination with *LPS-PG* did not induce major toxicity or significant cellular death. While our morphological assessment did not provide evidence of structural damage of the cells, our biochemical analysis verified that at some level there was cellular damage.

INTRODUCTION

Dental caries is a chronic condition affecting the teeth. If left untreated, dental caries can lead to infection and tooth loss and causes pain and disability across all ages [1]. To remedy decay, two forms of treatment are employed, extraction of the tooth involved or restoring the tooth with a restoration. There are several types of restorations such as amalgams, composites, or crowns. Adhesives aid the restoration in achieving and maintaining adhesion between the dental restorations and tooth structure [2]. Poly methacrylate (PMMA) is an adhesive that has been utilized in various medical professions including dentistry. PMMA has been widely utilized in the fabrication of dental adhesives, implants, obturators, and dentures. OptiBond® is a dental adhesives utilized in dentistry for both direct and indirect bonding of dental materials. Due to 0.4 micro filler, OptiBond® has high levels of protection against micro leakage. Prime & Bond® is a light cured self-priming adhesive designed to bond composite materials to enamel and dentin as well as to metals and ceramics. Both OptiBond® and Prime & Bond® have fluoride releasing properties which aid in preventing recurrent decay and sensitivity.

Dental caries is not the only common disease of the oral cavity. Periodontal disease has significant prevalence in the adult population. It has been estimated that 22% of the population has a moderate form of periodontal disease; while 13% have a severely advanced form that eventually leads to bone and tooth loss [3]. *Porphyromonas Gingivalis* lipopolysaccharide (*LPS-PG*) is a major component of the outer membrane of the gram negative bacteria commonly identified in periodontitis. *LPS-PG* is considered to be an important factor in the pathogenesis of periodontal disease; it is absorbed into the root surfaces of gingival tissues of patients [4].

Several cell types have been identified within the gingival connective tissue. Gingival fibroblasts have been identified as the predominant cell found in gingival connective tissue. Gingival fibroblasts function to manufacture extracellular components and are responsible for the continual adaptation of gingival connective tissue along with wound healing repair and regenerations [5]. *In vitro* studies have utilized gingival fibroblasts in studying periodontal disease, gingival overgrowth, pathologies, and restorative materials. This study aims to assess the morphology of human gingival fibroblasts upon exposure to Dental Adhesives in the presence of *Porphyromonas gingivalis* lipopolysaccharide.

METHODS

The human gingival fibroblast cells utilized for this study were obtained from the American Type Culture Collection (ATCC), (Manassas, VA). The cells utilized were pre-plated and plated with approximately 50,000 cells per tube. The fibroblasts were cultured in T-25 flasks until established and then transferred and plated in 24-well tissue culture plates. Dulbecco's modified Eagle's medium (90%) and fetal bovine serum (10%) was the media of choice per standard lab protocols. The cells were maintained at 37 °C in Carbon dioxide/ air incubation throughout the experiment.

Experimental Design: This study consisted of four experimental groups. Group one served as a control containing gingival fibroblasts and media only (n=12). The remaining three groups contained fibroblasts (n=36) and a bonding agent with LPS-PG; Polymethyl methacrylate (PMMA) (.1 g), OptiBond® (.1 g), or Prime & Bond® (.1 g), and each adhesive was combined with LPS-PG (2 µL). The bonding agents were cured and placed in ten mL of Dulbecco's modified Eagle's medium. In each phase the fibroblasts were exposed to a total of 100 µL of bonding agents (individually). All groups were incubated in culture plates at intervals of 24, 48, and 72 hours.

Biochemical Analyses: A biocinchonic acid (BCA) assay was used for protein determination. Lactate dehydrogenase utilized to assess cellular damage. A reduced glutathione was employed to ascertain cellular viability. All assays were measured by following standardized laboratory methods unless otherwise indicated.

Morphological Evaluation: Representative test tubes were used for morphological evaluation. After each incubation phase, the cells were washed with 1 mL of phosphate buffered saline (PBS) to remove any remaining proteins. Ethanol (50%) was used to fix the cells to the coverslips. The cover slips were stained using the hematoxylin and eosin staining procedure. Following staining, the coverslips were mounted cell side up to clear glass slides with mounting media. Imaging of the cells was performed using the Image Pro Plus System.

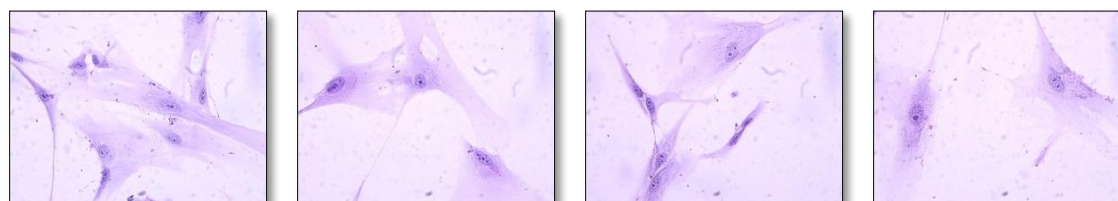
Statistical Analysis: All experiments were performed three times. In each analysis, controls were compared to the experimental groups in each phase. The results of the experiments were expressed using the descriptive statistics of mean ± SE. The statistical comparisons were performed using the Tukey test for non-parametric data where appropriate using the Jandel Computer Statistical Software (SigmaPlot 12.0). The significance level for the study was set at $p < 0.05$.

RESULTS

Cellular protein levels were evaluated in the gingival fibroblasts following exposure of combinations of the dental adhesives with LPS-PG: (1) PMMA, (2) OptiBond®, or (3) Prime & Bond® at 24, 48, and 72 hours. It was determined that there were no significant differences at any phase compared to the control. The lactate dehydrogenase assay was utilized to assess cellular damage. Lactate dehydrogenase is an enzyme which is part of normal cellular metabolism, and if it is found in the cell culture media, then cellular damage is evident. At 48 hours, the cells exposed to the Prime & Bond® adhesive combined with LPS-PG (25.954 ± 4.153 IU/mg Protein) demonstrated statistically significant increase ($P = 0.003$) in LDH activity in the media compared to the control (7.014 ± 1.395 IU/mg Protein).

Intracellular reduced glutathione levels were utilized to assess the oxidative stress level of the cell. No significant differences in intracellular levels were detected at 24, 48, or 72 hours. Morphological evaluation at all phases demonstrated that the exposure of the cells to the three dental adhesives in combination with LPS-PG did not induce major toxicity or significant cellular death (Figure 1). The large gingival fibroblasts displayed typical spindle shapes. The nuclei appeared hyper chromatic, prominent, and single arrangements; occasionally, multiple nuclei were noted. The cytoplasm was well defined and coarse.

(A.) 24 Hours



Control

OptiBond® + LPS

PMMA + LPS

Prime & Bond® + LPS

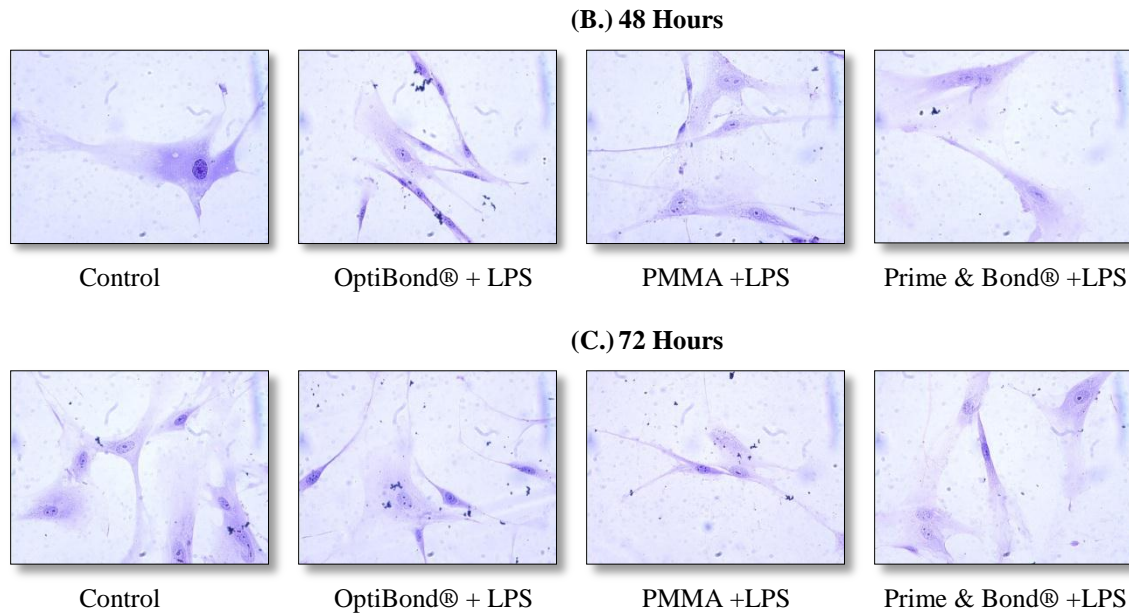


Figure 1: Morphological Evaluation of HGF-1 fibroblast cells exposed to PMMA+LPS, OptiBond®+LPS, and Prime & Bond® +LPS for (A) 24, (B) 48, and (C) 72 Hours (H&E staining) for more details see results section (X 40).

DISCUSSION

Fibroblasts from the oral connective tissue are the preferred cells to utilize when investigating the cytotoxicity of dental materials [6]. To achieve biocompatibility of dental materials, an appropriate host response is critical. Although cellular morphology indirectly reflects the degree of cell damage, this parameter was used for assessing the relative biocompatibility of fibroblast cells exposed to dental adhesives in the presence of LPS-PG.

Lactate dehydrogenase (LDH) is a stable cytoplasmic enzyme stored in viable cells. An increase in LDH leakage indicates that the stability of cell membranes is damaged, possibly due to oxidative injury [7]. At 48 hours, the cells exposed to the Prime & Bond® adhesive combined with LPS-PG demonstrated statistically significant increase ($P=0.003$) in LDH activity in the media compared to the control. Issa et al., 2004 utilized the LDH assay when assessing the cytotoxic effects of monomers leached from adhesives on gingival fibroblasts. Their study reported that lower concentrations of monomers caused fewer changes in LDH release. In contrast, they also noted that high monomer concentrations may cause progressive aggregation in phospholipid bilayer resulting in disruption of the membrane architecture and lysis [7]. Our study garnered at minimal exposure according to manufacture guidelines and recommendations of product usage. The increase in LDH at the 48 hour phase may be evident due to the time it takes for monomers to leach materials in laboratory situations; which is typically past the 24 hour time point. It has been reported that materials may continue to leach well after 24 hours at a slower rate [7].

The morphology of the cells assessed did not vary greatly from the control. The characteristic spindle shape of the fibroblast was evident throughout all phases. In studies conducted by Gomez-Florit et al., 2013 and 2014, the gingival fibroblasts exposed to implant materials demonstrated round-shape with few stress fibers growing without clear orientation and hyper-chromatic nuclei. The application of acid etchant is suspected to be the most obvious difference in application of their materials and ours.

CONCLUSION

Clinically all precautions should be taken to minimize toxicity to reduce any potential adverse effects of tissues that come in contact with dental materials. Previous evidence has shown that the correct manipulation and polymerization practices are of importance [8]. While our morphological assessment did not provide evidence of structural damage of the cells, our biochemical analysis verified that at some level there was cellular damage.

REFERENCES

- [1] E.D. Beltrán-Aguilar et al., "Surveillance for Dental Caries, Dental Sealants, Tooth Retention, Edentulism, and Enamel Fluorosis-United States, 1998-1994 and 1999-2002," *MMWR*, vol. 54, pp. 1-44, 2005.
- [2] J.L. Ferracane, "Direct Esthetic Anterior Restoratives," in *Materials in Dentistry: Principles and Applications*, Philadelphia, PA, J.B. Lippincott, 1995, ch. 5, Sec. Resins, pp. 88-94.
- [3] B.L. Philstrom, B.S. Michalowicz, and N.W. Johnson, "Periodontal diseases," *Lancet*, vol. 366, pp. 1809-1820, 2005.
- [4] M. Kiji et al., "Internal prostaglandin synthesis augments osteoprotegerin production in human gingival Fibroblasts stimulated by lipopolysaccharide," *British Society for Immunology, Clinical and Experimental Immunology*, vol. 149, pp. 327-334, 2007.
- [5] M. Gómez-Florit et al., "Differential response of human gingival fibroblasts to titanium- and titanium-zirconium-modified surfaces," *J Periodont Res*, doi:10.1111/jre.12121.
- [6] M. Gómez-Florit et al., "Human gingival fibroblasts function is stimulated on machine hydride titanium zirconium dental implants," *J Dent*, vol. 42, pp. 30-38.
- [7] Y. Issa, D.C. Watts, P.A. Brunton, C.M. Waters, and A.J. Duxbury, "Resin composite monomers alter MTT and LDH activity of human gingival fibroblasts in vitro," *Dental Materials*, vol. 20, pp. 12-20.
- [8] F. Öztürk, S. Malkoc, M. Ersöz, S.S. Hakki, and B.S. Bozkurt, "Real-time cell analysis of the cytotoxicity of the Components of orthodontic acrylic materials on gingival fibroblasts," *AJO-DO*, vol. 140, e243-e249.

AN EXCITATION-SCANNING HYPERSPECTRAL MICROSCOPE FOR BIOMEDICAL IMAGING OF GFP IN HIGHLY AUTOFLUORESCENT LUNG TISSUE

Peter Favreau^{1,2}, Thomas Rich^{2,3}, Ashley Stringfellow², Diego Alvarez^{2,4}, Prashant Prabhat⁵, Silas Leavesley^{1,3}

¹Chemical and Biomolecular Engineering, University of South Alabama, ²Center for Lung Biology, University of South Alabama, ³Pharmacology, University of South Alabama, ⁴Internal Medicine, University of South Alabama, ⁵Semrock, Inc., A Unit of IDEX Corp.

ABSTRACT

Hyperspectral imaging techniques have recently been applied to many biological applications to improve isolation of individual fluorophores in multi-label samples and identify fluorophores in the presence of highly autofluorescent tissue. Hyperspectral imaging is traditionally performed by collecting fluorescence emission over a broad wavelength range (emission scanning). However, significant light loss and long acquisition times can result from filtering the emission light.

Excitation scanning is a novel method of hyperspectral imaging that may provide higher sensitivity for detecting fluorophores than traditional emission-scanning techniques. Excitation scanning is performed by filtering the excitation light over many wavelengths, and subsequently collecting the emission at each excitation wavelength. This results in higher available signal, and shorter acquisition times.

Here, we report implementation of an excitation-scanning hyperspectral imaging microscope and preliminary results comparing excitation scanning to emission scanning. A comparative study was conducted using a model of lung injury featuring GFP-expressing pulmonary microvascular endothelial cells (PMVECs) in highly autofluorescent lung tissue. Our results indicate 1-2 orders of magnitude increased signal detection using excitation-scanning techniques compared to emission-scanning, and improved sensitivity for detection of GFP in autofluorescent lung tissue. Our future work will further test the efficacy of excitation scanning compared to emission scanning for applications in FRET detection, multi-label studies, and detection of changes in autofluorescence due to lung cancer.

Keywords: hyperspectral imaging, microscopy, fluorescence spectroscopy, tunable filters, thin films

INTRODUCTION

Fluorescence microscopy has traditionally been performed using bandpass filters to isolate peak fluorescence excitation and emission wavelengths for fluorescent labels. However, the emission spectra of many labels share similar peak emission wavelengths, resulting in poor spectral separation. Additionally, highly autofluorescent signals commonly possess broad emission spectra that can obfuscate dimly fluorescent labels [1].

Hyperspectral fluorescence microscopy combines spectroscopy and imaging techniques to quantify and separate multiple fluorescent probes. Hyperspectral imaging samples many wavelength bands to collect a contiguous emission spectrum. Consequently, hyperspectral imaging is capable of separating fluorophores based on a unique spectrum, notably in the separation of fluorescent probes from autofluorescence [2]. The traditional method of hyperspectral imaging filters the fluorescence emission in set increments across a broad wavelength range (emission scanning). Filtering can be accomplished using prisms [3], diffraction gratings [4], and tunable filters [5]. We have previously shown the efficacy of thin-film tunable filters for filtering fluorescence emission of GFP from lung autofluorescence [6]. However, emission-scanning hyperspectral imaging provides inherently low signal because the emission is sampled using narrow-bandwidth tunable filters. Consequently, emission scanning requires high acquisition times, making traditional hyperspectral approaches prohibitive for high-speed applications such as live-cell imaging or cell signaling.

We have developed a novel approach to hyperspectral imaging that overcomes the limitations of emission scanning by filtering the fluorescence excitation (excitation scanning), rather than fluorescence emission. Excitation scanning increases the available signal because the fluorescence emission is not filtered by a narrow-bandwidth filter. The increased signal results in shorter acquisition times, permitting high-speed hyperspectral imaging. Additionally, excitation scanning provides complimentary spectral information to emission scanning that can be used to better discriminate among multiple labels. In this work, we demonstrate the implementation of a novel

excitation-scanning hyperspectral imaging microscope and compare the new system to an emission-scanning hyperspectral microscope using detection of GFP in highly autofluorescent lung tissue.

METHODS

Cell, animal, and sample preparation was performed as described previously [2], [6]. Briefly, cell samples were acquired from pulmonary microvascular endothelial cells (PMVECs) and transfected with a lentivirus encoding GFP. CD adult rats were infected intratracheally with *P. aeruginosa* one week prior to injection of GFP-positive PMVECs in the jugular vein. Rats were euthanized after one week and samples removed from the most injured portions of the lung. Lungs were paraffin-embedded, sectioned, and placed on microscope slides. Rats not injected with GFP were injected with saline and euthanized for autofluorescence controls. Tissue samples were stained with Hoechst-33342 (Life Technologies, Carlsbad, California). Confluent monolayers of GFP-positive PMVECs were prepared on coverslips to obtain a pure GFP spectrum. Samples of wild-type PMVECs were stained with Hoechst to collect a pure Hoechst spectrum. A pure autofluorescence spectrum was obtained from unstained tissue slides.

An inverted fluorescent microscope (TE2000-U, Nikon Instruments) with a 40X oil-immersion objective (S Fluor, 40X/1.30 Oil DIC H/N2, Nikon Instruments) was used for imaging. Excitation scanning was performed using an array of thin-film tunable filters (VersaChrome, Semrock, Inc.) placed after a 300 watt Xe arc lamp (Titan 300, Sunoptic Technologies) in the optical lightpath (Fig. 1). A separate tunable filter array was positioned for emission scanning. A long-pass dichroic beamsplitter (BLP01-495R, Semrock, Inc.) and a long-pass emission filter (FF-495-Di03, Semrock, Inc.) separated excitation from emission light. Excitation scanning image acquisition was performed from 360-480 nm, in 5 nm increments. At each excitation wavelength, a 495 nm long-pass emission filter separated excitation from emission light. Emission scanning image acquisition was performed from 470 to 700 nm, in 5 nm increments. Excitation light was filtered with a 420/17 nm bandpass filter. An acquisition time of 300 ms and an EMCCD gain of 3800 were used for both systems, for all samples, except for the GFP control. An EMCCD gain of 3600 was used due to the high signal intensity of the confluent monolayer of GFP. Background subtraction and wavelength-dependent attenuation were characterized for all images.

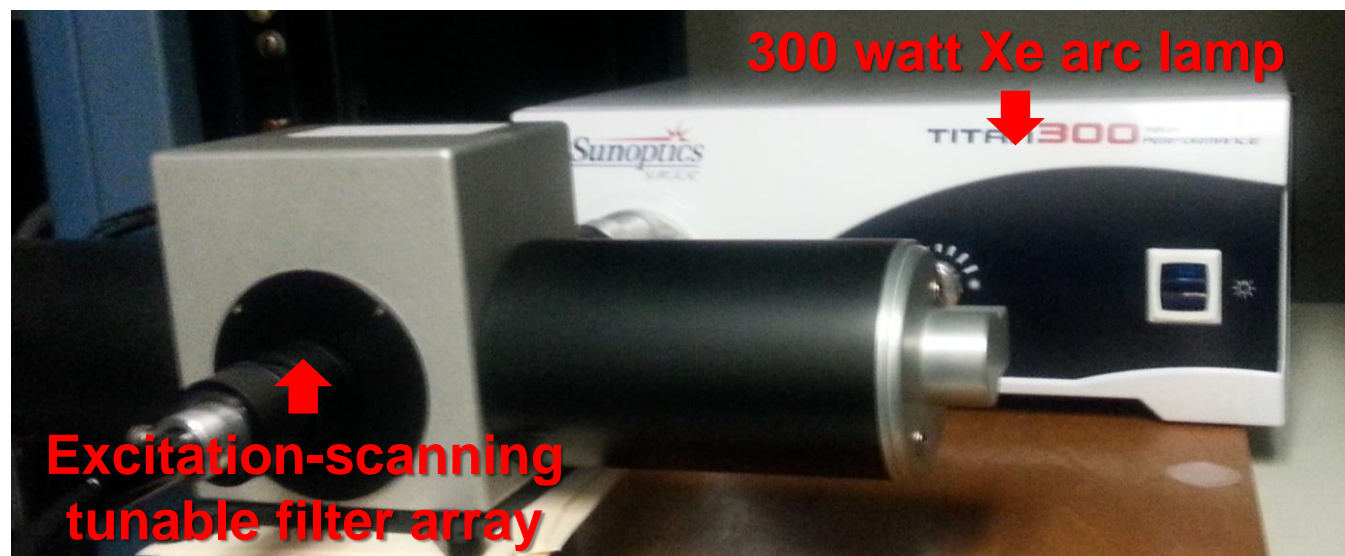


Figure 5: The excitation lightpath. The excitation-scanning tunable filter array was coupled to the Xe arc lamp with a liquid light guide. Filtered excitation light was transmitted to the microscope to excite the sample from 360-480 nm. Fluorescence emission was collected above 495 nm by a charge-coupled-device (CCD) camera.

RESULTS

Excitation scanning provided higher sensitivity for detection of GFP than emission scanning (Fig. 2a-d). Additionally, excitation scanning resulted in increased delineation of nuclear regions and lung structure. Excitation scanning also provided complimentary spectral information to emission scanning spectra.

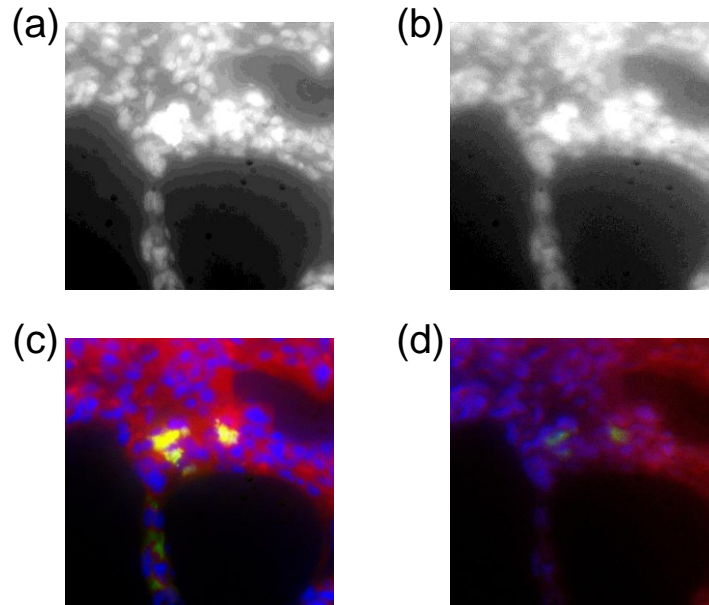


Figure 6: Summed fluorescence images of GFP in highly autofluorescent lung tissue with (a) excitation scanning and (b) emission scanning. The false-colored images from (c) excitation scanning compared to (d) emission scanning demonstrate higher sensitivity for GFP (green). There is also higher delineation of nuclear regions (blue), and more defined lung architecture (red) using excitation scanning.

DISCUSSION

In this work, we have demonstrated a novel hyperspectral imaging system that filters the fluorescence excitation instead of the emission (excitation scanning), and compared this technique to an emission-scanning hyperspectral microscope. Excitation scanning provided higher sensitivity for detection of GFP, and increased delineation of nuclear regions and lung structure. Time-dependent spectral measurements are possible with excitation scanning due to higher signal detection. Additionally, excitation scanning provided complimentary spectral information to emission scanning. Combining both spectral data sets would increase available spectral information unique to different labels, and consequently increase spectral discrimination of several fluorophores present in a single study.

CONCLUSIONS

Current fluorescence microscopy techniques utilizing several bandpass filters result in poor discrimination of fluorophores when multiple labels are present. Hyperspectral imaging is a recent technique that permits quantitative delineation of multiple labels by filtering and measuring the fluorescence emission spectrum of each fluorophore. However, filtering the emission results in reduced signal detection and long acquisition times, prohibiting time-lapse hyperspectral imaging studies. In this work, we have developed a novel excitation scanning hyperspectral microscope. We have compared excitation scanning to emission scanning by determining the efficacy for detecting GFP in highly autofluorescent lung tissue. Excitation scanning provided higher sensitivity for GFP than emission scanning, and complimentary spectral information to emission spectra. Our future work will involve time-lapse fluorescence imaging studies of multiple labels using excitation scanning. We anticipate increased temporal resolution for live-cell imaging.

ACKNOWLEDGMENTS

The authors would like to acknowledge support from NIH grant P01 HL066299, the Abraham Mitchell Cancer Research Fund, the Alabama Space Grant Consortium, and the University Committee on Undergraduate Research (UCUR). VersaChrome filters and tuning hardware for this study were provided by Semrock, Inc., a Unit of IDEX.

REFERENCES

- [1] J. R. Mansfield, K. W. Gossage, C. C. Hoyt, and R. M. Levenson, "Autofluorescence removal, multiplexing, and automated analysis methods for in-vivo fluorescence imaging," *J. Biomed. Opt.*, vol. 10, no. 4, p. 041207, 2005.
- [2] S. J. Leavesley, N. Annamdevula, J. Boni, S. Stocker, K. Grant, B. Troyanovsky, T. C. Rich, and D. F. Alvarez, "Hyperspectral imaging microscopy for identification and quantitative analysis of fluorescently-labeled cells in highly autofluorescent tissue," *J. Biophotonics*, vol. 5, no. 1, pp. 67–84, Jan. 2012.
- [3] D. T. Dicker, J. M. Lerner, and W. S. El-Deiry, "Hyperspectral Image Analysis of Live Cells in Various Cell Cycle Stages," *Cell Cycle*, vol. 6, no. 20, pp. 2563–2570, Oct. 2007.
- [4] J. N. Meyer, C. A. Lord, X. Y. Yang, E. A. Turner, A. R. Badireddy, S. M. Marinakos, A. Chilkoti, M. R. Wiesner, and M. Auffan, "Intracellular uptake and associated toxicity of silver nanoparticles in *Caenorhabditis elegans*," *Aquat. Toxicol.*, vol. 100, no. 2, pp. 140–150, Oct. 2010.
- [5] N. Gupta, "Acousto-optic-tunable-filter-based spectropolarimetric imagers for medical diagnostic applications—instrument design point of view," *J. Biomed. Opt.*, vol. 10, no. 5, pp. 051802–051802, Sep. 2005.
- [6] P. Favreau, T. Rich, A. Lindsey, D. Alvarez, P. Prashant, and S. J. Leavesley, "Thin-Film Tunable Filters for Hyperspectral Imaging of Lung Tissue," *J. Biomed. Opt.*, Feb. 2013.

HYPERSPECTRAL FRET IMAGING AND ANALYSIS APPROACHES TO DETERMINE cAMP COMPARTMENTALIZATION IN PMVECS

Naga S. Annamdevula¹, Andrea Britain², Thomas C. Rich^{2,3}, Silas J. Leavesley^{1,2}

¹Department of Chemical and Biomolecular Engineering, ²Department of Pharmacology, ³Center for Lung Biology, University of South Alabama, Mobile, AL, 36688

ABSTRACT

In the last 20 years, the importance of cAMP compartmentalization has been clearly demonstrated. These compartmentalized cAMP signals have differential effects in maintaining the pulmonary microvascular endothelial cell (PMVEC) barrier integrity. Several studies suggest that phosphodiesterases (PDEs) are key enzymes in regulating the spatial spread of cAMP signaling. PDE4 is primarily responsible for cAMP - PDE activity in PMVECS. However, the distribution of different PDE4 isoforms in PMVECS and their contribution cAMP compartmentalization is not well understood. This lack of knowledge is due in part to the dearth of studies that measured the localized cAMP signals and altered PDE localization and activity. State of the art probes for measuring cAMP signals in cells are based upon Förster resonance energy transfer (FRET). However, FRET signals are difficult to interpret due to weak signal strength and limited dynamic range. In this present study, we have used hyperspectral and analysis approaches to quantify multi-label FRET data with increased signal-to-noise ratios. To assess cAMP localization, we used soluble and plasma membrane targeted cAMP biosensors expressed in PMVECS isolated from wild type and PDE4A, B, and D knockout mice. This study provides preliminary information indicating the role of PDE4 isoforms in regulating the complex and spatially-distributed cAMP signaling in PMVECS. In future work, we plan to assess the spatial distribution of different PDE4 isoforms using isoform-specific antibodies. We will also investigate the role of different PDE4 isoforms in regulating the pulmonary endothelial barrier integrity.

Keywords: hyperspectral imaging, unbiased software analysis, Förster resonance energy transfer (FRET), cyclic AMP, phosphodiesterases, spatial distribution, pulmonary microvascular endothelial barrier integrity.

INTRODUCTION

Several studies have begun to demonstrate that cell signaling compartmentalization can help to regulate, or encode signaling specificity [1,2,3]. Cyclic AMP (cAMP) is an important second messenger that activates protein kinase A (PKA), cyclic nucleotide gated (CNG) channels, and exchange protein activated by cAMP (Epac) and regulates cellular and physiological functions. Recent studies have shown that cAMP signals are highly compartmentalized and dictate cellular or physiological function depending on where the cAMP is produced. For example, cAMP produced by plasma membrane- localized adenylyl cyclase (AC) enhances endothelial cell barrier integrity, whereas the cAMP produced by endogenous or heterologously-expressed soluble AC disrupts the endothelial barrier integrity [4]. However, the mechanisms underlying cAMP compartmentalization are not well understood. This lack of knowledge is due to the difficulty of quantitatively assessing subcellular cAMP concentrations. Recently, Förster resonance energy transfer (FRET) probes have been developed for measuring intracellular cAMP levels [5][6][7]. However, FRET signals are difficult to interpret due to weak signal strength and limited dynamic range. In our previous studies, we developed a methodological approach to improve the signal-to-noise ratio for a given hyperspectral imaging experimental assay [8]. We have also shown that hyperspectral imaging and analysis techniques offer an effective approach for quantitative analysis of multi-label FRET data, compared to traditional FRET techniques [9]. Based on these previous studies, we proposed to use hyperspectral imaging approaches and automated image processing analysis (image cytometry) to determine the role of PDE4 isoforms in regulating cAMP compartmentalization, and thus establishing their role in maintaining the endothelial barrier integrity. We used HEK293 cells transfected with Epac FRET probe to optimize our hyperspectral imaging and analysis approaches and to design automated cell analysis techniques to determine the subcellular localization of FRET signals[9]. We used a fusion protein comprised of a catalytically inactive cAMP binding protein, Epac, fused to a fluorescent donor (CFP) and acceptor (YFP) to infect PMVECS. In the basal state (low cAMP), the donor and acceptor fluorophores are in close proximity

such that FRET occurs efficiently. When cAMP binds to Epac, there is a conformational change such that FRET between CFP and YFP is reduced. The expression levels and signal intensity of these probes in cells is determined by the multiplicity of infection (MOI) value. Therefore, we used the imaging and analysis settings in our cell model (PMVECs) to determine the optimum multiplicity of infection. In our future studies, we will use these optimized parameters to determine the subcellular distribution of cAMP in PMVECs, the role of PDE4 isoforms in regulating cAMP compartmentalization, and the downstream effects on endothelial barrier integrity.

METHODS

Cell Culture, transfection and infection: HEK293 cells were cultured in 20 mm coverslip and were transfected with adenovirus encoding either plasma membrane-targeted or soluble Epac FRET probe. Prior to imaging, cells were labeled with Hoechst 33342 to visualize nuclei. For the spectral library, cells were transfected with adenovirus encoding either CFP or YFP. Non-transfected cells were labeled with Hoechst. For MOI optimization, PMVECs were cultured on 20 mm coverslips and were infected with different multiplicities of infection (MOI of 5, 15, 35, 70 and 100 were used) of adenovirus encoding soluble Epac FRET probe.

Hyperspectral imaging: All microscopy experiments were performed using an inverted spectral confocal microscope (Nikon A1R). Images were acquired using 405 nm excitation and hyperspectral emission was collected from 432 to 606 nm, in 6 nm increments (30 wavelength bands). All spectral images were acquired using a constant laser power, a constant photomultiplier voltage, and a confocal pinhole diameter of 4.9 Airy disc units.

Spectral Library: A spectral library containing the pure spectra (endmembers) of CFP, YFP, and Hoechst were constructed (Figure 1a). Each endmember of the spectral library was normalized to a peak value of one. Linearly unmixed images of Hoechst (Figure 1c), CFP (Figure 1d) and YFP (Figure 1e) were calculated using the “lsqnonneg” algorithm (MATLAB). Unmixed CFP and YFP images were used to calculate a FRET image (Figure 1f). The unmixed CFP and YFP images were also summed to produce a total fluorescent protein (CFP+YFP) emission image used for locating positively-expressing cells (Figure 1g).

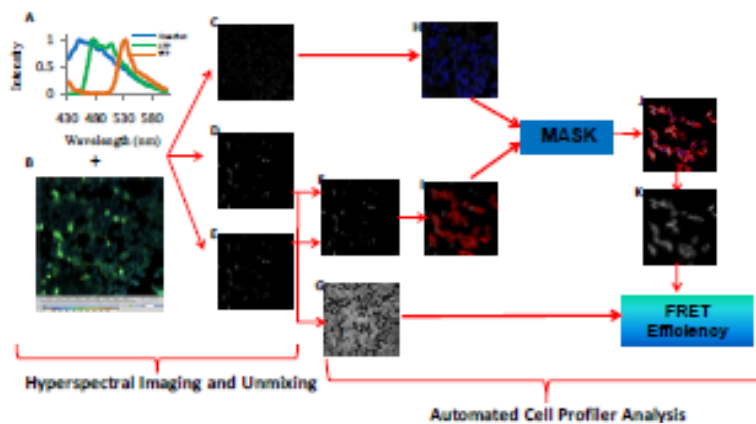


Figure 1: A spectral library containing pure spectra of each fluorophore was used to determine the abundance of Hoechst (C), CFP (D), and YFP (E) in the hyperspectral image (B). The unmixed CFP and YFP images were used to obtain a CFP+YFP total image (F) and FRET image (G). These unmixed images were used to determine the FRET efficiency using automated cell analysis.

Unbiased software analysis to estimate FRET efficiency in cells: FRET efficiency was measured using automated software analysis (Cell Profiler), as described previously[9]. Briefly, nuclei were identified in the unmixed Hoechst (Figure 1H) image and positively-expressing regions were identified in the CFP+YFP image (Figure 1I). Nuclei within expressing cells were then masked and subsequently propagated to estimate the borders of expressing cells (Figure 1J). Expressing cell cytoplasm (Figure 1K) was then identified by subtracting nuclear areas from expressing cell areas and the pixel-averaged FRET efficiency was measured. During experimentation, after 1 min basal activity, cells were either treated with vehicle control or with 10 μ M forskolin+ 10 μ M rolipram. Hyperspectral time-lapse images were then acquired for 10 minutes.

RESULTS

FRET Efficiency in HEK293 cells: FRET efficiencies were measured within each of the automatically identified ROIs. We observed differences in FRET responses among the cells expressing Epac^{cyt} (Figure 2A) and Epac^{PM} (Figure 2B) FRET probes, attributable to the differential production of cAMP in the cells in different compartments. Vehicle controls performed as expected (negligible cAMP change).

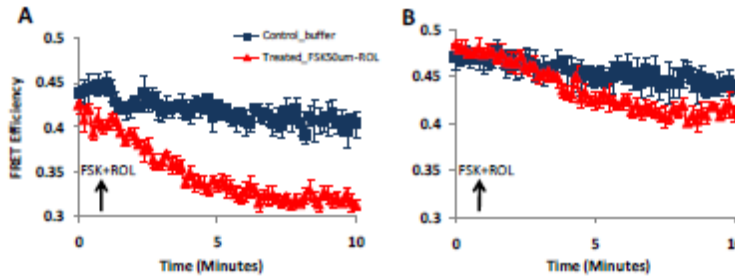


Figure 2: FRET efficiency measurements. FRET efficiency measurements in HEK293 cells expressing Epac^{cyt}, represents cytosolic cAMP (A) and Epac^{PM} FRET probes, represents cAMP near membrane (B).

Optimal MOI selection in PMVECs: We measured FRET efficiency in cells infected with different MOI values and observed that the measurable range of FRET efficiency lies with the MOI values of 35 and 70 as shown in Figure 3.

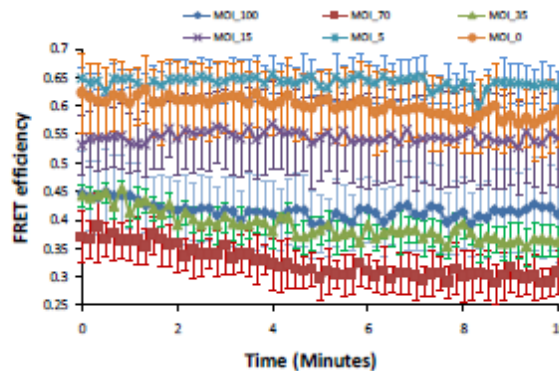


Figure 3: Time dependent measurements of FRET efficiency for different MOI values. After 1 minute of basal activity the cells were treated with forskolin and rolipram, due to which the FRET efficiency should decrease with time.

DISCUSSION

Hyperspectral imaging and analysis approaches offered increased SNR and allows quantitative measurement of multi-label FRET data. Traditional image analysis approaches require investigators to select regions of interest (ROIs) to interpret cyclic nucleotide signals in cells. Selecting ROIs manually may inadvertently bias data interpretation. We used unbiased image analysis to automatically select ROIs, which overcomes this limitation. We have previously shown that optimizing the hyperspectral imaging systems for any given hyperspectral assay is important [8] and hence we used well-documented cell model, HEK 293 cells to develop optimized hyperspectral and imaging analysis parameters to measure FRET in cells. We applied the optimized settings to measure FRET in PMVECs. In addition, we confirmed that there is a need to determine optimum MOI for the expression of fluorescent FRET probes in the PMVECs. While determining optimum MOI value, we need to make a compromise between acquiring maximum SNR and optimizing cell viability.

CONCLUSION

Our preliminary studies demonstrated that it is feasible to measure cAMP signals in localized cellular compartments (near-membrane and cytosolic) using hyperspectral FRET measurements with increased signal intensity and specificity. In addition, we observed differences in cytosolic and near membrane FRET response in HEK 293 cells. Future work will utilize hyperspectral imaging and automated analysis to determine the subcellular localization of cAMP and PDE4 isoforms in PMVECs.

ACKNOWLEDGEMENTS

The authors would like to acknowledge National Institutes of Health grants P01HL066299, NIHR01HL094455 and S10RR027535 for supporting this work

REFERENCES

- [1] S. L. Sayner, M. Alexeyev, C. W. Dessauer, and T. Stevens, "Soluble Adenylyl Cyclase Reveals the Significance of cAMP Compartmentation on Pulmonary Microvascular Endothelial Cell Barrier," *Circ. Res.*, vol. 98, no. 5, pp. 675–681, Mar. 2006.
- [2] T. C. Rich, K. A. Fagan, T. E. Tse, J. Schaack, D. M. F. Cooper, and J. W. Karpen, "A uniform extracellular stimulus triggers distinct cAMP signals in different compartments of a simple cell," *Proc. Natl. Acad. Sci.*, vol. 98, no. 23, pp. 13049–13054, Nov. 2001.
- [3] F. Rochais, A. Abi-Gerges, K. Horner, F. Lefebvre, D. M. F. Cooper, M. Conti, R. Fischmeister, and G. Vandecasteele, "A Specific Pattern of Phosphodiesterases Controls the cAMP Signals Generated by Different Gs-Coupled Receptors in Adult Rat Ventricular Myocytes," *Circ. Res.*, vol. 98, no. 8, pp. 1081–1088, Apr. 2006.
- [4] S. L. Sayner, D. W. Frank, J. King, H. Chen, J. VandeWaa, and T. Stevens, "Paradoxical cAMP-Induced Lung Endothelial Hyperpermeability Revealed by *Pseudomonas aeruginosa* ExoY," *Circ. Res.*, vol. 95, no. 2, pp. 196–203, Jul. 2004.
- [5] J. Creighton, B. Zhu, M. Alexeyev, and T. Stevens, "Spectrin-anchored phosphodiesterase 4D4 restricts cAMP from disrupting microtubules and inducing endothelial cell gap formation," *J. Cell Sci.*, vol. 121, no. 1, pp. 110–119, Jan. 2008.
- [6] B. Ponsioen, J. Zhao, J. Riedl, F. Zwartkruis, G. van der Krogt, M. Zaccolo, W. H. Moolenaar, J. L. Bos, and K. Jalink, "Detecting cAMP-induced Epac activation by fluorescence resonance energy transfer: Epac as a novel cAMP indicator," *EMBO Rep.*, vol. 5, no. 12, pp. 1176–1180, 2004.
- [7] B. E. Blackman, K. Horner, J. Heidmann, D. Wang, W. Richter, T. C. Rich, and M. Conti, "PDE4D and PDE4B Function in Distinct Subcellular Compartments in Mouse Embryonic Fibroblasts," *J. Biol. Chem.*, vol. 286, no. 14, pp. 12590–12601, Apr. 2011.
- [8] N. S. Annamdevula, B. Sweat, P. Favreau, A. S. Lindsey, D. F. Alvarez, T. C. Rich, and S. J. Leavesley, "An approach for characterizing and comparing hyperspectral microscopy systems.," *Sensors*, vol. 13, pp. 9267–9293, 2013.
- [9] S. J. Leavesley, A. L. Britain, L. K. Cichon, V. O. Nikolaev, and T. C. Rich, "Assessing FRET using spectral techniques," *Cytometry A*, p. 898-912, 2013.

TRANSVERSE RELAXATIONS OF SELECTIVELY EXCITED METABOLITES IN STROKE AT 21.1 T**Jens T Rosenberg^{1,3}, Noam Shemesh², Jean-Nicolas Dumez², Lucio Frydman^{1,2} and Samuel C. Grant^{1,3}**¹National High Magnetic Field Laboratory, The Florida State University, ²Chemical Physics, Weizmann Institute of Science, ³Chemical & Biomedical Engineering, FAMU-FSU College of Engineering, The Florida State University**ABSTRACT**

High magnetic fields can enhance the spectral sensitivity of Magnetic Resonance Spectroscopy. In this study, we used a 21.1-T magnet to investigate the apparent transverse relaxation (T_2) of metabolites under ischemic stroke. We utilize the Longitudinal Relaxation Enhancement (LRE) phenomena to measure T_2 -relaxation of selectively excited metabolites relevant to stroke to investigate their potential as stroke biomarkers. Spectra from the T_2 modified LRE sequence was of high fidelity, and importantly, no water contamination was observed. T_2 relaxation times were extractable, and variations in both T_2 and signal-to-noise ratio are seen. The apparent T_2 relaxation times of metabolites proved to be longer than expected, ranging from 101 ms (lactate) to 198 ms (N-acetylaspartate, NAA). At the investigated time point (24-h post occlusion), no statistically significant difference was seen for each respective metabolic T_2 when comparing the ipsilateral and the contralateral side. At only 16 averages, SNR for the shortest TE ranged from 11 (lactate on contralateral side) to 97 (choline on contralateral side) showing the increased sensitivity of using this sequence at ultra-high field. SNR measurements show significant difference between the ipsilateral and contralateral side for creatine (Cre) and NAA. These long T_2 s are interestingly accompanied by rather short T_1 s (~0.8 – 1.8 seconds). SNR measurements show significant difference between the ipsilateral and contralateral side for Cre and NAA. These findings suggest that the modified LRE sequence at high field increases MRS sensitivity and can potentially be used as biomarkers for stroke recovery.

Keywords: MRI, MRS, Relaxation enhancement, high field MRI, Stroke, Metabolites,**INTRODUCTION**

Utilizing high magnetic fields can enhance the spectral sensitivity of Magnetic Resonance Spectroscopy (MRS). In this study, the highest magnetic field currently available for MRS in animals, namely the 21.1-T magnet at the National High Magnetic Field Laboratory (NHMFL) [1], is employed to investigate the apparent transverse relaxation (T_2) of metabolites under ischemic stroke. In light of a recent report of Longitudinal Relaxation Enhancement (LRE) phenomena *ex vivo* [2], this study utilizes a similar technique to measure T_2 relaxation of selectively excited metabolites relevant to stroke in combination with high field MRS to investigate their potential to serve as stroke biomarkers.

METHODS

Cerebral ischemia was initiated by transient middle cerebral artery occlusion in Sprague-Dawley rats [3]. *In vivo* MRI were performed 24 hours following a 1.5-hour transient occlusion. The sequence, which is based on a previously reported LRE sequence [2], utilizes frequency selective, multiband excitation and refocusing pulses together with a 3D LASER module [4] to encode a voxel within the stroke region. The sequence was modified to increment the echo time (TE) and implemented on the 21.1-T magnet at the NHMFL. This ultra-wide bore magnet is equipped with a Bruker (Billerica, MA) Avance III spectrometer, and a homebuilt 33-mm quadrature coil resonating at 900 MHz was used to image all stroked animals. The spectrally selective pulse is based on a Shinnar-Le Roux (SLR) algorithm [2, 5] and was modified to target four metabolites: Lactate (Lac), N-acetylaspartate (NAA), Creatine (Cre) and Choline (Cho). Two 5-mm isotropic voxels were located in the brain, one covering the ischemic stroke and one in the contralateral side. For measuring metabolic T_2 , 14 TEs were varied between 58-110 ms, and the repetition time (TR) was set to 7.2 s. All scans were acquired with 16 averages and with gating applied during respiration. Datasets were zero filled, phase corrected and the magnitude of the data was applied before fitting each individual peak to a single exponential decay function in Topspin (Bruker, Billerica, MA).

RESULTS

Spectra arising from the T_2 modified LRE sequence at 21.1 T was of high fidelity, and importantly, no water contamination was observed (Fig. 1 and 2). Fig. 1 shows the TE dependence of each respective metabolite, which was used to extract apparent T_2 relaxation times. Variations in both T_2 and SNR are seen based on stroke lesion size, and the apparent T_2 relaxation times proved to be longer than expected, ranging from 101 ms (Lac) to 198 ms (NAA) on the ipsilateral side. At the investigated time point (24-hour post occlusion), no significant difference was seen for each respective metabolic T_2 when comparing the ipsilateral and the contralateral side as seen in Figure 3a. At only 16 averages, SNR for the shortest TE ranged from 11 (Lac on contralateral side) to 97 (Cho on contralateral side) showing the increased sensitivity of using this sequence at ultra-high field. In Figure 3b SNR measurements are shown and indicate significant difference between the ipsilateral and contralateral side for Cre and NAA. The long T_2 s measured are interestingly accompanied by rather short T_1 s (~0.8 – 1.8 seconds, data not shown), and are suggestive of high fidelity MRS in such high fields. SNR measurements show significant difference between the ipsilateral and contralateral side for Cre and NAA.

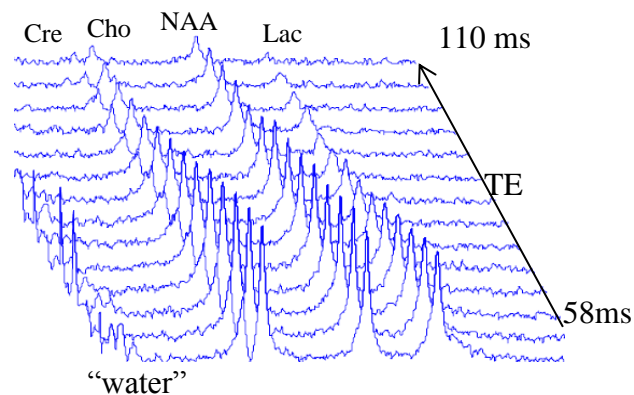


Fig 1: Stack plot of spectra with increasing TE of the selectively excited metabolites

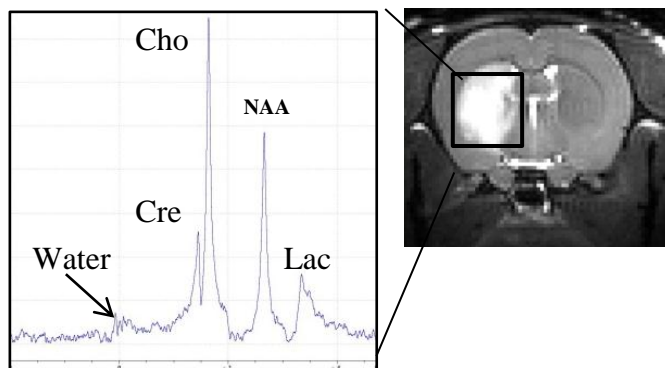


Figure 2: Spectrum showing selectively excited metabolites in a voxel covering the stroke lesion. Note the lack of water signal.

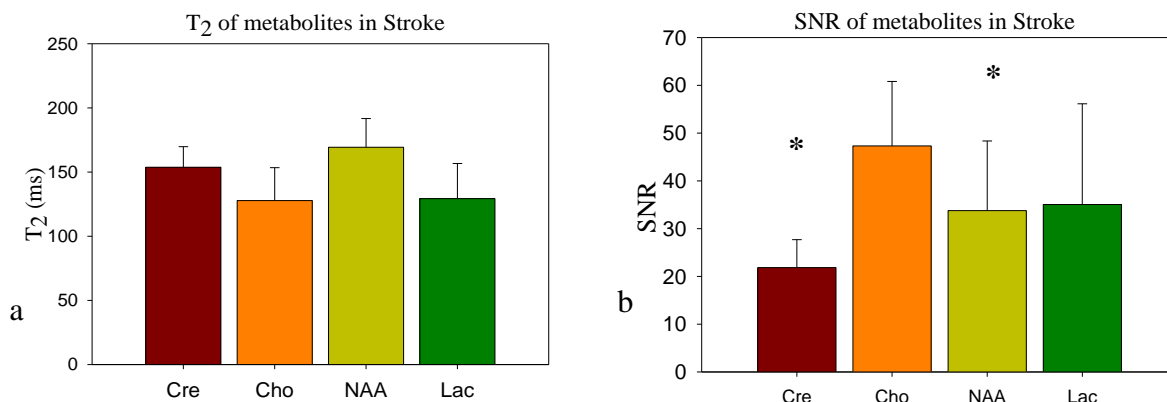


Figure 3: Graphs showing T₂ (a) and SNR (b) with the longest echo time (TE=58ms) of metabolites on the stroke side at (N=4). * Showing significant difference to the contralateral side (Student's t-test, p<0.05)

DISCUSSION

These findings suggest that the modified LRE sequence at high field increases the MRS sensitivity and can potentially be used as biomarkers for stroke recovery. The slow dephasing of the transverse spins will facilitate other quantitative studies of selectively excited metabolites (such as T₁ and diffusion) as a result of the preserved signal; furthermore, these long T₂s may offer the possibility of imaging metabolites with very good sensitivity. Furthermore, correlations between the lesion volume and metabolic T₂s are currently under investigation at different time points post-ischemia.

CONCLUSIONS

The results presented in this study strongly suggest that apparent T₂s at ultrahigh fields could provide unique insights into the complex chemistry and dynamic interactions of metabolites with their host tissues under ischemic processes.

ACKNOWLEDGMENTS

Work has been conducted in accordance with FSU Animal Care and User committee. Funding provided by the American Heart Association (10GRNT3860040), NSF (DMR-0084173), Florida State University and NHMFL, including a Visiting Scientist grant to N.S. (#12601). Support from EU's Marie Curie Action ITN METAFLUX (J-N Dumez, 264780) and a Helen and Kimmel Award (LF) are also appreciated.

REFERENCES

- [1] R. Fu, W. W. Brey, K. Shetty, P. Gor'kov, S. Saha, J. R. Long, S. C. Grant, E. Y. Chekmenev, J. Hu, Z. Gan, M. Sharma, F. Zhang, T. M. Logan, R. Bruschweiler, A. Edison, A. Blue, I. R. Dixon, W. D. Markiewicz and T. A. Cross, "Ultra-wide bore 900 MHz high-resolution NMR at the National High Magnetic Field Laboratory," *J. Magn. Reson.*, vol. 177, pp. 1-8, Nov, 2005.
- [2] N. Shemesh, J. N. Dumez and L. Frydman, "Longitudinal relaxation enhancement in 1H NMR spectroscopy of tissue metabolites via spectrally selective excitation," *Chemistry*, vol. 19, pp. 13002-13008, Sep 23, 2013.

- [3] J. T. Rosenberg, K. L. Sellgren, A. Sachi-Kocher, F. Calixto Bejarano, M. A. Baird, M. W. Davidson, T. Ma and S. C. Grant, "Magnetic resonance contrast and biological effects of intracellular superparamagnetic iron oxides on human mesenchymal stem cells with long-term culture and hypoxic exposure," *Cytotherapy*, vol. 15, pp. 307-322, Dec 17, 2013.

- [4] M. Garwood and L. DelaBarre, "The return of the frequency sweep: designing adiabatic pulses for contemporary NMR," *J. Magn. Reson.*, vol. 153, pp. 155-177, Dec, 2001.

- [5] J. Pauly, P. Le Roux, D. Nishimura and A. Macovski, "Parameter relations for the Shinnar-Le Roux selective excitation pulse design algorithm [NMR imaging]," *IEEE Trans. Med. Imaging*, vol. 10, pp. 53-65, 1991.

FRACTAL DIMENSION BASED DETECTION OF ARCHITECTURAL DISTORTION ANOMALIES IN MAMMOGRAPHY

Dr. Erol Sarigul, Dr. Kwabena Agyepong
Department of Advanced Technologies Alcorn State
University, Lorman, MS 39096

ABSTRACT

Breast cancer is one of the devastating, deadly diseases for women nowadays. Computer-aided detection (CAD) can assist radiologists in improving the mammographic screening process by suggesting mammographic regions with suspicion of malignancy. Architectural distortion (AD) is one of three common mammographic signs of breast cancer. The mammographic signs of AD can be easily confused due to the limitations of 2-D mammography and/or the effect of the superimposed tissues. As a result, AD is often missed in screening mammography by both radiologists and commercial CAD system. Although architectural distortion is such an important anomaly in breast cancer detection, very few detection algorithms have been developed in the literature. Fractal dimension based methods presents promising alternative to tackle problems in biomedical image processing field. The implemented algorithm analyzes and detects architectural distortion anomalies by utilizing fractal theory. Fractal analysis is a popular technique in biomedicine as increasingly more studies are being done to analyze many complex physical phenomena. The fractal dimension represents the rate of additional structural detail as the measurement scale changes. In mammography, normal breast parenchyma behaves as a fractal object. If any anomaly exist in breast parenchyma structure, that self-similarity behavior is disrupted and indication of anomaly. Therefore, the calculated fractal dimension for an image with architectural distortion should be lower than the fractal dimension of normal image. This algorithm has been developed to evaluate if fractal dimension can be applied effectively to indicate the presence of architectural distortion in screening mammograms. This paper presents the results in detail using publicly available DDSM mammography dataset.

Keywords: fractal dimension, mammography, architectural distortion, CAD, detection algorithm

INTRODUCTION

Architectural distortion (AD) is one of three common mammographic signs of breast cancer. The mammographic signs of AD can be easily confused due to the limitations of 2-D mammography and/or the effect of the superimposed tissues. Several descriptions of AD's appearance have been reported, including spiculations radiating from a point, focal retraction, and distorted parenchymal edge, etc. Furthermore, surgical scars, fibrocystic changes, and simply superimposition of breast tissues may generate similar parenchymal distortions. As a result, AD is often missed in screening mammography by both radiologists and commercial CAD system [1][2].

Despite extensive studies for masses and calcifications, the presence of architectural distortion is usually understudied and overlooked by radiologist. The detection of architectural distortion could be performed by identifying of more subtle sign of abnormality such as the presence of speculations and the distortion of the normal oriented texture pattern in the breast tissue, which could be easily missed by less experienced radiologist.

In the literature survey, it is reported that 50% of the architectural distortion cases is missed [2][3], and very few research papers for AD detection have been published [4][7] and very few reliable AD detection systems have been implemented or reported due to its difficulty to detect and to verify.

Therefore, there is still a big room to research on this challenging topic in terms of image processing, feature extraction, and the design of classifiers suited to AD detection and recognition.

DESCRIPTION OF THE DETECTION ALGORITHM

Fractal analysis is a popular technique in biomedicine as increasingly more studies are being done to analyze many complex physical phenomena. The fractal dimension represents the rate of additional structural detail as the measurement scale changes.

In mammography, normal breast parenchyma behaves as a fractal object. If any anomaly exist in breast parenchyma structure, that self-similarity behavior is disrupted and indication of anomaly. Therefore, the

calculated fractal dimension for an image with architectural distortion should be lower than the fractal dimension of normal image. The algorithm was implemented to evaluate if fractal dimension can be applied effectively to indicate the presence of architectural distortion in screening mammograms.

The algorithm utilizes circular average power spectrum method to estimate the fractal dimension. The steps of the algorithm are outlined in Figure 1. Region of Interest (ROI) image depicts region of interest which contains architectural distortion region which was cropped from full resolution mammography image. Initially, the two-dimensional power spectrum of the image is obtained using zero-padding and a carefully selected window function to ensure better estimation of the power spectrum. Radial hanning window is applied before power spectral analysis of ROI image. Finally, 2D power spectrum is transformed into one dimension by linear average along circle as a function of radial distance from zero frequency.



Figure 1. The outline of the algorithm

To find out fractal dimension, linear regression is applied on the whole frequency range to estimate the slope which is linearly related to the fractal dimension of the image. After linear regression analysis, the slope β is found then Equation (1) is used to find fractal dimension (FD).

$$FD = \frac{8 - \beta}{2} \quad (1)$$

To illustrate how fractal dimension based algorithm works, we chose one mammography case which contains architectural distortion. Figure 2(a) shows the MLO view of right breast for the selected case, the small inset picture shows zoomed out ROI region that is cropped and provided to the algorithm as input. The algorithm takes ROI image as input and determines its fractal dimension through power spectrum analysis. Power spectrum analysis provides image which is similar to Figure 2(b). Figure 2(c) presents circularly averaged 1D power spectrum plotted against the spatial log-frequency, linear line fitting regression is applied to find the slope of the graph. The slope of the fitted line determines the fractal dimension for that input image. If the calculated fractal dimension below certain threshold, it determines AD sign is present for given input image.

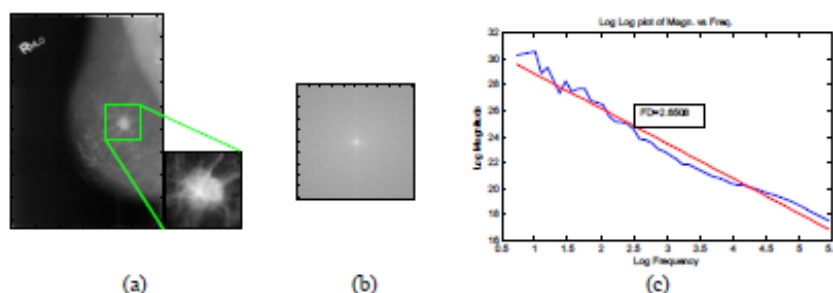


Figure 2. (a) Example mammography image that contains architectural distortion, green window shows selected ROI areas (inset picture shows zoomed out version). (b) its 2D power spectrum image after zero-padding and windowing using radial hanning window. (c) The circular averaged 1D power spectrum plotted on a log-log scale as a function of the spatial log frequency. The linear fit is also shown in (c) along with the calculated fractal dimension (FD=2.6508).

RESULTS AND DISCUSSION

The main database that we used for evaluation of the algorithm is the Digital Database for Screening Mammography (DDSM) [5][6]. DDSM is publicly available online database that contains a fair amount of architectural distortion screening mammograms to test our implemented algorithms. The mammograms were obtained in several hospital and they were transformed into digital domain (digitization) using three different digitizers. Our study used the DDSM cases using the LUMISYS and HOWTEK scanners at 50 μm and 43.5 μm per pixel respectively. For the both datasets, the pixel depth was 12 bits. We analyzed total of 108 digital mammography cases with annotated AD. Among those cases, 78 cases from the LUMISYS volumes and 30 cases from the HOWTEK volumes.

Each volume contains several architectural distortion cases in varying density, subtlety, and difficulty. Each case contains four different images (CC, MLO views for left and right breast) along with annotation information of detected image region. We manually cropped ROIs centered on the known location of each annotated AD case as input for the algorithm. Each extracted ROI is then analyzed by fractal algorithm to find fractal dimension of the ROI at hand. Extracted ROIs in both LUMISYS and HOWTEK volumes were analyzed by fractal algorithm, their corresponding fractal dimensions are calculated. Average fractal dimension for both volumes are presented in Table 1. Results were categorized based on breast density value to find out how breast density effect fractal dimension as well as detection performance.

Table 1. Average fractal dimension of AD ROIs, and normal ROIs and corresponding ROC area under curve (AUC) values for different breast parenchymal density for both LUMISYS and HOWTEK volumes.

	LUMISYS VOLUME			HOWTEK VOLUME		
	Average FD of AD ROIs	Average FD of normal ROIs	ROI AUC (AD versus normal)	Average FD of AD ROIs	Average FD of normal ROIs	ROI AUC (AD versus normal)
Total	2.559	2.777	0.83	2.539	2.761	0.85
Density 1	2.623	2.763	0.78	2.541	2.782	0.82
Density 2	2.637	2.689	0.71	2.556	2.789	0.77
Density 3	2.674	2.713	0.65	2.613	2.793	0.65

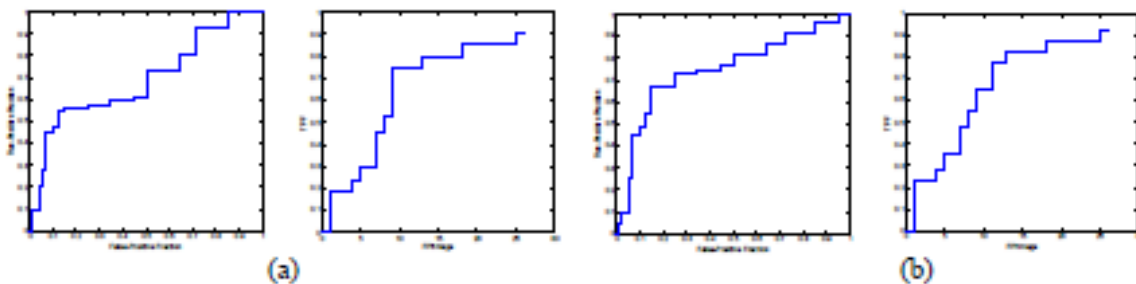


Figure 3. ROC and FROC curves for both LUMISYS (a) and HOWTEK volumes (b).

Figure 3. ROC and FROC curves for both LUMISYS (a) and HOWTEK volumes (b).

DISCUSSION AND CONCLUSION

We presented fractal based detection algorithm for detection of architectural distortion in mammography. Detection of architectural distortion requires complex texture analysis methods to detect anomaly texture in scanned/digital mammography. But analyzing image textures digitally still presents major hurdle despite ongoing research and studies on texture analysis. Fractal based methods provide promising tool for analysis of image texture. We utilized fractal based texture detection algorithm to analyze/detect presence of architectural distortion in ROI image, and we tested the performance of the algorithm against publicly available DDSM dataset. Our study reveals that fractal based image analysis could be utilized in processing mammography image for architectural distortion. But the algorithm shows sensitivity to breast density and detection performance degrades as breast density increases. One possible way is to fuse multiple algorithm output like, we found in recent literature [7] that attempt to fuse fractal dimension algorithm with gabor feature, phase portrait model.

ACKNOWLEDGMENTS

We thank Department of Defense by contract number W81XWH-06-1-0543 for funding of the research.

REFERENCES

- [1]. D.Kopans, Breast Imaging, 2nd ed. Philadelphia: Lippincott-Raven, 1998.
- [2]. Rangaraj M. Rangayyan, Fabio J. Ayres, J. E. Leo Desautels, A Review of Computer-Aided Diagnosis of Breast Cancer: Toward the Detection of Subtle Signs, Journal of The Franklin Institute, on-line.
- [3]. Scheider M.A, "Better detection: Improving our chances," in *Digital Mammography: Proc of the 5th Int. Workshop on Digital Mammography*, Toronto, Canada: Medical Physics Publishing, 2000, Pages 3-6.
- [4]. G.D. Tourassi, D.M. Delong, C.E. Floyd Jr., A study on the computerized fractal analysis of architectural distortion in screening mammograms, *Phys. Med. Biol.* 51 (5) (2006) 1299–1312.
- [5]. Michael Heath, Kevin Bowyer, Daniel Kopans, Richard Moore and W. Philip Kegelmeyer, The Digital Database for Screening Mammography in *Proceedings of the Fifth International Workshop on Digital Mammography*, M.J. Yaffe, ed., 212-218, Medical Physics Publishing, 2001. ISBN 1-930524-00-5.
- [6]. Michael Heath, Kevin Bowyer, Daniel Kopans, W. Philip Kegelmeyer, Richard Moore, Kyong Chang, and S. MunishKumaran, in *Digital Mammography*, "Current status of the Digital Database for Screening Mammography", Kluwer Academic Publishers, 1998; *Proceedings of the Fourth International Workshop on Digital Mammography*, pp 457-460.
- [7]. Rangaraj M. Rangayyan, Shormistha Prajna, Fabio Ayres, J. E. Leo Desautels, "Detection of architectural distortion in prior screening mammograms using Gabor filters, phase portraits, fractal dimension, and texture analysis", *Int. Journal CARS*, January 2008, Published online.

SMALL CLINIC DATA MANAGEMENT SYSTEM**Vikasini Chandrashekar, Ali Abu-El Humos, Hyunju Kim and Tzusheng Pei**

Department of Computer Science, Jackson State University, 1400 Lynch Street, Jackson, MS, U.S.A.

{ vikasini.chandrashekar@students., ali.a.humos@, hyunju.kim@, tzusheng.pei@jsums.edu**ABSTRACT**

Clinic Management systems are essential for tracking patient information, billing and scheduling appointments. Healthcare software systems are created to computerize manual operations in clinics. This Clinic Data Management system is tailored to manage day-to-day operations within a small clinic. It is a simple and cheap Desktop software solution that can be easily deployed and used. It identifies key information system characteristics and uses the software development life cycle to guide the implementation of the system as a proof-of-concept. Java Swing and MS Access technologies are used to create the software.

Keywords: Clinic Management Systems, Desktop software solution, Java Swing, MS Access

INTRODUCTION

Medical records are important to keep track of patient's medical history and current health status. Keeping track of medical records can be difficult, if the health information is captured on paper. As different people have different methods and forms of interpretation, it would be difficult to maintain the health information over a longer period of time. In addition, with the increased need of securing personal information, there is a critical need to maintain this information properly. With the development of many software solutions to maintain clinic records, better clinic data management is achieved. Data related to patient or doctor should be organized in a formal manner so it can be easily interpreted and maintained.

Clinic data management system is useful for the doctor, nurse, clerk and the clinic owner. It makes their lives easy and removes unnecessary human errors from their daily activities. It also helps in improved healthcare delivery by providing medical personnel with better data access and higher quality data. Moving patients' records from paper and physical filing systems to computers and their super storage capabilities creates great efficiencies for clinics. Even the federal government believes electronic record keeping is important, and it has invested its money and effort for that purpose [1].

In order for a software package to be considered a Clinic data management system, several characteristics have been identified that must be present [2]. The system should be user-friendly. It should be secure and affordable. Also, it should have an organized way of storing information, and finally, it should abide by the rules and regulations of the clinic.

The research has the following key contributions:

1. A comprehensive analysis of Clinic data management system tailored for small clinics.
2. The use of Java Swing and MS Access technologies to build a proof of concept Clinic data management system.

Related Work

Clinic data management systems are becoming more and more critical to the healthcare systems in the United States and many countries around the world.

Advancements in Technology make it more feasible and easier to store and retrieve medical records. Important information such as blood type, prescribed drugs, medical conditions and other aspects of medical history can be accounted for much more quickly with the use of Clinic data management system. Poorly maintained clinic management system could lead to masking of safety issues as discussed in Data management in clinical research journal [4].

Electronic Health Record (EHR) can save time at the doctor's office. At most, quick access to a specific patient's record can be lifesaving if an emergency occurs and answers to those questions are needed during the emergency decision-making process [1]. Tragic events like 9/11, Hurricane Katrina, and the California fires have showcased the benefits of digital record keeping. Those injured by any of the events mentioned and having an EHR were more easily treated and may have found better outcomes, than those for whom no EHRs were available [1].

Another benefit is safety. In the past, the way the doctor obtained the patient health history was by asking him in person each time a visit was made. Each time the patient visited a new doctor office, he had to fill out forms about his history, including previous surgeries, or the prescribed drugs on a regular basis. If the patient forgot a piece of

information, or if he did not write it down because it seemed unimportant to him, then the doctor did not have that piece of the patient medical puzzle to work with. The use of Electronic Health Records has resulted in saving money, not only the cost of paper and files folders, but also the cost of labor and space.

Simple Desktop applications eliminate the need of the Internet in contrast with the large number of web-based applications, which are prone to hacking and maintenance of servers. The developed Clinic data management software helps small clinics to maintain patient and doctor information, which can be accessed by the respective authorized persons. It can also be used for adding/modifying information of patient/doctor and scheduling appointments for patients.

REQUIREMENTS AND DESIGN SPECIFICATIONS

The purpose of this section is to show in detail the proposed Clinic data management system requirements and design. Clinic data management system is used to organize patient and doctor details. The application will allow the administrator (clerk) to enter the patient information like name, address, current problem, history etc. and doctor information like name, specialization, working hours etc. The administrator has also the privilege to schedule an appointment for the patient.

User Requirements Specification

1. Doctor/Administrator login to the application using their credentials username and password.
2. After login as a doctor, doctor can view and modify the patient information.
3. After login as an administrator, the administrator can do the following tasks:
 - a. Add new patient information.
 - b. Modify existing patient information.
 - c. Book appointment for patients.
 - d. Email appointment confirmation to the patient.
 - e. View patient information.
 - f. Add new doctor information.
 - g. Modify existing doctor information.
 - h. View doctor information.

Non-functional requirements represent constraints on the system, as well as other characteristics that are more difficult to verify than functional requirements. The following non-functional requirements have been identified:

Performance: As it is a simple desktop application with faster response time, one can search records of a particular patient/doctor within a short time, which is usually in couple of seconds.

Usability: The application is user-friendly and user interface is clean and intuitive. Features of the application shall be comparable to industry standard features.

3.2 Development Tools Interface Specification

Clinic data management system has to interact with Database entity to extract/insert information regarding patient/doctor.

The Database server used is Microsoft Access 2013 with JDBC data source on Windows XP/Windows 7. User Interface is developed using Java Swing technology.

CASE Workbench

CASE (Computer-Aided Software Engineering) tools workbench consists of:

1. Eclipse IDE for coding.
2. Project Folder for central repository.
3. MS Word for documentation.
4. UMLet for use cases, sequence and class diagrams.

Use Cases

Use cases are excellent means of depicting the functionality of a system in non-technical terms [3]. End users can look at use cases and understand what they represent intuitively. Use cases have been developed for Clinic data management system, which give a high-level understanding of what the system will be able to do. The use cases were developed from a collection of scenarios that describe user interaction with the system. Each use case has an accompanying narrative, as shown in Figure 1.

Design Goals

1. The system should have clear navigation.
2. The system should implement core functions as listed in requirements.
3. The system should have text based consistency throughout the application.

Design Methods

Standard pictorial models were used in creating the design documentation for this system [6]. A detailed entity relationship diagram depicts the layout of the Database design. Data flow diagrams are used to illustrate information flows and to give general overview of how to implement the described functionality. Sequence diagrams in Figures 2 and 3 are also used to explain the operations even further [5].

Also important is the diagram of the system decomposition based on the available use cases. This provides a necessary grouping of related functionality into system components, as shown in Figure 4.

User Interface Design

The user interface is designed with the following principles:

1. Explanation of features.
2. Error Handling.
3. Light weight User Interface for faster access.
4. Intuitive labels.

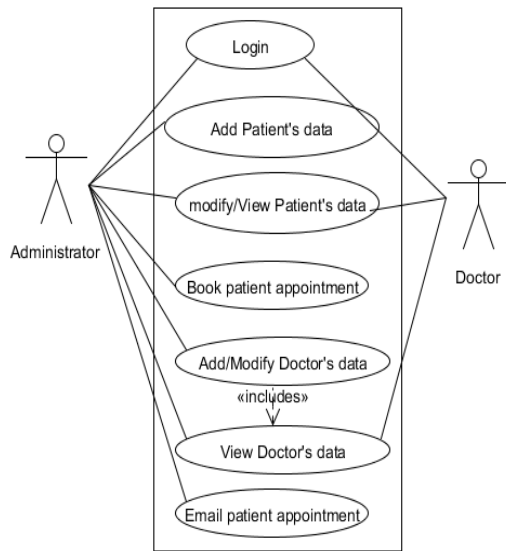


Figure1. Use Case Diagram

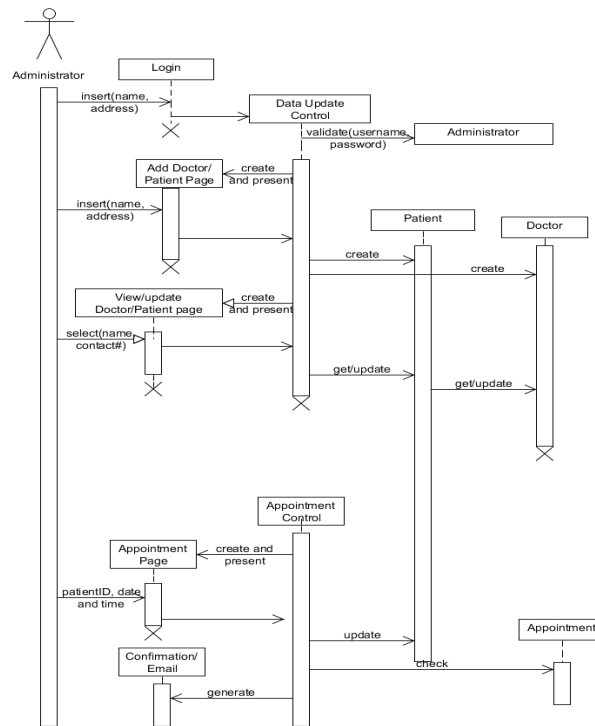


Figure 2. Sequence Diagram-Administrator login

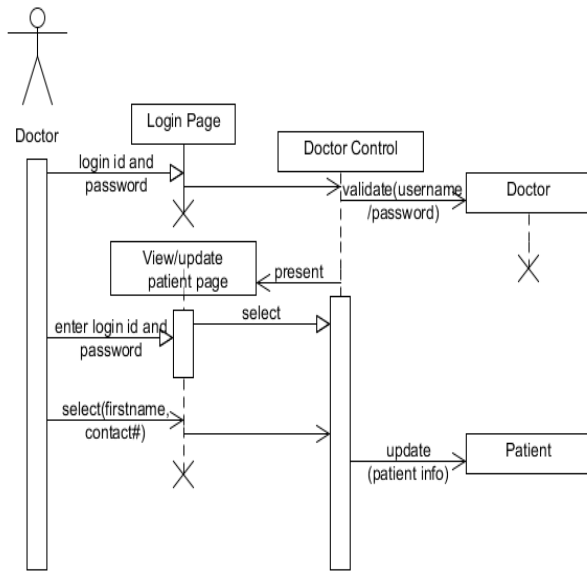


Figure 3. Sequence Diagram-Doctor login

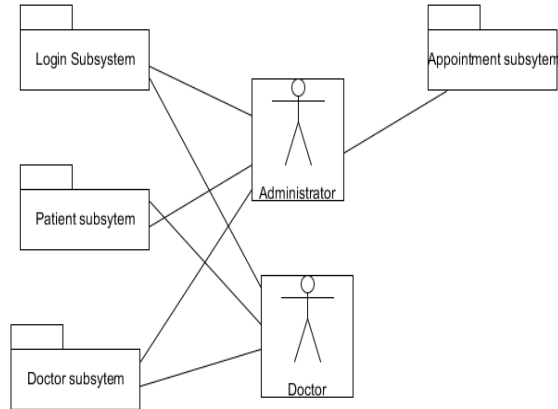


Figure 4. System Decomposition Diagram

5. Proper error messages for users on invalid actions/input performed by user. The resulting interface prototype consists of a navigation menu on the bottom. The color scheme consists of black text and gray buttons. Few diagrams of the application are shown below.



Figure 5. Application Diagram: Add patient window

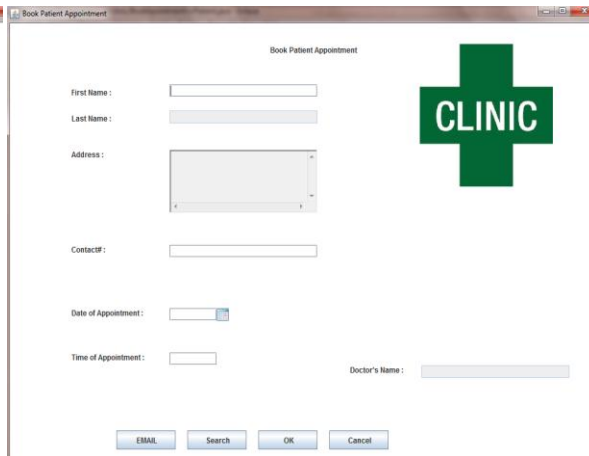


Figure 6. Application Diagram: Appointments

CONCLUSION AND FUTURE WORK

There is a demand to maintain effective data management system in healthcare industry. The problem was the need for organized data management system for small clinics to build a comprehensive system, which includes high availability of information, storing data in secure environment, and ease of use, all at a low cost. This work offers proof-of-concept system that satisfies these needs.

There is a potential for future work. Billing system could be developed to generate bills and store payment information. This concept consists of billing logic and integration with payment systems, and association Database tables. This concept could be implemented using Java swing, or similar technologies. Security features such as manual back up data, protecting system against brute force attack and data protection has to be incorporated in an efficient way too.

REFERENCES

- [1] "The Benefits of Electronic Health Records (EHRs)" available from <http://patients.about.com/od/electronicpatientrecords/a/EMRbenefits.htm>. Internet; accessed September 30, 2013
- [2] Reddy M, Pratt W, Dourish P, and Shabot M M. "Sociotechnical Requirements Analysis for Clinical Systems". Schattauer GmbH, 2003.
- [3] Jacobson I, Christerson M, Jonsson P, and Overgaard G. "Object Oriented Software Engineering: a use case driven approach". Addison Wesley, 1992.
- [4] Krishnankutty B. et al. "Data Management in Clinic Research". Indian Journal of Pharmacology, March 2012.
- [5] "UML basics: The sequence diagram" available from <http://www.ibm.com/developerworks/rational/library/3101.html>. Internet; accessed October 28, 2013
- [6] "Free UML Tool for Fast UML Diagrams" available from www.umlet.com. Internet; accessed October 28, 2013

STRESS-STRAIN ALTERATIONS IN THE MYOCARDIUM INDUCED BY MICROGRAVITY: A FINITE ELEMENT MODEL OF THE HEART

Richard L. Summers, Weston Smith², Ryan Gilbrech², Jun Liao², Benjamin C. Weed², Sourav Patnaik

Department of Emergency Medicine, University of Mississippi Medical Center, Jackson, Mississippi 39216
Cardiovascular Tissue Biomechanics Laboratory, Mississippi State University, Mississippi State, MS 39762.

ABSTRACT

Previous studies during have demonstrated a loss of ventricular mass after prolonged exposure to microgravity that is associated with changes in cardiac function. By Laplace's law, the geometry of the ventricle is important in determining the segmental wall stress. If microgravity exposure results in variations in the ventricular geometry then these changes could cause adjustments in the normal myocardial stress/strain patterns that might induce cardiac remodeling during extended spaceflights. This study analyzes the theoretical impact of microgravity on changes in the geometric conformation and stress strain patterns of a finite element mesh model (FEM) created from the 3-dimensional geometry of the left ventricle (LV) and attributed with material properties consistent with myocardial tissue. The Geometric Aspect Ratios (GAR, length to width quotient) of the LV were compared during simulations of the upright diastolic position in Earth's gravity and in microgravity. The application of microgravity conditions to the FEM model resulted in a 3.65% lower GAR of the LV as compared to that calculated for Earth's gravity. The stress and strain patterns of the myocardial wall were also modified especially around the base of the heart. This finding suggests that microgravity exposure could potentially result in changes in the ventricular radius of curvature and alter the segmental myocardial wall stress.

INTRODUCTION

physiologic and anatomic adaptations to microgravity exposure are considered one of the greatest barriers for human space exploration.¹ One of the most concerning of these changes is the 10-15% diminution in left ventricular mass that has been observed in astronauts.^{2,3,4} While some of these recorded changes in the myocardial volume can be attributed to simple fluid shifts, there appears to be a true loss of ventricular muscle mass when the exposure to microgravity is prolonged.^{3,5,6} The mechanism responsible for this loss of myocardial muscle is uncertain. While intuitively it could be assumed that the heart would work less in microgravity and result in an attrition of muscle mass, there is no convincing evidence to support this notion. Commonly measured hemodynamic parameters such as heart rate, blood pressure and cardiac output appear to be clinically near normal during spaceflight so it has been difficult to determine a driving force for the observed degree of cardiac atrophy.^{7,8,9,10,11}

A recent study demonstrated a linear relationship between the sphericity in the geometry of the left ventricular chamber as measured by echocardiography and the amount of gravitational forces.¹² The ventricles can be considered as fluid filled malleable vessels that are susceptible to the usual influences of physical forces. During conditions of free fall without the downward pull of gravitational forces, the ventricular chambers are thought to tend to become more spherical in their geometric conformation due to an equilibration of wall surface tensions.

The significance of this finding becomes clear when the resultant differences in myocardial wall tension forces induced by these changes are considered. In accordance with Laplace's law, the geometry of the ventricle is an important factor determining tension and segmental wall stress.^{13,14} The wall stress of any segment of the myocardium is therefore highly dependent upon the local geometry, particularly the radii of curvature of the ventricle wall at that location.¹⁵ It is thought that the ventricular myocardium hypertrophies or atrophies in an attempt to normalize wall stress and thereby optimize cardiac function.¹⁶ Such changes have been observed clinically in patients with valvular disease and other chronic pathologic conditions where the ventricles assume a more spherical shape.^{13,17,18} If microgravity exposure primarily induces alterations in local ventricular geometry and wall stress through conformational changes in the overall shape of the heart, then a general remodeling of myocardium might also occur. This mechanism could provide a possible explanation for the physiologic adaptation of the heart to its gravitational environment that is based upon simple physical forces as described by Laplace's Law. In this study a finite element model (FEM) of the left ventricle (LV) attributed with material properties consistent with myocardial tissue was used to examine the theoretical impact of microgravity on changes in the overall geometric conformation of the heart.

METHODS

Mimics, 3-matic software and Simpleware software were used to create a mesh model of the heart for finite element analysis. Three different mesh models of varying qualities (voxel mesh, low tetrahedral, and normal tetrahedral) were exported to ABAQUS for comparison of the finite element analyses. The heart tissue was considered as an isotropic material for simplification and myocardial mechanical material properties were incorporated into the elements of the mesh. The biaxial mechanical properties of tissue extensibility and tensile modulus used in the study were derived from published the literature.¹⁹ These properties have been characterized with a biaxial mechanical testing system in a square specimen trimmed from a native porcine myocardium engineered cardiac patch. In this preparation, biaxial loading was applied along the muscle scaffold fiber direction and cross-fiber directions of the specimen.

A series of simulation studies were carried out investigating changes in heart shape deformation in earth's gravity and during microgravity exposure. In the simulations, the model heart was situated in the anatomical position as if the person were standing, and the force of gravity (9.81 m/s^2) and microgravity ($1.0\text{e-}^6 \text{ m/s}^2$) were implemented vertically downward on the heart. The heart was also considered in the unpressurized state and without blood filling in the chamber in order to discern the independent impact of gravity on the heart tissue. The length and width of the left ventricle were recorded to calculate geometric aspect ratios (GAR) as an indicator of relative sphericity (equation below) and to assess the extent of global heart shape deformation in gravity and microgravity.¹² $\text{GAR} = \text{LV length} / \text{LV width}$. The LV sphericity index was calculated by dividing the LV maximal long-axis internal dimension by the maximal short-axis internal dimension at end-diastole. The percent change in the FEM GAR determined during simulations transitioning from the earth's gravity to microgravity was calculated.

RESULTS

Table 1 details the changes in values in length and width of the unpressurized left ventricle determined in the FEM analysis for both the microgravity and Earth's gravity states. The length of the unloaded ventricle is found to retract by 3.005% while the width expands slightly (0.55%). These changes resulted in an overall increase in the geometric aspect ratio of 3.65% as a global measure of the extent of alteration in the shape of the heart.

Gravity Condition	Length (mm)	Width (mm)	GAR
Microgravity	135	62.3122	2.16
Earth's Gravity	139.0563	61.9484	2.24
Percent Change	-3.005 %	+0.55 %	3.65 %

Table 1. This table depicts the values for changes in LV length,width and geometric aspect ratio (GAR) determined in the FEM analysis for both the unloaded (microgravity - $1.0\text{e-}^6 \text{ m/s}^2$) and loaded (Earth's gravity - 9.81 m/s^2) states. The length is found to retract by over 3% while the width expands slightly when the heart is unloaded. These changes results in an overall increased in the geometric aspect ratio of 3.65%.

DISCUSSION

In the current study, we provide a theoretical analysis using a FEM of the heart to explore the feasibility that a microgravity environment might generate conformational changes in the heart. The intent of the analysis is to provide support for the hypothesis that microgravity induced shape changes in the LV and their resultant changes in myocardial wall stress are a potential mechanism leading to a diminution in LV mass in astronauts. The mechanisms responsible for the changes in LV mass seen during spaceflight are probably multifactorial and can involve variations in workload, sympathetic inputs and a number of other influences that act synergistically. However, the complexity of this problem could potentially benefit from the perspective of a simple theoretical framework employing basic physical factors from which to develop a more comprehensive mechanistic hypothesis.

There is considerable evidence indicating that there is a direct relationship between ventricular wall stress and the extent of myocardial hypertrophy in chronic pathologic states such as hypertension and cardiac valvular

disease.^{13,17,18,20} Conventional wisdom suggests that the ventricular myocardium hypertrophies in an attempt to normalize wall stress and thereby optimize cardiac function.¹⁶ Since hypertrophy and atrophy of muscle begins at the cellular level it can be assumed that the stress factors driving these morphologic changes are also of a regional or segmental nature. The wall stress of any segment of the myocardium is highly dependent upon the local geometry as characterized by the radii of curvature of the ventricle wall at that location.^{14,15} Decrease in the segmental wall stress has been observed clinically in patients with valvular disease and other chronic pathologic conditions where the ventricles assume a more spherical shape.^{13,21,22} The current analysis indicates that microgravity could induce similar alterations in this local wall geometry through changes to the overall shape of the heart. If such conformational changes are found to occur during spaceflight, then this could provide a driving mechanism for the observed cardiac remodeling that is based upon simple physical forces as described by Laplace's Law.

There are several limitations to this study that should be noted. The material properties used for the cardiac tissue were derived from a porcine study performed on earth and may not accurately reflect those of the human heart in space. The FEM analysis also examined the effect of gravity on the heart in isolation from the rest of the body. However, the 3.65% change in GAR found in the current study seems reasonable when compared to the 5.3% change noted in a small sample of astronauts during spaceflight.¹² The intent of the present study was simply to determine if a significant conformational change in the global heart shape could be attributed to a loss of gravity influence alone. Such a shape modification and the resultant changes in the ventricular wall regional radii of curvature are central to the proposed hypothesis of a cardiac remodeling directly induced by wall stress changes.

The significance of a 3-5% shape change toward sphericity as it relates to cardiac remodeling is uncertain. A similar analysis by Herrold has predicted that clinically important ventricular remodeling can be induced by comparable spherical changes resulting from conditions of chronic volume overload.²³ Such remodeling is also a common occurrence in other cardiac pathologies in which the shape of the heart is changed.^{18,20,22} There may also be a direct and independent impact on global cardiac function. There is evidence suggesting that the shape of the heart is important in determining the efficiency of the twisting motion of the ventricles, particularly as it relates to their diastolic function.²⁴ Furthermore, recent spaceflight and long-term head down tilt bed rest studies used to simulate microgravity exposure have likewise demonstrated impairments in diastolic functioning due to inefficiencies with untwisting.^{25,26} Systolic function may also be dependent upon regional and global wall curvatures.²⁷ Myocardial shape changes and the possible resultant remodeling have also been implicated in the development of cardiac dysrhythmias.^{28,29,30} Such dysrhythmias have been observed during spaceflight.⁵

CONCLUSION

It has been suggested that the loss of ventricular mass in astronauts may be a result of changes in heart shape during microgravity exposure.^{3,12} Currently there is no direct causal evidence to support a conclusion that cardiac conformational changes during spaceflight result in reductions in LV mass or alter cardiac function. However, in accordance with Laplace's law, the geometry of the heart and its impact on the segmental wall stress should act as a driving force for cardiac remodeling. This study examined the theoretical impact of microgravity exposure on the shape of the LV.¹³ Changes in ventricular sphericity associated with changes in the radius of curvature of the myocardial wall of an FEM model were observed during simulated microgravity. Further study is required to link the observed loss of myocardial mass in astronauts to accompanying ventricular conformational changes.

REFERENCES

1. Summers RL, Johnston SL, Marshburn TH, Williams DR. "Emergencies in Space." *Ann Emerg Med* 46(02): 2005; 177-184.
2. Perhonen MA, Franco F, Lane LD, Buckey JC, Blomqvist CG, Zerwekh JE, Peshock RM, Weatherall PT, and Levine BD. "Cardiac atrophy after bed rest and spaceflight." *J Appl Physiol* 2001;91: 645-653.
3. Summers RL, Martin DS, Meck JV, Coleman TG. "Mechanism of Spaceflight Induced Changes in Left Ventricular Mass." *Am J Card* 2005; 95:1128-1130.
4. Goldstein MA, Edwards RJ, and Schroeter JP. "Cardiac morphology after conditions of microgravity during COSMOS 2044." *J Appl Physiol* 73:94S-100S, 1992.

5. Platts SH, Stenger M, Phillips T, Arzeno N, Brown AK, Levine B, Summers RL. "Risk of Cardiac Rhythm Problems During Spaceflight." *NASA's Human Research Program Evidence Books*: NASA-TP:2010: 1-17. Peer Review by IOM: ISBN: 0-309-12224-4.
6. Platts SH, Stenger M, Phillips T, Arzeno N, Summers RL. "Risk of Orthostatic Intolerance During Reexposure to Gravity." *NASA's Human Research Program Evidence Books*, NASA Document; 2010: HRP-47072. Peer Review by IOM: ISBN: 0-309-12224-4.
7. A Karemaker JM, Gisolf J, Stok WJ, van Montfrans GA. "24-hr blood pressure in HDT-bed rest and short-lasting space flight." *J Gravit Physiol*. 2007;14:49-50.
8. Baeovsky RM, Baranov VM, Funtova II, Diedrich A, Pashenko AV, Chernikova AG, Drescher J, Jordan J, Tank J. "Autonomic cardiovascular and respiratory control during prolonged spaceflights aboard the International Space Station." *J Appl Physiol*. 2007;103:156-61.
9. Verbanck S, Larsson H, Linnarsson D, Prisk GK, West JB, Paiva M. "Pulmonary tissue volume, cardiac output, and diffusing capacity in sustained microgravity." *J Appl Physiol*. 1997;83:810-6.
10. Gazenko OG, Shulzhenko EB, Turchaninova VF, Egorov AD. "Central and regional hemodynamics in prolonged space flights." *Acta Astronaut* 1988;17:173-9.
11. Fritsch-Yelle JM, Charles JB, Jones MM, Wood ML. "Microgravity decreases heart rate and arterial pressure in humans." *J Appl Physiol* 1996;80:910-4.
12. Summers RL, Martin DS, SH Platts, Mercado-Young R, Coleman TG, Kassemi M. "Ventricular Chamber Sphericity During Spaceflight and Parabolic Flight Intervals of Less Than 1 G." *Aviat Space Environ Med* 2010;81:506-510.
13. Gould KL, Lipscomb K, Hamilton GW, Kennedy JW. "Relation of left ventricular shape, function and wall stress in man." *Am J Cardiol*. 1974;34:627-34.
14. Yin FC. "Ventricular wall stress." *Circ Res* 1981;49:829-42.
15. Regen DM, Anversa P, Capasso JM. "Segmental calculation of left ventricular wall stresses." *Am J Physiol*. 1993;264:H1411-21.
16. Bader HS. "The stimulus to hypertrophy of the myocardium." *Circulation*. 1964;30:128-36.
17. Hood WP Jr, Rackley CE, Rolett EL. "Wall stress in the normal and hypertrophied human left ventricle." *Am J Cardiol*. 1968;22:550-8.
18. Barletta G, Di Donato M, Baroni M, Fantini A, Fantini F. "Left ventricular remodeling in chronic aortic regurgitation." *Int J Card Imaging* 1993;9:185-93.
19. Wang B, Borazjani A, Tahai M, Curry AL, Simionescu DT, Guan J, To F, Elder SH, Liao J. "Fabrication of cardiac patch with decellularized porcine myocardial scaffold and bone marrow mononuclear cells." *J Biomed Mater Res A*. 2010;94(4):1100-10.
20. Abi-Samra F, Fouad FM, and Tarazi RC. "Determinants of left ventricular hypertrophy and function in hypertensive patients. An echocardiographic study." *Am J Med* 1983;75:26-33.
21. Gibson DG, Brown DJ. "Continuous assessment of left ventricular shape in man." *Br Heart J*. 1975;37:904-910.
22. Yamazoe M, Tamura Y, Matsubara T, Igarashi Y, Tanabe Y, et al. "Circularity index of left ventricular shape in the assessment of heart disease." *J Cardiol*. 199;26:99-105.
23. Herrold, E.M.; Carter, J.N.; Borer, J.S. "Volume overload related shape change limits mass increase with wall thickening but only minimally reduces wall stress." *Computers in Cardiology* 1992; 11:287 – 290.
24. van Dalen BM, Kauer F, Vletter WB, Soliman OI, van der Zwaan HB, Ten Cate FJ, Geleijnse ML. "Influence of cardiac shape on left ventricular twist." *J Appl Physiol*. 2010;108(1):146-51.
25. Dorfman TA, Rosen BD, Perhonen MA, Tillery T, McColl R, Peshock RM, Levine BD. "Diastolic suction is impaired by bed rest: MRI tagging studies of diastolic untwisting." *J Appl Physiol*. 2008;104(4):1037-44.
26. Summers RL, Coleman TG, Platts S. "Systems Analysis of the Mechanisms of Cardiac Diastolic Function Changes After Microgravity Exposure." *Acta Astronautica* 2008;63:722-726.

27. Salgo IS, Tsang W, Ackerman W, Ahmad H, Chandra S, Cardinale M, Lang RM. "Geometric assessment of regional left ventricular remodeling by three-dimensional echocardiographic shape analysis correlates with left ventricular function." *J Am Soc Echocardiogr*. 2012;25(1):80-8.
28. Markowitz SM, Lewen JM, Wiggenhorn CJ, Abraham WT, Stein KM, Iwai S, Lerman BB. Relationship of reverse anatomical remodeling and ventricular arrhythmias after cardiac resynchronization. *J Cardiovasc Electrophysiol*. 2009;20(3):293-8.
29. Choi HF, Rademakers FE, Claus P. Left-ventricular shape determines intramyocardial mechanical heterogeneity. *Am J Physiol Heart Circ Physiol*. 2011;301(6):H2351-61.
30. Kerckhoffs RC, Faris OP, Bovendeerd PH, Prinzen FW, Smits K, McVeigh ER, Arts T. Timing of depolarization and contraction in the paced canine left ventricle: model and experiment. *J Cardiovasc Electrophysiol*. 2003;14(10 Suppl):S188-95.

DEVELOPMENT OF A NOVEL BENCH-TOP MODEL TO MIMIC THE LOWER EXTREMITY ARTERIES AND STENT MECHANICS

Nicholas Carroll and Saami K. Yazdani

Department of Mechanical Engineering
150 Jaguar Drive
Mobile, AL 36688

ABSTRACT

Atherosclerosis is the leading cause of heart attacks and strokes in the U.S., accounting for up to 800,000 deaths annually. Metallic stents are the number one choice to re-open clogged arteries but problems caused by stent fracturing are hindering their effectiveness. This is especially common in the superficial femoral artery and is reported to be more widespread of a problem in this area of the body than others. This high rate of fracturing is believed to be caused by the unique combination of biomechanical forces that the artery experiences in day to day activities. Although standalone failure tests are performed quite regularly on stents, the problem still continues. A different approach is needed to identify the specific cause of failure in these stents and its impact on the biological performance. Therefore, the purpose of this project was to design and build a medical testing device that can subject a stent to the axial and torsional biomechanical forces experienced by stents deployed in femoral arteries. The system was developed by utilizing a linear actuator to mimic the axial forces, and a servo motor to mimic torsional forces. All of these components were controlled using a custom LABVIEW© interface. The system is capable of linear movement at a rate of one inch per second and can deliver torsional force at any angle between zero and ninety degrees. The developed novel system is thus capable of mimicking a wide range of motion to better elucidate the relationship between biomechanical factors and device durability.

Keywords: Stent Mechanics, Axial, Torsional, Superficial Femoral Artery

INTRODUCTION

With atherosclerosis accounting for 1 in 4 of every death in the U.S. [1], the need for rigorous testing on stents deployed in the superficial femoral artery (SFA) is a real and relevant concern for patients and the doctors implementing this technology. As stated by Dr. Muller-Hulsbeck, “although it may be difficult to reproduce the dynamics of the SFA, it is imperative that improved standards should be developed in all aspects of nitinol stent processing and testing to better identify the failure modes of SFA stenting.”[2]. It is the intent of this undertaking to as accurately as possible recreate the dynamic environment that is experienced by a stent installed in the SFA. Products have been designed that subject bare stents to axial and torsional stresses, such as the Bose ElectroForce® Peripheral Stent Test Instrument and other in-house systems [3], however it is our belief that a more accurate in vivo environment is needed to truly understand the efficacy of the product. The novelty of our approach is to build a device that tests these biomechanical forces while the stent is installed in an artificially manufactured artery cultured with live cells. It is also imperative that our design be able to perform these tests while enclosed inside of an incubator.

METHODS

Design of the Novel Device

SolidWorks 3D CAD software (Dassault Systems) was chosen to design a device, **Fig. 1**, which incorporated both axial and torsional elements, accurately modeling the biomechanical forces experienced by the artery in daily motion. This software proved useful in ensuring snug fittings and suitable clearances for moving parts before the build. The hardware chosen was a combination of stepper motors and stepper drives. Stepper motors are DC electric motors that allow the rotation of the shaft to be subdivided into precise steps. This subdivision allows for smooth travel and more precise control over positioning of the motor. Stepper drives convert the signals sent by the controller into electrical pulses. Each electrical pulse equals one step of the motor. The axial component of the system was realized by using a combination of a “Digit” linear actuator (Model D-A.25-HT23-4-2NO-BR/EC4, Ultra

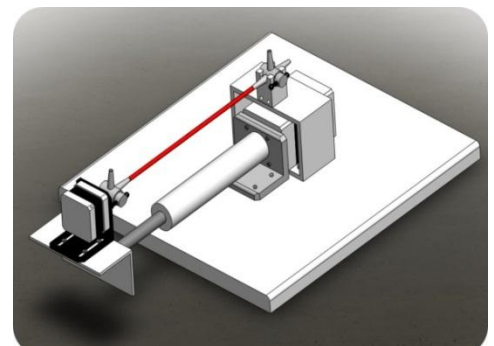
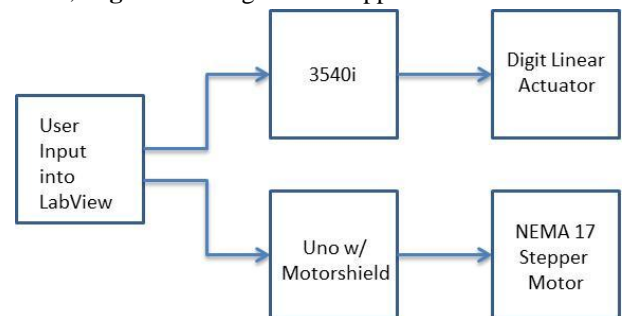


Fig. 1 3-D model of the testing device.

Motion LLC.) and a stepper drive (Model 3540i, Applied Motion Products, Inc.). A linear actuator is a stepper motor that converts the rotation of the motor shaft into linear motion by using a lead screw. The “Digit” has a lead screw with a pitch of 0.25 inches/revolution (in/rev), a stroke length of 4 inches, and a stepper motor with a step angle of 1.8 degrees (200 steps/rev). The 3540i stepper driver further enhanced the smooth travel of the lead screw by subdividing the step size to 20,000 steps/rev. The torsional component of the build was realized by using an Arduino Uno (arduino.cc) coupled with an Adafruit (Adafruit Industries) motor shield to control a NEMA 17 stepper motor with a step angle of 1.8 degrees (200 steps/rev).

Software Interface and Control

LabView, a graphical programming language that utilizes a block diagram scheme connected by wires to design a program, was used as the software interface for this project. The stepper drives are connected to the software by means of serial communication with a baud rate of 9600. The process begins with the user entering the desired movement parameters, for each motor, into the LabView control panel. These commands are then interpreted by the program and sent, in parallel, to the stepper drivers. The stepper driver then processes the command and executes the desired movement with the connected motor, **Fig. 2**. Although both stepper drives are capable of executing loops stored in their internal memory, the advantage gained in using LabView as the control is the ability to quickly introduce changes in speed and range of movement. Being able to accurately model the wide range of motion experienced by the stent when installed in the artery is a cornerstone of the success of this project.



RESULTS

Hardware

The assembled device, **Fig. 3**, demonstrates the successful design and their ability to support a bioreactor. The design was also successful in accomplishing the goal of being small enough to be operated from within an incubator, **Fig. 4**. This feature is key for recreation of the environment experienced by the deployed stent. Initial testing of the electrical components have shown that the device is able to perform the necessary range of movements needed to mimic the typical SFA in motion as indicated in the introduction. While traveling the 1 in/sec back and forth trajectory the motor controlling the linear actuator is being powered by 24 Volts and utilizing the full 20,000 steps/rev subdivision offered by the 3540i for smooth motion. The motor controlling the torsional movement of the artery is powered by 3.3 Volts. It has shown consistency in its movement and ability to stop at all predetermined angles between 0° and 90°.

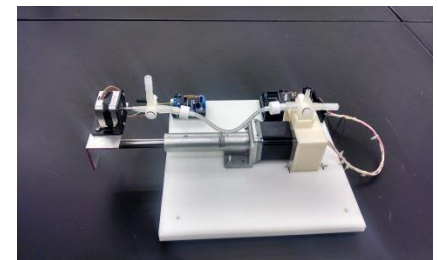


Fig. 3 Assembled Device

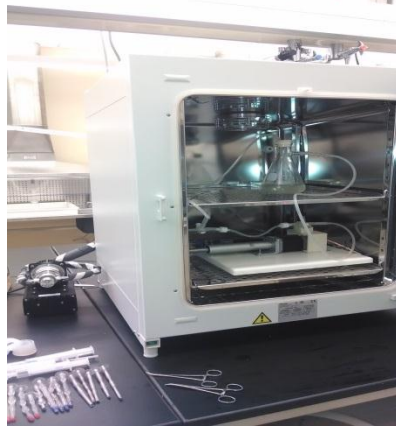


Fig. 4 Device installed inside of an incubator

Software

For initial testing of the device the native software programs supplied with their respective stepper drivers were used. The 3540i uses SI Programmer, screenshot seen in **Fig. 5**, and the Uno uses the native Arduino development environment, a variation on C-based language, also seen in **Fig. 5**. The motion parameters were entered into their respective interfaces and downloaded to the memory of the stepper drivers for testing. Both drives were successfully programmed to perform the movements required.

Fig. 5 Depictions of the programming environments.



DISCUSSION

We have successfully completed the design and build of an in vitro system that is capable of testing the biomechanical forces acting upon the stent in vivo. The chosen hardware allowed for the realization of a system that is small enough to perform its tasks while installed inside of an incubator and still have the flexibility to move through a wide range of motions smoothly and precisely. The precise ability of the system was further aided by the use of the stepper drives and the increased step subdivisions that they offered.

A current major limitation exists in current systems in their ability to study device fracture and the biological effects in vitro. Stents are known to fracture during varying hemodynamic conditions and the systems currently offered have been unable to address these conditions while testing mechanical stressors. With the system presented here it is evident that no such limitations will be imposed upon studies performed with this device. The ability to incorporate cells will add a new and exciting dimension to the scope of this research and allow for greater insights, and ultimately improvements, in stent design and use.

Though these initial studies have shown our capability to accomplish the goals laid out in the beginning, there is still more work to be done. From this point forward time will be spent in developing a comprehensive LabView (National Instruments) software program that will allow the user to test changing conditions with real-time control of the motion parameters. This will bring our project even closer to the recreation of truly in vivo like conditions while performing in vitro experiments.

CONCLUSION

With the undeniable need of more standardized testing of stent mechanics having been established, it has been the aim of this study to provide an answer to that call. With the system presented within this report it will be possible to not only study the effects of forces on the stent but also to analyze the real-time consequences of events like fractures on the vascular system. This will ultimately prove an indispensable tool for all medical professionals, and stent manufacturers, in their efforts to provide safe, reliable relief from such a deadly disease as atherosclerosis.

ACKNOWLEDGMENTS

We gratefully acknowledge the expert technical assistance of John Lion and Terry Pritchett in the machining of parts, and Stan Cotton with software installation

REFERENCES

- 1 M. V. L. R. E. J. B. J. D. B. M. J. B. S. D. E. S. F. C. S. F. S. F. H. J. F. C. G. S. M. H. J. A. H. V. J. H. Alan S. Go, "AHA Statistical Update: Heart Disease and Stroke Statistics—2014 Update: A Report From the American Heart Association," *Circulation*, vol. cir.0000441139.02102.80, pp. 129:e28-e292, 2014.
- 2 P. J. S. N. C. H. Y. M. H. a. T. J. Stefan Müller-Hülsbeck, "Comparison of Second-Generation Stents for Application in the Superficial Femoral Artery: An In Vitro Evaluation Focusing on Stent Design," *Journal of Endovascular Therapy*, vol. 17, no. 6, pp. 767-776, 2010.
- 3 H. B. S. K. O. M. B. S. S. L. B. S. Alexander Nikanorov, "Fracture of self-expanding nitinol stents stressed in vitro under simulated intravascular conditions," *Journal of Vascular Surgery*, vol. 48, no. 2, pp. 435-440, 2008.

TARGETED THERAPY TO TREAT CARDIOVASCULAR CALCIFICATION IN ESRD PATIENTS**Janice Cunningham, C. LaShan Simpson, Erick S. Vasquez, Keisha B. Walters**

PO Box 9632

Mississippi State, MS 39762

ABSTRACT

Vascular disease is the leading cause of death in populations suffering from advanced stages of chronic kidney disease (CKD). Cardiovascular calcification increases the risk of cardiac morbidity and mortality in sixty to eighty percent of dialysis patients with end-stage-renal-disease (ESRD). This paper will focus on developing a drug delivery system to de-mineralize calcified regions of the artery wall that cause arteriosclerosis in ESRD patients and provide preventative therapy to dialysis patients with early stages of CKD.

We are proposing a targeted drug therapy to reverse vascular calcification in patients with ESRD. A pH responsive polymersome will be developed for intravenous administration to carry, and release Fetuin-A to sites of calcification by binding to matrix (Gla) proteins (MGPs) when blood pH drops below 7.4. Fetuin-A, an inhibitor of extra-skeletal calcification, is made to solubilize calcium-phosphate minerals. MGPs inhibit soft-tissue mineralization and are up-regulated when pH falls below 7.4. Recruited to sites of calcification MGPs accumulate in the calcified lesions. Surface receptors on the polymersome will bind to MGPs present in calcified regions causing the targeted release of the drug Fetuin-A.

Our drug delivery system aims to improve the life expectancy of dialysis patients, especially non-transplant candidates and those on a transplant waiting list. Re-establishing physiological levels of Fetuin-A with targeted drug-delivery should reverse the pathological calcification in ESRD patients. In addition to providing a therapy for arteriosclerosis we aim to actively reduce the risk of cardiac morbidity and mortality associated with vascular calcification in dialysis patients with early stages of CKD.

Keywords: vascular calcification, arteriosclerosis, end-stage-renal-disease, Fetuin-A, matrix Gla proteins, chronic kidney disease, polymersome

INTRODUCTION

Cardiovascular disease (CVD) is the leading cause of mortality for patients at all stages of chronic kidney disease (CKD) [1]. Patients with CKD are more likely to die of cardiac related health events than to even reach late stage CKD, or end-stage renal disease (ESRD) [1]. There is clinical evidence that dialysis patients with ESRD are at higher risk of developing cardiovascular disease and cardiac related mortality due to the formation of vascular calcification (VC) of the arterial walls [2]. The most severe type of VC observed in ESRD patients is that of the medial tissue layer, also known as arteriosclerosis [3]. Variations between moderate to severe arteriosclerosis is found in sixty to eighty percent of dialysis patients [4]. Arterial medial calcification directly affects the vascular smooth muscle cells (VSMCs) by calcium-phosphate mineral growth between the cells matrixes, thus hardening the medial layer which results in a loss of compliance of the artery. This arterial wall stiffening is associated with an increase in cardiac workload and elevated systolic pressure both of which are risk factors for increased cardiac morbidity and mortality [1]. VC has been regarded as a highly regulated process that occurs in a way similar to physiological bone formation [5]. In ESRD patients, the duration of dialysis treatment has been shown to negatively impact mineral metabolism, resulting in excess phosphate uptake by VSMCs [1]. *In-vitro* studies have shown that when exposed to calcifying media, the excess phosphate contributes to the differentiation of VSMCs into osteoblast-like cells by down regulating VSMCs contractile proteins and up-regulating bone forming proteins [1, 5]. In addition to VSMC loss of phenotype clinical studies of dialysis patients showed a negative correlation between existing VC and decreased serum concentrations of Fetuin-A, an inhibitor of extra-skeletal calcification [2,6].

Fetuin-A, also known as alpha2-Heremans-Schmid glycoprotein (AHSG) is a physiological regulator of bone metabolism [2]. This serum glycoprotein functions as a de-mineralizing agent by solubilizing, and facilitating in the removal of unwanted calcium-phosphate minerals that form as a result of calcification process [2]. In addition to Fetuin-A's inhibitory effect on VC, there are also local inhibitors of calcification that exert their function in the tissues from which they are synthesized. One such group of proteins is MGP's (matrix Gla proteins) which are vitamin K dependent and are primarily made by VSMCs and chondrocytes [7]. Vitamin K is required for the γ -carboxylation of MGP, and only carboxylated MGP has the ability to act as a calcification inhibitor [1]. *In-vitro*

calcification studies of VSMCs have shown that un-carboxylated MGP (unMGP) accumulate at sites of calcification [8]. We will use the presence of the un-carboxylated MGP at sites of calcification as a biomarker to target VC within the artery wall. Fetuin-A encapsulated by pH sensitive carriers with a surface affinity for unMGP will allow for targeted delivery of Fetuin A to sites of VC. In addition to targeted treatment of VC, intravenous injections of this therapy will reconstitute physiological levels of serum Fetuin-A possibly having a preventative effect on the further development of VC.

METHODS

VSMC Culture and Morphology. Primary human aortic vascular smooth muscle cells (ATCC, Manassas, VA) were cultured in Vascular Cell Basal Medium with 5 ng/mL rh FGH-basic, 5 mg/mL rh insulin, 50 µg/mL ascorbic acid, 10 mM L-glutamine, 5% Fetal Bovine Serum, and penicillin/streptomycin. Cell morphology was visualized using light microscope.

Immunostaining. Antibody staining was used to verify VSMC phenotype. Goat primary antibody (1:200 dilution; Pierce, Waltham, MA) a polyclonal smooth muscle α -actin is reactive for porcine and selective for the α -actin found in vascular smooth muscle cells. Rabbit secondary antibody (1:200 dilution; Pierce, Waltham, MA) was tagged using a DAB substrate.

VSMC Calcification Model. Primary Human VSMCs, of passage 2 and 6, will be seeded into 4 different T75 cell culture flasks with 10 mL of growth medium, as previously described. Medium will be changed every 2 days until flasks reach confluence. Two controls will be established at this point and will continue with standard growth medium that will be replaced every 2 days for 2 weeks. Experimental flasks will be given calcification medium (standard growth medium supplemented with 10 mM β -glycerophosphate and 100 nM Dexamethasone) and medium will be changed every 2 days for 1 week. Cells will be examined regularly using a light microscope.

Quantification of Calcium Deposition. Following 1 week and 2 week time points the mineral content in the supernatant will be quantified using Calcium Assay Kit (Sigma, Waltham, MA). According to protocol, cells will be homogenized in 1.0 mL calcium assay buffer. A microcentrifuge will then be used to homogenize cell suspension at 10,000 g for 15 minutes. The supernatant will then be analyzed for calcium content using σ -cresolphthalein complexosone method. The calcium content of the cell layer will be normalized to protein concentration using BCA Protein Assay Kit (Pierce, Waltham, MA).

Protein Characterization. Dynamic light scattering (DLS) was used to determine the mean diameter by number of human Fetuin-A (Sigma-Aldrich (SA); St. Louis, MO) in two different solvents, water and a KOH solution at pH 7.37 (SA). Samples were prepared by centrifuging the protein in de-ionized (DI) water solution (14.5 rpm, 5 minutes), and redispersing in the pH buffer solution to mimic physiological blood pH. Both of these solutions were analyzed using DLS. A minimum of 5 DLS measurements was collected for each sample, and averages and standard deviations for the effective diameter are reported. The molecular structure of Fetuin-A was investigated with attenuated total reflection Fourier transform infrared (ATR-FTIR) spectroscopy using a diamond/zinc-selenide crystal (Miracle ATR[®] accessory, Pike Technology) and collecting at least 256 scans for each ATR-FTIR spectrum.

Polymersome Synthesis and Surface Topology. We will explore the use of PCL-b-PEG [poly(ϵ -caprolactone)-block-Poly(ethylene glycol)] and PMPC-b-PDPA [poly(methacryloyloxyethyl phosphorylcholine)-block-poly(diisopropanolamine ethyl methacrylate)]; both are known pH sensitive polymersomes used in biomedical applications for drug delivery purposes [9]. Protein release will be dictated by polymersome biodegradation via hydrolysis. Two methods will be evaluated for specific recognition of the polymersome by VSMC: (1) functional group attachment to polymer before vesicle formation via ligands or moieties; and (2) post functionalization of polymersomes via covalent or strong non-covalent interactions.

RESULTS

The results from the DLS of Fetuin-A in DI water and KOH in water solution yielded a mean diameter by number of 100.57 ± 120.51 nm and 201.28 ± 66.81 nm respectively. Analysis of the ATR-FITR absorptions reveals characteristic signatures for functional groups present in Fetuin-A (Figure 1): phenol, alkene, nitrile, alkyne, ester, aromatic hydrocarbon, amine, and amine oxide.

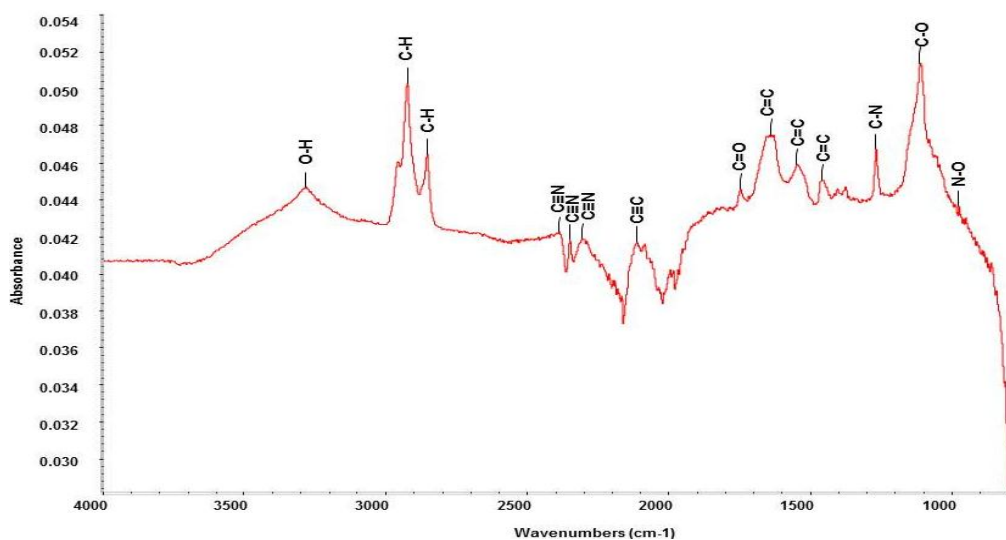


Figure 1: ATR-FTIR spectrum of Fetuin-A.

Discussion

With respect to the DLS results, the lower standard deviation (SD) values of the mean diameter by number for the pH solution suggest a more uniform interaction of Fetuin in the pH solution compared to that of water. In order to learn more about the potential adsorption ability of Fetuin, a deeper understanding with respect to Fetuin A concentration, solvent selection, and time of interaction must be gained. Figure 1 provides insight to potential chemical bonds that can be used to tailor molecular interactions during encapsulation and targeting of the protein to effectively treat VC.

CONCLUSIONS

This targeted drug therapy has the potential to reverse and prevent further cardiac disease progression that stems from vascular calcification. With no current cure for kidney failure, and with dialysis treatments being the only alternative to kidney transplantation, this targeted therapy could effectively improve the life expectancy of patients on dialysis. The efficacy of Fetuin-A to remove newly deposited mineral content versus removing mineral deposits that have accumulated over longer periods of time has not yet been assessed. In order to determine the potential of this targeted protein delivery for both calcification therapy and preventative care we must establish an appropriate dose to ensure an effective treatment. Synthesizing the desired biodegradation profile of the polymersome after successful encapsulation of Fetuin A would be the next focus after a safe and effective dosage is found. Testing of bio-distribution, and targeted delivery will require a 3D calcification model before progression to in-vivo testing.

ACKNOWLEDGEMENTS

I would like to thank the Agricultural & Biological Engineering Department and the Swalm C. School of Chemical Engineering at Mississippi State University for providing the laboratory equipment to conduct this research. Financial support for the acquisition of the dynamic light scattering equipment was provided by EPS-0903787.

REFERENCES

- [1] M. Shea and R. Holden. (2012). "Vitamin K Status and Vascular Calcification: Evidence from Observational and Clinical Studies American Society for Nutrition." *Adv. Nutr.* 3, pp. 158–165.
- [2] P. Stenvinkel, K. Wang, A. Rahid et al. (2005, January). "Low fetuin-A levels are associated with cardiovascular death: Impact of variations in the gene encoding Fetuin." *Kidney International.* 67, pp. 2383-2392.

- [3] A. Shioi and Y. Nishizawa. (2010). "Vascular calcification: Osteogenic transformation of vascular smooth muscle cells." *J Oral Biosci.* 52(1), pp. 26-32.
- [4] L. J. Schurgers, E.C.M. Cranenburg, and C. Vermeer. (2008, September). "Matrix Gla-protein: The calcification inhibitor in need of vitamin K." *Thromb Haemost.* 100, pp. 593–603.
- [5] D. Yonova. (2009). "Vascular calcification and metabolic acidosis in end stage renal disease." *Hippokratia.* 13(3), pp. 139-140.
- [6] U.S. Department of Health and Human Services. National Kidney and Urologic Diseases Information Clearinghouse. The growing burden of kidney disease. *Kidney Disease Statistics for the United States, 2012.* NIH Publication No. 12–3895
- [7] E. Theuwissen, E. Smit, and C. Vermeer. (2012). "The Role of Vitamin K in Soft-Tissue Calcification." *American Society for Nutrition. Adv. Nutr.* 3, pp.166–173.
- [8] H. M. Spronk, B. A. Soute, L. J. Schurgers et al. (2001). "Matrix Gla Protein Accumulates at the Border of Regions of Calcification and Normal Tissue in the Media of the Arterial Vessel Wall." *Biochemical and Biophysical Research Communications.* 289, pp. 485–490.
- [9] R. P. Brinkhuis, F.P.J.T. Rutjes and J. C.M. van Hest. (2011, March). "Polymeric vesicles in biomedical applications." *Polymer Chemistry.* 2, pp. 1449-1462.

CARDIOVASCULAR RESPONSE TO TWO AND FOUR MINUTES WALK USING A STANDARD WALKER AND/OR PLATFORM WALKER WITH WHEELS IN ONE FOOT NON-WEIGHT BEARING INDIVIDUALS

Felix Adah, Neva Greenwald, Joy Kuebler, Becca Pearson, Elgenaid Hamadain, Janet Slaughter and Min Huang

University of Mississippi Medical Center, Jackson, Mississippi

Keywords

Non-weight bearing, Standard Walker, Rolling Walker, Platform, Cardiovascular, Ambulation

Abstract

This study examined cardiovascular responses to different times of walk (two and four minutes), using standard walker and/or platform walker with wheels in one foot non-weight bearing individuals. Few studies have explored the physiological impact of various walkers and different walk times on the cardiovascular system. Male and female physical therapy students, (n=18, ages from 22 to 32 years) were studied at two different time periods. In Phase I, participants ambulated with a standard walker (SW) and a platform walker with wheels (RW) for 2 minutes. The heart rate (HR), respiratory rate (RR), and blood pressure (systolic blood pressure (SBP) and diastolic blood (DBP)) before and after walk were recorded. Phase II consisted of the same participants and the same vital sign measures but they ambulated for 4 minutes. Participants ambulated at a self selected pace. ANOVA was used to determine statistical significance and a confidence interval of 95% or a p value <0.05 was considered significant. Results indicated that ambulation for 2 or 4 minutes produced a statistically significant difference ($p < 0.05$) between before and after measurements of HR, SBP, and RR for SW, RW and DBP (for four minutes walk using RW only). Remaining DBP differences were not significant ($p > 0.05$). When all groups in each of the vital signs studied were compared, there was no statistical significant difference. Our study suggests that ambulation using any of the gait devices in 2 or 4 minutes walks significantly increased the vital signs of HR, PR, SBP and DBP (in only four minute walk using a platform rolling walker). It is highly suggested that extra precaution be taken when initiating ambulation especially in elderly patients after trauma and with other co-morbidities.

INTRODUCTION AND BACKGROUND

Orthopedic injuries such as fractures and dislocations are common phenomena in our society today. Injuries always affect normal walking and safety during ambulation. Interventions may include surgery and physiotherapeutic rehabilitation. Gait assistive devices may have to be prescribed temporarily or for a long term use. Many factors are used in choosing the appropriate assistive device. Such factors include the age, safety needs, and medical condition of the patient. Other factors may include the ability to bear weight on the hands and wrists and patient comfort. A standard walker must be lifted each time a step is taken during ambulation. Good upper extremity strength and function are needed to use this type of walker. On the other hand, a walker adapted with wheels and platforms don't have to be lifted with each step and good hand/wrist strength is not a requirement for usage. It is probable that these two types of walker would mediate different stress responses on the cardiovascular system. There are studies reported in the literature relating to cardiovascular stress mainly in the elderly population. *Baruch and Mossberg*, [5] reported that there was high demand put on the cardiovascular system while using a walker with non-weight bearing on one foot in elderly women ages 60 to 80 years old. Studies have shown a link between increased heart rate and physical exertion seen in patients ambulating with assistive devices. In 1993, *Holder et al.* [1] examined the effects of independent ambulation with non-weight bearing on one extremity using axillary crutches, standard walkers, and rolling walkers in nine female physical therapists. They compared oxygen cost, heart rate, blood pressure, rate-pressure product, and rating of perceived exertion. The authors reported that using an assistive device would increase cardiopulmonary demands compared with independent ambulation. Walking on different surfaces may exert varying cardiovascular demands on the body. *Murray et al.* [6] compared the heart rate of individuals walking on the treadmill and floor walking at varying speeds (slow; free and fast). The heart rate was higher for the free and fast walking on the treadmill compared to floor walking. The EMG showed increased heart activities during the free and fast walking on the treadmill which may indicate a slight apprehension during the treadmill walking. On the other hand, walking on a treadmill inside water and out of water did not produce a

significant difference in terms of cardiovascular perceived exertion [7]. The Guide to Physical Therapy Practice (Guide) recommends the HR and BP of new patients to be measured during examination, apparently under scoring the importance of these vital signs [9]. “The normal blood pressure response to dynamic upright exercise consist of a progressive increase in systolic blood pressure, and no change or a slight decrease in diastolic blood pressure” [8]. Systolic blood pressure is sensitive to activities and may be used to test the efficiency of assistive devices [1, 10, and 4]. Higher SBP when using a certain device indicates a less efficient assistive device. Oxygen consumption/or respiration can be affected when walking with or without an assistive device and on the condition of walk. *Murray et al.* [6] reported that O₂ consumption increased with walking speed, but they found no difference between treadmill and floor walking. *Holder and co-workers*, [1] reported that oxygen consumption with individuals that used axillary crutches for walking was less per unit distance compared to walking with standard walkers and rolling walkers, but oxygen consumption was more per unit time. Increasing walking exercise intensity can lead to increased oxygen consumption and walk training with someone who normally jogs will lead to deconditioning in coronary patients [2]. *Tudor-Locke* [3] reports no difference in blood pressure (systolic and diastolic) in individuals at rest compared to submaximal exercise based on the number of steps/day. Little is known about the effects of walking for two minutes or four minutes on the cardiovascular systems of individuals using different gait devices while walking on one foot. Therefore, the purpose of this study was to quantify and compare the effects of ambulation with a standard walker and platform rolling walker on cardiopulmonary functions during 2-minute and 4-minute walks in individuals who are non-weight bearing on one foot/extremity. We hypothesized that ambulation with the standard walker will result in higher cardiovascular stress when compared to ambulation with a standard walker adapted with wheels and platforms. Our second hypothesis is that a four minute walk will result in higher cardiovascular/physiological stress when compared to ambulation for two minutes. The specific objectives are: To determine the effect of ambulation with standard and/or standard walker adapted with wheels and platforms on the blood pressure (systolic (SBP) and diastolic blood (DBP) pressures); respirations (RR); and heart rates (HR) of university students and to compare the effects of two minutes and four minutes walks on the cardiovascular system using the two different type of walkers.

MATERIALS AND METHODS

Subjects: 14 subjects between the ages of 20 and 32 years old were randomly selected from a group of Physical Therapy students. The subjects signed an informed consent form prior to participate in the study. **Equipment:** adjustable adult aluminum standard four-point walker, standard walker with platform walker and wheels, and American Diagnostic Corporation digital BP monitor **Procedure:** The study consisted of 2 phases of different walk times. Prior to the ambulation, the subjects’ resting heart rate (HR), blood pressure (BP), and respiratory rate (RR) were measured and recorded. The walker was fitted to the subject. The subjects were allowed to choose which leg will be used for non-weight bearing (NWB) and they ambulated at a self-selected pace. In phase I of the study, the subjects ambulated using a standard walker (SW) over a smooth level surface for 2 minutes. The vital signs (HR, BP, and RR) were measured and recorded at the end of the 2-minute walk. The subjects returned the next day to perform the same procedure above using a platform walker with wheels (RW). The vital signs were measured and recorded prior to ambulation and after two minutes of walk with the platform walker and wheels. In Phase II which was done a week later, all the procedure performed in Phase I was repeated except that the walk using different assistive devices was carried out in four minutes (4-minute walk). The vital signs were measured and recorded before and after ambulation as in Phase I. **Analysis:** The collected data were analyzed using Stigma Stats software and Slide Write for the graphs with an alpha confidence level of less than 0.05 as significant. The data were analyzed using a paired t-test comparing resting vital signs to post ambulation vital signs. Inter group comparison was done using ANOVA. The procedure for this study was modified from the study of *Baruch and Mossberg* [5].

RESULTS AND DISCUSSION

There was a statistically significant difference ($p < 0.05$) between before and after measurements of HR, SBP, and RR for SW and RW for the 2 and 4-minute walks and DBP using RW for 4-minute walk. (Fig. 1-4) The remaining DBP differences were not significant. ($p > 0.05$) (Fig. 3). When the groups in each of the vital signs studied were compared, there was no statistical significant difference ($p > 0.05$). Normal blood pressure response to dynamic upright exercise has been shown to consist of a progressive increase in SBP, and no change or a slight change in DBP [8, 3] which was exactly what was observed in this study. Except for the four minute walk with rolling walker, the diastolic blood pressure was not different when both the before and after data were compared. The results of this

study is in accord with the findings of *Baruch and Mossberg* (5) that showed increased cardiovascular stress in elderly individuals who ambulated with non-bearing on one foot.

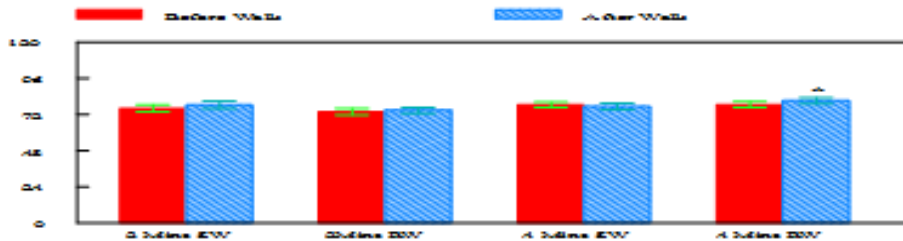


Figure 1: Pulse before and after walk at 2 and 4 minutes levels with SW and RW, *p < 0.05. SW = Standard Walker, RW = Rolling Walker.

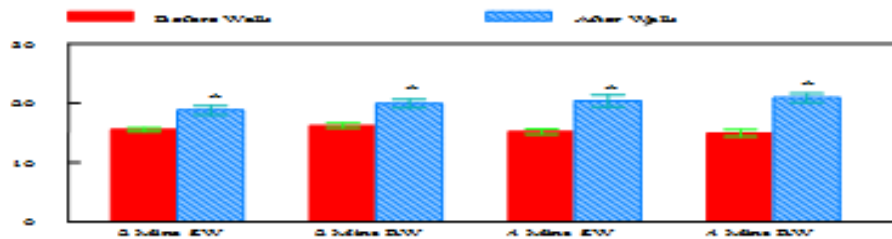


Figure 2: Systolic BP before and after walk at 2 and 4 minutes levels with SW and RW, *p < 0.05. SW = Standard Walker, RW = Rolling Walker.

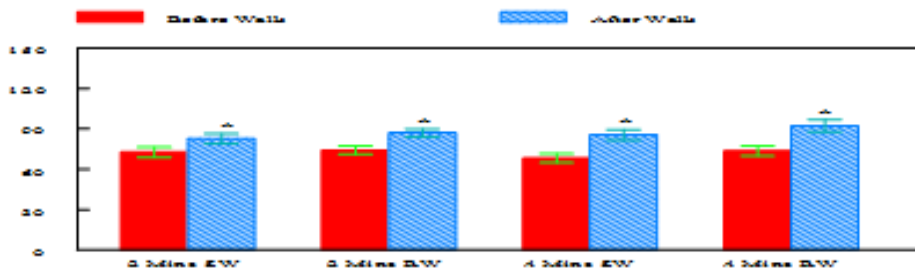


Figure 3: Diastolic BP before and after walk at 2 and 4 minutes levels with SW and RW, *p < 0.05. SW = Standard Walker, RW = Rolling Walker.

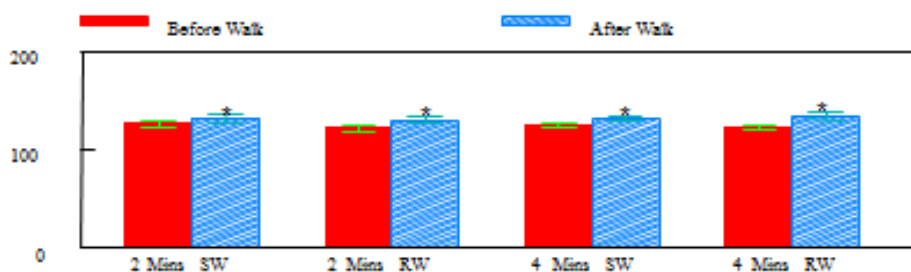


Figure 4: Respiration before and after walk at 2 and 4 minutes levels with SW and RW, *p < 0.05. SW = Standard Walker, RW = Rolling Walker.

The significant differences seen in the SBP, PR and RR in this study should be taken as a serious indication for precaution when ambulation training is being done with individuals recovering from an illness or injury. The subjects in this study were healthy young adults enrolled in a physical therapy program with no history of cardiovascular related problems. The increased cardiovascular demand depicted with increased HR, RR, and PR seen in this study is in agreement with the study of *Holder et al.* [1], who reported that an assistive device during ambulation increases cardiovascular demands. Our results suggest that there is no definitive difference between the two types of walkers tested which agrees with *Holder et al.* [1], but they found that the oxygen demand was less using axillary crutches for ambulation per unit distance walked. Axillary crutches were not tested in this study. With an increase in physical exertion, an increase in respirations and HR is normally seen as well. Our findings suggest statistically significant differences between pre- and post- ambulation in RR, HR, and SBP. The assistive device used (standard walker or platform rolling walker) and period of walk (two-minute or four-minute walk) did not show any significant difference in terms of cardiovascular responses ($p > 0.05$).

CONCLUSION

The study shows no significant difference with cardiopulmonary parameters when ambulating with the standard walker (SW) versus the rolling walker (RW) with platforms. However, ambulation using any of the gait devices in 2- or 4-minute walks significantly increased the vital signs of HR, PR, SBP and DBP (in a 4-minute walk using a platform rolling walker) from the resting or before values. Therefore, while patient comfort and/or preference should be the deciding factor when choosing a standard walker or platform walker with wheels, extra precaution is needed when ambulation time is two minutes and above. The extra precaution may be needed more with the elderly patients and individuals with much co-morbidity. A platform walker may also be recommended for a patient with or without hand/ wrist related problems as long as the device will enable easier mobility. Since both devices used in this study did not show any difference in cardiovascular demands. It is suggested that future studies should involve a wider age range, the elderly population, different time titration for lower and higher minutes of walk, and individuals with varying fitness levels.

REFERENCES

- [1]. Holder, C. G., Haskvitz, E. M., & Weltman, A. (1993). The effects of assistive devices on the oxygen cost, cardiovascular stress, and perception of nonweight-bearing ambulation. *Journal of Orthopedic & Sports Physical Therapy*, 18, 537-542.
- [2]. Dressendorfer, R. H., Franklin, B. A., Smith, J. L., Gordon, S., & Timmis, G. C. (1997). Exercise and the heart-rapid cardiac deconditioning in joggers restricted to walking. *Chest* 112, 1107- 1111.
- [3]. Tudor-Locke, C., Ainsworth, B. E., Whitt, M. C., Thompaon, R. W., Addy, C. L., and Jones, D. A. (2003). Ambulatory activity and simple cardiorespiratory parameters at rest and submaximal exercise. *Canadian Journal of Applied Physiology*, 28, 699-709.
- [4]. Hinton, C. A., & Cullen, K. E. (1982). Energy expenditure during ambulation with ortho crutches and axillary crutches. *Physical Therapy*, 62, 813-819.
- [5]. Baruch, I. M. & Mossberg, K. A. (1983). Heart-rate response of elderly women to nonweight-bearing ambulation with a walker. *Physical Therapy*, 63, 1782-1983.
- [6]. Murray, M. P., Spurr, G. B., Sepic, S. B., Gardner, G. M., & Mollinger, L. A. (1985). Treadmill vs. floor walking: kinematic, electromyogram, and heart rate. *Journal of Applied Physiology*, 59, 87-91.
- [7]. Fujishima, K. & Shimizu, T. (2003). Body temperature, oxygen uptake and heart rate during walking in water and on land at an exercise intensity based on RPE in elderly men. *Journal of Physiological Anthropology*, 22, 83-88.
- [8]. Balady, G. J., Berra, K. A., Golding, L. A., Gordon, N. F., Mahler, D. A., Myers, J. N., et al. (2000). ACSM's Guidelines for Exercise Testing and Prescription. Maryland: Lippincott, Williams, & Wilkins.
- [9]. *Guide to Physical Therapist Practice*, 2nd ed. Alexandria, Va. American Physical Therapy Association: 2001.
- [10]. Foley, M. P., Prax, B., Crowell, R., & Boone, T. (1996). Effects of assistive devices on cardiorespiratory demands in older adults. *Physical Therapy*, 76, 1313-1319.

OSTEOCLAST-MEDIATED DEMINERALIZING OF MEDIAL VASCULAR CALCIFICATION**Joshua Grant, C. LaShan Simpson**

Box 9632

Mississippi State, MS 39762

ABSTRACT

Vascular calcification is a cardiovascular disease divided into two distinct areas: intimal and medial. Intimal calcification involves plaque build-up in the arteries, which in turn leads to heart attack and stroke. Medial calcification is result of mineral deposition in the interior walls of the arteries. This results in complications including hypertension, heart attack, and stroke. Interestingly, research has shown that medial vascular calcification is physiologically similar to bone development in the body. Bone remodeling is a process that occurs continually in the body. This process keeps bone mass consistent through the continual resorbing of bone by osteoclasts and deposition of bone by osteoblasts. Smooth muscle cells in the artery walls are differentiating into osteoblast-like cells and depositing mineral inside the artery walls. Evidence has shown that osteoclast cell therapy is a potential pathway for treatment of vascular calcification. In this therapy, osteoclasts would resorb mineral the same way bone remodeling is done *in vivo*.

By introducing osteoclasts to sites of calcification, it is hypothesized that mineralization can be resorbed. To introduce osteoclast-like cells to sites of calcification, monocyte differentiation is a potential option. Monocytes are mobile inflammatory response cells normally found in bone and are also commonly found at sites of high calcification. Additionally, monocytes have the capacity to differentiate into osteoclast-like cells under the right conditions. Our objective is to take advantage of this by demineralizing vascular calcification through differentiation of monocytes to osteoclast-like cells *in vitro*.

Keywords: Vascular Calcification, Osteoclasts, Demineralization, Cardiovascular, monocytes, arteriosclerosis.

INTRODUCTION

Cardiovascular disease is the leading cause of death in the United States. According to the Center for Disease Control and Prevention, about 600,000 people succumb due to heart related complications every year in the United States. Each year, the United States spends over \$100 billion on cardiovascular disease [1]. Additionally, Mississippi has the highest rate of cardiovascular disease of any state [2]. There are many risk factors that are associated with cardiovascular disease. Among these includes a person's diet, tobacco use, and hereditary factors. Beyond just the heart, cardiovascular disease is an umbrella term referring to the entire cardiovascular network including arteries, veins, and capillaries. Some of these conditions associated with the vascular network include hypertension, intimal vascular calcification, and medial vascular calcification. Medial vascular calcification, hardening of the arteries, raises blood pressure and puts more work on the heart. This medial calcification is often viewed as a precursor for much more serious cardiovascular pathologies [3]. Interestingly, research has shown that the vascular calcification is being mediated by the same mechanism of bone mineralization [4]. Bone homeostasis is controlled by a delicate balance between osteoblast (bone-building cells) activity and osteoclast (bone-resorbing cells) activity. Under diseased conditions, vascular smooth muscles cells (vSMCs) in the medial layer of the arteries are differentiating into osteoblast-like cells and deposit mineral hydroxyapatite into the arteries; this is the same mineral found in bone [4]. It is hypothesized that vascular calcification can be reversed using the same mechanisms found in bone remodeling. Based on this, osteoclast delivery is a potential mechanism to resorb mineral deposits in the arteries

Many researchers have alluded to the use of monocytes as a potential pathway for treatment [5]. Monocytes are a type of white blood cell that are mobile and act in the inflammatory response in the body and are routinely found on bone and sites of calcification. They play several roles in the immune system including replenishing macrophage populations at sites of inflammation. Additionally, monocytes are known progenitor cells for both osteoblasts and osteoclasts. Due to this, some research suggests that they may be a contributing factor to medial vascular calcification [5]. However, it is hypothesized that the availability, mobility, and pre-osteoclast nature makes these cells excellent candidates for use in cell-targeted therapy for vascular calcification. The primary goal of the research is to demineralize calcified vascular calcification using osteoclast-like cells differentiated from monocytes. In order to proceed with this research, a static *in vitro* calcification model will be established. This calcification

model needs to show calcification can be produced *in vitro* in a repeatable/consistent manner. Various researchers have shown methods for inducing vascular calcification *in vitro* using β -glycerophosphate and dexamethasone as calcifying agents [6, 7, 8]. A combination of these methods was used to make this model.

METHODS

Cell Isolation, Cell Culture, and Cell Morphology

Several samples of porcine aorta were collected from a local abattoir and the medial layer separated from the intimal layer and connective tissue. The medial layer was cut into very small 2-3 mm sample sizes. Samples were digested in Type I Collagenase and the media was filtered to isolate cells. Cells were seeded into flasks with growth medium consisting of Dulbecco's Modified Eagle Medium (DMEM) with 10% Fetal Bovine Serum (FBS) and 1% Penicillin/Streptomycin (Pen/Strep). Growth medium was replaced every 2 to 3 days until cells were 80% confluent.

Additionally, primary human vSMCs (ATCC, Manassas, VA) were cultured in Vascular Cell Basal Medium with 5 ng/mL rhFGH-basic, 5 mg/mL rh insulin, 50 μ g/mL ascorbic acid, 10 mM L-glutamine, 5% Fetal Bovine Serum, and penicillin/streptomycin. Morphology of the cells was observed using light microscopy.

Porcine vSMC Calcification Model

The primary porcine vSMCs, all between passage 2 and passage 6, were seeded into 6-well cell culture plates with 4 mL of growth medium as previously established. Medium was changed every 2-3 days until all cells reached confluence. Upon confluency, controls continued to be fed standard growth medium. Test samples were fed growth medium supplemented with 10 mM β -glycerophosphate to accelerate mineralization. Data was collected at 2 week and 3 week time points.

Human vSMC Calcification Model

Primary Human vSMCs, all between passage 2 and passage 6, were seeded T75 cell culture flasks with 10 mL of Basal growth medium as previously established. Medium was changed every 2-3 days until all flasks reached confluency. Upon confluency, controls continued to be fed standard Basal growth medium. Tests samples were given basal growth medium supplemented with 10 mM β -glycerophosphate and 100 nM Dexamethasone to accelerate mineralization. Data was collected at 1 and 2 week time points.

Calcium Assay

Mineralization levels were analyzed using Calcium Assay Kit (Sigma, St. Louis, MO). According to protocol, cells will be collected by centrifugation at 1,000 RPM for 5 minutes. Following collection, cells will be homogenized in 1.0 mL calcium assay buffer. This homogenization will then be centrifuged at 10,000g for 15 minutes in a microcentrifuge. The supernatant was then be analyzed for calcium content using σ -cresolphthalein complexosone method.

RESULTS

Calcium Assay on Isolated Porcine Cells

After 2 weeks of culture in calcification medium, the primary porcine vSMCs isolated from tissue showed a statistically significant increase (using $\alpha = 0.05$) in calcium when compared to the calcium standard consisting of no calcium content and the control which consisted of primary porcine vSMCs cultured in regular growth medium without the addition of β -glycerophosphate (Figure 1). Interestingly, the 3-week trial did not show a statistically significant (using $\alpha = 0.05$) difference between the calcium standard, control, and calcification media samples (Figure 1).

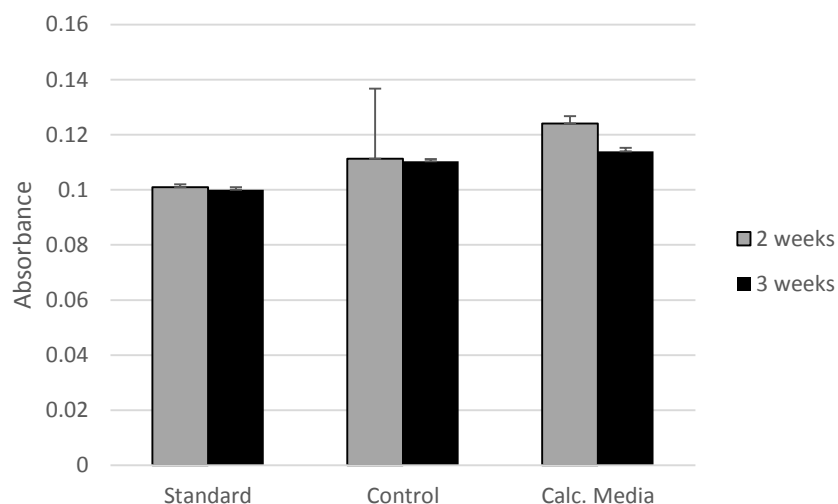


Figure 1: Calcium Analysis primary porcine vSMCs cultured in calcification medium.

DISCUSSION

We were able to induce calcification in the primary vSMCs in 2 weeks. The results showed that after 2 weeks of exposure to standard growth medium, the control samples did exhibit statistically significant ($\alpha = 0.05$) increase in calcification compared to that of the calcium standard sample containing no calcium. Additionally, after the 2 weeks the calcification medium samples also had statistically significant ($\alpha = 0.05$) increase in calcification in compared to the calcium standard containing no calcium and the 2 week control sample. It was expected that the calcification medium would accelerate the calcification. However, despite having a significant increase in calcium content compared to the calcium standard for zero calcium, the absorbance was small compared to expected values. In order to improve upon our previous study, the human vSMCs will have the study done in T75 flasks in order to increase the total quantifiable levels of calcification.

Interestingly, the three week samples produced different results. The 3-week trial did not show a statistically significant (using $\alpha = 0.05$) difference between the calcium standard, control, and calcification media samples. Additionally, the values for calcium content were actually higher in the 2-week study than the 3 week study. Perhaps this can be attributed to cell death during the extended cell culture period. Hopefully, reducing the study times from 2 and 3 weeks to 1 and 2 weeks, along with the addition of dexamethasone as a calcifying agent, will produce anticipated results. According to Mori et al, Dexamethasone can also be used to induce calcification in osteogenic progenitor cells [8]. To increase calcification in our samples, we plan to incorporate 100 nM Dexamethasone in addition to the 10 mM β -glycerophosphate to accelerate mineralization. Additionally, future work will have calcium content normalized to protein content using BCA Protein Assay (Sigma).

Also, the study lacked any way to qualitatively measure any mineralization in the cell cultures. In future studies, Alizarin Red and/or Von Kossa Staining will be performed on cell culture samples in order to visualize mineralization.

CONCLUSIONS

This preliminary study has confirmed that we were able to induce calcification of primary porcine vSMCs using β -glycerophosphate. However, we are refining the study by using primary human aortic vSMCs purchased from a commercial distributor to reduce the chance of a mixed population of cells. According to Mori et al, Dexamethasone can also be used to induce calcification in cell culture [8]. To increase calcification in our samples, we plan to incorporate 100 nM Dexamethasone in addition to the 10 mM β -glycerophosphate to accelerate mineralization. We anticipate great results from our new calcification model to be used to test the potential of osteoclast delivery as a treatment for vascular calcification.

ACKNOWLEDGMENTS

A special thanks is given to the Department of Agricultural and Biological Engineering Department at Mississippi State University and Katie McGuire for assistance with cell culture.

REFERENCES

1. Heart and Stroke Statistics. American Heart Association. Retrieved Oct 12 2013 from www.heart.org
2. Mississippi Burden of Heart Attack and Stroke. Center for Disease Control and Prevention Retrieved Oct 13 2013 from www.cdc.gov.
3. Persy V, and D'Haese P. Vascular Calcification and bone disease: the calcification paradox. Trends in Molecular Medicine. 2009. 15(9):405-416.
4. Simpson CL, Lindley S, Eisenberg C, Basalyga DM, Starcher BC, Simionescu DT, et al. Toward cell therapy for vascular calcification: osteoclast-mediated demineralization of calcified elastin. Cardiovascular Pathology Feb 2007;16:29-37.
5. Tintut Y, Patel J, Territo M, Saini T, Parhami F, and Demer LL. Monocyte/macrophage regulation of vascular calcification in vitro. Circulation. 2002. 105:650-655.
6. Park JB. The effects of dexamethasone, ascorbic acid, and β -glycerophosphate, on osteoblastic differentiation by regulating estrogen receptor and osteopontin expression. Journal of Surgical Research. 2012;173:99-104.
7. Jono S, McKee MD, Murry CE, Shioi A, Nishizawa Y, Mori K, et al. Phosphate regulation of vascular smooth muscle cell calcification. Circulation Research. 2000;87:10-17
8. Mori K, Shioi, Shuichi J, Nishizawa Y, Morii H. Dexamethasone enhances in vitro vascular calcification by promoting osteoblastic differentiation of vascular smooth muscle cells. Arterioscler thromb vasc boil. 1999;19:2112-2118.

FINITE ELEMENT ANALYSIS OF ARTERIAL VESSEL WALL STIFFNESS

Angel Huot, Saami K. Yazdani

University of South Alabama
Department of Mechanical Engineering

ABSTRACT

Coronary artery disease (CAD), which is the most common type of heart disease, accounts for nearly 400,000 annual deaths. In the coronary arteries, it is well established that plaque development correlates to endothelial cell (EC) dysfunction. ECs, which are strategically located at the interface of circulating blood and the vascular wall, sense and respond to their local mechanical environment. In addition to wall shear stress and cyclic strain, EC coronaries are exposed to varying wall stiffness values due to the cardiac contraction (motion of the heart). According to the wall strain-stiffening phenomenon, high stress sites correspond to stiffer sites in the arterial wall. The purpose of this investigation was to therefore compute stress and strain values with varying modulus values within an arterial vessel. A vessel with an inner radius of 2.9 mm and wall thickness of 0.6 mm was modeled as a linear elastic material. The modulus ranged from 0.02 MPa to 0.80 MPa. The vessel was then pressurized 80 and 120 mmHg and the peak stiffness compared.

Results indicated that higher stresses occurred at the transition of change in modulus. As the model became stiffer, the stress was increased to values up to 152% of baseline levels. These results demonstrate the significance of increased wall stiffness in vessels with varying modulus and the potential adverse impact on endothelial cell function due to these increased wall stress values.

Keywords: arterial wall, modulus, stiffness, stress, strain, FEA

INTRODUCTION

Arteries and veins *in vivo* are subjected to significant mechanical stresses generated by lumen blood flow, pressure, surrounding tissue tethering, and body movement [1, 2]. Arteries and veins, like water hoses or pipelines may also lose its mechanical stability under mechanical loads, and thus it is crucial that blood vessels under *in vivo* loads maintain its physiological function [3]. Atherosclerosis is a chronic, inflammatory, fibro-proliferative disease primarily of large and medium sized conduit arteries [4, 5]. Atherosclerosis occurs when plaque builds up inside the arteries, which eventually as it develops, alters the shape of the artery [6]. A narrowed artery would limit the flow of oxygen-rich blood to organs such as the heart and other parts of the body [6].

Coronary artery disease (CAD) is the most common type of heart disease, which is generated from atherosclerosis. The initiation of physiologic abnormalities in endothelial cell (EC) function has been recognized as the first identifiable phase in the development of atherosclerosis [7]. Due to cardiac contraction, EC coronaries are not only exposed to wall shear stress and cyclic strain but also varying wall stiffness throughout the artery. Markers of arterial stiffness have been correlated with cardiovascular outcomes, and have been classified as an emerging risk factor that provides prognostic information beyond standard stratification strategies [7]. According to the wall strain-stiffening phenomenon, high stress sites correspond to stiffer sites in the arterial wall. The purpose of this investigation was to therefore develop a finite element model of an artery with varying modulus to compute the stress and strain.

METHODS

A finite-element analysis requires the geometry and material properties of the blood vessel and the appropriate loading conditions to simulate the wall strain-stiffening phenomenon. The finite-element program used in this experiment was ANSYS.

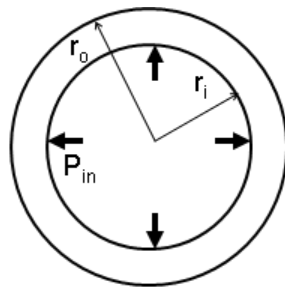
Geometric Model

The artery was modeled as an idealized vessel and represented by a symmetrical cylinder. The radial

dimensions of the artery are as follows: inner radius of 2.9 mm and wall thickness of 0.6 mm. To observe the stress-strain distribution due to changes in modulus values, the model was segmented into three solid parts. As the artery was considered a symmetrical cylinder, only $\frac{1}{4}$ of cylinder was taken into account for analysis. Three cases were analyzed for stress computation: modulus of 0.3, 0.5, and 0.8 MPa. Each case was compared to baseline levels (modulus of 0.02 MPa) for stress increase.

Material Properties

Vascular walls are composite structures composed of three concentric layers; however, considering all layers as a single material, and under small deformations, the wall exhibits an anisotropic, linear elastic behavior which is practically incompressible [8, 9]. The arterial vessel was modeled as a linear, elastic material. As the model consisted of three solid parts, this allowed the analyst to manually input the modulus values for each part. The Poisson's value used for the simulation was 0.3. The magnitude of stress in the artery is dependent on the internal pressure and on the ratio r/t (r – radius, t – thickness) [10]. The ratio r/t corresponds to the arterial wall as thick or thin in proportion to the radius. For this experimental case, a thick wall cylinder was considered (Figure 1).



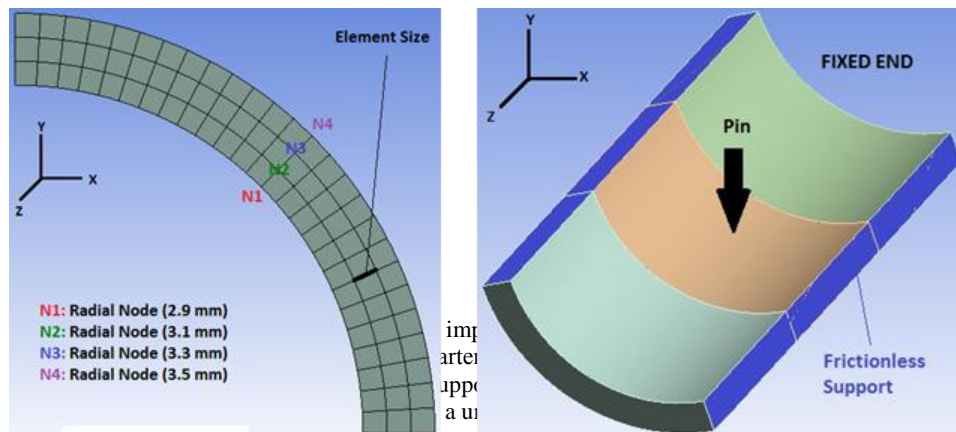
Symbols	Description
σ_θ	circumferential (hoop) stress
σ_r	radial stress
σ_z	axial stress
P_i	internal pressure
r_o	outer radius
r_i	inner radius
r	radius where stresses σ_θ and σ_r exists

Figure 1: Stress distribution from inside to outside of a thick arterial wall. Note that external pressure is considered as zero.

$$\sigma_\theta = \frac{P_i r_i^2}{r_o^2 - r_i^2} \left[1 + \frac{r_o^2}{r^2} \right] \quad \sigma_r = \frac{P_i r_i^2}{r_o^2 - r_i^2} \left[1 - \frac{r_o^2}{r^2} \right] \quad \sigma_z = \frac{P_i r_i^2}{r_o^2 - r_i^2}$$

Meshing and Boundary Conditions

The artery was meshed using solid elements. A convergence test was applied to the model comparing element type solsh90, solid185, and solid186. Comparing the theoretical versus ANSYS simulated data, solid186 (20-node brick elements) indicated an error percentage of less than 1%. Thus, solid186 was chosen for the wall-strain stiffening analysis. An element size of 0.2 mm was considered for the arterial model (Figure 2a). The arterial vessel was fixed at one end. A uniform internal pressure was applied to each node. As only $\frac{1}{4}$ of the cylinder was considered, a frictionless support was applied to both axial faces (Figure 2b).



RESULTS

The meshing incorporated into the simulations resulted in approximately 4,758 elements and 24,754 nodes. An observation of the nodal path (N1, N2, N3, N4) in respect to its radial stress was analyzed (Table 1, Figure 3). An increase in radial stress was observed only in the transition phases as seen in Figure 3. These increases in stress are reported in Table 1 as a percentage. Furthermore, the diameter compliance was also calculated for each analysis.

Table 1: Data shown represents the increase of radial stress (%) for transition phases 1 and 2 as a change in modulus occurred within the model. Stress percentage was compared to baseline levels. The diameter compliance was also observed for each modulus case.

Modulus Cases (MPa)	Transition Phase 1 Radial Stress Increase	Transition Phase 2 Radial Stress Increase	Diameter Compliance
0.02 - 0.3 - 0.02	107%	49%	4.5%
0.02 - 0.5 - 0.02	134%	109%	3.2%
0.02 - 0.8 - 0.02	154%	152%	2.4%

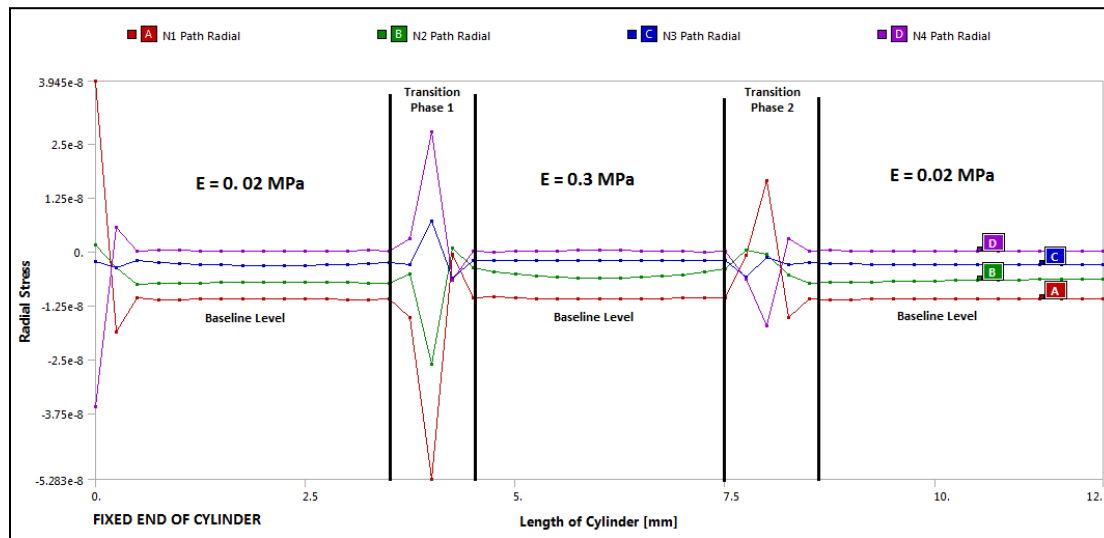


Figure 3: Radial stress in accordance to its nodal path (N1, N2, N3, N4) from 0 to 12 mm of the arterial model. Modulus values were assigned to sections within the model: 0.02 MPa, 0.3 MPa, and 0.02 MPa. Note: Unit of measure for radial stress is MN/mm^2 .

DISCUSSION

EC coronaries are exposed to varying wall stiffness values due to the cardiac contraction (motion of the heart). According to the wall strain-stiffening phenomenon, high stress sites correspond to stiffer sites in the arterial wall. In this study, a finite element model was constructed to observe the role of stiffness and its impact on stresses within an arterial wall. Results indicated that higher stresses occurred during the transition phase of change in modulus. As the model became stiffer, the radial stress was increased to values up to 152% of baseline levels. The diameter compliance indicated a decrease in percentage as the model became stiffer during transition phases.

CONCLUSIONS

A linear elastic finite element model was developed and demonstrated that stiffness affects the stresses within the arterial wall, and thus provides a basic understanding of the stiffness-stress relationship. Moreover, these results demonstrate the significance of increased wall stiffness in vessels with varying modulus and the potential

adverse impact on endothelial cell function due to these increased wall stress values. Future work will be to construct a nonlinear model, and introduce *in vivo* related mechanical loads such as buckling, bending and torsion.

REFERENCES

- [1] Fung, Y.C. Biomechanics: Circulation, Chap. 4 (2nd ed.). New York: Springer, 1997.
- [2] Han, H.C. Twisted blood vessels: symptoms, etiology and biomechanical mechanisms. *J. Vasc. Res.* 49(3):185-197, 2012.
- [3] Hai-Chao H., J.K.W Chesnutt, J.R Garcia, Q. Liu, and Q. Wen. Artery buckling: new phenotypes, models, and applications. *Annals of Biomedical Engineering*. Vol. 41, No. 7: 1399-1410, 2013.
- [4] Ross R. Atherosclerosis – an inflammatory disease. *N Engl J Med* 1999;340: 115-26.
- [5] Hansson GK. Inflammation, atherosclerosis, and coronary artery disease. *N Engl J Med* 2005;352:1685-95.
- [6] National Heart, Lung, and Blood Institute
- [7] Liao, J., and J. Farmer. Arterial stiffness as a risk factor for coronary artery disease. *Coronary Heart Disease*. 16:387, 2014.
- [8] C.G. Caro, T.J. Pedley, R.C. Schroter and W.A. Seed, *The Mechanics of Circulation*, Oxford Univ. Press, Oxford, 1978.
- [9] J.H. Storkholm, O. Frobert and H. Gregersen, Static elastic wall properties of the abdominal porcine aorta *in vitro* and *in vivo*, *European Journal of Vascular and Endovascular Surgery* **13** (1997), 31–36.
- [10] Thubrikar, M.J. *Vascular Mechanics and Pathology Book*. New York: Springer, 2007.

SPECTRAL- AND TIME-DOMAIN ANALYSIS OF HEART RATE VARIABILITY SIGNALS FROM MULTIPLE PHOTOPLETHYSMOGRAPHIC (PPG) SENSORS

Ajay K Verma, Sergio D Cabrera and Homer Nazeran
Department of Electrical and Computer Engineering, The University of Texas at El Paso,
El Paso, Texas, 79968 USA

ABSTRACT

Spectral and Time domain analysis of Heart Rate Variability (HRV) signal is widely used as a quantitative marker of the Autonomic Nervous System (ANS) activity. A robust algorithm was developed to derive HRV from photoplethysmographic (PPG) signals, compute FFT- and AR-based spectra of these signals, and determine their time- and frequency-domain features. This algorithm has detrending, sample-rate reductions, false-peak removal, automatic peak detection, peak-to-peak (PP) interval detection and correction, HRV signal generation, and spectral- and time-domain feature extraction from the HRV signal. Adapting to the very low spectral contents of the input PPG signal is very helpful in reducing the processing/computational effort. Standard spectrum estimation and measurements on the HRV signals were performed to generate spectral features, such as the LF/HF ratio, to quantify parasympathetic influences and sympathovagal balance. To validate the efficacy of the algorithm, PPG signals were recorded under different conditions such as stimulating an acupuncture point using a nanoscale patch, measuring relaxation after exercising, and others which are known to elicit changes in the ANS activity. Significant differences in LF/HF were observed due to these effects. The pNN50, a time domain measure of PP interval variability, was also considered for quantifying ANS activity and exploring its correlation with spectral features. Finally we used multiple sensors placed on different fingers to record PPG signals and to confirm that their respective spectral analysis was almost identical. We observed that a multiple sensor approach could be used to effectively reduce the impact of motion artifacts and of deterioration of signal quality due to loss of good PPG sensor contact.

Keywords: Photoplethysmography, Heart Rate Variability, Frequency Domain, Time Domain, Autonomic Nervous System, Spectral Analysis

INTRODUCTION

Heart rate variability (HRV) is one of the most important signals used in characterizing the health conditions impacting the autonomic nervous system activity. The HRV signal can be derived from photoplethysmographic (PPG) signals by detecting their peaks and calculating the Peak-to-Peak (PP) intervals followed by non-uniform interpolation. These signals are recorded using a PPG sensor usually placed on a fingertip. A PPG sensor uses a visible or infrared light emitting diode (LED) and a photodiode to measure blood volume changes in the capillary system with each heartbeat. With each cardiac cycle, the change in blood volume is detected by measuring the amount of light which is transmitted to the photodiode through the tissue [1]. Multiple PPG sensors can be used to collect signals from more than one finger in order to use the best signal in case some of these signals get corrupted due to loss of contact or motion artifacts. Once the HRV signal is derived, frequency domain analysis is usually performed to quantify the low frequency (LF) and high frequency (HF) contents of the HRV signal. It is well known that these measures can be used to estimate the state of the Autonomic Nervous System (ANS). It is believed that LF components correspond to sympathovagal part of ANS whereas the HF components correspond to the parasympathetic part [3]. Therefore, the ratio of low and high frequency spectral power, the LFHF ratio, is a marker of sympathetic dominance of stress response. We also used a time- domain feature, the pNN50, which measures the percentage of PP intervals that differs the previous PP interval by 50 msec. [3] as a separate marker of mental stress level. A preliminary comparison of time-domain and frequency-domain results does show a reasonable correlation between the two.

METHODS

The PPG signals were collected using multiple infrared PPG sensors placed on different fingers of the left hand. To record the signals, a National Instruments Elvis II board was used with the Matlab Data Acquisition using a very high sampling frequency (1000 Hz.). The very first signal processing step was to remove low frequency trends from the PPG signals. This detrending process was achieved by using a simple first order DC-notch IIR high-pass filter as discussed in [2]. Decimation to a lower sampling rate (100 Hz) was subsequently performed to find the PP intervals

to within less than 10 msec. of accuracy. In the following step, the positive part of the reduced rate PPG signal was squared to increase the dynamic range of the significant peaks compared to the rest of the signal. To accurately detect the location of peaks, a smart thresholding step was performed to obtain an initial determination of (uncorrected) PP intervals. The initial selection of peaks is done using a sub-interval accuracy, zero-crossing detection technique applied to the derivative of the signal and which operates only on sufficiently large peaks (above 150% compared to a local average of the clipped signal). Figure 1a) shows the result of the smart thresholding scheme for peak detection. We also incorporated an automatic missed peak detection and correction scheme in the algorithm. A peak is considered to be missed if the time duration between two detected peaks is more than 150% of the average time duration of the uncorrected PP intervals. The PP intervals signal $PP(n)$ (in units of seconds) is then obtained as the successive difference of the sample indices associated with the peaks $P(n)$ divided by the sampling frequency F_s (Hz.) to give: $PP(n) = (P(n) - P(n-1)) / F_s$. We computed the HRV signal from this PP intervals signal using a method of interpolation from non-uniform samples such as splines. This process is used to convert the arbitrary peak time locations into a uniformly sampled HRV signal whose amplitudes at the peak locations are equal to the PP interval [3]. The HRV signal is highly oversampled and its spectral contents of interest are known to be contained below 0.5 Hz. Thus, it can be severely decimated to a very low rate such as 2Hz as shown in Fig. 1b). In this case, an anti-aliasing filter should be used for such a large sample-rate reduction.

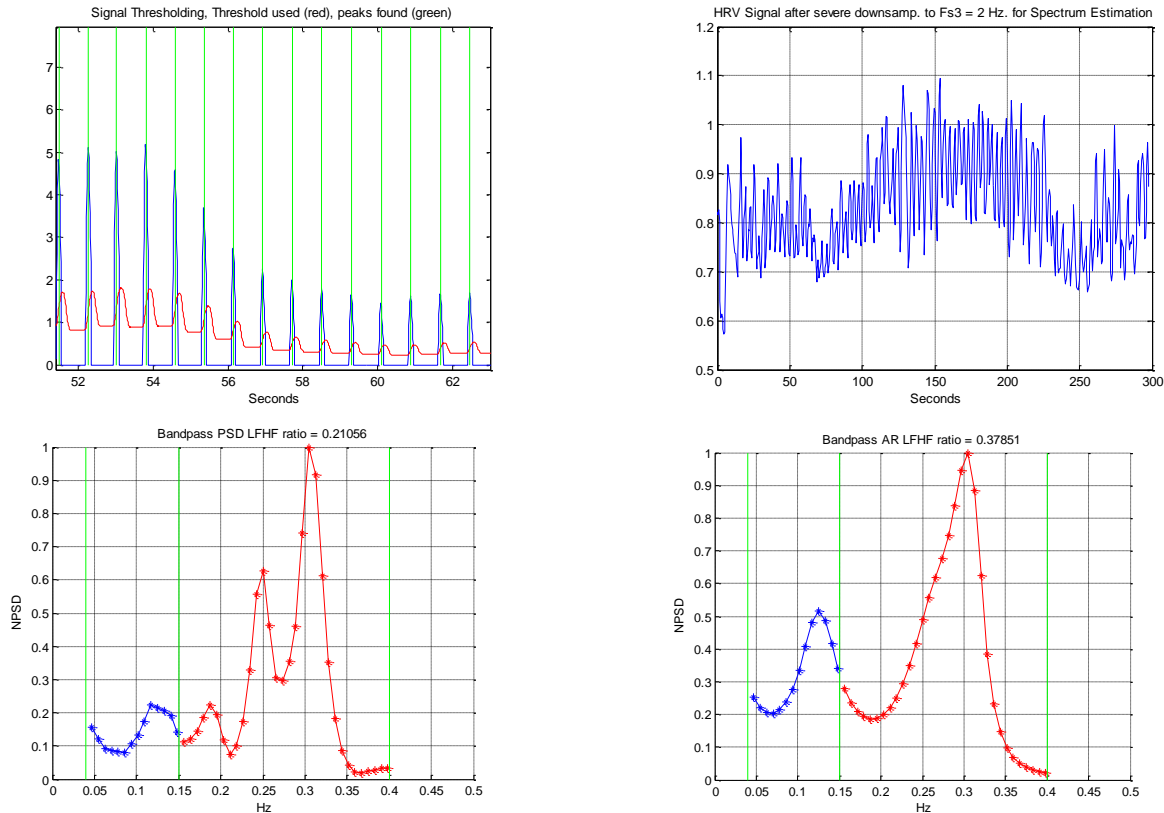


Figure 1: a) Smart peak detection, b) HRV signal after decimation, c) Normalized Welch Spectral Estimate of HRV signal in b) showing LF (blue) and HF (red) ranges., d) Normalized AR Spectral Estimate of HRV signal in b) showing LF (blue) and HF (red) ranges.

Once the HRV signal is derived there are a number of methods that can be used for its analysis. Commonly used HRV analysis methods are time-domain and frequency-domain, noting that time-domain analysis techniques are simpler to implement [3]. Of various time-domain features we emphasized the pNN50 measure which is the percentage of successive PP intervals that differ by more than 50 msec. . Our experimental results showed that pNN50 is proportional to the high frequency power present in the spectrum of the HRV signal. For frequency domain analysis we used parametric and non-parametric Power Spectral Density methods as described in [3]. The results obtained using both PSD methods were very comparable. For non-parametric case we used the normalized

Welch PSD method with a hamming window to compute the spectrum estimate of the HRV sampled at the very low rate of 2Hz. to separate the frequency components into low/LF (0.04Hz-0.15Hz) and high/HF (0.15Hz-0.4Hz) and then compute the LF/HF ratio of power to determine the dominance of sympathetic (high value) or parasympathetic (low value) part of the ANS. For parametric method we used the Auto Regressive PSD of order 16.

RESULTS

We explored an approach consisting of using multiple sensors (or redundant sensing) for recording PPG signals, which would give us an opportunity to discard signals that are affected by loss of contact and motion artifacts. Figure 2 below shows two signals recorded from different fingers where one case suffered from loss of contact. Figure 3 shows the complete block diagram of the working algorithm. To test the validity of this algorithm we recorded the signals of two of the authors belonging to two different age groups. Significant differences were obtained in LF/HF ratio and pNN50 value as shown in Tables I and II.

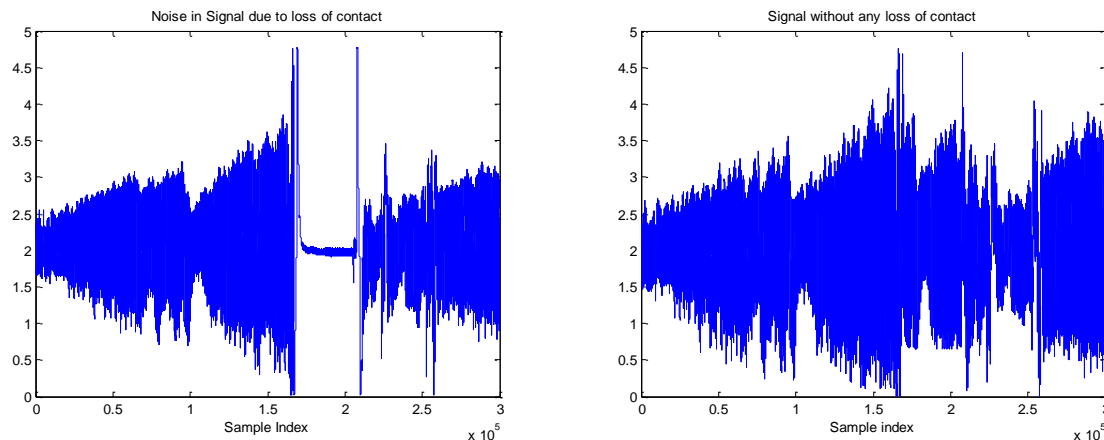


Figure 2: Simultaneous collection of PPG signals showing their equivalence and an example of a problematic interval of time where loss of contact is clearly noticeable on the left side.

Table I: Person A

Data#	Welch LF/HF	AR LF/HF	pNN50
1	0.260	0.412	64.44
2	0.519	0.566	69.77
3	0.395	0.478	61.72
4	0.897	0.914	63.06

Table II: Person B

Data#	Welch LF/HF	AR LF/HF	pNN50
1	6.74	6.61	3.31
2	4.86	3.69	3.11
3	13.87	13.78	3.21
4	11.86	10.77	3.58

DISCUSSION AND CONCLUSIONS

Heart Rate Variability signal analysis is very sensitive to accurate detection of PPG peaks location. Any imprecise detection of peak locations substantially compromises the correct determination of PP intervals and hence the quality of the time and frequency domain analysis of the HRV signals. An input signal containing distortion due to loss of contact or motion artifacts results in missed peaks which may be corrected using manual editing leading to bias in the results of analyzing the HRV signal in both time or frequency domains [3] Therefore, this problem may be avoided by the use of multiple sensors. To verify the functionality of the algorithm we used a nanoscale patch intended to stimulate an acupuncture point know to relax a person. Some brief results are shown in Table I. We also kept a track of the pNN50 count and showed that a low LF/HF index tends to correspond to a higher measure of pNN50 and vice versa. Thus, we found that there is reasonable agreement between time and frequency domain parameters of HRV signals in the determination of quantitative markers of the ANS activity. A review of pertinent

literature also indicates that a time domain parameter pNN50 has been used as a threshold to differentiate between stress and relaxation states [4].

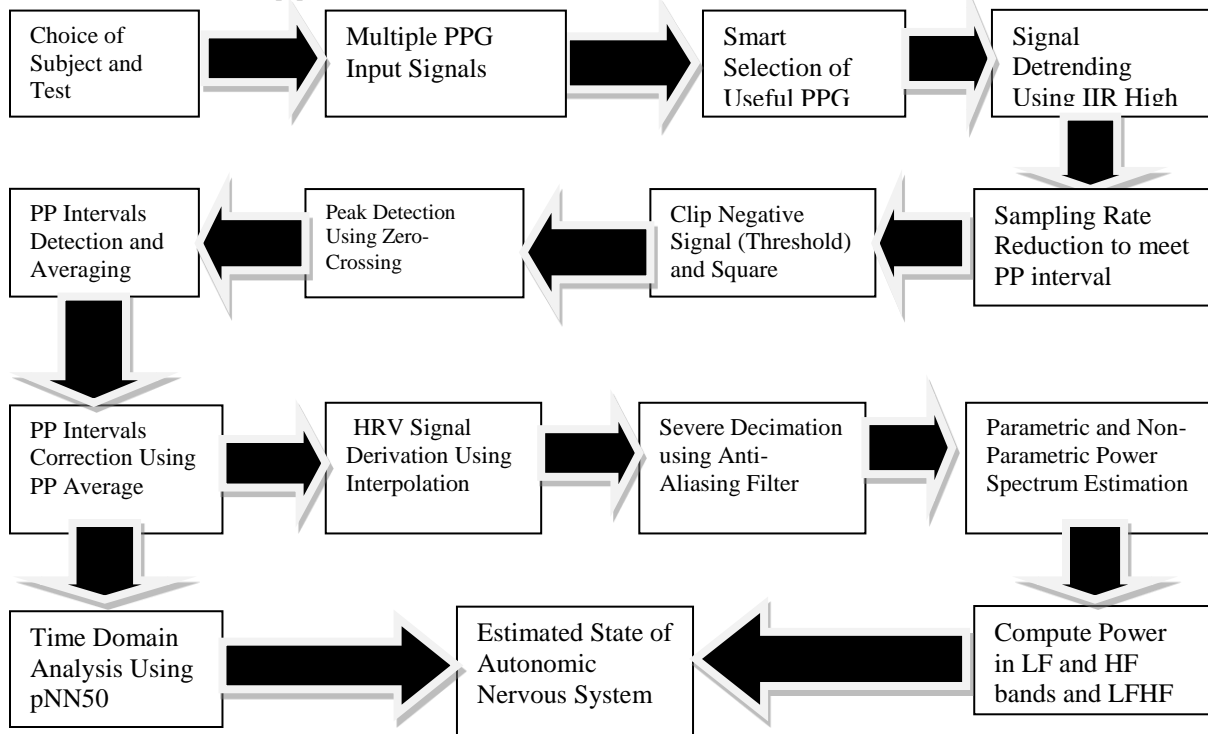


Figure 3: Complete Block Diagram of the PPG signal processing approach under development.

ACKNOWLEDGMENTS

We would like to thank *The Texas Instruments Foundation Endowed Scholarship Program* for providing financial support to graduate student Mr. Ajay K Verma to pursue a Master's degree in Electrical Engineering

REFERENCES

- [1] A.Petrenas, S.Daukantas, V. Marozas, A.Lukosevicius,"A Photoplethysmography based heart rate registration in rest and physical activity", Conference Biomedical Engineering.
- [2] A. Verma, S. Cabrera, A. Mayorga, H. Nazeran,"A Robust Algorithm For Derivation of Heart Rate Variability Spectra from ECG and PPG Signals", 29th Southern Biomedical Engineering Conference, pp. 35-36, May 3-5 2013, Miami, FL.
- [3] Camm, A. J., et al. "Heart rate variability: standards of measurement, physiological interpretation and clinical use. Task Force of the European Society of Cardiology and the North American Society of Pacing and Electrophysiology." *Circulation* 93.5 (1996): 1043-1065.
- [4] Olivia Manfrini, Carmine Pizzi, Davide Trere, Fiorella Fontana, Raffaele Bugiardini,"Parasympathetic failure and risk of subsequent coronary events in unstable angina and non-ST-segment elevation myocardial infarction" *European Heart Journal* 24, No. 17 (2003): 1560-1566.

AMINO ACID COATED UHMW-PE IMPLANTS MODIFY NEOVASCULARIZATION IN THE TISSUE-IMPLANT RESPONSE

Kenneth R. Butler, PhD, Hamed A. Benghuzzi, PhD, Michelle Tucci, PhD, Aaron D. Puckett, PhD

University of Mississippi Medical Center

Jackson, Mississippi—USA

ABSTRACT

Polyethylene materials used in orthopedic applications are biocompatible and non-immunogenic with host tissues. Recent studies in our laboratory have demonstrated the need to further study neovascularization associated with these devices in vivo to adequately elucidate methods to modulate the tissue-implant response. The purpose of this investigation was to determine differences in neovascularization after implantation of ultra-high molecular weight polyethylene (UHMW-PE) rinsed with saline (control) or coated with poly-L-lysine (PLL), arginine-glycine-aspartic acid (RGD), or arginine-glycine-glutamic acid (RGE) into 16 adult male rats intraperitoneally (I/P). Implants and surrounding tissue were harvested at 90 days post-implantation. The animals were euthanized; and the UHMW-PE implants and the fibrous tissue capsules surrounding them were harvested. Microscopic examination of routinely stained sections (5 microns, Hematoxylin & Eosin) of the fibrous tissue capsules revealed blood vessel counts were highest in the PLL coated group (19 ± 3.27 cells/high power field). There was a decreased mean number of blood vessels per high power field for saline (17.23 ± 4.57), RGE (2.81 ± 1.50), and RGD (2.56 ± 1.55). Analyses revealed blood vessel counts were significantly higher in saline and PLL treated group compared to RGD and RGE groups (ANOVA, $p < 0.05$). These findings indicate neovascularization in the fibrous tissue surrounding UHMW-PE can be reduced using amino acid combination coatings. In addition, these results provide evidence that the neovascularization can be modulated to some extent using amino acid coatings in soft tissue applications.

Keywords: polyethylene, amino acid coating, implant, soft-tissue, biocompatibility, angiogenesis

INTRODUCTION

Neovascularization is the process of new blood vessel formation from existing vasculature and occurs in the tissue-implant interaction. Though widely used in orthopedic applications such as hip and knee repair, ultra-high molecular-weight polyethylene (UHMW-PW) materials are being more widely used in soft tissue applications like sustained release drug delivery [1, 2]. An important component of the fibrous tissue capsule formation surrounding implants is neovascularization. The neovascularization process is an essential component of the fibrous tissue encasing the implant and is a fundamental requirement of biocompatibility for implants used in drug delivery applications [3-5]. These new vessels function by absorbing diffused bioactive compounds into the circulation for delivery to target organs in a sustained manner.

Previous studies in our laboratory have demonstrated that the thickness and cellular composition of the fibrous tissue capsule will affect the rate of release of drugs and other bioactive agents when used in drug delivery applications [1, 6-9]. However, few researchers have explored angiogenesis in UHME-PE in soft tissue applications. In previous biocompatibility studies, we conducted limited assessments of vascularity in the fibrous tissue surrounding TCP, hydroxyapatite, and aluminum calcium phosphate implants [6, 9-11]. Knowing how different bioactive compounds might affect neovascularity could be therapeutically advantageous in sustained release applications. Therefore, the objective of this study was to demonstrate the effect of amino acid coatings on the amount of neovascularity within the fibrous tissue capsules of extracted implants compared to a saline control. We hypothesized that the number and size of blood vessels formed within the fibrous tissue capsules surrounding UHMW-PE implants coated with RGD, RGE, and PLL would be significantly affected to the control group (saline).

METHODS

Twelve Sprague-Dawley male albino rats weighing 280-300g were obtained and acclimatized in the animal care facility for two weeks prior to surgery. These animals were randomly divided into four experimental groups and coated with RGD, RGE, or PLL amino acid solutions or saline (control). All animals in this investigation were kept on a 12-hour day/night cycle and were fed Purina Rodent Chow and water *ad libitum*.

UHMW-PE implants were cut in a similar fashion previously reported [1, 7]. One implant was placed into the peritoneal cavity of each rat. Aseptic surgical technique was employed for all the following procedure as

outlined in previous studies. Sterilized implants were inserted intraperitoneally (I/P) through the 1.5 cm incision in the lower left abdominal wall. The abdominal muscle wall was sutured with a 3-0 gut. Each abdominal incision site contained approximately four sutures. Following insertion, the skin was closed with four to six (9-mm) wound clips. Immediately following implantation, each rat was injected with 0.1 ml of 200,000 units of Penicillin G Procaine. At 90 days post-implantation, all animals from each group were euthanized using an overdose of halothane. UHMW-PE implants and the fibrous tissue surrounding them were collected and fixed in 10% neutral buffered formalin. Fibrous tissue was bisected in half for cross-sectional evaluation. Processing of these tissues included infiltration with paraffin and routine histologic processing.

Three-inch glass microscope slides were coated with 1% poly-L-lysine to aid in the tissue attachment to the glass slide. Sectioning was performed using a rotary microtome. Sections were floated in a 37° C degree water bath for stretching before being placed on glass slides. Three to five sections were cut at 5 µm and mounted to glass slides every 25 µm throughout the entire depth of the fibrous tissue mounted in the paraffin blocks. Total number of slides per animal varied from 250-400 because of loss of tissue due to processing. A randomly selected representation of 100 slides per animal (300 slides/group) were evaluated microscopically. Cellular observations were quantified by using digital analysis software (ImagePro) to count number of blood vessels per high power field (HPF) in a minimum of 10 random fields per slide throughout the thickness of the fibrous tissue. Blood vessels were identified and distinguished from the limited number of other inflammatory cells by their distinct histology and presence of red blood cells.

Statistical analysis was conducted using Stata statistical software (Stata Statistical Software: Release 13. College Station, TX). Quantification of blood vessels per HPF throughout the different layers of fibrous tissue was expressed as mean±sd. The number of blood vessels in each group were tested using analysis of variance (ANOVA, $\alpha=0.05$). Following ANOVA, post hoc Dunnett's t multiple comparison tests were used to describe which groups were significantly different.

RESULTS

Upon extraction of the implants from the peritoneal cavity, it was noted all were surrounded by a thin translucent layer of fibrous tissue with some vascularity notable grossly. Upon microscopic examination, characteristic layered capsules with all the proper cellular components and varying were noted. The PLL treated group had the highest number of vessels/HPF compared to the control (Figure 1). RGE and RGD treatment groups demonstrated similar neovascularization and fewer blood vessels/HPF compared to control and PLL. Within groups, digital analysis revealed the numbers of blood vessels per high power field were more consistently distributed throughout the tertiary fibro-adipose layer of the capsules (Figure 2).

ANOVA revealed statistically significant differences in the number of vessels/HPF ($F=35.34$, $p<0.001$). Post-hoc Dunnett's t revealed RGD and RGE treated groups had significantly fewer blood vessels/HPF compared to control (Table, $p<0.001$). The number of blood vessel/HPF in the PLL treated group was similar to control ($p=0.741$).

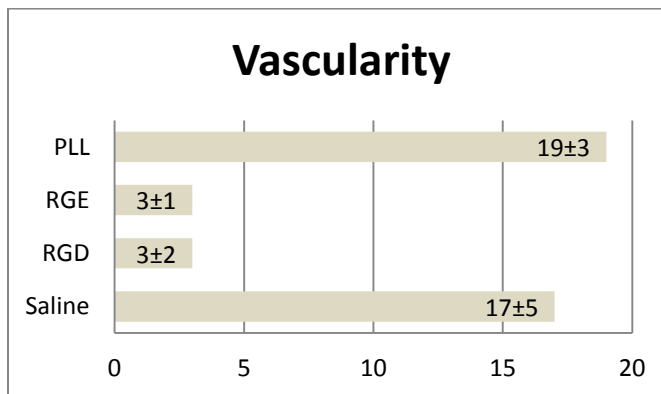


Figure 1. Mean±SD of blood vessels in the fibrous tissue matrix per high power field that developed surrounding UHMW-PE implants coated with PLL, RGE, and RGD compared to saline washed controls.

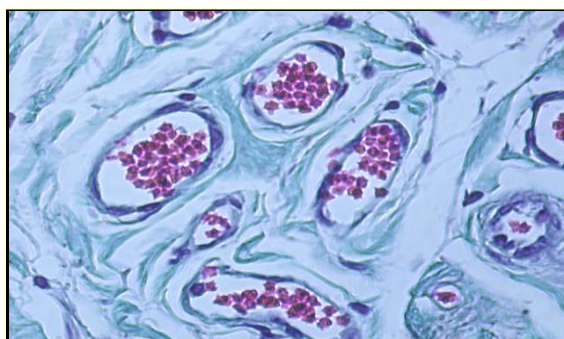


Figure 2. Representative photomicrographs highlighting vascularity in the fibrous tissue matrix surrounding UHMW-PE implants coated with amino acids. Vascularity was more dense in the tertiary layer of the fibro-adipose tissue.

Table. Results from Dunnett's t indicating significant differences of experimental groups compared to control. RGD and RGE demonstrated similar numbers of blood vessels/HPF that were significantly fewer in number compared to control. Blood vessels in the PLL treated group was similar to control.

Group		Mean Difference	Std. Error	P-value	95% CI	
					Lower Bound	Upper Bound
RGD	Saline	-14.68*	2.13	<0.001	-20.38	-8.97
RGE		-14.41*	2.13	<0.001	-20.12	-8.70
PLL		1.9	2.13	0.741	-3.92	7.49

DISCUSSION

In this investigation, we demonstrated that amino acid coatings can markedly modify neovascularization in the fibrous tissue capsule surrounding TCP bioceramic implants. Using both conventional histological laboratory techniques and digital image analysis software, we quantified neovascularization occurring within the fibrous tissue surrounding implants coated with PLL, RGD, and RGE at 90 days post-implantation.

Observing a significant decrease in the number of blood vessels/HPF in RGD and RGE treatment groups was unexpected. Neovascularity is important to any tissue-implant response and ultimate integration with host tissue[3-5]. Previous studies in our laboratory have yielded limited insight into development of new blood vessels in the fibrous tissue surrounding UHMW-PE implants. To our knowledge, this is the first study to demonstrate differences in neovascularization resulting from administration of amino acid coatings in soft tissue applications. Extending our previous findings combined with data from this analysis suggest neovascularization within the fibrous tissue surrounding implants treated with amino acid solutions is highly variable and dependent on the amino acid being administered [1, 7]. Though UHMW-PE alone has good angiogenic properties, which is excellent for drug delivery applications, our present findings indicate the addition of RGD and RGE demonstrated good potential for limiting the angiogenic response surrounding the implants.

The data from this study will allow us to enhance our ability to predict neovascularization in UHMW-PE and similar implants. Both RGD and RGE demonstrated the ability to decrease the number of blood vessels surrounding the implant, which may be important in low dose sustained release drug delivery applications. Conversely, PLL could be used to enhance the release of biological compounds.

CONCLUSIONS

The use of amino acid coatings, when used to control or enhance the development of neovascularity in the tissue implant response, have the potential of widespread use in both human and veterinary applications. Different amino acid combinations affect neovascularity differently as we observed in this investigation. RGD and RGE severely limit the number of observable blood vessel lumen. The use of digital image analysis to evaluate histological sections of fibrous capsule developed around the implants is considered instrumental in visualizing the detailed inflammatory responses such as angiogenesis. A range of additional evaluations that combine

morphological, immunohistochemical, and electron microscopy techniques are warranted to better characterize neovascularization in these implants.

ACKNOWLEDGMENTS

The authors thank Ms. Gerri Wilson and Ms. Lisa McCammon, from the Department of Orthopedic Surgery and Rehabilitation for their technical and administrative support.

REFERENCES

- [1] K. Butler, H. Benghuzzi, and S. Tucci, "Tissue-implant response following soft tissue implantation of poly-L-lysine coated UHMW-polyethylene into adult male rats," *Biomed Sci Instrum*, vol. 37, pp. 19-24, 2001.
- [2] R. Johnson, D. Harrison, M. Tucci, A. Tsao, M. Lemos, A. Puckett, J. L. Hughes, and H. Benghuzzi, "Fibrous capsule formation in response to ultrahigh molecular weight polyethylene treated with peptides that influence adhesion," *Biomed Sci Instrum*, vol. 34, pp. 47-52, 1997.
- [3] L. Tang and W. Hu, "Molecular determinants of biocompatibility," *Expert review of medical devices*, vol. 2, pp. 493-500, 2005.
- [4] K. M. Nuss and B. von Rechenberg, "Biocompatibility issues with modern implants in bone-a review for clinical orthopedics," *The open orthopaedics journal*, vol. 2, p. 66, 2008.
- [5] P. Thevenot, W. Hu, and L. Tang, "SURFACE CHEMISTRY INFLUENCE IMPLANT BIOCOMPATIBILITY," *Current topics in medicinal chemistry*, vol. 8, p. 270, 2008.
- [6] K. R. Butler, Jr. and H. A. Benghuzzi, "Morphometric analysis of the hormonal effect on tissue-implant response associated with TCP bioceramic implants," *Biomed Sci Instrum*, vol. 39, pp. 535-40, 2003.
- [7] K. R. Butler, Jr., H. Benghuzzi, M. Tucci, and A. Puckett, "Amino Acid coated uhmw-pe implants modify macrophage migration in the tissue-implant response - biomed 2011," *Biomed Sci Instrum*, vol. 47, pp. 240-5, 2011.
- [8] K. R. Butler, Jr., H. Benghuzzi, M. Tucci, and A. Puckett, "Androgen administration and macrophage behavior in the tissue-implant response - biomed 2011," *Biomed Sci Instrum*, vol. 47, pp. 228-33, 2011.
- [9] K. R. Butler, H. Benghuzzi, M. Tucci, and A. Puckett, "Neovascularization is influenced by androgenic hormones in the tissue implant response," *Biomed Sci Instrum*, vol. 48, pp. 49-56, 2012.
- [10] K. Butler, H. Benghuzzi, and A. Puckett, "Cytological evaluation of the tissue-implant reaction associated with S/C and I/P implantation of ALCAP and HA bioceramics in vivo," *Pathol Res Pract*, vol. 197, pp. 29-39, 2001.
- [11] K. R. Butler, H. A. Benghuzzi, and A. Puckett, "Morphometric evaluation of tissue-implant reaction associated with ALCAP and TCP bioceramics in vivo," *J Invest Surg*, vol. 14, pp. 139-52, May-Jun 2001.

ELECTRICAL AND MAGNETIC PARAMETERS AS A PREDICTOR OF RUST SCORE FOR FRACTURE UNION

Kanika Gupta¹, G.K. Singh², Pravin Gupta³, Vikas Verma⁴, Santosh Kumar¹

¹Department of Orthopaedics, King George's Medical University, Lucknow, Uttar Pradesh, India

²Founder- Director, All India Institute of Medical Sciences-Patna, Bihar, India

³Department of Orthopaedics, Indraprastha Appolo Hospital, New Delhi, India

⁴Department of Orthopaedics, All India Institute of Medical Sciences-Patna, Bihar, India

ABSTRACT

Clinical practice lacks a Gold Standard method for early diagnosis of union, delayed and non unions of fractures. We studied electrical and electro-magnetic parameters for predicting Radiographic Union Scale for Tibial fractures (RUST) at week 20 for diagnostic assessment of fracture healing. 30 patients with compound fracture of tibia (Gustillo Grade I&II), treated by insulated external fixators of class VI standard biomaterial, permitted measurements of electrical and electro-magnetic properties of bone excluding soft tissue. At week 20, normal union had RUST Score ≥ 9 and delayed union < 9 . Capacitance, Conductance, Impedance at week 8 and inductance at week 4 correctly predicted union in 70%, 75%, 92%, 58% patients respectively and in delayed union 94%, 61%, 76%, 69% patients respectively; precision rate for positive test (normal union) was 94%, 61% 76%, 69% respectively and precision of negative test result (delayed union) was 88%, 94%, 90%, 56% respectively; positive likelihood ratio were 14.8, 1.95, 4, 1.91 respectively; negative likelihood ratios were 0.13, 0.40, 0.1, 0.59 respectively. Impedance at week 8 is the best indicator (OR=63.09, $p=0.0013$) in prediction model for rust score 9 or above as compared to conductance (OR=0.12, $p=0.17$). Capacitance was complicated by unstable readings, inductance showed least sensitivity and specificity, therefore were excluded from prediction model. Electrical and electro-magnetic parameters of bone are measurable and could predict union (RUST Scores). This study outlined the baseline methodology and data for further research. Impedance was found to be the best predictor of union but other parameters require investigation with larger sample size.

INTRODUCTION

Delayed union and non union are diagnosed many weeks after the injury (16 weeks for delayed union and 36 weeks for non-union after the treatment). An early diagnosis of these could reduce the time and costs related to the treatment. Literature and Clinical Practice lacks a Gold Standard [1] to diagnose delayed and non-unions early. Radiological Union Scale for Tibial fractures (RUST Score) [2] provides an indication of the healing status of a tibial fracture on a continuous with high inter-rater reliability but it is unable to diagnose delayed and non-unions early.

The process of fracture healing and remodeling is governed by biological signaling pathways, generic signals, mechanical stress, chemical pathways and ionic movements generating electrical signals [3]. Bone being a biological semi-conductor displays a combination of many electrical and magnetic properties like resistance, impedance, conductance, dielectric permittivity, specific capacitance and inductance generated due to piezoelectric and junctional diode effects [3]. Bone is also diamagnetic [4]. Magnetic signals were reported as a result of induced vibrational signals in long bones [5]. Piezoelectric properly and elastic waves also contributes to the magnetic property which is independent of mechanical quality of soft tissues and may be used to investigate bone remodeling [6].

A description of impedance, capacitance, conductance and inductance in fractured segment and normal segments of bone is essential to generate baseline data for future reference. Using the diagnostic assessment it could be possible to propose a model to predict union or delayed union early.

METHODOLOGY

After attaining ethical clearance, 30 patients aged 12-70 years with Compound Fracture Both Bone Legs, Gustillo's grade I and II, treatable by external fixators, without associated injuries or complications, reporting to the trauma center of KGMU, Lucknow, UP-India giving written informed consent were studied.

Wounds were debrided and fractures reduced and externally fixed using class VI bio-compatible epoxy coated Schanz pins and rods sterilized by plasma sterilization which permitted the measurements excluding noise from soft tissue. To protect the Epoxy coating, holes were drilled and tapped in the bones using normal pins which were taken out and Epoxy quoted pins screwed in. The fractured tibia was hypothetically divided into three segments separated

by shanz pins. The segment near the knee joint was not fractured and was called as proximal segment. The segment near the ankle was not fractured and called distal segment. The segment in between the proximal segment and distal segment was fractured and was called fractured segment. Patients were assessed at day 1 after intervention, week 2, week 4, week 6 and week 8 for electrical and magnetic parameters using LCR-Q meter[7]. The readings were standardized for length of bone segment. At the end of 8th weeks fixator was removed and functional brace (plaster cast) was applied till union judged sound at week 10, 12, 14, 16,18, 20 during their physiotherapy sessions by 3 blinded clinicians for classification into union and delayed union.



Figure 1: Photograph showing measurement of Electrical Properties via LCR-Q Meter

RESULTS

The mean age of the patients was 42.83 ± 13.83 years. All 30 were males. 66.66% had fracture in the proximal portion of the diaphysis of tibia. Patients reported after mean $2.23 \pm .33$ days of injury and were surgically managed after 14.7 ± 8.08 days of injury. The mean circumference of the wound was 24.98 ± 28.11 centimeters. 56.67% wounds were circular, 16.67% were oval, 20% were punctured and 6.6% were irregular in shape. The mean distance of the wound from the ankle was 11.9 ± 7.1 centimeters. Wounds of the 20 patients were contaminated by dirt. 10 patients had comminuted fractures. Pus was present in 60% of the patients. The mean haemoglobin was 10.3 ± 2.12 gram%. Mean TLC count was 7595 ± 2325 cells/mm³, polymorphs 67.8 ± 6.4 cells/mm³, Lymphocytes 29 ± 6.6 cells/mm³, Eosinophils 4 ± 14 , Monocytes 0.87 ± 1.38 .

Table 1: Diagnostic assessment of electrical parameters predicting Normal union for RUST Score above 9

	Capacitance > 2.14E-03 micro farad at week 2	Capacitance > 2.14E-03 at week 8	Impedance > 30,000 micro ohms at week 8	Conductance < 54501 micro Siemens at week 8	Inductance < -0.12 micro Henry at week 4
Sensitivity	0.90	0.70	0.92	0.75	0.58
Specificity	0.71	0.94	0.76	0.61	0.69
Positive Predictive Value	0.41	0.94	0.76	0.61	0.69
Negative Predictive Value	0.83	0.88	0.90	0.94	0.56
(+) likelihood ratio	1.54	14.8	4	1.95	1.91
(-)Likelihood ratio	0.86	0.13	0.1	0.40	0.59
True Positives	9	7	12	3	10
True Negatives	5	8	10	16	9
False Positives	2	0 (0.5)	3	10	4
False Negatives	1	3	1	1	7

Since 93% of the patients at week 20 with RUST score < 9 went into delayed union, the cut off used was ≥ 9 . Outcome of interest was normal union. Various cutoffs for electrical parameters were evaluated using sensitivity and specificity. The best cutoff was found to be 30,000 micro ohms for impedance, 2.14E-03 micro farad for capacitance, 54501 micro Siemens for conductance, for -0.12 micro Henry for inductance.

Capacitance at weeks 2 correctly predicted union in 90% cases and delayed union in 71 % cases. The precision rate for a positive on test for normal union was 41% and for delayed union is 83%. The likelihood of

positive diagnosis is minimal and for wrong diagnosis is less (see table 1). Capacitance at week 8 correctly predicted union in 70% cases and delayed union in 94% cases. The precision rate for a positive on test for normal union was 94% and for delayed union is 88%. The likelihood of positive diagnosis is high for capacitance at week 8 (+LR=14.8) and for wrong diagnosis is significantly less (-LR=0.13) as compared to capacitance at week 2 (-LR=0.86). The capacitance at week 8 is able to predict RUST Score at week 20 better than capacitance at week 2 (see table 1). However, measuring capacitance was complicated by unstable readings and hence loss of data (as capacitance could be recorded in only 17 cases at week 2 and 18 at week 8).

Impedance at 8 weeks correctly predicted union in 92% cases and delayed union in 76% cases. The precision of positive test for normal union was 76% and for delayed union is 90%. There is small increase in likelihood of normal union (+LR=4) and moderate decrease in delayed union (-LR=0.1).

Conductance at week 8 correctly predicted normal union in 75% cases and delayed union in 61% cases. The precision for positive test for normal union was 61% and for delayed union is 94%. There is minimal increase in likelihood of normal union (+LR=1.95) and small decrease in the likelihood of union (-LR=0.40).

Inductance at week 4 is the worst indicator. Only 58% patients were correctly diagnosed for normal union and 69% for delayed union. The predictive values and likelihoods also suggest that inductance is the weakest indicator. Impedance at week 8 is the best indicator (OR=63.09, $p=0.0013$) in the prediction model for rust score for 9 or above as compared to conductance (OR=0.12, $p=0.17$).

A comparative study for difference revealed that a statistically significant difference exists in impedance at week 8 ($p=0.01$) between the normal proximal segment (mean=3099268.73, variance=2.2E+13) and fractured segment (mean=1168159.52, variance=4.91E+12). On comparing impedance between normal distal segment and fractured segment at different points of time, we found significant difference at week 2 ($p=0.006$) and 4 (0.021)

DISCUSSION

Diagnostic assessment of the electrical parameters suggests that impedance is the best predictor having the highest sensitivity and specificity values in contrast to others. A +ve Likelihood ratio of 4 as reported by us implies that impedance at 8 weeks may be used to predict RUST score at week 20 in other populations. Primary evidence also suggests that electrical impedance can be used for measuring the healing rate of the transverse fractures of bovine tibia [8] and distal radius fractures of humans [9]. Impedance has also been used to determine the time for the removal of the external fixator in rabbits by correlating them to the change in cross sectional area of the callus [10]. Capacitance is not good method to predict RUST score as the readings were unstable resulting in loss of data. Using capacitance requires further study as the circuitry used by us resulted in unstable readings. Inductance has the advantage of diminishing the confounding due to area of cross section but the sensitivity and specificity was too low. We believe that we are the first to perform a diagnostic assessment of electrical parameters that may be used to predict RUST Score at week 20. Impedance imaging [11] and Magnetic resonance electrical impedance tomography [12] are subjective processes and direct measurement of impedance values is objective. If incorporated and standardized against these processes, it can be used for changing subjective assessment into objective assessment.

We standardized our measurements against the length of the segment from where the electrical property was measured. High variance reported by us could be because we did not take into consideration factors like BMD mechanical properties of bone, area of cross section, blood flow and ionic content [7] as the fracture healed. It has been reported that blood flow and ionic content at the fractured segment may influence the readings [7] but no method is reported in literature to account for them. Monitoring and standardization against these confounders is necessary as the healing progresses [3].

CONCLUSION

Diagnostic assessment of the electrical and electromagnetic parameters confirms that impedance is the best predictor having the highest sensitivity and specificity values in contrast to conductance, inductance or capacitance. A +ve Likelihood ratio of 4 as reported by us implies that impedance at 8 weeks may be used to predict RUST score at week 20 in other populations as well. Further research is required considering this study as baseline for developing a methodology controlling all identified confounders.

ACKNOWLEDGEMENT

I am extremely thankful to Uttar Pradesh Council of Science and Technology for funding this project. I am also thankful to Mr Jhon Frey, Dr Naren Naik, Dr Vishal Saxena and Dr KS Venkatesh for their technical advice regarding instrumentation.

REFERENCES

- [1] S. Morshed, L. Corrales, H. Genant and T. Miclau. Outcome assessment in clinical trials of fracture-healing. *J Bone Joint Surg Am.* 2008;90(1):62-67.
- [2] B.W. Kooistra, B.G. Dijkman, J.W. Busse, S. Sprague, E.H. Schemitsch, M Bhandari. The Radiographic Union Scale in Tibial Fractures:Reliability and Validity. *J Orthop Trauma.* 2010 Mar;24(1):S81-6
- [3] K. Gupta, P. Gupta, G.K. Singh, S. Kumar, R.K. Singh, R.N. Srivastava. Changes in electrical properties of bones as a diagnostic tool for measurement of fracture healing. *Hard Tissue.* 2013 Jan 21;2(1):3
- [4] M.D. Simon, L.O. Heflinger, A.K. Geim. Diamagnetically stabilized magnet levitation *Am. J. Phys.*,2001 Jun; 69(6): 702-715
- [5] S. Saha, R.S. Lakes. A non-invasive technique for detecting stress waves in bone using the piezoelectric effect. *IEEE Trans Biomed Eng.* 1977 Nov;24(6):508-512.
- [6] R.S. Lakes, S. Saha. A noncontacting electromagnetic device for the determination of in vivo properties of bone. *Med Instrum.* 1978 Mar-Apr;12(2):106-109.
- [7] J. Sierpowska, M.A. Hakulinen, Töyräs J, Day JS, Weinans H, Jurvelin JS, Lappalainen R. Prediction of mechanical properties of human trabecular bone by electrical measurements. *Physiol Meas.* 2005 April;26(2):119-131
- [8] T. Yoshida, W.C. Kim, K. Kawamoto, T Hirashima, Y. Oka, T. Kubo. Measurement of bone electrical impedance in fracture healing. *J Orthop Sci.* 2009 May;14(3):320-9
- [9] T. Hirashima, W.C. Kim, K. Kawamoto, T. Yoshida, T. Kubo. Evaluating Bone Union of Distal Radius Fractures by Measuring Impedance Values. *Orthopedics.* 2009 Jan;32(1):31.
- [10] T. Yoshida, W.C. Kim, Y. Oka, N. Yamada, T. Kubo (2010). Assessment of distraction callus in rabbits by monitoring of the electrical impedance of bone. *Acta Orthop.* 2010 Oct;81(5):628-33.
- [11] I.K. Ritchie, R.B. Chesney, P. Gibson, V. Kulkarni, J.M. Hutchison. Impedance osteography: a technique to study the electrical characteristics of fracture healing. *Biomed Sci Instrum.* 1989;25:59-77.
- [12] E.J. Woo, J.K. Seo. Magnetic resonance electrical impedance tomography (MREIT) for high-resolution conductivity imaging. *Physiol Meas.* 2008 Oct;29(10):R1-26

A COMPARISON OF DECELLULARIZATION METHODS APPLIED TO PORCINE OSTEOCHONDRAL XENOGRAPTS FOR ARTICULAR CARTILAGE REPAIR

Mark Mosher¹, Ryan Butler³, Steven Elder¹, Andrew Claude³, Jim Cooley², Eric Gilbert¹, Anuhya Gottipati¹, Jun Laio¹, Robert Meyer³

¹Agricultural & Biological Engineering, Mississippi State University, Mississippi State, Mississippi

²Department of Pathobiology and Population Medicine, College of Veterinary Medicine, Mississippi State University, Mississippi State, Mississippi

³Department of Clinical Sciences, College of Veterinary Medicine, Mississippi State University, Mississippi State, Mississippi

ABSTRACT

The objective of this research was to compare decellularization methods for porcine osteochondral xenografts, which may have potential application in articular cartilage repair. Ø5.0 mm porcine osteochondral dowels were obtained from adult pig knee joints. Method 1 was a technique that had been developed for osteochondral xenografts. Method 2 had been used to decellularize xenogenic myocardium for cardiac tissue engineering. Method 3 was designed to partially demineralize and deproteinize xenogenic bone for bone defect filling. Evaluations of the osteochondral xenografts biochemistry, biomechanics, and histology were performed. In addition, they were assessed for their ability to resurface the trochlear groove of adult New Zealand white rabbits *in vivo* for up to 8 weeks. Method 1 removed almost all of the glycosaminoglycans and DNA, but this severely compromised the compressive stiffness. Methods 2 and 3 both extracted about half the glycosaminoglycan, and Method 3 was more effective than Method 2 at removing DNA (roughly 75% vs. 50% removed). Both methods reduced the compressive stiffness by 50% or more. The rabbit experiment showed that none of the methods caused severe adverse immune response, and by 8 weeks the bone phase was gradually integrating into the native bone. The joint resurfacing was acceptable in some cases. The results suggest Method 1 is too destructive to the extra cellular matrix. However, it is believed that Methods 2 and 3 could be refined to provide an optimal balance between DNA removal and retention of biomechanical properties.

Keywords: articular cartilage, xenograft, pig, decellularization

INTRODUCTION

Many young physically active individuals frequently suffer from joint injuries, which result in osteochondral and cartilage lesions. These lesions lead to pain, swelling, and loss of functionality of the joint. One of the most popular treatments is osteochondral allograft transplantation (OAT). This treatment has the advantage of immediately restoring a resistance to mechanical stress. The big disadvantage to OAT is that there is a low supply of allografts available. This why using a xenograft is a very appealing alternative because they are in high supply and have a low cost. Decellularization of the xenograft can reduce the immunogenicity of the graft, and it can also help integration into the host tissue. Several studies have already shown that osteochondral xenografts (OCXG) have potential to repair articular cartilage, but they still have room for improvement [1, 2]. The aim of this study is to evaluate the ability of previously published decellularization protocols on the removal of antigenic cellular material, structural biochemistry, and biomechanics of porcine OCXGs, and to study the *in vivo* response of the OCXGs in a rabbit articular cartilage defect model.

MATERIAL AND METHODS

Tissue Samples:

Ø5.0 mm osteochondral dowels were harvested using a trephine from adult porcine stifle joints obtained from a local meat processor. All samples were rinsed with PBS and frozen at -20 °C , and when samples were ready for processing or testing they were thawed.

Method 1

Decellularization was based on the method described by Khier et al [3]. First, OCXGs were exposed to two freeze/thaw cycles. The plugs were then exposed to two more cycles of freeze/thaw in hypotonic buffer. OCXGs were then incubated with agitation in detergent. This was then followed by two washes in PBS with aprotinin. After, the wash samples were then incubated in nuclease. Once completed OCXGs were then washed in PBS with protease inhibitors. Decontamination was achieved by incubating samples in 0.1% (v/v) peracetic acid in PBS for 3h at room temperature.

Method 2

This method was designed for the decellularization of myocardium and was developed by Wang et al [4]. Osteochondral plugs were decellularized in a solution of 0.25% SDS, 1mM PMSF, 0.01%, 20 ug/ml RNase, and 0.2 mg/ml DNase under agitation for 11 days under room temperature. During the 11 days solution was changed every 3 days and samples received 10min ultrasonic treatment (50Hz). After 11 days samples were washed in PBS twice for 1h. Following that they were sterilized in two washes of 70% EtOH for 2h each and then washed with sterile PBS.

Method 3

This method was adapted from Xie et al [5] and is a partial demineralization and deproteinization. First, OCXGs were immersed in 10% hydrogen peroxide for 24h at 38°C. Next the plugs were partially demineralized in 0.6 N hydrochloric acid for 3-4 h at room temperature. Then they were incubated at room temperature for 1h in chloroform/ methanol (1:1) and then in 0.25% trypsin for 12h at 4°C. Lastly, they went through multiple extensive washes with distilled water and were lyophilized. They were gas sterilized for the *in vivo* experiment.

Animal Testing

All experiments involving New Zealand White rabbits were approved by the Mississippi State Animal Care and Use Committee. This experiment involved 6 healthy male rabbits weighing approximately 4kg. Rabbits were anesthetized by intubation using 1% isoflurane and oxygen. Full-thickness cylindrical defects, 5mm diameter by 7mm depth, were created bilaterally in the central part of the patellofemoral groove of both stifle joints. The defects were then filled with one of the decellularized OCXGs matching the defects size so the grafts and the host cartilage was flush. The xenografts were selected so no rabbit received the same type in both knees and each method was represented 4 times. Three rabbits containing 2 constructs from each method were euthanized at 2 weeks and 8 weeks after surgery to assess the inflammatory response and cellular infiltration of the xenograft. Following this the joints were radiographed to assess bone healing.

Histology, Biomechanical Testing, and Biochemistry

Samples were fixed in formalin and decalcified in formic acid. Sections were then embedded in paraffin and stained with H&E, Toluidine Blue, and Picrosirius Red. Biomechanical testing of the non-implanted tissue required the separation of the cartilage from the bone with a scalpel. The cartilage pieces (n=5) were then loaded to 10% strain under confined compression, and the aggregate modulus was found by fitting the stress relation curve to the biphasic model. The bone cylinders (n=5) were then loaded to failure in unconfined compression at a rate of 0.01mm⁻¹. Five samples from each group were digested in papain buffer (pH 6.5) for 24h at 60°C. DNA was then quantified using Hoechst 33258. Glycosaminoglycan (GAG) was quantified using the Biocolor Blyscan Assay based on dimethyl- methylene blue dye-binding. Bone (n=5) cylinders were tested for their calcium content using the Stanbio Calcium (CPC) LiquiColor kit after extraction with HCL.

H&E staining showed that cell nuclei were completely removed by method 1, but many nuclei remained after processing by methods 2 and 3. The Toluidine blue staining showed that method 1 almost completely stripped the tissue of proteoglycans, but methods 2 and 3 only partially removed the proteoglycans from the tissue (Fig. 1). Picrosirius red staining showed that method 1 removed a lot of the collagen in the tissue (Fig. 1). The results from the biochemistry and biomechanical testing shown in Table 1

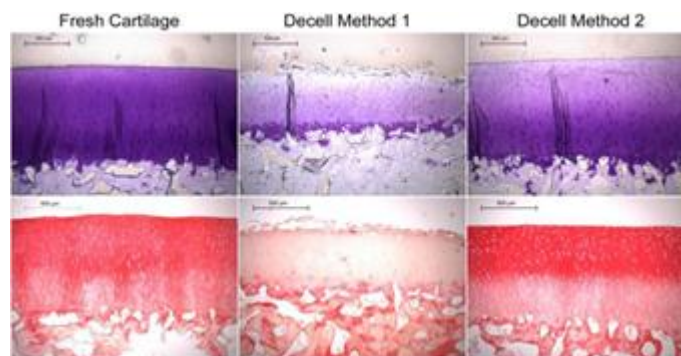


Fig. 1. Histology of decellularized OCXGs. (top: Toluidine blue, bot: Picrosirius red)

Table 1. Biochemical and Biomechanical data of OCXG. (* designates a statistical difference wrt controls)

	Method 1	Method 2	Method 3	Frozen/Thawed Controls
DNA normalized to wet	0.1982± 0.0364*	0.8498± 0.2017*	0.4186± 0.2067*	1.5076± 0.3310
GAG normalized to wet	3.742± 3.25*	54.736± 9.96*	44.765± 16.81*	99.018± 28.26
Calcium normalized to dry	137.0± 11.45	93.21± 33.31	30.79± 23.62*	115.93± 21.34
Aggregate Modulus of Cartilage (MPa)	0.0213± 0.0026*	0.0552± 0.0039*	0.077± 0.0084*	0.1397± 0.04
Young's Modulus of Bone	79.32± 39.69	167.93± 44.56	97.58± 49.25*	167.88± 82.58

Animal Experiment

After 2 weeks of implantation the grafts were strongly demarcated from the surrounding bone and had evoked a sclerotic reaction. By 8 weeks the grafts had begun to integrate with the native bone as shown in Figure 2. Qualitatively, method 1's grafts were the best integrated followed by method 3 and then method 2, but the variation was minor. Synovitis was present in all of the synovial membrane/ joint capsules to some degree, but it was generally mild.



Fig 2. OCXG 8 week radiograph.

DISCUSSION

The goal of decellularizing the OCXGs was to remove as much antigenic cellular material as possible while still leaving an extra cellular matrix still intact and having the xerograph still retain its mechanical

properties. Method 1 was able to completely remove all cells for the cartilage phase, while method 2 and 3 only removed some of the nuclei. Method 1 removed almost all the DNA in the OCXG while, method 3 removed 75% of the DNA, and method 2 only removed 50% of it. The histology and biochemistry showed that method 1 removed almost all of the GAG molecules from the tissue and methods 2 and 3 only removed about half of the GAG in their OCXGs. Method 3 stripped about 75% - 50% of the calcium from the

bone of the OCXGs, but methods 1 and 2 showed little to no calcium loss. Method 3 reduced the aggregate modulus of the cartilage by about 50%, but method 2 was not far behind reducing it by 60%. The biggest reduction was seen in method 1, which reduced the modulus by 85%. The decellularization of the bone did not affect the Young's modulus in method 2. The other methods reduced the Young's modulus by about 50%. The animal experiment showed that none of methods had any severe adverse immune responses. Also, all the OCXGs had started to integrate into native bone and cartilage with an acceptable level of joint resurfacing. Considering all the factors method 1 is not acceptable because it compromised too much of the mechanical strength by stripping out most of the collagen and the GAG. Methods 2 and 3 look very promising they have a good balance of DNA removal and retention of the collagen and GAG. Also, they preserve the mechanical strength of tissues. Method 2 does have a little more priority over method 3 because it did not harm the bone matrix as much. It is believed that methods 2 and 3 could be refined to create better OCXGs because they only have just been adapted to decellularization of cartilage and bone.

CONCLUSIONS

OAT is a viable option when repairing osteochondral and cartilage lesions. The drawback is that allografts are hard to come by. Xenografts are widely available and come at cheap cost. Decellularization of xenografts promotes cell infiltration and integration into the tissue, while not causing a severe immunogenic response from the host. The evaluation of these three decellularization techniques shows that methods 2 and 3 were the most advantageous and promising to use. They stripped DNA and cells from the tissue, while still preserving some of the GAG and the mechanical properties of the xenograft. Method 2 was just slightly favored because it had less of an impact on the bone phase. With further research these two methods could be improved upon since there were adapted to this task.

ACKNOWLEDGMENTS

Research reported in this publication was supported by the National Institute of Arthritis and Musculoskeletal and Skin Diseases of the National Institutes of Health under Award Number 1R15AR057934. The content is solely the responsibility of the authors and does not necessarily represent the official views of the National Institutes of Health.

REFERENCES

- [1] Toolan B, Frenkel S, Pereira D, Alexander H. Development of a novel osteochondral graft for cartilage repair. *J Biomed Mater Res*. Vol. 41, no. 2, pp. 244-250. Aug, 1998
- [2] von Rechenberg B, Akens M, Nadler D, et al. Mosaicplasty with photooxidized, mushroom shaped, bovine, osteochondral xenografts in experimental sheep. *Vet Comp Orthop Traumatol*. Vol. 19, no. 3, pp. 147-56. 2006
- [3] Kheir E, Stapleton T, Shaw D, Jin Z, Fisher J, Ingham E. Development and characterization of an acellular porcine cartilage bone matrix for use in tissue engineering. *J Biomed Mater Res A*. vol. 99, no. 2, pp 283-94. Nov, 2011.
- [4] Wang B, Borazjani A, Tahai M, Curry AL, Simionescu DT, Guan J, To F, Elder SH, Liao J. Fabrication of cardiac patch with decellularized porcine myocardial scaffold and bone marrow mononuclear cells. *J Biomed Mater Res A*. vol. 94, no.4, pp. 1100-10. Sep, 2010.
- [5] Xie H, Yang F, Deng L, Luo J, Qin T, Li X, Zhou GQ, Yang Z. The performance of a bone-derived scaffold material in the repair of critical bone defects in a rhesus monkey model. *Biomaterials*. vol. 28, no.22, pp.3314-24. Aug, 2007.

EFFECTS OF GENIPIN ON DECELLULARIZED PORCINE CARTILAGE**T. King¹, S. Elder²**¹**Department of Animal and Dairy Sciences, Mississippi State University**²**Department of Agricultural and Biological Engineering, Mississippi State University****ABSTRACT**

This research aims to develop an alternative method to osteochondral articular transfer using decellularized, crosslinked porcine osteochondral xenografts (OCXGs). Crosslinking collagenous tissue results in greater mechanical strength, more resistance to enzymatic degradation, and reduced immunogenicity. This study used genipin, a chemical substance from the *Gardenia jasminoides* Ellis fruit. Genipin is inexpensive and simple to use. In this study, porcine articular cartilage disks were decellularized via a previously published method for porcine nasal septal cartilage decellularization. The process extracts glycosaminoglycan to allow for greater infiltration of nutrients and host cells. The disks were then crosslinked with 0.01% and 0.1% aqueous genipin for 3 days at room temperature with agitation. Prior to decellularization, the cartilage disks' biphasic properties were determined by confined compression testing. The test was repeated after decellularization and after crosslinking. The aggregate modulus was notably lessened after decellularization but returned to, and in most cases, exceeded that of the fresh disks after crosslinking. Genipin fixation also tended to lower the hydraulic permeability. In a separate experiment, genipin fixation of fresh cartilage was shown to slow the rate of tissue destruction by collagenase. This study demonstrates that genipin seems to be a viable alternative for crosslinking OCXGs.

Keywords: xenografts, crosslinking, genipin, cartilage, mechanical properties

INTRODUCTION

Orthopaedic surgeons come into contact with numerous patients experiencing articular cartilage lesions. According to a study that analyzed 25,124 knee arthroscopies from 1989-2004, 60% of the patients suffered at least one chondral lesion. Of that, 7% accounted for candidates suitable for restorative procedures, being 40 years of age or younger with one to three moderate to severe cartilage lesions [1]. Currently there is only one procedure that immediately restores hyaline cartilage to the joint surface and is capable of bearing normal loads, osteochondral articular transplantation. An osteochondral autograft transplantation removes cartilage from the edges of the patient's own joint to repair the defect. Disadvantages of this method include donor site morbidity and limited supply. On the other hand, an osteochondral allograft transplantation uses cartilage pieces from other donors. Disadvantages include graft rejection and disease transmission [2,3,4,5,6]. The purpose of this research is to develop an alternative to conventional treatments which will utilize decellularized porcine osteochondral xenografts (OCXG). Osteochondral dowels could be harvested from a porcine stifle joint, cleaned, decellularized, and crosslinked. The plugs could then be used to repair articular cartilage defects during exploratory surgery using standard OAT surgical procedures. The pig is an appropriate source of human replacement tissue due to its similar size and physiology as well as its rapid growth rate [7]. In addition to the benefits mentioned, decellularized xenografts are low cost, available in abundance, low risk for disease transmission, able to support weight and provide a solid anchorage within the joint.

The long-term goal of this research is to advance the development of decellularization and crosslinking processes to make OCXGs more biocompatible and durable. The immediate aim is to further develop a non-cytotoxic means of chemically crosslinking collagen. A previously published study on glutaraldehyde fixation of collagenous tissue showed that crosslinking simultaneously increases mechanical strength and decreases degradation by enzymatic processes. Crosslinking also masks antigen, resulting in a less immunogenic product [8]. Glutaraldehyde has often been used to chemically crosslink bioprosthetic heart valves but is quite cytotoxic. Leaching of any glutaraldehyde residues into nearby tissue results in necrosis [9]. Therefore, this research studies the use of non-cytotoxic genipin as a means of chemically crosslinking cartilage collagen. Genipin is derived from geniposide which is harvested from the fruit of *Gardenia jasminoides* Ellis. A study comparing the effects of glutaraldehyde and genipin for fixation of decellularized porcine xenografts in sheep found glutaraldehyde to be extremely cytotoxic while genipin succeeded in depressing the host's inflammatory response [10]. In addition, genipin-crosslinked matrices with at least a 50% crosslinking degree were biocompatible and the cells within, viable [11]. We hypothesize that, in general, crosslinking via genipin has positive effects on mechanical strength and

resistance to enzymatic degradation.

METHODS

Ten samples of 5 mm articular cartilage discs were harvested from porcine stifle joints and biphasic properties (aggregate modulus and hydraulic permeability) measured via stress-relaxation tests performed in confined compression. The cartilage samples were then decellularized according to previously published protocol for porcine nasal septal cartilage [12]. Biphasic properties were re-tested on each of the samples and compared to the fresh cartilage values. Five of the discs were crosslinked in 0.01% aqueous genipin for 24 hours at room temperature with agitation. The remaining 5 were crosslinked in 0.1% aqueous genipin under the same conditions. The biphasic properties of all 10 samples were tested in confined compression and compared to the pre-crosslinking values.

A separate experiment was conducted to investigate resistance to collagenase digestion. Articular cartilage discs (n=30) 5 mm in diameter were harvested from pig stifle joints. Ten samples were maintained as a control group, 10 were fixed in 0.01% genipin, and 10 in 0.1% genipin. All samples were incubated at 37°C with agitation for 18 hours. The non-crosslinked control group was incubated in PBS without genipin. The genipin concentration and exposure duration were determined based on a previous study of genipin-fixed bovine pericardium [13]. Collagenase resistance testing (n=10 per group) was then performed. Samples were weighed prior to exposure to collagenase treatment and placed in individual wells of 24-well plates. Samples were covered with 1 ml of 1 mg/ml collagenase type 2 (300 U/mg) solution and incubated at 37°C with agitation. Samples 1-5 of each group (control, 0.01% genipin, and 0.1% genipin) were removed from solution after 30 min, blotted, and weighed. Samples 6-10 of each group were incubated with agitation for 60 min before being weighed.

RESULTS

Figure 1 illustrates the results of the stress-relaxation tests in confined compression to determine biphasic properties. In both the 0.01% and 0.1% genipin fixed samples, the aggregate modulus was usually higher after decellularization and genipin crosslinking compared to fresh samples. Both differences were statistically significant ($p < 0.05$, paired t-test). Figure 1a also demonstrates the reduction in aggregate modulus caused by decellularization alone. Figure 2 demonstrates the effect of decellularization and genipin crosslinking on the hydraulic permeability of porcine articular cartilage. At both genipin concentrations, the hydraulic permeability tended to decrease in comparison to fresh samples. Figure 3 represents the effect of genipin crosslinking on enzyme degradation resistance of the cartilage samples. At 30 minutes, the 0.01% and 0.1% genipin crosslinked samples had lost significantly less weight than the control group ($p < 0.05$, ANOVA). This trend continued through 60 minutes but the differences were not statistically significant.

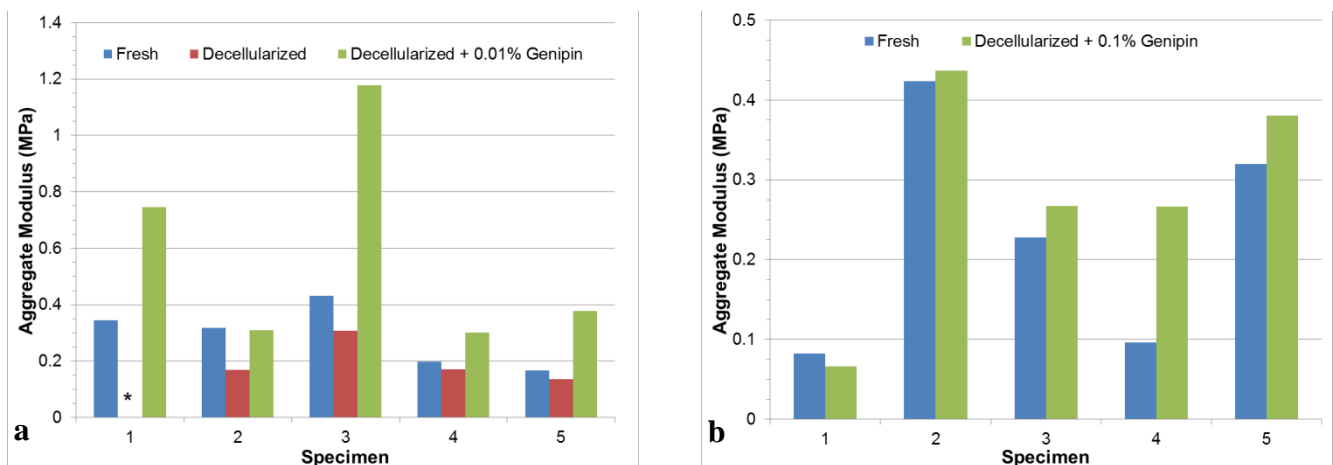


Figure 1. Effect of tissue processing on aggregate modulus of porcine articular cartilage. a – low genipin concentration; b – high genipin concentration. *Data not available due to irregular stress relaxation profile.

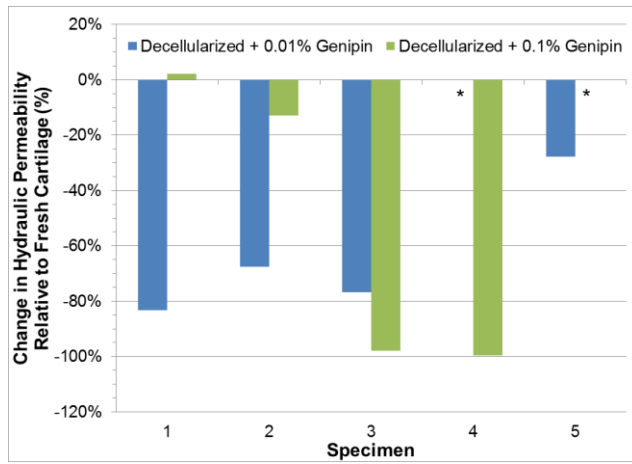


Figure 2. Effect of genipin on hydraulic permeability of porcine articular cartilage. *Data not available due to irregular stress relaxation profile.

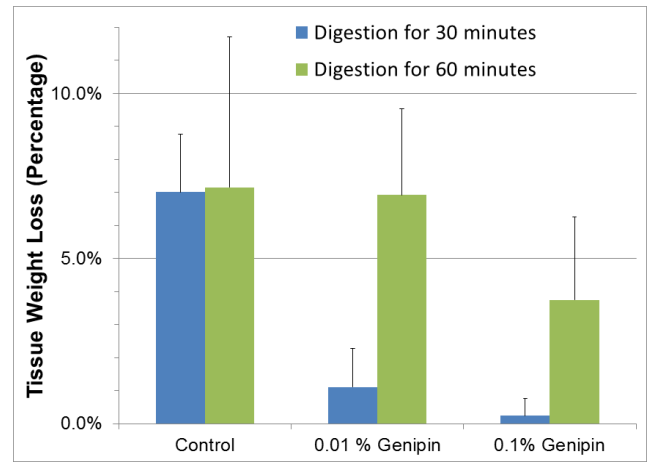


Figure 3. Effect of genipin fixation on resistance of porcine cartilage to degradation by collagenase type 2.

DISCUSSION

As hypothesized, decellularization and genipin crosslinking increased the aggregate modulus for the 0.01% and 0.1% genipin-fixed porcine articular cartilage discs when compared to fresh samples. Simultaneously, the hydraulic permeability of crosslinked samples was decreased. A high aggregate modulus and low hydraulic permeability are what provide articular cartilage with its ability to withstand high magnitude and repetitive compressive joint loads. The samples that were chemically crosslinked with genipin performed better in the collagenase resistance test than those in the control group that were not crosslinked. The crosslinked samples were better able to resist enzyme degradation and maintain more of their original mass after being exposed to collagenase for the given time periods. Overall, these findings are consistent with those of Okamura et al. in their *in vivo* study of decellularized, crosslinked cartilage which suggested that crosslinked cartilage better withstood biodegradation by host enzymes than non-crosslinked cartilage [8]. Further tests will be performed with larger sample sizes to improve precision of measurements and to enhance statistical power.

CONCLUSIONS

It can be concluded that crosslinking porcine articular cartilage discs with genipin is a successful means of enhancing mechanical properties and resisting enzyme degradation. As seen in this study, the samples that had been cross-linked with 0.01% and 0.1% genipin experienced increased aggregate modulus, decreased hydraulic permeability, and greater resistance to degradation by collagenase than those that had not been crosslinked. This proves significant toward identifying genipin as a successful tool for increasing biphasic mechanical properties and reducing degradation by enzyme activity. This knowledge is consistent with the findings of literature previously cited and will be useful in developing durable osteochondral xenografts.

REFERENCES

- [1] W Widuchowski, J Widuchowski, and T Trzaska, "Articular cartilage defects: study of 25,124 knee arthroscopies," *Knee*, vol. 14, no. 3, pp. 177-82, 2007.
- [2] BJ Cole, C Pascual-Garrido, and RC Grumet, "Surgical management of articular cartilage defects in the knee," *J Bone Joint Surg Am*, vol. 91, no. 7, pp. 1778-90, 2009.

- [3] K Zaslav et al., "A prospective study of autologous chondrocyte implantation in patients with failed prior treatment for articular cartilage defect of the knee: results of the Study of the Treatment of Articular Repair (STAR) clinical trial," *Am J Sports Med*, vol. 37, no. 1, pp. 42-55, 2009.
- [4] JE Browne et al., "Clinical outcome of autologous chondrocyte implantation at 5 years in US subjects," *Clin Orthop Relat Res*, vol. 436, pp. 237-45, 2005.
- [5] AE Gross, N Shash, and P Aubin, "Long-term followup of the use of fresh osteochondral allografts for posttraumatic knee defects," *Clin Orthop Relat Res*, vol. 435, pp. 79-87, 2005.
- [6] PC McCulloch, RW Kang, MH Sobhy, JK Hayden, and BJ Cole, "Prospective evaluation of prolonged fresh osteochondral allograft transplantation of the femoral condyle: minimum 2-year follow-up," *Am J Sports Med*, vol. 35, no. 3, pp. 411-20, 2007.
- [7] RH Chen, A Kadner, RN Mitchell, and DH Adams, "Mechanism of delayed rejection in transgenic pig-to-primate cardiac xenotransplantation," *J Surg Res*, vol. 90, pp. 119-125, 2000.
- [8] K Okamura et al., "Antigen depressant effect of glutaraldehyde for aortic heterografts with a valve, with special reference to a concentration right fit for the preservation of grafts," *Surgery*, vol. 87, no. 2, pp. 170-6, 1980.
- [9] WJ Revell and FW Heatley, "Functional restoration of an articular surface using a heterotopic xenograft: biology of host-implant interaction in the canine patella," *Biomaterials*, vol. 9, pp. 173-180, 1988.
- [10] P Somers et al., "Genipin blues: an alternative non-toxic crosslinker for heart valves?," *J Heart Valve Dis*, vol. 17, no. 6, pp. 682-8, 2008.
- [11] NC Cheng, BT Estes, TH Young, and F Guilak, "Genipin-crosslinked cartilage-derived matrix as a scaffold for human adipose-derived stem cell chondrogenesis," *Tissue Eng Part A*, vol. 19, no. 3-4, pp. 484-96, 2013.
- [12] S Schwarz et al., "Processed xenogenic cartilage as innovative biomatrix for cartilage tissue engineering: effects on chondrocyte differentiation and function," *J Tissue Eng Regen Med*, vol. Published online in Wiley Online Library, no. DOI: 10.1002/term.1650, 2012.
- [13] H-C Liang, Y Chang, C-K Hsu, M-H Lee, and H-W Sung, "Effect of crosslinking degree of an acellular biological tissue on its tissue regeneration pattern," *Biomaterials*, vol. 25, pp. 3541-3552, 2004.

DESIGN AND IMPLEMENTATION OF EMG/EEG FINITE STATE MACHINE FOR PROSTHETIC HAND CONTROLLING

Mustaffa Alfatlawi and Dean Aslam

Electrical and Computer Engineering Department
Michigan State University

East Lansing, USA

ABSTRACT

In this work a finite state machine is designed to combine both Surface Electromyography (SEMG) and Electroencephalography (EEG) signals in actuating a prosthetic hand. Also single electrode EEG and two electrodes EMG Wireless data acquisition circuits are designed and implemented to reduce the communication complexity of the system and to have more freedom in allocate the electrodes. The system was tested successfully by five healthy subjects. The results using combination of SEMG and EEG showed more sustainability in doing tasks than using either SEMG or EEG signals.

Keywords: SEMG, Brain Waves, prosthetics, non-pattern recognition.

INTRODUCTION

There are two main sources for actuating the upper limbs prosthetics; Surface Electromyography (SEMG) and Electroencephalography (EEG). SEMG contains rich information about the intention of the handicapped person which can be used in controlling prosthetics [1]. Two main methods can be used to exploit the SEMG signal to control prosthetics, pattern recognition [2, 3], and non-pattern recognition [4, 5]. Many challenges have faced this approach; the most important ones can be addressed by: unintuitive way of controlling, weakness of the controlling muscle, resulted exhaustion from the continuous physical reaction.

The independence on the neuromuscular actions makes EEG a good candidate to overcome the weak points of EMG-controlled prosthetics. Many researches have focused on using the EEG signal to control prosthetics [6, 7]. A lot of weak points should be taken care of before using this signal. For example, distance between the source of EEG signal and the scalp degrades accuracy of the delivered information. Another weak point is that the detected signal from the scalp is not exclusively sourced from the brain; many environmental and biological sources can participate in composing such signals [8].

In this paper a finite state machine algorithm is designed to combine both EEG and EMG signals in the decision making process in order to creates more intuitive motion with less physical effort. Wireless SEMG and EEG data acquisition systems are designed to give more freedom in choosing the controlling muscle instead of being limited to the weak muscles in the rest of the defected arm, and to decrease the hardware complexity of the system.

METHODS

1. Theory

In this work a parallel analyses are done for SEMG and EEG signals in order to produce a decision to actuate a single degree of freedom robotic hand.

1.1. SEMG Detection and Analysis

The SEMG signal is formed form the overlap of action potentials (AP) which result from the discharge of the active motor units during the contraction of muscles.

According to a research by Clancy et al. [9], Laplacian probability density function represents a better fit for the SEMG than the Gaussian model, which makes Mean absolute Value (MAV) more accurate than the RMS in estimating the amplitude of the SEMG. The MAV value can be obtained by the following formula:

$$MAV = \frac{1}{N} \sum_{i=1}^N |x_n| \quad (1)$$

where:

N : number of samples.

MGH algorithm is used to determine the state of muscle out of the MAV value [10]. This algorithm is based on sliding two adjacent windows (leading and trailing) on the SEMG signal. The value of the MAV is calculated for two windows, and then the difference between them is calculated (ΔMAV). A contraction in the muscle is assumed

to be occurred if $\Delta\text{MAV} > K$, and a relaxation is assumed to occurred if $\Delta\text{MAV} < -K$, where K is a predefined threshold which is chosen according to the average level of contraction during the first operation time.

1.2. EEG Detection and Analysis

EEG signal is a dynamic, stochastic, nonlinear, and non-stationary bioelectrical signal. A single dry electrode TGAM chip manufactured by NeuroSky Inc. is used in this work. The chip produces the raw brain waves in addition to two values, which represents the attention and meditation status on scale of 1 to 100. The attention level is used as a control signal in the decision making process by comparing it to a single threshold value. The threshold value is chosen according to the convenience of the user.

1.3. Finite State Machine.

The finite state machine which is responsible for decision making can be described as follows: the system stays in the idle mode if the attention level is below the threshold regardless of the muscle state. If the user intends to use the robotic hand, the attention level should be increased above the threshold to transform the system from the idle mode to the active mode. After that, the grip is either closed if the muscle is contracted, or opened if the muscle is relaxed. A flow chart for the finite state machine is shown in figure (1).

2. Circuit Design.

The system is mainly composed of three main subsystems which communicate between each other in a wireless RF mode. Two of those sub systems are data acquisition systems for EEG and EMG signals, while The third one in the driver circuit for the robotic hand.

2.1. SEMG Detection Circuit

First the SEMG signal is detected by using two $Ag/AgCl$ electrodes. As a result of using wireless communication, these electrodes can be placed on any muscle which can be controlled by the user and can produce a strong SEMG signal. The signal then is fed to the analogue signal processing circuit shown in figure (2).

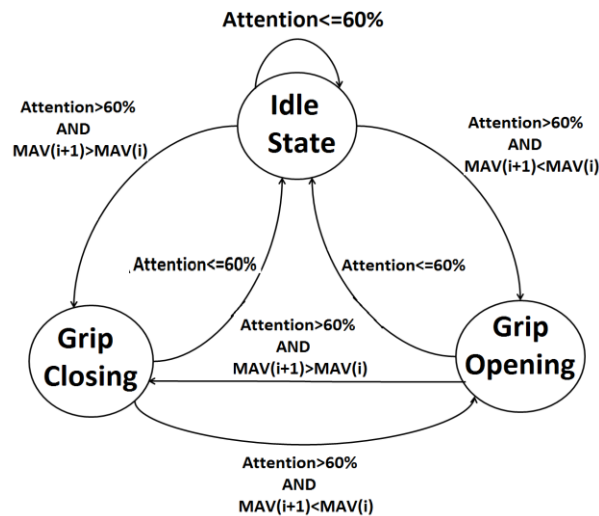
The output analogue signal is supplied then to the MSP430F2274 microcontroller to extract the MAV of this signal and apply the MGH algorithm to it. The decoded resulted state of muscle (0XFF for contraction, 0X00 for relaxation) is transmitted to the driver circuit of the robotic hand through CC2500 RF chip.

2.2. Attention Detection Circuit.

The resulted data from TGAM chip is supplied serially through UART lines to the MSP430F2274 microcontroller. The microcontroller parse the data to extract the attention level value and then sends this value to the CC2500 RF chip to be transmitted to the robotic hand driver circuit.

3.2. Robotic Hand Driver Circuit.

This subsystem has three tasks; first, collecting all the transmitted data from the data acquisition systems. The second task is to process these data according to finite state machine to make a decision. The third and final task is to actuate a single degree of freedom robotic hand according to the made decision.



Figure(1): Finite State Machine

RESULTS

The output signal from the analogue signal processing circuit and its MAV for SEMG signal in a sequence of two contraction is shown in the upper and lower plots in figure(3) respectively. The attention readings over a period of time are shown in figure (4). The system was tested in the Micro and Nano Technology laboratory by 5 healthy subjects. After a preliminary training session, they were able to close and open the grip of robotic hand to hold and release a phone handle respectively. The system also was tested by using three different actuation methods. In the beginning, the hand was actuated using attention level and SEMG signal independently, and then the combination of two values was used after applying the finite state machine in figure (1).

DISCUSSION

The process of actuation using the finite state machine showed more sustainability in holding the object than the other two methods. The wireless communication helped in minimizing the hard ware complexity since there are two different sources of signals (Attention and SEMG) with one sink(robotic hand).

CONCLUSIONS

Combining EMG and EEG signal can be the solution for the problem of intuitiveness and continuous reaction in the EMG-controlled prosthetics. Also this approach enhances the accuracy of decision by relying on two different sources of information instead of one. The involvement of wireless techniques in transmitting signals provides a wide range of freedom to choose the location of electrodes for both EEM and EEG data acquisition system, and minimize the hardware connections complexity.

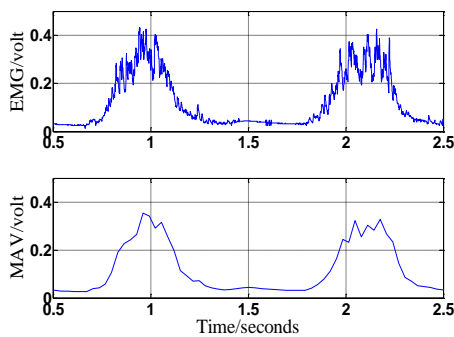


Figure (2): SEMG signal and MAV

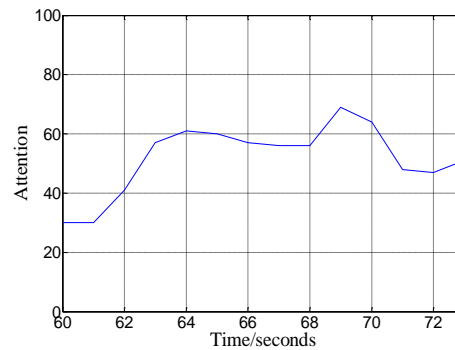


Figure (3): Attention Level

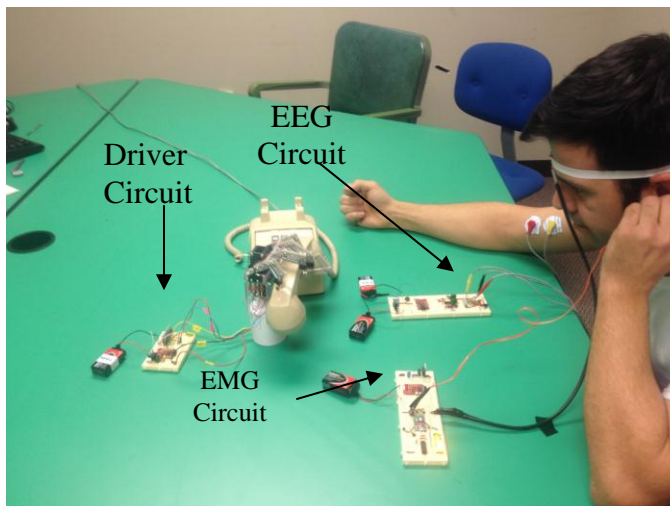


Figure (4): Closing the Grip

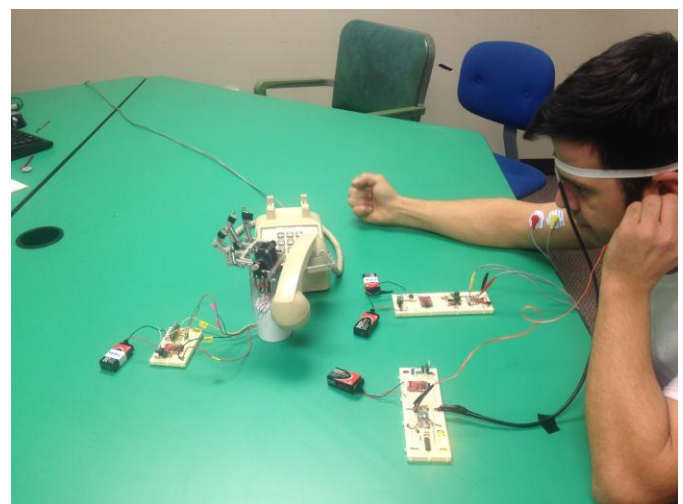


Figure (5) opening the Grip

REFERENCES

- [1] M. Oskoei and H. Hu, "Myoelectric Control Systems-A survey," in *Biomedical signal Processing and control*, 2007.
- [2] A. T. C. Au and R. F. Kirsch, "EMG-Based Prediction of Shoulder and Elbow," *IEEE TRANSACTIONS ON REHABILITATION ENGINEERING*, vol. 8, no. 4, pp. 471-480, 2000.
- [3] B. Karlik, M. O. Tokhi and M. Alci, "A Fuzzy Clustering Neural Network Architecture for Multifunction Upper-Limb Prosthesis," *IEEE TRANSACTIONS ON BIOMEDICAL ENGINEERING*, vol. 50, no. 11, p. 1255, 2003.
- [4] S. A. Dalley, H. A. Varol and M. Goldfarb, "A Method for the Control of Multigrasp Myoelectric Prosthetic Hands," *IEEE TRANSACTIONS ON NEURAL SYSTEMS AND REHABILITATION ENGINEERING*, vol. 20, no. 1, pp. 58-67, 2012.
- [5] I. Moon, M. Lee, J. Chu and M. Mun, "Wearable EMG-based HCI for Electric-Powered Wheelchair Users with Motor Disabilities," in *International Conference on Robotics and Automation*, Barcelona, Spain, 2005.
- [6] S. Sequeira, C. Diogo and F. Ferreira, "EEG-signals based control strategy for prosthetic drive systems," in *2013 IEEE 3rd Portuguese Meeting in* .
- [7] E. Lavelly, G. Meltzner and R. Thompson, "Integrating Human and Computer Vision with EEG Toward the Control of a Prosthetic Arm," in *HRI '12 Proceedings of the seventh annual ACM/IEEE international conference on Human-Robot Interaction*, New York, USA, 2012.
- [8] D. J. MCFARLAND and J. R. WOLPAW, "Brain-Computer Interface Operation of robotic and Prosthetic Devices," *Advances in computer*, vol. 79, pp. 169-187, 2008.
- [9] E. Clancy and N. Hogan, "Probability density of SEMG and its relation to amplitude detectors," *IEEE Transaction Biomedical Engineering*, vol. 8, no. 3, pp. 330-341, 2000.
- [10] Q. Sun, Y. Sun and Z. M. Ding, "Onset determination of muscle contraction in SEMG signal analysis," in *IEEE international conference on information acquisition* , Hong Kong, 2005.

OCT IMAGING FOR SMALL ANIMALS – A SWEEP SOURCE PLATFORM

José P. Domingues^{1,2}, Susana F. Silva¹, António Miguel Morgado^{1,2} and Rui Bernardes^{1,3}

¹IBILI – Institute for Biomedical Imaging and Life Sciences, University of Coimbra, Portugal

²Department of Physics, Faculty of Sciences and Technology, University of Coimbra Portugal

³Centre of New Technologies for Medicine, AIBILI, Coimbra, Portugal

ABSTRACT

Optical Coherence Tomography (OCT) has been recognised as a very powerful tool for ophthalmologic diagnosis. Based on the optical interference phenomenon, it is capable of producing high-resolution cross-sectional images of non-homogeneous ocular structures such as the retina.

OCT application on small animal studies with enough accuracy and resolution is a fundamental issue they are often used as physiological models to test and develop new medical techniques and therapies. Therefore, it is our main goal to develop a dedicated OCT platform for small animal ocular image acquisition using most recent technological advances, mainly in laser sources. Laser swept-source (1060nm, 110 nm bandwidth and sweep frequency of 100 kHz), InGaAs balanced detector and a fast multi I/O 400 MSPS data acquisition board installed on a personal computer (PC) are the main structural parts. Digitized data undergoes Fourier analysis to produce the final OCT image, a task performed with a dedicated acquisition/control software which has been developed to show real-time OCT images with different angle spans, B-scan pixels, scanning speed and other image features.

So far, preliminary results let us conclude that system demonstrates performance parameters that meet the final goal. Axial resolution (8 μm) and imaging speed (175 ms/image for B-scans) are comparable to other described OCT systems. Sensitivity, sensitivity roll-off, dynamic range and lateral resolution are being improved to meet the needs for biomedical OCT applications, namely imaging rats' retinas.

Keywords: OCT, Swept Source, High Speed Data Acquisition, Fast Fourier Transform, Retinal Imaging

INTRODUCTION

Soon after its appearance in early nineties, OCT - Optical Coherence Tomography - has become a very promising optical imaging technique and new developments and applications confirm its huge potential in living tissue assessment. Based on the light interference phenomenon [1][2] it is widely used in the field of ophthalmology as a diagnostic tool by allowing cross-sectional real-time imaging of ocular structures such as the retina [2][3].

Currently, two main types of OCT systems can be considered: Time-Domain OCT (TD-OCT) and Fourier-Domain OCT (FD-OCT) – that can be further divided in Spectral Domain OCT (SD-OCT) and Swept Source OCT (SS-OCT) as we will see [1,4]. TD-OCT was the first to be developed and its working principle is quite similar to a Michelson interferometer [5]. Light from a low-coherence source is directed into a beamsplitter where it is divided in two paths: reference and sample. Interference fringes occur with backreflected light under the condition that both path lengths match to within the coherence length of the light. OCT interferogram is obtained by moving the position of the reference mirror changing the reference path by a certain amount (Δz) to match multiple sample optical structure and a depth profile (A-Scan) of the sample can be acquired [1].

In FD-OCT the reference mirror is fixed and the interference profile is acquired by detecting the output spectrum using a spectrometer and an array detector (often CCD camera) and, then, Fourier transformation. A recent approach for FD-OCT has been the so-called Swept-Source OCT (SS-OCT). In SS-OCT the novelty is the light source – a swept source – that is a tunable narrowband laser that is swept over a broad range of optical frequencies with a sweep frequency of 100 kHz or more. In this configuration, spectrometer and camera, are replaced by an InGaAs dual balanced photodiode detector and a high sample rate digitizer. This type of OCT presents advantages: reduced fringe washout, improved sensitivity with imaging depth, longer image range and higher detection efficiencies [4, 5].

METHODS

1.Theory. In a simple theoretical formulation let us consider an open-air OCT system with a beamsplitter, reference

and sample paths and a Gaussian-shape broadband source. Light coming from the source can be represented by its electric field wave component $E(w, t)$ expressed as a complex exponential [1][2]:

$$E(w, t) = A(w)e^{-i(wt+kz)} \quad (\text{eq. 1})$$

$A(w)$ is the source amplitude spectrum, w the angular frequency and k the wavenumber. The second term in the exponential accounts for phase which can be arbitrarily considered zero at input electric field. At the end (detector), phase appears due to different interactions throughout the interferometer both for reference and sample arms as follows, respectively:

$$E_R(w, t) = E(w, t)e^{-\frac{izwnz_R}{c}} \quad E_S(w, t) = E(w, t)e^{-\frac{izwnz_S}{c}} \quad (\text{eq. 2})$$

n represents refraction index, z_R and z_S the path lengths in reference and sample arms and the factor of two arises from light double pass. Off course the sample is not a simple reflecting surface and has a layered refraction index structure which determines a reflectance, r , for each layer given by the Fresnel's equations. At the end we can consider that there is a sample response function $R(w)$ given by [1]

$$R(w) = \int_{-\infty}^{+\infty} r(w, z)e^{\frac{izn(w,z)wz}{c}} dz \quad (\text{eq. 3})$$

leading to

$$E_R(w, t, \Delta z) = E(w, t)e^{-\frac{izwn\Delta z}{c}} \quad E_S(w, t) = E(w, t)R(w) \quad (\text{eq. 4})$$

where Δz represents the reference mirror translation distance.

After interference the resultant field into the detector is $E_T = E_R + E_S$ and optical detector are really sensitive to Irradiance, I , which, by the square law, can be written as $I = \langle E_T E_T^* \rangle$. After proper calculations it can be shown that $I = I_0 + 2\text{Re} \langle E_S E_R^* \rangle$, containing, the second term, the relevant cross-interference information [1][2].

- Implementation.** The high speed SS-OCT system developed is represented in fig. 1. It includes a commercially available swept source laser, AXP50125-3 1060nm (Axsun Technologies, USA) with a central wavelength of 1060 nm, bandwidth 110 nm and sweep frequency of 100 kHz; a fast I/O 400 MSPS acquisition board, X5-400M (Innovative Integration, USA) and an InGaAs balanced amplified photodetector, PDB145C (Thorlabs GmbH, Germany). In this balanced mode only cross-interference optical signal is detected rejecting the common-mode or dc component and enhancing sensitivity. A fully customized software program has been developed. Data processing and OCT imaging are executed on the graphics processing unit (GPU) through NVIDIAS's Compute Unified Device Architecture (CUDA) technology. To perform B or C-scans over a sample, the laser beam is directed along one and two axes, respectively, by a Scanning Galvo System GVS002 (Thorlabs GmbH, Germany). With current hardware implementation, about 2048 points in sagittal plane (A-scan) are digitalized in 10 μs and a maximum of 200 points in 2 ms are allowed in the transverse plane (B-scan). Consequently, 200 lines in the coronal plane (C-scan) can be obtained in 400 ms.

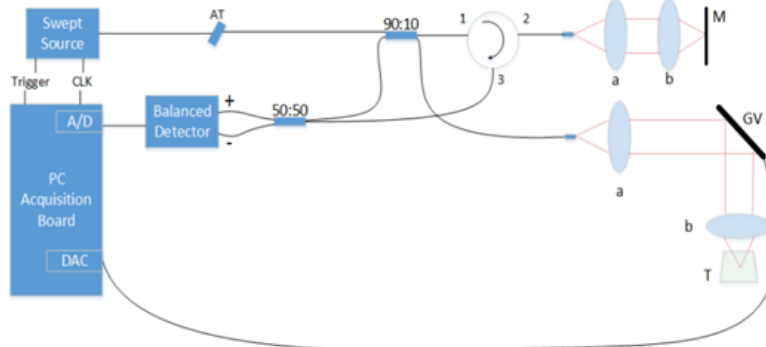


Fig. 1 – SS-OCT layout

RESULTS

Balanced detector output signal show the interference fringes signal. Digitalization with equal k -spacing sampling can be achieved by clocking the high speed A/D channel of the acquisition board with the clock (so-called optical clock) provided by the source. The Fourier transform analysis can be directly applied on the acquired data.

Moreover, the laser source also provides a trigger signal which is connected to the SYNC port of the acquisition board. This signal is responsible for starting the I/O module. Fig. 2 represent program acquisition panel for a three layer sample.

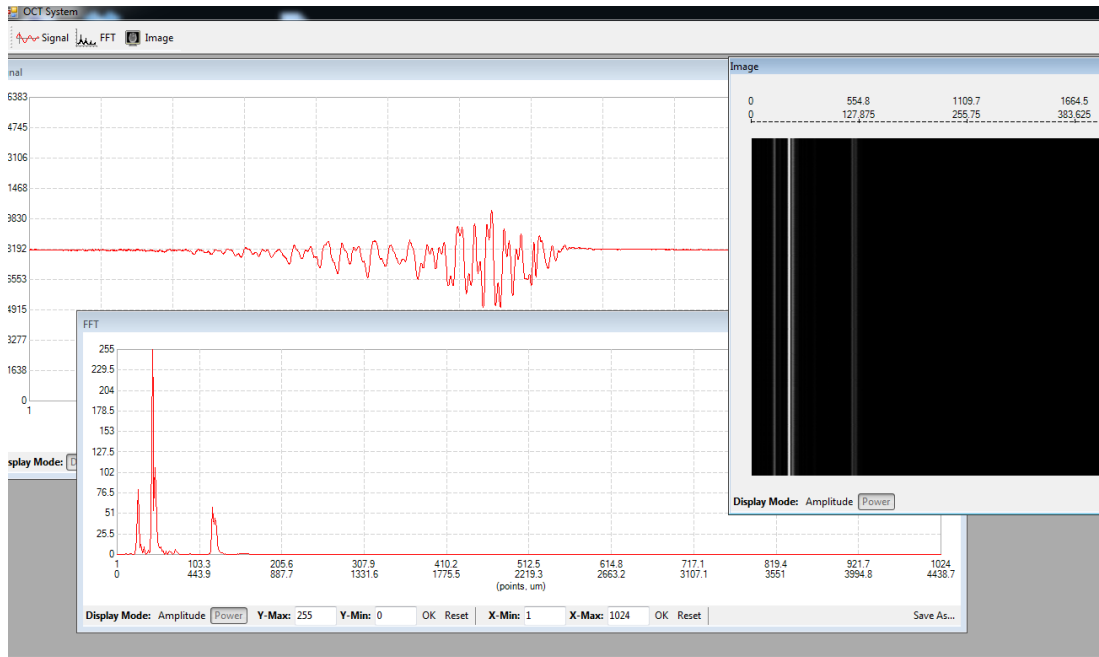


Fig. 2 - Acquisition panel with detected signal, FFT and image windows for a multilayer target B-Scan.

The total axial with present optical layout was 500 μm . It could be demonstrated that the position of the Fourier transform peak varies linearly with the distance of the sample, as expected, with 8 μm resolution. Sensitivity around 55 dB has already been achieved but can be optically improved.

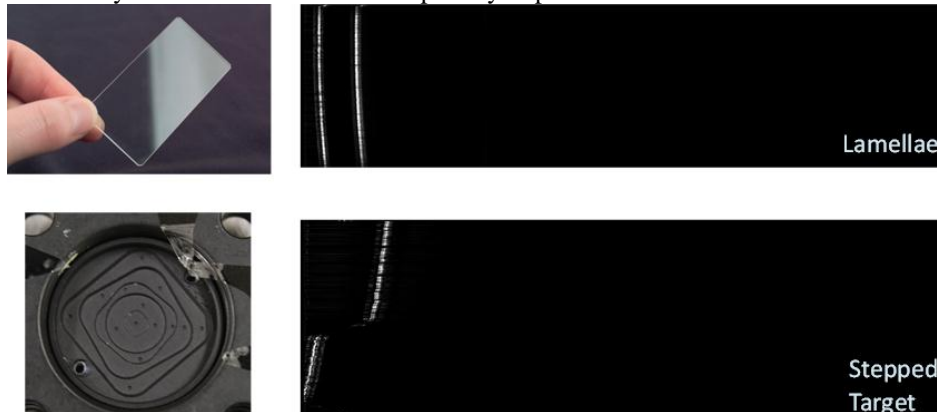


Fig. 3 – B-Scan of test samples showing accurate spatial resolution and sensitivity

DISCUSSION AND CONCLUSION

OCT images of small animals retinal structure can give researchers the means to understand physiology, pathology and phenotypes of intact living systems similar to human beings and the instrument will be a valuable tool for research on retinal physiology. It will also be used as a development platform for new OCT instrumentation and methods. Currently, two-dimensional images in amplitude scale are generated. Noise removal, averaging and neighboring scans interpolation algorithms are being tested to improve contrast and image quality. The current developed program provides flexible control of the data acquisition and overall system with high automation. One parameter under consideration is the polarization control. Polarization sensitive evaluation of the interferograms can

give additional information about sample birefringence enhancing image quality. Fiber polarization controller has been used with promising results (better sensitivity and SNR) [6]. Improvement of the binomial depth of view - for at least one or two mm - and lateral resolution proceeds as well as image reconstruction algorithm speed.

ACKNOWLEDGMENTS

This work was supported by PEST/C/SAU/UI3282/2013 and also by FEDER, through the Programa Operacional Factores de Competitividade – COMPETE and by National funds through FCT – Fundação para a Ciência e Tecnologia in the frame of the project PTDC-SAL-ENB-122128-210.

REFERENCES

1. Tomlins, P H.; Wang, R. K.. Theory, developments and applications of optical coherence tomography. Institute of Physics Publishing, Journal of Physics D: Applied Physics, vol. 38, no. 15, pages: 2519-2535, Jul. 2005.
2. Brezinski, M. E.. Optical Coherence Tomography-Principles and Application. ISBN 978-0-12-133570-0, Academic Press - Elsevier (Burlington, USA), 2006.
3. Marschall S, Sander B et al (2011) Optical coherence tomography – current technology and applications in clinical and biomedical research. Anal Bioanal Chem 400 pp. 2699-2720 DOI 10.1007/s00216-011-5008-1
4. Huang D, Swanson C et al (1991) Optical Coherence Tomography. Science, 254(5035) pp. 1178-1181
5. Popescu D P, Choo-Smith, LP (2011) Optical Coherence Tomography: fundamental principles, instrumental designs and biomedical applications. Biophys Rev 3:155-169 DOI 10.1007/s12551-011-0054-7
6. Zhang, J.; Nelson, J. S.; Chen, Z.. Removal of a mirror image and enhancement of the signal-to-noise ratio in Fourier-domain optical coherence tomography by use of an electro-optical phase modulator. Optics Letters, vol. 30, no. 2, Jan. 2005

DEVELOPMENT OF A THREE-DIMENSIONAL DIGITAL IMAGE CORRELATION FOR DISPLACEMENT AND STRAIN MEASUREMENT OF SEEDED ENDOTHELIAL CELLS

Emily Gould, Nicholas Carroll, Dr. Gail D. Jefferson, and Dr. Saami K. Yazdani

Department of Mechanical Engineering, 150 Jaguar Drive, Shelby Hall, Mobile, AL 36688

ABSTRACT

Atherosclerosis, a progressive disease of the large arteries, is the primary cause of heart disease, and stroke. Endothelial cell (EC) dysfunction precedes the development of atherosclerosis. ECs are mainly affected by three mechanical factors; pressure from pulse, shear stress from blood flow, and strain due to the elasticity of the blood vessel. ECs require these mechanical factors to function at optimal levels. Deviation from these levels can result in damage to ECs and lead to disease initiation. An additional factor for EC dysfunction is increased wall stiffness due to the non-linear mechanical properties of the arterial wall. As the main coronaries are located on the epicardium, these vessels stretch and twist with each heartbeat, resulting in a non-uniform spatial distribution in strain and thus in wall stiffness. Therefore, the purpose of this investigation was to develop a non-invasive method to characterize local strain stiffness responsible for changes in EC function. To this end, a commercially available digital image correlation (DIC) was used to characterize local strain measurements under physiological conditions. Sylgard 184 was used to create synthetic models with varying elastic modulus that mimic arterial geometry. The models were then coated with micron size particles and local strain measurements could then be estimated on a Sylgard tube to an approximate accuracy of 2.1%. These preliminary results demonstrate the potential of such a system to characterize local strain undergoing arterial hemodynamics.

INTRODUCTION

Atherosclerosis is a progressive disease of the large arteries [1]. It is the primary cause of heart disease and stroke, and is the underlying cause of about fifty percent of all deaths in westernized societies. Atherosclerosis is characterized by the accumulation of lipids and fibrous elements in the large arteries. It is also distinguished by abnormal thickening and hardening of arterial wall resulting in loss of elasticity [2]. Studies have shown that endothelial dysfunction precedes and thought to play a major role in the development of atherosclerosis. Endothelial dysfunction is a condition where endothelial cells (ECs), cells that form a thin membrane that lines the inside of blood vessels, do not function properly [3]. The endothelium functions as a selectively permeable barrier between blood and tissue [1]. Damage to the endothelial cells leads to an increase in permeability across the membrane to macromolecules such as low-density lipoprotein (LDL) and are ideal sites for lesion formation. This can lead to atherosclerosis because a primary initiating event in atherosclerosis is the accumulation of LDL.

Endothelial cells are mainly affected by three mechanical factors; pressure from pulse, shear stress from blood flow, and strain due to the elasticity of the blood vessel [4]. Endothelial cells require these mechanical factors to function at certain levels. Deviation from these levels can result in damage to the cells and lead to disease. The arterial wall is constantly subjected to both the flow-induced shear stress and wall strain. The vascular wall stiffens as it is stretched. This nonlinear elastic response may be a factor for plaque formation.

The goal of this project is to characterize local strain stiffness responsible for changes in endothelial cell function. In order to do this, synthetic models that mimic arterial geometry and mechanical properties will be developed. Developing a non-invasive method to characterize strain would be beneficial in examining how strain effects endothelial cell function.

METHODS

Model Development. Sylgard Elastomer was used to create the models that simulate human tissue [5]. The mechanical properties of Sylgard 184 were tested for various mixing ratios of Sylgard 184. Mixing ratio of 1:10, 1:20, and 1:30 created for this project. The ratios correspond to the curing agent and the base by mass. For the 1:10 ratio, there was one gram of curing agent to every nine grams of base. The Sylgard 184 base was poured into a container and weighed on a mass balance. While the container remained on the mass balance, the curing agent was slowly added until the desired mass ratio was achieved. The mixture was stirred and placed under a vacuum to remove any air bubbles.

Once the air bubbles were removed, the mixture was used to make Models A and B (Figure 1). For Model

A, the sylgard mixture was poured into a petri dish, approximately 2mm in thickness. Grounded coffee was distributed over the sylgard. The DIC needed particles of random geometry to track in order to calculate strain. Grounded coffee was chosen since it could be made into the model (would not come off like ink), easily accessible, and could reasonably control the size. The model was placed in an incubator at 37°C to cure overnight. After curing, the model was removed and cut into a rectangle approximately three inches by a half an inch. This model was used for a control test. For Model B, the mixture was poured over a slow turning rod, one-fourth inch in diameter, over heat. Grounded coffee was distributed over the turning rod. After curing, more of the Sylgard 184 mixture was poured over the rod, creating another layer covering the coffee. After curing, the model was carefully removed from the rod. Model B simulates the correct geometry of the artery and were used to test strain due to fluid.

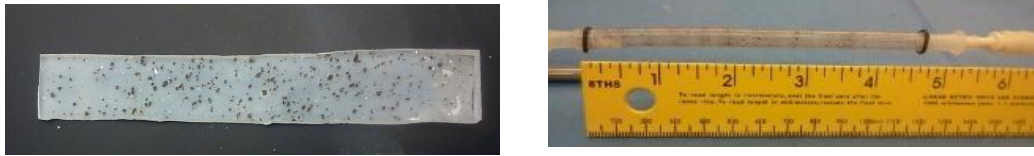


Figure 7: Sylgard models. Model A used for control test. Model B simulates correct geometry

VIC-3D Measurement System. Type B models were used to test the strain due to hydrostatic pressure variation. This was done through the use of the VIC-3D Measurement System. This system consists of a pair of digital cameras that utilizes Digital Image Correlation, DIC, and a computer with VIC-3D software [7]. DIC is a method of measuring deformation on an object surface. This method involves tracking random patterns created by small areas of particles of random geometry (grounded coffee) on an object surface during deformation.

Development of a control test apparatus. A control test was needed to compare the strain calculated by the DIC and the theoretical strain. A linear actuator with a clamping system and a flat sample, shown in Figure 2, was used to perform this test. The linear actuator was programed to move back half an inch in a second and forward half an inch in a second.

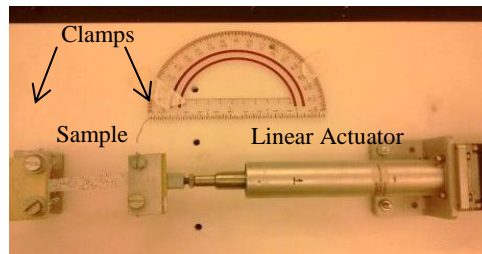


Figure 8: Control test step up with sample

RESULTS

The theoretical strain was calculated by using the first image taken, before the linear actuator started moving, and the image where the linear actuator was fully compressed, sample fully extended.

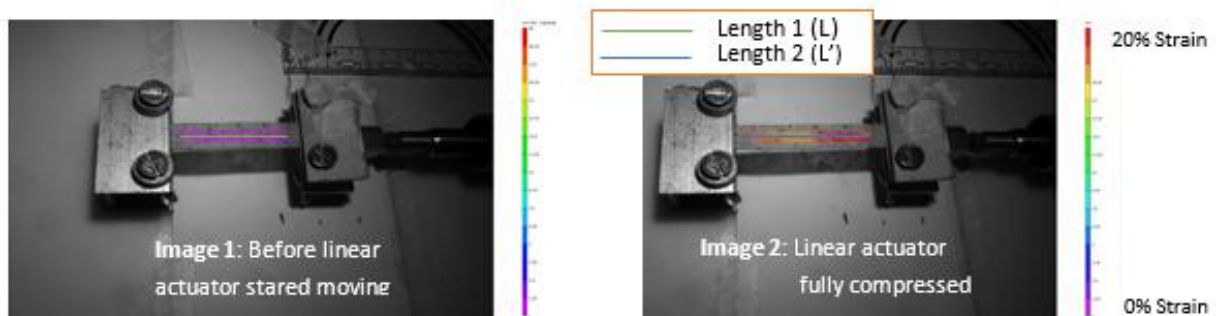


Figure 9: Control test used to compare strain calculated by DIC to theoretical strain.

The length from image 1 and the length for image 2 were measured. The strain was then calculated by subtracting the two lengths, dividing it by the original length, and multiplying by a hundred for a percentage.

Length 1 (L) was 1.12 inches and length 2 (L') was a 1.302 inches. So the change in length (ΔL) was 0.182 inches, making the strain 16.25%. Figure 4 was last image before the linear actuator was fully compressed. The region between yellow and orange was 16.25% strain, calculated by DIC.

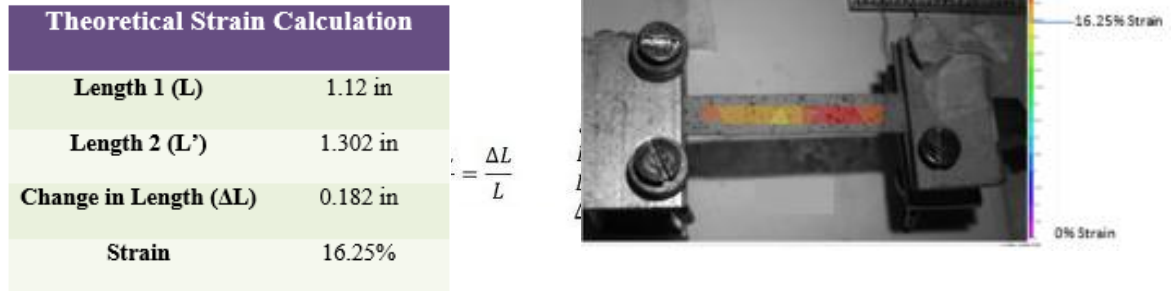


Figure 10: Results from control test

Strain Measurements in Model B. For this test, hydrostatic pressure variation was used to induce strain. Milk was used as the fluid in this test to create the necessary contrast needed by the DIC. A two meters tall tube was connected to the sample, 1:10 ratio, and filled with milk. When a valve was opened it released the fluid. The change in the height of the fluid created pressure. From this, the theoretical strain could be calculated.

For this test, the valve was opened for two seconds and the height of the fluid changed by 1.5m. Modulus of elasticity for Sylgard 184, 1:10 ratio, was 1.45MPa [5]. The density for milk was 1.032kg/L. The radius of the sample was 4mm and the thickness was 1mm. So the theoretical hoop strain was 4.19% and the theoretical longitudinal strain was 2.09%. The highest strain the DIC calculated was about 2.1% strain in the yy-direction. More pressure or a lower modulus of elasticity was needed to see a higher percentage of strain.

DISCUSSION

The goal of this project was to develop a non-invasive method to characterize strain that could be used to characterize local strain stiffness responsible for change in endothelial cell function. Throughout this project, synthetic models that mimic arterial geometry and mechanical properties that could be tested with DIC were successfully made. Also, a control test apparatus was successfully built. The biggest challenge faced was getting the models to work with DIC due to size of particles and contrast. The challenge of the size of the particles was overcome by grinding coffee and using mesh to apply it. The contrast was solved by using milk and whiteout applied so that it would not crack when the sample was stretched. These type of experiments are needed in the development of a noninvasive technique to characterize the strain on EC cells and to confirm computational data. Noninvasive techniques are important because these are safer and cheaper than other techniques. Since computational data is theoretical, experimental data is used to confirm for it is more real world. Digital Mechanical Analysis tests will be done on Sylgard 184 samples in order to determine more of its mechanical properties. During this project, a successful control test to compare the strain calculated by the DIC and the theoretical strain was developed. Also, was able to come up with a method to test and tested strain due to fluid on synthetic models that mimic arterial geometry and mechanical properties.

CONCLUSIONS

During the duration of this project, synthetic models that mimic arterial geometry and mechanical properties were made and tested with DIC. A successful control test was developed in order to compare the strain calculated by DIC and the theoretical strain. Also, was able to test strain due to fluid on synthetic models that simulated arterial geometry and mechanical properties. Overall, these results demonstrate the potential to measure strain on endothelial cells by use of DIC.

REFERENCES

- [1] A. J. Lusis, "Atherosclerosis," *Nature*, vol. 407, no. 6801, pp. 233-241, 2000.
- [2] "Endothelial Function Testing," Cedars-Sinai, [online] 2013, <http://www.cedars-sinai.edu/Patients/Programs-and-Services/Womens-Heart-Center/Services/Endothelial-Function-Testing.aspx>
- [3] R. N. Fogoros M.D., "Endothelial Dysfunction," (About.com), [online] 2011, <http://heartdisease.about.com/od/coronaryarterydisease/g/Endothelial-Dysfunction.htm>
- [4] J. Ohayon, A. M. Gharib, A. Garcia, J. Heroux, S. K. Yazdani, M. Malve, P. Tracqui, M.-A. Martinez, M. Doblare, G. Finet and R. I. Pettigrew, "Is arterial wall-strain stiffening an additional process responsible for atherosclerosis in coronary bifurcations?: an in vivo study based on dynamic CT and MRI," *American Journal of Physiology*, vol. 301, no. 3, 2011.
- [5] Martin, Bryn; Kotsakos, Tom; Stevens, Justin; Nicolaon, Sebastien; Cespedes, Steven;, "Quantification of the Modulus of Elasticity and Dynamic Properties of Sylgard for Various Mixing Ratios, 2003-2006", (neurohydrodynamics), [online] 2011, http://www.neurohydrodynamics.com/wiki/index.php?title=Quantification_of_the_Modulus_of_Elasticity_and_Dynamic_Properties_of_Sylgard_for_Various_Mixing_Ratios,_2003-2006
- [6]"Introduction to Dynamic Mechanical Analysis (DMA): A Beginner's Guide", (PerkinElmer), [online] 2013, http://www.perkinelmer.com/CMSResources/Images/44-74546GDE_IntroductionToDMA.pdf
- [7] " The VIC-3D Measurement System", (Correlated Solutions), [online] 2013, <http://www.correlatedsolutions.com/marketing/Brochures/VIC-3D%20System%20Specs.pdf>

DEVELOPMENT OF SILICONE CORONARY BIFURCATION MODELS FOR *IN VITRO* FLOW EVALUATION

Alex Parks, Saami K. Yazdani
Department of Mechanical Engineering
University of South Alabama

ABSTRACT

Bifurcations throughout the vascular system are among the most common locations that atherosclerosis may form. Within the span of an arterial bifurcation, uniform flow is disrupted and more complex mechanical situations exist. Analysis of a flow path complicated by a change in direction is much more complex than studying flow patterns through a single channel. For this purpose, modeling an arterial bifurcation with sylgard 184 may allow for extensive analysis of the system. Therefore, the purpose of this study is to develop a rapid and inexpensive method to develop consistent bifurcation models. In order to model an arterial bifurcation with precise dimensions, a two-stage mold design has been strategized. The initial mold is injected with a material to form the inner cast, which is then placed into the secondary mold. Sylgard is injected into the secondary mold to cover the inner cast. Once the sylgard cures, the coated inner cast is removed from the secondary mold and then melted out of the sylgard, leaving a bifurcation shaped tube behind. Three types of materials, molding wax, polymers, and low-temp melting metals, were tested as the inner mold. Results demonstrated that the low-temp melting metal possesses the best properties for our application. Upcoming challenges will focus on the injection procedures and the manufacture of the mold. With a repeatable process for modeling bifurcations, these studies will potentially lead to more accurate testing of cardiovascular devices, such as stents, in a laboratory setting.

INTRODUCTION

Atherosclerosis and hypertension are the most common causes of cardiovascular disease. Atherosclerosis is the thickening of a vessel wall due to absorption of fatty materials such as cholesterol and triglyceride. This absorption is due to compromised endothelial cell function lining the interior wall of a vessel and allows plaque to accumulate (2). Other than prescription medications, treatments for atherosclerosis include different strategies such as the use of catheters with drug coated balloons and stents. Bifurcations throughout the vascular system are among the most common locations that atherosclerosis may form (2). Within the span of an arterial bifurcation, uniform flow is disrupted and more complex mechanical situations exist (1). Analysis of a flow path complicated by a change in direction is much more complex than studying flow patterns through a single channel. Any situation regarding design optimization and procedure involving a stent implant for a bifurcation also requires greater understanding of the mechanics involved with these complications. For these purposes and possibly many more applications, modeling an arterial bifurcation may allow for widespread analysis of the system. Therefore, the purpose of this study is to develop a rapid and inexpensive method for developing consistent bifurcation models.

Sylgard 184 (provided by Dow Corning), a clear silicone based material, has been selected as an ideal compound for creating these models. The material has uniform elastic properties, it cures clear, and it can handle the higher temperatures used in the molding processes described below. Also, the mixture ratio may be altered to allow for multiple trials involving alternative material compliancy. After the Sylgard is cured, it is crystal clear. This aspect will allow for visual study of the internal conditions once an arterial model is affixed inside a bioreactor and flow is introduced. The curing process occurs relatively quickly at moderate temperatures, these restraints have proven to be appropriate for the methods involved with our procedure.

METHODS

Injection Molding Process

In order to model an arterial bifurcation with precise dimensions, a two-stage mold design has been developed and designed using Solidworks as shown in FIGURE 1. Production of this design may be machined. However, approaching more complex compound bifurcation molds may require stainless steel 3D printing. The initial mold, made of stainless steel, will be injected with a low temperature melting material to form the inner cast, which is then placed into the secondary mold. An optically clear silicone based material is then injected into the secondary mold to cover the inner cast. Once the sylgard cures, the coated inner cast must be removed from the secondary mold and then melted out of the silicone, leaving a bifurcation shaped phantom.

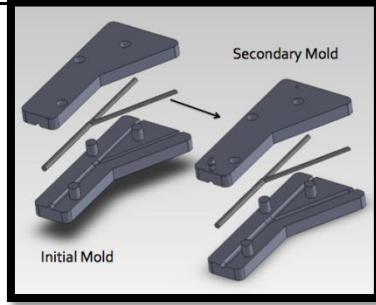


FIGURE (1): Two stage mold design modeled using SolidWorks

Silicone Bifurcation Tubing and Preparation

For our purposes, sylgard may be injected into a mold to create a vessel shaped cast. The challenges involved with this approach include a need for a two-stage process. This gives rise to the selection process regarding suitable material for shaping the inner walls of the sylgard model. After the second stage, a bifurcation model formed around this material must be separated. In order to remove the inner cast from the model, it has been determined that a suitable material for this process could be melted out of the Sylgard, leaving a bifurcation shaped tube behind. The thermal elastic properties of the sylgard must also be taken into consideration. Once formed into the shape of a bifurcation, this cast may be used for extensive bench testing.

In order to fit the scale of our procedures, 10 grams of sylgard was used. Initially using a 10:1 ratio, 9 grams of the base material was mixed with 1 gram of the curing agent included in the Sylgard 184 silicone elastomer kit. Each 10-gram batch is used to create a single model.

Material Selection

To experimentally establish suitable materials for shaping the interior walls of the arterial model, an electric DC motor operating at 2 Volts was used. Straight cylindrical rods were then molded to size, 125mm in length and 5mm diameter, from the various materials tested which served as horizontal rotating shafts. 10 grams of Sylgard was then applied to the surface of these rotating rods and cured for one hour at 100°F to form a tube. Materials tested in this fashion include modeling wax, thermoplastic (HEA-500) provided by Education Innovations, and Cerrosafe alloy consisting of 42.5% Bismuth, 37.7% Lead, 11.3% Tin, and 8.5% Cadmium. Once the rods were coated with sylgard, trials were carried out to insure that the materials could be removed from the model.

Cerrosafe Trials

Cerrosafe alloy was selected as a suitable material to serve as the inner cast used for shaping the inner walls of the arterial model, surface smoothness was then addressed. Five samples were created from three different cooling rates including: room temperature cooling, quenching with running tap water, and quenching in a 40-50°F bath. These fifteen samples were then compared to establish the most reliable method. Once consistently smooth samples were created, trials were carried out to establish an adequate removal process. Glass tubing with an inner diameter of 5mm was used to create fifteen 125mm long cylindrical Cerrosafe rods. A syringe was attached and used to draw liquid Cerrosafe preheated at 225°F, approximately 20% above Cerrosafe melting temperature, into the glass tube. Once sealed from the bottom, the arrangement was quenched in 40-50°F water to achieve a smooth finished surface. Thirty minutes following solidification, the glass tubes were fragmented to remove the Cerrosafe rods. These rods were then rotated on a horizontal axis for sylgard application. Next, the Cerrosafe filled sylgard tubes were set in a 225°F oven with a vertical orientation. Of the fifteen trials, five were left alone, five were pre-treated by inserting a film of water between the contacting surfaces of the Sylgard and Cerrosafe, and the last five were pre-treated by injecting a film of glycerin. Once the bulk of the material was removed, the Sylgard tubes were flushed with boiling water to remove remaining particles.

RESULTS

Material Trials

The modeling wax results demonstrated that the removal process compromised the clarity of the resulting Sylgard tube. The foggy appearance left behind was unsatisfactory for our purposes. The thermoplastic presented an even more difficult removal process due to its high viscosity and flow resistance. Results demonstrated that the low-temp melting metal possessed the best properties for our application as it does flow well in its liquid phase. This Cerrosafe alloy has been chosen to serve as the inner cast for the two-stage design.

Cerosafe Alloy

The Cerosafe sample results, shown in FIGURE 2, infer that the most suitable method was quenching the alloy in a 50°F bath. After attempting multiple techniques for removing Cerosafe from Sylgard models, it proved most efficient to inject a film of glycerin between the contacting surfaces of these materials before using heat to melt the Cerosafe for removal. The chance of the oil film being broken at the operating temperature of 212° F is insignificant. This method resulted in transparent Sylgard arterial models.

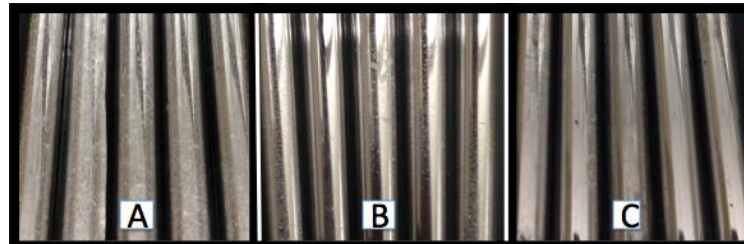


FIGURE (2): Fifteen Cerosafe samples cooled with: A) Room temperature, B) Running tap water, C) 50°F bath.



Figure (3): Fifteen Sylgard Samples After Cerosafe Removal Using: A) No Surface Separation, B) Injecting A Film Of Water Between Surfaces, C) Injecting A Film Of Glycerine Between Surfaces

DISCUSSION

Based on results, it is apparent that Cerosafe alloy may be used for the inner cast of the proposed two-stage mold design. After initial injection, this material may be quenched in a 40-50°F water bath to achieve a smooth finished surface. Once this inner cast is coated with sylgard, glycerine may be injected to aid in removing Cerosafe from within the Sylgard construct.

The significance of developing models for arterial bifurcations relate to the fact that disease mostly occurs near arterial bifurcations. Flow separation at bifurcations lead to low shear stress experienced by endothelial cells, leading to endothelial dysfunction and the progression of vascular disease.

Further stages of this study will involve manufacturing the two-stage mold design for testing. Upon completion of the bifurcations, non-invasive flow diagnostics will be used to measure and quantify temporal and spatial wall shear stress values of the models under physiological conditions.

CONCLUSIONS

This study has successfully identified Sylgard 184 and Cerrosafe alloy as compatible materials for a two-stage injection molding strategy. The process will be used to model arterial bifurcations for the purpose of optically evaluating flow disturbances at bifurcation regions and their impact on vascular disease.

ACKNOWLEDGMENTS

The authors acknowledge Mr. John Lyons and Mr. Terry Pritchett from The University of South Alabama: Engineering Machine Shop for their technical assistance.

REFERENCES

1. Colombo A, Moses JW, Morice MC, Ludwig J, Holmes DR, Jr., et al. Randomized study to evaluate sirolimus-eluting stents implanted at coronary bifurcation lesions. *Circulation* 109: 1244–1249. 2004.
2. Alexander, R. Wayne, “Hypertension and the Pathogenesis of Atherosclerosis Oxidative Stress and the Mediation of Arterial Inflammatory Response: A New Perspective,” Division of Cardiology, Emory University School of Medicine, Atlanta, GA.

HIGHLY SENSITIVE CONTINUOUS FLOW MICROFLUIDIC CHIP SENSOR WITH INTEGRATED BI/SB THERMOPILE FOR BIOCHEMICAL APPLICATIONS

Varun Kopparchy^{1,2}, Joshna Nimmala^{1,2}, Eric. J. Guilbeau^{1,2}

¹ Center for Biomedical Engineering and Rehabilitation Science,

² Institute for Micromanufacturing, Louisiana Tech University, Ruston, LA, 71272.

ABSTRACT

Chip calorimetry offers a power tool for fast and high throughput analysis of biochemical process. However, it is challenging to realize an inexpensive, easy to fabricate microfluidic chip based calorimeter with high sensitivity. This study describes the design of a novel, highly sensitive, continuous flow microfluidic chip sensor with an integrated Sb-Bi thin-film thermopile heat detection element. The geometry and the design of the microfluidic device facilitate hydrodynamic flow focusing, and the integration and design of the thermopile sensor into the microfluidic device eliminates the need for reference temperature control. The microfluidic device is fabricated using an inexpensive fabrication method, Xurography. The device contains a single flow channel that is 120 μm high and 10 mm wide with two fluid inlets and one fluid outlet. An Sb-Bi thin film thermopile is fabricated on the inner surface of the bottom channel wall using thermal evaporation and was passivated with a 3 μm SU-8 photoresist layer. The device has been successfully used to measure the dynamic temperature changes resulting from heat generation following the mixing of glycerol and water. The effect of flow rates on the sensor's response was measured. The sensor was capable of detecting dynamic temperature changes in the order of 10^{-6} K. The limit of detection of heat power of the device was calculated to be 8.8 pW. With the obtained remarkable sensitivity and heat power detection limit, the microfluidic chip sensor can be used to investigate biochemical processes such as enzyme-catalyzed reactions, and metabolic activity of cells.

Keywords: Thermoelectric, Thermopile, Glycerol, Microfluidic, Biochemical sensor, Calorimetry.

INTRODUCTION

Measuring biochemical process has showed increasing importance with the development of chip calorimeters [1]. Chip calorimetry is generally achieved by integrating the calorimetric detection using sensors such as thermistors and thermopiles with the micro flow channels for sample handling. Several groups have shown the advantages of chip calorimeters for the analysis of biochemical process [2], [3]. Often, chip calorimeters are realized using MEMS fabrication to achieve high heat power sensitivities. MEMS techniques are highly complex, time consuming, expensive and require sophisticated equipment. To monitor biochemical process such as metabolic activity of cells and binding event measurements of bio molecules, the heat power sensitivities of the chip calorimeters must be in the range of nW to pW [4]–[6]. Rapid prototyping has shown great promise in realizing inexpensive and easy to fabricate fluidic chips with micrometer features enabling lab-on-chip analysis [7]. Thermopile sensors generally used in chip calorimeters need extreme reference temperature control. Common mode rejection of thermal signals by the thermopile sensors was explored recently by a few groups [8], [9] and in our earlier work [10] to eliminate the need for reference temperature control. In this study, we fabricated a microfluidic chip sensor by integrated a thin film thermopile sensor on to a microfluidic device fabricated using rapid prototyping technique.

METHODS

Fabrication of thin film thermopile

Thin film thermopile with antimony (Sb) and bismuth (Bi) metals (Sigma Aldrich) was fabricated using thermal evaporation technique. Complementary metal shadow masks (Towne Technologies) were used to fabricate the thermopile structure. First, a Bi layer of thickness 0.8 μm with a mask pattern is deposited and a complementary pattern is aligned and then a Sb layer of thickness 1.2 μm is deposited on a glass coverslip of thickness 170 μm (Electron microscopy sciences). Second, a metal mask with a pattern for the connector leads is also fabricated on the same coverslip by depositing 1.2 μm Sb layer. Thermopiles were also fabricated on 100 μm thick Kapton® sheet (Kapton.com). This fabrication procedure described in detail in ref [10]. The fabricated thermopiles typically have a resistance of 20 K Ω and showed a Seebeck coefficient of 7.14 μV (mK)⁻¹.

Microfluidic chip sensor (MCS) fabrication

A microfluidic chip sensor (MCS) is fabricated by integrating the thermopile on the glass coverslip as the channel wall of the microfluidic device. Inlet holes (Inlet 1 and Inlet 2) and an outlet hole are drilled onto the microscope glass slide along the length. The microfluidic device is fabricated using an inexpensive rapid prototyping technique called Xurography. A dual side adhesive tape (kapton.com) is cut to form the channel and is sandwiched between a microscope glass slide and a glass coverslip (thermal conductivity, $k=1.05 \text{ W (m.K)}^{-1}$) with the fabricated thermopile. Two configurations of the microfluidic chip sensors (MCS-1, MCS-2) were fabricated, tested and evaluated. MCS-1 was fabricated by sandwiching the dual side adhesive tape between the microscope glass slide and the glass coverslip. A thermopile sensor is attached to the coverslip using superglue, and the thermopile is facing outside the channel (Fig. 1A). Attaching a $25 \mu\text{m}$ thick tape passivates thermopile facing outside the channel. MCS-2 is fabricated by sandwiching a dual side adhesive tape with the glass coverslip with thermopiles, which is coated with a $3\text{-}\mu\text{m}$ thick SU-8 (Microchem) photoresist layer and the microscope glass slide. The thermopiles in the MCS-2 configuration are facing inside the microfluidic channel and the SU-8 (thermal conductivity, $k=0.2 \text{ W (m.K)}^{-1}$) layer passivates the thermopiles (Fig. 1B). MCS-2 fabrication was an improvement to the fabricated MCS-1.

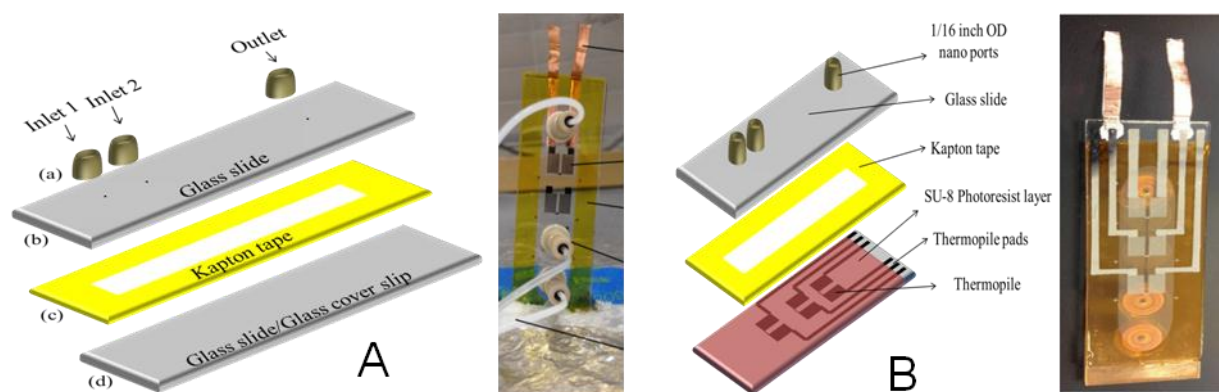


Figure 1: A) MCS-1 configuration showing the fabrication of microfluidic device with thermopiles outside the fluidic channel. B) Schematic of the MCS-2 configuration with a SU-8 passivation later on thermopiles facing inside of the channel. Pictures next to the schematics in A and B are the fabricated MCS configurations. The microfluidic channel dimensions are $60 \text{ mm} \times 12 \text{ mm} \times 0.1 \text{ mm}$ and the channel volume is $86.4 \mu\text{l}$.

Experimental procedure

The experimental setup used for this study consists of syringe pumps, which continuously flow water into the inlets of the MCS. An injection valve is used to inject the sample into the inlet 2 flow for generating a chemical reaction. The inlet 2 flow is hydro-dynamically focused into the MCS. The reaction is generated over the measuring junctions of the thermopile, which generates a proportional voltage. This voltage is detected by a nano-voltmeter (Agilent 34420A) and is recorded in a computer. A $13 \mu\text{l}$ sample volume injected into the flow is injected using the sample injection valve. To demonstrate the operation of the MCS, the exothermic nature of glycerol water mixing reaction is utilized.

RESULTS

MCS-1 response to glycerol-water mixing

The fabricated MCS-1 was connected to the experimental setup and varying concentrations of glycerol were injected to measure the response of the thermopile. Flow rates of $100 \mu\text{l min}^{-1}$ and $25 \mu\text{l min}^{-1}$ were used to continuously inject the water in inlet 1 and 2 respectively. Once the sample was injected into the inlet 2 flow stream, the sample traveled to the microfluidic device and was hydrodynamically focused over the measuring junctions of the thermopile. The glycerol sample mixed with the water flowing from inlet 1 at the interface and generated heat. As the sample passed over the measuring junctions of the thermopile, the voltage increased and then returned to its baseline once the sample flowed past the thermopile. Fig. 2 shows the typical response of the thermopile for 10 % (V/V) glycerol. The magnitude of the signal represents the total temperature change detected by the thermopile, and

the area under the curve (AUC) represents the total heat detected by the thermopile.

MCS-2 response to glycerol-water mixing

The MCS-2 device fabricated with thermopiles passivized with a 3 μm layer of photoresist facing inside the microfluidic channel was also tested for glycerol-water mixing reaction. Varying concentrations of glycerol were injected into the MCS-2 and the response of the thermopile was recorded. Fig. 3 compares the response of MCS-1 and MCS-2 for 10% V/V glycerol. Flow rate dependency of the MCS-2 sensor was also investigated for flow rates of 100 $\mu\text{l min}^{-1}$ and 25 $\mu\text{l min}^{-1}$, and 50 $\mu\text{l min}^{-1}$ and 25 $\mu\text{l min}^{-1}$ inlet 1 and inlet 2 respectively (Fig. 4). The sensitivity of the sensors (in terms of AUC) MCS-1 and MCS-2 were evaluated and plotted in Fig. 5. MCS-2 showed 3.5-fold increase in sensitivity compared to MCS-1.

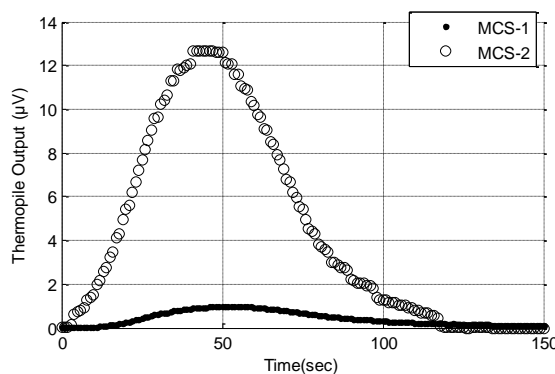
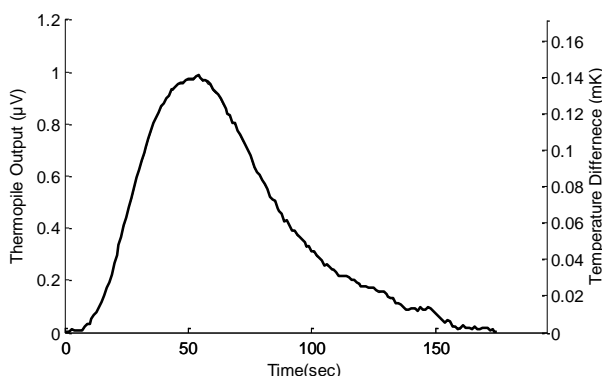


Figure 2: Response of the MCS-1 for 10% (V/V) glycerol.

Figure 3: Peak height comparison of MCS-1 and MCS-2 for 10% (V/V) glycerol.

DISCUSSION

Both MCS-1 and MCS-2 showed responses for the exothermic reaction of glycerol-water mixing. The heat power sensitivity of the fabricated thermopile was characterized in our earlier paper as 0.045 V W^{-1} . The lowest concentration of glycerol injected was 0.1% V/V, for which a voltage of 400 nV response was recorded by MCS-2. MCS-1 measured no voltage for 0.1% (V/V) glycerol concentration, because of the high thermal resistance for heat transfer to the thermopile. Considering the Seebeck coefficient of the thermopile, 400 nV corresponds to a detected temperature of $57.2 \mu\text{C}$. Similarly, considering the heat power sensitivity of the thermopile, the lowest heat power detected by the thermopile was calculated to be $\sim 8.8 \text{ pW}$. MCS-2 showed better sensitivity compared to MCS-1, due to the thermal resistance in the heat transfer region for MCS-1 is higher compared to MCS-2. The total thermal resistance in the MCS-1 is due to the thermal resistance of the glass coverslip, which is 6.07 KW^{-1} , and the total thermal resistance in the MCS-2 only the 3 μm thick SU-8 layer which is 0.833 KW^{-1} .

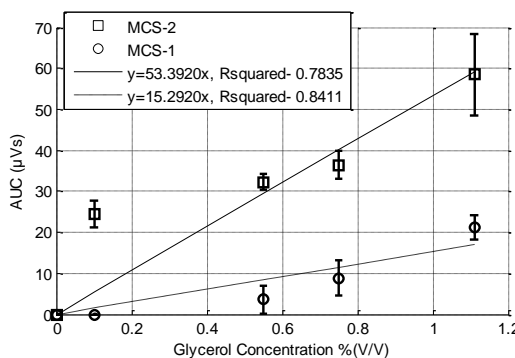
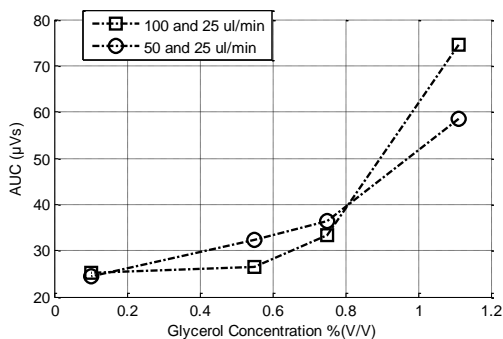


Figure 4: Effect of flow rate on MCS-2 response for varying concentrations of glycerol.

Figure 5: Sensitivity of the MCS-1 and MCS-2 configurations for varying concentrations of glycerol. Error bars represent the standard error when $n=3$.

CONCLUSIONS

A thermoelectric microfluidic chip sensor was developed to measure dynamic temperature changes in the order of 10^{-6} K. High sensitivity was obtained by an inexpensive and easy to fabricate MCS without any extreme measures and complex procedures to control reference temperatures. Two configurations of the sensors were fabricated and tested MCS-1 and MCS-2. An improved sensor with low thermal resistance (MCS-2) showed a low heat power detection of 8.8 pW. The sensitivity obtained with the simple to fabricate MCS is suitable for monitoring bioprocesses such as cell metabolism, enzymatic reactions, and binding event measurements.

ACKNOWLEDGEMENTS

The authors would like to thank the Institute for Micromanufacturing at Louisiana Tech University for their support.

REFERENCES

- [1] W. Lee, "Development and applications of chip calorimeters as novel biosensors," *Nanobiosensors Dis. Diagnosis*, p. 17, Apr. 2012.
- [2] Y. Zhang and S. Tadigadapa, "Calorimetric biosensors with integrated microfluidic channels," *Biosens. Bioelectron.*, vol. 19, no. 12, pp. 1733–1743, 2004.
- [3] W. Lee, W. Fon, B. W. Axelrod, and M. L. Roukes, "High-sensitivity microfluidic calorimeters for biological and chemical applications," *Proc. Natl. Acad. Sci.*, vol. 106, no. 36, pp. 15225–15230, Sep. 2009.
- [4] J. Lerchner, A. Wolf, F. Buchholz, F. Mertens, T. R. Neu, H. Harms, and T. Maskow, "Miniaturized calorimetry — A new method for real-time biofilm activity analysis," *J. Microbiol. Methods*, vol. 74, no. 2–3, pp. 74–81, 2008.
- [5] E. A. Johannessen, J. M. R. Weaver, P. H. Cobbold, and J. M. Cooper, "A suspended membrane nanocalorimeter for ultralow volume bioanalysis," *NanoBioscience, IEEE Trans.*, vol. 1, no. 1, pp. 29–36, 2002.
- [6] K. Verhaegen, K. Baert, J. Simaels, and W. Van Driessche, "A high-throughput silicon microphysiometer," *Sensors Actuators A Phys.*, vol. 82, no. 1–3, pp. 186–190, 2000.
- [7] D. A. Bartholomeusz, R. W. Boutté, and J. D. Andrade, "Xurography: rapid prototyping of microstructures using a cutting plotter," *Microelectromechanical Syst. J.*, vol. 14, no. 6, pp. 1364–1374, 2005.
- [8] S.-I. Yoon, S.-C. Park, and Y.-J. Kim, "A micromachined microcalorimeter with split-flow microchannel for biochemical sensing applications," *Sensors Actuators B Chem.*, vol. 134, no. 1, pp. 158–165, 2008.
- [9] B. S. Kwak, B. S. Kim, H. H. Cho, J. S. Park, and H. I. Jung, "Dual thermopile integrated microfluidic calorimeter for biochemical thermodynamics," *Microfluid. Nanofluidics*, vol. 5, no. 2, pp. 255–262, 2008.
- [10] V. L. Kopparchy, S. M. Tangutooru, G. G. Nestorova, and E. J. Guilbeau, "Thermoelectric microfluidic sensor for bio-chemical applications," *Sensors Actuators B Chem.*, vol. 166–167, no. 0, pp. 608–615, May 2012.

INTELLIGENT MEDICATION DISPENSER

M. H. Mohammed, W. M. Ahmedhassan, K. S. Ali, G. Skelton, E. Hamadain

Jackson State University,
Computer Engineering Department,
Department of Diagnostic and Clinical Health Sciences,
University of Mississippi Medical Center, Jackson, MS

ABSTRACT

This paper describes a system that utilizes smart devices to alert the user when medications (Pills or Tablets) are not taken on time. The system comprises a multi compartment box in which medications are stored. Each compartment houses the medications to be taken at a particular time. All compartments are equipped with a transmitter detector pair that can detect the existence of medication in that compartment. A microcontroller system attached to the compartment box checks for the existence of medications at the dosage programmed time and at subsequent user determined intervals. This microcontroller communicates via WiFi or Bluetooth with a smart device application. The smart device application will then alert the user if medication is not taken on time. This alert can be done through SMS, Voice or any variety of other alarm stimuli. The system will also alert the user to refill compartments at the end of the week. The system can also be connected to the user's pharmacy system to request refills at the appropriate time. All system's records are stored and made accessible to the user to share with his or her health providers. It is anticipated that this system will improve compliance with medication orders as well as allow the health providers track such compliance.

INTRODUCTION

The idea of this project is to alert the user when it is time to take his/her medications. This can be done through the user's smart device or home computer. By adding a light emitter and detector to a pill box, the system can then identify if pills were taken or if they are still in the box. The system will then send an appropriate notification to the user.

As shown in Figure 1. the pill box is modified to ensure that any pill can be detected. This was accomplished by making the bottom of each compartment concave with the detector at the center. This will ensure that any pill will immediately cover the detector.

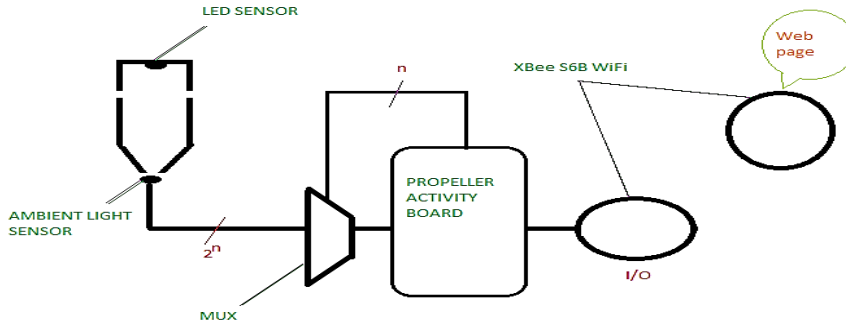
Communication between the pill box and the server (home computer) can be accomplished through any of several techniques such as Bluetooth, 802.11. However, due to the availability of components XBee radio was used.

System's Operation.

The components used in this system are:

- Pill box.
- Light Emitting Diodes.
- Propeller Activity Board.
- Ambient light sensors.
- XBee S6B WiFi.
- Xbee SIP Adapter.

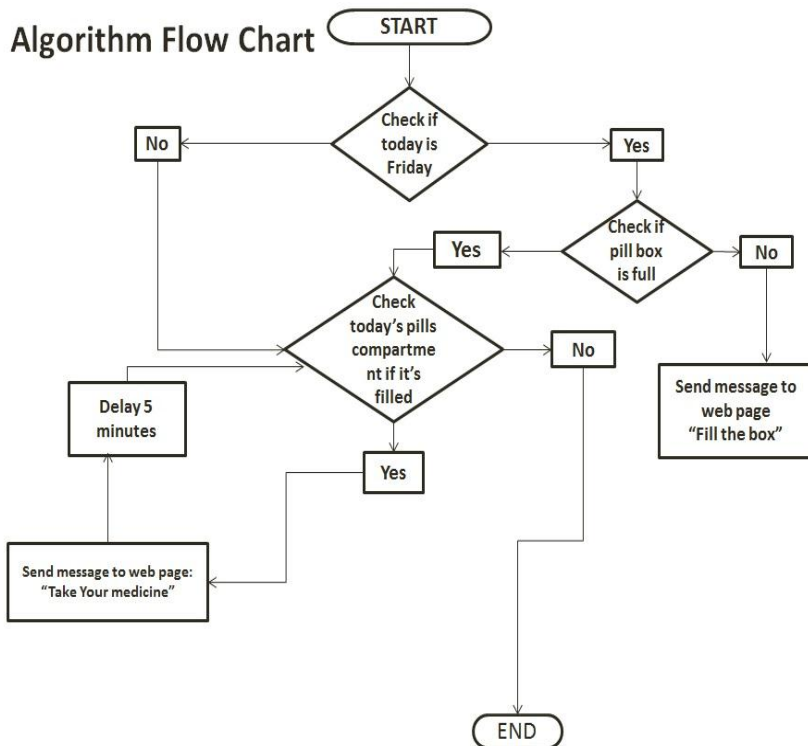
Hardware Flow Chart:-



The system operates by turning on the LEDs with a modulated signal, to ensure that ambient light may not interfere with the system's operation. Once lights are turned on, the appropriate day detector is then checked for the existence or lack thereof Pills.

At the end of the week, and at a day chosen by the user, the pill box will alert the user to re-stock the box with pills. From then and on, the box will check the appropriate day at the appropriate pill time and send out an alert if the pills are still in the box.

This data, when pills were taken, is also logged on the webpage to provide a record for the health providers on the level of medication compliance.



FLOW CHART:-

CONCLUSION

At a cost of less than \$100, a pill box can be made to alert the user of when to take medication and when to refill the pill box. The same system can be used to provide a record of medication compliance for health providers.

REFERENCES

- 1- Propeller Activity Board (#32910) data sheet : <http://www.adafruit.com/datasheets/32910-Propeller-Activity-Board-Guide-v1.0.pdf>
- 2- XBee and XBee-PRO ZB data sheet : http://www.vintagecomputercables.com/datasheet/ds_xbeezbmodules.pdf

Index of Authors

Adah, Felix	240, 267, 339	Grant, Joshua	343	Puckett, Aaron D.	182, 195, 353
Adah, Osasu	240	Grant, Samuel C.	314	Pyakurel, Ashmit	363
Adkinson, Joshua	221, 231	Greenwald, Neva	339	Rich, Thomas, C.	186, 191, 306, 310,
Agyepong, Kwabena	318	Gui, Jian-Wei	267	Roseburg, Jens T.	165, 314
Ahmedhassan, WM	391	Guilbeau, Eric J.	267	Russell, George	235
Alfatlawi, Mustaffa	371	Gupta, Kanika	359	Sarigul, Erol	318
Ali, KS	391	Gupta, Pravin	359	Sayner, SL	186
Alvarez, Diego	306	Hamadain, Elgenaid	249, 279, 339, 391	Scruggs, AK	186
Amruthwar, Shruti S.	199	Harpole, Jennifer L.	209, 293	Shemesh, Noam	314
Aneja, Arun	235	Hayes, Antonio V.	267	Silva, Susana F.	375
Annamdevula, Naga S.	310	Hester, Robert	235	Simpson, C. LaShan	170, 335, 343
Aslam, Dean	371	Horstemeyer, M.F.	162	Skeleton, G	391
Atigh, Marzieh, K	174	Huang, Min	267, 339	Slaughter, Janet	339
Bagwell, Jana	245	Humos, Ali Abu-El	322	Smith, Kristan	174
Baird, Michelle,	165	Huot, Angel	347	Smith, Weston	327,
Bauer, N	186	Iasemidis, Leonidas	221, 231	Spoonamore, Janet	158, 213
Bejarano, Fabian Calixto	165	Janorkar, Amol V.	178, 199, 283	Stokic, Dobrivoje S.	267
Benghuzzi, Hamed A.	182, 195, 209, 217, 225, 240, 245, 258, 267, 272, 279, 287, 293, 297, 302, 353	Jefferson, Gail D.	379	Stringfellow, Ashley	306
Bennett, Kevin A.	170	KamaKim, Hyunju	322	Summers, Richard L.	327
Bernardes, Rui	375	King, T.	367	Tardy, Felicia M.	217
Bishop, Charles E.	249	Kopparthy, Varun	387	Tomblyn, Seth	204
Black, David	272	Kuebler, Joy	339	Tucci, Michelle	182, 195, 209, 217, 225, 240, 245, 272, 279, 287, 293, 297, 302, 353
Britain, Andrea	310	Kumar, Santosh	359	Turner, Emily	204
Burnett, Luke	204	Laio, Jun	327,	Turner, Paul A.	283
Butler, Kenneth R.	182, 195, 353	Leavesley, Silas	191, 306, 310,375	Valachos, Ioannis	221, 231
Butler, Ryan	363	Lee, Nayeon	162	Vance, Stacy Hull	225
Cabrera, Sergio D.	351	Leftin, Avigdor	165	Vasquez, Erick S.	335
Cameron, Joseph A.	297	Liao, Jun	363	Verma, Ajay K	351
Carroll, Nicholas	332, 379	Liu, Boshen	235	Verma, Vikas	359
Chandrashekar, Vikasini	322	Liu, Howe	267	Walker, Clark	235
Claude, Andrew	363	Liu, Rui	221, 231	Walters, Keisha B.	335
Cooley, Jim	363	Ma, Teng	166	Wang, Cliff	158
Cunningham, Janice	335	Meyer, Robert	363	Wang, Jenny	158, 213
Davidson, Michael M.	165	Mittwede, Peter	235	Wang, Xuexiang	267
Domingues, Jose P.	375	Mohamed, Adel	297	Webb, Kristal J.	191
Dumez, Jean-Nicolas	314	Mohammed, MH	391	Weed, Benjamin C.	327
Elder, Steven	363, 367	Moore, La'Toya Richards	279	Weeks, C. Andrew	178
Farah, Ibrahim O.	252	Morgado, Antonio Miguel	375	Wilkins, Renee	287
Favreau, Peter	306	Mosher, Mark	363	Williams, Lakiesha N.	162
Frydman, Lucio	314	Nazeran, Homer	351	Wilson, Gerri	240, 272
Garner, Angie	302	Nimmala, Joshna	387	Xiang, Lusha	235
Ghonim, Elham	258	Parks, Alex	383	Yang, Edward	235
Gilbert, Eric	263	Patnaik, Sourav	327	Yazdani, Saami K	174, 204, 332, 347, 383
Gilbrech, Ryan	363	Pearson, Rebecca H.	267, 339		
Gottipati, Anuhya	363	Pei, Tzusheng	322		
Gould, Emily	379	Prabhat, Prashant	306		
		Prabhu, R	162		